Experimental study of nucleon resonance contributions to η-photoproduction on the neutron

Inauguraldissertation

zur

Erlangung der Würde eines Doktors der Philosophie
vorgelegt der
Philosophisch-Naturwissenschaftlichen Fakultät
der Universität Basel

von

Dominik Werthmüller

aus Utzenstorf, BE

Basel, 2014

Genehmigt von der Philosophisch-Naturwissenschaftlichen Fakultät auf Antrag von

Prof. Dr. B. Krusche
Prof. Dr. V. Metag

Basel, 26. März 2013

Prof. Dr. Jörg Schibler
Dekan

Abstract

Nucleon resonances play an important role in the process of understanding the low energy regime of the strong force. Quantum Chromodynamics (QCD), being the established theory for the description of this interaction, cannot be applied directly using perturbation theory, as the coupling constant is large at typical energies around 1 GeV. Therefore, effective models are used, which introduce higher lying degrees of freedom compared to the quarks and gluons of QCD, but on the other hand incorporate also certain features of the fundamental theory. Validation of these models needs experimental input that was obtained until twenty years ago mainly via πN scattering, in which a large number of nucleon resonances were identified. Unfortunately, most models predict an even higher number of states, leading to the problem of 'missing resonances'.

From the experimental side, the problem was approached by performing measurements of photoexcitation of nucleons. It was hoped that resonances coupling only weakly to πN could be identified by using this different formation channel. In the last years, a firm base of high precision data of meson photoproduction reactions was obtained at various facilities, such as MAMI, ELSA, ESRF and JLab.

The present work aims at contributing to the experimental base of photoproduction data by measuring unpolarized differential cross sections of the reaction $\gamma n \to \eta n$ with high precision. Several previous experiments observed an unusual structure in the total cross section around $W \sim 1680$ MeV. One of the various and heavily debated interpretations of this phenomenon is the existence of an exotic antidecuplet with $J^P = 1/2^+$ containing five quark states. As statistics of the previous measurements is moderate, especially for the angular distributions, a new precision measurement was urgently needed to shed more light on the issue.

The experiment for this work was performed at MAMI (Mainz, Germany) in December 2007, February 2009 and May 2009, resulting in 471 hours of data. A real photon beam was produced via tagged bremsstrahlung technique from the 1.5 GeV electron beam of MAMI-C. A liquid deuterium target was surrounded by an almost 4π-covering combined detector setup consisting of the Crystal Ball and the TAPS calorimeters. Discrimination of charged and neutral particles was performed by dedicated Veto detectors in both calorimeters. The η-mesons were

identified using the $\eta \to 2\gamma$ and the $\eta \to 3\pi^0$ decays. The reactions $\gamma p \to \eta p$ and $\gamma n \to \eta n$ were measured exclusively in quasi-free kinematics along with an inclusive measurement of $\gamma N \to \eta(N)$. In the analysis of the $\eta \to 2\gamma$ decay channel, 1.2×10^6 events with coincident protons and 4.5×10^5 events with coincident neutrons were reconstructed. The analysis of the $\eta \to 3\pi^0$ decay channel provided 6.3×10^5 events with coincident protons and 1.8×10^5 events with coincident neutrons.

Differential cross sections were calculated as a function of the center-of-mass energy $W = \sqrt{s}$ and $\cos(\theta^*_\eta)$ determined from the initial state. The resulting cross sections are affected by a loss of resolution due to the Fermi motion of the initial state nucleons. In addition, the center-of-mass energy was reconstructed from the final state using both a kinematic reconstruction and a time-of-flight measurement of the nucleons in forward direction. The corresponding cross sections are not affected by Fermi motion but only by the resolution of the applied W-reconstruction.

The consistency of the neutron measurement was verified by a comparison with the proton and the inclusive measurement. From the comparison of the quasi-free proton results to free proton measurements, it was found that nuclear effects play a minor role or are sufficiently under control in the quasi-free analysis. This justifies the interpretation of the extracted observables from the quasi-free neutron measurement as approximated observables of the free neutron.

The results of this work confirm the presence of a structure around a center-of-mass energy $W \sim 1670$ MeV in the total cross section of $\gamma n \to \eta n$ with unprecedented statistical evidence. The best overall estimate for the position is $W_R = (1670 \pm 5)$ MeV and an upper limit for the width of $\Gamma_R \leq (51 \pm 10)$ MeV was extracted. Taking into account the resolution of the kinematic W-reconstruction leads to an estimation of the intrinsic width of $\Gamma_R \approx (30 \pm 5)$ MeV. Assuming that the structure is caused by a single $J = 1/2$ state, the coupling strength is determined to be $\sqrt{b_\eta} A^n_{1/2} = (12.4 \pm 0.8)\, 10^{-3}\, \text{GeV}^{-1/2}$.

The differential cross sections obtained in this work show for the first time the angular dependence of the structure with high precision. This should allow more detailed studies in terms of partial-wave analyses that will hopefully yield in a better understanding of the phenomenon.

Contents

List of Figures

List of Tables

Chapter 1

Introduction

In this chapter a short introduction to the investigation of nucleon resonances will be given, to which this work contributes. After a general introduction in section 1.1, the formalism of photoproduction of pseudoscalar mesons will be presented in section 1.2. Particularities of η-photoproduction will be shown in section 1.3. In section 1.4 previous measurements of η-photoproduction on the neutron will be presented followed by a selection of theoretical interpretations in section 1.5. Finally, the motivation for this work will be given in section 1.6.

1.1 Nucleon resonances

The measurement of the magnetic moment of the proton performed in 1933 by Stern resulted in a value different from the theoretical prediction for point-like spin 1/2 particles of $\mu_p = e\hbar/2m_p$ [1]. This was the first hint that the proton is in fact not elementary but holds a substructure.

Later in the 1950s, electron scattering experiments by Hofstadter showed that the measured cross section could not be described by scattering off a point-like particle and a root-mean-square charge radius for the proton of $\sqrt{\langle r_p^2 \rangle} = 0.74$ fm was deduced [2].

In the meantime, Fermi performed scattering experiments on hydrogen using a beam of charged pions and obtained total cross sections that showed a steep rise at center-of-mass energies around $W = 1200$ MeV [3] (see figure 1.1). Such a behavior can be explained by a resonance phenomenon, i.e., the inner structure of the proton is excited to a state of higher energy. With the ratio of the cross sections of positively and negatively charged pions the isospin of the resonance was determined to be $I = 3/2$. This first excited state of the nucleon is called the Δ-resonance and is denoted as $P_{33}(1232)$ in the notation used in the spectroscopy of nucleon resonances:

$$L_{2I2J}(M)$$

with

L   angular momentum of decay into $N\pi$ with $S = 0, P = 1, D = 2, ...$
I   isospin of resonance
J   spin of resonance
M   mass of resonance

In the following forty years a plethora of excited states was identified in scattering experiments using beams of charged pions and kaons, protons, deuterons and α-particles. Compared to atomic spectroscopy, the experimental exploration of the nucleon spectrum is complicated by the fact that the states are massively overlapping due to the small spacings and the large widths. The latter is due to the large coupling of the strong interaction, which leads also to problems in the theoretical understanding of the spectrum. Namely, the fundamental theory of the strong force, Quantum Chromodynamics (QCD), cannot be applied using perturbative methods, because the strong coupling constant α_s is not $\ll 1$ in the energy range of the nucleon resonances. This means that effective theories have to be constructed to model the excitation spectrum as, e.g., constituent quark models, in which three equivalent valence quarks are confined in an effective potential. The degrees of freedom are thus not current quarks and gluons, as in QCD, but less fundamental objects.

Presumably, the main new contributions in the future will come from lattice QCD calculations. This method discretizes the QCD Lagrangian in a space-time lattice with spacing a and evaluates it numerically. Physical results are then
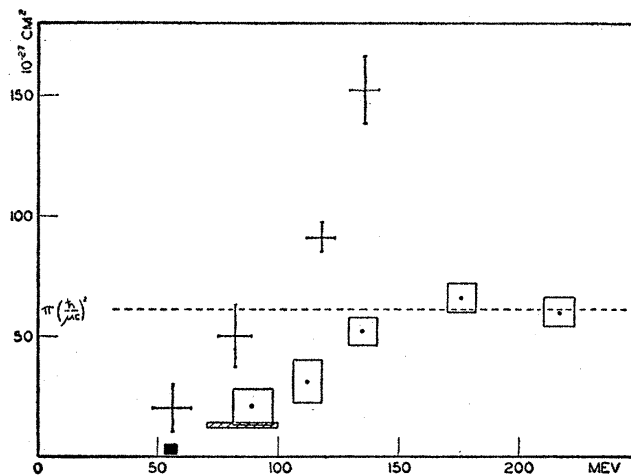
Fig. 1.1: Total cross sections of charged pion scattering in hydrogen as a function of the pion energy: Crosses: π^+p. Boxes: π^-p. Taken from [3].

obtained by extrapolation to the continuum $a \to 0$. Recent calculations of the nucleon excitation spectrum [4] reproduce the states that are also obtained by the nonrelativistic constituent quark model. Because computational power grows constantly and rapidly, effects caused by the numerical evaluation will become less important in the future and thus the extraction of precise results should be possible.

Constituent quarks models can describe many of the properties of the lowest lying baryon states, especially when QCD-inspired features are incorporated into the model for the calculation of the dynamics [5, 6]. On the other hand, these models predict excited states that were not observed experimentally so far. This could be due to the fact that the number of degrees of freedom is too high in the models. Reducing this number by, e.g., assuming quark-diquark structures, reduces the number of states but even in such reduced models more states than observed are predicted.

This problem, referred to as the problem of 'missing resonances', could also be due to reasons on the experimental side of view. Namely, around twenty years ago, most experimental data of nucleon states were deduced from measurements using long-lived mesons beams, as mentioned above. Thereby, signatures of resonances coupling only weakly to the corresponding formation channels are hardly seen in the scattering cross sections. To circumvent this bias, large efforts were made in the 1990s to build up experiments for the photoexcitation of nucleons, looking for resonances that couple stronger to γN than πN. Due to challenges in the realization of high energetic and high intensity beams of real photons, this was not possible at earlier times.

Photoproduction of mesons gives access to the electromagnetic transition amplitudes of the resonances, which is an additional important ingredient for the investigation of the resonances. Compared to meson-induced reactions, there are some drawbacks that have to be taken into account. First, the scattering cross sections are much smaller in the electromagnetic interaction. Secondly, there are notable background terms that contribute along with the resonance excitation to the cross sections. Isolating the resonance contributions relies therefore on reaction models, which introduce model-dependencies in the analysis.

In the last twenty years, photoproduction experiments at JLab, MIT-Bates, LEGS, SPring-8, MAMI, ELSA, and ESRF have substantially improved the knowledge of nucleon resonance parameters. Either evidence for unknown resonances was found or the properties of already known resonances could be extracted more precisely from the photoproduction data. An overview of the current status concerning the N-resonances with $I = 1/2$ is given in table 1.1. The table of the Δ-states ($I = 3/2$) is omitted because they cannot be subject of this work, as will be explained in section 1.3. The star-rating system used by the Particle Data Group (PDG) is used to mark how well the existence of the states is supported

					Status as seen in —						
Particle	J^P	Status overall	πN	γN	$N\eta$	$N\sigma$	$N\omega$	ΛK	ΣK	$N\rho$	$\Delta\pi$
N	$1/2^+$	****									
$N(1440)$	$1/2^+$	****	****	****		***				*	***
$N(1520)$	$3/2^-$	****	****	****	***					***	***
$N(1535)$	$1/2^-$	****	****	****	****					**	*
$N(1650)$	$1/2^-$	****	****	***	***			***	**	**	***
$N(1675)$	$5/2^-$	****	****	***	*			*		*	***
$N(1680)$	$5/2^+$	****	****	****	*	**				***	***
$N(1685)$	$?^?$	* ←									
$N(1700)$	$3/2^-$	***	***	**	*			*	*	*	***
$N(1710)$	$1/2^+$	***	***	***	***		**	***	**	*	**
$N(1720)$	$3/2^+$	****	****	***	***			**	**	**	*
$N(1860)$	$5/2^+$	**	**							*	*
$N(1875)$	$3/2^-$	***	*	***			**	***	**		***
$N(1880)$	$1/2^+$	**	*	*		**		*			
$N(1895)$	$1/2^-$	**	*	**	**			**	*		
$N(1900)$	$3/2^+$	***	**	***	**		**	***	**	*	**
$N(1990)$	$7/2^+$	**	**	**				*			
$N(2000)$	$5/2^+$	**	*	**	**			**	*	**	
$N(2040)$	$3/2^+$	*									
$N(2060)$	$5/2^-$	**	**	**	*				**		
$N(2100)$	$1/2^+$	*									
$N(2150)$	$3/2^-$	**	**	**				**			**
$N(2190)$	$7/2^-$	****	****	***			*	**		*	
$N(2220)$	$9/2^+$	****	****								
$N(2250)$	$9/2^-$	****	****								
$N(2600)$	$11/2^-$	***	***								
$N(2700)$	$13/2^+$	**	**								

****	Existence is certain, and properties are at least fairly well explored.
***	Existence is very likely but further confirmation of quantum numbers and branching fractions is required.
**	Evidence of existence is only fair.
*	Evidence of existence is poor.

Tab. 1.1: Status of the $N(I = 1/2)$ nucleon resonances: The red arrow denotes the speculative $N(1685)$ state for which the base of experimental evidence should be augmented with this work. Taken from [7].

by the data [7]. According to the PDG, well established states with a three- or four-stars rating have to be confirmed by independent analyses using complete information, i.e., the minimum number of required observables for the description of the formation channel (see next section). In addition, these resonances have to be seen in one of their strongest decay modes.

Several experiments (see section 1.4) collected evidence for a new state denoted as $N(1685)$, which is marked by the red arrow in table 1.1. The major goal of this work is to augment the base of experimental evidence for this state, as further discussed in section 1.6.

1.2 Formalism of pseudoscalar meson photoproduction

In scattering theory [8] the transition of an initial state $|i\rangle$ into a final state $|f\rangle$ can be described by the scattering matrix S, which represents the probability P that $|i\rangle$ goes to $|f\rangle$ via

$$P(|i\rangle \rightarrow |f\rangle) = |\langle f|S|i\rangle|^2. \tag{1.1}$$

For the process of photoproduction of a pseudoscalar meson m on a nucleon N

$$\gamma + N \rightarrow m + N' \tag{1.2}$$

with kinematics

$$p_\gamma + p_N = p_m + p_{N'} \tag{1.3}$$

the matrix elements S_{fi} can be written as

$$S_{fi} = \frac{1}{(2\pi)^2} \delta^4(p_{N'} + p_m - p_N - p_\gamma) \sqrt{\frac{M_N^2}{4E_{N'}E_m E_N E_\gamma}} \cdot i\mathcal{M}_{fi}, \tag{1.4}$$

where M_N is the nucleon mass and E_i, p_i are the total energies and four-momenta of the corresponding particles, respectively [9]. The different terms take into account the reaction phase space, four-momentum conservation and the interaction. $\mathcal{M}_{fi}$ are the Lorentz invariant matrix elements that describe the transition from initial to final state. They can be expanded in terms of Dirac spinors of the final and initial state nucleon as

$$i\mathcal{M}_{fi} = \bar{u}(p_{N'}, s_{N'}) \left[\sum_{j=1}^{4} A_j M_j\right] u(p_N, s_N), \tag{1.5}$$

where M_j are operators that depend on the four-momenta and the polarization vector of the photon, and contain the Dirac matrices. A_j are the invariant am-

plitudes, which incorporate the dynamics of the transition. The matrix elements $\mathcal{M}_{fi}$ can also be expressed using Pauli spinors χ, resulting in

$$\mathcal{M}_{fi} = \frac{4\pi W}{M_N} \langle \chi(N')|\mathcal{F}|\chi(N)\rangle, \tag{1.6}$$

with the center-of-mass energy W

$$W = \sqrt{s} = \sqrt{(p_\gamma + p_N)^2}, \tag{1.7}$$

and the 2×2 matrix $\mathcal{F}$

$$\begin{aligned} \mathcal{F} = {}& i\vec{\sigma} \cdot \vec{\epsilon}\,\mathcal{F}_1 + (\vec{\sigma} \cdot \hat{p}_m)(\vec{\sigma} \cdot (\hat{p}_\gamma \times \vec{\epsilon}))\,\mathcal{F}_2 \\ & + i(\vec{\sigma} \cdot \hat{p}_\gamma)(\hat{p}_m \cdot \vec{\epsilon})\,\mathcal{F}_3 + i(\vec{\sigma} \cdot \hat{p}_m)(\hat{p}_m \cdot \vec{\epsilon})\,\mathcal{F}_4\,, \end{aligned} \tag{1.8}$$

with the photon and meson unit vectors $\hat{p}_\gamma = \vec{p}_\gamma/|\vec{p}_\gamma|$ and $\hat{p}_m = \vec{p}_m/|\vec{p}_m|$, respectively. $\vec{\epsilon}$ is the polarization vector of the photon and $\vec{\sigma}$ is a vector containing the Pauli matrices. $\mathcal{F}_i$ are the CGLN amplitudes [10]. From the $2 \times 2 \times 2$ spin configurations of the reaction four are removed by parity conservation, which leads to four remaining complex amplitudes. They depend on the center-of-mass energy W and on the polar angle of the meson θ_m^* in the center-of-mass frame. In addition to the amplitudes shown above other amplitudes such as the helicity amplitudes H_i or the transversity amplitudes b_i can be constructed. Each set of amplitudes can be converted into an other one by linear relations. Depending on the observable, it is sometimes convenient to choose a different parametrization.

Knowing all four complex amplitudes $\mathcal{F}_i$ allows a model-independent description of the reaction. The determination of the number of required observables to be measured for a 'complete experiment' is nontrivial. Finally, it was shown that at least eight measurements of properly chosen observables are sufficient for an unambiguous determination of the amplitudes [11]. However, for the analysis of nucleon resonances, the amplitude analysis of such a set is not useful, because there is still an overall phase depending on W and θ_m^* that cannot be determined either by experiment or by model-independent theory [12]. The solution is to perform a truncated partial wave analysis on the observables themselves, where the overall unknown phase is only depending on W and can be constrained by theory without strong model dependence. A large number of measurements of different observables can then help to constrain solutions of the partial wave analysis. In addition to the cross section measurements, single and double polarization observables can be measured that relate the helicity of the photon and the spin of the initial and final state nucleon with each other in different combinations.

The unpolarized cross section in the center-of-mass frame can be written using the CGLN amplitudes as

$$
\begin{aligned}
\frac{p_\gamma^*}{p_m^*} \frac{d\sigma}{d\Omega} =\ & \left[|\mathcal{F}_1|^2 + |\mathcal{F}_2|^2 + \frac{1}{2}|\mathcal{F}_3|^2 + \frac{1}{2}|\mathcal{F}_4|^2 + \mathrm{Re}\left(\mathcal{F}_1 \mathcal{F}_3^*\right) \right] \\
& + \left[\mathrm{Re}\left(\mathcal{F}_3 \mathcal{F}_4^*\right) - 2\mathrm{Re}\left(\mathcal{F}_1 \mathcal{F}_2^*\right) \right] \cdot \cos(\theta_m^*) \\
& - \left[\frac{1}{2}|\mathcal{F}_3|^2 + \frac{1}{2}|\mathcal{F}_4|^2 + \mathrm{Re}\left(\mathcal{F}_1 \mathcal{F}_4^*\right) + \mathrm{Re}\left(\mathcal{F}_2 \mathcal{F}_3^*\right) \right] \cdot \cos^2(\theta_m^*) \\
& - \left[\mathrm{Re}\left(\mathcal{F}_3 \mathcal{F}_4^*\right) \right] \cdot \cos^3(\theta_m^*),
\end{aligned}
\tag{1.9}
$$

where '*' means evaluation in the center-of-mass frame for $p_\gamma^*, p_m^*, \theta_m^*$ and complex conjugate for the $\mathcal{F}_i^*$ [13].

The CGLN amplitudes can be expanded in terms of electric and magnetic multipoles via

$$
\begin{aligned}
\mathcal{F}_1(\theta_m^*) &= \sum_{l=0}^{\infty} \left[lM_{l+} + E_{l+} \right] P'_{l+1}(\cos(\theta_m^*)) + \left[(l+1)M_{l-} + E_{l-} \right] P'_{l-1}(\cos(\theta_m^*)), \\
\mathcal{F}_2(\theta_m^*) &= \sum_{l=0}^{\infty} \left[(l+1)M_{l+} + lM_{l-} \right] P'_l(\cos(\theta_m^*)), \\
\mathcal{F}_3(\theta_m^*) &= \sum_{l=0}^{\infty} \left[E_{l+} - M_{l+} \right] P''_{l+1}(\cos(\theta_m^*)) + \left[E_{l-} + M_{l-} \right] P''_{l-1}(\cos(\theta_m^*)), \\
\mathcal{F}_4(\theta_m^*) &= \sum_{l=0}^{\infty} \left[M_{l+} - E_{l+} - M_{l-} - E_{l-} \right] P''_l(\cos(\theta_m^*)),
\end{aligned}
\tag{1.10}
$$

where l denotes the relative orbital angular momentum of the final nucleon-meson system and P', P'' are derivates of the Legendre polynomials. The sign in the index of the electric and magnetic photon multipoles $E_{l\pm}$ and $M_{l\pm}$, respectively, indicates if the nucleon spin is added to or subtracted from l to obtain the total angular momentum in the intermediate state. From the initial state with total angular momenta of the photon L_γ and the nucleon $J_N = 1/2$, it follows for the intermediate state that

$$
\begin{aligned}
|L_\gamma - 1/2| \leq\ & J_{\mathrm{im}} \leq |L_\gamma + 1/2|, \tag{1.11} \\
& P_{\mathrm{im}} = P_\gamma \cdot P_N = P_\gamma, \tag{1.12}
\end{aligned}
$$

with the corresponding parities P_i. For the final state including a pseudoscalar meson ($S_m = 0$, $P_m = -1$) with relative angular momentum L_m, it must hold true that

$$
\begin{aligned}
|L_m - 1/2| \leq\ & J_{\mathrm{im}} \leq |L_m + 1/2|, \tag{1.13} \\
& P_{\mathrm{im}} = P_N \cdot P_m \cdot (-1)^{L_m} = (-1)^{L_m+1}, \tag{1.14}
\end{aligned}
$$

Photon M-pole	IS L_γ^P, J_γ^P	IMS $J_{\rm im}^P$	FS J_N^P, L_m^P	Multi-pole	$\dfrac{p_\gamma^*}{p_m^*}\dfrac{d\sigma}{d\Omega}$
E1	1^-, $1/2^+$	$1/2^-$	$1/2^+$, 0^-	E_{0+}	$\lvert E_{0+}\rvert^2$
		$3/2^-$	$1/2^+$, 2^-	E_{2-}	$1/2\,\lvert E_{2-}\rvert^2\,(5-3x^2)$
M1	1^+, $1/2^+$	$1/2^+$	$1/2^+$, 1^+	M_{1-}	$\lvert M_{1-}\rvert^2$
		$3/2^+$	$1/2^+$, 1^+	M_{1+}	$1/2\,\lvert M_{1+}\rvert^2\,(5-3x^2)$
E2	2^+, $1/2^+$	$3/2^+$	$1/2^+$, 1^+	E_{1+}	$9/2\,\lvert E_{1+}\rvert^2\,(1+x^2)$
		$5/2^+$	$1/2^+$, 3^+	E_{3-}	$9/2\,\lvert E_{3-}\rvert^2\,(1+6x^2-5x^4)$
M2	2^-, $1/2^+$	$3/2^-$	$1/2^+$, 2^-	M_{2-}	$9/2\,\lvert M_{2-}\rvert^2\,(1+x^2)$
		$5/2^-$	$1/2^+$, 2^-	M_{2+}	$9/2\,\lvert M_{2+}\rvert^2\,(1+6x^2-5x^4)$

Tab. 1.2: Lowest order multipole amplitudes for pseudoscalar photoproduction: abbreviations: initial state (IS), intermediate state (IMS), final state (FS). $x = \cos(\theta_m^*)$. [13].

which gives the following conditions for parity and angular momentum conservation:

$$P_\gamma = \quad P_{\rm im} \quad = (-1)^{L_m+1}\,, \tag{1.15}$$

$$L_\gamma \pm 1/2 = \quad J_{\rm im} \quad = L_m \pm 1/2\,, \tag{1.16}$$

with independent signs in equation 1.16. For magnetic ML-multipoles with parity $P_\gamma = (-1)^{L+1}$ this can only be fulfilled if

$$ML : L_\gamma = L_m\,. \tag{1.17}$$

Electric ML-multipoles with parity $P_\gamma = (-1)^L$ obey therefore

$$EL : L_\gamma = L_m \pm 1\,. \tag{1.18}$$

This leads to the fact that each intermediate state with $J_{\rm im} \neq 1/2$ can be excited by one electric and one magnetic multipole. For states with $J_{\rm im} = 1/2$ only one multipole is possible [13]. Table 1.2 shows an overview of the lowest order multipoles with the corresponding angular distributions of the cross sections. It can be seen that from the angular distribution alone, spin and parity of a possible resonance cannot be determined simultaneously, but polarization observables are needed to resolve these ambiguities.

1.3 η-photoproduction on protons and neutrons

Direct extraction of single nucleon resonance properties from the angular distributions of photoproduction cross sections, as discussed in the previous section, is only possible for rare special cases. In general, as the resonances are broad and overlapping, interferences can occur that affect the angular distributions. In case of the already mentioned $P_{33}(1232)$ resonance, the expected angular distribution of the M_{1+} multipole excitation is indeed observed in the $\pi^0 p$ final state, as the resonance is well separated from the higher lying states. But already the measurement of the $\pi^+ n$ isospin companion differs significantly from the expected distribution. This is due to another problem that complicates in general the extraction of resonance parameters from photoproduction data. Namely, contributions to the cross sections are not only made by resonant terms, but also nonresonant 'background' terms are present. The magnitude of the latter depends on the reaction channel. Going back to the example of the $P_{33}(1232)$, background contributions are significantly higher in the charged isospin channels of pion production than in the neutral one, which results in a distortion of the angular distributions. Hence, when extracting resonance properties from photoproduction data, reaction models, which take into account the background contributions, have to be used.

In the case of η-production, the leading contributions to the process are shown in figure 1.2. In addition to the resonant term in the s-channel, a resonant term in the u-channel and nonresonant Born terms in the s- and u-channels contribute as well. Moreover, the high energy photon can couple via vector meson exchange in the t-channel to the nucleon. A particularity in η-production is the fact that the sum of these background terms is small. According to the Eta-MAID model [14], Born terms and t-channel contributions are not negligible but compensate each other. Also, the ηNN coupling is small.

Because of the small background contributions, η-photoproduction is well suited for the study of nucleon resonances. Also, due to the isospin $I = 0$ of the η-meson, isospin conservation of the strong force prevents a Δ-state to decay into the ηN final state. Therefore, only N-states with $I = 1/2$ can contribute to η-photoproduction, which simplifies the interpretation of the data.
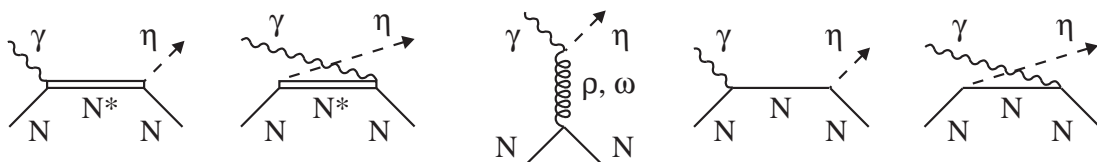
Fig. 1.2: Leading contributions to η-photoproduction: From left to right: resonant s- and u-channels, vector meson exchange in the t-channel, Born terms in the s- and u-channels. Taken from [13].

Measurements on the free proton were performed to a great extent in the past at different experimental facilities (see references in [15]). Near the threshold around $E_\gamma \sim 707$ MeV, the cross section is dominated by the excitation of the $S_{11}(1535)$ resonance. Because contributions of other resonances are small in that region and due to the other facts mentioned above, a similar situation as for the $P_{33}(1232)$ in π^0-production arises and resonance parameters could be directly extracted from the cross section. Nevertheless, very small contributions of the $D_{13}(1520)$, which interferes with the $S_{11}(1535)$, were identified as well. Going to higher energies, the cross section decreases due to a destructive interference with the $S_{11}(1650)$ resonance. For higher energies, the various models suggest different resonance contributions and the situation is less clear.

Measurements on the neutron are experimentally more challenging since there is no free neutron target. Therefore, light nuclei, such as the deuteron, ^{3}He or ^{4}He, have to be used to measure in quasi-free kinematics and nuclear effects have to be studied carefully in the analysis of the data. In addition, more reliable results can be obtained in exclusive measurements only, which require the detection of the recoil neutrons. The detection efficiency of neutrons is generally lower than for, e.g., protons so that the experimental setup needs to fulfill certain requirements.

The motivation for the first measurements of η-photoproduction on the neutron was the extraction of the isospin decomposition of the electromagnetic excitation of the $S_{11}(1535)$ resonance. Namely, as the isospin in the γNN^* vertex is not conserved, the amplitudes can be decomposed into an isoscalar A^{IS} ($\Delta I = 0$) and isovector A^{IV} and A^{V3} ($\Delta I = 0, \pm 1$, respectively) parts. For η-production ($\Delta I = 0$) this leads then to the following relations for the cross sections [13]:

$$\sigma_p \quad \sim \quad |A^{\text{IS}}_{1/2} + A^{\text{IV}}_{1/2}|^2 \tag{1.19}$$

$$\sigma_n \quad \sim \quad |A^{\text{IS}}_{1/2} - A^{\text{IV}}_{1/2}|^2 \tag{1.20}$$

With measurements of coherent η-production on the deuteron, where

$$\sigma_d \sim |A^{\text{IS}}_{1/2}|^2 \tag{1.21}$$

has to hold true and measurements on helium nuclei, it was found that the excitation of the $S_{11}(1535)$ is dominantly isovector and a ratio of $\sigma_n/\sigma_p \approx 2/3$ was extracted [16, 17]. This ratio is often used in this work to scale the neutron cross sections to the ones of the proton to obtain a normalization in the region dominated by the $S_{11}(1535)$. After that region, model predictions on σ_n/σ_p differ due to the contributions of different resonances. For example, the Eta-MAID model [14] predicts a strong rise of the ratio due to the $D_{15}(1675)$ resonance. This resonance cannot be excited from the proton in the quark model due the Moorehouse selection rules [18] and, therefore, very weak contribution to the cross section on

the proton is expected. On the other hand, the predicted branching ratio into the $N\eta$ channel disagreed significantly from the PDG values [7]. Experimental clarification on $\gamma n \to \eta n$ above $E_\gamma \sim 1$ GeV was needed and measurements at various facilities were performed. An overview of the results will be given in the next section.

1.4 Previous measurements of $\gamma n \to \eta n$

Previous measurements of η-photoproduction on the neutron were performed by GRAAL at the ESRF in Grenoble, at the LNS in Sendai and by CBELSA/TAPS in Bonn. In the following parts, the different experiments and their results will be discussed.

1.4.1 GRAAL

The GRAAL experiment [19, 20] was located at the ESRF in Grenoble. High energetic photons were produced by backscattering of laser light off the electrons in the storage ring. This technique allows the production of highly polarized photons. The energy of the photons was determined by measuring the deviation of the scattered electrons from the normal orbit. Maximum photon energies of 1.5 GeV could be reached. The liquid deuterium target was surrounded by an electromagnetic spectrometer made of 480 bismuth germanate (BGO) crystals with a thickness of 21 radiation lengths, detecting particles with polar angles between 25 and 155 degrees. Charged particle identification and discrimination from neutral particles was provided by a cylindrical barrel of plastic scintillators installed between the target and the calorimeter. In addition, two cylindrical multi-wire proportional chambers (MWPC) allowed a more precise tracking of charged particles. At forward angles below 25 degrees, two planar MWPC were installed for tracking of charged particles. Furthermore, a double layer plastic scintillator hodoscope could be used for tracking, identification and time-of-flight (TOF) measurements of charged particles. Finally, a lead-scintillator sandwich TOF shower detector was used for the detection of photons and the recoil protons/neutrons. This setup covered a solid angle of almost 4π.

Cross sections of $\gamma p \to \eta p$ and $\gamma n \to \eta n$ were simultaneously measured using a deuterium target in exclusive measurements, i.e., the recoil nucleons were detected [21]. The η-meson was identified via its $\eta \to 2\gamma$ decay and background was rejected by application of analysis cuts. The center-of-mass energy W was reconstructed either from the incoming photon and assuming the nucleon at rest or from the final state η-meson and the recoil nucleon. In case of the latter, the energy of the nucleons was determined in forward direction by a time-of-flight measurement and for nucleons in the BGO detector by kinematic constraints. This led to an overall
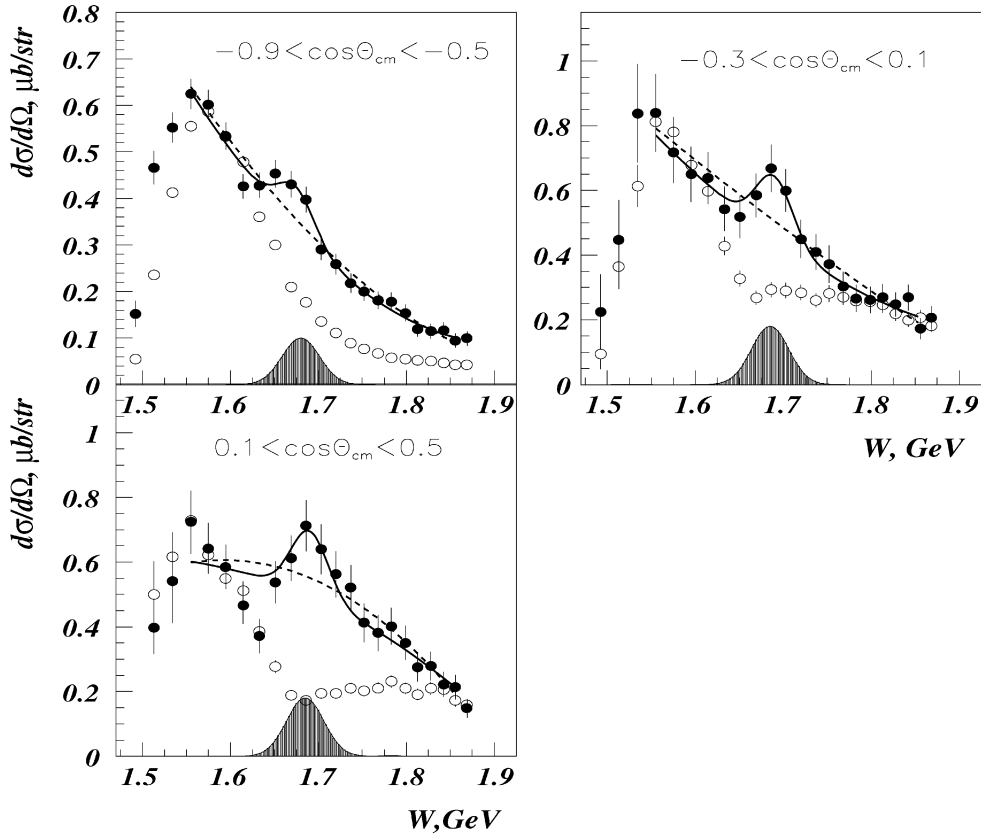
Fig. 1.3: GRAAL cross section results for quasi-free η-production on the neutron and proton: The shown cross sections were calculated from the initial state assuming the nucleon at rest. Filled circles: cross section of $\gamma n \to \eta n$. Open circles: cross section of $\gamma p \to \eta p$ normalized to neutron results in the maximum of the $S_{11}(1535)$ resonance. Curves: fits to data. Histograms: contributions of narrow resonance with $\Gamma = 10$ MeV. Taken from [21].

FWHM resolution in W of 40–60 MeV for both initial and final state reconstruction. In the first case, the finite resolution was due to the Fermi momentum of the nucleon and in the second case it was caused by detector resolution.

The results were published in 2007 by part of the GRAAL collaboration. Surprisingly, as shown in figure 1.3, they did not only show an increase in σ_n/σ_p, but revealed a narrow structure in the cross sections on the neutron around $W \sim 1.68$ GeV. On the proton, no structure of this kind was observed. It was argued that the structure may be caused by a very narrow resonance, as the width of the structure is despite the notable resolution caused by Fermi motion relatively narrow. This was illustrated by the simulated line shape of a resonance with a width of $\Gamma = 10$ MeV, which shows a similar width as the observed structure, when the latter was fitted with a polynomial of third order and a Breit-Wigner function.
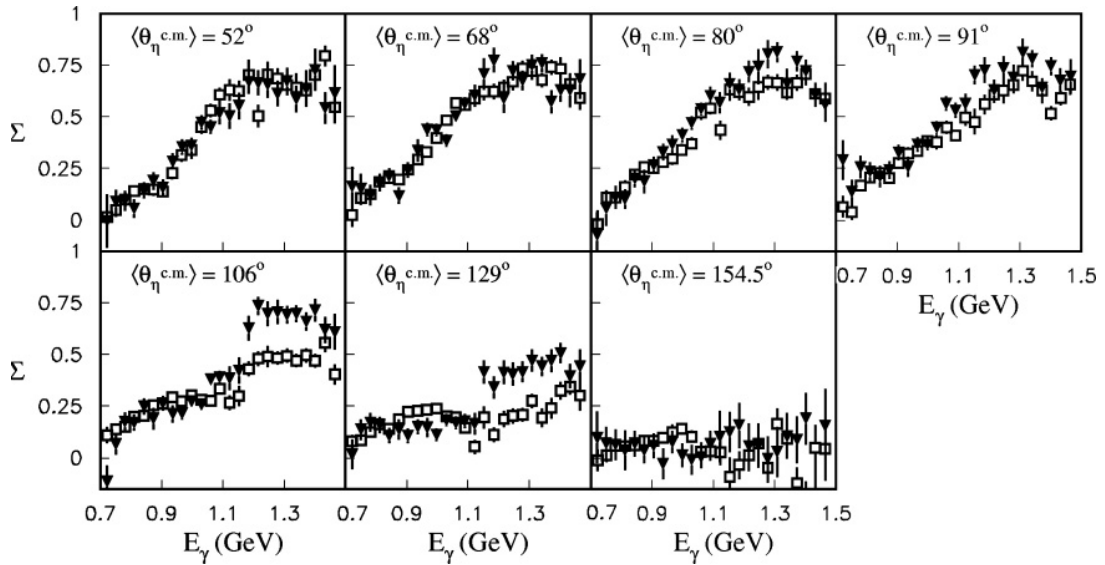
Fig. 1.4: GRAAL beam asymmetry results for quasi-free η-production on the neutron and proton: Full triangles: data of $\gamma n \to \eta n$. Open squares: data of $\gamma p \to \eta p$. Taken from [20].

In 2008, first measurements of the beam asymmetry Σ for η-photoproduction on the neutron were published by the GRAAL collaboration [20]. This polarization observable has other dependencies from the electromagnetic multipoles than the cross sections and can thus be more sensitive to contributions of certain resonances. The results are shown in figure 1.4 for different angular bins as a function of the photon beam energy. Up to $E_\gamma \sim 1.05$ GeV, the asymmetries are very similar for proton and neutron. For higher energies, the neutron asymmetries are higher, especially at backward angles. In the bins $\theta_\eta^* = 106°$ and $\theta_\eta^* = 129°$ an instant rise in the asymmetry can be seen, corresponding to $W \sim 1715$ MeV.

Finally in 2011, an other analysis of the GRAAL data was performed leading to results for Compton scattering off the neutron [22]. The analysis of this reaction is complicated by the fact that massive background from π^0-production contaminates the true signal, for which the cross section is orders of magnitudes lower. It was argued that this background could be successfully rejected and the results shown in figure 1.5 were extracted. Again, a narrow peak around $W \sim 1685$ MeV is visible in the excitation function obtained for the neutron. From a fit using a second order polynomial and a Gaussian function, the position of the peak was determined to $W = (1686 \pm 7_{\text{stat}} \pm 5_{\text{sys}})$ MeV and a width of $\Gamma \approx (28 \pm 12)$ MeV was estimated.
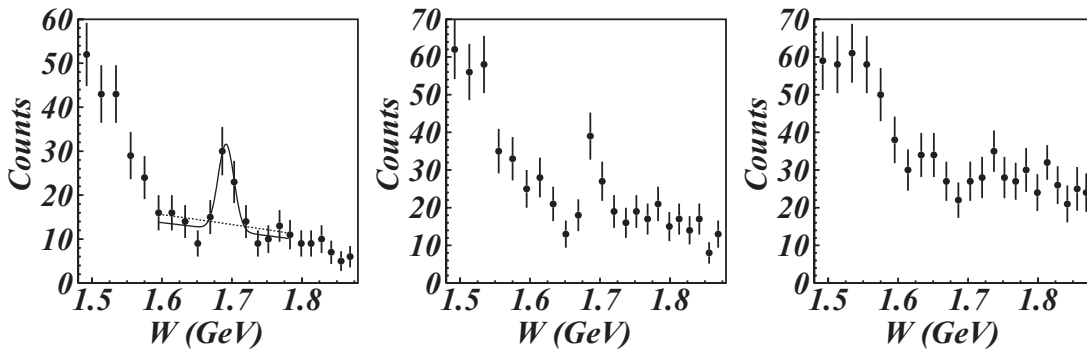
Fig. 1.5: GRAAL results for quasi-free Compton scattering off the neutron: From left to right: results of standard analysis, results with wider cut on missing energy, results of simulated data. Taken from [22].

1.4.2   LNS-Sendai

The setup for real photon physics at the LNS in Sendai was as follows [23]. Photons of energies from 580 to 1160 MeV were produced via bremsstrahlung off a thin carbon fiber installed in the electron stretcher-booster ring (STB). The photon energies were determined from the recoiling electrons detected in a tagger detector. Particles leaving the target were detected in 206 pure cesium iodide (CsI) crystals that were divided into four blocks. Two blocks with each 74 crystals of 30 cm length were installed in forward direction, covering polar angles from 15 to 72 degrees and azimuthal angles from -17 to 17 degrees. Two blocks of 29 crystals of 25 cm length placed backward covered polar angles from 95 to 125 degrees and azimuthal angles from -12 to 12 degrees. Plastic scintillators of 5 mm thickness were placed in front of the crystals for charged particle identification. They were used to discriminate charged particles, neutrons and photons and provided time-of-flight measurements.

In 2007, preliminary results of $\gamma n \to \eta n$, as shown in figure 1.6, were published [25]. First, cross sections were obtained for $\gamma N \to \eta(N)$ in an inclusive measurement using a deuterium target, where η-mesons were reconstructed from the $\eta \to 2\gamma$ decay. The proton contribution to the total cross section was estimated by folding the Eta-MAID [14] prediction with the Fermi momentum distribution inside the deuteron. Assuming $\sigma_{\mathrm{inc}} = \sigma_p + \sigma_n$, the cross section of the neutron was then obtained by subtracting the estimated proton contribution from the measured inclusive cross section. The shoulder already seen in the inclusive cross section around $E_\gamma \sim 1$ GeV becomes a clear structure in the neutron cross section. It was fitted with a smooth background function and a Breit-Wigner signal function and the position in the center-of-mass system was estimated to $W = (1666 \pm 5)$ MeV with a width of $\Gamma \leq 40$ MeV.
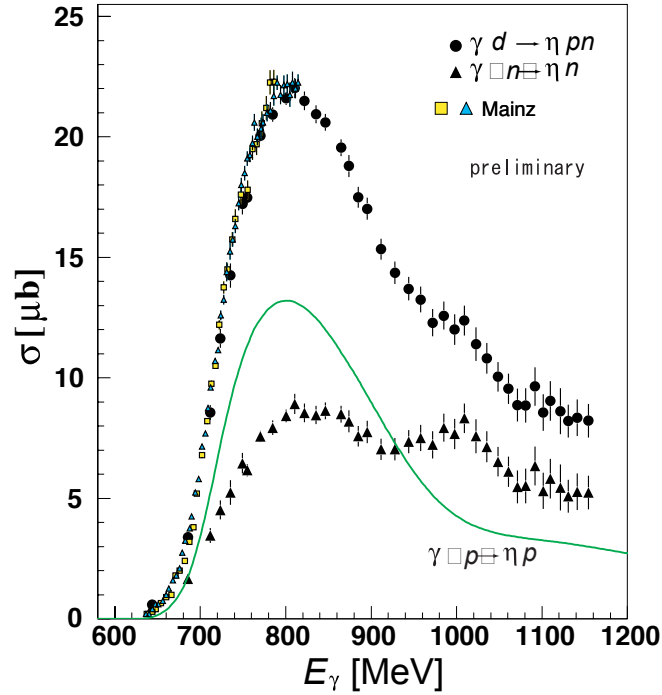
Fig. 1.6: LNS-Sendai cross section results for quasi-free η-production on the neutron obtained from an inclusive measurement of $\gamma N \to \eta(N)$: Black circles: data of $\gamma N \to \eta(N)$. Black triangles: data of $\gamma n \to \eta n$. Yellow squares: MAMI data from [17]. Blue triangles: MAMI data from [24]. Green curve: Eta-MAID [14] folded with Fermi motion. Taken from [25].

1.4.3 CBELSA/TAPS

The CBELSA/TAPS experiment is located at ELSA in Bonn. In this facility, the tagged bremsstrahlung technique is used to produce photons from an electron beam. Photon energies up to 2.5 GeV can be tagged. The setup, as described in the following, refers to the corresponding status used for the later presented results. The target was positioned inside the Crystal Barrel detector, which consists of 1290 thallium doped cesium iodide (CsI(Tl)) crystals of 16 radiation lengths thickness. This detector covers the full azimuthal angle and polar angles from 30 to 168 degrees. For particle identification a three layer scintillating fiber detector was surrounding the target that could be used to discriminate charged and neutral particles. The acceptance hole in forward direction was closed by the TAPS detector wall that was made of 528 barium fluoride (BaF$_2$) crystals of 12 radiation lengths thickness. Full azimuthal angle coverage was achieved for polar angles starting from 4.5 degrees. In front of every crystal a 5 mm thick plastic scintillator was installed for charged particle vetoing. Almost the complete solid angle could be covered by this combined setup.
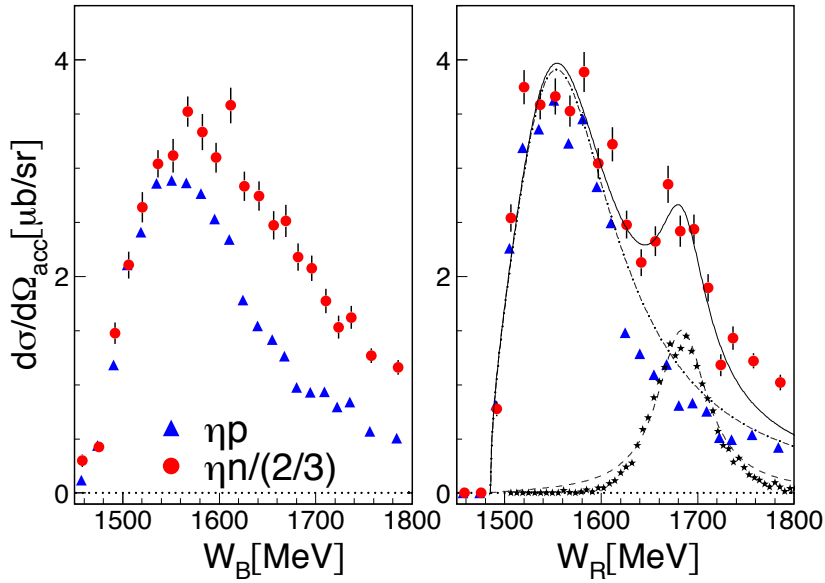
Fig. 1.7: CBELSA/TAPS cross sections for quasi-free η-production on the neutron for $\cos(\theta_\eta^*) < -0.1$: Left-hand side: W reconstructed from initial state assuming the nucleon at rest. Right-hand side: W reconstructed from final state using time-of-flight measurement. Blue triangles: data of $\gamma p \to \eta p$. Red circles: data of $\gamma n \to \eta n$ scaled by 3/2. Black stars: simulated resolution. Curves: fits to neutron data. Taken from [26].

In the measurements using a deuterium target, the η-mesons were identified by the $\eta \to 3\pi^0$ decay. Exclusive measurements were performed and results for the quasi-free proton and neutron were obtained simultaneously. For the first results [26], the center-of-mass energy W was calculated from the initial state, assuming the nucleon at rest, and from the final state by measuring the kinetic energy of the recoil nucleons with a time-of-flight measurement using TAPS. The latter led to the fact that the resulting cross sections were restricted to $\cos(\theta_\eta^*) < -0.1$ for kinematic reasons. As shown in figure 1.7, a slight shoulder can be seen in the cross section on the neutron calculated from the initial state, which is becoming a clear structure when effects from Fermi motion are removed by the W-reconstruction using TOF. The width of this structure, on the other hand, is dominated by the experimental resolution, denoted by the black stars. Using a combined fit of two Breit-Wigner functions, a position of $W = 1683$ MeV and a width of $\Gamma \approx (60 \pm 20)$ MeV was extracted.

It will be shown in section 4.5.1 that the center-of-mass energy W can be reconstructed from kinematics with good resolution. This technique was used in the further analysis of the CBELSA/TAPS data resulting in total and differential cross sections for the complete angular range [15]. The first ones are shown in figure 1.8. Good agreement between free proton and quasi-free proton results was found.
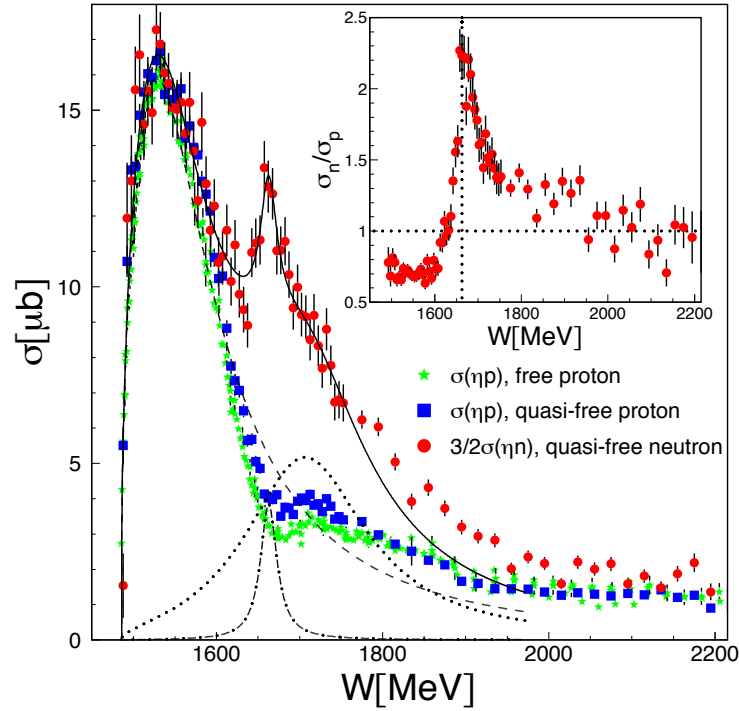
Fig. 1.8: CBELSA/TAPS total cross sections for quasi-free η-production on the neutron as a function of W_{kin}: Blue squares: data of $\gamma p \to \eta p$. Red circles: data of $\gamma n \to \eta n$ scaled by 3/2. Green stars: free proton data. Curves: fits to data. Taken from [15].

The peak in the neutron cross section is now even more clearly visible. Position and width were estimated from a combined fit of three Breit-Wigner functions to $W \approx 1670$ MeV and $\Gamma \approx 25$ MeV, whereas the latter is again comparable to the resolution of the W-reconstruction in the corresponding analysis.

For the theoretical interpretation, precise angular distributions are needed to check the quality of a model description. The differential cross sections obtained by CBELSA/TAPS are shown in figure 1.9. The statistical quality of the data allowed the creation of four bins in $\cos(\theta_\eta^*)$. The quasi-free proton distributions show again good agreement to the free proton data, which means that nuclear effects could be successfully removed by the analysis or play a minor role in case of a deuteron target. The neutron results show some major deviations from the selected model predictions. However, having only four data points in the whole angular range complicated the interpretation of the deviations, since also statistical and systematic errors have to be taken into account. In addition, fits to the angular distributions consisting of four points only can have at the most four free parameters. Therefore, it was desirable to increase the statistical quality, which finally led to the proposal for the current work (see section 1.6).
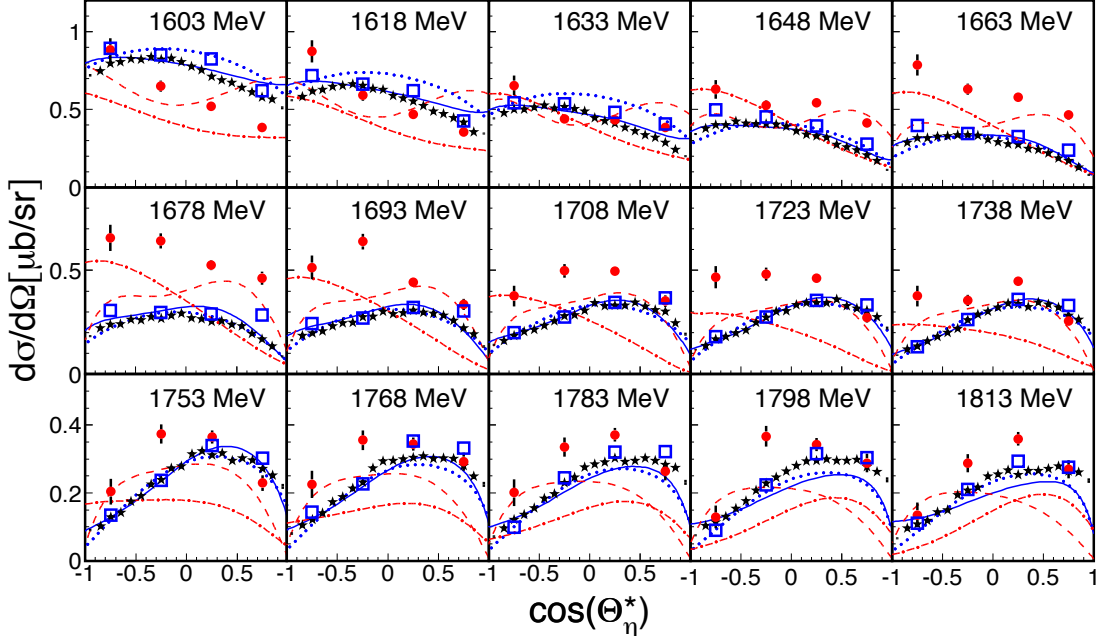
Fig. 1.9: CBELSA/TAPS differential cross sections for quasi-free η-production on the neutron as a function of W_{kin}: Blue squares: data of $\gamma p \to \eta p$. Red circles: data of $\gamma n \to \eta n$. Black stars: free proton data. Red curves: neutron model predictions. Blue curves: proton model predictions. Taken from [15].

1.5 Interpretations of previous measurements

In the following section, the interpretations of a selection of models are presented that aimed at giving an explanation for the phenomenon seen in η-photoproduction on the neutron using various theoretical approaches.

1.5.1 New narrow resonance

The chiral quark soliton model (χQSM) states that light baryons can be viewed as solitons of the pion (or chiral) field [28]. In the model, a space rotation of the field is equivalent to that in isospin space. This leads to the view that N- and Δ-states can be seen as different rotational states of the 'classical nucleon'. The model can be generalized to include hyperons with SU(3) flavor symmetry and the lowest lying states can then be identified with the $J^P = 1/2^+$ baryon octet and the $J^P = 3/2^+$ decuplet. Several characteristic properties of the multiplet members can be deduced from the model. Considering the next rotational excitation, the antidecuplet with $J^P = 1/2^+$ emerges. It contains some states with exotic quantum numbers, e.g., a member with strangeness $S = +1$ that cannot be explained in the quark model picture by three quarks. Instead, five quarks have to be assumed denoting the states as pentaquarks. They can also be seen as bound states of a
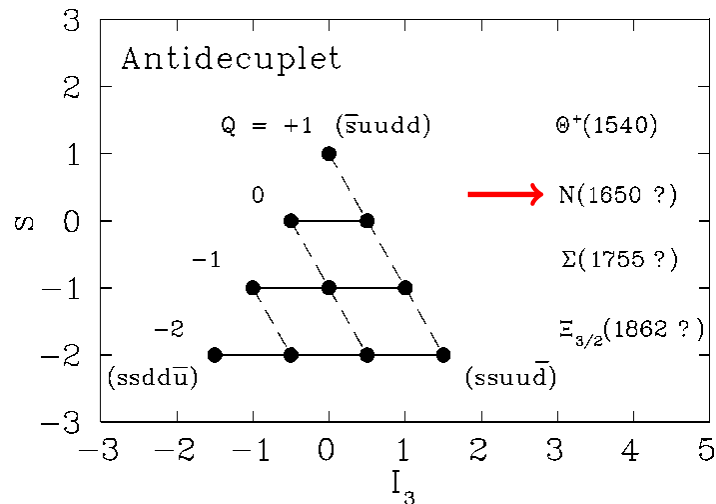
Fig. 1.10: Exotic antidecuplet of baryons with $J^P = 1/2^+$: The red arrow denotes the speculative $N(1685)$ state for which the base of experimental evidence should be augmented with this work. Taken from [27].

baryon and a meson. The exotic baryon antidecuplet is sketched in figure 1.10. Common to all states is the fact that their masses are relatively low, considering a five quark content including one or more strange quarks, and a narrow width of $\Gamma \leq 30$ MeV.

The most famous member of the antidecuplet, the Θ^+, has a long and eventful history of experimental confirmation and denial. The review on pentaquarks by the PDG [7] calls it a 'curious episode in the history of science'. After a series of negative results from high statistics measurements, there is at the moment no evidence to believe that the Θ^+ might exist.

The nonstrange member N of the antidecuplet was first identified as the three-star $P_{11}(1710)$ resonance and from its (rather uncertain) parameters, properties of all the antidecuplet members were estimated. Due to the differences in widths between the Θ^+ ($\Gamma \sim 1$ MeV) and the $P_{11}(1710)$ ($\Gamma \sim 100$ MeV), it was suspected to be improbable that both belong to the same multiplet. Later, it was shown by a modified partial wave analysis of πN scattering data that the nonstrange member N could be an $N(1680)$ or $N(1730)$ or a mixing of the two [27]. It was also predicted that the decay width of N^* into $N\eta$ is rather 'large'. In addition, it was shown that the electromagnetic excitation of the N^* is suppressed on the proton in contrast to the neutron [29]. These facts were the main motivation for the measurement of $\gamma n \to \eta n$ at GRAAL.

Considering the cross section results for $\gamma n \to \eta n$ that followed, the conclusion with respect to the chiral quark soliton model is that the peak in the total cross section of $\gamma n \to \eta n$ is due to the $P_{11}(1685)$, the nonstrange member of the antidecuplet with a mass $M \sim 1650$–1730 MeV and a width $\Gamma \leq 40$ MeV [30].

In [31] an effective Lagrangian approach was used for a qualitative interpretation of the GRAAL $\gamma n \to \eta n$ data. Born terms and vector meson exchange were included along with the resonances $S_{11}(1535)$, $S_{11}(1650)$, $P_{11}(1710)$ and a narrow $N(1675)$ with unknown spin and parity. The results showed that the $N(1675)$ is responsible for the peak observed in the neutron cross section and simultaneously leads to a dip in the proton cross section around $W = 1675$ MeV.

In [32] preliminary total cross sections for η-production on the quasi-free proton and neutron obtained by CBELSA/TAPS were analyzed with a Reggeized model of Eta-MAID [33], in which, in addition to the eight resonances in the standard version of the model, a narrow $P_{11}(1670)$ with a width of $\Gamma = 10/30$ MeV was introduced. The data could be described and estimations for other channels were given.

1.5.2   Interference of known resonances

Interferences of resonances belonging to the same partial wave can show up in the total cross section. Several models presented in the following suggest such an effect as explanation for the bump structure seen in the total cross section of $\gamma n \to \eta n$.

In the work of [34], data from GRAAL and CBELSA/TAPS were studied with a chiral quark model approach. In this model an effective chiral Lagrangian accounts for the quark-pseudoscalar-meson coupling. Six resonances were included, which were treated equivalently at the quark level and only a limited number of parameters was needed for the resonance description. Most of the resonance parameters extracted from the model were near the PDG values [7]. Also included were u-channel contributions, which were found to be important, but no vector meson exchange in the t-channel was modeled. The bump in the total cross section on the neutron could be described by a constructive interference between the $S_{11}(1535)$ and the $S_{11}(1650)$ resonances. A destructive interference of the same two states was found to produce a dip near $W \sim 1.68$ GeV in the total cross section on the proton, which is clearly seen in the latest high precision measurements from MAMI-C [35]. Therefore, also the ratio σ_n/σ_p was well described in this work.

A partial wave analysis was performed in [36], where the earlier CBELSA/TAPS cross section data [26] were used in addition to various other data as, e.g., π^0, $2\pi^0$ and $\pi^0\eta$-production. Again, it was found that the structure could be naturally interpreted as interference between the $S_{11}(1535)$ and the $S_{11}(1650)$ resonances. As the authors cannot exclude that the $S_{11}(1650)$ could have small photocouplings to the neutron, also a P_{11} could play an important role. The data could be described with either a broad or a narrow P_{11} state, although the scenario of a broad resonance is probably ruled out by the latest results of the CBELSA/TAPS collaboration [15].

1.5.3 Coupled-channel effects

In [37] a coupled-channel effective Lagrangian approach was used to analyze the earlier CBELSA/TAPS data. The model used the K-matrix approach to simplify the coupled Bethe-Salpeter equations of meson-nucleon scattering. All important final states ($\pi N, \eta N, \phi N, \rho N, \gamma N, K\Lambda, K\Sigma$) were included and contributions from nucleon Born terms, t-channel exchange of mesons, nucleon and resonance terms in the u-channel and baryonic resonances in the s-channel were taken into account. Eleven nucleon resonances were included in the model. It was found that the peak in $\sigma(\gamma n \to \eta n)$ was generated by interference effects of the resonances $S_{11}(1535)$, $S_{11}(1650)$, $P_{11}(1710)$ and $P_{13}(1720)$. The authors argued that structures seen in photoproduction cross sections could be caused by channel coupling instead of resonances and, therefore, a full coupled-channel approach would be essential to interpret the data correctly.

The Giessen model is a coupled-channel model, that includes πN and γN reactions similar to the model mentioned above. It uses also a K-matrix effective Lagrangian approach. In [38] preliminary results of the neutron cross sections obtained at CBELSA/TAPS were included in the model and calculations for the total and differential cross sections of $\gamma n \to \eta n$ were presented. The observed bump was explained as threshold effect coming from the opening of the $K\Lambda$ channel. It was found that the overall magnitude of the structure was very sensitive to the helicity amplitudes of the $S_{11}(1650)$ and the $P_{11}(1710)$ states. These parameters were constrained by the preliminary CBELSA/TAPS results, which could have affected the accuracy of the estimation. The predicted differential cross sections for energies near the bump position showed a rise at backward angles.

Finally, in [39] an S-wave model for the study of $\gamma N \to \pi N$ and $\pi N \to \pi N$ was extended to include $\gamma N \to \eta N$, $\pi N \to \eta N$, $\gamma N \to KY$ and $\pi N \to KY$ with $Y = \Lambda, \Sigma$. The hadronic interaction in this model is mediated by the Weinberg-Tomozawa interaction in the lowest order chiral Lagrangian. The neutron total cross sections could be reproduced along with the peak in σ_n/σ_p. It was pointed out that the $K\Lambda$ and the $K\Sigma$ thresholds were located just at the beginning of the peak and near the end, respectively. Therefore, it was argued that the peak could be due to the intermediate strangeness states of the model. For the proton channel, there is a cancellation effect due to the intermediate $K^+\Lambda$ photon loop, that is absent in the neutron channel, leading to the observed neutron-proton ratio in the total cross sections.

1.6   Motivation for this work

As seen in section 1.4, the current base of experimental data regarding cross
sections of $\gamma n \to \eta n$ consists of three measurements:

- The GRAAL data provides differential cross sections for three angular regions with relatively low statistics [21].

- The LNS-Sendai data are still preliminary and statistics is moderate [25]. The measurements are inclusive only.

- The CBELSA/TAPS data consists of differential cross sections for four angular bins [15]. Statistics is generally moderate, but lower at backward angles in $\cos(\theta_\eta^*)$ due to trigger restrictions in the experimental setup.

Considering the numerous possibilities of theoretical interpretations (see section
1.5), it is clear that this situation needs clarification. Therefore, in proposal A2-
10/05 submitted to the PAC in 2005 [40], it was suggested to start a new high
precision measurement at MAMI-C using a deuterium target. The goal of the
first part of the proposal, namely the extraction of high precision unpolarized
differential cross sections for $\gamma n \to \eta n$, was achieved in this work and the results
will be presented in the following.

Chapter 2

Experimental setup

In this chapter the experimental setup that was used to carry out the measurements for this work will be described. In the first sections, details about the electron accelerator, the target and the different detectors will be given. The data acquisition will be described in section 2.6. Software needed for the data analysis is discussed in section 2.7. Finally, details about the data sets used in this work are summarized in section 2.8.
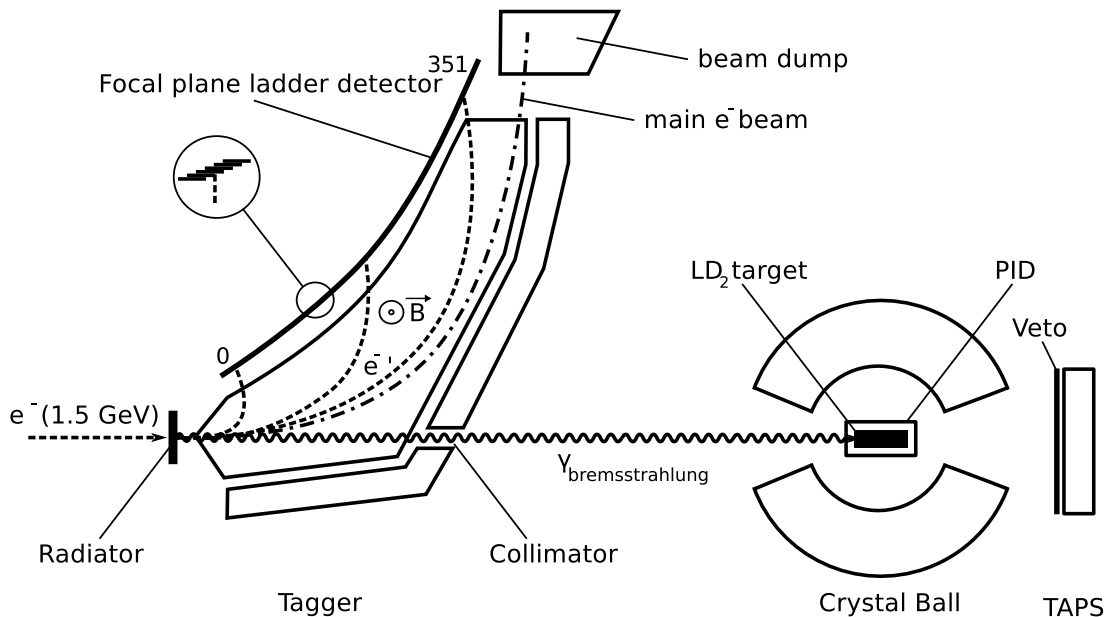
Fig. 2.1: Overview of the experimental setup: The principal detectors are the Glasgow photon tagger, the Crystal Ball and the TAPS detector.

The data that were analyzed in this work were measured at the tagged photon facility in the A2 hall of MAMI at the University of Mainz in Germany. Figure 2.1 shows an overview of the experimental setup. A photon beam is obtained via bremsstrahlung in a radiator from a 1.5 GeV electron beam produced by the

MAMI accelerator. The scattered electrons are deflected by a dipole magnet and energy tagged in the Glasgow photon tagger which allows the reconstruction of the energy of the produced photons. The photon beam is collimated and impinges on the liquid deuterium target located at the center of the Crystal Ball (CB) detector. The target is surrounded by the Particle Identification Detector (PID) used for the identification of charged particles in CB. The hole in forward direction of CB is covered by the TAPS detector. In front of every TAPS detector element, a thin Veto detector is installed for charged particle identification.

2.1   The MAMI electron accelerator

The electron accelerator MAMI (Mainz Microtron) at the Institute for Nuclear Physics of the University of Mainz consists of a cascade of several accelerators, which allows the production of a unpolarized or polarized continuous wave (cw) electron beam with nominal energies up to 1.5 GeV [41, 42]. Continuous wave machines are essential for coincidence experiments to reduce background from accidental coincidences. The electron bunches in MAMI have a very small spacing, which cannot be seen by the detectors, thus fulfilling this requirement.

The floor plan of the MAMI accelerator is shown in figure 2.2. Unpolarized electrons are produced by a thermic electron cannon, whereas longitudinally polarized electrons with polarizations up to 85% can be produced by a semi-conductor crystal (GaAsP) and polarized laser light [44]. The electrons are preaccelerated to 611 keV and injected to the injector linear accelerator, in which they are brought to an energy of 3.97 MeV. Afterwards, the first race track microtron (RTM1) accelerates them to 14.86 MeV.

A race track microtron consists of a linear accelerator with radio-frequency cavities of 2.45 GHz and two dipole magnets with uniform fields, which deflect the electrons by 180 degrees at both sides of the apparatus. The electrons gain a constant fraction of energy each time they pass the accelerator step, which leads to

	Injector	RTM1	RTM2	RTM3	HDSM
inject. energy	611 keV	3.97 MeV	14.86 MeV	180 MeV	855 MeV
extr. energy	3.97 MeV	14.86 MeV	180 MeV	855 MeV	1508 MeV
σE	1.2 keV	1.2 keV	2.8 keV	13 keV	110 keV
# of turns	—	18	51	90	43
magn. field	—	0.1026 T	0.5550 T	1.2842 T	1.53-0.95 T
magn. weight	—	4.2 t	92.3 t	911.6 t	1030 t
linac length	4.93 m	0.80 m	3.55 m	8.87 m	8.57/10.10 m

Tab. 2.1: Main parameters of the MAMI accelerator stages [43].
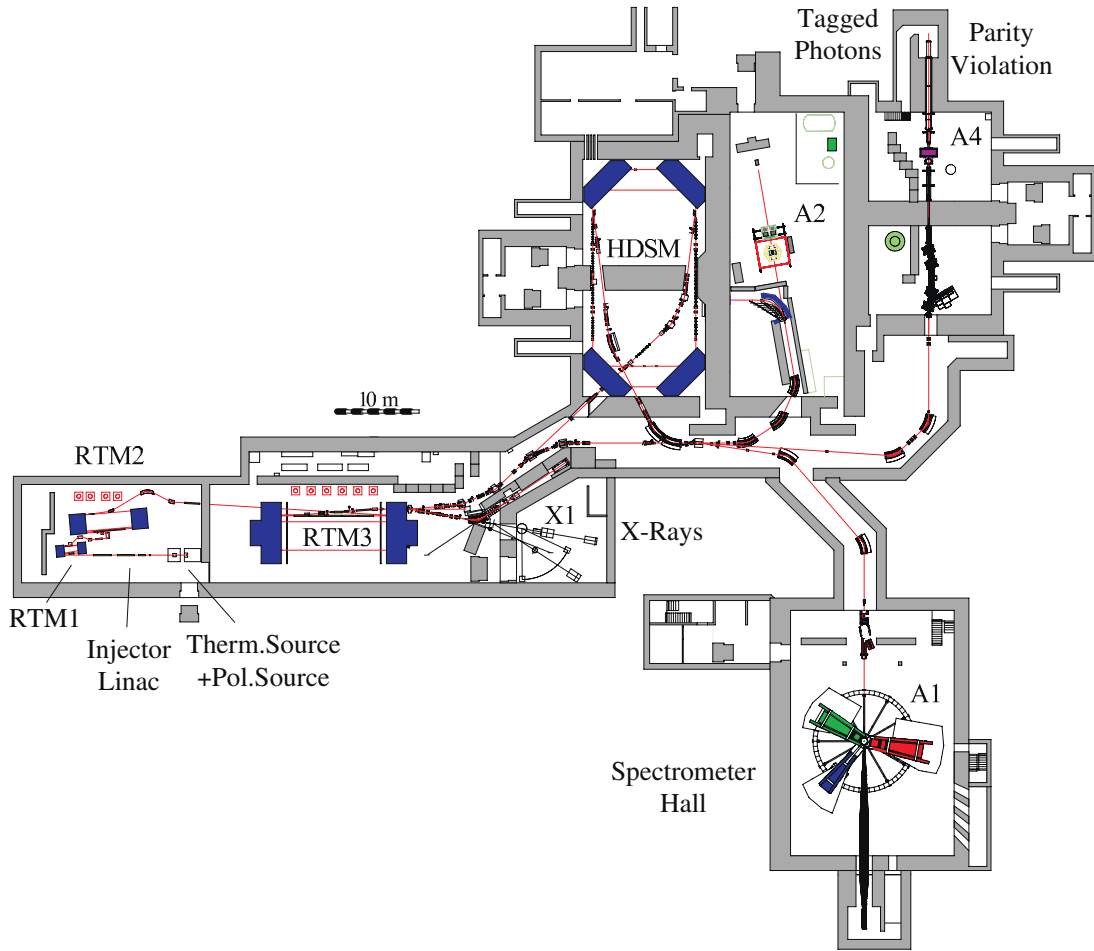
Fig. 2.2: Floor plan of the MAMI electron accelerator facility: The current experiment was performed in the A2 hall. Taken from [42].

larger radii of the electron trajectories in the magnets with each turn. The beam is finally extracted when the most outer orbit and the corresponding maximum energy is reached.

After having passed RTM1, the electron beam is further accelerated in two other race track microtrons RTM2 and RTM3 to 855 MeV (MAMI-B). Due to the increasing energy, the radii of the electron orbits in the magnets become larger and the magnetic fields have to be stronger to keep the RTMs at a reasonable size. However, the standard race track microtron design was not feasible due to weight and space restrictions for the last accelerator step from 855 MeV to 1.5 GeV (MAMI-C). Therefore, a harmonic double-sided microtron (HDSM) was built for this purpose. It replaces the two dipole magnets on each side by four dipole magnets in the corners, each deflecting the electron beam by 90 degrees. This gives also the advantage that two accelerator stages can be used at the long sides of the HDSM. From the HDSM the electrons are led to the experimental halls.

A summary of the parameters of the different accelerator stages can be found in table 2.1. In summary, MAMI produces a high quality and stable electron beam with low emittance, energies up to 1.5 GeV (recently even up to 1.6 GeV) and a maximum current of 100 μA.

2.2   The Glasgow photon tagger

The Glasgow photon tagger is an electron spectrometer which serves for the reconstruction of the energy of the photons that impinge on the target and the determination of the corresponding flux [45, 46, 47]. A photo of the apparatus can be seen in figure 2.3.

High energetic photons are produced via bremsstrahlung off a thin radiator. In the current experiment, a 10 μm copper foil or, in case of the Møller radiator, Vacoflux 50 (alloy of cobalt and iron) were used as radiators. Due to the heavy masses of the recoil nuclei compared to the electron, only a negligible amount of energy in the order of a few keV is transferred to the nuclei and, therefore, the energy of the emitted photon E_γ can be calculated via

$$E_\gamma = E_0 - E_{e^-}, \tag{2.1}$$

with the incoming electron energy E_0 and the energy of the scattered electron E_{e^-}. The cross sections of bremsstrahlung show the following characteristic energy and angular dependences [48, 49]:

$$\frac{d\sigma}{dE_\gamma} \quad \propto \quad \frac{1}{E_\gamma} \tag{2.2}$$

$$\frac{d\sigma}{d\theta_\gamma} \quad \propto \quad \frac{\theta_\gamma}{\left(\theta_\gamma^2 + \theta_c^2\right)^2} \tag{2.3}$$

$$\theta_c \quad = \quad \sqrt{\langle \theta_\gamma^2 \rangle} \propto \frac{m_e}{E_0} \tag{2.4}$$

Half of the photons are emitted within the characteristic angle θ_c. From the ratio of electron mass m_e and incoming electron energy E_0, it is clear that this angle is very small, i.e., most photons are emitted in forward direction having small angles θ_γ. To have an even better defined fine photon beam on the target, the photons were collimated with a lead collimator of 4 mm diameter. This led to a beam spot size of ≈ 1.3 cm diameter on the target. The photon flux, i.e., the number of photons reaching the target, is determined from the number of detected electrons and the tagging efficiency $\epsilon_{\text{tagg}} = N_\gamma / N_{e^-}$ (see section 4.9).

The electrons are deflected horizontally by a large dipole magnet with a weight around 70 t. Using a maximum current of 440 A, a magnetic field strength of 1.9
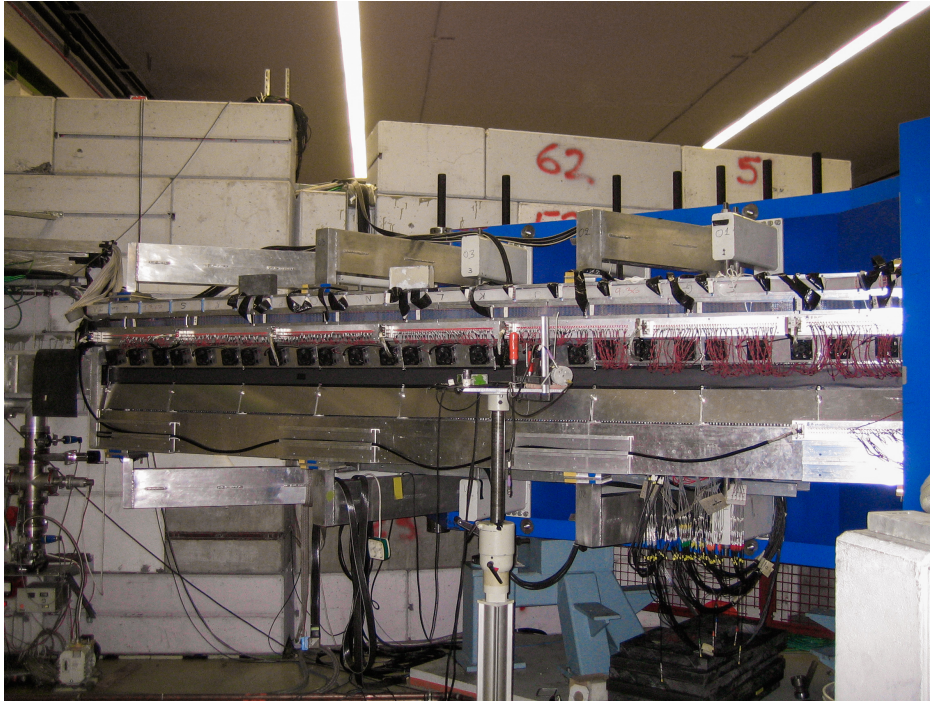
Fig. 2.3: Photo of the Glasgow photon tagger: The dipole magnet (blue) deflects the scattered electrons to the focal plane detector ladder seen in the central part of the image.

T can be produced. The main electron beam is led into a shielded beam dump, where a Faraday cup is installed for monitoring of the electron beam current. The scattered bremsstrahlung electrons are spread out in the magnetic field according to their momentum and electrons with energies $5\% < E_{e^-}/E_0 < 93\%$ are detected in a ladder of detectors installed in the focal plane. Using the detected position, the electron energy can be reconstructed with an appropriate calibration (see section 3.5.3). The detector array consists of 353 EJ-200 scintillators of 80 mm length, 2 mm thickness and widths from 9 to 32 mm to keep a constant energy coverage per detector. The detectors are partly overlapping so that a coincidence condition on passing electrons can be established, requesting a coincident signal in two adjacent detectors. This leads then to 352 logical detectors with resolutions of 2–5 MeV for an incoming beam energy of 1.5 GeV. The scintillators are read out individually by Hamamatsu R1635 photomultiplier tubes that are shielded from the magnetic field by steel plates.

Due to the $\propto 1/E_\gamma$ bremsstrahlung spectrum, a high beam intensity can saturate the tagger detectors at high electron energies and cause radiation damage. Therefore, for the current experiment only detectors 1 (low electron energy) to 272 (high electron energy) were activated, resulting in a tagged photon energy range of $\sim$400–1400 MeV (see table 2.4).

Fig. 2.4: Photo of the liquid hydrogen/deuterium target cell. Taken from [50].

2.3   Cryogenic target

A liquid deuterium target [51] was used in the current experiment to achieve a high density of scattering centers, i.e., neutrons and protons. Gaseous deuterium is kept in a storage tank at typically 1400 mbar at the beginning of the cooling. When cooled down to approximately 20 K, about 25% of the deuterium is liquified and the pressure in the gas drops to 1080 mbar. The liquid deuterium is led to a storage reservoir and finally to the target cell. The temperature in the target cell is monitored and adjusted automatically by either adding cool liquid or heating.

The target cell, as shown in figure 2.4, is a cylinder made of 125 μm Kapton with a diameter of 4 cm. The length of the target cell can be changed by different entrance window adapters. For this work, cell lengths of (4.72 ± 0.05) cm and (3.02 ± 0.03) cm were used. When installed, the cell was surrounded by eight layers of super-isolating foil (8 μm Mylar plus 2 μm aluminum) for thermic isolation. The cell is then placed inside a 1 mm carbon-fiber-reinforced plastic tube with a diameter of 82 mm. Inside the tube, there is a vacuum of around 3×10^{-7} mbar.

2.4   The Crystal Ball detector

The Crystal Ball detector (CB) is a highly segmented spherical calorimeter having a main geometry of a icosahedron [52, 53, 54]. This is a regular polyhedron with twenty identical equilateral triangular faces (major triangles), as shown in figure 2.5. Each major triangle is divided into four smaller equilateral triangles (minor
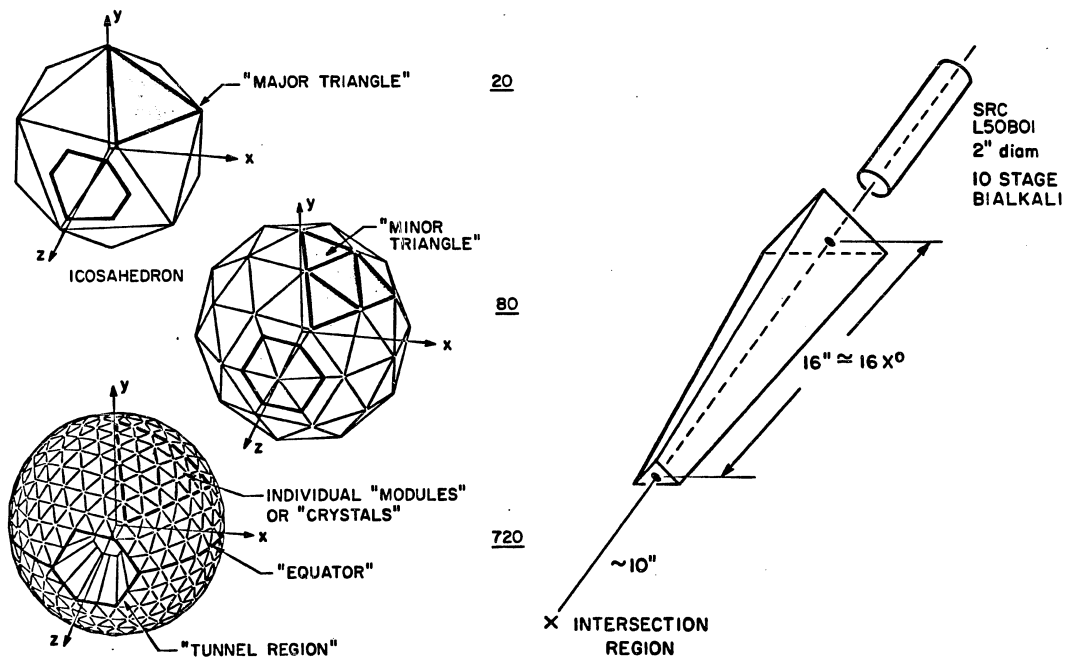
Fig. 2.5: Geometry of the Crystal Ball detector and the NaI(Tl) crystals: Left-hand side: The icosahedron-shaped detector has 20 major and 80 minor triangles. Right-hand side: crystal geometry. Taken from [52].

triangles). Finally, each minor triangle holds nine triangle-shaped thallium doped sodium iodide (NaI(Tl)) crystals. This yields in a total amount of 720 segments, but to have entrance and exit windows for the beam, 24 crystal positions in backward and forward direction are not filled (tunnel regions). Hence, CB consists in total of 672 NaI(Tl) crystals.

For practical reasons, CB is divided into two hemispheres with inner and outer radii of 25 cm and 66 cm, respectively. Both are evacuated since the NaI(Tl) crystals are hygroscopic and have to be protected from moisture. The vacuum is also needed for mechanical stability. Between the two hemisphere, there is an inactive region caused by 2×1.5 mm steel plates and an air gap of 5 mm. The upper hemisphere can be lifted for maintenance work, which is shown in figure 2.6.

Due to the geometry, eleven different shapes of crystals exist. Each is a truncated triangular pyramid with a length of 40.6 cm corresponding to 15.7 radiation lengths. The sides of the triangular faces are around 5.1 cm at the front of the crystals and 12.7 cm at the back. All crystals were optically isolated by wrapping them in reflector paper and aluminized Mylar. Photomultipliers of the type SRC L50B01 are installed outside the hemispheres for each crystal. The optical coupling is made by glass windows, where part of the light is lost due to air gaps between crystal, glass and photocathode. Some characteristic properties of NaI(Tl) crystals can be found in table 2.2.
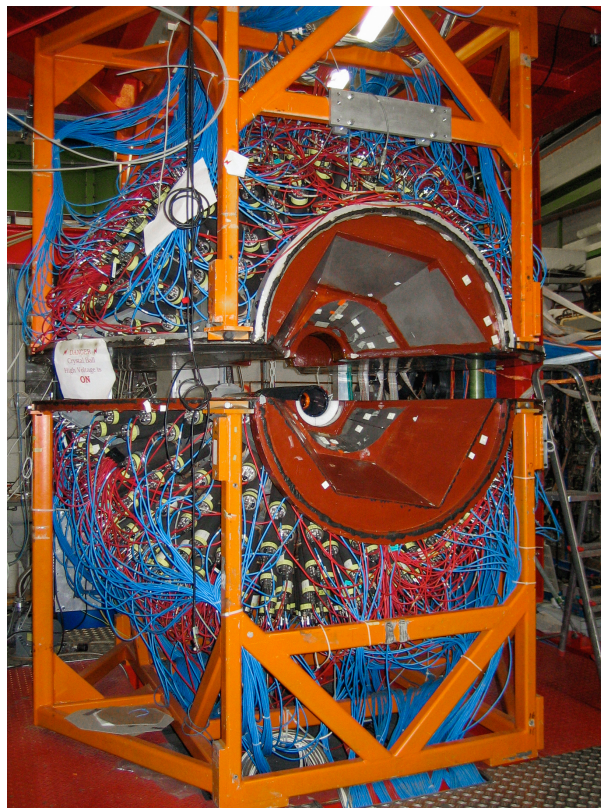
Fig. 2.6: Photo of the Crystal Ball detector: The upper hemisphere is lifted for maintenance work.

Photons deposit typically 98% of their energy in 13 adjacent crystals. Charged pions can be stopped up to kinetic energies of 240 MeV, protons up to energies of 425 MeV. The full acceptance in the azimuthal angle is only slightly reduced by the gap between the hemispheres. The polar angular acceptance is around $20° \leq \theta \leq 160°$. The energy and the angular resolutions will be discussed in section 3.6.

Property	Value
density	3.67 g cm^{-3}
critical energy (e^-)	13.37 MeV
radiation length	2.59 cm
Molière radius	4.13 cm
primary decay time	245 ns
wavelength of emission max.	410 nm

Tab. 2.2: Properties of NaI(Tl) crystals used in Crystal Ball [7, 55].
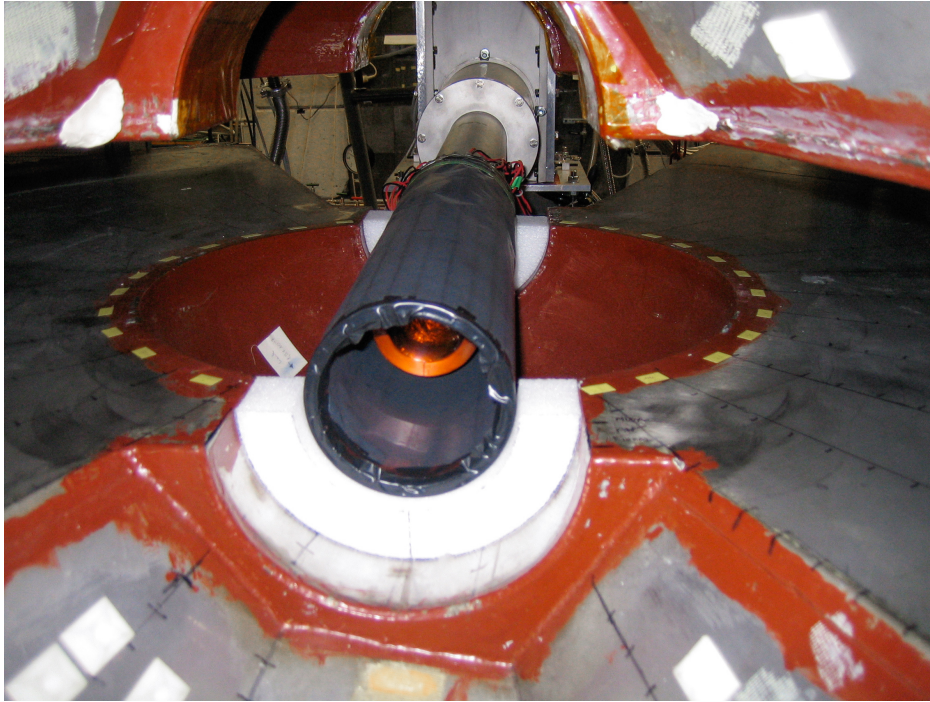
Fig. 2.7: Photo of the PID detector and the target: The upper hemisphere of CB was lifted for maintenance work.

2.4.1 Particle Identification Detector

The Particle Identification Detector (PID) [56] is part of the inner detector system of CB (see figure 2.7). For this work, it was the only inner detector that could be used, as the multi-wire proportional chamber (MWPC) was not functional. The PID is used for the identification of charged and neutral particles (veto detector). Furthermore, protons, pions and electrons can be discriminated by plotting the coincident deposited energy in the PID versus the cluster energy in CB. The different particles are then located in fairly separated areas and can be separated to a certain degree.

The PID consists of a 10 cm diameter barrel of 24 EJ-204 plastic scintillators, which is installed between the target cell and CB. The scintillators are 500 mm long, 4 mm thick and have a trapezoidal cross section to minimize the gaps between each other when formed to the barrel. Optical isolation is achieved by aluminum foil and a layer of black Tedlar. All scintillator elements are read out by their own photomultipliers of the type Hamamatsu H3164-10 connected via lucite light guides and installed in the upstream direction to avoid additional material in forward direction. When the PID is installed at its nominal position, the complete solid angle of CB is covered, in which one PID element covers 15 degrees of the azimuthal angle.
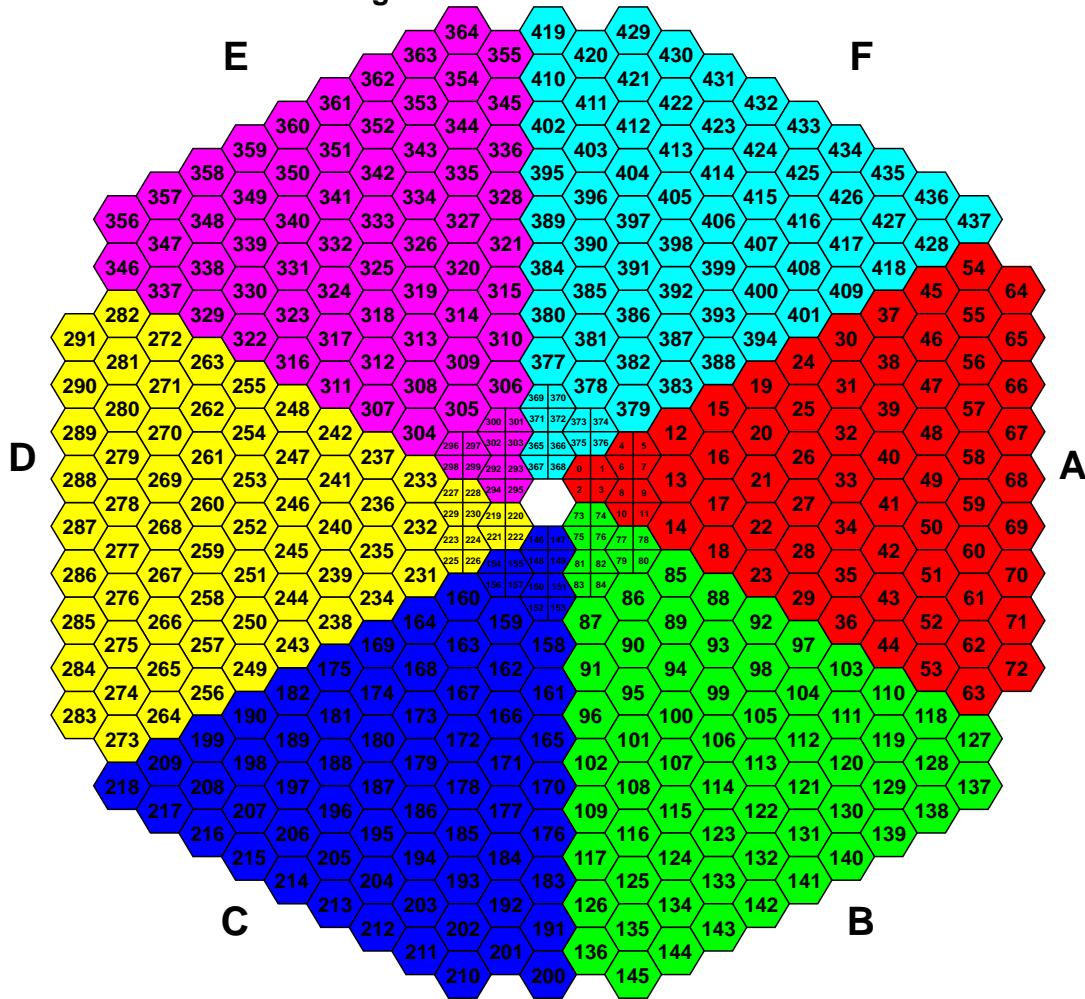
Fig. 2.8: Geometry of the TAPS detector: The shown configuration corresponds to the one installed since 2009 with two inner rings of $PbWO_4$ crystals.

2.5 The TAPS detector

TAPS is a versatile calorimeter [57, 58] that is configured as forward wall for the current experiment. It covers the full azimuthal angle for polar angles from around 5 degrees to approximately 20 degrees. The crystals are arranged in a hexagon-like structure with eleven rings and six logical sectors. In the December 2007 beamtime, TAPS consisted of 384 barium fluoride (BaF_2) crystals. Before the beamtimes in February and May 2009, the two most inner rings containing 18 crystals were replaced by smaller lead tungstate ($PbWO_4$) crystals for a better handling of the high rates at smaller forward angles. Each BaF_2 crystal was replaced by four $PbWO_4$ crystals, resulting in a total configuration of 72 $PbWO_4$ plus 366 BaF_2 crystals (see figure 2.8).

Property	Value for BaF_2	Value for $PbWO_4$
density	4.89 g cm^{-3}	8.3 g cm^{-3}
critical energy (e^-)	13.78 MeV	9.64 MeV
radiation length	2.03 cm	0.89 cm
Molière radius	3.10 cm	2.00 cm
fast decay time	0.9 ns	10 ns
wavelength of emission max.	220 nm	420 nm
slow decay time	650 ns	30 ns
wavelength of emission max.	300 nm	425 nm

Tab. 2.3: Properties of BaF_2 and $PbWO_4$ crystals used in TAPS [7, 55].

The BaF_2 crystals have a hexagonal shape with a front face diameter of 5.9 cm. The length is 22.5 cm plus 2.5 cm of the cylindric end cap with a diameter of 5.4 cm. The overall length of 25 cm corresponds to 12 radiation lengths. Charged pions can be stopped up to 185 MeV and protons up to 380 MeV. A summary of the properties of BaF_2 is given in table 2.3. A special property of BaF_2 is the presence of a fast ($\tau \sim 0.9$ ns) and a slow ($\tau \sim 650$ ns) scintillation light component. The first provides a very good time resolution needed for time-of-flight measurements (up to $\Delta t \approx 170$ ps for a single detector), whereas the latter is responsible for the good energy resolution because of the high light yield. Due to the different mechanisms of energy deposition of photons and, e.g., hadrons, these two light components lead to different signal shapes for the corresponding particles. The relative contribution of the fast component to the total light output is higher in the case of photons than for, e.g., protons or neutrons. This can be used for particle identification by integrating the signal over a short and a long time interval and comparing the two resulting calibrated energies (see section 3.5.2).

The BaF_2 crystals are optically isolated by a wrapping of eight layers of 38 μm thick reflecting Teflon foil and one layer of 15 μm aluminum foil. Individual photomultiplier tubes of the type Hamamatsu R2059-01 are connected to the cylindrical ends of the crystals. Light tightness is achieved by a black shrinking tube.

The $PbWO_4$ crystals were installed in the two most inner rings of TAPS to better resist the high rates at small forward angles [59, 60]. This is achieved by the short decay time of around $\tau \sim 10$ ns. In addition, the higher density compared to BaF_2 (see table 2.3) allowed the installation of smaller crystals. They have a trapezoidal shape so that a combination of four $PbWO_4$ crystals gives the geometry of one BaF_2 crystal, which allows an easy integration into the TAPS geometry. The length of the crystals is 20 cm which corresponds to 22.5 radiation lengths. Each crystal is wrapped in 70 μm reflector foil VME 2000 and an additional layer
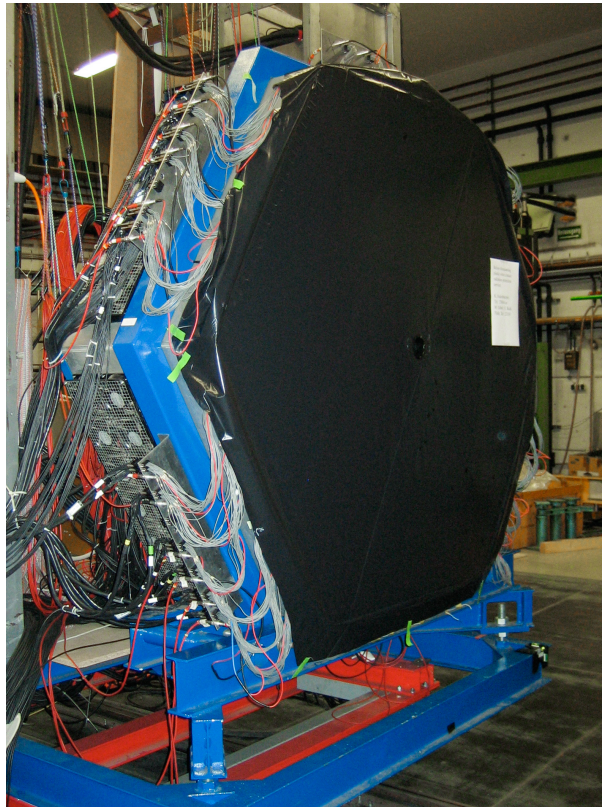
Fig. 2.9: Photo of the TAPS forward detector: The black foil serves as light isolation for the Veto wall.

of 20 μm aluminum foil, and is connected to a photomultiplier tube of the type Photonis XP 1911. Due to the installation on short notice before the deuterium beamtimes in 2009, the $PbWO_4$ crystals were not ready to be used in the analysis. This led to an acceptance hole in TAPS because of the lack of the most inner two rings consisting of these crystals.

2.5.1 Veto detectors

In front of every BaF_2 crystal and, respectively, every group of four $PbWO_4$ crystals, a thin plastic scintillator is installed that is used for charged and neutral particle discrimination. Similar to the PID detector, also a separation of electrons, charged pions and protons is possible to a certain degree, although with worse resolution than in the PID due to the inferior optical coupling to the photomultipliers (see below).

The scintillators are made of 5 mm thick EJ-204 and have the same hexagonal shape as the face of the BaF_2 crystals. They are connected via BCF-92 wavelength-shifting fibers to multi-anode photomultipliers of the type Hamamatsu H6568 with 16 channels. The Veto detectors are hold by a hexagonal frame that is placed in

front of TAPS. The frame is light-tightened with a black foil. A photo of the Veto wall mounted on TAPS can be seen in figure 2.9.

2.6 Data acquisition

The analog signals that are produced in the photomultipliers of all detectors are digitized by the electronics. The data acquisition system collects all obtained information and stores them to digital files. This will be discussed briefly in section 2.6.1. Electronics is also needed for the experimental trigger which decides whether an event is recorded or not. An overview of the trigger will be given in section 2.6.2.

2.6.1 Readout

The various detectors are readout by different systems that will be presented in the following part.

Tagger

During standard data taking, only the hit times and the number of electron hits in the focal plane detectors are recorded. The deposited energies are only needed for calibration purposes. The signals have to pass a discriminator and are then led to a CATCH (COMPASS Accumulate, Transfer and Control Hardware) multi-hit TDC (time to digital converter). This unit is capable of recording the times of multiple hits per event. In addition, the signals are sent to FASTBUS scaler units, which count the number of hits in the corresponding detectors.

Crystal Ball

A schematic view of the CB electronics can be seen in figure 2.10. The signals of the NaI(Tl) crystals are first led to an active splitter in groups of 16 channels. There, the analog sum of all signals is created that is used for the energy sum trigger (see next section). One part of the split signals is delayed and fed to the ADC (analog to digital converter) for the integration of the signals. The other part is led to leading-edge discriminators (LED) with 16 input channels, where the signals are compared to two thresholds. If the low threshold is passed, the signal of the corresponding channel is sent to the CATCH TDC. The outputs of the 16 high threshold discriminator lines are connected with each other via logical OR and are later used for the multiplicity trigger.

The delayed signals are sent to sampling ADCs that sample the signals with a rate of 38.88 MHz. Due to limitations in the data recording, not all samples
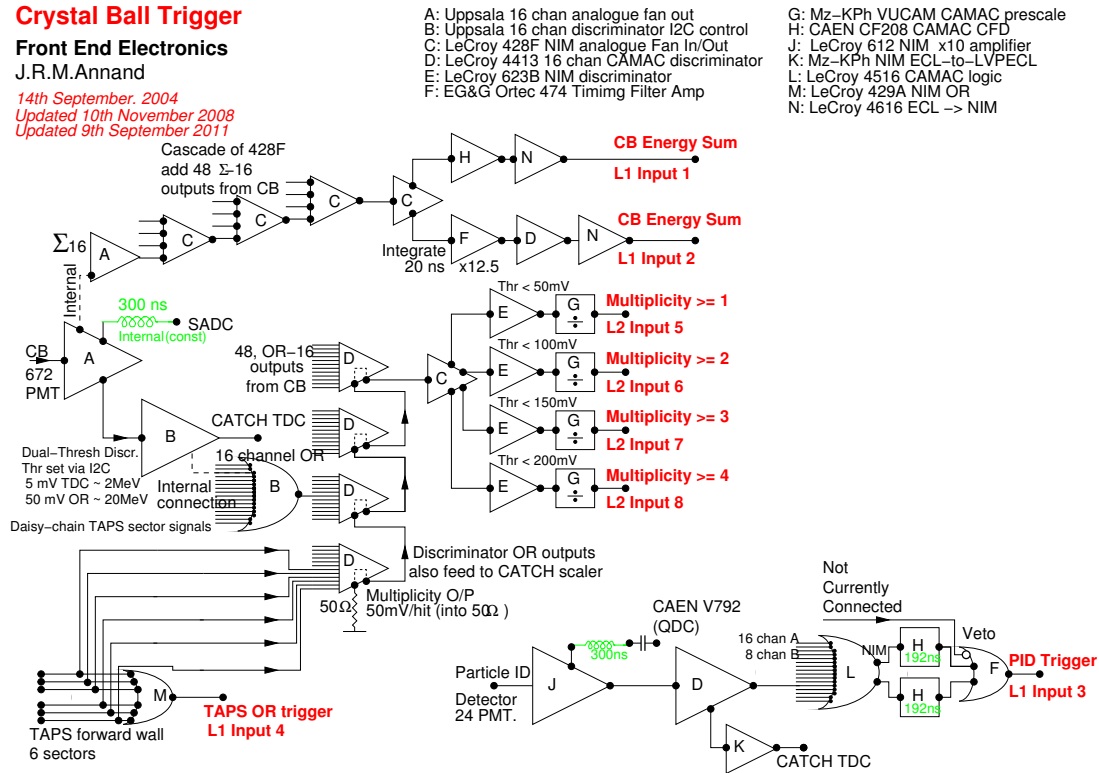
Fig. 2.10: Schematic view of the Crystal Ball electronics. Taken from [50].

are saved, but integrals of three time intervals are calculated. These correspond to the pedestal (baseline), the signal and the tail. The pedestal is automatically subtracted from the signal event-by-event, therefore only the gain had to be calibrated later (see section 3.2.1). The tail information is not used at the moment.

The signals of the PID are amplified and split. Delayed signals are led to ADCs for the signal integration, while the other line is passing through a discriminator and finally goes to CATCH TCDs for the time measurement.

TAPS

The readout of TAPS is performed by customized VME (Versa Module Eurocard) boards. One board integrates discriminators and analog to digital converters for 4 BaF_2 channels. A constant-fraction discriminator (CFD) is used to check if a channel detected any signal. The corresponding thresholds are normally set as low as possible just above the noise level (equivalent to around 3 MeV). Two LEDs per channel can be used for trigger purposes. The time measurement is performed by time to amplitude converters (TAC), whereas the energy information is obtained by charge to amplitude converters (QAC). Digitalization is made by 12 bit ADCs. As discussed in section 2.5, the signals are integrated over a short interval (40 ns) and a long one (2 μs) to take into account the two scintillation light components of the BaF_2 crystals.

Similar VME boards were designed for the readout of the TAPS Veto detectors. One board can handle 8 channels, for which the processing is more simple compared to the crystal channels. One LED per channel is used to start the time measurement and the energy integration over a gate of 110 ns.

2.6.2 Trigger

The data acquisition system used in the current experiment cannot record data continuously, as a finite time is needed for the readout of the detectors and the digitalization of the measured data. Therefore, a trigger is used to reduce the event rate and to keep the dead time of the detector system at a reasonable level. This trigger performs a preselection of the events so that only events of possible interest for the offline analysis are recorded.

The first level trigger is built from the analog sum of all CB signals, implementing an energy sum trigger (see figure 2.10). A threshold can be set in a discriminator, to which the total signal is compared. Knowing the relationship between the amplitude of the signal and the deposited energy in CB, a threshold in terms of energy can be set. When set at a moderate value, this trigger is mainly used to reject events from cosmics. Higher thresholds can be used to, e.g., reject events of photoproduction of certain mesons. For the current experiment, a threshold of about 300 MeV was applied to suppress events from single pion production, as the main object of the measurement was the study of η-photoproduction.

The second level trigger used for this work consists of the multiplicity trigger, which aims at putting a condition on the approximated number of detected particles. As already mentioned before, this is implemented in CB by applying a threshold of around 30 MeV to a group of 16 adjacent channels, which form a logical group. If at least one of the channels is above threshold, the group contributes to the multiplicity. TAPS is divided into six sectors (see figure 2.8), which also contribute to the total multiplicity if at least one crystal in a sector is above the LED1 threshold. Due to the coarse and static logical groups used for the multiplicity trigger, the number of detected particles can only be approximately determined. Namely, if two particles are detected in the same group, they only count as one. On the other hand, when one particle cluster spreads over multiple logical groups, it can contribute several times.

In the beamtimes of December 2007 and May 2009, the multiplicity trigger was set to M2+, which means that two multiplicity hits or more fulfill the trigger condition. This was chosen to select events originating from the $\eta \rightarrow 2\gamma$ decay. In the February 2009 beamtime, M3+ was chosen to increase statistics for the $\eta \rightarrow 3\pi^0$ decay and other reactions.

An overview of the trigger logic and electronics is given in figure 2.11. In the December 2007 and the February 2009 beamtimes, the CB energy sum trigger
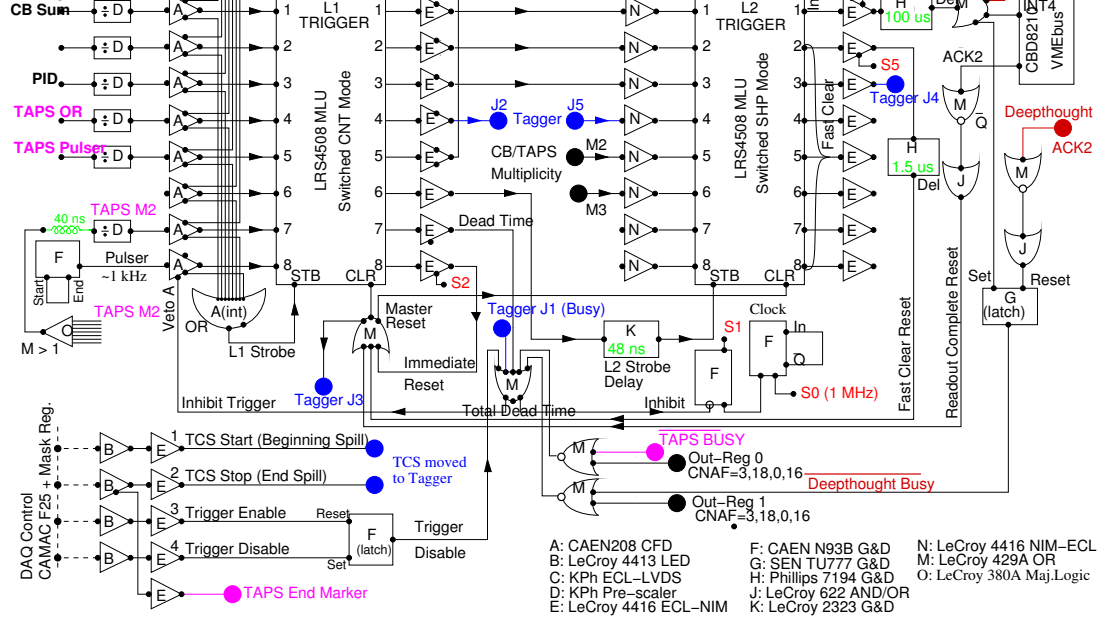
Fig. 2.11: Schematic view of the trigger electronics. Taken from [50].

was the only used first level trigger. In May 2009, also the TAPS M2 trigger was activated, which allowed the recording of events with two sectors in TAPS over the LED2 thresholds but without fulfilling the CB energy sum condition. This trigger was implemented for the detection of forward going π^0-mesons, which created two clusters in TAPS with no or few energy deposition in CB. Events originating from the TAPS M2 trigger were skipped in the analysis of this work, as such events do not exist in η-production but could lead to unwanted trigger effects.

2.7 Software

The following two sections present the main software packages that were used for the data analysis of this work. AcquRoot was used for the analysis of experimental and simulated data, whereas the A2 simulation was used to produce the latter. In section 2.7.3 additional software developed as part of this work will be briefly discussed.

2.7.1 AcquRoot

AcquRoot is the main software package that is used for data acquisition, data analysis and Monte Carlo (MC) event generation for experiments performed by

the A2 collaboration [61]. It is based on the CERN ROOT framework [62] and written in C++ following an object-oriented approach. The experimental data for this work was still obtained by ACQU, the predecessor of the DAQ module of AcquRoot called AcquDAQ, which is currently replacing ACQU step by step. Instead of the AcquRoot MC generator (AcquMC), a custom event generator that is part of the OSCAR library was used for MC event generation in this work (see section 2.7.3).

The AcquRoot analyzer is used to decode the binary raw files produced by ACQU and the simulated data files produced by the A2 simulation. Furthermore, all detectors are modeled in classes, which are derived from base classes that incorporate common features and properties. The application of calibrations is implemented via ASCII configuration files. The detector objects are filled with calibrated experimental or simulated data and clusters in CB and TAPS are reconstructed. Physics analysis classes can be added and easy access within these classes to the detector information is provided by the framework.

For this work, a more flexible calibration system (CaLib) was implemented and coupled to the AcquRoot framework (see section 2.7.3). In addition, a parallelized analysis was developed as part of the OSCAR library that was used for the analysis of presorted events. The preselection was performed in the AcquRoot analyzer, where all the detector calibrations and rough analysis cuts were applied, so that only events of interest could be saved for further accelerated processing. By using the presort, the duration needed for the analysis could be decreased by at least one order of magnitude.

2.7.2 A2 Geant4 simulation

The A2 simulation is a model of the experimental setup used for this work [63]. It is based on the Geant4 framework [64, 65], which is a toolkit for simulating the passage of particles through matter. The main purpose of the simulation is the determination of detection efficiencies that are, e.g., needed for the normalization of cross sections. Other applications are the testing of analysis cuts or the estimation of data taking durations. In addition, new detector developments can be tested with the simulation.

The geometries of the detectors and other relevant materials are described as accurately as possible in the code of A2, so that the algorithms in Geant4 are able to track a variety of particles within this model of the setup. A visualization of the modeled geometry is shown in figure 2.12. Most of the geometry descriptions were converted from an older simulation based on GEANT3. Inaccuracies in the current geometry led to some problems in the determination of the detection efficiencies for nucleons that will be discussed in section 4.8.3. Also related to that are the Geant4 physics lists, which are discussed in section 4.8.2.
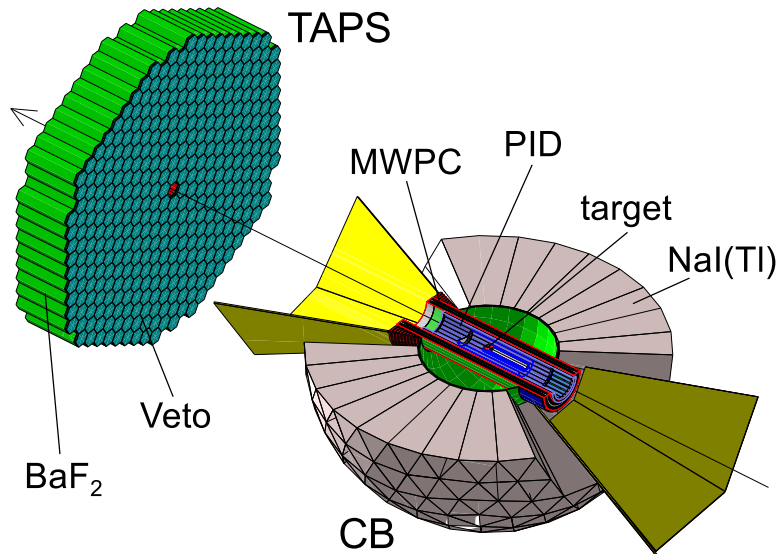
Fig. 2.12: Visualization of the Geant4-based model of the experimental setup: CB was cut in half to show the inner parts of the setup.

The events to be simulated can be created by the simple built-in generator or various external event generators, such as AcquMC, Pluto [66] or the OSCAR event generator. All particles that were enabled for tracking are then passed to Geant4 and, starting from the generated vertex, the passage through the materials is simulated. The detectors are marked as sensitive volumes in the simulation, which allows the determination of deposited energies and hit times. These information are then saved and can be processed with the AcquRoot analyzer similarly to experimental data.

As Geant4 is continuously modified and improved, it is important to note that version 9.5 (patch-01) was used in this work.

2.7.3   Additional software

Three software projects worth mentioning were developed as part of this work. The OSCAR library provides basic functions useful in the data analysis that are not included in the ROOT framework. CaLib was developed for a convenient calibration process during offline analysis. Finally, TAPSMaintain is used for the precalibration of TAPS during preparation for data taking.

OSCAR

The OSCAR library (OSCAR Simplifies Coding and Analyzing with ROOT) is a collection of ROOT-based classes that were developed for various purposes during this work. The initial development was started to provide additional functionality

to ROOT classes. Later, more extensive implementations were added. OSCAR contains several modules of classes with similar fields of application:

- **A2** : event classes for the AcquRoot presort, basic meson reconstructions

- **analysis** : presort analysis classes, calculation of cross sections, photon fluxes, Fermi momentum distributions, kinematic calculations, handling of theoretical model predictions

- **graph** : data plotting

- **MC** : Monte Carlo event generator classes

- **utils** : file readers, histogram/graph utility functions, cross section data storage and manipulation

- **math** : implementation of special mathematical functions

Apart from the classes in the A2 module and a few other exceptions, OSCAR does not depend on the experiment, in which the data to be analyzed was obtained. For example, the presort analysis had to be only slightly modified for the data analysis of the CBELSA/TAPS experiment [67]. OSCAR was also tested in the data analysis of other data sets and reaction channels. Therefore, further development will be encouraged.

CaLib

During data taking, experimental parameters can change over time. Some of them as, e.g., a change in temperature in the experimental hall can sometimes not be avoided but have great influence on some of the detectors. Other changes are made on purpose, e.g., to improve the experimental conditions. In any case the calibration procedure has to take into account all instabilities of the detectors.

The time dependence of the calibrations was checked by extracting the key quantities of the corresponding calibrations (e.g., π^0-peak position in the two photon invariant mass, photon time coincidence) for each data run. The behavior of these quantities over time was checked in detail. If unstable time frames were found, multiple calibration sets were created based on the magnitude of the deviations and the remaining statistics in the data set to establish a separate calibration.

This results in a time-dependent calibration for all detectors, whereas the time frames a certain calibration is valid are not the same for the different calibrations but overlapping. The existing mechanism to read calibration parameters within the analysis software AcquRoot (see section 2.7.1) using ASCII files was not flexible enough to handle these complex and numerous calibration time frames. Therefore, a more convenient solution had to be found.
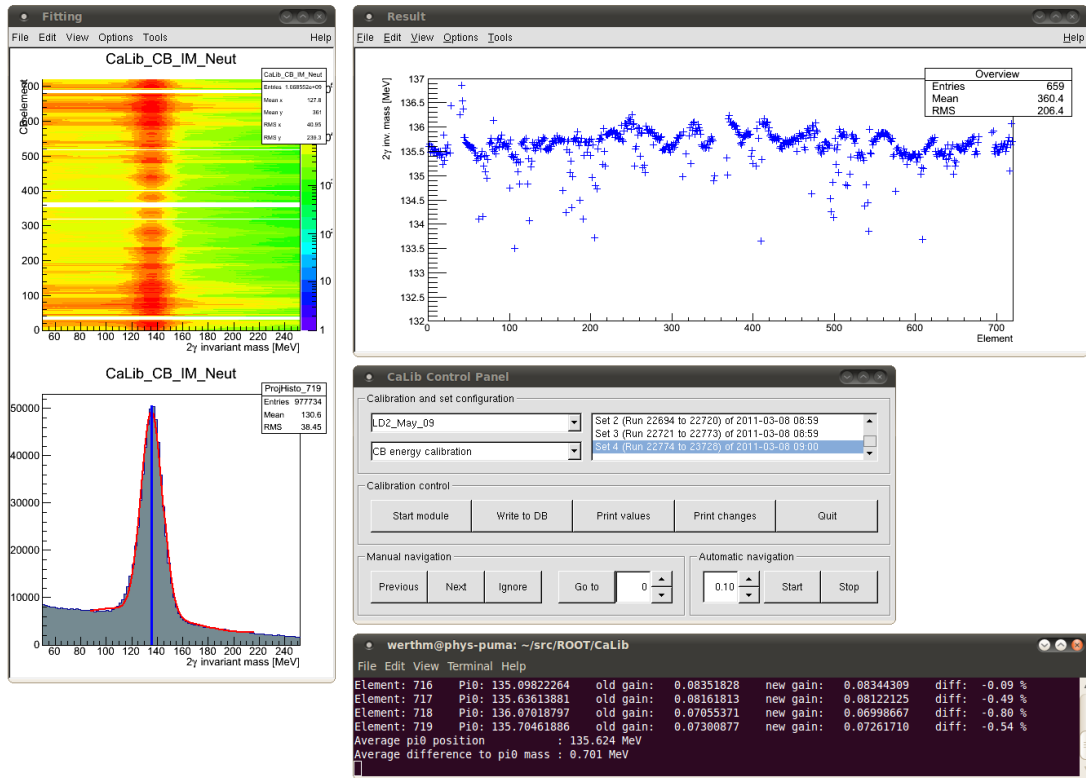
Fig. 2.13: The user interface of the CaLib software: After the selection of the beamtime, the run set and the type of the calibration, the user usually iterates over all detector elements (manually by clicking a button or automatically). Fits can be checked and corrected. An overview of all elements is shown helping to estimate the accuracy and status of the calibration. The shown active module is used for the energy calibration of CB.

I. Keshelashvili started the development of the CaLib calibration software, which is based on an SQL database system. The main principle is to have an SQL table for each calibration parameter containing columns for all detector elements. For every calibration time frame a row can be added that consists of the calibration parameters as well as a run number interval this calibration is valid. Finally, during data analysis the correct parameters for all the calibrations are read by a special class that was added to the AcquRoot analysis software.

CaLib is using the ROOT framework and contains modules that can be used to create almost all of the calibrations that will be discussed in the next chapter. Moreover, classes are included that provide interaction with the SQL database, reading and writing of AcquRoot calibration files, reading headers of ACQU raw data files as well as importing and exporting calibrations. Also a graphical user interface was implemented (see figure 2.13) to simplify and accelerate the calibration process.
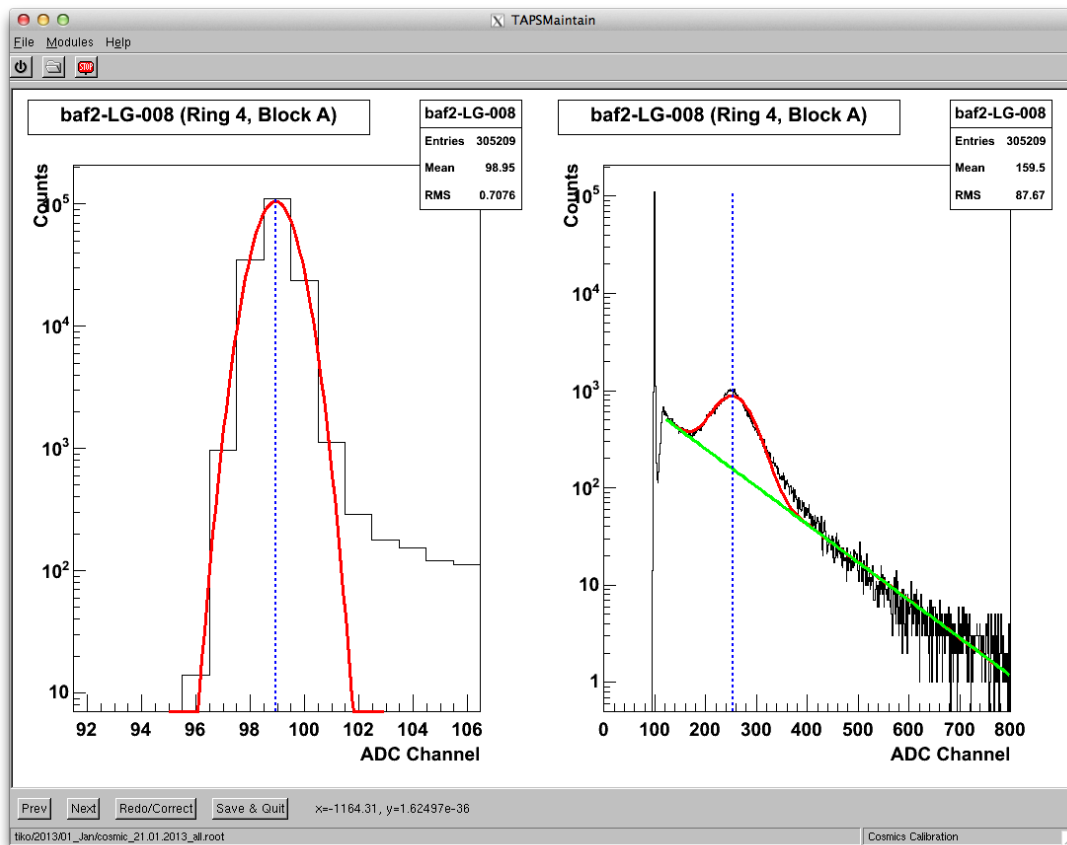
Fig. 2.14: The user interface of the TAPSMaintain software: The shown active module is used for the cosmics calibration.

The common procedure of the calibration modules is as follows: First, histograms created by the corresponding calibration analysis are loaded and merged depending on the calibration time frame to which they belong (calibration sets). Depending on the selected calibration, the necessary calculations are performed for every detector element. The user has the possibility to process all the elements automatically or to check the outcome of the calculation element by element. After all elements have been processed the newly determined calibration parameters can be saved to the database.

As part of this work, CaLib was extended and brought to a first production version that was tested intensively during the calibration for the present work. It was then also used for the calibration of the data sets measured in 2010–2011 for the extraction of polarization observables.

TAPSMaintain

TAPSMaintain was developed for the preparation of the TAPS detector before data taking. It has a flexible modular architecture so that new tasks can be easily

added in the future development cycle. At the moment, the following modules are available:

- Convenient checking of the spectra provided by the analysis of the standalone acquisition data

- Editor for the parameter database

- Transfer module for the parameter setting on the high voltage mainframes

- Cosmics energy calibration including calibration of high voltage settings and LED thresholds

- TDC gain calibration

A screenshot of the TAPSMaintain user interface showing the module for the cosmics energy calibration can be found in figure 2.14.

2.8   Beamtime overview

The data sets used in this work were obtained during three beamtimes in December 2007, February 2009 and May 2009. For each data taking, the experimental settings were slightly different. An overview of the most important parameters is given in table 2.4. The beamtime hours correspond to the data that could be used in the analysis.

Parameter	Dec. 2007	Feb. 2009	May 2009
beamtime hours	140	141	190
electron energy	1508.4 MeV	1508.4 MeV	1557.5 MeV
electron current	10 nA	5 nA	4.5 nA
tagger mean magnetic field	1.8321770 T	1.8281117 T	1.89601 T
tagged photon energies	410–1401 MeV	413–1401 MeV	423–1447 MeV
collimator	4 mm	4 mm	4 mm
radiator	10 μm Cu	10 μm Cu	Møller foil
target	LD_2	LD_2	LD_2
target length [cm]	(4.72 ± 0.05)	(4.72 ± 0.05)	(3.02 ± 0.03)
CB energy sum trigger	> 300 MeV	> 300 MeV	> 300 MeV
multiplicity trigger	M2+	M3+	M2+

Tab. 2.4: Overview of the experimental parameters of the analyzed data sets.

Chapter 3

Calibrations

In this chapter, the steps necessary for the actual data analysis will be discussed. First, the methods for the reconstruction of particles are presented in section 3.1. Subsequently, the main calibrations of energy, time and thresholds are discussed in sections 3.2 to 3.4. In section 3.5, additional calibrations that were performed will be shown. Some points concerning the simulation will be discussed in section 3.6. Finally, a summary will be given in section 3.7.

3.1 Reconstruction of particles

Slightly different methods, although based on the same principle, were used for the reconstruction of particles in the CB and TAPS detectors. In contrast, the reconstruction of electrons in the tagger is much simpler.

3.1.1 Tagger

As mentioned in section 2.2, a coincidence condition on two adjacent focal plane detector elements is made by the tagger electronics. Valid hits are stored by the data acquisition including all the times recorded by the multi-hit TCSs. Knowing the number of the focal plane tagger channel, the energy of the electron E_{e^-} is obtained in the offline analysis by the tagger energy calibration (see section 3.5.3). Finally, the energy of the bremsstrahlung photon E_γ is obtained via

$$E_\gamma = E_0 - E_{e^-},\tag{3.1}$$

where E_0 is the energy of the incoming electron beam. Subsequently, for each event in the offline analysis a list of tagger hits is created that is associated with a list of corresponding photon energies and hit times. Up to 3 hits per tagger channel provided by the multi-hit TDCs were taken into account in one event.

3.1.2   Crystal Ball

Clusters in CB are formed by an iterative algorithm. The list of hits in CB, i.e., detectors having a signal over the threshold of around 2 MeV, are sorted according to their energy. The cluster search is started with the element of maximum energy. It is marked as the logical center of the cluster and provides the hit time of the cluster. Afterwards, the detected energies in up to 13 neighboring elements are checked. If they are higher than the threshold, the corresponding elements are added to the cluster and removed from the list of hits, because one element is only allowed to contribute to one cluster. Elements with larger distances from the central cluster are not taken into account since it was found that generally 98% of the deposited energy of a photon is spread over 13 detector elements. When all neighbors were processed, the total energy of the cluster E_{cl} is calculated via

$$E_{\text{cl}} = \sum_{i=1}^{n} E_i \,, \tag{3.2}$$

using the individual energies E_i of the n detector elements that are part of the cluster. A threshold to the total cluster energy is then applied, i.e., clusters having total energies less than 20 MeV are rejected. For valid clusters, the impact position $\vec{r}_{\text{cl}}$ is estimated by calculating the square root energy weighted mean via

$$\vec{r}_{\text{cl}} = \frac{\sum\limits_{i=1}^{n} \sqrt{E_i} \cdot \vec{r}_i}{\sum\limits_{i=1}^{n} \sqrt{E_i}} \,, \tag{3.3}$$

where $\vec{r}_i$ are the centers of gravity of the single detector elements. This iterative procedure is continued until the list of hits is empty and no more clusters can be formed.

Once the list of clusters is established, possible coincidences with the PID are searched. Out of all possible hits in the PID, the best match with each cluster in CB is assigned by taking the hit with the minimal difference in the azimuthal angle. If the difference is lower than 15 degrees, the corresponding cluster is marked as charged. This angular limit was determined by taking into account the number of PID elements and the reaction vertex distribution due to the finite beam spot size on the target.

Because the PID does not provide information about the polar angle of a hit, neutral particles can be wrongly marked as charged if they are detected in the same azimuthal solid angle slice as a charged particle which fired the relevant PID element. It was found that this deficiency of the current experimental setup decreases the detection efficiency in the $\eta \to 3\pi^0$ analyses quite significantly.
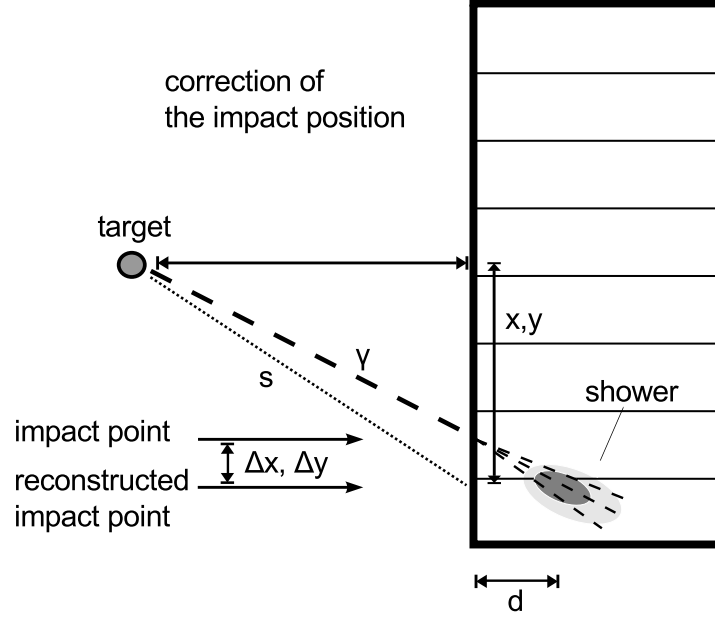
Fig. 3.1: Correction of the impact position in TAPS. Taken from [68] and edited.

3.1.3 TAPS

The cluster search in TAPS starts with the list of detector hits which passed the CFD thresholds ($\sim$3–5 MeV). The element with maximum deposited energy is established as logical cluster center and the hit time of the element is assigned as the cluster time. In the following, neighboring elements of the center are checked and added to the cluster, if they contain a valid hit. In contrast to CB, a full iteration is performed in TAPS, i.e., no limit on the added number of elements is put. The building of a cluster is stopped when no more adjacent elements containing hits are found. The total energy is calculated as in equation 3.2. For the determination of the position, logarithmic weighting is used via

$$W_i = \max\left\{0,5 + \log\frac{E_i}{\sum\limits_{i=1}^{n} E_i}\right\}, \tag{3.4}$$

$$\vec{r}_{\text{cl}} = \frac{\sum\limits_{i=1}^{n} W_i \cdot \vec{r_i}}{\sum\limits_{i=1}^{n} W_i}, \tag{3.5}$$

as determined in [69, 70]. As the faces of the TAPS detector elements are not pointing to the target (as the elements of CB) but are positioned as a detector wall, a correction on the impact position has to be performed for photons. The situation

is sketched in figure 3.1. Due to the shower depth d, which depends on the photon energy, the following correction has to be applied on the x, y-coordinates [71]:

$$x' = x - x\left(\frac{s}{d} + 1\right)^{-1} , \tag{3.6}$$

$$y' = y - y\left(\frac{s}{d} + 1\right)^{-1} , \tag{3.7}$$

$$d = X_0 \cdot \left(\log\left[\frac{E_{\mathrm{cl}}}{E_C}\right] + 1.2\right) , \tag{3.8}$$

with the radiation length $X_0 = 2.05$ cm and the critical energy $E_C = 12.7$ MeV of BaF_2, and the particle flight path s.

All clusters detected in TAPS are checked for coincidences with the Veto detectors. It is possible that a charged particle passes through the Veto detector of a neighboring detector element instead of the one installed in front of the central element of the cluster. Due to the smaller angles of the particle trajectories with respect to the TAPS surface, this is especially the case for elements in the outer rings. Therefore, not only the Veto detector in front of the central element is checked, but also the corresponding Veto detectors of all neighbors of the central element and in addition the ones in front of all cluster members. If at least one coincident signal in a Veto element is found, the cluster is marked as charged.

3.2   Energy calibrations

Energies deposited in scintillators are normally measured by integrating an electrical signal over a specific time getting an electrical charge. The corresponding analog to digital converters are called charge to digital converters (QDC). When using this kind of energy measurement, the produced charge is in first approximation linearly dependent on the deposited energy. Hence, the following relation between the digitized and discretized charge in terms of the digital channel c and the physically deposited energy E_{dep} [MeV] can be established:

$$E_{\mathrm{dep}} = g \cdot (c - p) \tag{3.9}$$

The constant of proportionality g [MeV/channel] is called conversion gain. p [channel] is the pedestal position representing the channel that corresponds to zero energy (base signal). The goal of the energy calibration is to find the correct values for g and p.
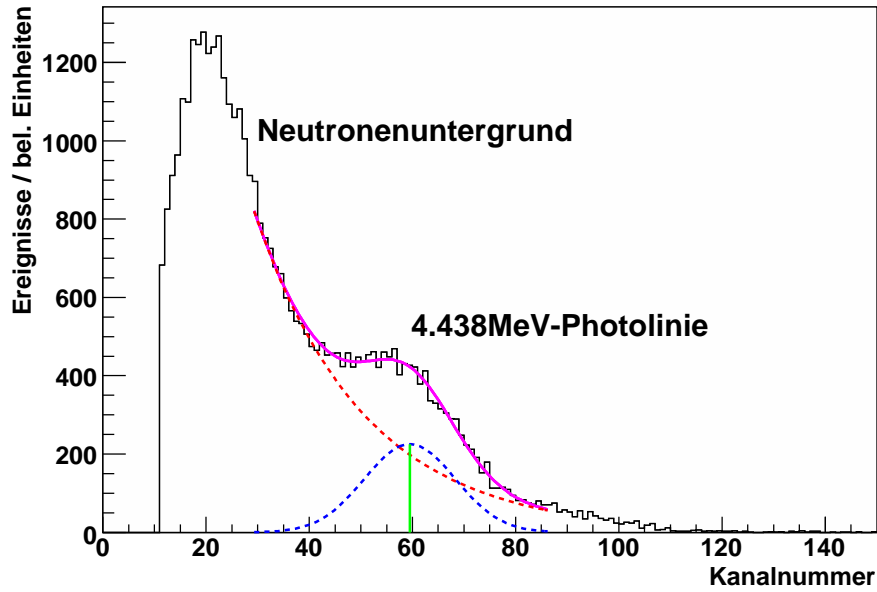
Fig. 3.2: Raw energy spectrum of a single NaI(Tl) crystal obtained with a ^{241}Am/^{9}Be source: Red curve: exponential function for neutron background. Blue curve: Gaussian for photon peak. Magenta curve: total fitting function. The position of the photon peak corresponds to 4.438 MeV. Taken from [72].

3.2.1 Crystal Ball

The energy calibration of the Crystal Ball was performed in several steps. First, a low energy calibration that is mainly important for the acquisition system was obtained. For the offline analysis, a second calibration valid for higher photon energies had to be made. Finally, a higher order correction was applied.

Low energy calibration

In the trigger electronics (see section 2.6.2) thresholds to Crystal Ball detector signals are applied in various places. Therefore, a good relative energy calibration of all detector signals with respect to each other is needed in order to ensure equal discrimination of all the signals. For this calibration, a ^{241}Am/^{9}Be source was used [73]. The α-particles emitted by the radioactive ^{241}Am are captured by ^{9}Be leading to a reaction chain that ends with an excited state of ^{12}C, which finally emits monochromatic photons with an energy of 4.438 MeV. The gains of all photomultipliers were adjusted in a way that the peak caused by these photons was located at the same position in the ADC spectrum for all detector elements (see figure 3.2).
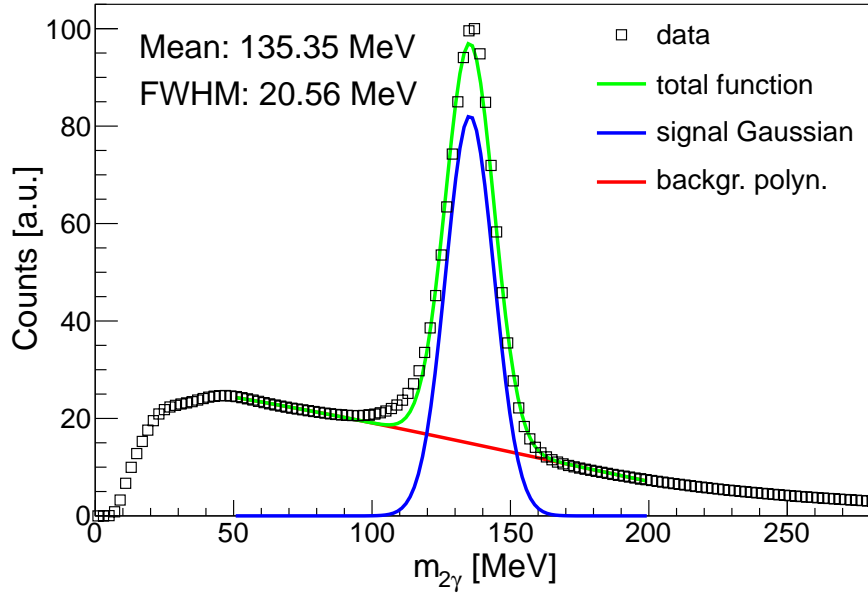
Fig. 3.3: Peak of π^0-meson in the two photon invariant mass used for the CB high energy calibration: Black squares: experimental data (sum of all detector elements). Red curve: polynomial for background. Blue curve: Gaussian for signal. Green curve: total fitting function. Data from May 2009 beamtime.

High energy calibration

During the experiment, photons detected in the Crystal Ball have energies up to two orders of magnitude higher than the ones used for the low energy calibration. Therefore, a calibration method involving photons with higher energies has to be applied to obtain the best precision. When a hydrogen target is used in the experiment, an exclusive measurement of the reaction $\gamma p \to \pi^0 p$ can be used for that purpose. Its kinematics is overdetermined, i.e., the energy of the π^0-meson and consequently the energies of the decay photons can both be calculated and measured. The conversion gains of the QDCs can then be adjusted until an agreement between the two values is found. When using nuclear targets, the kinematics of this reaction is no longer overdetermined and an other calibration method has to be applied. In this work, the peak of the π^0-meson in the invariant mass spectrum of two photons (see section 4.3.2) was used as a reference point. Using all neutral clusters, the invariant mass was calculated for all cluster pairs and filled into different histograms depending on the central detector element of the clusters. The mean position of the π^0-meson in the invariant mass spectrum of two photons, one of them having the central element i, can be approximated as

$$\langle m_{\pi^0, i} \rangle = \sqrt{2 \langle E_{\pi^0, i} \rangle \langle E_{\pi^0, o} \rangle \left(1 - \cos \langle \psi_{\pi^0, io} \rangle \right)}. \tag{3.10}$$

$\langle E_{\pi^0,i} \rangle$ and $\langle E_{\pi^0,o} \rangle$ are the mean photon energies of the element i and the other elements, respectively. $\langle \psi_{\pi^0,io} \rangle$ is the mean opening angle of one photon detected in element i and one photon detected in an other detector. The mean energy $\langle E_{\pi^0,i} \rangle$ is directly proportional to the mean value of the integrated signal $\langle I_{\pi^0,i} \rangle$ in the sampling ADCs due to the automatic pedestal subtraction (see section 2.6.1):

$$\langle E_{\pi^0,i} \rangle = g_i \cdot \langle I_{\pi^0,i} \rangle \tag{3.11}$$

The goal of the calibration is now to find the appropriate conversion gain g'_i so that

$$\langle m'_{\pi^0,i} \rangle = \sqrt{2 \langle E'_{\pi^0,i} \rangle \langle E_{\pi^0,o} \rangle \left(1 - \cos \langle \psi_{\pi^0,io} \rangle \right)} \stackrel{!}{=} m_{\pi^0} , \tag{3.12}$$

i.e., the mean invariant mass should be equal to the mass of the π^0-meson. Writing equation 3.11 for the uncorrected gain g_i and the corrected gain g'_i leads to

$$g'_i = g_i \cdot \frac{\langle E'_{\pi^0,i} \rangle}{\langle E_{\pi^0,i} \rangle} , \tag{3.13}$$

and from equations 3.10 and 3.12 the following relation can be found to obtain the corrected gain:

$$g'_i = g_i \cdot \frac{m_{\pi^0}^2}{\langle m_{\pi^0,i} \rangle^2} \tag{3.14}$$

Because changing the gain of one detector influences the calibration of the other detectors via $\langle E_{\pi^0,o} \rangle$ and $\langle \psi_{\pi^0,io} \rangle$, and because $\langle E_{\pi^0,i} \rangle$ contains also contributions from its neighboring elements, the corrected gains have to be calculated iteratively. Depending on the quality of the initial values, up to 15 iterations had to be performed to align the peak of the π^0-meson at the correct position for all elements. $\langle m_{\pi^0,i} \rangle$ was determined as the center of a Gaussian that was fitted in combination with a polynomial to the invariant mass spectrum of the detector element i. A typical summed spectrum of all elements after the performed high energy calibration is shown in figure 3.3.

Quadratic energy correction

When the high energy calibration is finished, the peak of the π^0-meson is located at the correct position in the spectrum of the two photon invariant mass. However, the peak of the η-meson in the same spectrum is located at a higher value with respect to its nominal mass. This is caused by an overcorrection of the energy calibration at higher deposited energies. Because part of the photon energy is lost due to detector thresholds and shower losses (the latter most clearly visible for detector elements at the edge of CB), the high energy calibration described above incorporates corrections for these effects as the peak of the π^0-meson is finally at the correct position. Since the relative weights of the energy losses are smaller

for higher cluster energies, the calibration leads to an overcorrection at higher energies in case of, e.g., decay photons of η-mesons.

A quadratic function applied to the deposited energy E is chosen [68] to correct wrongly reconstructed energies:

$$E' = a \cdot E + b \cdot E^2 \tag{3.15}$$

The parameters a, b are determined under the condition that the corrected energies should result in correct invariant masses for both the π^0- and the η-meson, i.e., the mean values of their invariant mass distributions should correspond to their nominal masses:

$$\langle m'_{\pi^0} \rangle = \sqrt{2 \langle E'_{\pi^0} \rangle^2 (1 - \cos \langle \psi_{\pi^0} \rangle)} \overset{!}{=} m_{\pi^0} \tag{3.16}$$

$$\langle m'_{\eta} \rangle = \sqrt{2 \langle E'_{\eta} \rangle^2 (1 - \cos \langle \psi_{\eta} \rangle)} \overset{!}{=} m_{\eta} \tag{3.17}$$

The mean energies of photons $\langle E'_{\pi^0} \rangle$ and $\langle E'_{\eta} \rangle$ coming from π^0- and η-meson decays, respectively, were determined from the experimental data. Knowing these values, the parameters a, b can be calculated using equations 3.16 and 3.17 under the assumption that the mean opening angles of the decay photons of both mesons do not change when applying the energy correction. Individual correction parameters were determined for every detector element.

3.2.2 TAPS

As for the Crystal Ball detector, the energy calibration of TAPS was performed in several steps: The first rough calibration using cosmic radiation is necessary for data taking, whereas for the offline analysis further procedures were needed to obtain a precise calibration.

Cosmics calibration

Most of the electromagnetic background and a significant part of the recoil nucleons (depending on the reaction) is emitted in forward direction and is detected in TAPS. Therefore, already during data taking it is crucial to have an accurate energy calibration, which allows a precise setting of thresholds.

In contrast to CB, the TAPS detector elements are all placed horizontally and hence cosmic radiation can be used for calibration, as the distribution of their trajectories are equal for all crystals. Making use of cosmic radiation has the advantage that neither a beam nor a radioactive source is needed and the calibration can be performed at any time. Normally, calibration measurements were carried out before and after data taking and sometimes during breaks to monitor the stability of the calibration.
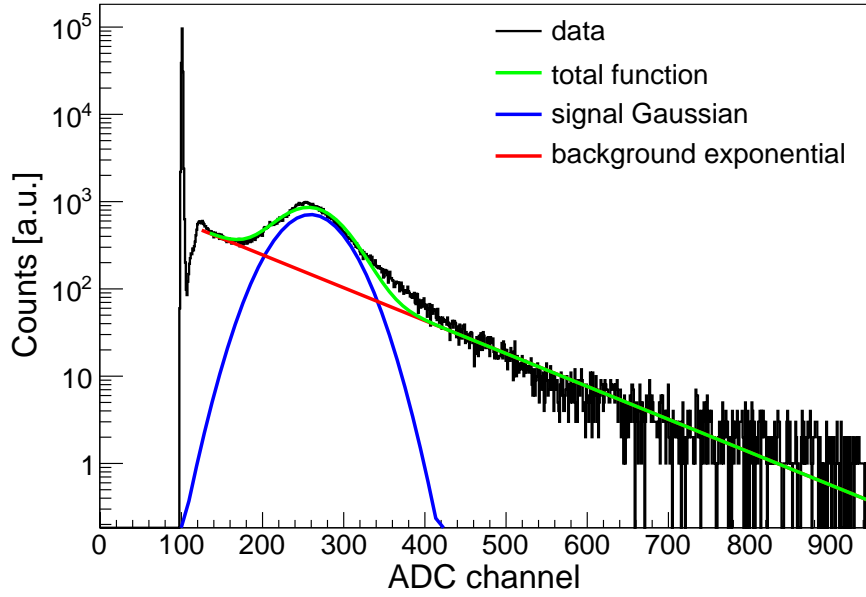
Fig. 3.4: Raw energy spectrum of a single BaF$_2$ crystal obtained with cosmics: Black histogram: data. Red curve: exponential for background. Blue curve: Gaussian for cosmics peak. Green curve: total fitting function. The position of the cosmics peak corresponds to 37.7 MeV. The pedestal is located around channel 100.

The mean deposited energy of minimum ionizing particles in the BaF$_2$ crystals was determined to be 37.7 MeV [74]. A typical raw spectrum is shown in figure 3.4. The distribution can be fitted with a Gaussian and an exponential background function, and consequently the channel that corresponds to the mean deposited energy can be extracted. Also the pedestal position can be determined and using equation 3.9 the conversion gain can be calculated. This was done before all beamtimes to normalize the gains of the individual detectors by adjusting the high voltage of the photomultipliers and to establish a first rough energy calibration.

High energy calibration

In the offline analysis, the pedestal position was determined from the raw ADC spectra of the production data runs. For the calibration of the gains, the same method as used for CB was applied. Due to insufficient statistics, π^0-mesons with both decay photons in TAPS could not be used. One photon was required to be in CB, making the calibration dependent from the CB energy calibration. As a consequence, the TAPS energy calibration had to be made after the final CB energy calibration was established.

Quadratic energy correction

Requesting again one of the decay photons of the π^0- and the η-meson, respectively, in TAPS and the second one in CB, the same procedure for the quadratic energy correction as for CB was applied for TAPS.

3.2.3   PID

The method described in [75] was used to calibrate the deposited energy in the PID. The basic idea is to determine the correct pedestal and conversion gain values such that the deposited energy of a proton agrees with the simulated value. Consequently, events involving protons were simulated (see section 2.7.2) and their energies deposited in the PID were plotted versus the energies deposited in CB (see section 4.4.3). For the experimental data, the same plots were made (selecting $\gamma p \rightarrow \pi^0 p$ events), but instead of taking the deposited energies in the PID (which would already require an initial calibration), the raw ADC values were plotted versus the energy in CB. Subsequently, projections of this histogram were made for different energy ranges in CB and the proton peak positions were fitted both for simulated and experimental data. In the end, the fitted values obtained from real data were plotted versus the corresponding values from simulation and the dependence was fitted with a linear function. Using the two fit parameters, the pedestal value and the conversion gain could be directly calculated.

3.2.4   Veto

Due to their vertical installation, cosmic radiation can normally not be used to calibrate the Veto detectors. However, for maintenance work the complete Veto wall can be dismounted and placed horizontally on the floor, which allows a calibration using cosmics. As this was not done during the beamtimes for this work, the Veto detectors were calibrated directly using the production data. The pedestal positions could be extracted from the raw ADC spectra. The conversion gain was calculated, similarly to the PID, by comparing the proton energy deposition in experimental data and simulation.

3.3   Time calibrations

Detector hit times can be measured with time to digital converters (TDC). Giving a start and a stop signal, TDCs map the timespan to a discrete channel value. The relation between the physical time t [ns] and the channel number c is

$$t = g \cdot (c - o), \tag{3.18}$$

Detector	Start	Stop	Time
Tagger CB PID	trigger	detector	$t = t_{\text{det}} - t_{\text{trig}}$
TAPS Veto	detector	trigger	$t = t_{\text{trig}} - t_{\text{det}}$

Tab. 3.1: Overview of detector timings: t is the TDC time, t_{trig} is the trigger time and t_{det} is the detector time.

where g is the conversion gain [ns/channel] and o [channel] is an offset. The goal of the time calibration is to find the correct values for g and o. Whereas the conversion gain is an intrinsic value of the used TDC, the offset can be chosen freely. Normally, the offsets of all detectors are adjusted in a way that the coincidence peaks of photons are centered at zero.

Depending on the detector, different start and stop times are used. Some TDCs are started by the signal of their associated detector and are stopped by the trigger (common stop), whereas others are started by the trigger and are stopped individually (common start). Table 3.1 gives an overview of all detector timings. When calculating time differences between different detectors, it is important to ensure that the trigger time cancels, as it is affected by jittering which decreases the resolution. Hence, depending on the detector combination, the time 'difference' is either the sum or the difference of their individual times.

A precise time calibration is crucial for the subtraction of the tagger random coincidences, time-of-flight measurements and coincident hit analyses. In the following sections, the time calibrations of the different detectors are described. The main principle remains the same, however, for some detectors special corrections have to be applied.

3.3.1 Crystal Ball

Signals of NaI(Tl) crystals have a rather slow rise time. Therefore, the time at which the signal exceeds the threshold in the LEDs strongly depends on the amplitude of the signal, i.e., the deposited energy in the crystal. For this effect, known as time walk, a special correction has to be applied.

The conversion gain g of the CATCH TDCs used for the CB timing is fixed to 117 ps. Therefore, only the offset o has to be determined. In total, three steps were necessary in order to achieve a precise time calibration for CB.
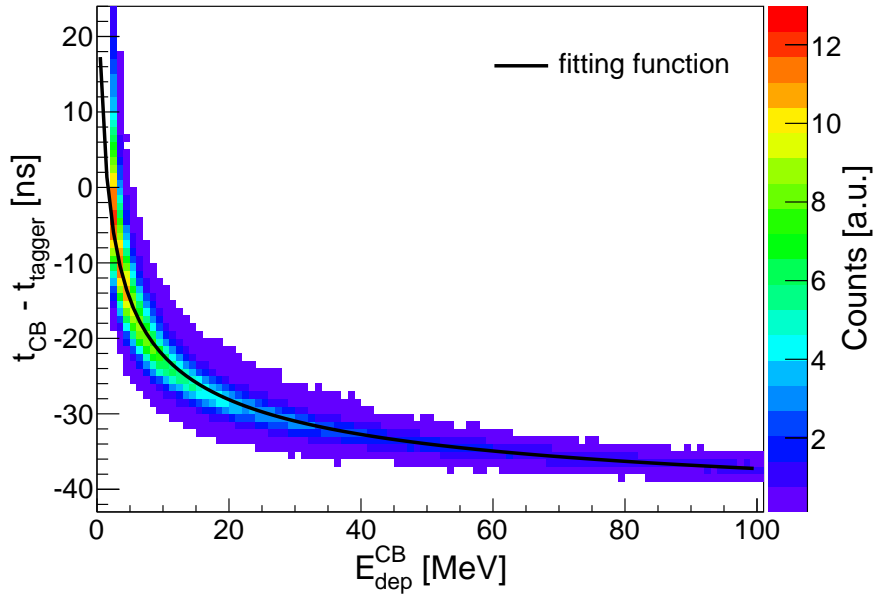
Fig. 3.5: CB time depending on deposited energy showing the time walk effect: Black curve: fitting function (equation 3.20). Data from May 2009 beamtime.

Time prealignment

First, the time differences of all cluster hit combinations in Crystal Ball were calculated depending on the central elements of the clusters. As no coincident hit in the PID was requested, mostly clusters originating from photons were selected and slow charged particles with larger times were rejected. The distributions of the time differences for every detector element i were fitted with Gaussians and from the mean values m_i new individual offsets o'_i were calculated via

$$o'_i = o_i + \frac{m_i}{g_i} \,, \tag{3.19}$$

with the old offsets o_i and the gains g_i, whereas the latter were the same for all elements in case of CB. This procedure was performed iteratively and converged sufficiently fast, so that in the end the mean values of all time differences were centered at zero.

Time walk calibration

Because the signals in the NaI(Tl) crystal have a slow rise time and LEDs are used in the electronics, the time signals are affected by time walk. This energy dependence of the time has to be corrected to maximize the time resolution in CB.

The main principle to establish the time walk correction is to plot the time versus the energy for every detector element, followed by a fit of an appropriate

function to the energy dependence. For background suppression, only events from π^0-production were used for that purpose, selected by cuts on the invariant mass of two photons and on the π^0 missing mass (see section 4.3.3). The relative timing to the tagger was used to calculate the time of all detector elements of the two photon clusters. Spectra of these times depending on the deposited energies in the detectors were obtained as shown in figure 3.5. They were fitted with the function

$$t(E_{\text{dep}}) = a + \frac{b}{(E_{\text{dep}} + c)^d} \, , \tag{3.20}$$

with four free parameters a, b, c, d. These parameters, individually determined for all detector elements, were used in the following to correct the energy dependence of the detector times via

$$t' = t - \left(a + \frac{b}{(E_{\text{dep}} + c)^d} \right) . \tag{3.21}$$

The corrected times t' are then automatically centered at zero with respect to the tagger because the time difference to the tagger was used to calculate the correction.

Final rise time calibration

Due to inaccurate fits during the time walk correction, especially for low statistics backward detector elements, the relative timing between CB detector elements could be slightly shifted. This can be restored by fitting the mean values of the relative times again after having applied the time walk correction. The rise time parameter a in equation 3.21 can then be readjusted to center the relative times at zero again.

3.3.2 TAPS

Since the distance from the target to TAPS is sufficiently long and the BaF_2 crystals have a very good time resolution, time-of-flight measurements can be performed for particles detected in TAPS. To maximize the resolution, a precise time calibration of the TAPS TDCs was performed. As the time measurement for the BaF_2 elements is started by CFDs and due to the short signal rise time, it was not necessary to perform a time walk correction.

TDC gain calibration

The TDC conversion gains are usually determined before data taking using the following procedure [76]. The common stop signal of all the TAPS detectors is
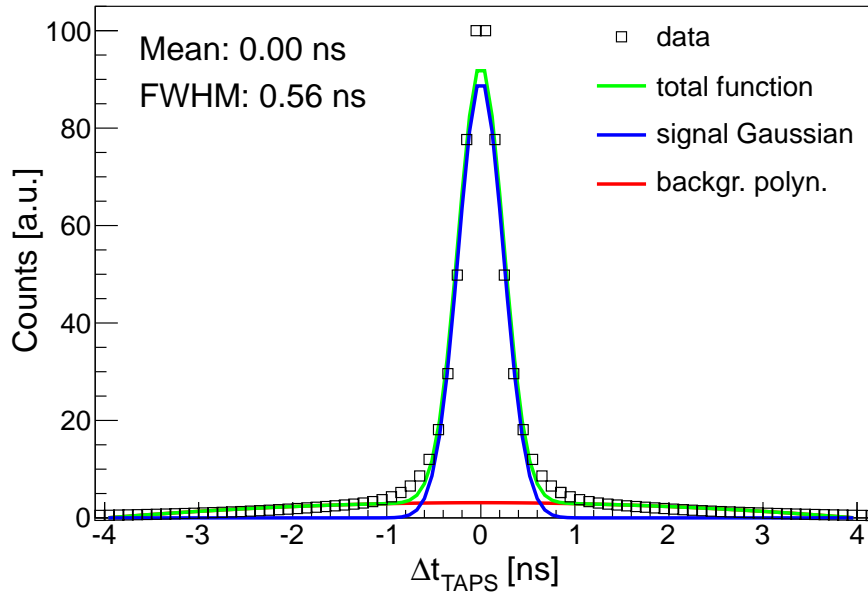
Fig. 3.6: TAPS-TAPS coincidence time spectrum: Black squares: experimental data (sum of all detector elements). Red curve: polynomial for background. Blue curve: Gaussian for signal. Green curve: total fitting function. Data from May 2009 beamtime.

delayed by adding a series of cables with known delay to the electronic circuit one by one. The exact delays of the used 10 ns cables were measured using a signal generator and an oscilloscope. The frequency of the pedestal pulser is increased and short TAPS standalone measurements are performed. The position of the pedestal pulser signal is then fitted for every measurement. Afterwards, the differences of the delays are plotted versus the differences of the pulser positions. Finally, the data points are fitted linearly and the gain is extracted as the slope of the fitting function. This procedure was carried out for all the BaF$_2$ elements resulting in individual TDC gains for all detectors.

TDC offset calibration

The time offsets were calibrated in the offline analysis using the production experimental data. Spectra of the time differences of all combinations of neutral particles in TAPS were created with respect to the corresponding central cluster detectors. In the following, the same technique as for the time prealignment of the CB time was used. The positions of the coincidence peaks were fitted and new offsets were calculated using equation 3.19. This was done iteratively until all peaks were centered at zero. Figure 3.6 shows the summed spectrum of all detector elements after the calibration for the May 2009 beamtime.
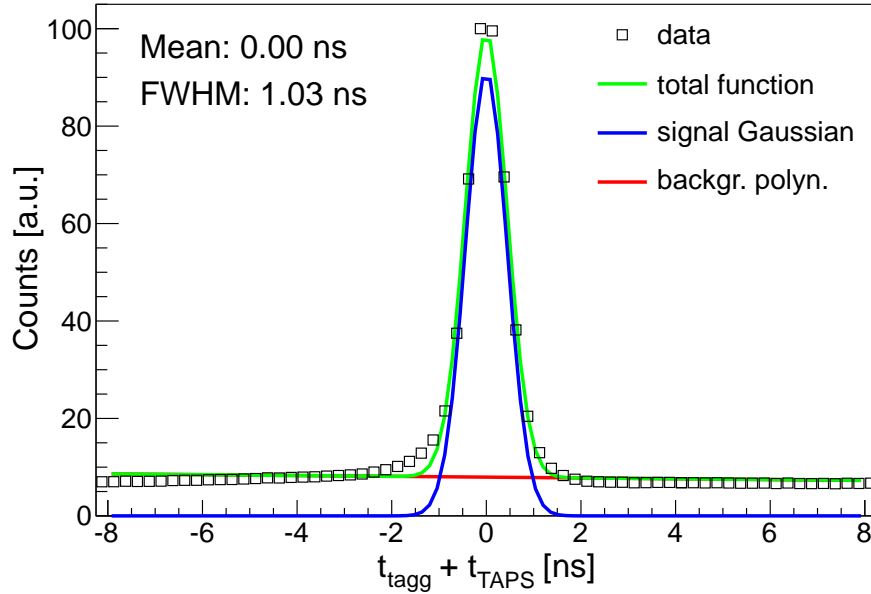
Fig. 3.7: Tagger-TAPS coincidence time spectrum: Black squares: experimental data (sum of all detector elements). Red curve: polynomial for background. Blue curve: Gaussian for signal. Green curve: total fitting function. Data from May 2009 beamtime.

3.3.3 Tagger

The time measurements in the tagger were also performed by CATCH TDCs with fixed conversion gains, leaving only the offsets to be calibrated. This was implemented by the use of TAPS. Hence, TAPS had to be already fully calibrated before the tagger calibration could be started. Spectra of the time differences of all combinations of neutral particles in TAPS and hits in the tagger were created individually for each tagger channel. The positions of the coincidence peaks were determined and new offsets were calculated from equation 3.19. If the positions were estimated properly, one iteration was sufficient to achieve the final calibration, as there is no dependence between the tagger channels. Figure 3.7 shows the summed spectrum of all detector elements after the calibration for the May 2009 beamtime.

3.3.4 PID and Veto

The times of the PID and the Veto detectors were not used in this work. Therefore, only a rough calibration was performed to align the relative timings of the individual elements. This was done using the same iterative method described above by centering the relative coincidence peaks of the individual detectors at zero.

3.3.5   Order of calibration

As some time calibrations are made by making use of other detectors, there are some dependencies, which lead to a fixed order of calibration. TAPS had to be calibrated first, because its calibration is independent but needed for the calibration of the tagger. The calibration of TAPS sets the relative differences in the hit times of photons to zero. Calibrating then the tagger by using TAPS shifts the TAPS-tagger photon coincidence peaks to zero as well. Consequently, the time walk coefficients of CB are determined relative to the tagger times, which leads to the fact that also the CB-tagger photon coincidences are located at zero. Therefore, also the relative CB-TAPS timings are finally aligned.

3.4   Detector threshold calibrations

Thresholds were used in the trigger process and for individual detector elements. In both cases, they affected strongly the detection efficiency of the setup. Therefore, thresholds applied to the experimental data had to be determined accurately since the same thresholds had to be used in the simulation.

3.4.1   CB high thresholds

The CB high thresholds are applied in 45 discriminator blocks, each processing signals of 16 CB elements connected via logical OR. These discriminators are used for the multiplicity trigger in CB (see section 2.6.2). Although the signal threshold is the same for all 16 detectors, the resulting thresholds in terms of calibrated energies are different, since the individual signals have different calibration parameters. Unfortunately, the indices of the elements that passed the threshold are not recorded in the data stream. Therefore, the method described in [48, 72] was applied to reconstruct the individual energy thresholds for all CB detector elements.

For each discriminator block, the element having the maximum of deposited energy was determined, as this was considered to be the element that passed most probably the threshold. A list consisting of the maximum energies and the corresponding element indices was then created from all blocks and sorted according to the energies. Using the same method for TAPS with its six logical discriminator segments, this list was completed with the information of TAPS. The hits in TAPS had to be taken into account because the TAPS blocks were also allowed to contribute to the total multiplicity. For events with M2+ or M3+ triggers, the two or, respectively, three highest energies were then filled into a spectrum for the corresponding detector element (either of CB or TAPS).
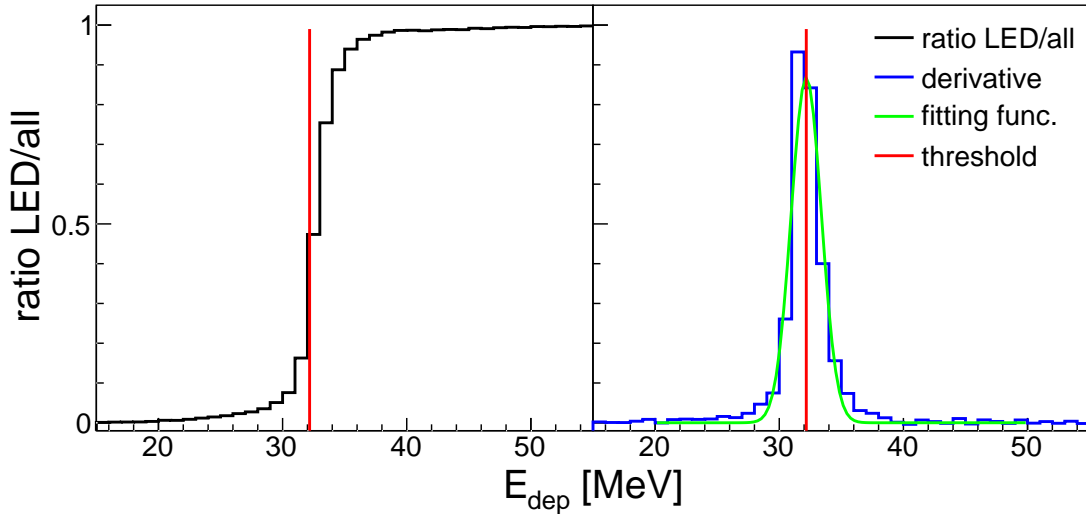
Fig. 3.8: Determination of the TAPS LED thresholds: Left-hand side: ratio of LED hits and all hits (black histogram). Right-hand side: scaled derivative of ratio (blue histogram), Gaussian fitting function (green curve). Red line: threshold marker. Data from May 2009 beamtime.

The resulting spectra for the CB elements showed the clear influence of the thresholds. At a certain energy, a steep rise of the counts could be observed. In each spectrum, the threshold value was determined by calculating the discrete derivative of the spectrum. The resulting distribution showed a maximum at the threshold position that was fitted with a Gaussian. The so obtained mean was then used as threshold value for the corresponding detector element. The CB high thresholds were in the order of ∼10–30 MeV in the current experiment.

The obtained spectra for TAPS could in principle be used for the determination of the LED thresholds in TAPS, using the same method as for CB. But, as the LED pattern is recorded in the data stream in case of TAPS, the thresholds were determined directly from the pattern, which was considered to be more accurate.

3.4.2 TAPS LED thresholds

The TAPS LED thresholds, which are used for the multiplicity trigger, can be set individually for all BaF_2 detectors. The actual values depend on the experiment and are normally set at the beginning of data taking. Often, the thresholds are varied with respect to the detector ring, e.g., the thresholds for inner rings are increased to suppress contamination from electromagnetic background in the trigger. However, for this work equal thresholds of around 30 MeV were set. The threshold values were calculated using the cosmics calibration. Therefore, an additional redetermination using the final photon calibration had to be performed in the offline analysis.

As the LED pattern is recorded in the data stream, the calibration is rather straight-forward. For each TAPS element, an energy spectrum containing all hits, and one containing only hits with a coincident LED hit were created. The ratio of the two spectra showed a sharp rise from 0 to 1 due to the threshold. This can be seen in a typical spectrum shown in the left part of figure 3.8. As for CB, the peak in the distribution of the derivative was fitted with a Gaussian to extract the threshold value, as shown on the right-hand side of figure 3.8. As intended, the resulting thresholds were in the order of $\sim$30 MeV.

3.4.3   TAPS CFD and Veto LED thresholds

The thresholds for individual BaF_2 and Veto elements are set by CFDs and, respectively, LEDs. An accurate calibration of the corresponding thresholds is essential, especially for the detection efficiencies of neutrons and protons. Instead of using a common maximum value for all elements, a relative calibration for both was estimated.

The raw ADC spectra of the BaF_2 and the Veto detectors were created from the standard production data. The positions of the threshold were then estimated from the derivatives of the spectra, as discussed above. The conversion from channel to energy was performed by using the calibration of the corresponding calibration set. Finally, individual channel thresholds for the complete data set were calculated by the maximum values of all calibration sets.

3.5   Other calibrations

Apart from energy, time and threshold calibrations, several other types of calibrations were performed, which will be described in the following part.

3.5.1   PID azimuthal angle calibration

The mean azimuthal angle for all PID elements has to be known for the identification of charged particles in CB, where correlations of hits in the PID and clusters in CB are established by comparing the ϕ-differences.

The PID detector has to be removed during maintenance of the MWPC or the target. When reinstalled, the correlation with CB in the azimuthal angle has to be redetermined. This is done in the offline analysis by selecting events with exactly one cluster in CB and one hit in the PID. Using this strong event condition reduces statistics but helps on the other hand to extract the coincidence signal with less background. Spectra for each of the 24 PID elements are created containing the azimuthal angle of the clusters detected in CB. A typical spectrum is shown in
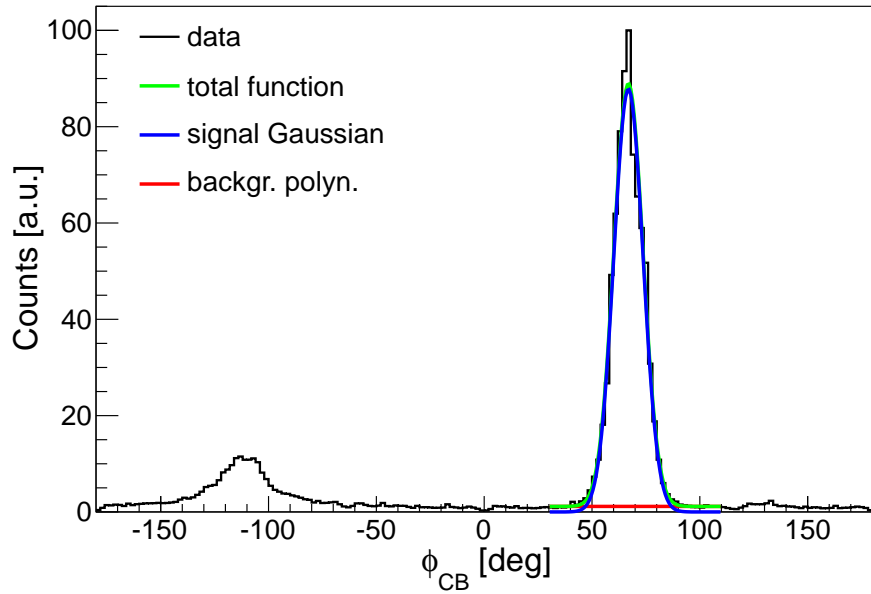
Fig. 3.9: Spectrum of CB cluster azimuthal angle with coincident PID hit: Black histogram: data of one PID element. Red curve: polynomial for background. Blue curve: Gaussian for coincidence peak. Green curve: total fitting function. Data from May 2009 beamtime.

figure 3.9. A clear coincidence peak can be seen, which is fitted with a Gaussian function combined with a polynomial for the small background contribution. The lower peak at azimuthal angles shifted by 180 degrees is caused by reactions which emit a charged and a neutral particle back-to-back, where the charged one is not detected in CB.

Systematic uncertainties of the individual fits are reduced by a global fit of all extracted angles. This is done by plotting the ϕ-angles versus the PID element indices. A linear fit is performed and from the fitting function the corresponding azimuthal angles of all PID elements can be calculated.

3.5.2 Barium fluoride short gate calibration

The signals of the BaF_2 crystals are integrated over a short and a long time interval to take into account the two scintillation light components of BaF_2 (see section 2.6.1). The correlation of the two resulting energies can be used for the discrimination of photons and protons/neutrons in TAPS using pulse-shape-analysis (PSA).

Having already calibrated the energies of the standard (long) integration gate, pedestal and gain of the short gate ADCs are initialized with the values obtained in the cosmics measurement. For particle discrimination, it was found convenient
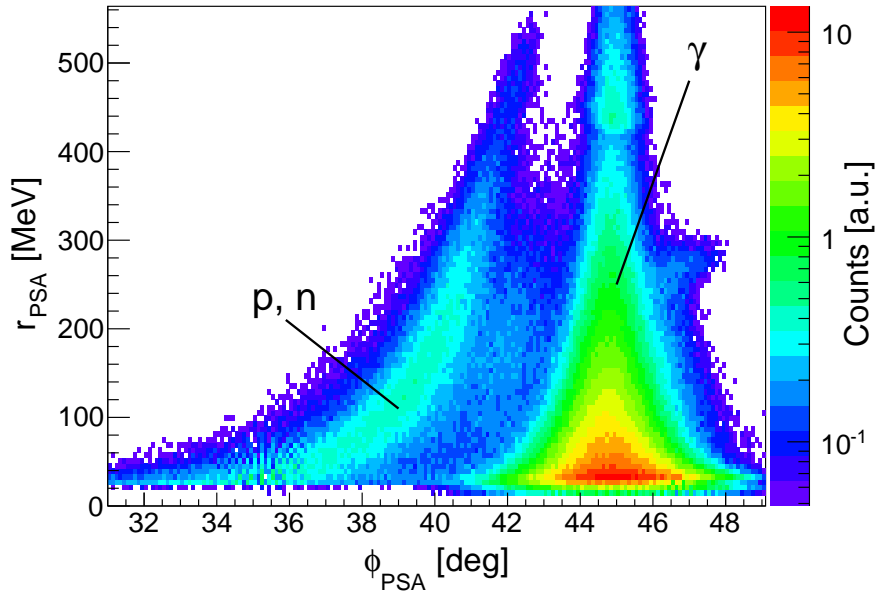
Fig. 3.10: TAPS BaF$_2$ PSA spectrum: Nucleons are located in the banana-shaped structure below 45 degrees, while photons are distributed around 45 degrees for all radii. Data from May 2009 beamtime.

[71] to use the following transformation for the long gate energies E_l and the short gate energies E_s:

$$\phi_{\text{PSA}} = \arctan\left(\frac{E_s}{E_l}\right) \tag{3.22}$$

$$r_{\text{PSA}} = \sqrt{E_s^2 + E_l^2} \tag{3.23}$$

When the PSA-radius r_{PSA} is plotted versus the PSA-angle ϕ_{PSA}, characteristic band-like structures can be seen for the different particles, as shown in figure 3.10. The short gate energies are calibrated such that $E_s = E_l$ for photons, i.e., the photons should be located at PSA-angles of 45 degrees for all PSA-radii. Protons and neutrons have smaller PSA-angles and their PSA-radii show a typical dependence of the PSA-angles (banana-shaped structures).

For the calibration process, all clusters in TAPS are selected and their ϕ_{PSA} and r_{PSA} are calculated using the short- and long-gate energies of their central elements. Spectra as shown in figure 3.10 are filled depending on the central elements. The positions of the photon bands are determined within two r_{PSA}-intervals at low and high PSA-radii, respectively, using Gaussian fits to the interval projections on the ϕ_{PSA}-axis. From the two estimated PSA-angles and the two mean PSA-radii of the projected intervals, new values for the pedestal and gain were calculated requesting $E_s = E_l$. This problem has in principle one analytic solution, as there are two equations for two unknown variables. But, due to systematic errors in the

fitting procedure described above, several iterations had to be performed until convergence was reached.

The calibration was carried out for all detector elements individually, which resulted finally in an alignment of the particle bands in the summed spectrum of all detectors.

3.5.3 Tagger energy calibration

The calibration of the electron energies in the tagger depends on the magnetic field strength of the tagger dipole magnet and the incoming electron beam energy. The latter is very stable, while the first can vary between beamtimes. During a beamtime, on the other hand, the magnetic field is normally very stable and is monitored continuously via an NMR measurement.

The association of electron energies with tagger channels was performed by the calibration program `ugcalv2ua` [47, 77]. It takes into account the incoming electron beam energy and the average magnetic field of a beamtime and calculates an electron energy calibration for all tagger channels. The calculation is using a uniform field map, which is based on several field measurements. In addition, tagger calibration measurements were performed, for which the electron beam is bent at low intensity directly into the tagger magnet and is detected in the focal plane detectors. Measurements at different electron energies and magnetic fields were performed to determine a linear relationship between the electron energies and the tagger channel numbers. The calibration is interpolated for all channels and additional phenomenological corrections for nonuniformities are applied. Finally, the mean electron energies and the widths of the corresponding energy windows can be calculated for all channels.

3.6 Calibration of the simulation

The following steps were performed on and using the data generated by the simulation before it was used in the same data analysis as experimental data.

Energy calibration

The high energy and the quadratic energy calibrations for CB and TAPS were performed with simulated data equivalently as for experimental data to shift the peak positions of π^0- and η-mesons in the two photon invariant mass to their nominal masses.
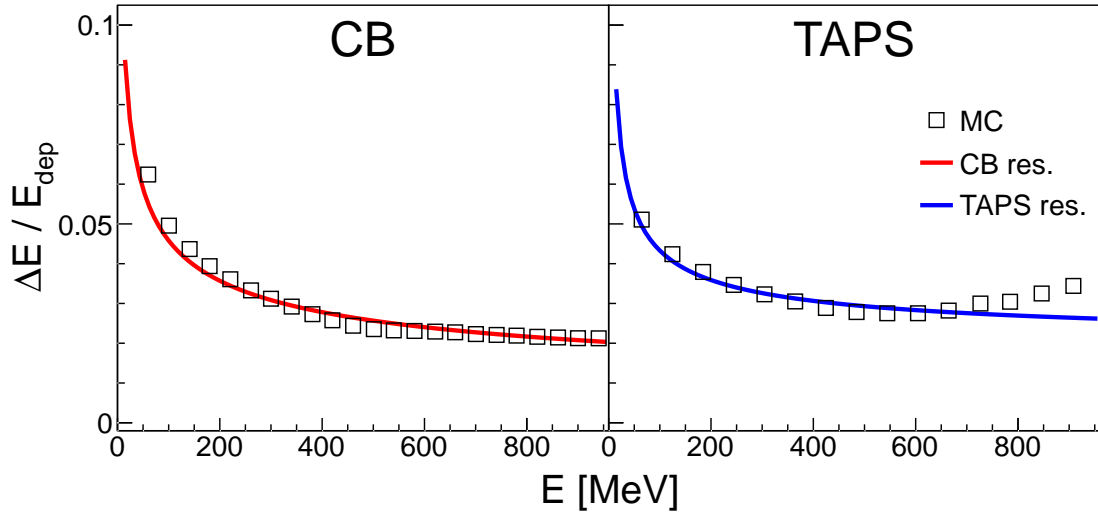
Fig. 3.11: Energy resolution for photons in CB and TAPS obtained from simulation: Left-hand side: CB. Right-hand side: TAPS. Black squares: simulated data. Curves: resolution parametrizations for CB (red, eq. 3.24) and TAPS (blue, eq. 3.25).

Energy resolution

The simulated deposited energies in the NaI(Tl) crystals of CB and the BaF$_2$ crystals of TAPS were artificially smeared to reproduce the photon energy resolution in the corresponding detectors given by the following parametrizations [35]:

$$\frac{\Delta E}{E_{\text{dep}}} = \frac{2\%}{(E[\text{GeV}])^{0.36}} \qquad \text{(CB)} \qquad (3.24)$$

$$\frac{\Delta E}{E_{\text{dep}}} = 1.8\% + \frac{0.8\%}{(E[\text{GeV}])^{0.5}} \qquad \text{(TAPS)} \qquad (3.25)$$

This was done by simulating isotropically distributed photons with random energies up to 1 GeV. The deposited energy and its resolution was then determined for several intervals of generated energies by fitting the corresponding line shapes with tailed Gaussian functions [58]. The resulting energy dependent resolutions are shown in figure 3.11. An overall good agreement with the parametrized resolutions could be achieved for the simulated data. There are some small deviations for TAPS starting around 800 MeV that could not be corrected without losing the agreement in the low energy region. This is no problem for the $\eta \to 3\pi^0$ analyses, since the η-meson decay photons do not reach these high energies. The majority of the decay photons coming from the $\eta \to 2\gamma$ decay are also below 800 MeV.

Equations 3.24 and 3.25 were used to calculate the absolute values of the energy errors needed in the χ^2-minimization of the two photon invariant mass (see section 4.2).

Smearing was also applied to the simulated energies in the PID and the Veto detectors to reproduce the experimentally observed resolutions.

Angular resolutions

The angular resolutions in CB and TAPS had to be determined for the estimation of the angular errors in the χ^2-minimization of the two photon invariant mass (see section 4.2). Similar to the determination of the energy resolutions, simulated data of isotropically distributed photons were used for that purpose. Knowing the generated direction of the photon for each event, spectra of the differences to the detected azimuthal and polar angles were created depending on the generated polar angle. The energy dependence was neglected. The distributions were fitted with Gaussians and the θ-dependent errors $\Delta\phi$ and $\Delta\theta$ were extracted. They can be found in figures 3.12 for CB and 3.13 for TAPS, respectively. Two separate resolution functions were determined for the two different targets that were used for this work. However, the better resolution in case of the shorter target is only visible in the polar angle resolution of CB. The shown resolution functions of TAPS for the shorter target correspond to the May 2009 beamtime, where the inner two rings were replaced by $PbWO_4$ crystals that could not be used in the analysis. The lack of the two rings causes a significant loss in both azimuthal and polar angular resolution at small polar angles.

Thresholds

In the analysis of simulated data, the same thresholds as used in the corresponding analysis of experimental data were applied. These thresholds included

- PID detector thresholds

- Veto detector thresholds

- TAPS CFD (detector) and LED (trigger) thresholds

- CB low (detector) and high (trigger) thresholds
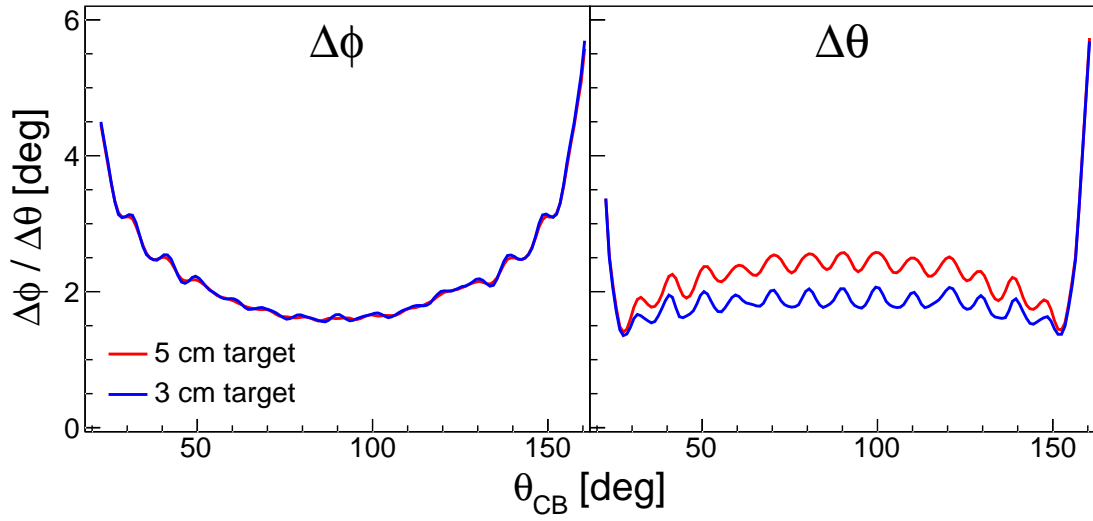
Fig. 3.12: Angular resolution for photons in CB obtained from simulation: Left-hand side: azimuthal angle resolution. Right-hand side: polar angle resolution. Red curves: resolutions for 5 cm target. Blue curves: resolutions for 3 cm target.
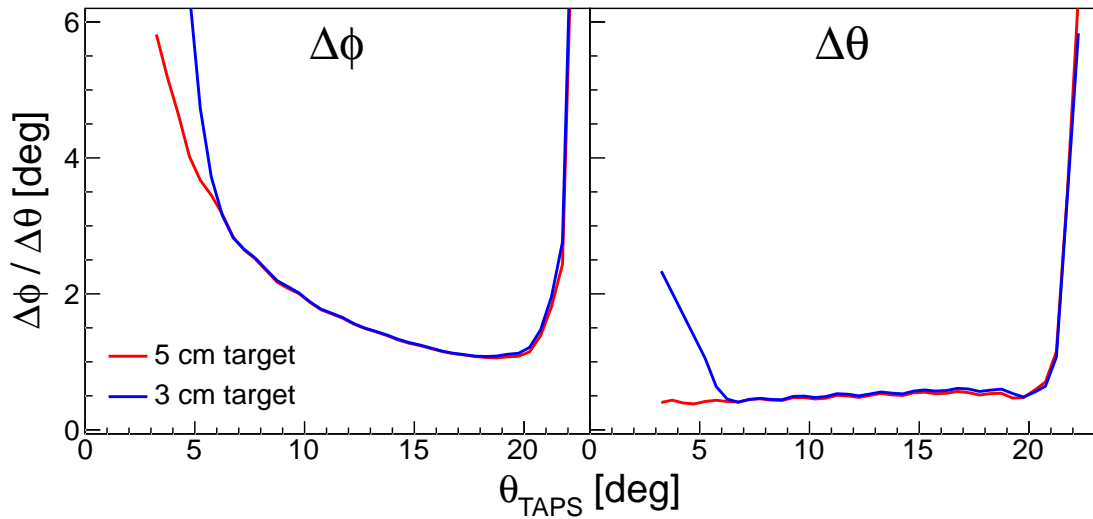
Fig. 3.13: Angular resolution for photons in TAPS obtained from simulation: Left-hand side: azimuthal angle resolution. Right-hand side: polar angle resolution. Red curves: resolutions for 5 cm target. Blue curves: resolutions for 3 cm target.

3.7 Summary

Table 3.2 gives a summary of the overall achieved resolutions in energy, as seen in different invariant masses, and in time. The averaged values were extracted from the η-analyses and all analysis cuts were applied.

Type	Quantity	ΔE or Δt
Energy	η in $m_{2\gamma}$	44 MeV
	η in $m_{3\pi^0}$	29 MeV
	π^0 in $m_{2\gamma}$	19 MeV
Time	TAPS-TAPS	0.52 ns
	CB-CB	2.23 ns
	CB-TAPS	1.67 ns
	Tagger-CB	2.00 ns
	Tagger-TAPS	1.02 ns

Tab. 3.2: Overview of average energy and time resolutions (FWHM).

Chapter 4

Data analysis

After the successful calibration of all detector systems, the actual data analysis of the physical reactions to be investigated can be started. This chapter will describe all the steps necessary for the extraction of differential and total cross sections of the following reactions:

$\gamma N \to \eta(N)$ quasi-free inclusive η-photoproduction on the deuteron
$\gamma p \to \eta p$ quasi-free exclusive η-photoproduction on the proton
$\gamma n \to \eta n$ quasi-free exclusive η-photoproduction on the neutron

In each case separate analyses for the $\eta \to 2\gamma$ and the $\eta \to 3\pi^0$ decays were performed. Apart from the event selection, the subsequent steps of the data analysis were the same for both decay analyses.

The exclusive analyses contain some additional steps compared to the inclusive analyses due to the detection of the recoil nucleon.

Following the analysis philosophy of this work, reconstructed clusters in the detectors are first classified into neutral and charged particles (see section 3.1). Depending on the reaction to be analyzed, events are then selected or rejected based on the number of neutral and charged clusters, and the intermediate state η-meson is reconstructed from the detected decay photons. This will be discussed in section 4.1 and 4.2, respectively. The event candidate is successively tested with a series of mostly kinematic cuts that will be described in section 4.3. Finally, additional information obtained from the detectors that was not used up to this point, can be checked to ensure a proper identification of the event, as will be described in section 4.4.

It should be stressed that the analysis sequence described above does not classify the detected clusters into real particles at a first step. Rather, the particle classification is performed by checking the most probable assignment with kinematic cuts. The most probable assignment again does not use additional detector information, such as deposited energies in the PID/Veto detectors and time-of-flight, but relies only on the reconstruction of the intermediate state η-

meson. These further measured quantities are only used to check the quality of the event selection after all analysis cuts. In contrast to an analysis which would take into account all available detector information in the first place, creating definite particle classifications, the reconstruction efficiency of the method used in this work may be inferior. On the other hand, this sequence allows a better reproduction of the analysis with simulated data. This is due to the fact that the correct simulation of most of the extended detector information mentioned above requires an excellent modeling of the detector simulation and a very accurate knowledge of the experimental setup. This is most important for, e.g., the detection of protons and neutrons, which is required in this work aiming at exclusive measurements of $\gamma p \rightarrow \eta p$ and $\gamma n \rightarrow \eta n$ with the detection of the complete final states. In addition, certain detector information are difficult to reproduce in the simulation, e.g., the two scintillation light components of BaF_2 used in the PSA or the time-of-flight for neutrons. Therefore, in this work the analysis was performed in the sequence described above without using any detector information other than deposited energies and hit times in the calorimeter crystals and hits in the PID/Veto detectors for the primary particle identification.

In section 4.5 the two methods used for the reconstruction of the center-of-mass energy $W = \sqrt{s}$ from the final state particles will be presented. Subsequent steps in the extraction of the reaction yields include the subtraction of the tagger random coincidences (section 4.6), the application of the software trigger (section 4.7) and the determination of the detection efficiencies (section 4.8). In section 4.9 the calculation of the photon flux will be discussed that is required for the extraction of the cross sections (section 4.10). The merging of the multiple data sets and the combining of the results of the two η-meson decay analyses will be presented in section 4.11. In order to remove the contribution of the target cell from the final results, the empty target data were analyzed and the corresponding subtraction procedure is shown in section 4.12. Finally, section 4.13 will discuss the main sources of the systematic uncertainties of the measurements performed in this work.

4.1   Event selection and analysis overview

The basic particle reconstruction described in section 3.1 creates disjoint sets of neutral and charged particles. According to the expected final states of the studied reactions, corresponding criteria on the multiplicities of the detected charged and neutral particles are put in the analysis. An overview is shown in table 4.1 and the details are given in the next subsections. Also a short overview of the subsequent analysis steps is given for each analysis.

| Analysis | Exactly required clusters | | |
	Neutral	Charged	
	2	0	OR
$\gamma N \to \eta(N) \to 2\gamma(N)$	2	1	OR
	3	0	
	6	0	OR
$\gamma N \to \eta(N) \to 3\pi^0(N)$	6	1	OR
	7	0	
$\gamma p \to \eta p \to 2\gamma p$	2	1	
$\gamma p \to \eta p \to 3\pi^0 p$	6	1	
$\gamma n \to \eta n \to 2\gamma n$	3	0	
$\gamma n \to \eta n \to 3\pi^0 n$	7	0	

Tab. 4.1: Overview of the cluster selection criteria for the different analyses: Each exclusive analysis has exactly one cluster condition while the inclusive analyses have three conditions connected via logical OR.

4.1.1 Analysis of $\gamma N \to \eta(N)$

In the inclusive analysis of $\gamma N \to \eta(N)$ at least the η-meson has to be detected. The detection of the final state proton or neutron is optional. Therefore, three independent conditions on the detected neutral and charged particles can be placed:

1. Two (six) photons of the $\eta \to 2\gamma$ ($\eta \to 3\pi^0$) decay, no recoil nucleon detected $\to$ two neutral, no charged (six neutral, no charged) particles

2. Two (six) photons of the $\eta \to 2\gamma$ ($\eta \to 3\pi^0$) decay, recoil proton detected $\to$ two neutral, one charged (six neutral, one charged) particles

3. Two (six) photons of the $\eta \to 2\gamma$ ($\eta \to 3\pi^0$) decay, recoil neutron detected $\to$ three neutral, no charged (seven neutral, no charged) particles

The statements in parentheses correspond to the $\eta \to 3\pi^0$ analysis (see table 4.1). If one of these conditions is valid (connection via logical OR), the event is accepted.

Further steps in the inclusive analysis are the reconstruction of the η-meson, the application of the PSA, invariant mass and missing mass cuts and the subtraction of the tagger random coincidences. Finally, the extracted yields are normalized using the detection efficiency and the photon flux to obtain differential and total cross sections.

4.1.2 Analysis of $\gamma p \to \eta p$

The analysis of $\gamma p \to \eta p$ requires the detection of the final state η-meson as well as the detection of the recoil proton. Therefore, only events with two neutral and one charged particle have to be considered for the $\eta \to 2\gamma$ analysis. In the $\eta \to 3\pi^0$ analysis six neutral particles and one charged particle have to be present (see table 4.1).

After the reconstruction of the η-meson, kinematic cuts are applied for background rejection. In addition to the cuts applied in the inclusive analysis, further cuts as, e.g., the coplanarity cut and cuts on the polar angle of the proton in the laboratory system can be applied because of the detection of the recoil proton. After the subtraction of the coincidental background in the tagger, the yields can be normalized using the detection efficiency and the photon flux. The determination of the detection efficiency is more complex compared to the inclusive analysis since the proton has to be considered along with the η-meson decay photons. As the complete final state is detected, the center-of-mass energy W can be reconstructed from it, removing effects from Fermi motion in contrast to the calculation using the initial state and assuming the proton at rest. The two methods that were used in this work to perform this reconstruction are described in section 4.5.

4.1.3 Analysis of $\gamma n \to \eta n$

The analysis of $\gamma n \to \eta n$ is equivalent to the analysis of $\gamma p \to \eta p$. The only differences are the different cluster criteria for the event selection and the lack of certain detector observables such as deposited energies in the PID/Veto detectors in case of the neutron analysis. In the $\eta \to 2\gamma$ analysis in total three neutral particles have to be detected, whereas the $\eta \to 3\pi^0$ analysis requires the detection of exactly seven neutral particles. In both cases no charged particle is allowed to be detected (see table 4.1).

4.2 Reconstruction of the η-mesons

The first step in the reconstruction of the η-meson is the identification of the decay photons out of all detected particles. Afterwards the energy resolution can be optimized by a correction of the energy of the final state η-meson and, in case of the $\eta \to 3\pi^0$ decay analysis, the intermediate state π^0-mesons.

4.2.1 Identification of the η-decay photons

In the $\eta \to 2\gamma$ analysis with only two detected neutral particles, the reconstruction of the η-meson is trivial. When three neutral particles are detected, including one

possible neutron candidate, the two photons originating from the η-meson decay are found by a χ^2-test. For all three photon pair combinations that are possible when having in total three photons, the following expression is calculated:

$$\chi^2_{ij} = \left(\frac{m_{\gamma_i \gamma_j} - m_\eta}{\Delta m_{\gamma_i \gamma_j}} \right)^2 , \quad i, j = 1, 2, 3, \, i \neq j , \tag{4.1}$$

where $m_\eta = 547.85$ MeV is the nominal mass of the η-meson [7], $m_{\gamma_i \gamma_j}$ is the invariant mass of the photons γ_i and γ_j and $\Delta m_{\gamma_i \gamma_j}$ is the associated error of the invariant mass. The latter is evaluated separately for each photon combination and depends on the errors of the deposited energies and the errors of the azimuthal and polar angles of the two photons, as shown in appendix A.1. These errors were determined individually for the Crystal Ball and the TAPS detectors using the simulation of the detector setup (see section 3.6) and they are themselves depending on the photon energies and the polar angles. It is clear from equation 4.1 that the best photon combination, i.e., the two true photons of an η-meson decay, should minimize the χ^2-value. Therefore, the photons of the combination that minimizes χ^2_{ij} are assumed to originate from the η-meson decay. The remaining neutral particle is marked as neutron candidate.

In case of the $\eta \to 3\pi^0$ analysis a similar procedure is performed. Having detected six or seven neutral particles the following χ^2-test is used to find the best combination to form three π^0-mesons out of 15 or $7 \times 15 = 105$ total combinations, respectively:

$$\chi^2_{ijklmn} = \left(\frac{m_{\gamma_i \gamma_j} - m_{\pi^0}}{\Delta m_{\gamma_i \gamma_j}} \right)^2 + \left(\frac{m_{\gamma_k \gamma_l} - m_{\pi^0}}{\Delta m_{\gamma_k \gamma_l}} \right)^2 + \left(\frac{m_{\gamma_m \gamma_n} - m_{\pi^0}}{\Delta m_{\gamma_m \gamma_n}} \right)^2 , \tag{4.2}$$

with $i, \ldots, n = 1, \ldots, 6$ and $i, \ldots, n$ all different, and $m_{\pi^0} = 134.98$ MeV [7]. As before the errors of the invariant masses $\Delta m_{\gamma\gamma}$ are calculated for each photon combination. Again, the combination with the minimal χ^2-value is assumed to originate from an $\eta \to 3\pi^0$ decay and in case of 7 detected neutral particles, the leftover particle is marked as neutron candidate.

In the $\eta \to 2\gamma$ analyses, additionally a χ^2-test checking for a single π^0-meson is performed. If the resulting χ^2-value is smaller than the one from the η-χ^2-test, the event is rejected.

4.2.2 χ^2-distribution and confidence level

The distributions of the χ^2-values of the best photon combinations calculated using equations 4.1 and 4.2 contain more information about the quality of the η-meson reconstructions. Definitions and further mathematical supplements to the object of the following part can be found in appendix A.2.
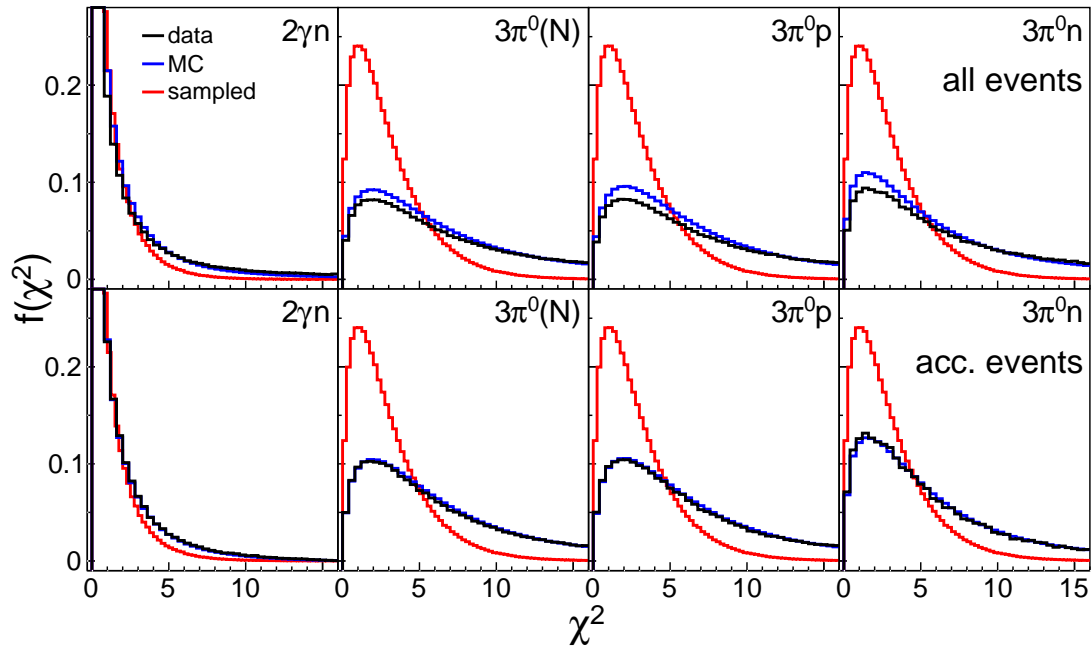
Fig. 4.1: Overview of the normalized χ^2-distributions of the η-reconstructions: Upper row: all events. Lower row: accepted events after all cuts. Distributions: experimental data (black), simulation (blue), sampled χ^2-distributions (red).
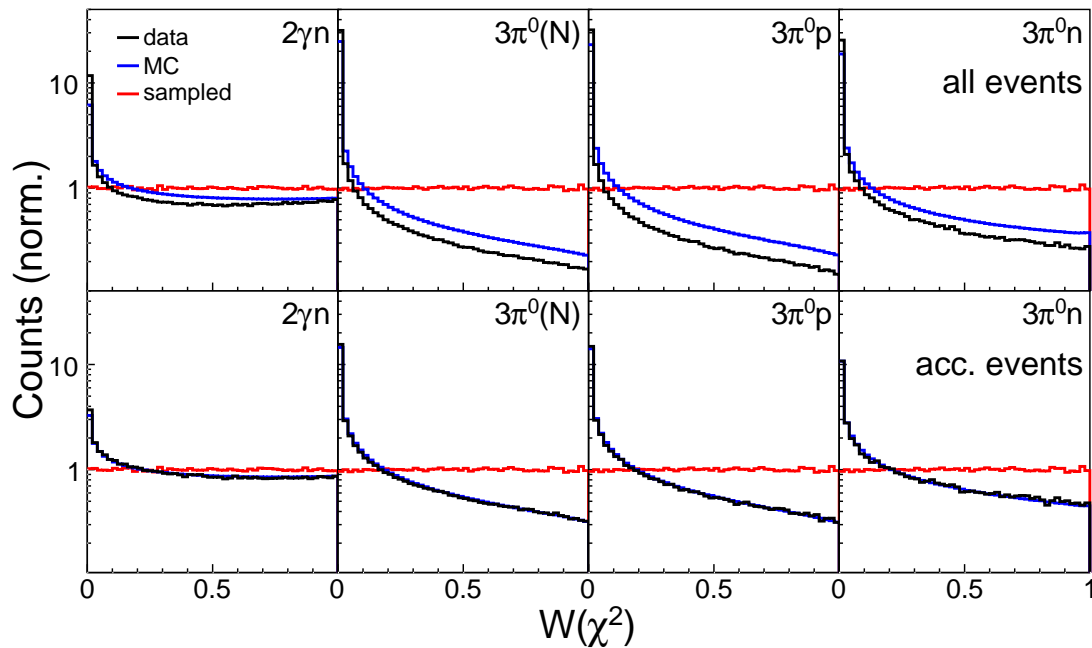
Fig. 4.2: Overview of the normalized confidence level distributions of the η-reconstructions: Upper row: all events. Lower row: accepted events after all cuts. Distributions: experimental data (black), simulation (blue), sampled confidence level distributions (red).

If the measured invariant masses $m_{\gamma\gamma}$ are independent and normally distributed random variables and their errors $\Delta m_{\gamma\gamma}$ are correctly estimated (i.e., are equal to the standard deviations of the corresponding Gaussian distributions), the χ^2-values calculated using equations 4.1 and 4.2 should be distributed according to the χ^2-distributions with one and, respectively, three degrees of freedom. In figure 4.1 the χ^2-distributions obtained in the analyses of the different channels are shown. In the $\gamma p \to \eta p \to 2\gamma p$ analysis no combinatorial η-reconstruction is needed. The χ^2-distribution obtained in the $\gamma N \to \eta(N) \to 2\gamma(N)$ analysis is equal to the one obtained in the $\gamma n \to \eta n \to 2\gamma n$ analysis. These channels are therefore not shown. The distributions obtained from the experimental data are compared to their counterparts of simulated data (MC) and to distributions that were sampled from the exact χ^2-distributions with the corresponding degrees of freedom. The distributions of all events are shown as well as the ones of the accepted events, i.e., the events that passed all analysis cuts described in section 4.3. All distributions were normalized since they can be interpreted as probability density functions.

The agreement between experimental data and simulation is excellent after all cut were performed. Without cuts, there are visible differences due to the fact that the measured data contain background events that are absent in the simulation. Discrepancies are found with respect to the sampled χ^2-distributions. The experimental and simulated distributions are shifted towards higher χ^2-values which is especially visible in the $\eta \to 3\pi^0$ analyses. This could be due to different reasons.

First, the measured invariant masses are not Gaussian distributed but asymmetric, having a low energy tail caused by the detector resolution (see figures 4.4 and 4.5, respectively). In addition, in the $\eta \to 3\pi^0$ analyses, the combinatorial background increases due to the high number of possible combinations. Interestingly, the reconstruction in the $\gamma n \to \eta n \to 3\pi^0 n$ analysis seems to yield smaller χ^2-values. This is maybe caused by the fact that the probability of finding the correct combination is higher because all combinations of seven neutral particles are taken into account. In the corresponding proton analysis, the charged particle is already assumed to be the proton so there are less possible combinations. Having seven detected particles there is a nonnegligible probability that a neutral particle in the Crystal Ball detector is wrongly marked as charged because the coincidence with the PID detector is established regarding the azimuthal angle only (see section 3.1.2). Hence, it is possible that the correct combination to form the three π^0-mesons cannot be found since a photon is wrongly assumed to be the proton and is not considered in the combinations. Nevertheless, as it can be seen later, no drastically increased background in the $\gamma p \to \eta p \to 3\pi^0 p$ analysis can be found.

The other reason for the shifts in the χ^2-distributions could be wrongly estimated errors $\Delta m_{\gamma\gamma}$. An overestimation of these errors would lead to lower χ^2-values while an underestimation would increase them. The obtained χ^2-distributions seem to support the fact that the errors were underestimated. This could be because the errors of energy and angles were added quadratically for the calculation of $\Delta m_{\gamma\gamma}$ (see equation A.3) and no correlation was taken into account. This method of error propagation leads generally to smaller errors compared to, e.g., the linear sum of the absolute errors, which was found to yield overestimated errors. More detailed studies including the investigation of the correlation between energies and angles are needed for a more exact estimation of the error $\Delta m_{\gamma\gamma}$.

Another quantity of interest is the confidence level $W(\chi_i^2)$ corresponding to a χ_i^2-value. This is the probability that a random χ^2-value is greater or equal than a given χ_i^2-value. It is pointed out in appendix A.2 that a large χ^2-value corresponds to a small confidence level and vice versa. Figure 4.2 shows the normalized distributions of the confidence levels associated with the χ^2-distributions of figure 4.1. One can see that a true χ^2-distribution leads to a flat distribution of the confidence level. In the distributions without analysis cuts the accumulation of events with very low confidence levels is caused by background events or wrong combinations with high χ^2-values. This is obviously more pronounced in case of experimental data. After all analysis cuts were applied, the very good agreement between experimental data and simulation is confirmed again. The distribution of the $\gamma n \rightarrow \eta n \rightarrow 2\gamma n$ analysis is relatively flat and close to the sampled distribution while the distributions of the $\eta \rightarrow 3\pi^0$ analyses decrease to higher confidence level values. As mentioned before, this is a direct consequence of the underestimated errors. The effect is probably stronger in these spectra as the χ^2-expression has three degrees of freedom and hence the χ^2-values are more affected by the deviations of the single errors.

In summary, the obtained χ^2- and confidence level distributions show an excellent agreement between experimental and simulated data that indicates an equivalent selection of events, which is important for the calculation of the detection efficiencies. The underestimated errors $\Delta m_{\gamma\gamma}$ pose no systematic problem since it was found that the calculation of these errors has little influence on the event selection. Cuts on the confidence levels that are sometimes used in other analyses did not change significantly the final results and were therefore not applied.

4.2.3   Correction of the η-meson energy

All detectors were energy calibrated using the decay photons of π^0- and η-mesons such that the position of the corresponding peaks in the invariant mass distributions of the decay photons are located at the right position (see chapter 3.2).

These peaks have finite widths which means that the invariant mass in each single event is not exactly equal to the nominal meson mass but only approximately normally distributed around the correct mass. It is shown in [68] that this can be corrected event-by-event, i.e., the energies of the decay photons E_{γ_1,γ_2} can be adjusted to E'_{γ_1,γ_2} resulting in an invariant mass that corresponds exactly to the nominal meson mass. Neglecting the angular resolutions, the photon energy correction is calculated in case of the η-meson via

$$E'_{\gamma_1,\gamma_2} = \frac{m_\eta}{m_{\gamma_1\gamma_2}} E_{\gamma_1,\gamma_2} = c \cdot E_{\gamma_1,\gamma_2} \,. \tag{4.3}$$

In the current analysis the uncorrected four-momentum of the η-meson obtained from the four-momenta of the decay photons is directly scaled by c

$$p'_\eta = c \cdot p_\eta = c \cdot (p_{\gamma_1} + p_{\gamma_2}) = c \cdot \begin{pmatrix} E_{\gamma_1} + E_{\gamma_2} \\ \vec{p}_{\gamma_1} + \vec{p}_{\gamma_2} \end{pmatrix}, \tag{4.4}$$

resulting in

$$m'_{\gamma_1\gamma_2} = \sqrt{[c \cdot (E_{\gamma_1} E_{\gamma_2})]^2 - [c \cdot (\vec{p}_{\gamma_1} + \vec{p}_{\gamma_2})]^2} = c \cdot m_{\gamma_1\gamma_2} = m_\eta \,. \tag{4.5}$$

This correction improves significantly the resolution of, e.g., the missing mass calculation.

In the $\eta \to 3\pi^0$ analyses the correction is applied first to the intermediate state π^0-mesons. This increases the resolution of the $3\pi^0$ invariant mass. After the four-momentum of the η-meson has been reconstructed from the corrected four-momenta of the π^0-mesons, the correction is once again performed on the η-meson four momentum.

4.3 Analysis cuts

The correct number and type (neutral/charged) of detected particles and even a reconstructed η-meson candidate from the procedure described before do not ensure that only true signal events were selected. There is a plethora of possibilities for background events, i.e., events originating from other reactions, to enter the event selection performed so far. For example, particles can be undetected or secondary particles can be created when primary particles pass through the detector materials. Inefficiencies of the PID and Veto detectors can mark charged particles as neutral and, on the other hand, accidentally coinciding signals in these detectors can mock charged particles when they were in reality neutral. Therefore, additional conditions on the selected events have to be put to reject background events. These analysis cuts can be divided into two groups.
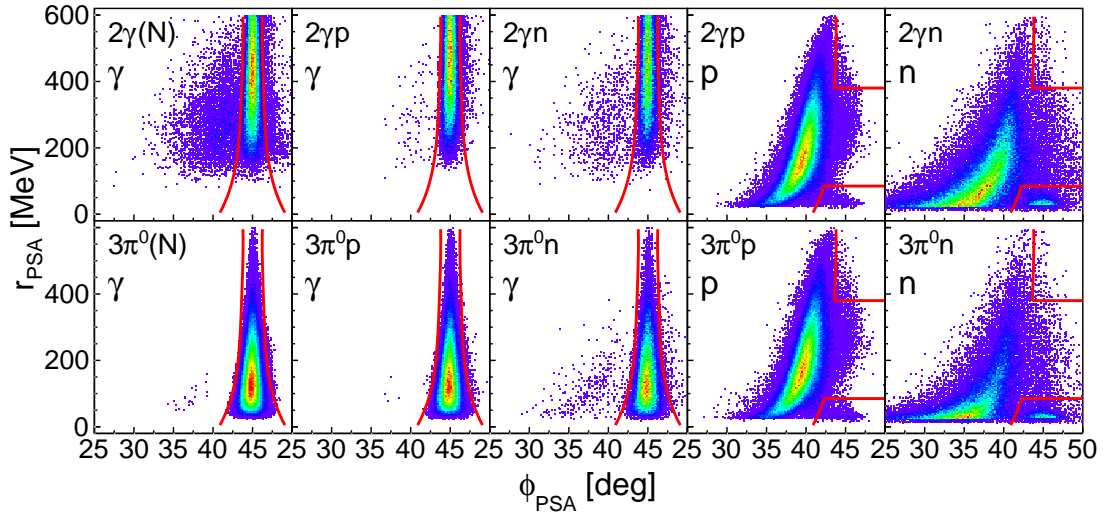
Fig. 4.3: Overview of the PSA cuts: Upper row: $\eta \to 2\gamma$ analyses. Lower row: $\eta \to 3\pi^0$ analyses. Red lines: cut markers. Color code: counts increase from violet to red.

The first group is used to achieve an unambiguous identification of the detected particles by using all available information from the detectors. Typically, these cuts are performed for each particle individually and do not include correlated checks of multiple particles. As explained in the introduction of this chapter, it was tried to minimize this kind of cuts in the current work due to the sometimes problematic reproducibility in the simulation. The only exception is the pulse-shape-analysis (PSA) that will be discussed in subsection 4.3.1.

The second group of cuts acts on an ensemble of particles and puts conditions on specific correlations of these particles. Most of the conditions are deduced from the kinematics of the signal reaction. The goal is to suppress a maximum number of background events while rejecting a minimum number of signal events, i.e., to maximize the signal-to-background ratio. At times, this is nontrivial since signal and background events are hardly separable with respect to a certain observable and trade-offs are required. With a series of cuts on different quantities a good signal-background separation could be achieved in this work. They will be discussed in subsections 4.3.2 to 4.3.6. Finally, an overview of all analysis cuts will be given in subsection 4.3.7.

4.3.1   Pulse-shape-analysis

The first cut that is already applied in the presort analysis (AcquRoot) is the pulse-shape-analysis (PSA) cut. It is applied to all particles detected in TAPS. The complete event is rejected, if at least one particle does not fulfill the cut condition. Because the two scintillation light components of BaF_2 were not simulated, this

cut is only applicable to experimental data (see section 3.5.2). Therefore, the cut has to be performed in a rather conservative manner so that the number of good events, which are rejected, is kept at a minimal level. The typical PSA plots including all particles of all analyses are summarized in figure 4.3. The additional cuts that will be described in the following sections were already applied to the shown spectra. Hence, the events that are solely rejected by the PSA cuts are visible more clearly.

After successful calibration photons should be located at PSA-angles of 45 degrees due to the definition of the PSA-angles (see section 3.5.2). This can be clearly seen in the plots. Also, the different energy ranges of the $\eta \to 2\gamma$ photons and the $\eta \to 3\pi^0$ photons are visible. There is very few background contamination in all spectra. Nevertheless, as nucleons are located at lower PSA-angles, a safe cut is performed that rejects events which are located outside a 3σ zone with respect to the mean value of the photon band. Mean and sigma values were determined for each TAPS crystal individually. In figure 4.3 the global averages of the cut positions are represented by the red lines.

The nucleons are located in the banana-shaped regions below 45 degrees. Neutrons are located at lower PSA-radii because they deposit less energy in the crystals. From the study of reaction channels with more high energetic nucleons in forward direction, e.g., π^0-production, it was found that punch-through nucleons can be located at higher PSA-angles for PSA-radii between 85 and 380 MeV. Therefore, no cut is applied in this region. For the complementary regions nucleons are rejected if they are located below the photon band (photon mean position minus 3σ, see figure 4.3). Only in the neutron analyses a notable number of events located at 45 degrees are rejected. These photon signatures are coming from wrongly assigned photons/electrons or from (n, γ) reactions of the neutron. The loss of events is small and should be corrected via the nucleon detection efficiency correction (see section 4.8.4).

In summary, the PSA that is only applied to experimental data has a minor influence on the event selection as most of the background is already rejected by the other cuts.

4.3.2   Invariant mass cut

The invariant mass of two particles m_{12} coming from a two body decay of a parent particle P is equal to the rest mass of the parent particle m_P

$$m_P = \sqrt{p_P^2} = m_{12} = \sqrt{(p_1 + p_2)^2} = \sqrt{p_1^2 + p_2^2 + 2p_1 p_2} \,, \qquad (4.6)$$
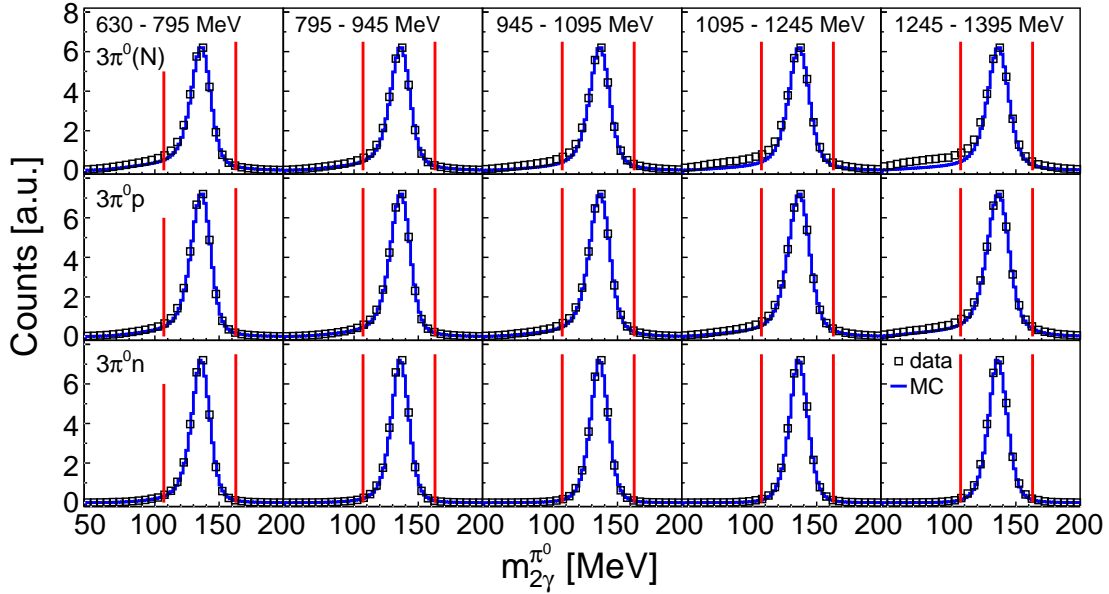
Fig. 4.4: Overview of the invariant mass cuts for the intermediate π^0-mesons: Columns (left to right): bins of increasing photon beam energy E_γ. Rows: analysis channels. Black squares: experimental data. Blue histograms: simulation. Red lines: cut markers.

with the corresponding four-momenta p_P, p_1, p_2. In case that the two decay particles are photons, equations 4.6 becomes

$$m_{12} = \sqrt{2E_1 E_2 (1 - \cos \phi_{12})}\,, \tag{4.7}$$

with the photon energies E_1, E_2 and the opening angle ϕ_{12}.

In this work the invariant mass of the detected photons was used to identify the η-mesons. In the $\eta \to 2\gamma$ analysis the invariant mass spectrum of the two photons is directly accessible. In the $\eta \to 3\pi^0$ analysis an additional step consisting of the reconstruction of the intermediate state π^0-mesons was performed, as described in section 4.2. The invariant masses $m_{2\gamma}^{\pi^0}$ of the three photon pairs, which were formed in the χ^2-reconstruction, are shown in figure 4.4. The total range of the photon beam energy E_γ is split into five bins and the corresponding spectra of all $\eta \to 3\pi^0$ analyses are presented. All other analysis cuts were applied to the spectra to emphasize the events that are only rejected by this cut. When comparing to the spectra obtained from simulation, it can be seen that the π^0-peaks are very well reproduced. Some combinatorial background can be seen in the inclusive analysis at higher photon energies, as no analysis cuts on the recoil nucleon can be performed. In general there is almost no energy dependence of the line shapes and, therefore, a fixed 3σ cut around the π^0-mass was applied. All three intermediate state π^0-mesons of a single event had to fulfill this cut.

Once the intermediate state π^0-mesons passed the cuts and their invariant masses were constrained to the theoretical mass (see section 4.2.3), the $3\pi^0$ invariant masses $m_{3\pi^0}^\eta$ were calculated for the identification of the η-mesons. They are shown in figure 4.5 together with the 2γ invariant masses $m_{2\gamma}^\eta$ of the $\eta \to 2\gamma$ analyses. All complementary cuts were applied to obtain the specta. Again, experimental data and simulation agree very well with the exception of the
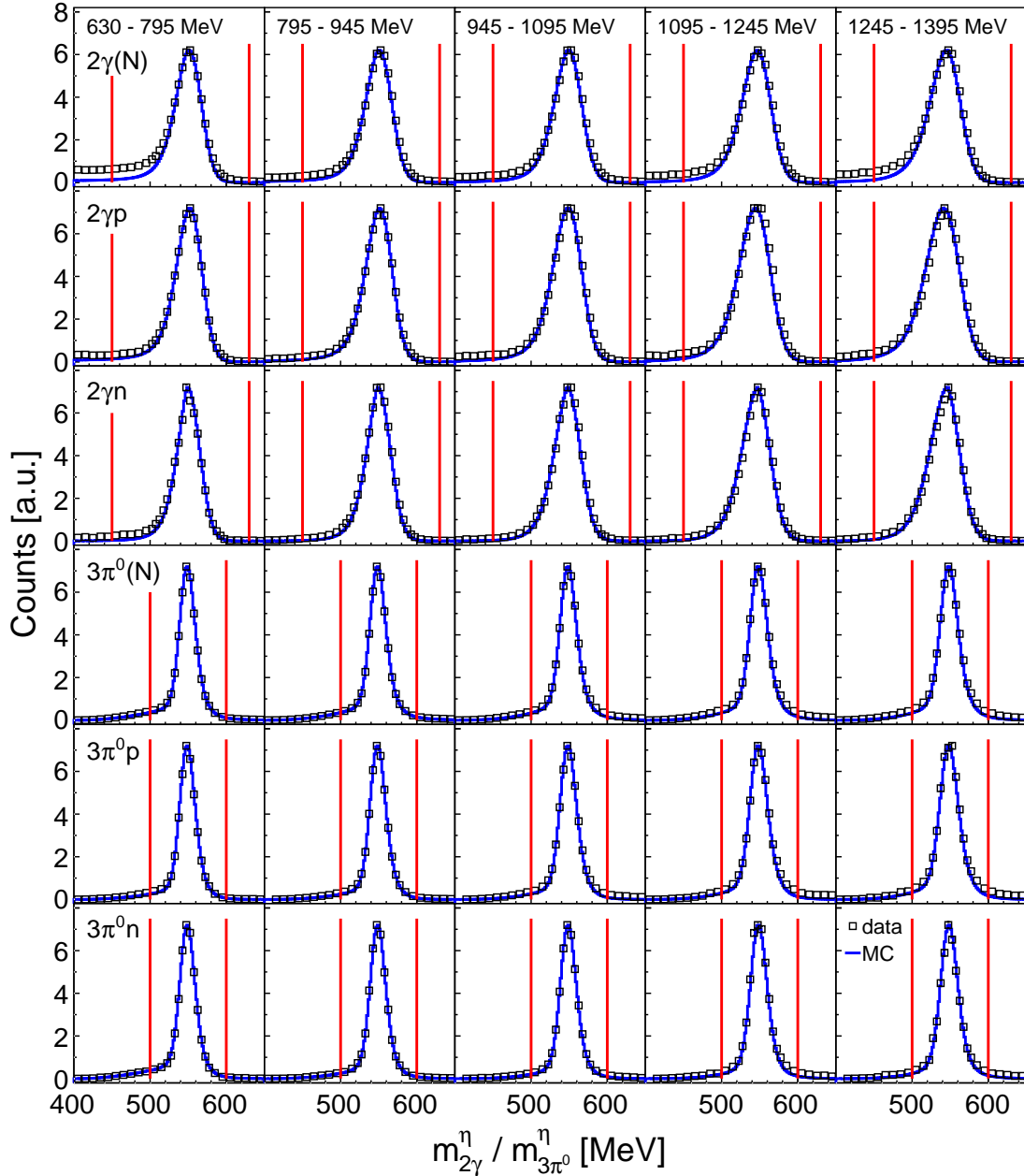
Fig. 4.5: Overview of the invariant mass cuts: Columns (left to right): bins of increasing photon beam energy E_γ. Rows: analysis channels. Black squares: experimental data. Blue histograms: simulation. Red lines: cut markers.

$\gamma N \rightarrow \eta(N) \rightarrow 2\gamma(N)$ spectra, where some background is present in the experimental data. The resolution in the $3\pi^0$ invariant mass is better than in the two photon case because of the π^0-mass constraints that were applied. As there is only a slight dependence of the line shapes on the photon beam energy E_γ, once again fixed cut limits were used. Due to the broader signal in the $\eta \rightarrow 2\gamma$ analyses the corresponding cuts were set more open.

The 2γ and, respectively, $3\pi^0$ invariant mass spectra are also used for the calculation of the yields that will be discussed in section 4.10.1.

4.3.3   Missing mass cut

Having identified the η-meson and, in case of the exclusive analyses possible recoil nucleon candidates, it has to be checked that these final states particles were produced in the reaction to be studied. The reaction kinematics imposes some strong constraints and several quantities can be used for analysis cuts. One of them is the missing mass m_X defined as the mass of the missing (e.g., undetected) particle X of a reaction. It is calculated as the invariant mass of the difference of the sums of initial state and final state four-momenta:

$$m_X \;=\; \sqrt{\Delta p^2} = \sqrt{\left(\sum_i p_i^{\mathrm{is}} - \sum_j p_j^{\mathrm{fs}}\right)^2} = \sqrt{(\Delta E)^2 - (\Delta \vec{p})^2} \tag{4.8}$$

$$\Delta E \;=\; \sum_i E_i^{\mathrm{is}} - \sum_j E_j^{\mathrm{fs}} \tag{4.9}$$

$$\Delta \vec{p} \;=\; \sum_i \vec{p}_i^{\,\mathrm{is}} - \sum_j \vec{p}_j^{\,\mathrm{fs}} \tag{4.10}$$

When measuring quasi-free η-production on the deuteron $\gamma d \rightarrow \eta X$, the missing particle has to be either a proton or a neutron and m_X should be equal to the proton or, respectively, neutron rest mass. If additional particles are produced in the final state and they are not detected or wrongly assigned to the expected products of η-production, m_X will be different from this value. Therefore, the missing mass can be used to separate signal from background events.

Assuming the initial state nucleon at rest, the missing mass in quasi-free η-production is calculated via

$$m_X = \sqrt{\left(E_\gamma + m_N - E_\eta\right)^2 - \left(\vec{p}_\gamma - \vec{p}_\eta\right)^2}. \tag{4.11}$$

In this case m_X is correctly denoted as η missing mass since the mass is missing with respect to the detected η-meson. In the literature also the expression proton/neutron missing mass is common since one expects it to be equal to the
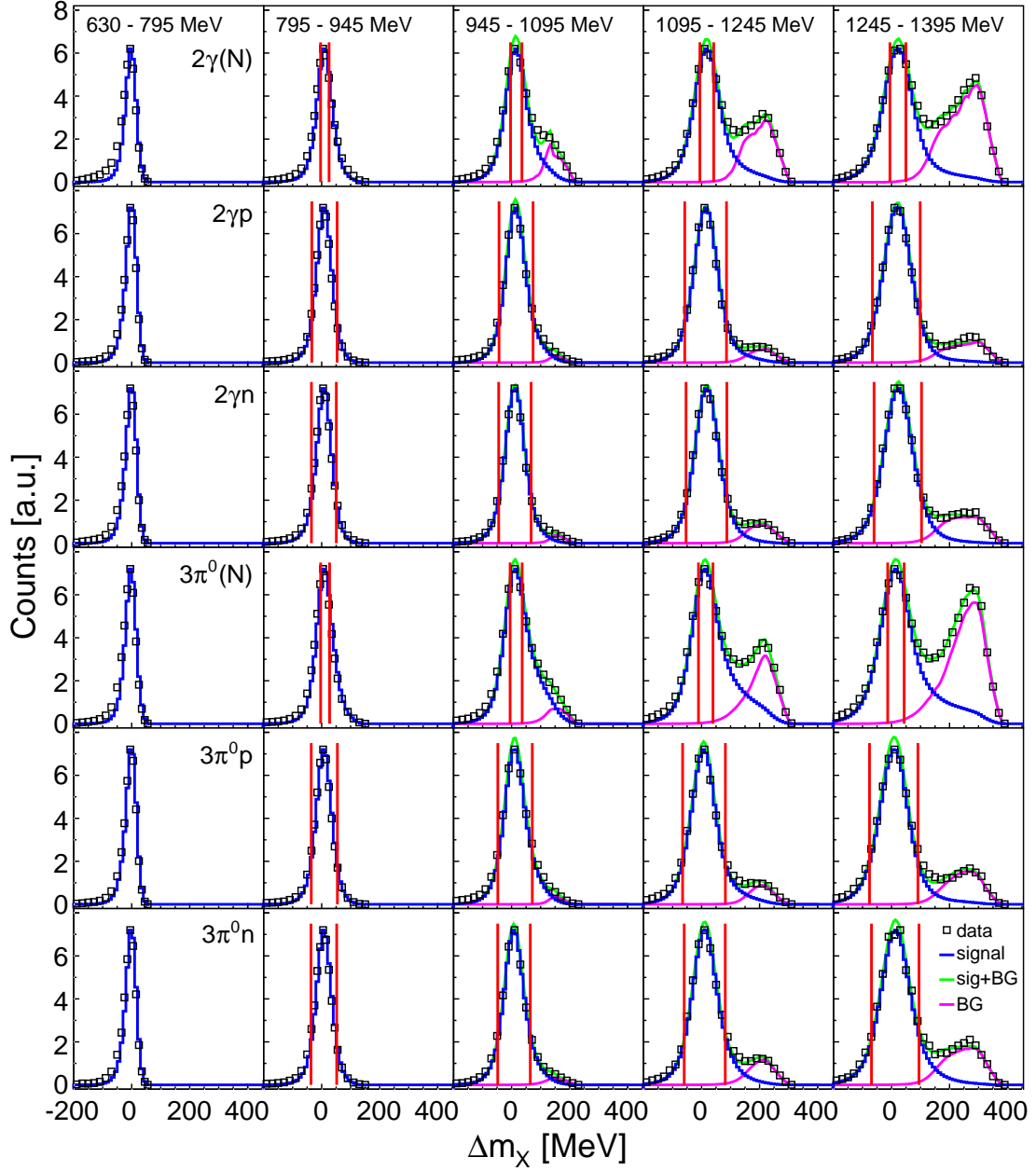
Fig. 4.6: Overview of the η missing mass cuts: Columns (left to right): bins of increasing photon beam energy E_γ. Rows: analysis channels. Black squares: experimental data. Blue histograms: signal simulation. Green curves: signal + background simulation fitted to data. Magenta curves: $\eta\pi$-background contribution of combined fits. Red lines: cut markers.

proton/neutron rest mass. In this work the nucleon mass is subtracted from m_X so that

$$\Delta m_X = m_X - m_N \, , \tag{4.12}$$

and hence true signal events should be distributed around zero.

An overview of the η missing masses of all analyses and the corresponding cuts that were applied is given in figure 4.6. The photon beam energy bins correspond to the bins used in figure 4.5 for the $2\gamma/3\pi^0$ invariant masses. All other cuts were applied to the presented spectra. Clear signal peaks at values around zero can be seen. The worse energy resolution of the $\eta \to 3\pi^0$ analysis due to the six particle final state could be successfully improved by the mass constraint discussed in section 4.2.3. The width of the peaks does only partially reflect the intrinsic resolution of the calorimeter. Because the initial state nucleons inside the deuteron are not at rest as it was assumed in the calculation of the missing mass, the signal peaks are smeared. The Fermi motion of the nucleons is also reflected in the asymmetric signal line shapes in the first energy bin since at threshold Fermi momenta in negative z-direction are predominant.

Agreement between experimental data and signal simulation is good up to around 800 MeV. In this region $\eta\pi$-production becomes possible which is the dominant background. In the exclusive analyses the background is more suppressed due to the fact that the nucleons were detected and additional cuts could be applied. The background level in the neutron analyses is only slightly higher than in the proton analyses.

Due to the strong photon beam energy dependence of the signal peak and the varying background contribution, no fixed missing mass cuts could be applied. The signal peaks in all energy bins were approximated by Gaussian fits and energy dependent mean and sigma values $m_{\mathrm{mm}}(E_\gamma), \sigma_{\mathrm{mm}}(E_\gamma)$ were calculated. Below the $\eta\pi$-threshold around 807 MeV no cut was applied. For higher energies a symmetric cut $m_{\mathrm{mm}}(E_\gamma) \pm f \cdot \sigma_{\mathrm{mm}}(E_\gamma)$ was used, where the factor f was chosen to be 1.5 for the exclusive analyses. For the inclusive analyses a more conservative value of 0.5 was chosen to rule out contamination from the broad background distribution.

Simulations of the $\eta\pi$-background channels $\gamma p \to \eta\pi^+ n$, $\gamma n \to \eta\pi^- p$ and $\gamma n \to \eta\pi^0 n$ were performed. They can contaminate the signal when neutrons or charged pions are not detected. The experimental data histograms were fitted with the sums of the signal and background line shapes, which are represented by the green curves in figure 4.6. The so determined pure background contributions are shown by the magenta curves. It can be seen that the applied cuts are performed at a safe level and do not include background events. The plots of the inclusive analyses demonstrate that the choice of a narrower cut is necessary because the background contribution enters considerably into the signal region.

An asymmetric cut accepting only events with negative missing masses could minimize the risk of background contamination. However, it was found [78] that asymmetric cuts are shifting the position of the structure in the excitation function of the neutron, whose investigation is the main topic of this work. This is due to the nontrivial correlations of Fermi motion, center-of-mass energy and missing mass. Therefore, symmetric cuts were chosen to ensure a reliable extraction of the properties of this structure.

4.3.4 η–N coplanarity cut

The coplanarity cut is another analysis cut that can be used for the identification of the signal reaction. It imposes a condition on the η-meson and the detected recoil nucleon and, therefore, it can only be used in the exclusive analyses. Namely, if the η-meson and the recoil nucleon are originating from $\gamma N \to \eta N$, the recoil nucleon has to lie in the reaction plane that is spanned by the incoming photon and the η-meson due to momentum conservation. As $\vec{p}_\gamma = (0, 0, E_\gamma)$ this condition can be easily checked by the calculation of the difference in azimuthal angles

$$\Delta\phi = \begin{cases} \phi_\eta - \phi_N & \text{if } \phi_\eta - \phi_N \geq 0 \\ 2\pi - |\phi_\eta - \phi_N| & \text{if } \phi_\eta - \phi_N < 0 \end{cases} \quad (4.13)$$

of η-meson and recoil nucleon. Since ϕ is independent of the z-direction, along which the Lorentz-boost to the laboratory system takes place, $\Delta\phi$ can also be directly calculated in the laboratory frame. Strictly speaking, this is only true if the initial state nucleon is at rest. The fact that the nucleons have finite momenta will decrease the resolution of the calculation of $\Delta\phi$. But, similar to the missing mass cut, the separation of signal and background will not be affected too much.

The coplanarity spectra are shown in figure 4.7. Again, five photon beam energy bins for all the exclusive analyses are presented and all other analysis cuts were applied to the spectra. It can be noticed from the comparison of experimental data and simulation that all spectra are basically free of contamination from other channels, with the only exception of the $\gamma n \to \eta n \to 2\gamma n$ analysis. The origin of the background in the latter channel is mainly π^0-production on the neutron (plus smaller contributions from $\eta\pi^0$-production) that enters the event selection when the recoil neutron is wrongly assigned to an η-meson decay photon and a π^0-decay photon is assumed to be the neutron. This background channel was simulated and a combined fit with signal and background line shapes (green curve in figure 4.7) describes the experimental data very well. The increased background in the $\gamma n \to \eta n \to 3\pi^0 n$ analysis is reproduced by the signal simulation and is thus not related to contamination from other channels but due to combinatorial background.
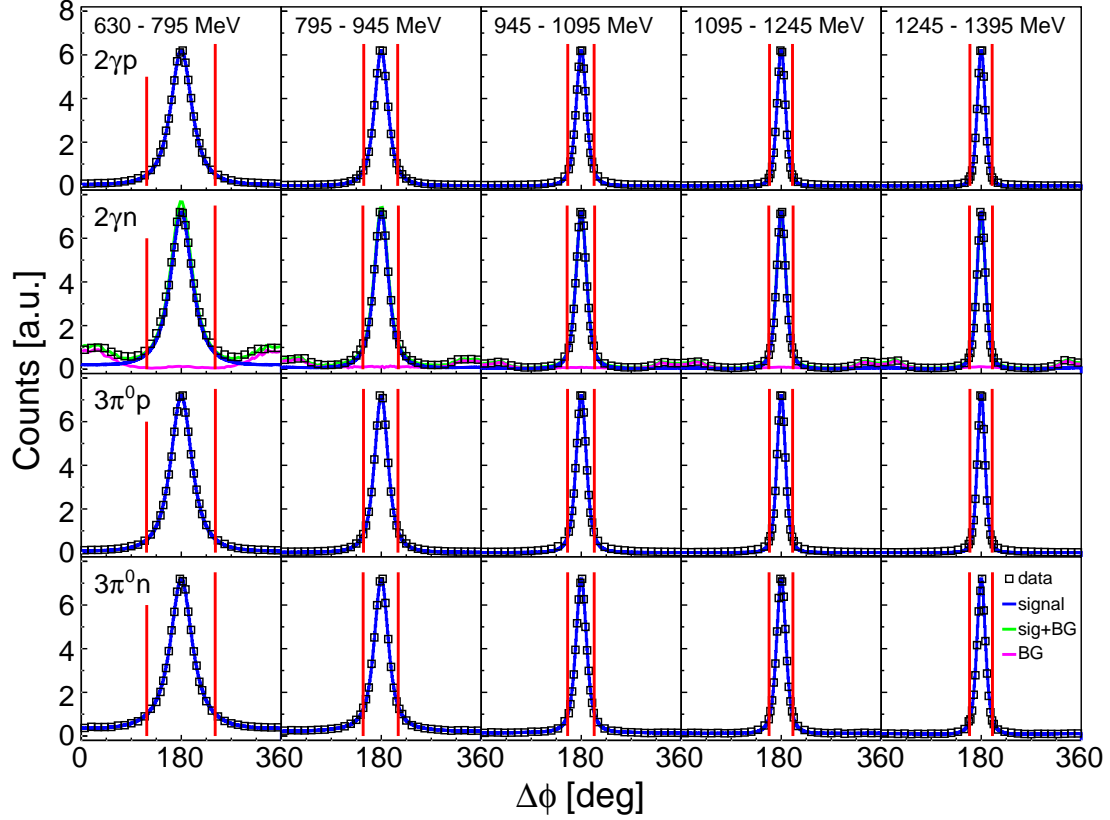
Fig. 4.7: Overview of the η-nucleon coplanarity cuts: Columns (left to right): bins of increasing photon beam energy E_γ. Rows: analysis channels. Black squares: experimental data. Blue histograms: simulation. Green curves: signal + background simulation fitted to data. Magenta curves: π^0-background contribution of combined fits. Red lines: cut markers.

The signal shapes in the $\Delta\phi$-spectra are highly energy dependent. At threshold the resolution is much worse than for higher beam energies. This is due to the fact that the η-mesons have very few kinetic energy at threshold and their four-momenta in the laboratory frame are strongly influenced by the Lorentz-boost leading to a decrease in resolution. Therefore, it was necessary to establish a photon beam energy dependent coplanarity cut, equivalent to the missing mass cut. The signal peaks were approximated by Gaussians and energy dependent mean and sigma values $m_{\text{cop}}(E_\gamma), \sigma_{\text{cop}}(E_\gamma)$ were calculated. Afterwards, a symmetric cut around the mean value $m_{\text{cop}}(E_\gamma) \pm 2 \cdot \sigma_{\text{cop}}(E_\gamma)$ was applied for all energies in all analysis channels. The previously mentioned background contamination in the $\gamma n \to \eta n \to 2\gamma n$ analysis, represented by the magenta curves in figure 4.7, is sufficiently rejected by this cut.
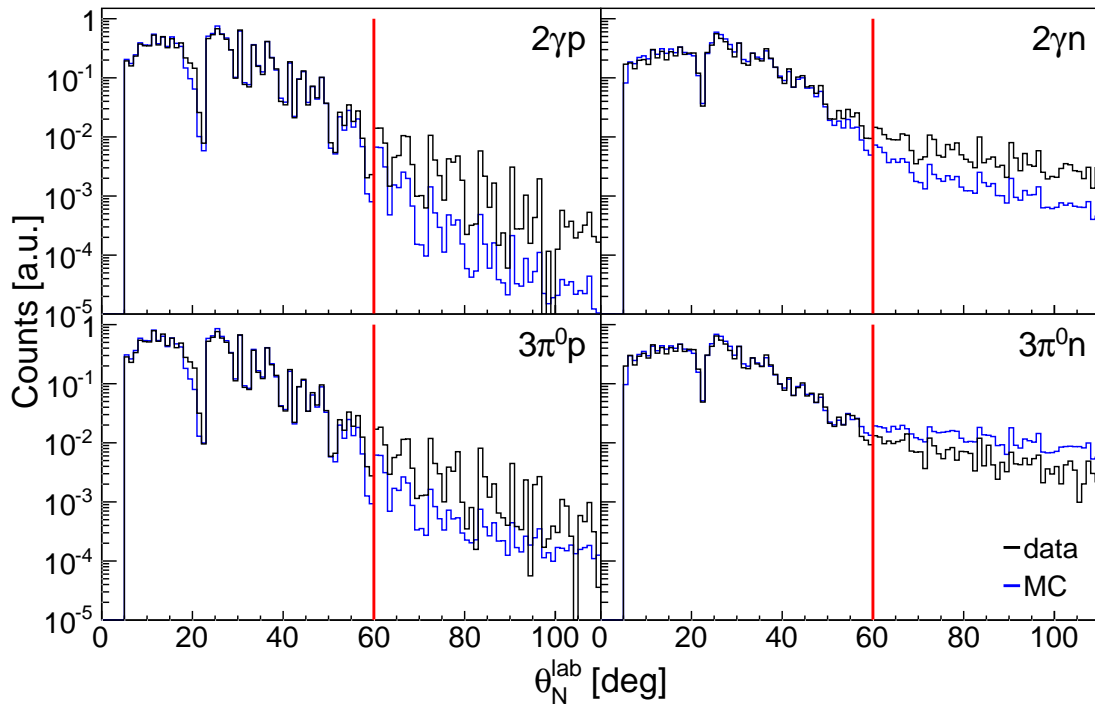
Fig. 4.8: Overview of the nucleon polar angle cuts: Black histograms: experimental data. Blue histograms: simulation. Red lines: cut markers.

4.3.5 Nucleon polar angle cuts

Within the good approximation of quasi-free kinematics, i.e., without having extremely large Fermi momenta, there is a kinematic limit for the laboratory polar angle θ_N^{lab} of the recoil nucleons of $\gamma N \to \eta N$. It was determined via simulation to be around 60 degrees. Figure 4.8 shows the polar angle spectra for the exclusive analysis channels and compares experimental and simulated data. The histograms were normalized in the range $30° < \theta_N^{\mathrm{lab}} < 50°$. All other analysis cuts were applied. The spectra start at 5 degrees, where the nucleons are detected in the third ring of TAPS (see section 2.5). Around 22 degrees the acceptance hole caused by the gap between TAPS and CB is clearly visible. The fluctuations in the spectra come from the segmentation of the calorimeters and the small cluster sizes for protons and neutrons, which results in accumulations of events in certain polar angle bins.

The overall agreement between experimental and simulated data is good. Only in the proton spectra some discrepancies at higher TAPS angles around 17 degrees can be seen. They are caused by the inaccuracy of the proton efficiency correction, which will be discussed in section 4.8.4. Without application of the proton efficiency corrections the discrepancies were found to be even higher.

Although the counts are shown logarithmically so that absolute differences are small around 60 degrees, the histograms of experimental and simulated data

start to deviate from each other. Therefore, a cut on the nucleon laboratory polar angle was set at 60 degrees in all exclusive analyses.

In addition to the cut described above an additional cut on the nucleon polar angle had to be applied in the analysis of the December 2007 data. During the beamtime in December 2007 the PID was not located at its nominal position but was shifted in negative z-direction (upstream) by approximately 15–16 cm [79]. It was found that this had an influence on the discrimination of charged and neutral particles in CB and on the detection efficiency of nucleons due to the changes in material budget.

First, charged particles can be marked as neutral since no coincidence with the PID was found and, hence, can enter the event selection as photon or neutron candidates. Due to the rigorous kinematic cuts, from all possible scenarios of background contamination only a misidentification of protons as neutrons poses a real risk since they directly move events from $\gamma p \rightarrow \eta p$ to $\gamma n \rightarrow \eta n$. Therefore, a conservative but strict approach would be the rejection of all events with a recoil nucleon in the affected angular region.

At its nominal position the PID covers polar angles down to approximately 15 degrees and thus overlaps with the outer TAPS detector elements. Due to the shifted position, the detection efficiency of nucleons detected in these elements is modified. As expected, the influence on protons was found to be much larger than for neutrons. Nevertheless, low energetic neutrons emitted into that region are affected as well. It was taken account for the shifted PID in the geometry of the detector simulation but as the nucleon detection efficiency correction (see section 4.8.4) would require hydrogen data measured under the same experimental conditions, a reliable determination of the nucleon detection efficiency was not possible for the December 2007 beamtime.

As a result of the two described problems caused by the shifted PID detector, an additional cut on the laboratory polar angle of the nucleons was applied in the analysis of the December 2007 data. All events having nucleons with $15° < \theta_N^{\text{lab}} < 27°$ were rejected. The handling of the limited acceptance in this data set will be discussed in section 4.11.1.

4.3.6   Fermi momentum cut

In section 4.5.1 it will be shown that the momentum of the undetected spectator nucleon can be reconstructed. This has by definition the same value in the final and in the initial state and is in the latter also the same for the participant nucleon, although with opposite direction. In first approximation the obtained momentum distribution must correspond to the Fermi momentum distribution inside the deuteron. The distributions of the different analyses are shown in figure 4.9. Spectra of experimental data and simulation are compared to the calculation
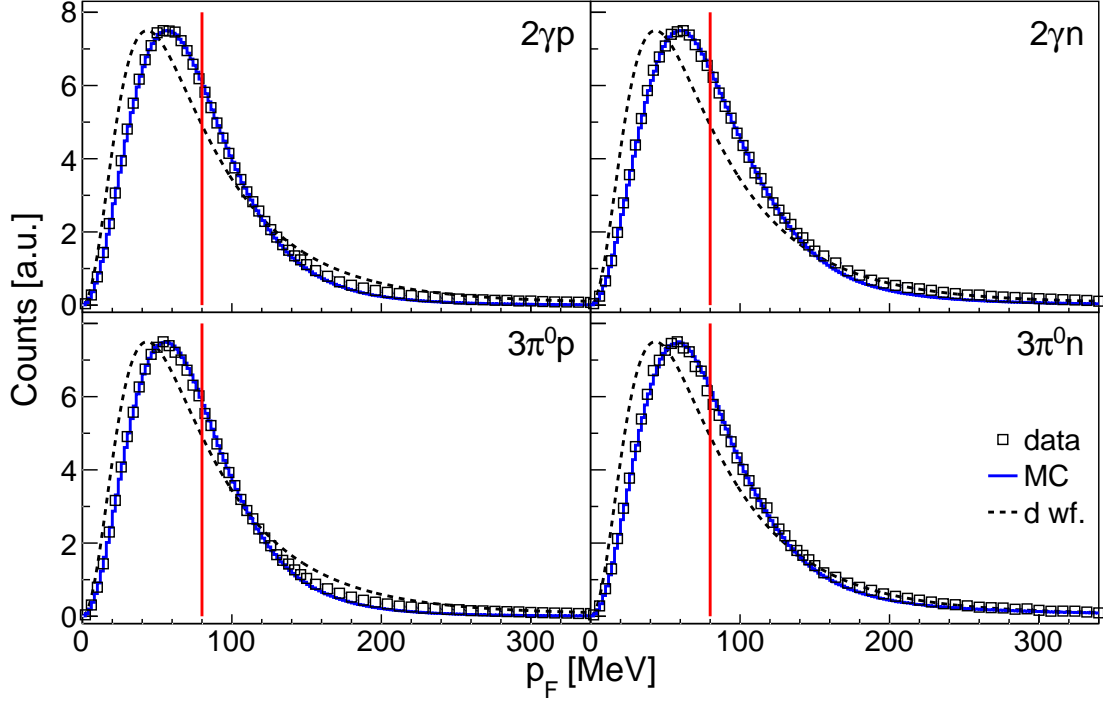
Fig. 4.9: Overview of the Fermi momentum cuts: Black squares: experimental data. Blue histograms: simulation. Dashed curve: theoretical calculation from [80]. Red lines: cut markers.

of the deuteron wave function from the Paris N–N potential [80]. In all analysis channels there is a good agreement between experimental data and simulation. The position of the most probable value is shifted from the predicted value of 45 MeV to about 55 MeV in the data spectra. Since also the rise to the maximum is less steep in the data, this could be caused by the resolution of the recoil energy reconstruction (more details are given in section 4.5.1). Nevertheless, the obtained momentum distributions look reasonable with respect to the theoretical calculation confirming the validity of the kinematic reconstruction.

In the standard analysis (Analysis I) no cut was applied to the reconstructed Fermi momentum. It was found that even a cut at rather high values has strong influence on the extracted cross sections at threshold. This was expected because the quasi-free η-production threshold is lowered compared to the free threshold by these large Fermi momenta and because of the immediate and sharp rise to the $S_{11}(1535)$ resonance the effect of this cut are clearly visible.

In the second analysis (Analysis II), where analysis cuts were tightened to optimize the resolution in the cross sections (see section 5.4.3), a cut on the Fermi momentum was performed that rejected events with large reconstructed momenta. As these events are either outside the approximation of quasi-free kinematics and the participant-spectator model, or were badly reconstructed, the cut was expected

Type of cut	$\eta \to 2\gamma$			$\eta \to 3\pi^0$		
	inc.	exc. p	exc. n	inc.	exc. p	exc. n
Common cuts						
PSA			3σ (exclusion zone for nucleons)			
2γ inv. mass $(3\pi^0)$		—			3σ	
$2\gamma/3\pi^0$ inv. mass [MeV]		$450 < m_{2\gamma} < 630$			$500 < m_{3\pi^0} < 600$	
nucleon lab polar angle	—	$\theta_N < 60°$		—	$\theta_N < 60°$	
nucleon lab polar angle[1]	—	$15° < \theta_N < 27°$		—	$15° < \theta_N < 27°$	
Analysis I						
missing mass	0.5σ	1.5σ		0.5σ	1.5σ	
η–N coplanarity	—	2σ		—	2σ	
Analysis II						
missing mass	—	0.5σ		—	0.5σ	
η–N coplanarity	—	0.5σ		—	0.5σ	
Fermi momentum [MeV]	—	$p_F < 80$		—	$p_F < 80$	

Tab. 4.2: Overview of the analysis cuts: The two major columns represent the two η-meson decays, the sub-columns the analysis channels $\gamma N \to \eta(N)$ (inc.), $\gamma p \to \eta p$ (exc. p) and $\gamma n \to \eta n$ (exc. n). [1]only applied to December 2007 data.

to improve the resolution of the kinematic reconstruction. It will be shown later that this was indeed the case. The cut position at 80 MeV was determined by taking into consideration the gain in resolution and the decreased statistics caused by this cut.

4.3.7   Summary

All analysis cuts that were discussed in the previous parts are summarized in table 4.2. The table lists separately the cuts of the different analysis channels of the two η-meson decays that were performed in this work. Analysis I refers to the standard analysis, whereas Analysis II denotes the analysis with more strict cuts that is described in section 5.4.3.

4.4   Checking the event selection

As described in the introduction to this chapter, the additional information provided by the detectors is used in this work to check the event selection, which itself is mainly done using kinematic cuts. It will be shown in the following that these information show no signs of possible contamination of background events and thus no additional cuts for the event selection are needed.
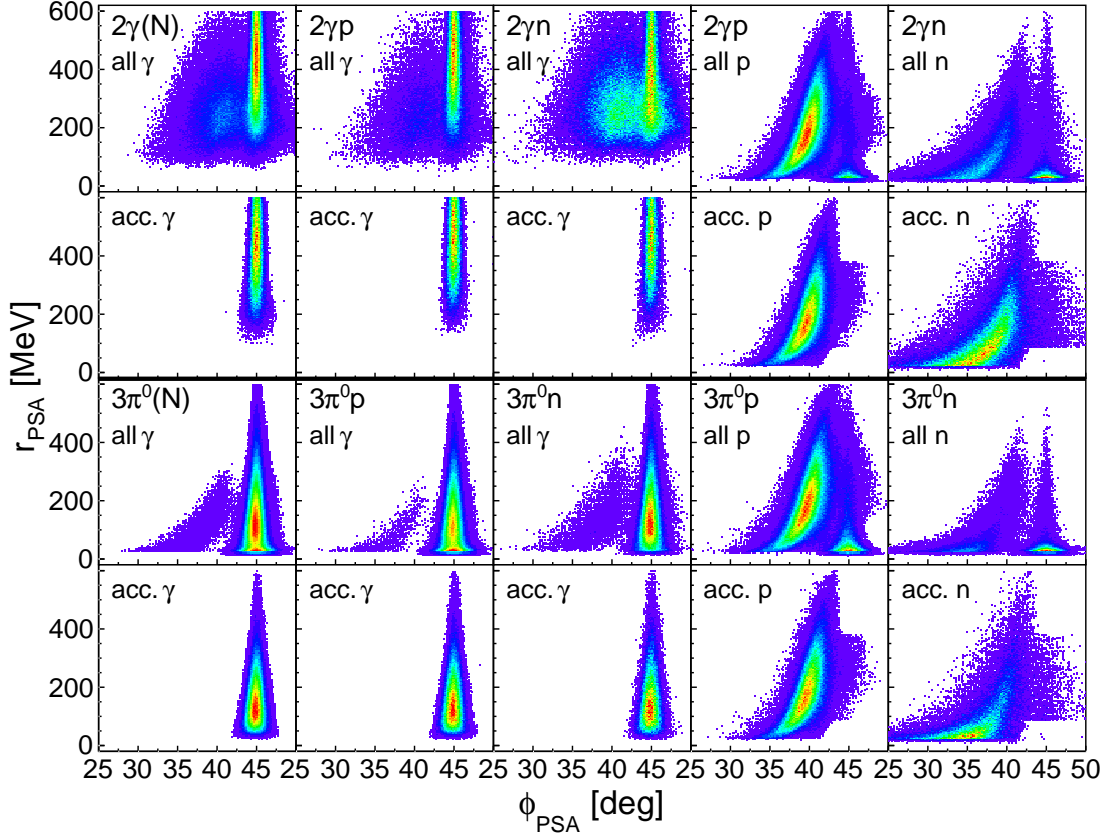
Fig. 4.10: Overview of the TAPS pulse-shape-analysis (PSA) spectra: Columns: analysis channels. Upper two rows: $\eta \to 2\gamma$ analysis channels. Lower two rows: $\eta \to 3\pi^0$ analysis channels. Spectra with all events (no cuts) are denoted by 'all', spectra including all cuts are denoted by 'acc.'.

4.4.1 Pulse-shape-analysis

The pulse-shape-analysis (PSA) spectra obtained for all particles in TAPS are shown in figure 4.10. The spectra of all analysis channels are shown for all events (no cuts applied) and for the finally selected events including all analysis cuts. Obviously, as also a cut on the PSA is performed, the spectra for the accepted events are free of any background (see section 4.3.1). But, from the comparison to the spectra of all events, the massive impact of all other cuts can be seen. Without any cuts, there is a significant contamination of neutrons in the photon spectra and vice versa, especially in the $\eta \to 2\gamma$ analysis. Also photons are taken as proton candidates.

4.4.2 Time-of-flight analysis

The time-of-flight (TOF) is a useful quantity that can be used for particle identification, especially for the discrimination of photons and massive particles. It
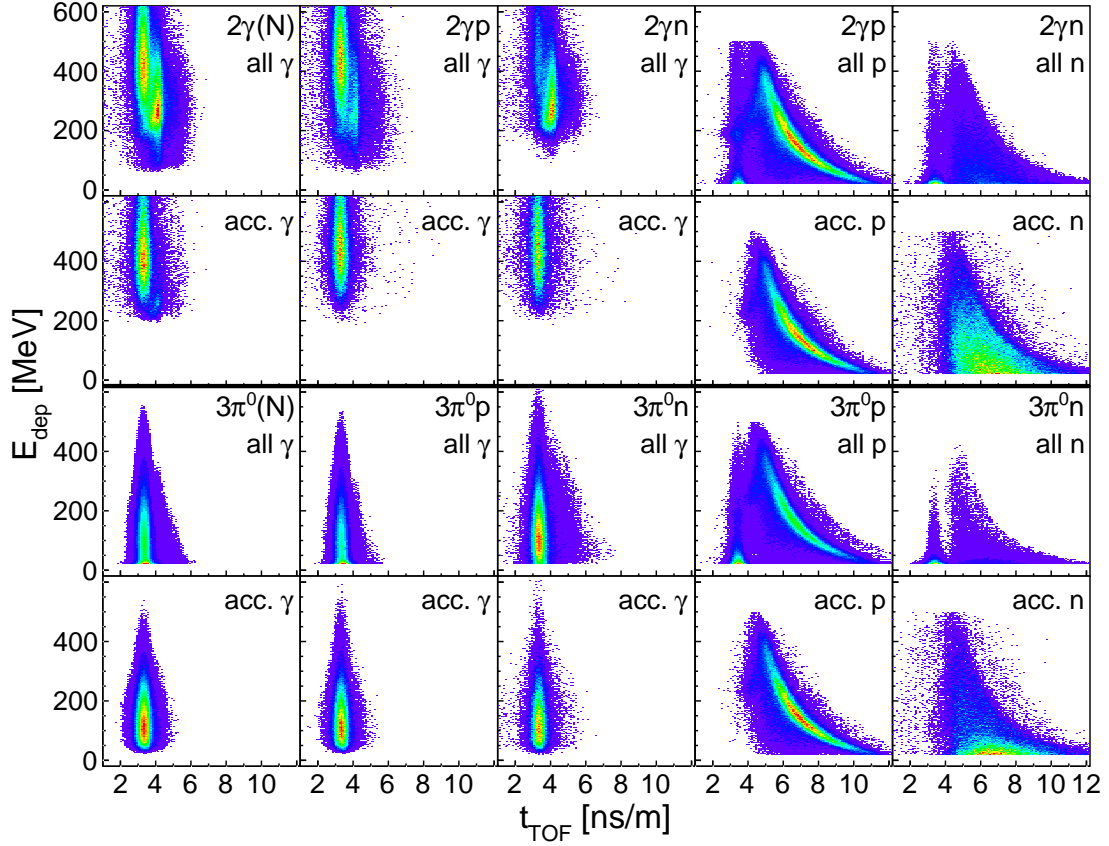
Fig. 4.11: Overview of the TAPS time-of-flight (TOF) spectra: Columns: analysis channels. Upper two rows: $\eta \to 2\gamma$ analysis channels. Lower two rows: $\eta \to 3\pi^0$ analysis channels. Spectra with all events (no cuts) are denoted by 'all', spectra including all cuts are denoted by 'acc.'.

requires that the flight path of the particles has a certain length to achieve the necessary resolution in the time measurement. With a distance of about 25 cm from target to detector this is not fulfilled for the Crystal Ball detector. The distance to TAPS on the other hand, which is around 1.5 m, is sufficiently long and, therefore, the TOF analysis can be performed for particles in TAPS.

In the TOF analysis the deposited energy in TAPS is plotted versus the time-of-flight t_{TOF} that is calculated as

$$t_{\text{TOF}} = \frac{\Delta t}{s} + \frac{1}{c} \mathrel{\hat{=}} \frac{1}{v} \quad [\text{ns/m}] . \tag{4.14}$$

Δt is the time difference between TAPS and the photon tagger that provides better time resolution than a time measurement with respect to the Crystal Ball (see section 3.3 for the time difference calculation). Due to the different lengths of the flight paths s, the time-of-flight is normalized to 1 meter leading to the unit ns/m of this 'time'. As all time calibrations were performed such that the photon time

differences are located at zero for all detector elements, the normalized photon flight time $1/c$ has to be added to the time-of-flight. Hence, using this definition the 'time-of-flight' is the inverse of the velocity.

The TOF spectra for all analysis channels and particles are shown in figure 4.11. The photon bands are located around 3.3 ns for all energies. In the spectra of the $\eta \to 2\gamma$ analyses without cuts, a large background contamination of minimum ionizing pions or protons is present. It is successfully removed by the analysis cuts. Only in the inclusive analysis a tiny fraction is still visible that will be removed by the signal fitting (see section 4.10.1). The proton spectra are clean and the very low energetic photons signatures, which could be caused by primary or secondary (back-scattered) electrons, are removed by the analysis cuts. As the neutrons deposit their energy via various reactions in the detector as, e.g., elastic and inelastic scattering, nuclear reactions (n, γ), (n, p), (n, d), (n, α) which also produce secondary particles, there is no correlation between the deposited energy and the initial energy. This can be seen in the neutron spectra, where no dependence of the deposited energy from the time-of-flight can be identified. Due to inefficiencies of the TAPS Veto detectors, it is important to check if protons were wrongly marked as neutrons in the analysis. A notable contamination would lead to the typical proton band in the neutron spectra. A structure of this kind cannot be clearly seen in the current spectra. In the accepted spectrum of the $\gamma n \to \eta n \to 2\gamma n$ there is a minor accumulation of events in the suspected region, although hardly visible. To rule out possible contamination, a cut on this region was applied but the influence on the resulting cross sections was negligible, especially in the region of interest around $W = 1680$ MeV. Therefore, no cut on the neutron TOF was applied in the final analyses.

4.4.3 ΔE–E analysis

For charged particles there is another detector information that can be used, namely the deposited energy in the PID and the Veto detectors. Charged particles are marked as charged in the analysis when any coincident signal above threshold was deposited in these detectors, but looking at the amount of deposited energy, further particle discrimination becomes possible. The typical plots that are made are shown in figure 4.12. The energy deposited by the proton candidate of the two $\gamma p \to \eta p$ analyses in the PID or Veto detector ΔE is plotted versus the energy deposited in the corresponding calorimeter E. The ΔE values of the protons show a strong dependence on E reflected by the banana-shaped bands. Pions are almost minimum ionizing and thus their band is located at lower energies and shows only a minimal energy dependence. Electrons are located at low ΔE and low E. The resolution for particles in TAPS is worse because there is a large loss of the Veto signals because the scintillation light is led via long and thin optical fibers to the
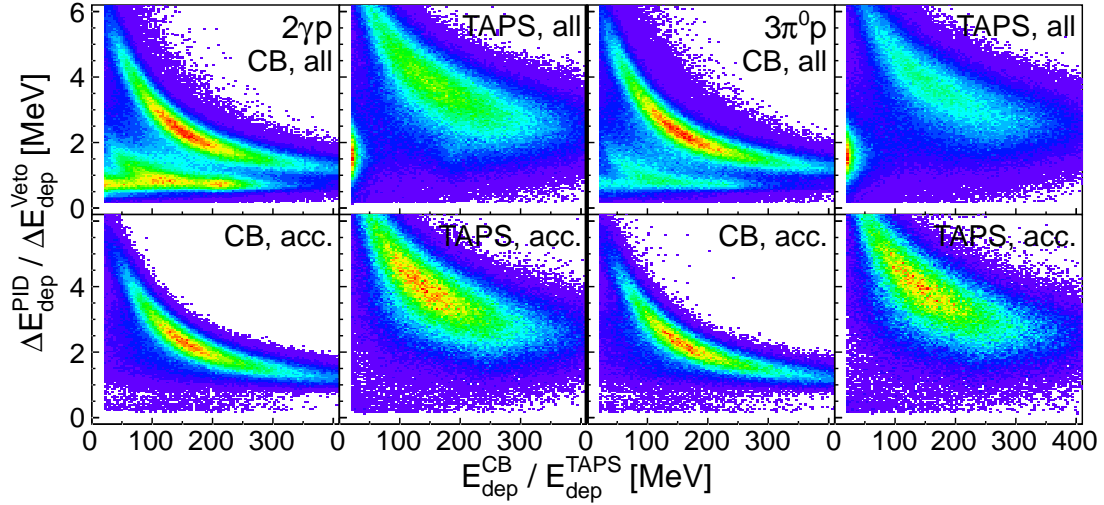
Fig. 4.12: Overview of the ΔE–E spectra: Left two columns: $\gamma p \to \eta p \to 2\gamma p$ analysis. Right two columns: $\gamma p \to \eta p \to 3\pi^0 p$ analysis. Spectra with all events (no cuts) are denoted by 'all', spectra including all cuts are denoted by 'acc.'.

photomultipliers. It can be seen that in the spectra without analysis cuts there is a large contamination of pions and electrons in CB, whereas in TAPS only electrons seem to be present. All this background is successfully removed by the analysis cuts leaving only the proton bands in the spectra.

4.5 *W*-reconstruction from the final state

Due to the Fermi motion of the nucleons inside the deuteron, the 'true' center-of-mass energy $W = \sqrt{s}$ cannot be calculated from the initial state. W can be approximated by assuming the nucleon at rest which leads to quasi-free cross sections that correspond to the free cross sections folded with the Fermi momentum distribution. Sharp structures are then smeared and in case of the structure seen in the η-production cross section on the neutron, a direct and model-independent estimation of the intrinsic width is not possible.

Therefore, the center-of-mass energy has to be determined from the final state products, namely as the ηN invariant mass. This requires the reconstruction of the four-momenta of the η-meson and the nucleon. With the experimental setup used for this work, which is optimized for the detection of photons, this can be achieved with high precision for the η-meson. The nucleon measurements have much larger systematic uncertainties. First, the measurement of the direction is less precise because the typical cluster sizes for protons and neutrons are much smaller than for photons, as the energy deposition is more concentrated. Secondly, the reconstruction of the kinetic energy from the deposited one is impossible for neutrons, as discussed in section 4.4.2. The proton kinetic energy could be reconstructed

by applying various corrections to the deposited energy, as the calorimeters were calibrated for the energy measurement of photons. These corrections require also simulations of the energy loss in the detector materials, which is again a source of significant systematic uncertainty. Fortunately, there are two other methods for the reconstruction of the kinetic energy of the recoil nucleons, namely by making use of the reaction kinematics and a time-of-flight measurement, which can be used for both protons and neutrons in an equivalent way. Using the same method is important for consistency between proton and neutron data, as the neutron measurement itself is already exhibiting a notable systematic uncertainty.

4.5.1 Kinematic W-reconstruction

In the participant-spectator model (see appendix B.1) neglecting the deuteron binding energy of about 2 MeV, the kinematics of the reaction $\gamma d \to \eta pn$ being

$$\begin{pmatrix} E_\gamma \\ \vec{p}_\gamma \end{pmatrix} + \begin{pmatrix} m_d \\ 0 \end{pmatrix} = \begin{pmatrix} E_\eta \\ \vec{p}_\eta \end{pmatrix} + \begin{pmatrix} E_P \\ \vec{p}_P \end{pmatrix} + \begin{pmatrix} E_S \\ \vec{p}_S \end{pmatrix}, \qquad (4.15)$$

with either the proton or the neutron as participant P or, respectively, spectator S, is completely determined if the following quantities are known or were measured:

- initial state: E_γ, $\vec{p}_\gamma = (0, 0, E_\gamma)$, m_d

- final state: $\vec{p}_\eta$, m_P, m_S, m_η, θ_P, ϕ_P

θ_P, ϕ_P are the polar and azimuthal angles of the participant nucleon and the m_i denote the masses of the corresponding particles. The four remaining unknown variables are therefore

- final state: T_P, $\vec{p}_S$,

i.e., the kinetic energy of the participant T_P and the three-momentum of the spectator $\vec{p}_S$. As equation 4.15 contains four constraints in terms of energy and momentum conservation, the system is determined and the four remaining variables can be calculated. In [81] the closed-form expression for T_P was derived and the final result can be found in appendix B.2 of this work. Knowing now the full four-momentum of the recoil participant nucleon, cross sections as a function of the ηN invariant mass $W = m(\eta N)$ can be obtained, where no effects from Fermi motion are present.

For the estimation of the intrinsic with of the structure seen in the η-production cross section on the neutron, it is important to estimate the resolution of this W-reconstruction. This was done by simulating events created by a special event generator (see section 4.8.1), which created phase space decays of an intermediate state with fixed mass and zero width (δ-function) into an η-meson and a proton
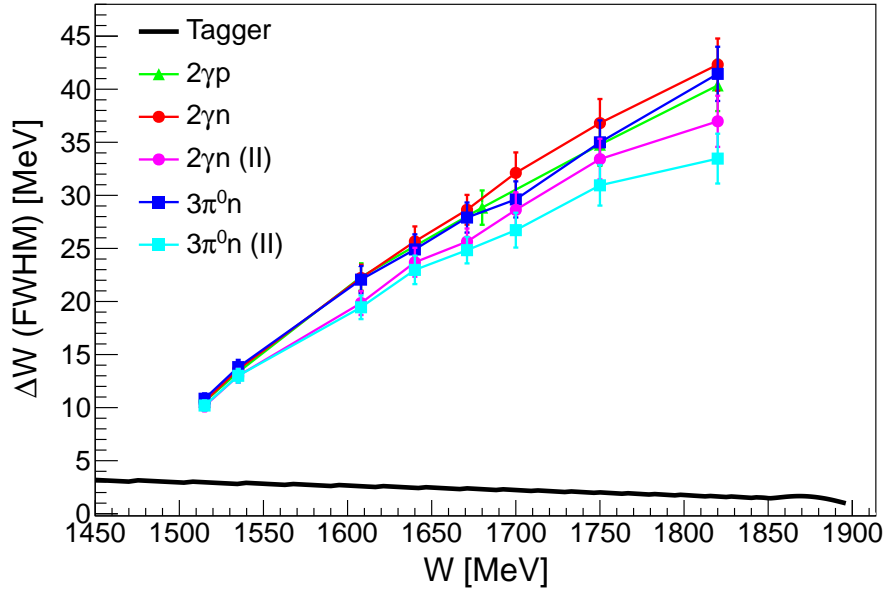
Fig. 4.13: W-dependence of the resolution of the kinematic W-reconstruction: The FWHM resolutions were extracted approximately by Gaussian fits. Green triangles: $\gamma p \rightarrow \eta p \rightarrow 2\gamma p$ analysis. Red/magenta circles: $\gamma n \rightarrow \eta n \rightarrow 2\gamma n$ Analyses I/II. Blue/cyan squares: $\gamma n \rightarrow \eta n \rightarrow 3\pi^0 n$ Analyses I/II. The black curve represents the intrinsic resolution of the photon tagger for comparison.

or a neutron. The same analysis used for the experimental data was performed and the ηN invariant mass was reconstructed. Due to the finite angular and energy resolutions of the detectors, a distribution around the fixed value of W was then obtained. The resolution distributions are slightly asymmetric but can be approximately fitted with a Gaussian function.

Several simulations at fixed W-values were performed to estimate the resolution in the complete W-range. In figure 4.13 the so obtained FWHM resolutions of the two neutron analyses (Analysis I and II for both η-meson decay channels) along with the one of the $\eta \rightarrow 2\gamma$ proton analysis are compared to the intrinsic resolution of the photon tagger. The latter is much better by nearly one order of magnitude. The resolutions of the standard analyses for proton and neutron channels are very similar considering the errors of the Gaussian fits. They rise nearly linearly from $\Delta W = 10$ MeV at 1515 MeV to $\Delta W = 42$ MeV at 1820 MeV. The corresponding resolutions for the Analysis II including more strict cuts (see section 4.3.7) are improved by $\sim$10%.

The simulation of ηN-decays at fixed values of W was used to check the method of the W-reconstruction by replacing the measured input quantities by the generated ones. Then, by re-replacing the generated quantities by the measured ones, it is possible to estimate the contributions of the different error sources to the final resolution one-by-one. This cannot be done analytically as the interference
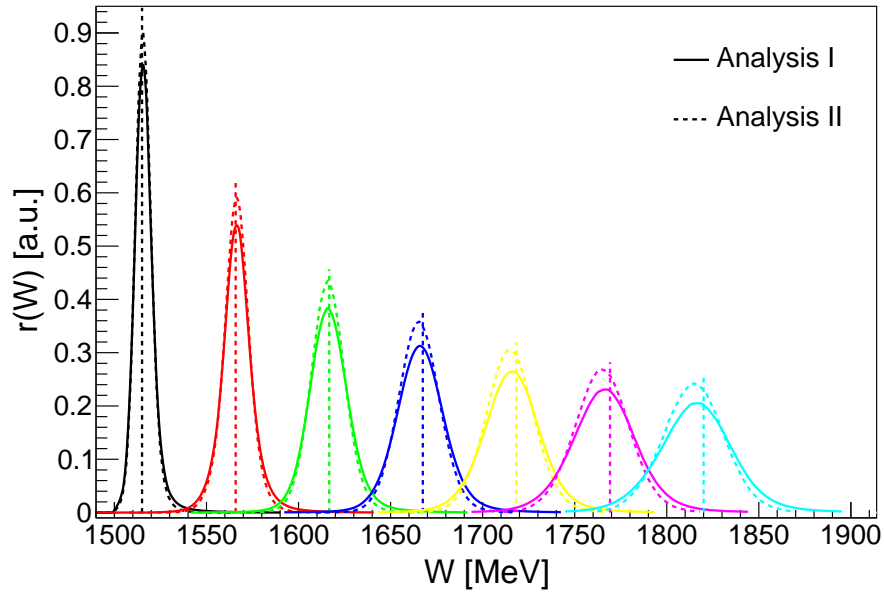
Fig. 4.14: Resolution distributions of the kinematic W-reconstruction for the $\gamma n \to \eta n \to 2\gamma n$ analysis: Solid curves: distributions of Analysis I. Dashed curves: distributions of Analysis II. Dashed vertical lines: simulated fixed W-value leading to the corresponding distribution.

between the different error sources due to kinematics and angular distributions of the different reactions is nontrivial.

The error of the incoming photon beam energy ΔE_γ was found to be negligible, which was expected since it is smaller than 1% for all tagger channels. Therefore, the resolution is made up of the four-momentum measurement of the η-meson and the direction measurement of the recoil nucleon. The decreasing resolution with rising W was found to be caused by the degradation of both of them with higher W.

In case of the η-meson four-momentum measurement, this is caused by the worse energy resolution for higher energetic η-mesons, which could be due to shower losses of the high energetic decay photons. The direction measurement of the η-meson on the other hand improves with higher energy since the decay photon clusters are larger, which leads to a better triangulation of the impact positions. Nevertheless, this apparently does not compensate the worse energy resolution so that the overall resolution of the four-momentum measurement declines with rising W.

The resolution of the nucleon direction measurement is itself only weakly depending on the energy of the nucleon. It is slightly better for protons than for neutrons because neutrons can make large energy deposits in remote detector elements with respect to the impact element, which smears the position calculation. The worsening with rising W comes from the fact that above $W \sim 1550$ MeV the

majority of nucleons are detected in Crystal Ball. As the resolution in the polar angle $\Delta\theta$ is much worse in CB than in TAPS ($\Delta\phi$ being similar), the resolution of the direction measurements becomes worse with higher W.

For the neutron analyses eight simulations with fixed values of W between 1515 and 1820 MeV were performed (see figure 4.13). From these nodes the resolution distributions at any value of W could be sampled by interpolation. This was needed for the convolution fit presented in section 4.5.3, because of the strong dependence of the W-resolution on W itself and due to the non-Gaussian line shapes. Figure 4.14 shows the resolution distributions for the $\gamma n \to \eta n \to 2\gamma n$ analysis with standard (Analysis I) and more strict cuts (Analysis II). The deviations from Gaussian distributions are hardly visible in this plot. The broadening of the resolution with higher W is obvious. Also a shift of the resolution maxima relative to the generated fixed W-value can be seen. This is probably due to some systematic effects in the W-reconstruction for higher energies. Finally, the effect of the stronger cuts in Analysis II is reflected by narrower resolution distributions.

4.5.2   Time-of-flight W-reconstruction

The second method that can be used for the reconstruction of the kinetic energy of the recoil nucleon is the time-of-flight (TOF) measurement. This is only possible for nucleons in TAPS, as the distance from the target to the Crystal Ball detector elements is too small (see section 4.4.2). This limited acceptance leads to the fact that cross sections can only be obtained for a limited angular region. In case of η-production measured with the current experimental setup the resulting range is $-1 < \cos(\theta_\eta^*) < -0.5$, where θ_η^* is the polar angle of the η-meson in the center-of-mass frame.

The kinetic energy of the recoil participant nucleon T_P can be calculated from the measured time-of-flight t_{TOF} of equation 4.14 via

$$T_P \;=\; m_P(\gamma - 1) = m_P \left(\frac{1}{\sqrt{1 - \beta^2}} - 1 \right), \qquad (4.16)$$

$$\beta \;=\; \frac{v}{c} = \frac{1}{t_{\mathrm{TOF}} \cdot c}, \qquad (4.17)$$

where m_P is the mass of the participant.

Instead of using t_{TOF} from the relative timing between the tagger and TAPS, it is also possible to obtain the time-of-flight using TAPS itself as reference detector. In this case, at least one photon has to be detected in addition to the nucleon in TAPS and provide a reference time. The extraction of cross sections in case of η-production and using the $\eta \to 2\gamma$ decay is impossible, since the angular distribution of the two decay photons has a strong energy dependence and the
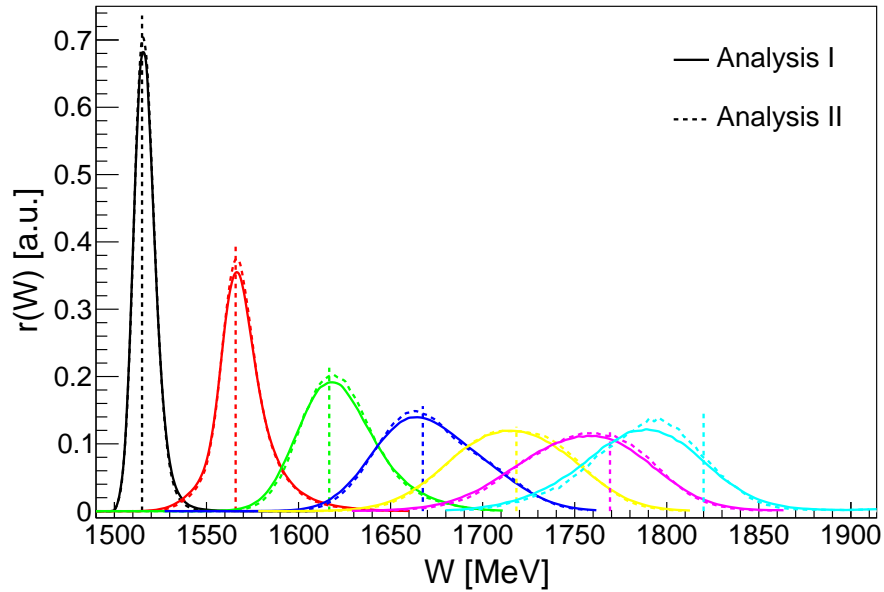
Fig. 4.15: Resolution distributions of the TOF W-reconstruction for the $\gamma n \to \eta n \to 2\gamma n$ analysis: Solid curves: distributions of Analysis I. Dashed curves: distributions of Analysis II. Dashed vertical lines: simulated fixed W-value leading to the corresponding distribution.

photon multiplicity is too small. At low beam energies, the opening angle between the two photons in the laboratory frame is close to 180 degrees. Hence, there is a notable probability that when one photon is going to TAPS, the second one escapes through the backward hole of CB and the event is not detected. Due to the Lorentz-boost the opening angle becomes smaller at higher beam energies which allows the detection of one photon in TAPS and one in CB. Nevertheless, due to the small angular acceptance of TAPS and because only two decay photons are available, the probability of having suitable events is very low. On the other hand, in the $\eta \to 3\pi^0$ analyses the more isotropic distribution of the six decay photons allows the extraction of cross sections using the TAPS-TAPS time-of-flight measurement (see section 5.3.1). Still, the detection efficiency of this method is very low and the cross sections were extracted for crosscheck purposes only and were not used any further. All following discussions refer therefore to the standard TOF W-reconstruction using the tagger as reference detector.

Similarly to the studies performed for the kinematic W-reconstruction, the resolution of the TOF W-reconstruction was investigated using the same simulated data of ηN-decays at fixed W-values. First, the validity of the method was successfully checked by reconstructing the kinetic energy using the exact generated input variables. Then, the contributions of the different variables to the total resolution was studied.

As in the kinematic reconstruction, the four-momentum of the η-meson accounts to the total resolution. Due to the reasons explained before, the η-resolution becomes worse at higher W. Nevertheless, the relative contribution to the total resolution is small in contrast to the situation in the kinematic method.

Also the influence of the nucleon direction measurement plays a minor role. The angular resolution is similar for all TAPS elements, it degrades only for the most inner and outer elements. Contributions can therefore be larger, when a nucleon is detected in the inner rings, which leads to larger relative errors due to the short flight path and the worse angular resolution.

The largest contribution to the total resolution is caused by the time resolution. For photons, the typical tagger-TAPS time resolution determined from experimental data is around 620 ps for the tagger channels corresponding to 1600 MeV $< W <$ 1700 MeV. However, the resolution for neutrons is worse because of the energy deposition via nuclear reactions in the crystals that is not as homogeneous as for photons. The relative importance of this effect is higher when the flight times are smaller, i.e., when the neutron energies are higher. This process is hard to simulate. In order to achieve reasonable agreement between simulation and experimental data, the neutron time-of-flight was determined manually by smearing the exact time-of-flight calculated from the generated four-momentum of the neutron. Also an additional correction of the reconstructed W was necessary, that was calculated using the W-value of the kinematic reconstruction. Finally, the W-resolution of the time-of-flight method could be estimated.

Figure 4.15 shows the resolution distributions of the analysis $\gamma n \to \eta n \to 2\gamma n$ for several values of W. They were again obtained via interpolation of the distributions of the eight simulations with fixed W between 1515 and 1820 MeV. Due to the declining resolution in the time measurement of higher energetic neutrons, the W-resolution also declines with higher W. Despite the correction that was mentioned above, the distributions become also asymmetric and their maxima are shifted with respect to the generated W position. At $W = 1671$ MeV, the FWHM resolution is around 70 MeV. Possibly narrow structures in cross sections that are obtained using the TOF W-reconstruction are thus expected to be substantially smeared. It can also be seen that the more stringent cuts applied in Analysis II do not change the resolution significantly. This shows that the TOF W-resolution is dominated by the time measurement and events well outside the quasi-free approximation have a minor influence on the resolution.

4.5.3 Convolution of the *W*-resolution

The measurement of experimental data is often affected by a finite resolution, i.e., the measured distribution $m(x)$ is a convolution of the true signal distribution $s(x)$ and the experimental resolution $r(x)$:

$$m(x) = s(x) \otimes r(x) = \int_{-\infty}^{\infty} s(x)\, r(x-u)\, du = \int_{-\infty}^{\infty} s(x-u)\, r(x)\, du \qquad (4.18)$$

This integral can only be solved analytically in special cases for certain $s(x)$ and $r(x)$. Normally, it is solved numerically using either direct numerical integration or via Fourier transformation since a (circular) convolution can be performed via simple multiplication in the frequency domain. Assuming a model for the signal distribution and knowing the resolution, the convolution of the two can be fitted to the measured data and properties of the true signal can be extracted via the signal model distribution.

In the current work properties will be extracted from cross section data depending on the center-of-mass energy W, which was reconstructed as described in the previous two sections. The resolutions for both reconstruction methods were estimated from simulated data and, therefore, the cross sections can be fitted with a convolution of a signal model distribution and the resolution. This kind of fit is needed because the width of the structure seen in the total cross section of η-production on the neutron is of the same order as the resolution (see section 5.4.3). If this would not be the case, either the signal or the resolution would dominate the convolution and a convoluted fit would not be necessary or possible, respectively.

The convolution of the signal function and the W-dependent W-resolution was implemented in this work by simple numerical integration using the composite trapezoidal rule. As mentioned before the resolutions were interpolated and normalized at any values of W from the resulting line shapes of eight simulations of δ-functions at fixed values of W. The integration limits were determined from the resolution line shapes and corresponded roughly to 3σ.

The fitting method was tested with simulated data as follows. An intermediate state, whose mass was sampled according to a Breit-Wigner distribution with fixed width Γ_G, was generated and the final state particles from its decay into $\eta n \rightarrow 2\gamma n$ were tracked in the detector simulation. The spectrum of the reconstructed center-of-mass energy W using the kinematic reconstruction is shown in figure 4.16 by the black circles. Three states at $W = 1671$ MeV with $\Gamma_{G,i} = 25, 30, 35$ MeV were simulated. The spectra were then fitted with a convolution of a Breit-Wigner function and the W-dependent resolution of the kinematic W-reconstruction, and a polynomial of second order, which accounts for combinatorial background. The data points are very well described by this fitting function represented by the black
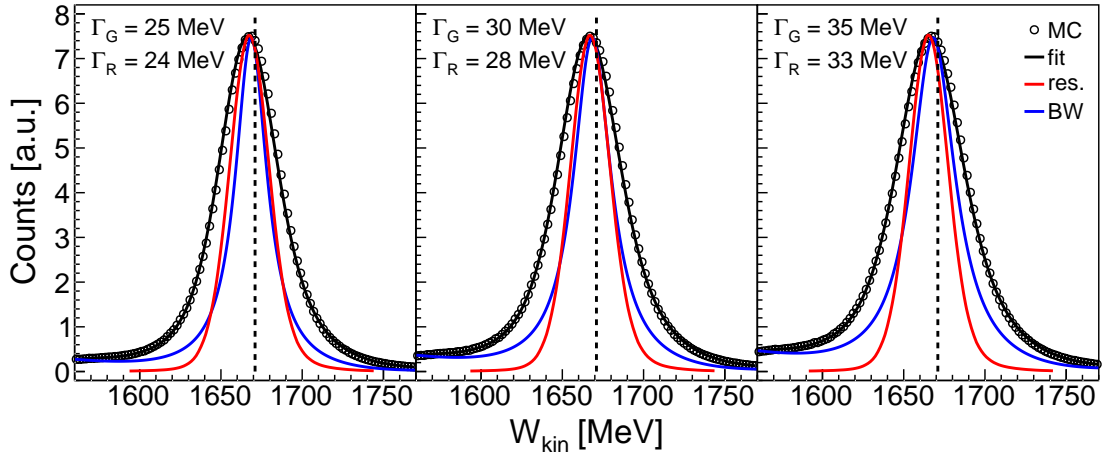
Fig. 4.16: Reconstruction of the intrinsic widths of simulated Breit-Wigner distributions using convolution fits of signal and background distributions: Γ_G: generated width. Γ_R: reconstructed width. Black circles: simulated data. Black curves: total fitting function. Red curves: resolution at the obtained mean value. Blue curves: pure Breit-Wigner signal function. Dashed lines: generated mean at 1671 MeV.

curve. All obtained Breit-Wigner mean values are close to 1668 MeV and thus slightly shifted with respect to the generated value. This means that despite using the resolutions in the convolution fit, the latter is not quite able to compensate for these shifts caused by the W-reconstruction. The obtained widths of the Breit-Wigner functions account to $\Gamma_{R,i} = 24, 28, 33$ MeV and are close to the generated ones. The red and the blue curves show the resolutions at the obtained mean position and, respectively, the pure Breit-Wigner signal functions with intrinsic widths $\Gamma_{R,i}$. The normalization of these functions in the figure is arbitrary.

The performed test described above gives confidence that using a convolution fit including the reconstruction resolution, intrinsic parameters of the signal distribution can be reasonably approximated from the spectra obtained by the kinematic W-reconstruction. Therefore, it was applied to the measured data as will be described in section 5.4.3.

4.6 Subtraction of tagger random coincidences

During the event time window (gate) all electron hits in the tagger were registered. One of them is the true coincident electron, which produced the bremsstrahlung photon that triggered the event recording by undergoing a reaction in the target. However, due to the high intensity of the electron beam, additional electrons are detected within the event gate, which are not correlated to the photon that triggered the event. Depending on the exact beam intensity, the number of tagger
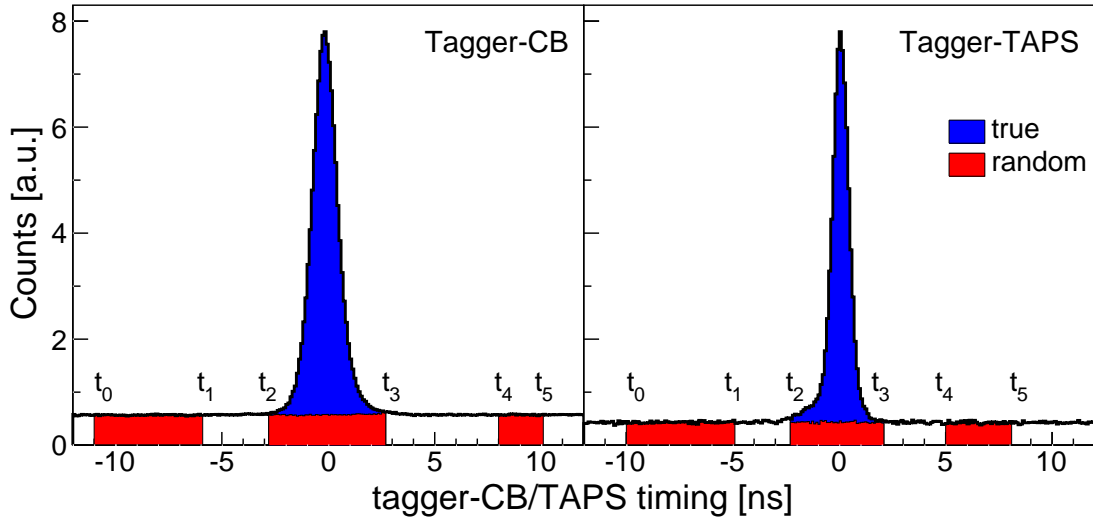
Fig. 4.17: Tagger-calorimeter coincidence time spectra: Left-hand side: timing between tagger and Crystal Ball. Right-hand side: timing between tagger and TAPS. Read areas: random background. Blue areas: true coincidences. The widths of the time intervals are figurative only.

hits in the current experiment had mean values around 35 hits. This leads to the fact that with such an experimental setup the incoming photon beam energy cannot be known on an event-by-event basis. Rather, a statistical subtraction of the uncorrelated background has to be performed on all quantities calculated in the analysis that incorporate information of the incoming photon. The classical method applied also in this work uses the coincidence time spectra between the calorimeter and the photon tagger for a sideband subtraction. A detailed discussion can be found in [82].

The subtraction method uses the fact that, obviously, coincidence should be seen in the timing between the photon tagger and the calorimeters. Figure 4.17 shows the timing (see section 3.3) between all tagger hits and the calorimeter times for all events of the $\gamma p \rightarrow \eta p \rightarrow 2\gamma p$ analysis. The calorimeter time is obtained by averaging the hit times of the η-meson decay photons. Whenever one or more photons were detected in TAPS, only their time information was used because of the better resolution. This can be seen in the tagger-TAPS spectrum, where the clear coincidence peak is narrower compared to the tagger-CB timing. The constant and flat background is caused by the uncorrelated electron hits. Under the assumption that the time and energy distributions of the uncorrelated hits are purely random, their contributions to the distributions of any quantity calculated using the incoming photon are equal in the intervals of uncorrelated events $[t_0, t_1]$, $[t_2, t_3]$ and $[t_4, t_5]$ (red areas). Therefore, the distribution of the true coincidences in the prompt interval $[t_2, t_3]$ (blue area) can be calculated by subtracting the normalized random distributions obtained in the intervals $[t_0, t_1]$ and $[t_4, t_5]$ from the total distribution in the interval $[t_2, t_3]$.

In this work the limits of the prompt intervals were determined separately for the tagger-CB and tagger-TAPS timings and individually for every tagger channel, as the resolutions of the latter vary strongly. Due to bad tagger channels having very asymmetric coincidence peaks, rather safe limits of $\pm 4\sigma$ were applied. The subtraction of the random coincidences was implemented by filling the same histograms with different weights for events of the prompt interval and the two random intervals. The prompt weight was set to $w_p = 1$ and the random weight w_r was calculated from the normalization of the time intervals as

$$w_r = -\frac{t_3 - t_2}{t_1 - t_0 + t_5 - t_4} \,. \tag{4.19}$$

The number of true entries N_t and its statistical error calculated from the number of prompt entries N_p and random entries N_r are then

$$N_t = N_p + \sum_{i=1}^{N_r} w_r = N_p + w_r N_r \,, \tag{4.20}$$

$$\Delta N_t = \sqrt{N_p + w_r^2 N_r} \,, \tag{4.21}$$

where ΔN_t is calculated as the square root of the sum of weights. The statistical error can be improved when w_r is minimized by using large intervals for the random coincidences. In this work w_r was in the order of -0.012, i.e., the random intervals were about 80 times larger than the prompt interval.

A technical detail that should be added here is the fact that special attention has to be paid in the subtraction of the random coincidences from time-of-flight spectra, when the tagger is used as reference detector. In the TOF calculation of events from the random intervals, the actual tagger times cannot be used as reference times, since they lead to unphysical flight times due to the position of the random intervals. The solution is to calculate a random tagger time for all random events that is uniformly distributed within the prompt time interval, corresponding to the possible times of random events inside that interval.

Finally, it should also be noted that the subtraction of the tagger random hits is only necessary for experimental data. In the analysis of simulated data, there is exactly one coincident hit in the tagger without any random background present (see section 4.8.1).

4.7   Software trigger

In order to determine the detection efficiencies for the measured reactions, the conditions set by the hardware trigger (see section 2.6.2) have to be applied to the simulated data as well via a software trigger. This trigger has to be modeled

such that it is as close to the hardware trigger as possible. In particular, all events rejected by the hardware trigger should also be rejected by the software trigger. However, in this analysis a more strict condition was implemented in the software trigger compared to the one in the hardware. Namely, the conditions on the CB energy sum and the multiplicity that will be described below, were checked using the η-meson decay photons only. The recoil nucleons were not allowed to contribute to the trigger decision. The reason for that is the very different interaction of protons and neutrons with the detectors compared to each other. Including these particles in the trigger decision would lead to a source of systematic uncertainty when comparing the final proton and neutron results.

4.7.1 CB energy sum trigger

The CB energy sum trigger is checking the total sum of the analog signals of all NaI(Tl) crystals against a threshold, which corresponds to a certain energy. Because the analog signals are used to build up the total sum, the calibrated energies cannot be used to calculate the total energy sum in the modeling of the software trigger. Depending on the calibration constants of a single detector, its contribution to the analog sum would be under- or overestimated. Therefore, the procedure developed in [48, 72] was used. Based on the calibration constants, the analog signal is reconstructed via a de-calibration of the calibrated energy which leads to an approximation of the relative contributions of the single detectors to the analog signal sum. The same procedure was applied to the simulated data using the same values for the de-calibration as for the experimental data.

The spectra of the CB photon energy sum E_{sum} for the exclusive analysis channels of the May 2009 beamtime are shown in figure 4.18. All analysis cuts were applied to the spectra. The distributions of the $\eta \to 2\gamma$ analyses show an additional maximum around 300 MeV, which is caused by events with only one detected photon in the Crystal Ball. The corresponding distribution for the proton and neutron channels are slightly different. This is due to the fact that the photon energy sum depends on the energy and angular distribution of the η-meson and thus a certain model dependence is introduced. Therefore, the settings of the CB photon sum software trigger had to be determined for all analysis channels individually.

Experimental and simulated data were normalized in the intervals $[400, 700]$ MeV ($\eta \to 2\gamma$) and $[600, 900]$ MeV ($\eta \to 3\pi^0$), where the influence of the CB energy sum trigger was expected to be negligible. For lower energies, a depletion of events can be observed for the experimental data caused by the hardware trigger (upper row). This can be seen even more clearly when the ratio of the experimental and the simulated spectra is calculated (middle row). The sharp rise from 0 to 1 near 300 MeV is consistent with the CB energy sum threshold
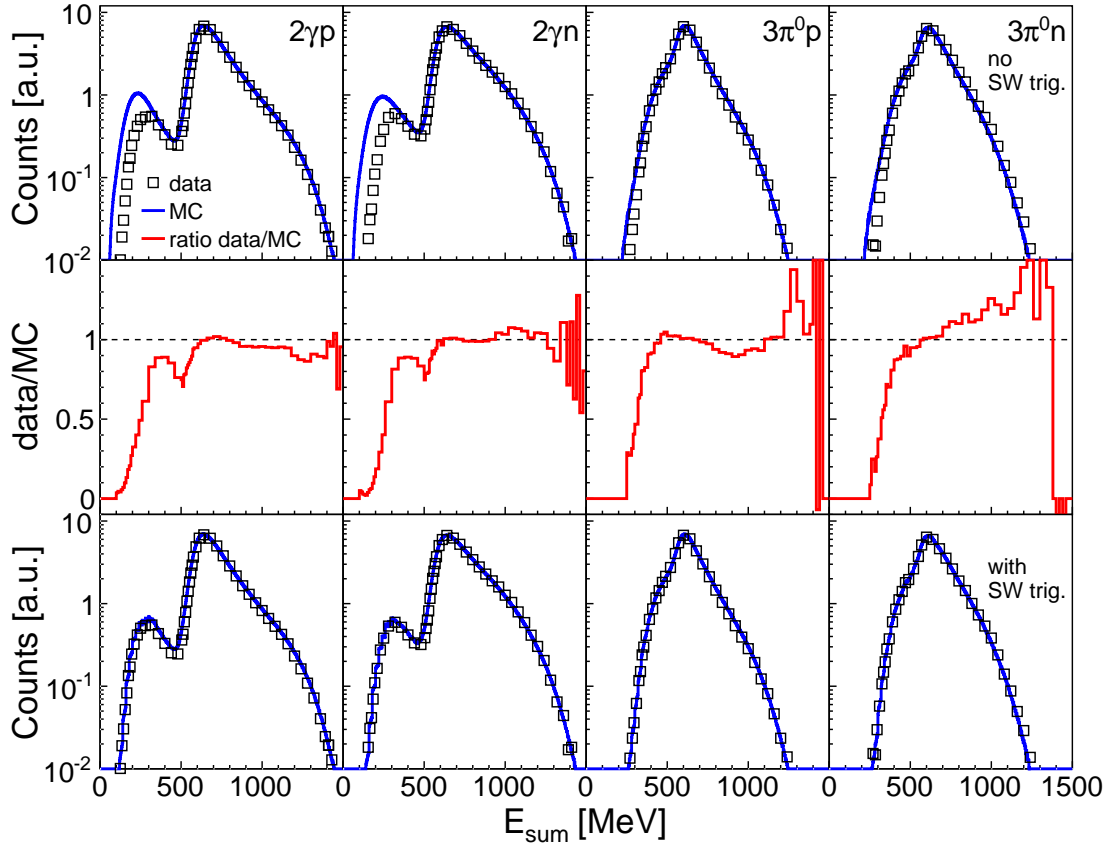
Fig. 4.18: Overview of the CB energy sum software trigger: Columns: exclusive analysis channels of May 2009 beamtime. Upper row: CB photon energy sum without software trigger. Middle row: ratio of experimental and simulated data. Lower row: CB photon energy sum with software trigger. Black squares: experimental data. Blue histograms: simulated data. Red histograms: ratio data/MC. Note the logarithmic y-axes for the sum spectra.

that was set around 300 MeV during data taking. The deviations from a value of 1 at higher energies are caused by normalization effects from inaccuracies of the simulated event distributions.

The software trigger for the energy sum was modeled similarly to the one in [75]. Instead of fitting the ratio histogram with a cumulative distribution function and rejecting events according to that function, in the current work the simulated events were weighted with a factor $f_{MC} < 1$ obtained directly from the ratio histogram. The weighting was performed up to $E_{sum} \sim 700$ MeV, where the ratio is reaching a value of one. The comparison of the resulting simulated distributions with the experimental spectra, shown in the last row of figure 4.18, shows a very good agreement between the two. Hence, the effect of the CB energy sum hardware trigger could be successfully reproduced and applied to simulated data.
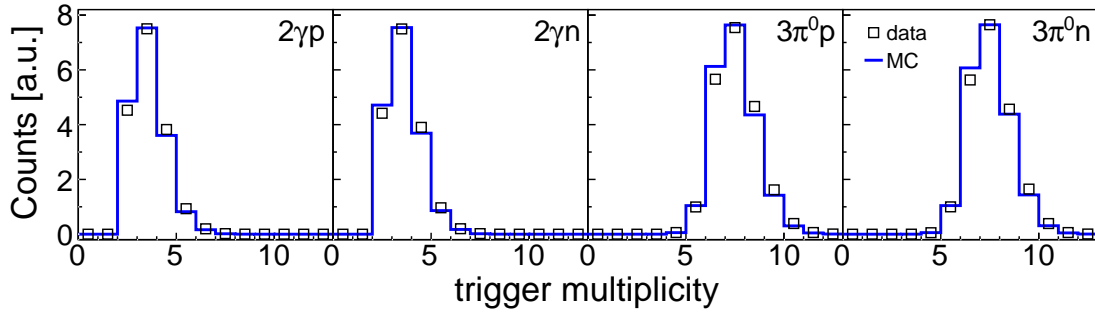
Fig. 4.19: Overview of the multiplicity software trigger: Columns: exclusive analysis channels of May 2009 beamtime. Black squares: experimental data. Blue histograms: simulated data.

4.7.2 Multiplicity trigger

The multiplicity trigger allows an approximate selection of the number of detected particles with different granularities for CB and TAPS. In CB 16 adjacent detectors are grouped together resulting in 45 blocks. Each block contributes to the multiplicity if at least one detector signal is above threshold. TAPS is divided into six sectors that contribute to the multiplicity by forming the logical OR of all detectors in one sector (see section 2.6.2 for more details).

In the software model of the multiplicity trigger, TAPS elements belonging to either the three most inner rings or the most outer ring were not allowed to contribute to the sector-wise logical OR. Otherwise electromagnetic background, which is mostly present in very forward direction and detected in the most inner rings, could fudge the trigger decision. In the most outer ring, there is considerable shower loss due to the detector geometry and, therefore, possible unclean clusters detected in this region are ignored in the trigger decision as well.

The software multiplicity trigger was applied to experimental and simulated data acting on the η-meson decay photons only, as described before. The individual thresholds in terms of calibrated energies for all CB and TAPS detectors were determined for the experimental data (see sections 3.4.1 and 3.4.2) and the same values were used in the analysis of simulated data. For the December 2007 and May 2009 beamtimes a minimum multiplicity of 2 was required for an event in order to be accepted. For the February 2009 data the minimal multiplicity was 3, which allowed the analysis of the $\eta \to 3\pi^0$ decays only.

Figure 4.19 shows a comparison of the trigger multiplicity distributions of experimental and simulated data for the exclusive analyses of the May 2009 beamtime. All analysis cuts were applied to produce the shown spectra and the normalization was calculated by the total integral of the histograms. The agreement between measured data and simulated data is reasonably good. The expectedly very different distributions for the two η-meson decay analyses with

two and, respectively, six detected photons are well reproduced by the simulated data, which indicates that the implementation of the multiplicity software trigger is appropriate.

4.8   Detection efficiency correction

The detection efficiency corrections needed for the absolute normalization of cross sections were determined using the simulation software A2, which is a Geant4-based model of the experimental setup (see section 2.7.2). Detection efficiencies were determined individually for all analyses and types of cross sections as functions of the η-meson polar angle in the center-of-mass frame $\cos(\theta_\eta^*)$ and an energy e, either being the incoming photon beam energy E_γ or the center-of-mass energies $W_{\mathrm{kin}}, W_{\mathrm{TOF}}$. In general, efficiencies were calculated using the same binning as for the corresponding excitation functions, which allowed a straight-forward normalization of the latter. Knowing the generated and the detected parameters of the simulated events, effective efficiencies ϵ_e were calculated as

$$\epsilon_e(e_{\mathrm{det}}, \cos(\theta_{\eta,\mathrm{det}}^*)) \quad = \quad \frac{N_{\mathrm{det}}(e_{\mathrm{det}}, \cos(\theta_{\eta,\mathrm{det}}^*))}{N_{\mathrm{gen}}(e_{\mathrm{gen}}, \cos(\theta_{\eta,\mathrm{gen}}^*))} \,, \tag{4.22}$$

using the number of detected (N_{det}) and generated (N_{gen}) events. As the energies e and the values of $\cos(\theta_\eta^*)$ are not necessarily the same for the generated (subscript 'gen') and the detected (subscript 'det') events, these effective efficiencies can also take values $\epsilon_e > 1$. It was found that the use of effective efficiencies improves the normalization, especially at threshold, where resolution effects are better taken into account with this parametrization compared to efficiencies obtained only from generated parameters. In the next section, details about the event generation and the adjustment of the simulation to the experimental conditions will be given.

In contrast to most of the previous measurements conducted with the current experimental setup, an exclusive measurement was performed in this work, i.e., the final state recoil nucleons had to be detected as well. It was found that this leads to various complications in the determination of the detection efficiency correction that are not encountered in inclusive analyses, where only decay photons are detected. For a better understanding of the various effects, hydrogen data were analyzed to reduce the complexity of the analysis. Using the cross sections of $\gamma p \to \eta p$ extracted from this data in an exclusive measurement, it was found that several correction were needed in order to achieve reliable nucleon detection efficiencies. They will be described in the following.

4.8.1 Generation and analysis of simulated events

Events for the reactions $\gamma p \to \eta p$ and $\gamma n \to \eta n$ were generated using the OSCAR `TOMCGenReaction` class (see section 2.7.3). This is a versatile event generator based on `TGenPhaseSpace` of the ROOT framework [62], which itself is based on the n-body Monte Carlo event generator `GENBOD` of CERNLIB [83]. The energy of the incoming photon beam was randomly chosen from a uniform distribution starting at the coherent production threshold on the deuteron and ending at the last tagger channel. The initial state momentum of participant and spectator nucleon was randomly taken according to the Fermi momentum distribution inside the deuteron from [80]. Using the participant-spectator model, the intermediate state was built from the four-momenta of the photon beam and the participant nucleon, and its two-body decay into the final state participant nucleon and η-meson was calculated. Depending on the η-meson decay channel the corresponding further decays to the final decay photons were calculated as well. All decays were calculated according to pure phase space.

For the generation of events with fixed center-of-mass energies (δ-functions) or Breit-Wigner mass distributions, the class `TOMCGenResDecay` was implemented and added to the OSCAR library. The event generation is very similar to the one used in the standard class described above. The only difference is that the photon beam energy is calculated backwards from the center-of-mass energy and the four-momentum of the participant nucleon, the latter being sampled from the Fermi momentum distribution.

Finally, the four-momenta of the incoming photon, the η-meson decay photons and the final state participant and spectator nucleons were saved to a file for further processing. In addition, for each event a random reaction vertex inside a cylindrical volume located around the target position was chosen. The height of this cylinder was set to the target length and the diameter was set to the estimated beam spot size on the target, which was approximated to be 1.3 cm in diameter.

The quantities calculated by the event generator were used as input for the A2 simulation (see section 2.7.2), which was configured according to the experimental setup of the corresponding beamtime. The decay photons of the η-meson were tracked along with the participant and the spectator nucleons and their deposited energies and hit times in the sensitive detector volumes were saved for further processing. For the reaction on the proton, 100 million events were simulated for every η-meson decay channel and every beamtime. For the reaction on the neutron, the event number was doubled to 200 million to account for the lower neutron detection efficiency.

The output of the A2 simulation was read by the AcquRoot analysis (see section 2.7.1) similarly to measured experimental data. Additional smearing was applied to deposited energies and hit times when necessary in order to reproduce

the resolutions obtained in experimental data (see section 3.6). The events were associated with tagger channels by comparing the generated photon beam energies with the energy ranges of the tagger channels. As only one photon hit per simulated event was created, the subtraction of random coincidences was not implemented for simulated data. The same detector thresholds used for the experimental data sets were applied in the analysis of the corresponding simulated data. Ignored and bad detector elements were omitted in the exact same way for both data types.

In order to compare experimental and simulated data, the latter had to be weighted accordingly on an event-by-event basis, as it was produced using a uniform E_γ-distribution and pure phase space decays of the intermediate states. Compared to a simulation that creates events directly according to the $1/E_\gamma$-bremsstrahlung distribution and that includes angular distributions of the resonance decays from models or measured cross sections, the method used in this work has several advantages:

- The statistical errors of the generated events are the same for all energy and angular bins. By using sampled events, bins of low cross section values will not only suffer from high statistical errors of the yield measurements but also from higher statistical errors of the detection efficiency corrections obtained from simulated data.

- The simulated data is more versatile since, e.g., angular distributions of different models can be compared with each other without redoing the simulation. Performing simulations is computationally expensive and can thus take a considerable time.

- The method is the only applicable method when the angular distributions of the resonance decays are unknown.

In this work all simulated events were first weighted with $1/E_\gamma$ to account for the bremsstrahlung spectrum of the experimental photon distribution. The η-meson decays were always assumed to be phase space. In the proton simulation events were weighted according to the SAID calculation [84, 85]. The previous measurements on the neutron [15] were used to weight the neutron simulation in a first step. Later, the extracted cross sections of this work were directly used to weight the simulated data for the neutron. It was made sure that this iterative-like procedure was not introducing artificial effects in the final results.

4.8.2   Geant4 physics list selection

Simulations based on the Geant4 framework can choose from several physics lists that include different techniques for modeling the particle interactions in different energy ranges. For medium energy applications, QGSP_BIC and QGSP_BERT
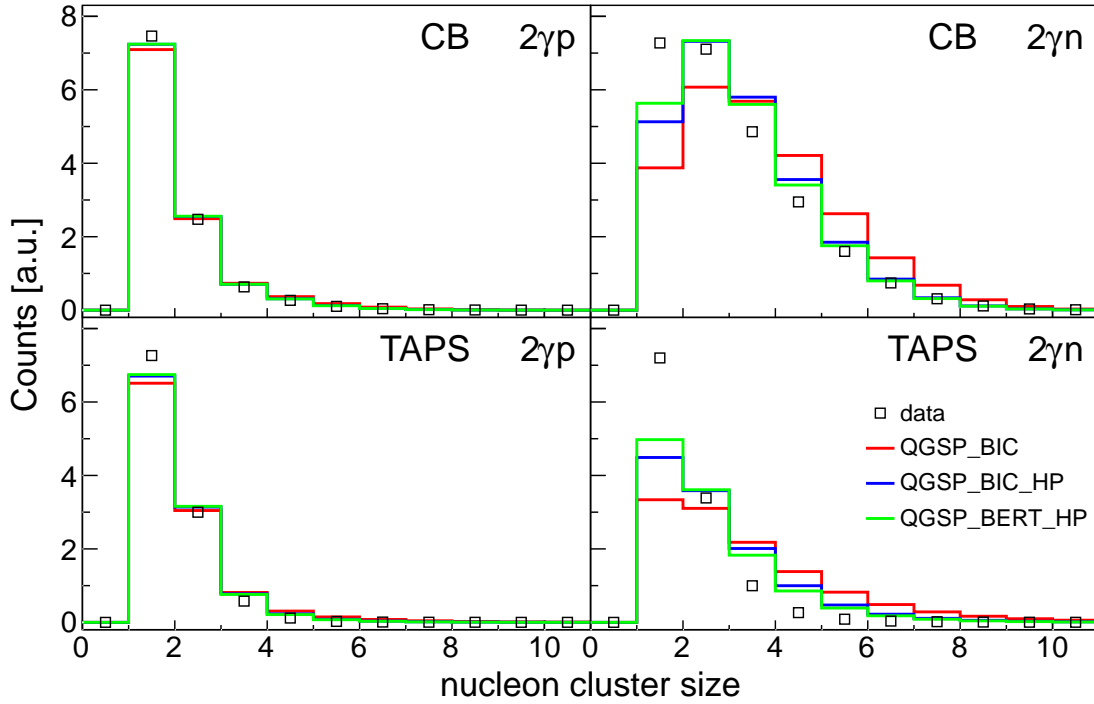
Fig. 4.20: Comparison of nucleon cluster sizes for different Geant4 physics lists: Left column: $\gamma p \rightarrow \eta p \rightarrow 2\gamma p$ analysis. Right column: $\gamma n \rightarrow \eta n \rightarrow 2\gamma n$ analysis. Upper row: CB cluster sizes. Lower row: TAPS cluster sizes. Black squares: experimental data. Histograms: simulation with different physics lists (see legend).

are recommended, which use either the Binary cascade or the Bertini cascade models for the calculation of inelastic hadronic interactions below 10 GeV [86]. For the accurate treatment of neutrons, it is also recommended to use the high precision neutron package (_HP). This consists of a large database of measured cross sections and calculates the transport of neutrons from 20 MeV down to thermal energies.

Simulations of $\gamma p \rightarrow \eta p \rightarrow 2\gamma p$ and $\gamma p \rightarrow \eta p \rightarrow 2\gamma p$ using the physics lists QGSP_BIC, QGSP_BIC_HP and QGSP_BERT_HP were performed and compared. It was found that one of the most indicative quantity for the validation of the different physics lists is the cluster size of the detected nucleons. Figure 4.20 shows an overview of the proton and neutron cluster sizes in CB and TAPS obtained from the standard analysis using all cuts. The spectra of the different simulations are compared to the experimental results by normalization of the total integrals of the spectra. Practically no dependence of the proton cluster size on the used physics list is noticeable. In case of the neutron the distributions from the different models change significantly. The QGSP_BIC physics list seems to produce too large clusters in both calorimeters. Activation of the high precision neutron package improves the agreement considerably, which indicates clearly that this package is needed for the tracking of neutrons in the current application.

The differences between the Bertini cascade and the Binary cascade models are not too large but visible. Overall, the spectra of the first are systematically closer to the experimental distributions. In addition, it was found in the studies of the detection efficiency correction factors (see section 4.8.4) that the neutron detection efficiencies obtained using the Bertini cascade model were closer to the efficiencies extracted from experimental data. Therefore, QGSP_BERT_HP was chosen as the default physics list for all simulations performed in this work and is recommended for future activities involving the detection of neutrons.

4.8.3   Correction of the CB geometry

During the analysis of the deuterium data, significant deviations to the results of previous η-production measurements were observed, especially in the region dominated by the $S_{11}(1535)$ resonance corresponding to $640 < E_\gamma < 900$ MeV. After various successful checks of all the analysis steps, it was decided to perform an analysis of $\gamma p \to \eta p$ using hydrogen data to identify the problem using a less complex analysis. It was found that the exclusive measurement, where the detection of the recoil nucleon is required, leads indeed to some problems caused by the detection efficiency determination for the nucleons. This problems could be mostly solved by applying various corrections, one of them being an update of the detector geometry in the simulation that will be discussed in this section.

An equivalent analysis of $\gamma p \to \eta p$ as used for the main measurement of this work was performed using the hydrogen data set measured in April 2009. The total and differential cross sections obtained by the basic analysis are shown in figures 4.21 and 4.22, respectively, denoted by the red points. For comparison the results of a previous inclusive measurement using hydrogen data obtained at MAMI-C [35] are used. Above $E_\gamma \sim 900$ MeV ($W \sim 1600$ MeV) there is a reasonable agreement of the shapes of the angular distributions to this data, whereas the overall normalization is around $\sim 10\%$ too low. On the other hand, below $E_\gamma \sim 900$ MeV the deviations in shape and normalization are massive, e.g., an enormous dip at η-meson forward angles can be seen in bin $W = 1514$ MeV, which leads to discrepancies in the total cross section up to 30%. In that region due to the reaction kinematics the recoil protons are emitted to forward angles in the laboratory frame and for certain values of $\cos(\theta_\eta^*)$ they have very few kinetic energy. Such protons are strongly affected by the interaction within the material that is located between the target and the detectors, such as the PID detector, the MWPC detector and the holding structure of CB. Therefore, the detection efficiency in this energy range is very sensitive to the modeling of the actual detector geometry and material budget in the simulation.

Due to the old age of the Crystal Ball detector, its geometry was implemented manually in the A2 simulation by converting older FORTRAN code of the
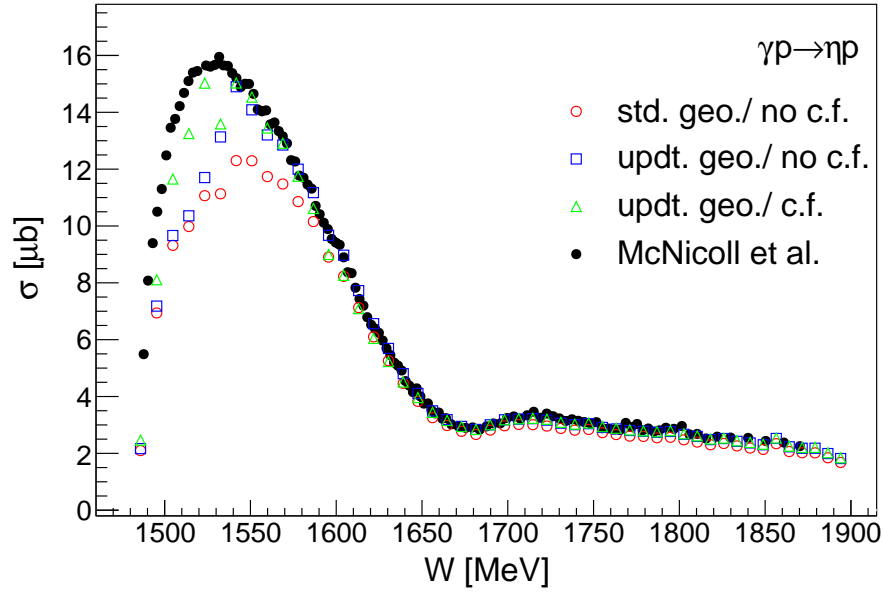
Fig. 4.21: Comparison of total cross sections of $\gamma p \to \eta p$ from hydrogen data: Red circles: standard simulation, no efficiency correction factor. Blue squares: updated CB geometry, no efficiency correction factor. Green triangles: updated CB geometry, including efficiency correction factor. Black circles: MAMI-C proton data [35].

GEANT3-based simulation to C++, rather than using a digital reproduction from electronic construction plans (e.g., CAD). Therefore, the highest accuracy needed for exclusive measurements can not be expected. During checks of the modeled geometry it was suspected that some material was missing in the simulation between the skirting and the tunnel of CB [87]. The geometry in the simulation is visualized in figure 4.23 and can be compared to the real world situation shown in figure 4.24. In the standard version of the A2 simulation, the forward tunnel region was similarly built as the backward tunnel region, which consists of the tunnel cylinder (blue) and the skirting (yellow). In the simulation used for this work additional iron material (red) was placed around the forward tunnel cylinder between the skirting and the inner can of CB (green). It was implemented by surrounding the tunnel cylinder with several half-open cylinders on both side of the hemispheres. The inner radius was chosen close to the outer radius of the tunnel. The outer radius decreases from the radius of the circle described by the skirting to the radius of the tunnel. Nevertheless, as it can be seen from the comparison to the real tunnel region, the geometry in the simulation is still a rough approximation. In the future, more effort should be put on a more exact modeling of the skirting geometry in the forward tunnel of CB.

The updated geometry improves significantly the exclusively measured cross sections, especially in the bins from $W = 1533$ MeV to $W = 1604$ MeV, as shown
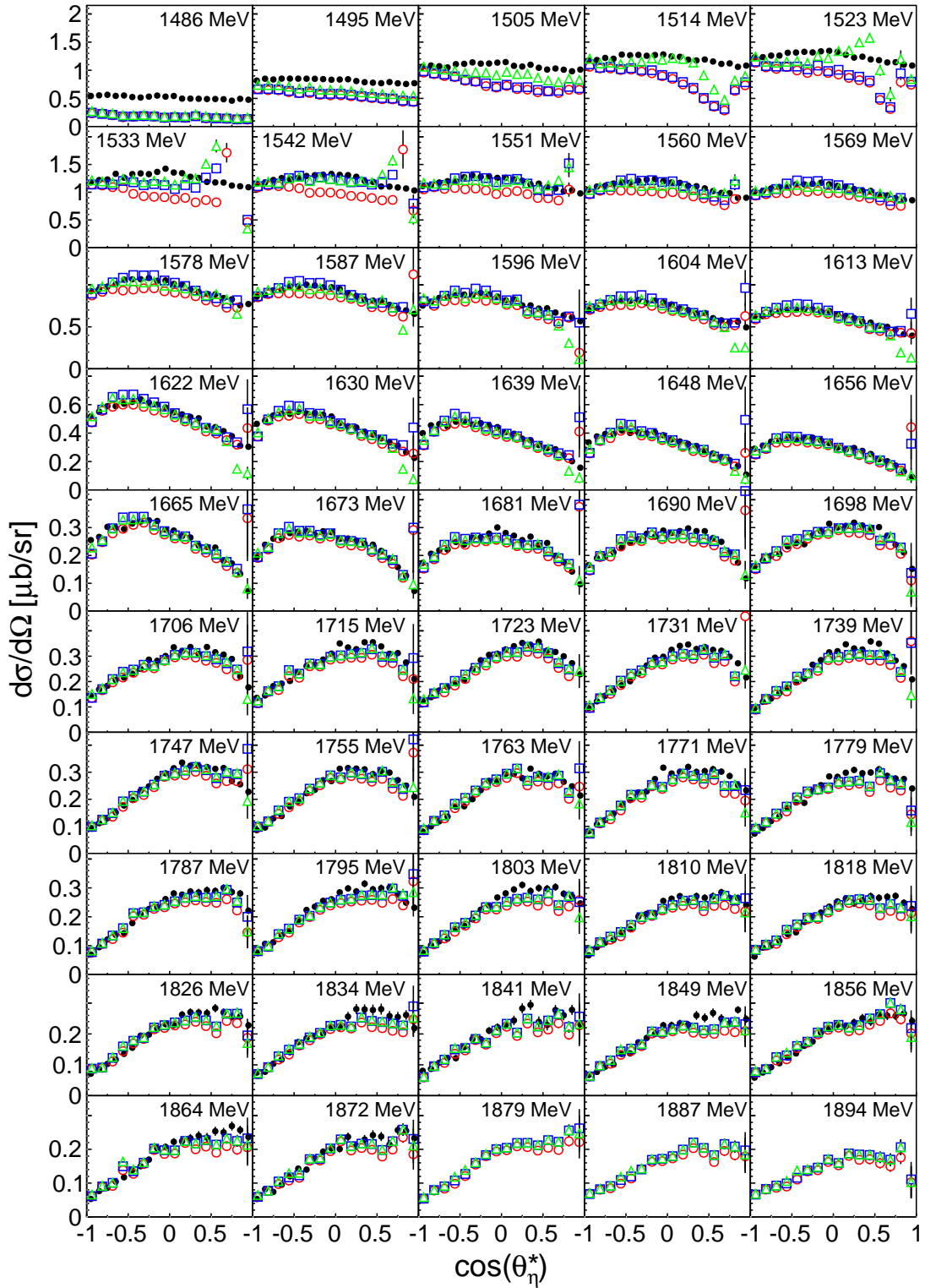
Fig. 4.22: Comparison of differential cross sections of $\gamma p \to \eta p$ from hydrogen data: Red circles: standard simulation, no efficiency correction factor. Blue squares: updated CB geometry, no efficiency correction factor. Green triangles: updated CB geometry, including efficiency correction factor. Black circles: MAMI-C proton data (rebinned) [35].
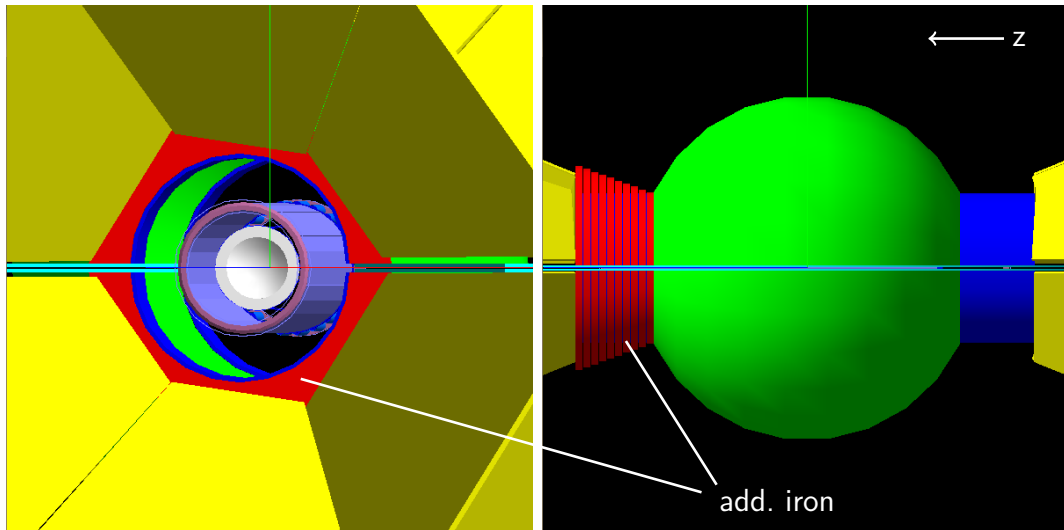
Fig. 4.23: Visualization of the additional iron structure introduced in the A2 simulation: Left-hand side: view from TAPS to target. Right-hand side: lateral view. The additional iron structure is shown in red.

Fig. 4.24: Photo of the Crystal Ball exit tunnel region including target cell and PID detector: The complex geometry of the beam exit tunnel is at the moment not exactly modeled in the simulation.

by the blue squares in figures 4.21 and 4.22. But the fall-offs at larger values of $\cos(\theta_\eta^*)$ in the 1514/1523 MeV bins are still present. This indicates that other types of corrections have to be applied that will be discussed in the following.

4.8.4   Nucleon detection efficiency correction

For the final correction of the nucleon detection efficiencies calculated from simulation, experimental data were used. It is possible by choosing suitable reactions to extract the detection efficiency of protons and neutrons directly from this data. In this work, the following two reactions on the free proton target with protons and, respectively, neutrons in the final state were used:

$$\gamma p \;\; \rightarrow \;\; \eta p \tag{4.23}$$
$$\gamma p \;\; \rightarrow \;\; \pi^0 \pi^+ n \tag{4.24}$$

The hydrogen data measured in April 2009 were fully calibrated and analyzed for that purpose. It should be stressed that the method described here could only be applied because the experimental setups in the hydrogen beamtime and the deuterium beamtimes of February 2009 and May 2009 were similar. As already mentioned in section 4.3.5, the PID detector was shifted upstream during the December 2007 beamtime and to ensure a clean discrimination of protons and neutrons, a strict cut on the nucleon polar angle was applied in the data analysis. The large range of this cut was also necessary because the detection efficiency, which is altered due to the shifted PID, could not be corrected in this region with the method described in the following. This is because of the other material budget in this sensitive area during the hydrogen beamtime, where the PID was installed at its nominal position. The affected cross section bins of the December 2007 data were omitted in the calculation of the final results (see section 4.11.1).

The corrections described in the following were determined individually for all deuterium beamtimes by setting the same detector thresholds in the hydrogen analysis and the corresponding deuterium analysis. This is most crucial for the PID and Veto thresholds that have a strong influence on the proton detection efficiency, and the TAPS CFD thresholds, which are important for the detection of neutrons.

The nucleon detection efficiencies were determined by calculating the ratio of events, where the final state nucleon was detected with respect to the total number of events:

$$\epsilon_p^{\text{data}}(T_p, \theta_p) \;\; = \;\; \frac{N(\eta p)}{N(\eta) + N(\eta p)} \tag{4.25}$$

$$\epsilon_n^{\text{data}}(T_n, \theta_n) \;\; = \;\; \frac{N(\pi^0 \pi^+ n)}{N(\pi^0 \pi^+) + N(\pi^0 \pi^+ n)} \tag{4.26}$$

The efficiencies were calculated as functions of the nucleon kinetic energies T_p, T_n and the polar angles in the laboratory frame θ_p, θ_n. These quantities were calculated from kinematics, independently from the fact if the nucleons were detected or not. As the experimental setup is not completely symmetric in the azimuthal angle due to, e.g., the gap between the CB hemispheres, it was checked if an additional dependence on ϕ was needed. As no notable changes in the final results were found, the dependence on the ϕ-angle was omitted.

The choice of the reaction $\gamma p \to \eta p$ for the proton efficiency calculation was obvious, since its analysis incorporates similar systematic uncertainties as the analysis of the deuteron data, in which ϵ_p^{data} is later applied. Also the phase space of the proton is close to its quasi-free counterpart. In case of the neutron there is no reaction equivalent to η-production that could be used. The cross section of $\gamma p \to \eta \pi^+ n$ is too small and would lead to low statistics. $\gamma p \to \pi^+ n$ could not be used due to the experimental trigger in the hydrogen data set. In addition, this reaction would suffer from systematic uncertainties in the trigger due to the sole charged pion and background contamination caused by misidentified protons. Also the subtraction of the tagger random coincidences would be less precise because there is no photon in the final state providing a good time measurement. Therefore, $\gamma p \to \pi^0 \pi^+ n$ had to be used for the extraction of the neutron efficiencies.

Efficiencies extracted from experimental data include several components that are not taken into account in the simulation, such as, e.g., exact geometries and material budget, and PID/Veto efficiencies. But, on the other hand, new systematic uncertainties are introduced by the analyses of the reactions 4.23 and 4.24. Also, due to phase space holes of these reactions, no efficiency values could be present for certain T_N, θ_N combinations needed in the quasi-free η-production analyses. Therefore, the experimentally determined efficiencies were not applied directly in the deuterium analyses, but a relative correction of the simulated efficiencies was established. This was done by simulating the free reactions $\gamma p \to \eta p$ and $\gamma p \to \eta \pi^+ n$ and extracting the nucleon efficiencies ϵ_N^{MC} equivalently to experimental data using equations 4.25 and 4.26. In the following, the ratios of the two efficiencies were calculated, in which also systematic terms are expected to cancel to some degree:

$$f_c(T_N, \theta_N) = \frac{\epsilon_N^{\text{MC}}(T_N, \theta_N)}{\epsilon_N^{\text{data}}(T_N, \theta_N)} \tag{4.27}$$

This correction factor f_c, being a measure for the deviation of the simulated nucleon efficiencies from the experimentally obtained ones, was in the end then applied in the efficiency determination of the quasi-free analyses. When simulated quasi-free data of $\gamma p \to \eta p$ and $\gamma n \to \eta n$ was analyzed, the detected events were weighted with $1/f_c$. The correction factor was evaluated using the measured θ_N and the reconstructed T_N (see section 4.5.1). If no correction factor was available for a certain point in the T_N, θ_N phase space, the next available value of the nearest point was used because extrapolation led to wrong factors.
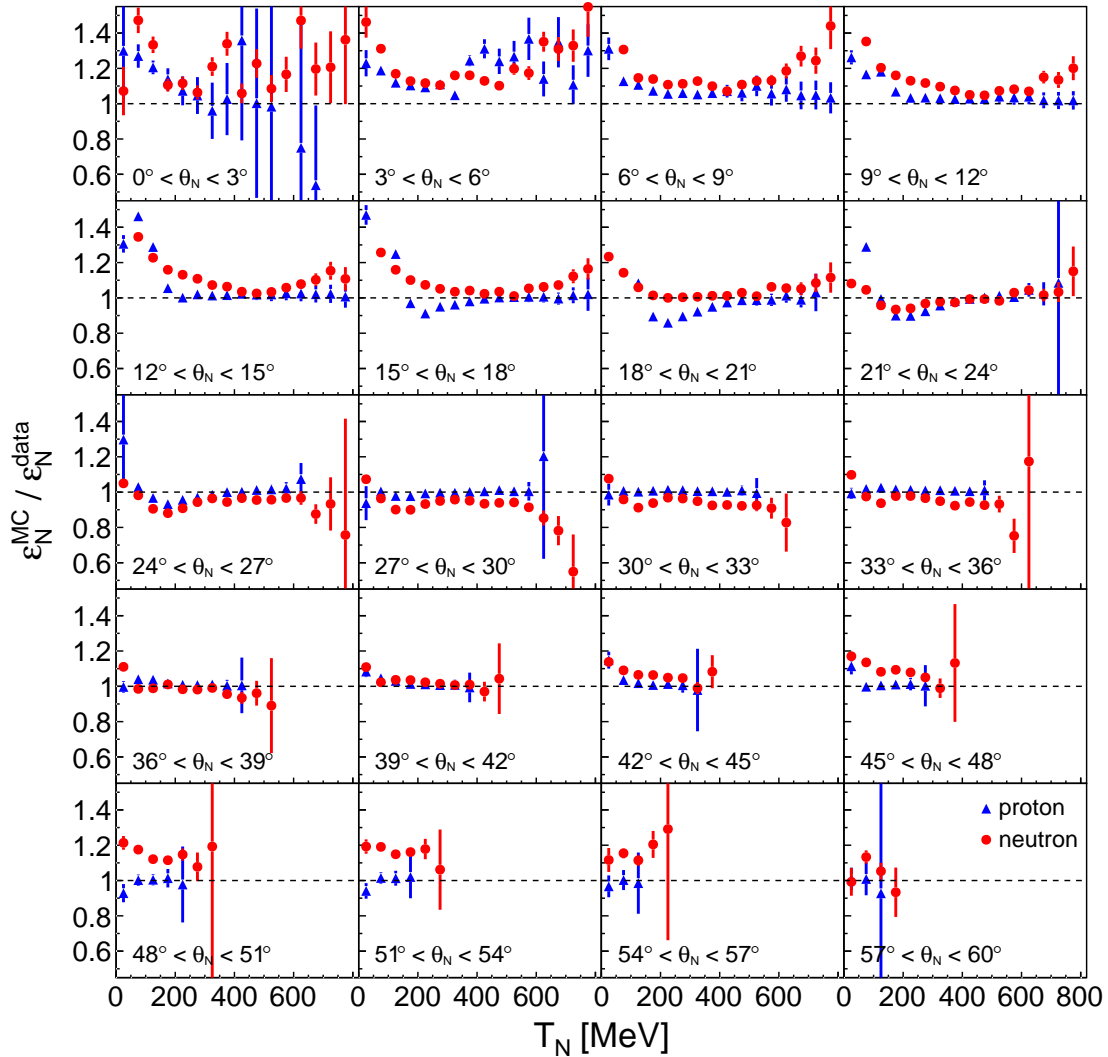
Fig. 4.25: Ratios of nucleon detection efficiencies extracted from experimental data and simulation as a function of the nucleon kinetic energy for different nucleon polar angles in the laboratory frame: Blue triangles: proton efficiency ratios. Red circles: neutron efficiency ratios. The shown ratios were determined for the May 2009 beamtime.

Figure 4.25 shows the ratios of the nucleon detection efficiencies extracted from experimental and simulated data as a function of the nucleon kinetic energy for different nucleon polar angles. It can be seen that the ratios for both proton and neutron deviate significantly from 1, especially for low nucleon energies and smaller polar angles. This is because the simulation is less accurate when the nucleons are going to forward direction, where they pass additional material, as discussed in the sections before. Also, the signals of nucleons differ more from the signals of photons in the BaF_2 crystals of TAPS than in the NaI(Tl) crystals of CB, which leads to a strong dependence of the detection efficiency on the

TAPS detector thresholds. In general, the interaction in BaF$_2$ is probably worse described in the simulation which leads to higher deviations of the ratio for nucleons in TAPS. Up to $\theta_N \sim 18°$ the ratio is larger than 1, which means that the simulated efficiencies are overestimated. For larger angles there is a dip in the ratio to values below 1 around 200 MeV that is more pronounced for the proton, indicating that the efficiencies are underestimated in that region. In general, the proton efficiency is well described for larger angles, while the neutron efficiency seems to be slightly underestimated up to 40 degrees and overestimated above. Nevertheless, the strongest deviations with the largest impact on the normalization of the cross section results of this work are found for low energetic nucleons in TAPS.

As a check, the proton efficiency correction factors were determined and applied for the analysis of $\gamma p \to \eta p$ on the free proton. The correction factor was evaluated with the reconstructed proton energy from kinematics and the measured θ-angle to mimic the situation in the quasi-free analyses, where θ_N and T_N cannot be reconstructed simultaneously from kinematics. The resulting total and differential cross sections are shown in figures 4.21 and 4.22, respectively, by the green triangles. With the help of this correction and including the updated geometry (see section 4.8.3) the angular distributions of the problematic 1514/1523 MeV bins could be improved to a certain amount. The region near $\cos(\theta_\eta^*) \sim 1$ is still affected by strong deviations in four bins, but for smaller values of $\cos(\theta_\eta^*)$ the agreement with the inclusive measurement of [35] is much better. Also some data points that were obviously overcorrected by the updated geometry alone (blue points) are restored and fit now better to the inclusive measurement. Above $W = 1600$ MeV the influence of the detection efficiency correction factor is less strong.

It is not exactly clear why this method is not correcting the efficiencies completely, leading to cross sections that agree perfectly with the inclusive measurement. One reason could be the fact that the calculation of the correction factor uses the reconstructed θ_N while evaluation uses the measured angle. These angles could be very different in certain regions. It is clear that this correction introduces additional systematic uncertainties that are estimated in section 4.13. Nevertheless, it was found that the influence of this correction is mainly in the $S_{11}(1535)$ region of the η-production cross section and thus the main region of interest of this work around $W = 1680$ MeV is only weakly affected. Finally, the kinematics of η-production seems to yield a quite 'unfortunate' nucleon distribution for the current experimental setup compared to other reactions. The influence of the nucleon detection efficiency correction on cross sections for, e.g., π^0- and $\pi^0\pi^0$-production was determined in preliminary analyses to be much lower [88, 89].
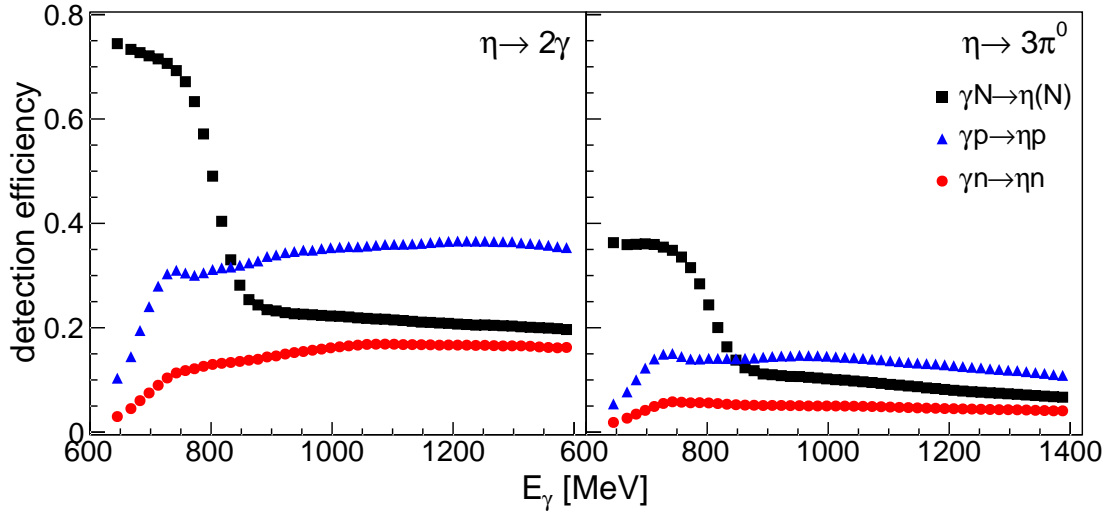
Fig. 4.26: Comparison of integrated detection efficiencies as a function of E_γ for the May 2009 beamtime: Left-hand side: $\eta \to 2\gamma$ analyses. Right-hand side: $\eta \to 3\pi^0$ analyses. Black squares: $\gamma N \to \eta(N)$ analyses. Blue triangles: $\gamma p \to \eta p$ analyses. Red circles: $\gamma n \to \eta n$ analyses.

4.8.5   Summary

After all corrections described in the previous sections were performed, the detection efficiencies for all analysis channels and all beamtimes were calculated as functions of $\cos(\theta^*_\eta)$ and energies $E_\gamma, W_{\mathrm{kin}}, W_{\mathrm{TOF}}$ using the same binning as the corresponding excitation functions. This allowed a straight-forward normalization to finally obtain cross sections.

For the visualization of the energy dependence, the detection efficiencies were integrated over all angular bins. They are shown in figures 4.26, 4.27, 4.28 as functions of $E_\gamma, W_{\mathrm{kin}}, W_{\mathrm{TOF}}$, respectively. Below $E_\gamma = 800$ MeV the efficiencies of the inclusive analyses are rather large, between 30–70% for the $\eta \to 2\gamma$ analysis and 20–35% for the $\eta \to 3\pi^0$ analysis. Above this energy the strict missing mass cut (see section 4.3.3) reduces the efficiencies to nearly constant values of 20% and 10%, respectively. The efficiencies of the exclusive analyses rise from zero at threshold to nearly flat values above $E_\gamma \sim 900$ MeV ($W \sim 1600$ MeV). The smaller efficiencies of the $\eta \to 3\pi^0$ analyses compared to the $\eta \to 2\gamma$ analyses are caused by several mechanisms. Assuming 98% single photon efficiency, the difference in the number of photons of the two η-meson decay channels accounts to a reduction of the efficiency of only 7%. The rest is due to the increased probability of cluster overlaps, combinatorics and other effects.

The angular efficiencies are shown in figures 4.29, 4.30 and 4.31. As effective efficiencies were calculated, the values can be larger than 1 (see beginning of this section). This can be seen in the bins at threshold for the inclusive analyses. The inclusive efficiencies are relatively flat through the whole energy range whereas the exclusive ones decrease significantly to forward $\cos(\theta^*_\eta)$ bins. This is due to
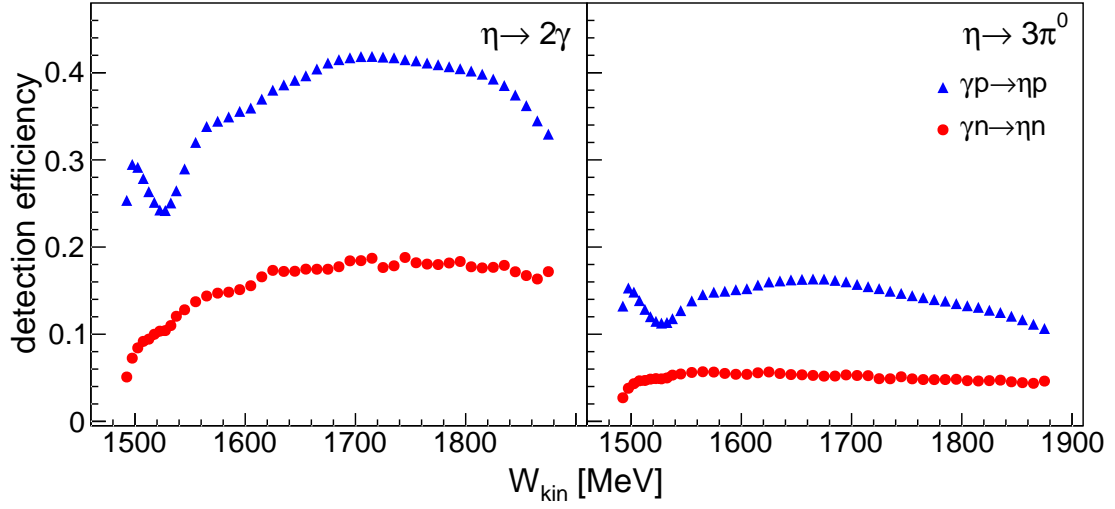
Fig. 4.27: Comparison of integrated detection efficiencies as a function of W_{kin} for the May 2009 beamtime: Left-hand side: $\eta \to 2\gamma$ analyses. Right-hand side: $\eta \to 3\pi^0$ analyses. Blue triangles: $\gamma p \to \eta p$ analyses. Red circles: $\gamma n \to \eta n$ analyses.
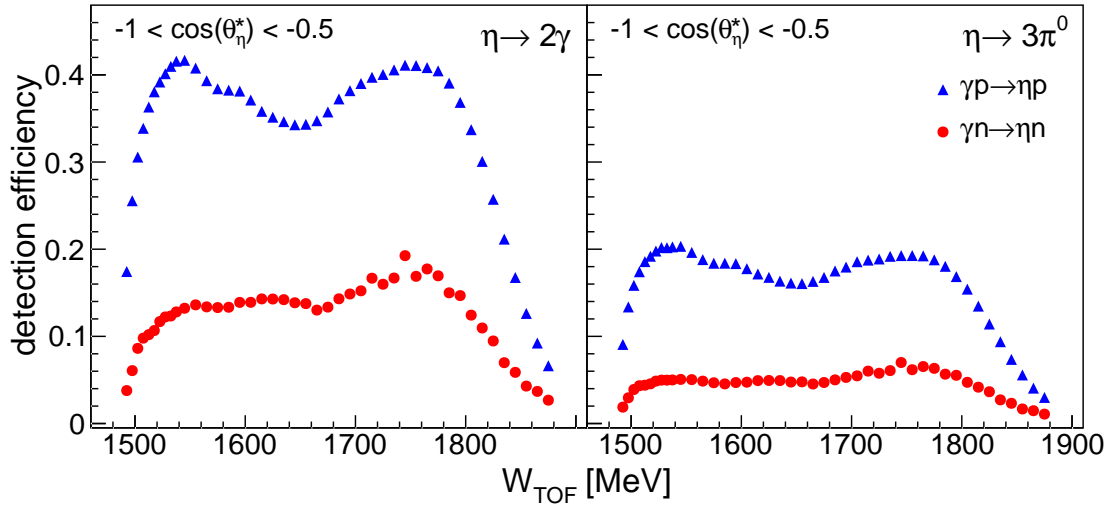
Fig. 4.28: Comparison of integrated detection efficiencies as a function of W_{TOF} for $-1 < \cos(\theta_\eta^*) < -0.5$ for the May 2009 beamtime: Left-hand side: $\eta \to 2\gamma$ analyses. Right-hand side: $\eta \to 3\pi^0$ analyses. Blue triangles: $\gamma p \to \eta p$ analyses. Red circles: $\gamma n \to \eta n$ analyses.

the fact that the nucleons have very few kinetic energy in these bins and thus only a small fraction is able to reach the detectors and to produce a detectable signal. Also a dip around $\cos(\theta_\eta^*) \sim -0.5$ can be observed in the exclusive efficiencies, most pronounced in the ones of the proton depending on W_{kin}. This is caused by the material in the Crystal Ball tunnel region, which reduces especially the detection efficiency of protons.
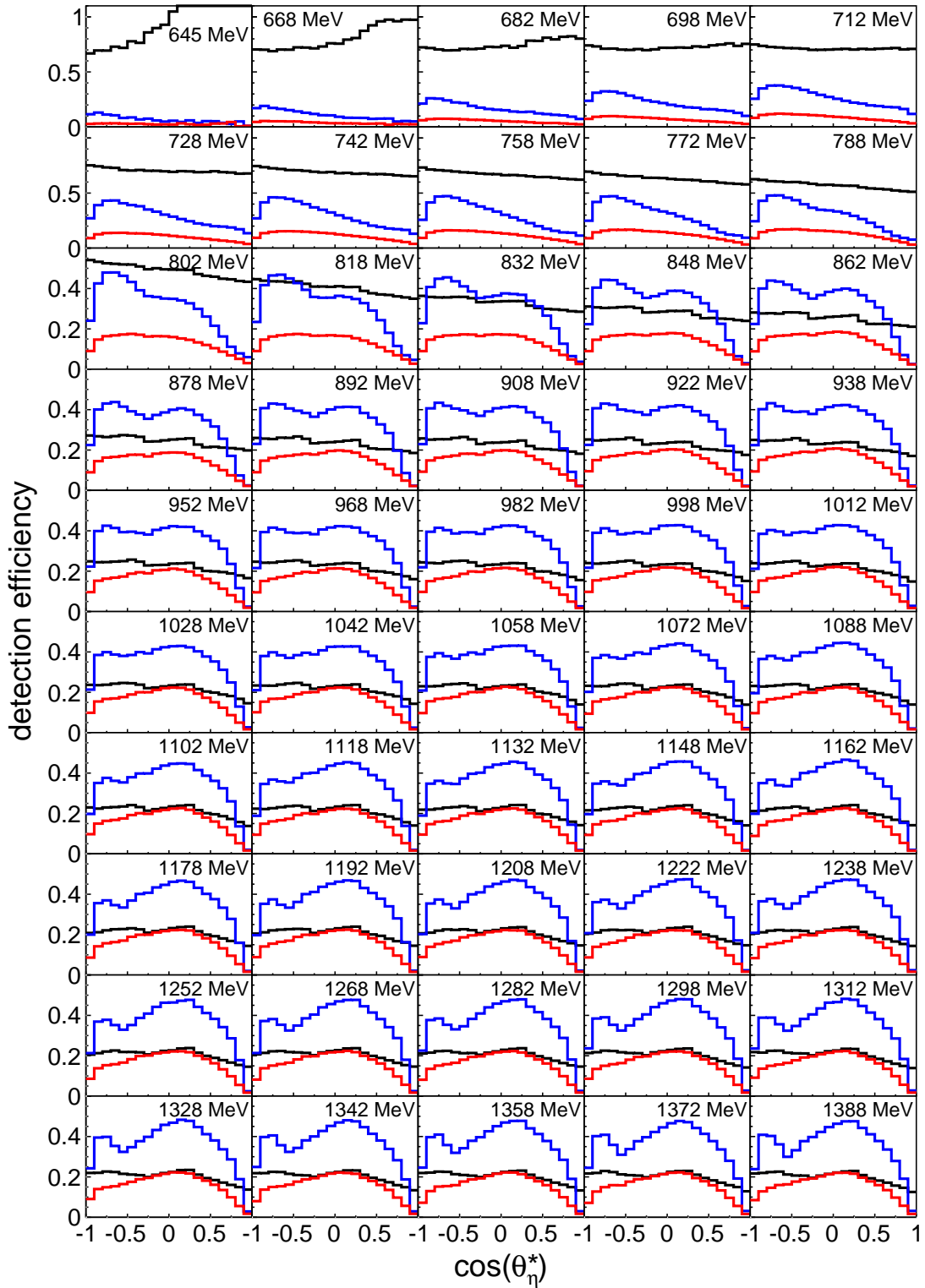
Fig. 4.29: Comparison of angular detection efficiencies of the $\eta \to 2\gamma$ analyses as a function of E_γ for the May 2009 beamtime: Black histograms: $\gamma N \to \eta(N)$ analysis. Blue histograms: $\gamma p \to \eta p$ analysis. Red histograms: $\gamma n \to \eta n$ analysis.
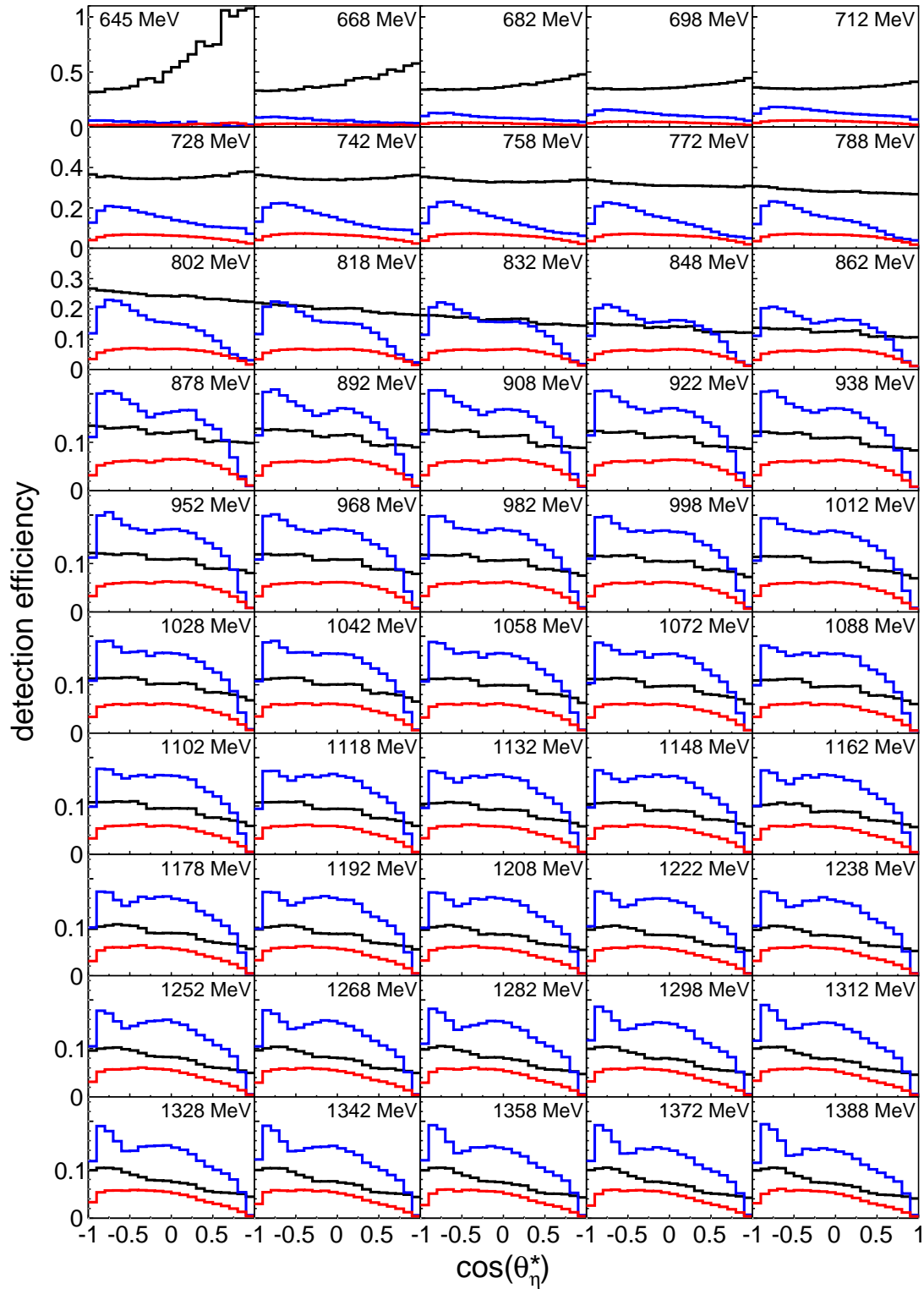
Fig. 4.30: Comparison of angular detection efficiencies of the $\eta \to 3\pi^0$ analyses as a function of E_γ for the May 2009 beamtime: Black histograms: $\gamma N \to \eta(N)$ analysis. Blue histograms: $\gamma p \to \eta p$ analysis. Red histograms: $\gamma n \to \eta n$ analysis.
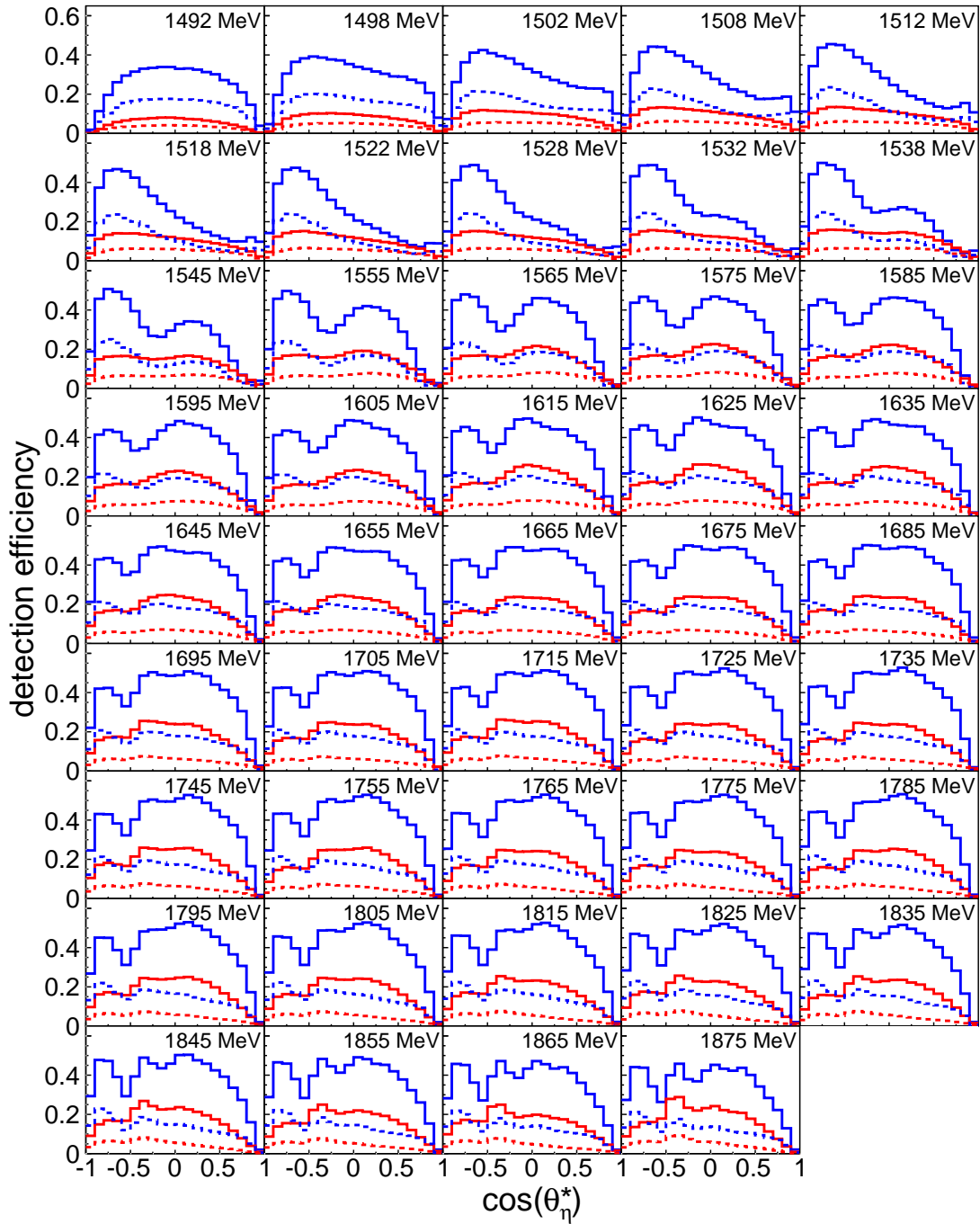
Fig. 4.31: Comparison of angular detection efficiencies as a function of W_{kin} for the May 2009 beamtime: Blue solid histograms: $\gamma p \to \eta p \to 2\gamma p$ analysis. Red solid histograms: $\gamma n \to \eta n \to 2\gamma n$ analysis. Blue dashed histograms: $\gamma p \to \eta p \to 3\pi^0 p$ analysis. Red dashed histograms: $\gamma n \to \eta n \to 3\pi^0 n$ analysis.
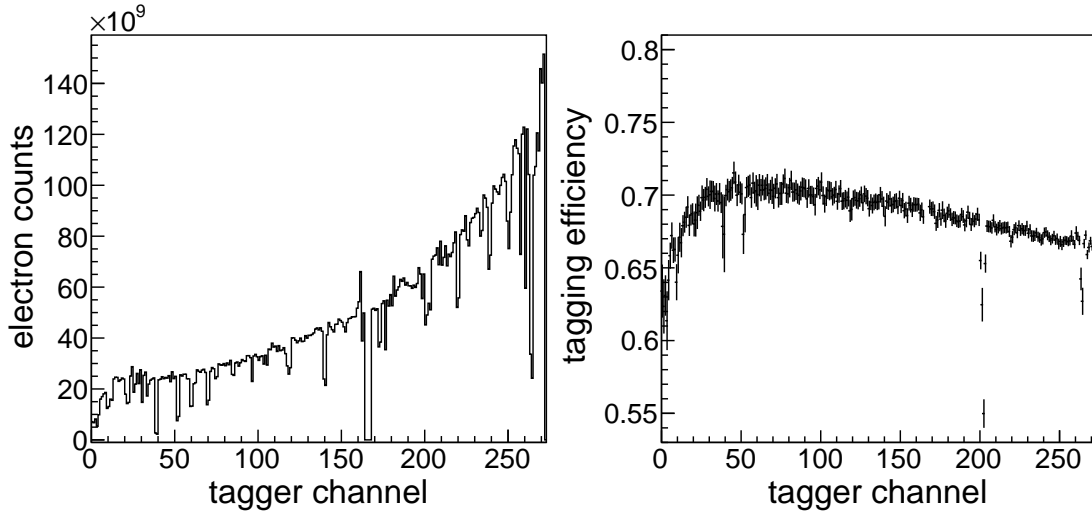
Fig. 4.32: Tagger electron scaler spectrum and tagging efficiency: Left-hand side: electron spectrum measured by scalers as a function of tagger channels. Right-hand side: average of tagging efficiency measurements as a function of tagger channels. Both spectra taken from the May 2009 beamtime.

4.9 Photon flux normalization

The knowledge of the photon flux is necessary for the normalization of cross sections. In the current experimental setup the number of photons impinging on the target $N_\gamma(c)$ is calculated via the number of electrons $N_{e^-}(c)$ detected in the tagger channel c and the tagging efficiency $\epsilon_{\text{tagg}}(c)$ of the corresponding channel, which is defined as

$$\epsilon_{\text{tagg}}(c) = \frac{N_\gamma(c)}{N_{e^-}(c)} < 1 \,. \tag{4.28}$$

$N_{e^-}(c)$ is constantly recorded during data taking via scaler modules. $\epsilon_{\text{tagg}}(c)$ is measured during dedicated tagging efficiency measurements that are performed regularly during a beamtime. These measurements will be described in section 4.9.1.

A typical electron scaler spectrum is shown in the left part of figure 4.32. Low tagger channels correspond to low electron energies, i.e, high photon energies. The characteristic shape is caused by the $\sim 1/E_\gamma$ bremsstrahlung distribution. As the detection efficiencies and thresholds of the focal plane detectors are varying, small fluctuations can occur. Also a few broken elements can be seen showing no counts at all. These elements along with noisy channels were skipped in the analysis.

The electron scalers were inhibited by the tagger DAQ busy signals, i.e., the scalers were not counting when the detectors were readout and the event information was collected. During this time the detectors are not ready to trigger another event and, therefore, also the flux integration has to be stopped. The tagger DAQ

is independent from the DAQ of the rest of the detectors and the busy times of the two DAQ systems are different (the tagger DAQ was normally faster). Hence, a correction had to be applied on the electron scalers in the offline analysis to account for the different busy times of the tagger and the other detectors [90]. The live time of the tagger Γ_{tagg} and the total live time Γ_{tot} (logical OR of all coupled detectors) were separately determined by the ratios of free running scaler clocks and inhibited ones, which were halted when the corresponding system was busy. The corrected number of electrons N'_{e^-} was then calculated as

$$N'_{e^-} = N_{e^-} \cdot \frac{\Gamma_{\text{tot}}}{\Gamma_{\text{tagg}}} \, , \qquad\qquad (4.29)$$

with $N'_{e^-} < N_{e^-}$ due to the higher live time of the tagger. For the current experiment this correction was in the order of 25–30%.

An other correction concerning a technical detail was the use of the multi-hit recording capabilities of the tagger TDC modules. With higher beam currents the probability that a focal plane detector is detecting more than one electron during one events increases. Consequently, the multi-hit readout had to be enabled for these detectors and up to 3 hits per detector and event could be registered. As a consequence, the background of the random coincidences was found to be more flat, which improved the systematic uncertainty of the random subtraction (see section 4.6).

4.9.1   Tagging efficiency

During the beamtimes dedicated measurements of the absolute tagging efficiency were performed. This was done by moving a lead glass detector into the photon beam line behind the TAPS detector. At low beam intensities this detector has a photon detection efficiency of nearly 100% and therefore the number of photons reaching the target could be measured. The low intensity is also required to avoid random coincidences in the tagger. As the tagging efficiency is mainly depending on the photon beam collimator and the electron beam energy, but only weakly on the beam intensity, the obtained values of ϵ_{tagg} are then assumed to be the same at normal production running with higher beam currents.

Before and after the tagging efficiency measurements with beam, background measurements without any beam were performed. This was necessary as a notable amount of the counts in the tagger at these low beam intensities are caused by cosmic radiation and nuclear decays in activated material in the vicinity of the focal plane ladder. The two background measurements were averaged and subtracted with proper time normalization from the counts obtained with the beam switched on. The average values of all tagging efficiency measurements of the May 2009 beamtime are shown in the right part of figure 4.32.
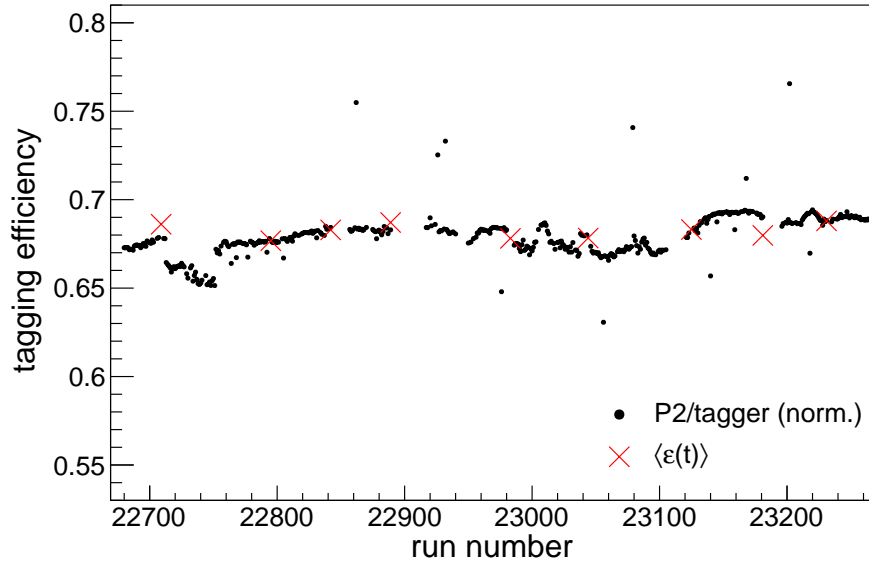
Fig. 4.33: Time-dependence of channel-averaged tagging efficiency as a function of the data run number: Black points: normalized P2/tagger ratio. Red crosses: channel-averaged absolute tagging efficiency measurements $\langle \epsilon(t) \rangle$. Data from May 2009 beamtime.

Because the tagging efficiency depends on the position and quality of the beam, which could change during data taking, the obtained tagging efficiency measurements could not simply be averaged for the flux calculation but the time dependence had to be taken into account. During normal production data taking the photon beam is led to an ionization chamber (P2), whose counts are proportional to the photon flux. By calculating the ratio of counts in the P2 and the tagger detectors, the relative tagging efficiency could be measured constantly during normal data taking. The absolute measurements were then used to normalize this ratio to finally obtain the time dependent tagging efficiency.

To minimize the influence of the statistical fluctuations in the absolute measurements, the tagging efficiencies $\epsilon(c, t)$ for a channel c at a time t were calculated by separating the energy and the time dependences using

$$\epsilon(c, t) = \frac{\bar{\epsilon}(c)}{\langle \bar{\epsilon} \rangle} \cdot \langle \epsilon(t) \rangle \,, \tag{4.30}$$

$$\bar{\epsilon}(c) = \frac{1}{N_m} \sum_{i=1}^{N_m} \epsilon_i(c) \,, \tag{4.31}$$

$$\langle \bar{\epsilon} \rangle = \frac{1}{N_c} \sum_{i=1}^{N_c} \bar{\epsilon}(c_i) \,, \tag{4.32}$$

where N_m is the number of absolute measurements and N_c is the number of tagger channels. The first term in equation 4.30 describes the ratio of the efficiency of
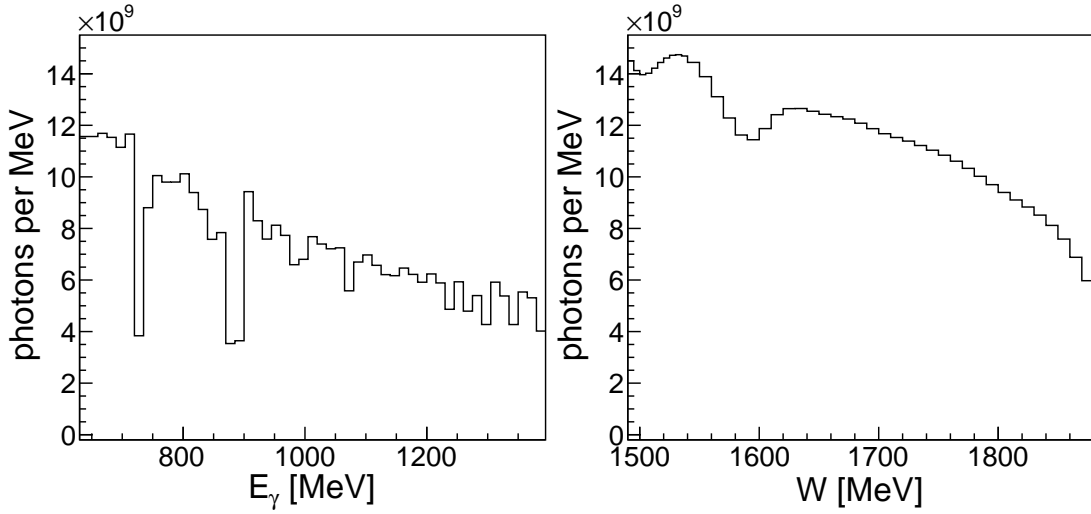
Fig. 4.34: Photon fluxes as functions of E_γ and W for the May 2009 beamtime: Left-hand side: E_γ-dependent flux. Right-hand side: W-dependent flux (neutron as participant nucleon).

a channel averaged over all measurements to the mean global average of all measurements and channels. This contains the energy dependence that is in fact only weak, as shown in figure 4.32. The next term introduces the time dependence by means of the time dependent efficiency averaged over all channels. As mentioned before, the latter is obtained by the normalized P2/tagger ratio shown in figure 4.33 by the black points. The tagger counts were calculated by integrating the scaler counts of all tagger channels. The ratio could in principle be determined after all scaler read events (every 20'000 events) but as the beam was rather stable in the current experiment, it was calculated on a run-by-run basis ($\sim$30 minutes corresponding to about 2×10^6 events). Normalization to the absolute measurements averaged over all channels, denoted by the red crosses, was performed by a χ^2-minimization. Finally, using equation 4.30 the tagging efficiencies for all single channels were calculated individually for all data runs.

4.9.2 E_γ-dependent flux

In the analysis the photon flux $N_\gamma(c)$ depending on the tagger channel c was integrated run-by-run using the both run-dependent number of electrons $N_{e^-}(c)$ and tagging efficiencies $\epsilon_{\text{tagg}}(c)$. Before the resulting spectra could be used for the normalization of the E_γ- and W-dependent cross sections, the flux had to be converted to a function depending on those variables.

In case of the flux depending on E_γ, the bin-overlap method (see appendix C) was used to distribute the counts into an E_γ-dependent histogram taking into account the finite and individual energy bin sizes of the tagger channels. The
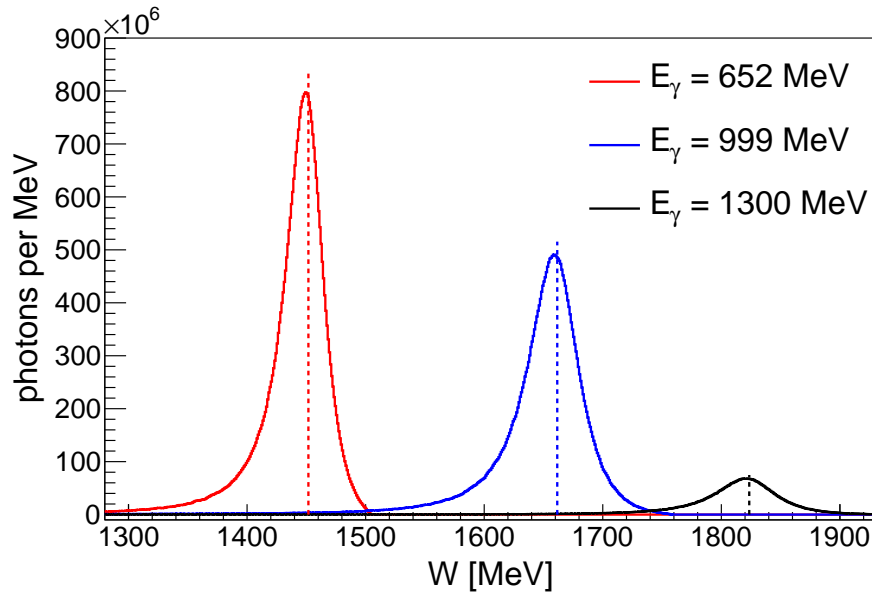
Fig. 4.35: Contributions of three single tagger channels to the W-dependent photon flux (neutron as participant): Solid lines: photon flux contributions. Dashed lines: values of $W = \sqrt{2E_\gamma m_n + m_n^2}$ of the tagger channels. Data from May 2009 beamtime.

resulting spectrum is shown on the left-hand side of figure 4.34. The two bins with notably less counts compared to the other ones are caused by broken tagger channels that are omitted from the analysis. The energy binning of this histogram matches the binning of the excitation function histograms and thus the latter can be easily divided by the flux to achieve the normalization to cross sections.

4.9.3 *W*-dependent flux

The calculation of the W-dependent flux needs slightly more effort compared to the E_γ-dependent one. The flux $N_\gamma(c)$ representing the number of photons corresponding to a tagger channel c has to be converted to $N_\gamma(W)$, namely the number of possibilities to reach a certain W in the kinematics. It is clear that in the participant-spectator model the Fermi momentum distribution inside the deuteron has to be taken into account for the calculation of $N_\gamma(W)$. The algorithm developed for this purpose is shown in figure 4.36 represented by pseudocode. The basic idea is to calculate the W-distribution for each tagger channel by sampling a large number of possible W-values using the photon energy of the channel and the deuteron Fermi momentum distribution. The resulting distributions are normalized and added up to the final $N_\gamma(W)$-distribution.

First, an empty histogram is initialized with the same binning as used in the excitation functions depending on W. This ensures a straight-forward normaliza-

Input: photon flux $N_\gamma(c)$, spectator mass m_S, deuteron mass m_d, deuteron
          Fermi momentum distribution, tagger energies and errors
Output: $N_\gamma(W)$
initialize empty histogram for $N_\gamma(W)$;
$n \leftarrow$ 1e6;
foreach *tagger channel c* **do**
    $e \leftarrow$ photon energy of channel c;
    $\Delta e \leftarrow$ photon energy error of channel c;
    $f \leftarrow$ photon flux of channel c;
    $w \leftarrow f \div n$;
    $i \leftarrow 0$;
    while $i < n$ **do**
        $p \leftarrow$ random Fermi momentum;
        $p_z \leftarrow$ random z-component of Fermi momentum;
        calculate W, ΔW from $(e, \Delta e, p, p_z, m_S, m_d)$;
        fill W to histogram using ΔW and weight w (overlap-bin method);
        $i \leftarrow i + 1$;
    end
end
return histogram of $N_\gamma(W)$;

Fig. 4.36: Algorithm in pseudocode for the calculation of the W-dependent photon flux.

tion to cross sections. Then, for each tagger channel, a large amount of events n (e.g., one million) are sampled as follows: The absolute value of the participant Fermi momentum is taken randomly according to the distribution of [80]. The corresponding z-component is chosen from a random isotropic distribution. Knowing the masses of the spectator nucleon m_S and the deuteron m_d, the Fermi momentum and the photon energy of the tagger channel, the center-of-mass energy $W = \sqrt{s}$ was calculated using equation B.7. This value was then filled into the histogram using as weight the ratio of the photon flux $N_\gamma(c)$ of the channel c and the number of sampled entries n. Hence, after calculating n events the integral of the filled entries is equal to $N_\gamma(c)$ and proper normalization is achieved. The histogram was filled using the bin-overlap method (see appendix C), which requires the energy range ΔW that was calculated using the Jacobian

$$dW \approx \Delta W = \frac{m_d - \sqrt{m_S^2 + \vec{p}_F^2} - p_{F,z}}{W} \cdot \Delta E_\gamma \qquad (4.33)$$

of equation B.7, although it was found that the direct filling of the calculated W without the bin-overlap method did not yield a significantly different final photon flux.

Single contributions of three tagger channels to the W-dependent flux are shown in figure 4.35. They have asymmetric line shapes with a maximum close to $W = \sqrt{2E_\gamma m_N + m_N^2}$, the center-of-mass energy for a nucleon at rest, and their integrals, equal to $N_\gamma(c)$, are decreasing with higher values of W due to the $1/E_\gamma$-bremsstrahlung distribution. The final flux $N_\gamma(W)$ being the sum of the contributions of all tagger channels is shown in the right part of figure 4.34. The binning in E_γ and W is different and not equidistant, hence the entries were normalized to the bin widths in the plots. The bin entries are higher in the E_γ-dependent flux as the interval $[630, 1400]$ MeV in E_γ is transformed into the W-interval $[1490, 1880]$ MeV. The dips around $W = 1510$ MeV and $W = 1600$ MeV are due to broken tagger channels that can also be seen in the E_γ-dependent flux.

4.10   Extraction of cross sections

The yields of the reactions to be analyzed were determined using two methods that will be described in the following. In section 4.10.2 the calculations needed to finally obtain differential and total cross sections are discussed.

4.10.1   Extraction of the yields

The reaction yields were determined from the 2γ and $3\pi^0$ invariant mass distributions in the $\eta \to 2\gamma$ and, respectively, the $\eta \to 3\pi^0$ analyses. Histograms with finite binnings in $E_\gamma, W_{\text{kin}}, W_{\text{TOF}}$ and $\cos(\theta_\eta^*)$ were filled for that purpose in the analyses. The bin-overlap method (see appendix C) was used to fill the E_γ-dependent spectra.

The residual background contributions in the spectra of the exclusive analyses were negligible and, therefore, the corresponding histograms were directly integrated in the same interval that was also used for the invariant mass cut, which was applied when other histograms than the invariant mass were filled (see table 4.2).

In the spectra of the inclusive analyses the background levels were higher due to the smaller number of analysis cuts that could be applied. They were especially noticeable in the analysis of $\gamma N \to \eta(N) \to 2\gamma(N)$ at threshold and at higher energies in $\cos(\theta_\eta^*)$-bins at very forward angles. As an example, the 20 $\cos(\theta_\eta^*)$ bins for the energy $E_\gamma = 713$ MeV are shown in figure 4.37. To extract the signal yields the spectra were fitted with the green functions consisting of a signal and a background term. For the signal terms, shown in blue, the invariant mass line shapes extracted from simulated data were used to account for the slightly E_γ- and $\cos(\theta_\eta^*)$-dependent line shapes of the signals. It was found that by choosing polynomials of second order, which are represented by the red curves, the
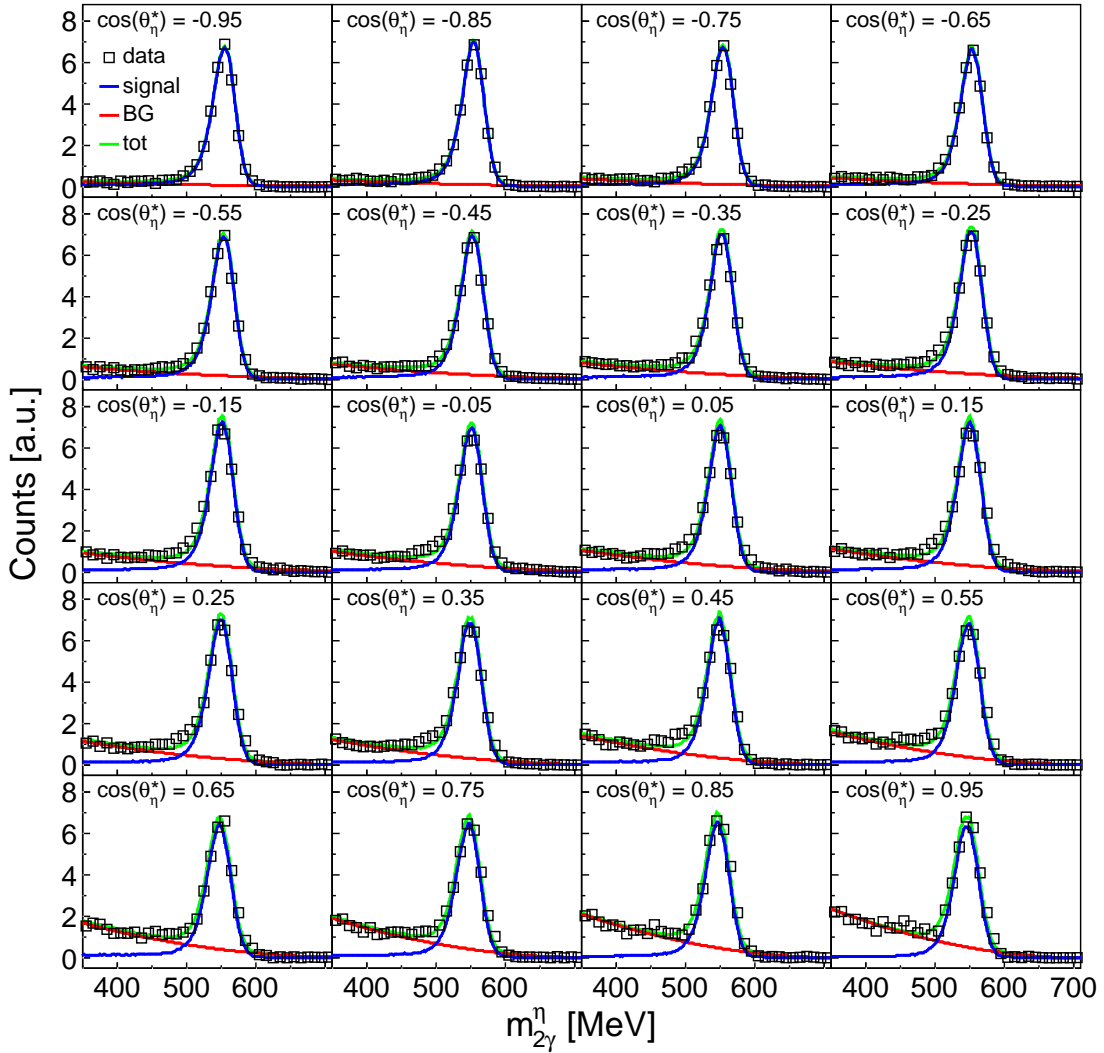
Fig. 4.37: Extraction of yields with signal fitting of the 2γ invariant mass distribution in the $\gamma N \rightarrow \eta(N) \rightarrow 2\gamma(N)$ analysis: Black squares: data of the 20 bins in $\cos(\theta_\eta^*)$ for the energy $E_\gamma = 713$ MeV. Blue curve: signal function. Red curve: background function. Green curve: combined total signal + background fitting function. Data from May 2009 beamtime.

background contributions could be well described. The yields were then extracted by integrating the pure signal curves taking into account the statistical errors of the data.

4.10.2 Calculation of cross sections

The differential cross sections $d\sigma/d\Omega$ as functions of the energy e and the cosine of the polar angle of the η-meson in the center-of-mass frame $\cos(\theta_\eta^*)$ were calculated via

$$\frac{d\sigma}{d\Omega}(e, \cos(\theta_\eta^*)) = \frac{N(e, \cos(\theta_\eta^*))}{N_\gamma(e) \cdot \epsilon_{\text{det}}(e, \cos(\theta_\eta^*)) \cdot \rho \cdot \Gamma_i/\Gamma \cdot \Delta\Omega}, \qquad (4.34)$$

using

e	energy E_γ, W_{kin} or W_{TOF},
$N(e, \cos(\theta_\eta^*))$	e- and $\cos(\theta_\eta^*)$-dependent number of detected events,
$N_\gamma(e)$	e-dependent number of photons,
$\epsilon_{\text{det}}(e, \cos(\theta_\eta^*))$	e- and $\cos(\theta_\eta^*)$-dependent detection efficiency,
ρ	target density [scattering centers/barn],
Γ_i/Γ	η-meson decay branching ratios [7]
	$\eta \to 2\gamma$: $(39.31 \pm 0.20)\%$
	$\eta \to 3\pi^0$: $(32.57 \pm 0.23)\%$,
$\Delta\Omega$	solid angle of $\cos(\theta_\eta^*)$-bin [sr].

The target density ρ, which is equal to the number of deuteron nuclei per barn (1 barn $= 10^{-24}$ cm^2), was calculated via

$$\rho = \frac{N_A \cdot l \cdot \rho_{\text{LD2}}}{M_D}, \qquad (4.35)$$

using

N_A	Avogadro constant: 6.02214×10^{23} mol^{-1},
l	target length
	December 2007 and February 2009: (4.72 ± 0.05) cm
	May 2009: (3.02 ± 0.03) cm,
ρ_{LD2}	density of liquid deuterium: 0.16324 g cm^{-3} at 1080 mbar,
M_D	molar mass of atomic deuterium: 2.014 g mol^{-1},

resulting in

$\rho_1 \approx 0.23039$ b^{-1} for December 2007 / February 2009 and
$\rho_2 \approx 0.14741$ b^{-1} for May 2009.

Calculating the differential cross sections as a function of $\cos(\theta_\eta^*)$ rather than θ_η^* via the transformation $\theta \to \cos\theta$ with $d\cos\theta = -\sin\theta\,d\theta$ is convenient since the bin solid angle $\Delta\Omega$ is then constant for all bins and equal to

$$\Delta\Omega = \frac{4\pi}{N_b}, \qquad (4.36)$$

where N_b is the number of bins in $\cos(\theta_\eta^*)$ ($N_b = 20$ in this work). Hence, the total cross section can be obtained simply by summing the bins of the differential cross sections via

$$\sigma(e) = \int \frac{d\sigma}{d\Omega}(e, \cos(\theta_\eta^*)) \, d\Omega \approx \frac{4\pi}{N_b} \sum_{i=1}^{N_b} \frac{d\sigma}{d\Omega}(e, \cos(\theta_\eta^*)) \,. \qquad (4.37)$$

In the current work this was used for the calculation of the cross sections depending on W_{TOF}, for which only five angular bins could be integrated corresponding to $-1 < \cos(\theta_\eta^*) < -0.5$ due to the limited angular acceptance of TAPS. For the calculation of the E_γ- and W_{kin}-dependent total cross sections the differential cross sections were first fitted with an expansion using the Legendre series

$$f_L(e, \cos(\theta_\eta^*)) = \frac{q_\eta^*(e)}{k_\gamma^*(e)} \sum_{i=0}^{3} A_i(e) P_i(\cos(\theta_\eta^*)) = \sum_{i=0}^{3} B_i(e) P_i(\cos(\theta_\eta^*)) \,, \qquad (4.38)$$

where P_i are the Legendre polynomials and A_i, B_i are the expansion coefficients. q_η^*, k_γ^* are the momenta in the center-of-mass frame of the η-meson and the incoming photon, respectively. Finally, the fitting functions were integrated to obtain the total cross section via

$$\sigma(e) = \int_{-1}^{1} f_L(e, \cos(\theta_\eta^*)) \, d\cos(\theta_\eta^*) = 4\pi \cdot B_0(e) \,. \qquad (4.39)$$

4.11   Data merging

Data from several measurements were merged at multiple levels of the analysis. Having three data sets available, the results have to be merged at a certain step to obtain the full statistical quality. This will be discussed in section 4.11.1. As cross section measurements were performed using the two η-meson decays, $\eta \to 2\gamma$ and $\eta \to 3\pi^0$, it is also reasonable to calculate combined results to further improve statistics and also to average systematic uncertainties. This procedure will be presented in section 4.11.2.

4.11.1   Merging of data sets

Once it was made sure that there were no systematic deviations amongst the data sets (see chapter 5), the cross section results of the different data sets were merged. This was done at the yield and flux level, i.e., all beam time dependent corrections as, e.g., target density, detection efficiency and empty target subtraction were applied to the yields so that they could be summed. Also the photon fluxes were summed and finally the normalized cross sections were derived. The advantage

Beamtime	Time	$\eta \to 2\gamma$ events			$\eta \to 3\pi^0$ events		
		inc.	exc. p	excl. n	inc.	exc. p	exc. n
December 2007	140	1.53	0.54	0.20	0.65	0.21	0.06
February 2009	141	—	—	—	0.34	0.17	0.05
May 2009	190	1.31	0.69	0.25	0.49	0.25	0.07
total	471	2.84	1.23	0.45	1.48	0.63	0.18

Tab. 4.3: Overview of the statistics of the analyzed data sets: Unit of time is hours, number of events in millions.

of this method is that for the signal fits of the yield histograms, used in the calculation of the inclusive cross sections, the full statistics could be used, which reduced the systematic errors of the fitting procedure significantly compared to the fitting of single data sets.

Another reason for the convenient data merging at yield and flux level was the fact that not all data points of the December 2007 beamtime could be used for the merged results. In the analysis of that data set, nucleons had to be excluded from a large angular region in the laboratory system due to large systematic uncertainties in the detection efficiency correction (see sections 4.3.5 and 4.8.4). This cut led to cross section bins for certain values of $\cos(\theta_\eta^*)$ and $E_\gamma, W_{\mathrm{kin}}, W_{\mathrm{TOF}}$ with enormous statistical and systematic uncertainties. As the source of the problem was systematic and known, the affected data points were ignored in the data merging. But, omitting these data is only approvable when a systematic procedure is used to decide whether a bin is affected or not. As a measure, the contribution of events removed by the cut to the total number of events was calculated for every cross section bin. This ratio was obtained by analyzing simulated data without any application of the cut at all (all events) and with the complementary cut (removed events). When the ratio exceeded 30% the corresponding data point was omitted. Consequently, around 35% percent of the proton data and 44% of the neutron data obtained from the December 2007 data set were ignored in the merging of the E_γ- and W_{kin}-dependent yields. In the range of $-1 < \cos(\theta_\eta^*) < -0.5$, where cross sections as a function of W_{TOF} could be measured, a majority of the data points was affected. Therefore, the December 2007 data were completely ignored in the merging of the W_{TOF}-dependent yields.

Table 4.3 shows an overview of the statistics of the data that was analyzed in this work. The beamtime hours correspond to the amount of data that was finally used in the analysis. All analysis cuts were taken into account for the determination of the number of events but the empty target contribution is not subtracted and neither are the ignored bins of the December 2007 beamtime.

4.11.2   Merging of η-meson decay channel data

A combined result of the data obtained in the $\eta \to 2\gamma$ and, respectively, $\eta \to 3\pi^0$ analyses for all reaction channels was created by calculating averages $\bar{x}$ from the data points x_i weighted with their statistical errors as $1/(\Delta x_i)^2$ using

$$
\bar{x} = \frac{\displaystyle\sum_{i=1}^{2} \frac{x_i}{(\Delta x_i)^2}}{\displaystyle\sum_{i=1}^{2} \frac{1}{(\Delta x_i)^2}}, \quad \Delta\bar{x} = \frac{1}{\sqrt{\displaystyle\sum_{i=1}^{2} \frac{1}{(\Delta x_i)^2}}}, \tag{4.40}
$$

where the associated statistical errors $\Delta\bar{x}$ were derived via standard error propagation. For $x_1 \pm \Delta x_1$ the differential cross section data of the $\eta \to 2\gamma$ analysis was used and for $x_2 \pm \Delta x_2$ the corresponding ones of the $\eta \to 3\pi^0$ analysis. The resulting combined differential cross sections were then used to calculate the combined total cross sections (see section 4.10.2).

4.12   Empty target subtraction

A nonnegligible fraction of the detected η-mesons is not produced inside the target cell but in the thin target windows made of Kapton. This material contains a large amount of carbon and nitrogen nuclei which have large cross sections for quasi-free production of η-mesons. The current analysis is not able to reject these events completely as the reaction vertex cannot be reconstructed using, e.g., a kinematic fit or reconstructed tracks of charged particles. Therefore, the degree of contamination was estimated from dedicated empty target measurements, for which the liquid deuterium was removed from the target cell. These measurements were performed for the December 2007 and for the May 2009 beamtimes, but due to a normalization problem the December 2007 data could not be used.

The empty target data were analyzed in the same way as the normal data using the exactly same analysis cuts. By normalizing the obtained yields, empty target cross sections as functions of $E_\gamma, W_{\mathrm{kin}}, W_{\mathrm{TOF}}$ were calculated. Due to the limited statistics no angular distributions could be obtained but only energy dependent total cross sections with a rather coarse energy binning. The ratios to the cross sections measured with the filled target were calculated and used to scale down the filled target yields to remove the empty target contributions. As the degree of contamination depends on the target length, the relative contributions determined using the May 2009 data were scaled to the target lengths of the December 2007 and February 2009 beamtimes.

As an example, the relative empty target contributions to the total cross sections as a function of E_γ for the May 2009 beamtime are shown in figure 4.38.
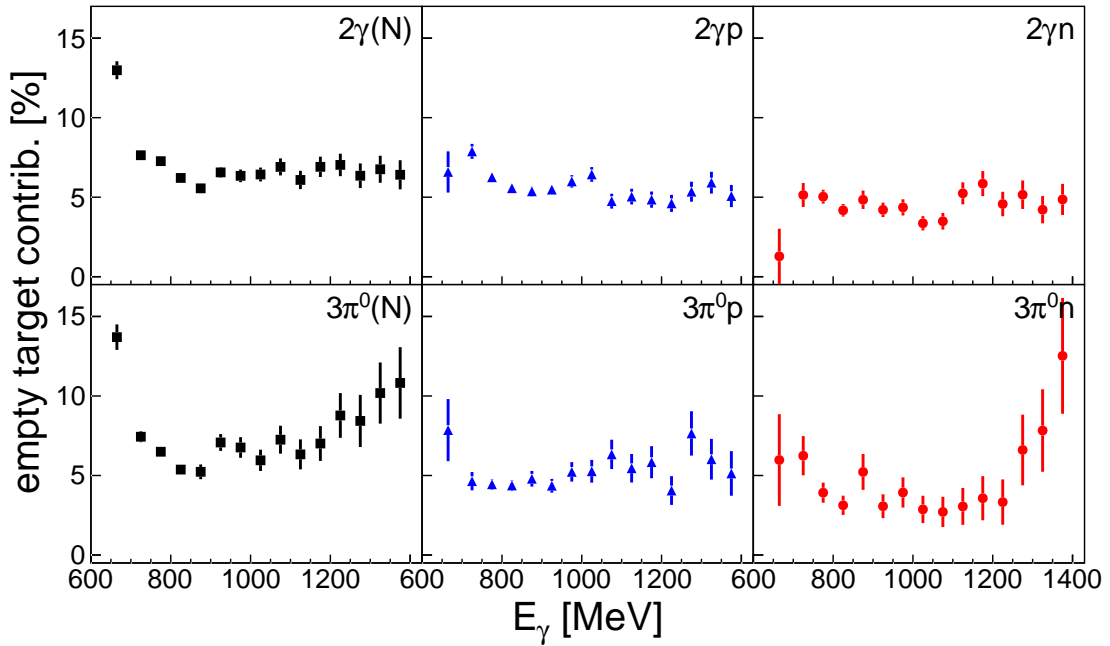
Fig. 4.38: Overview of the relative empty target contributions to the total cross sections as a function of E_γ for the May 2009 beamtime: Black squares: $\gamma N \to \eta(N)$ analyses. Blue triangles: $\gamma p \to \eta p$ analyses. Red circles: $\gamma n \to \eta n$ analyses.

In general, there is no strong energy dependence and the contributions are in the order of 5–7%. Higher values at very low and high photon beam energies are caused by statistical fluctuations. The estimated contributions in the December 2007 and the February 2009 beamtimes are reduced by a factor of $3.02/4.72 \approx 0.64$, i.e., the ratio of the target lengths.

4.13 Systematic uncertainties

In addition to statistical uncertainties, the results of this work are also affected by systematic uncertainties. A selection of sources that are suspected to be the most substantial ones will be discussed in the following. The sources can be divided into common ones, which have the same values for all analysis channels (section 4.13.1), and other contributions that have to be determined separately for each analysis channel (section 4.13.2). In section 4.13.3 the total systematic uncertainties including all the contributions will be derived and discussed.

The procedure for the estimation of the systematic uncertainties is as follows: Changes according to the sources of systematic uncertainties are applied to the analysis and the final cross section data are calculated. The relative differences of these data to the cross section data of the standard analysis correspond to the relative systematic errors. The relative errors of all sources discussed in the following were calculated for all analysis channels and all types of cross sections.

4.13.1   Common systematic uncertainties

The systematic errors presented in this section are caused by global sources, i.e., they are common for all analyses and had, therefore, only to be calculated once.

Photon flux

The dominating systematic error in the calculation of the photon flux is the tagging efficiency measurement. As described in section 4.9.1, the data run dependent tagging efficiency is calculated from the normalized relative tagging efficiency, obtained from the P2/tagger ratio, using the absolute measurements. In doing so, the ratio was adjusted to the absolute measurements via χ^2-minimization. The systematic uncertainties in both the relative and the absolute measurements were estimated by calculating a minimal and a maximal normalization by forcing the ratio to cross either the minimum or the maximum absolute measurement. Consequently, two sets of data run dependent tagging efficiencies were created and the two resulting integrated photon fluxes were calculated. The relative difference of the latter to each other was found to be 2.8%, which was used as systematic error of the photon flux.

Target density

The value of the target density is affected by systematic uncertainties in the measurement of the target length. The main uncertainty in this measurement is the deformation of the inner target window [51]. Using the values (4.72 ± 0.05) cm (December 2007 / February 2009) and (3.02 ± 0.03) cm (May 2009) as target lengths a common systematic error for all data sets of 1.1% was estimated.

Empty target subtraction

Due to the low statistics and the coarse binning in the cross section data obtained from the empty target runs (see section 4.12) a rough estimation of the systematic uncertainity of the empty target subtraction of 2.5% was assumed. This account approximately to half of the relative empty target contribution to the measured cross sections.

η-decay branching ratio

The systematic uncertainties of the η-meson decay branching ratios Γ_i/Γ of $(39.31 \pm 0.20)\%$ for the decay $\eta \to 2\gamma$ and of $(32.57 \pm 0.23)\%$ for the decay $\eta \to 3\pi^0$ [7] are very small and basically negligible. For the visualizations of the different contributions in section 4.13.3 the common maximum value of 0.7% was used for completeness.

4.13.2   Channel-dependent systematic uncertainties

The systematic uncertainties that are discussed in the following are depending on the analysis channel and were, therefore, determined for all channels and all bins of the cross section data individually.

CB energy sum trigger

The CB photon energy sum trigger that was modeled for the analysis of simulated data (see section 4.7.1) has a strong influence on the detection efficiency, which is mainly derived from the simulation. This is especially the case for photon energy sums below 400 MeV, where simulated events are weighted down by the software trigger to achieve agreement with the experimental data. Therefore, the systematic error of the sum trigger was estimated by extracting cross sections without events having photon energy sum values below 400 MeV, thus ignoring the affected energy region. Due to the distinct photon energy sum distributions in all channels of the $\eta \to 2\gamma$ and the $\eta \to 3\pi^0$ analyses the resulting systematic errors are suspected to be different and, therefore, individual calculations for all analysis channels were required.

Analysis cuts

Variations in the analysis cuts (see section 4.3) caused by, e.g., systematic problems in fitting procedures when calculating the cut limits, change inevitably the event selection. Hence, the signal-to-background ratio could be changed, the phase space of the signal events could be reduced or equivalent events could be handled differently in the analysis of experimental and simulated data. All this will have an influence on the final cross section data. As it is not feasible to study the influence and correlation of all the different cuts by checking all possible combinations of variations, the following procedure was performed in this work. The cuts on the missing mass, the η-nucleon coplanarity and the 2γ or, respectively, $3\pi^0$ invariant masses were found to be the dominating cuts with respect to the extracted yields. Therefore, two analyses with either wider limits for all cuts or more narrow ones were performed for all analysis channels. The cut limits were varied by $\pm 3\%$ with respect to the limits of the standard analysis. Finally, the systematic errors were calculated from the averaged deviations of the cross section data obtained by the two analyses from the standard data.

Geant4 physics models

In the exclusive analyses two additional sources of systematic uncertainties caused by the nucleon detection efficiency corrections were considered. One of them is the estimation of the influence of the physics models used in the Geant4 simulation

of the detector setup. As discussed in section 4.8.2, for the simulation of the hadronic interactions both the Binary cascade and the Bertini cascade models were recommended for applications in medium energy physics experiments. It was found that the Bertini cascade model results in a slightly better description of the neutron cluster sizes and hence this model was chosen in this work. By comparing the final cross section results to the ones obtained using the Binary cascade model in the detection efficiency calculation, the systematic uncertainty of both models in general was estimated.

Nucleon detection efficiency correction

The second additional source of systematic uncertainty in the exclusive analyses is the calculation of the correction factors for the nucleon detection efficiencies (see section 4.8.4). For this purpose, the reactions $\gamma p \to \eta p$ and $\gamma p \to \pi^0 \pi^+ n$ were analyzed using hydrogen data. As also in these analyses the software trigger modeling the photon energy sum condition in CB was used, its influence on the correction factors had to be estimated. Also the impact of the analysis cuts had to be considered. Therefore, the influence of these two sources on the deuterium cross sections via the detection efficiency correction factor was studied using the same procedures as described before. From the resulting deviations the maximum values were taken as the total systematic uncertainties of the nucleon detection efficiency correction factor.

4.13.3   Sum of systematic uncertainties

The systematic uncertainties $\Delta_i^{\mathrm{sys}}(e, \cos(\theta_\eta^*))$ with $e = E_\gamma, W_{\mathrm{kin}}, W_{\mathrm{TOF}}$ of all n sources described above were combined individually for all analysis channels to the total systematic uncertainties $\Delta_{\mathrm{tot}}^{\mathrm{sys}}(e, \cos(\theta_\eta^*))$ by summing them quadratically:

$$\Delta_{\mathrm{tot}}^{\mathrm{sys}}(e, \cos(\theta_\eta^*)) = \sqrt{\sum_{i=1}^{n} \left[\Delta_i^{\mathrm{sys}}(e, \cos(\theta_\eta^*)) \right]^2} \qquad (4.41)$$

Quadratic summation is justified by the facts that the sources are independent in first approximation and that the number of sources is rather large and thus cancelation effects have to be considered. The resulting total relative errors were then multiplied with the cross section data to obtain the absolute errors.

The final relative systematic errors of the total cross sections as functions of $E_\gamma, W_{\mathrm{kin}}, W_{\mathrm{TOF}}$ are shown in figures 4.39, 4.40 and 4.41, respectively. The errors of the proton analysis show almost no energy dependence and are in the order of 5%. The errors of the inclusive analysis using the $\eta \to 2\gamma$ decay channel are very similar and also around 5%, whereas the corresponding ones of the $\eta \to 3\pi^0$ analysis are 10% at threshold and decline smoothly to 6% at maximum beam
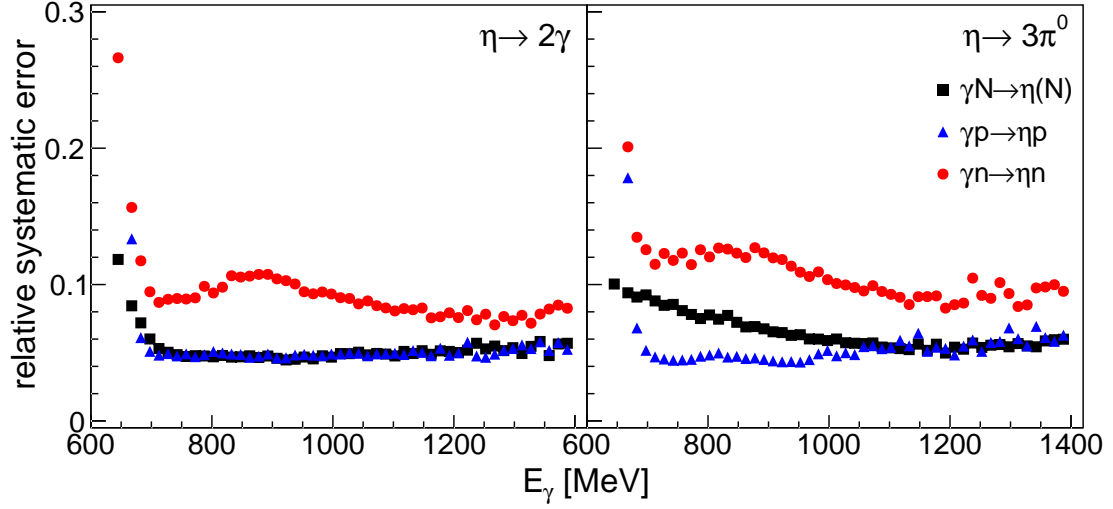
Fig. 4.39: Comparison of relative systematic errors of the total cross sections as a function of E_γ: Left-hand side: $\eta \to 2\gamma$ analyses. Right-hand side: $\eta \to 3\pi^0$ analyses. Black squares: $\gamma N \to \eta(N)$ analyses. Blue triangles: $\gamma p \to \eta p$ analyses. Red circles: $\gamma n \to \eta n$ analyses.

energy. As expected, the systematic errors of the neutron analyses are higher. The uncertainties in the two decay channel analyses show a similar, characteristic energy dependence, the errors of the $\eta \to 3\pi^0$ analysis being around 10% higher compared to the $\eta \to 2\gamma$ analysis. At threshold, the errors account to 15–20% decreasing to 8–12% at higher beam energies.

As an example, the relative systematic errors of the differential cross sections for the $\eta \to 2\gamma$ analyses as a function of E_γ are shown in figure 4.42. The corresponding figures for the $\eta \to 3\pi^0$ analysis as well as for cross sections as a function of W_{kin} can be found in appendix D. It is visible that for the neutron results there is also a clear angular dependence of the systematic errors in addition to the energy dependence, whereas the errors for the inclusive and the proton analysis are relatively flat apart from energy bins right at threshold and some $\cos(\theta_\eta^*)$ bins at very forward angles. This is mainly caused by the high systematic uncertainties in the neutron detection efficiencies due to the systematic uncertainties in the simulation of low energetic neutrons and the neutron efficiency correction factor derived from experimental data.

To study the composition of the total systematic error $\Delta_{\text{tot}}^{\text{sys}}(e, \cos(\theta_\eta^*))$ out of the different sources $\Delta_i^{\text{sys}}(e, \cos(\theta_\eta^*))$ the following measure for the single contributions $c_i(e, \cos(\theta_\eta^*))$ was calculated:

$$c_i(e, \cos(\theta_\eta^*)) = \frac{\left[\Delta_i^{\text{sys}}(e, \cos(\theta_\eta^*))\right]^2}{\left[\Delta_{\text{tot}}^{\text{sys}}(e, \cos(\theta_\eta^*))\right]^2}, \tag{4.42}$$
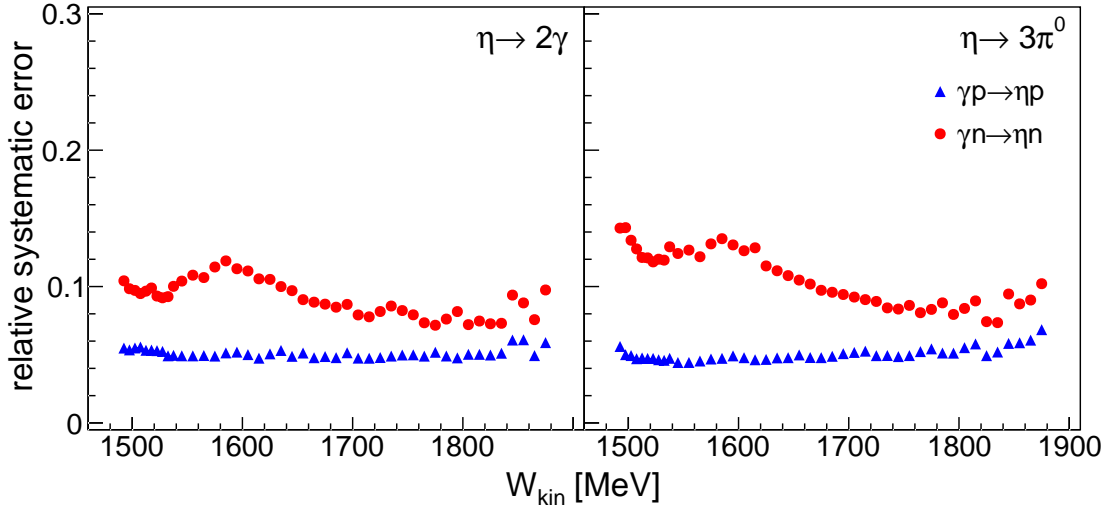
Fig. 4.40: Comparison of relative systematic errors of the total cross sections as a function of W_{kin}: Left-hand side: $\eta \to 2\gamma$ analyses. Right-hand side: $\eta \to 3\pi^0$ analyses. Blue triangles: $\gamma p \to \eta p$ analyses. Red circles: $\gamma n \to \eta n$ analyses.

with $\sum_i c_i = 1$ fulfilled. Figure 4.43 shows as an example the composition of the systematic errors of the differential cross sections as a function of E_γ obtained in the $\gamma n \to \eta n \to 2\gamma n$ analysis. In the region dominated by the excitation of the $S_{11}(1535)$ resonance, the total systematic error is dominated by the neutron detection efficiency, as already stated above. This is caused by the fact that the neutrons are detected in TAPS, where the detection efficiency is very sensitive to detector thresholds. Also the material budget plays a role, although a minor one compared to the proton case. With increasing beam energy, the other sources start to contribute, especially in forward bins of $\cos(\theta_\eta^*)$. At backward angles, the systematic error of the neutron detection efficiency continues to dominate as a major part of the corresponding neutrons are detected in TAPS. An interesting fact is also the strong influence of the nucleon detection efficiency correction factors for intermediate $\cos(\theta_\eta^*)$ values in the energy range from 832 MeV to 968 MeV. This is mainly caused by the software trigger in the $\gamma p \to \pi^0 \pi^+ n$ analysis that is used to derive the correction factors.

The plots showing the contributions to the total systematic errors for the other reactions were moved to appendix D. Generally, the compositions of the total errors show very distinct angular dependencies and different sources are dominating in the $\eta \to 2\gamma$ and the $\eta \to 3\pi^0$ analysis channels. The most striking features are:

- $\gamma N \to \eta(N) \to 2\gamma(N)$: dominance of analysis cuts at threshold, strong influence of CB energy sum trigger in forward direction at higher beam energies.
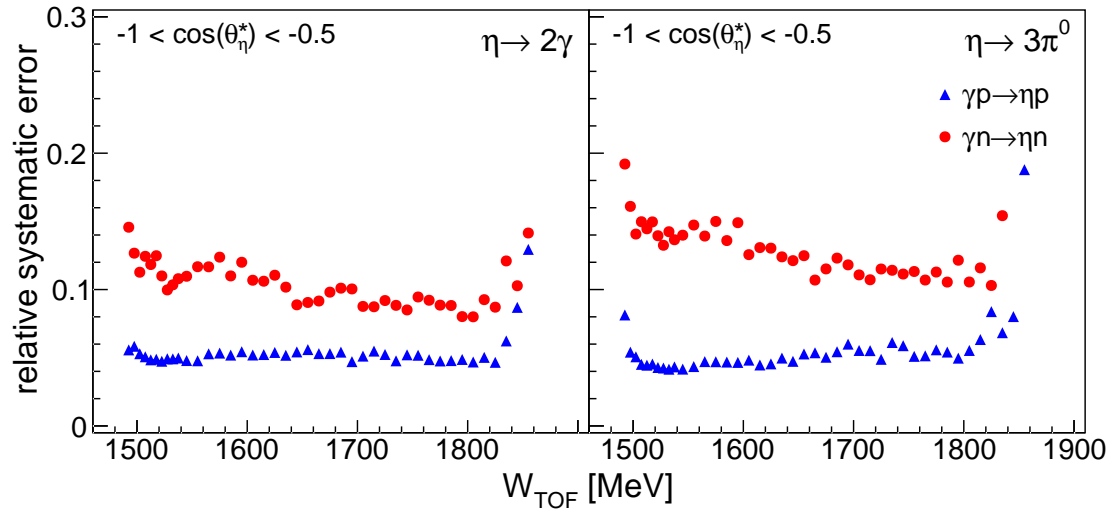
Fig. 4.41: Comparison of relative systematic errors of the total cross sections as a function of W_{TOF}: Left-hand side: $\eta \to 2\gamma$ analyses. Right-hand side: $\eta \to 3\pi^0$ analyses. Blue triangles: $\gamma p \to \eta p$ analyses. Red circles: $\gamma n \to \eta n$ analyses.

- $\gamma N \to \eta(N) \to 3\pi^0(N)$: dominance of CB energy sum trigger from threshold to $E_\gamma \sim 1$ GeV, influence of analysis cuts at higher energies.

- $\gamma n \to \eta n \to 2\gamma n$: dominated by neutron detection efficiency (Geant4 physics model and correction factor), other sources at higher beam energies.

- $\gamma n \to \eta n \to 3\pi^0 n$: dominance of neutron detection efficiency and CB energy sum trigger in the $S_{11}(1535)$ region, analysis cut contributions at higher beam energies.

Absolute values of the systematic errors will be shown in chapter 5 along with the extracted cross section data. Numerical values can be found in the data tables of appendix F.
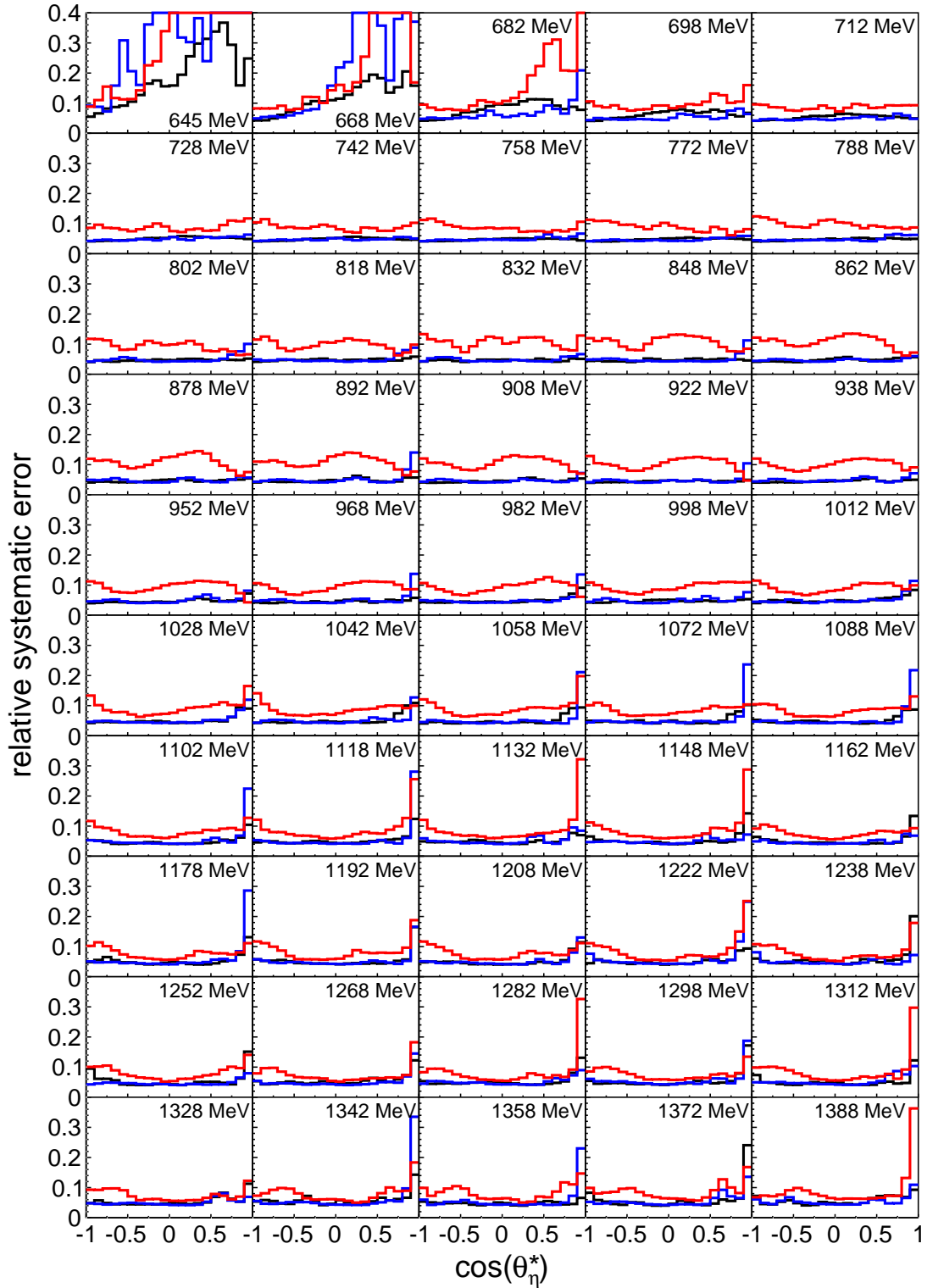
Fig. 4.42: Comparison of relative systematic errors of the differential cross sections for the $\eta \to 2\gamma$ analyses as a function of E_γ: Black histograms: $\gamma N \to \eta(N) \to 2\gamma(N)$ analysis. Blue histograms: $\gamma p \to \eta p \to 2\gamma p$ analysis. Red histograms: $\gamma n \to \eta n \to 2\gamma n$ analysis.
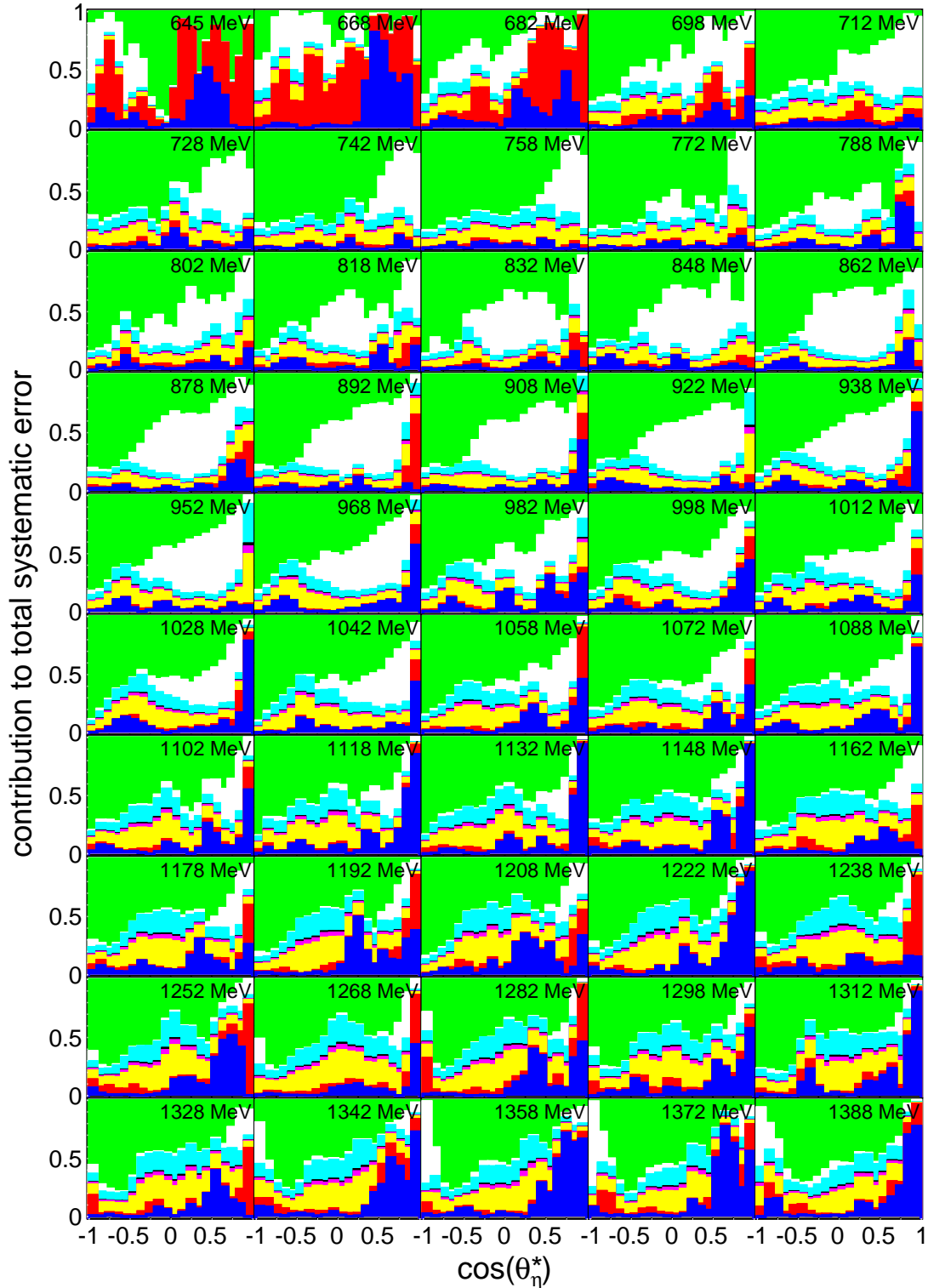
Fig. 4.43: Contributions to the total systematic error of the differential cross sections of $\gamma n \rightarrow \eta n \rightarrow 2\gamma n$ as a function of E_γ: CB energy sum trigger (blue), analysis cuts (red), photon flux (yellow), target density (magenta), empty target subtraction (cyan), η-meson decay branching ratio (black), nucleon detection efficiency correction (white), Geant4 physics model (green).

Chapter 5

Results and discussion

The results that were obtained in this work will be presented in this chapter. In the first sections the results of the three principal cross section measurements will be discussed including comparisons of data sets and η-meson decay channels. The combined results are then compared to previous measurements. In section 5.4 further investigations concerning the structure seen in the η-photoproduction cross section on the neutron are shown. Finally, conclusions originating from this work are drawn in section 5.5.

The main results of this work are differential and total cross section measurements of the following reactions on a deuteron target:

$\gamma N \to \eta(N)$ quasi-free inclusive η-photoproduction on the deuteron
$\gamma p \to \eta p$ quasi-free exclusive η-photoproduction on the proton
$\gamma n \to \eta n$ quasi-free exclusive η-photoproduction on the neutron

Two neutral decay channels of the η-meson, namely $\eta \to 2\gamma$ and $\eta \to 3\pi^0$, were used in the analysis. Cross sections for all three reactions were calculated from threshold up to $E_\gamma \sim 1.4$ GeV as a function of E_γ and $\cos(\theta_\eta^*)$, which is the cosine of the polar angle of the η-meson in the photon-nucleon center-of-mass frame. For the exclusive reactions on the bound nucleons, in addition cross sections were calculated as a function of the center-of-mass energy $W = \sqrt{s}$ reconstructed from the final state η-meson and the recoil nucleon. The values of $\cos(\theta_\eta^*)$ were calculated in the corresponding center-of-mass frames. The W-dependent cross sections are not affected by smearing effects from Fermi motion of the bound nucleons but only by the resolution of the W-reconstruction. Two methods were used for the latter, namely a kinematic calculation (see section 4.5.1) and a time-of-flight (TOF) measurement (see section 4.5.2). The second method requires the detection of the recoil nucleon in forward direction using the TAPS detector, which leads to a limited acceptance in $\cos(\theta_\eta^*)$. Therefore, only cross sections for $-1 < \cos(\theta_\eta^*) < -0.5$ could be calculated using this method, whereas for the kinematic method differential cross sections over all the angular range could be

measured. Depending on the method that was used, the center-of-mass energy W is denoted in the following sections as W_{kin} or W_{TOF}, respectively.

The available high statistics of three data sets allowed a very fine binning of the data. Having still in most bins statistical errors below 10%, 20 bins in $\cos(\theta_\eta^*)$, a 15 MeV binning in E_γ and a 5–10 MeV binning in W_{kin} and W_{TOF} was feasible. Because of the unsuitable experimental trigger in the February 2009 data, only the December 2007 and the May 2009 data could be used for the $\eta \to 2\gamma$ analyses. Nevertheless, the same binning was applicable as statistics was still higher than for the $\eta \to 3\pi^0$ analyses due to the higher detection efficiencies (see section 4.11.1 for more details).

Total cross sections as functions of E_γ and W_{kin} were obtained from integration of the Legendre fits of the corresponding angular distributions. These fits are shown in the figures of the final angular distributions in the following sections. Cross sections as a function of W_{TOF} were calculated using direct integration of the available $\cos(\theta_\eta^*)$ bins. More information about the calculation of cross sections can be found in section 4.10.

Figures of total cross sections showing comparisons of data sets as well as comparisons of differential cross sections extracted from the two analyzed η-meson decays were moved to appendix E for a better readability of the text. In all plots the error bars of the data points correspond to the statistical error only. It should be noted that in most of the plots showing total cross sections the error bars are too small to be visible due to the good statistics of the measurements.

Data tables with the numerical values of all measured differential and total cross sections including statistical and systematic errors can be found in appendix F.

5.1 Quasi-free inclusive η-photoproduction on the deuteron

In this section the results of the $\gamma N \to \eta(N)$ analyses are discussed. Details about the analysis of this channel can be found in section 4.1.1.

5.1.1 Comparison of data sets and η-decay channels

Figure E.1 shows a comparison of the total cross sections of $\gamma N \to \eta(N)$ of the three data sets and the two η-meson decays that were analyzed in this work. There is a good agreement between the two data sets in the $\eta \to 2\gamma$ analysis, only a few points in the sharp rise to the $S_{11}(1535)$ peak show some deviations smaller than 10%. In the $\eta \to 3\pi^0$ analysis the results obtained from the December 2007 data set are up to 10% lower between 750 MeV and 900 MeV compared to the other
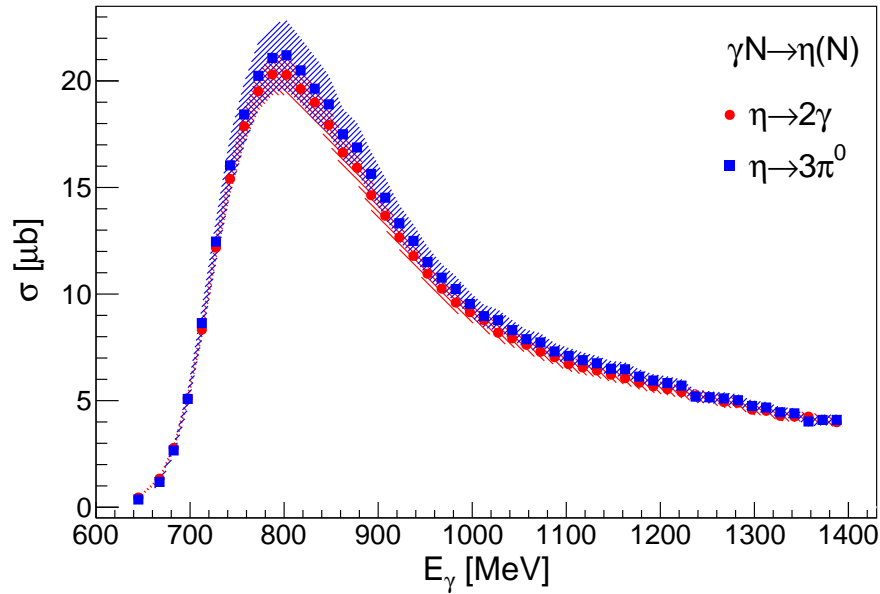
Fig. 5.1: Comparison of the total cross sections of $\gamma N \to \eta(N)$ of the two η-meson decay analyses as a function of E_γ: Red circles: $\eta \to 2\gamma$ analysis. Blue squares: $\eta \to 3\pi^0$ analysis. The estimated systematic errors are shown by the hatched red and, respectively, blue areas.

data sets. This could be due to unreliable results from the signal fitting procedure (see section 4.10.1), as the statistics of a single data set is limited. The problems occurring in the fitting procedure can also be seen in the fluctuating points of the February 2009 data set, which has lower statistics compared to the other two. The fitting problems will be reduced when the data sets are merged and the fits can be performed using the combined statistics of all the data sets.

Overall no notable systematic deviations can be seen in the comparison of the data sets. The shapes and magnitudes of all cross sections are in reasonable agreement and, therefore, the data sets can be merged (see section 4.11.1).

The total cross sections from the two η-meson decays obtained using the merged data sets are compared in figure 5.1. Taking into account the systematic errors for the analyses of the two decays, the results are in good agreement. As shown in section 4.13, the systematic errors for the $\eta \to 2\gamma$ analysis are around 10% at threshold reaching a nearly constant value of 5% starting around $E_\gamma = 700$ MeV. In case of the $\eta \to 3\pi^0$ analysis the systematic uncertainties are slightly higher, starting from 10% at threshold and decreasing linearly to a constant value of approximately 6% for $E_\gamma = 1$ GeV and above.

A comparison of the differential cross sections is shown in figure E.8. Apart from systematically lower values of the $\eta \to 2\gamma$ analysis in the first four forward bins for E_γ below ~950 MeV that could be due to analysis cuts or the CB energy sum trigger, there are no global discrepancies in the magnitudes and the shapes

Fig. 5.2: Total cross section of $\gamma N \to \eta(N)$ from the combined results of the $\eta \to 2\gamma$ and $\eta \to 3\pi^0$ analyses as a function of E_γ: Red circles: combined result of this work. Red hatched area: combined systematic error. Blue squares: CBELSA/TAPS data [15]. Black triangles: TAPS data [17].

of the angular distributions of the two η-meson decay channels. For photon beam energies above 1.2 GeV the statistical quality of the data decreases, especially for the $\eta \to 3\pi^0$ decay, which leads to fluctuations of single data points caused by unreliable signal fits.

5.1.2 Combined results

The results of the $\gamma N \to \eta(N) \to 2\gamma(N)$ and the $\gamma N \to \eta(N) \to 3\pi^0(N)$ analyses were used to calculate a combined result for the $\gamma N \to \eta(N)$ reaction. The data were averaged according to their statistical weights and the same weights were used to estimate a combined systematic error (see section 4.11.2).

Figure 5.2 shows the total cross section of $\gamma N \to \eta(N)$ that was obtained in this work. It is compared to the measurements by the CBELSA/TAPS collaboration [15] and the results of the TAPS collaboration [17]. These results agree well with each other while a discrepancy up to 10% in the $S_{11}(1535)$ region to the current results can be seen. The sources of the systematic uncertainties of the other measurements may be different compared to this measurement, as they were obtained in other experiments, but the magnitudes are surely of similar order. Thus, within systematic errors the results of this work can be seen compatible with the previous measurements.

Fig. 5.3: Differential cross sections of $\gamma N \to \eta(N)$ from the combined results of the $\eta \to 2\gamma$ and $\eta \to 3\pi^0$ analyses as a function of E_γ: Red circles: combined result of this work. Red hatched histograms: combined systematic error. Blue squares: CBELSA/TAPS data [15]. Black curves: fit of data.

From the differential cross sections that are shown in figure 5.3 it can be seen that the differences to the CBELSA/TAPS measurements are due to systematic differences of the angular distributions in forward direction, whereas the agreement at backward angles is good for most bins with coinciding data. The lower values in forward direction of the current results are caused by the data of the $\eta \to 2\gamma$ decay channel, which dominate the combined measurement because of their higher statistical weights. The $\eta \to 3\pi^0$ decay channel on the other hand shows a similar behavior, at least for lower beam energies, as the CBELSA/TAPS results, which were also obtained by the analysis of the $\eta \to 3\pi^0$ decay channel. Therefore, the differences between the current results and the results from CBELSA/TAPS could be due to systematic uncertainties in the $\eta \to 2\gamma$ analysis.

Major features of previous measurements of the differential cross sections of $\gamma N \to \eta(N)$ are confirmed by the results of this work. At threshold there is a strong forward-backward asymmetry caused by the Fermi motion of the quasi-free nucleons. The threshold for η-production can be reached more easily by nucleons with large momenta in negative z-direction and, therefore, the average of the nucleon momenta at these energies is shifted. Since the center-of-mass frame is calculated assuming nucleons at rest, which is a reasonable approximation when the nucleon momentum distribution is isotropic, this frame has a systematic deviation from the true center-of-mass frame. In fact, the calculated frame is faster than in reality which results in a shift of the flat angular distribution of the η-meson in the real frame to backward angles in the calculated frame due to the wrongly calculated Lorentz boost. For higher beam energies up to 900 MeV, the typical isotropic behavior of the angular distribution caused by the dominating excitation of the $S_{11}(1535)$ resonance can be seen. Also the curvature in this region caused by the interference of the $S_{11}(1535)$ and the $D_{13}(1520)$ resonances is reproduced.

5.2   Quasi-free exclusive η-photoproduction on the proton

In this section the results of the $\gamma p \to \eta p$ analyses are discussed. Details about the analysis of this channel can be found in section 4.1.2.

5.2.1   Comparison of data sets and η-decay channels

In figure E.2 the total cross sections of $\gamma p \to \eta p$ as a function of the photon beam energy E_γ originating from the different data sets and the two η-meson decay channels are compared. There is an excellent agreement between the data sets for the analyses of the two decays. In figures E.4 and E.6 the corresponding cross
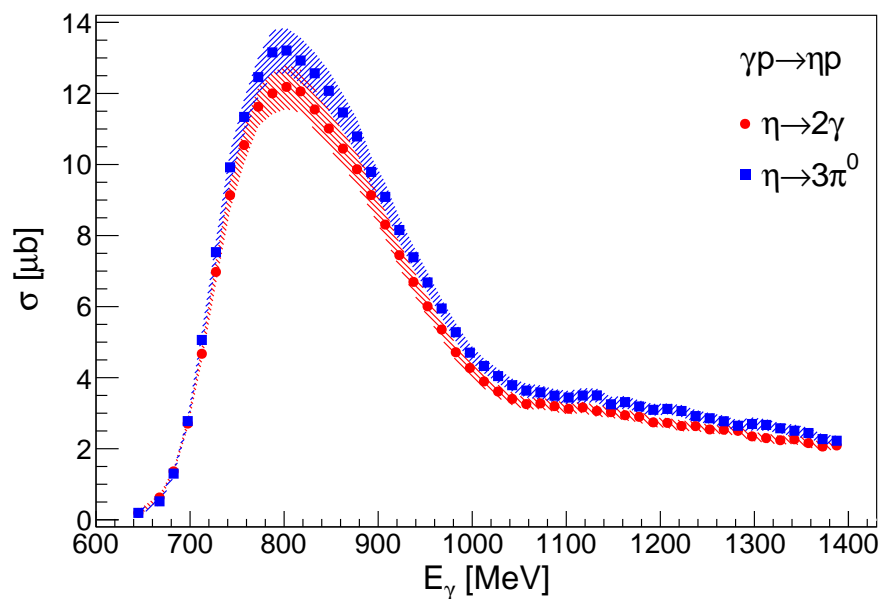
Fig. 5.4: Comparison of the total cross sections of $\gamma p \to \eta p$ of the two η-meson decay analyses as a function of E_γ: Red circles: $\eta \to 2\gamma$ analysis. Blue squares: $\eta \to 3\pi^0$ analysis. The estimated systematic errors are shown by the hatched red and, respectively, blue areas.

sections as functions of the center-of-mass energy W reconstructed from kinematics and, respectively, by using time-of-flight can be found. The overall agreement between the data sets is good. There are some deviations in the December 2007 data set, which are caused by the cut on the proton polar angle as described in section 4.3.5. The cross section depending on W_{TOF} is affected most strongly by this cut on forward going protons, as it reduces drastically the statistics for protons in TAPS. Also the effect is more visible in $\sigma(W_{\mathrm{kin}})$ than $\sigma(E_\gamma)$ because there is no smearing of the affected angular bins by Fermi motion. However, when merging the data sets, all affected bins for all the differential cross sections of the December 2007 data set are ignored and thus have no influence on the merged result. In case of the cross section $\sigma(W_{\mathrm{TOF}})$ the December 2007 data set is completely omitted due to its large statistical and systematic uncertainty (see section 4.11.1).

Having merged the data sets, the results of the two η-meson decays can be compared. The comparison of the total cross sections as functions of E_γ, W_{kin} and W_{TOF} can be seen in figures 5.4, 5.5 and 5.6, respectively. The results of the $\eta \to 2\gamma$ decay analysis are showing smaller values than the ones obtained by the $\eta \to 3\pi^0$ analysis. The difference is only weakly depending on the energy and accounts to 8–10%. As the bands indicating the estimated systematic errors are only barely overlapping, this difference is probably due to an unknown or underestimated source of systematic uncertainty. There is a slight dependence of this difference on $\cos(\theta_\eta^*)$, as can be seen in the angular distributions shown in figures E.9 and E.11. The differences seem to be larger at backward angles.
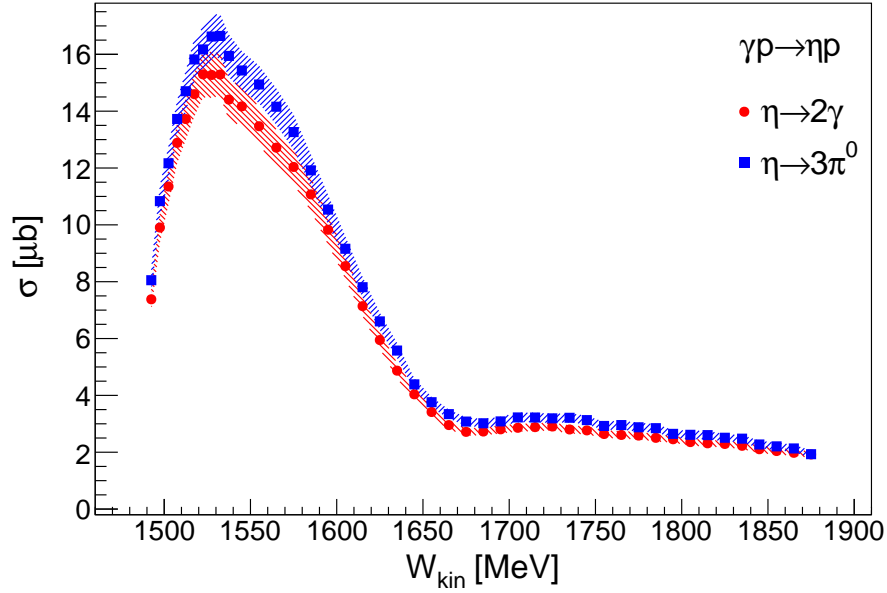
Fig. 5.5: Comparison of the total cross sections of $\gamma p \rightarrow \eta p$ of the two η-meson decay analyses as a function of W_{kin}: Red circles: $\eta \rightarrow 2\gamma$ analysis. Blue squares: $\eta \rightarrow 3\pi^0$ analysis. The estimated systematic errors are shown by the hatched red and, respectively, blue areas.
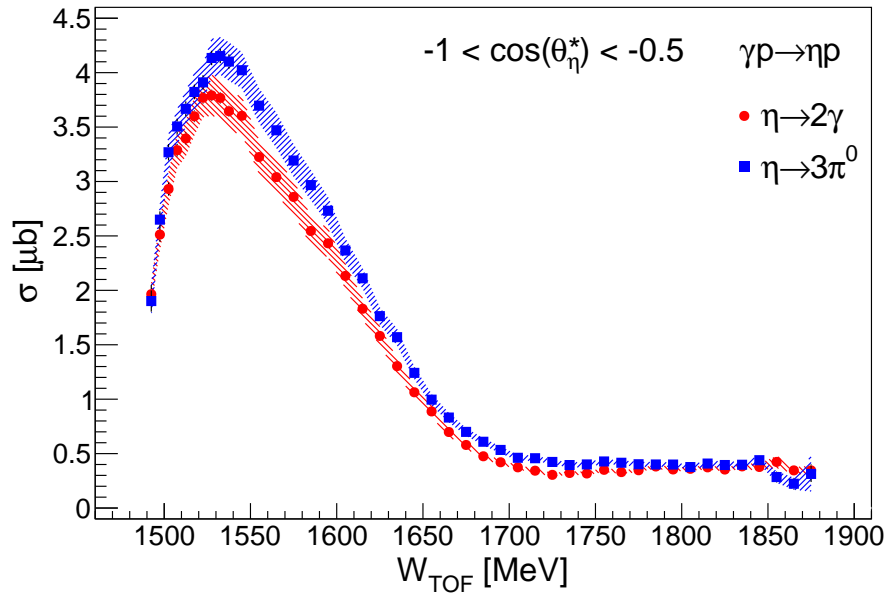
Fig. 5.6: Comparison of the total cross sections of $\gamma p \rightarrow \eta p$ of the two η-meson decay analyses as a function of W_{TOF} for $-1 < \cos(\theta_\eta^*) < -0.5$: Red circles: $\eta \rightarrow 2\gamma$ analysis. Blue squares: $\eta \rightarrow 3\pi^0$ analysis. The estimated systematic errors are shown by the hatched red and, respectively, blue areas.
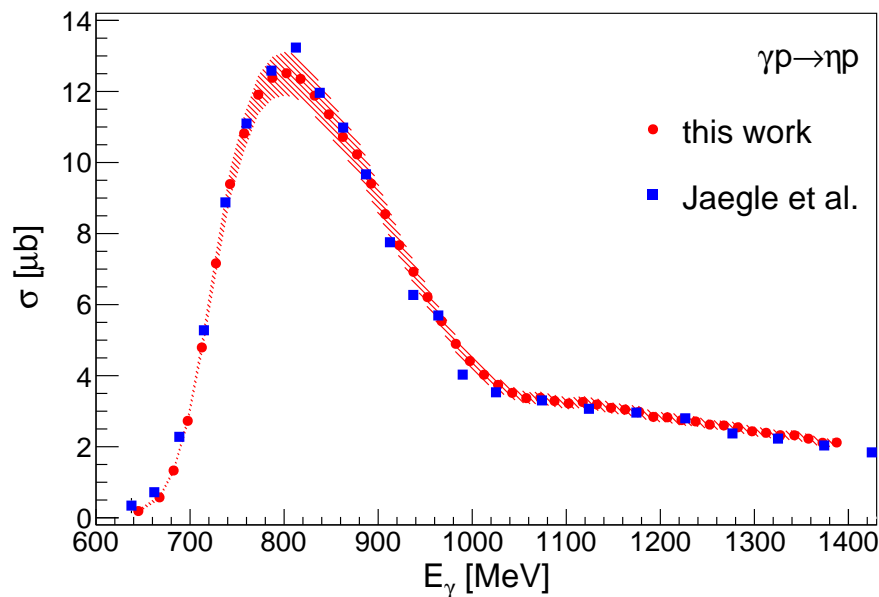
Fig. 5.7: Total cross section of $\gamma p \to \eta p$ from the combined results of the $\eta \to 2\gamma$ and $\eta \to 3\pi^0$ analyses as a function of E_γ: Red circles: combined result of this work. Red hatched area: combined systematic error. Blue squares: CBELSA/TAPS data [15].

One possibility might be contamination in the $\eta \to 3\pi^0$ analysis of events coming from direct $3\pi^0$-photoproduction. In the free measurement of $\gamma p \to \eta p$ at MAMI-C a contamination up to 4.4% at $E_\gamma = 1.4$ GeV was estimated [35]. This work was using event-by-event kinematic fitting, which usually results in a very good background suppression. For the current analysis, where this technique was not possible due to the lack of an overdetermined reaction kinematics, contamination of direct $3\pi^0$ events could be even higher. A clean separation and subtraction of this contamination was not performed in this work. Using the current analysis, a separation is rather difficult because the background events that pass all cuts in the analysis are hardly separable from real events. A rough estimation of the degree of contamination was performed using unpublished cross section data from [91]. The obtained values were unrealistically large (up to 30% at 1.4 GeV) considering the good agreement of various distributions of simulated and experimental data, and the actual differences to the results of the $\eta \to 2\gamma$ analysis. Therefore, the results of the $\eta \to 2\gamma$ and the $\eta \to 3\pi^0$ analyses were merged directly without subtraction of any kind. Nevertheless, the overall shape is in good agreement and the nearly energy independent discrepancy is not changing the final conclusions of this work.
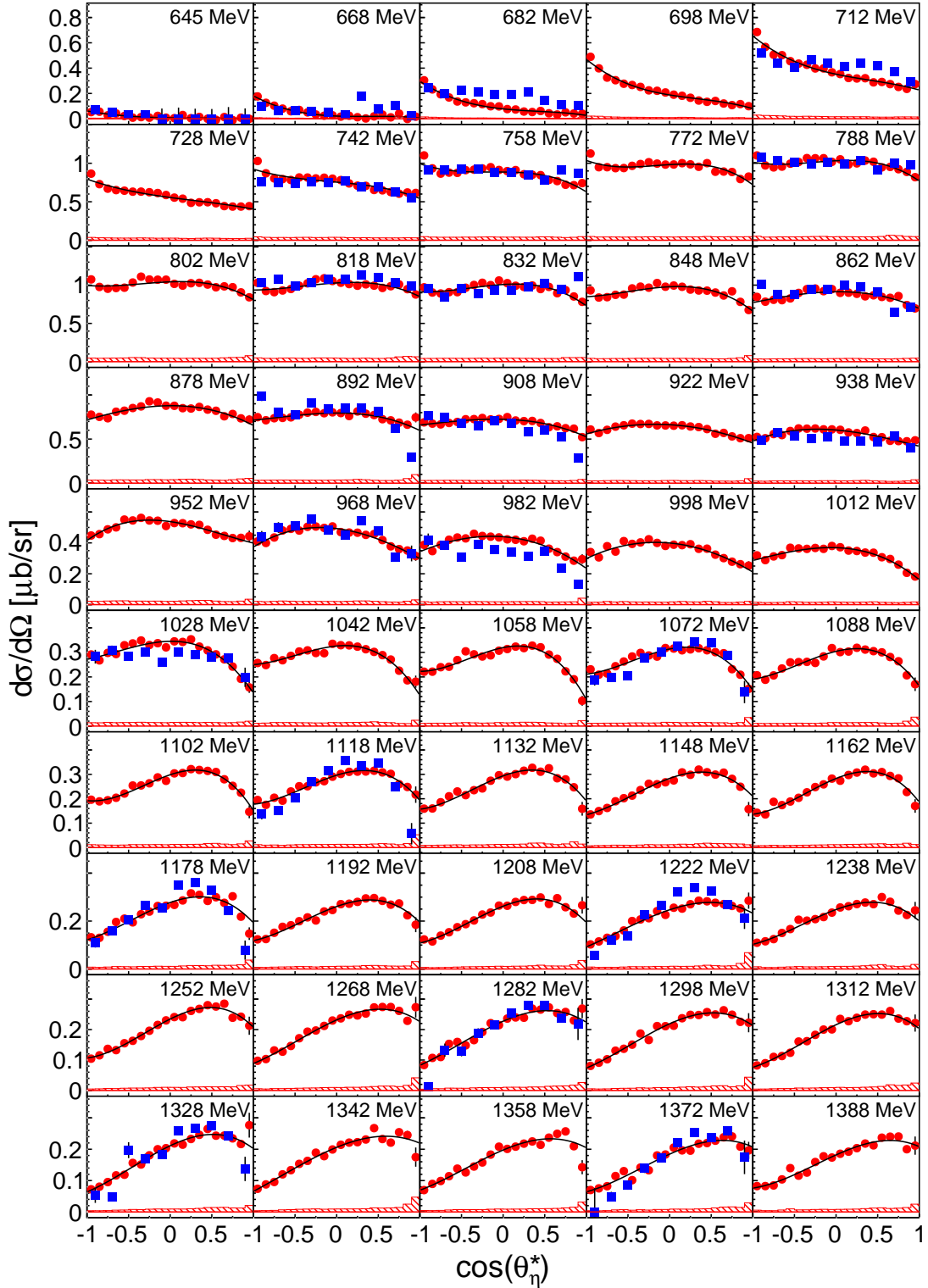
Fig. 5.8: Differential cross sections of $\gamma p \to \eta p$ from the combined results of the $\eta \to 2\gamma$ and $\eta \to 3\pi^0$ analyses as a function of E_γ: Red circles: combined result of this work. Red hatched histograms: combined systematic error. Blue squares: CBELSA/TAPS data [15]. Black curves: fit of data.
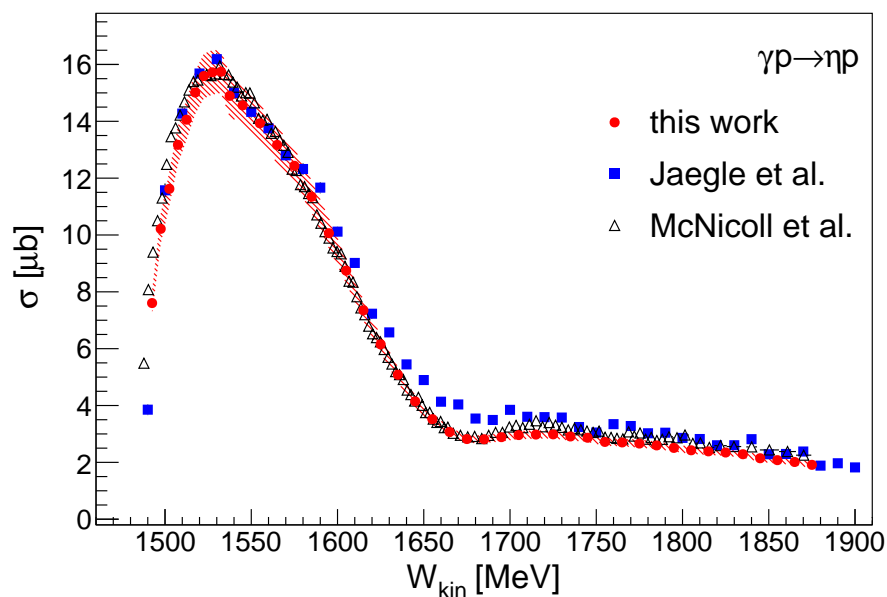
Fig. 5.9: Total cross section of $\gamma p \to \eta p$ from the combined results of the $\eta \to 2\gamma$ and $\eta \to 3\pi^0$ analyses as a function of W_{kin}: Red circles: combined result of this work. Red hatched area: combined systematic error. Blue squares: CBELSA/TAPS data [15] (rebinned). Black triangles: MAMI-C free proton data [35].

5.2.2 Combined results

The results of the $\gamma p \to \eta p \to 2\gamma p$ and the $\gamma p \to \eta p \to 3\pi^0 p$ analyses were used to calculate a combined result for the $\gamma p \to \eta p$ reaction. The data were averaged according to their statistical weights and the same weights were used to estimate a combined systematic error (see section 4.11.2).

First, the cross sections depending on the photon beam energy E_γ are discussed. The total cross section is shown in figure 5.7 and the angular distributions in figure 5.8, respectively. The results are compared to the CBELSA/TAPS measurements [15]. The global agreement of normalization and shape is good. Most of the previously measured data points coincide within systematic errors with the current measurements. There are some larger deviations for four data points, one around a beam energy of 820 MeV and three between 900 MeV and 1 GeV. As it can be seen in the angular distributions, this is caused by some fluctuations in the data of CBELSA/TAPS. It is also visible that the agreement in the total cross section above 1 GeV is somehow accidental, because there are some deviations in opposite directions in the differential cross sections. The current results tend to have larger values at backward angles while they fall off with respect to the CBELSA/TAPS data at $\cos(\theta_\eta^*) \sim 0.5$. Considering the fluctuations of these data at lower energies, where statistics should be better, it is not quite clear if the deviations are systematic or purely statistical.
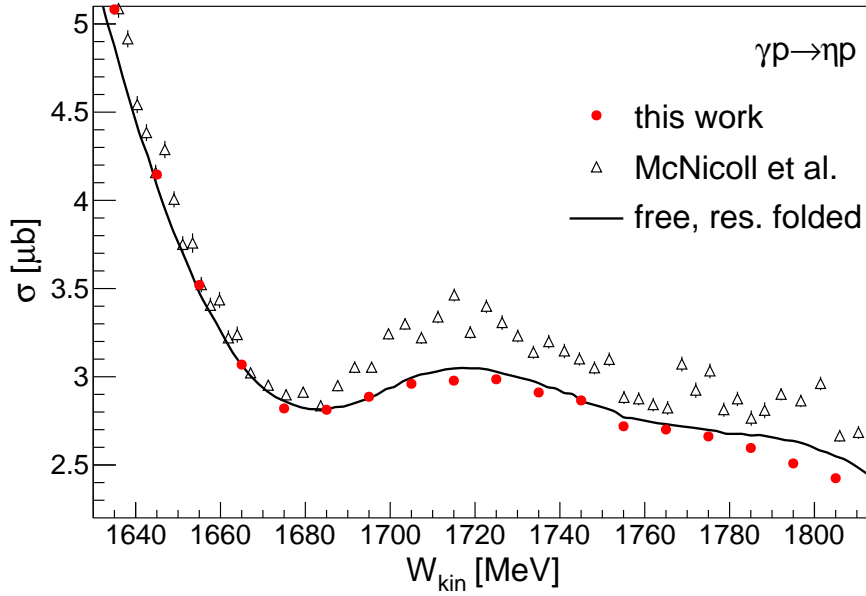
Fig. 5.10: Influence of the W_{kin}-reconstruction resolution on the total cross section of $\gamma p \to \eta p$ as a function of W_{kin}: Red circles: this work. Black triangles: MAMI-C free proton data [35]. Black line: free proton data folded with W_{kin}-resolution (normalized).

In figure 5.9 the total cross section of $\gamma p \to \eta p$ as a function of the center-of-mass energy W_{kin} is shown, which was obtained from the reconstruction of the reaction kinematics (see section 4.5.1). In addition to the previously mentioned data from CBELSA/TAPS [15], the high precision data obtained from the measurement on the free proton at MAMI-C [35] can be used for a comparison with the result of this work. There are some major discrepancies with the first one, whereas the agreement to the latter data is very good, having deviations smaller than 5% for energies from 1520 MeV up to 1700 MeV. There are some larger (but still < 10%) differences right at threshold and around 1700 MeV. Both could be due to the resolution of the W_{kin}-reconstruction. The measurement on the free proton is only affected by the tagger energy resolution resulting in a significantly better resolution of the center-of-mass energy (see section 4.5.1).

Resolution effects are most visible in the vicinity of sharp structures, e.g., as stated above, at threshold or near the dip-like structure around $W = 1680$ MeV in the total cross section, whose presence was finally confirmed by the MAMI-C measurement. The situation at this energy is shown in figure 5.10, where the total cross section of the MAMI-C measurement on the free proton was folded with the resolution of the W_{kin}-reconstruction obtained in this work. For a better comparison the folded cross section was normalized to the result of this work in the interval [1660, 1680] MeV. It can be clearly seen that the folded free measurement reproduces fairly well the quasi-free measurements: Normalized to the preceding
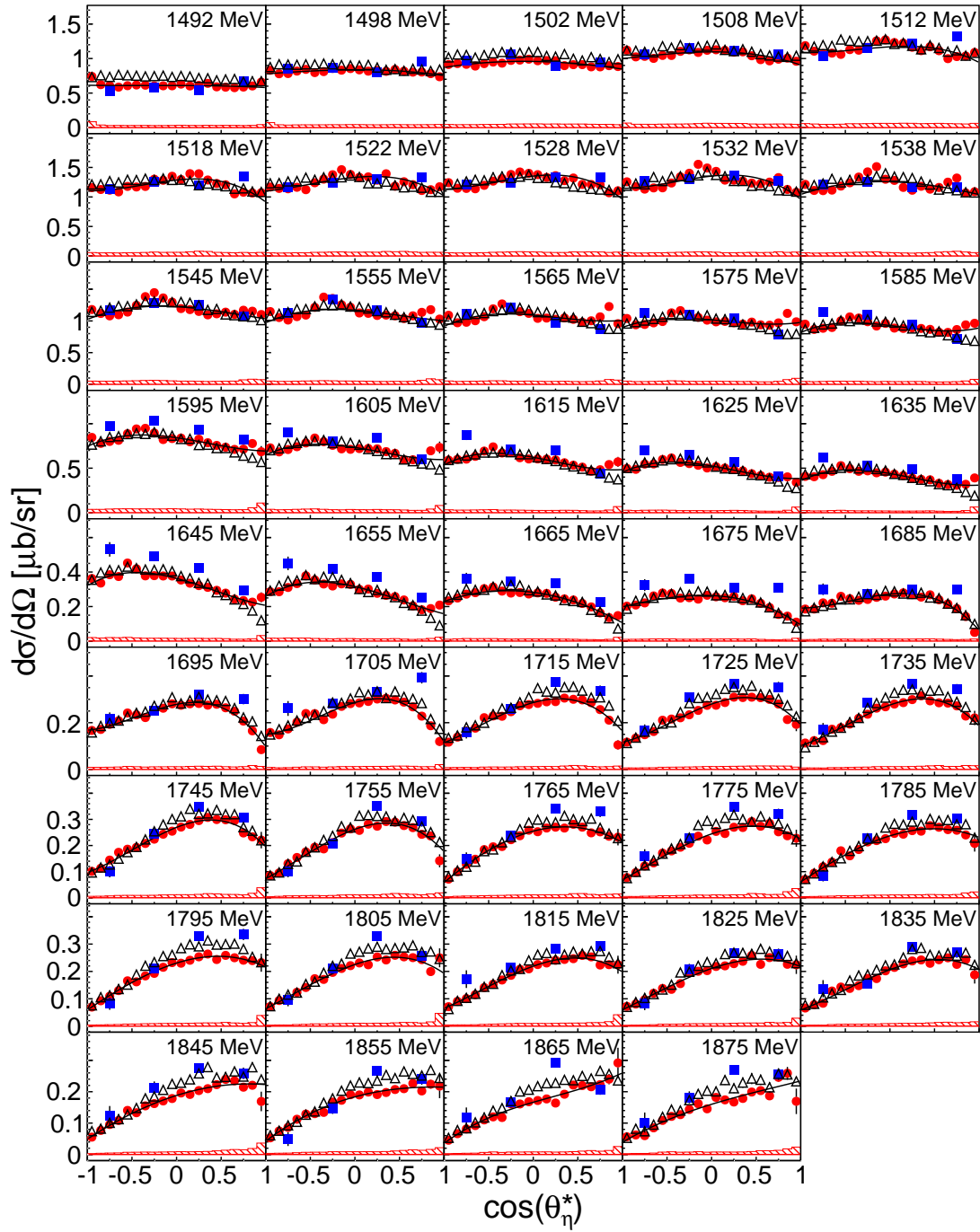
Fig. 5.11: Differential cross sections of $\gamma p \rightarrow \eta p$ from the combined results of the $\eta \rightarrow 2\gamma$ and $\eta \rightarrow 3\pi^0$ analyses as a function of W_{kin}: Red circles: combined result of this work. Red hatched histograms: combined systematic error. Blue squares: CBELSA/TAPS data [15]. Black triangles: MAMI-C free proton data [35] (rebinned). Black curves: fit of data.
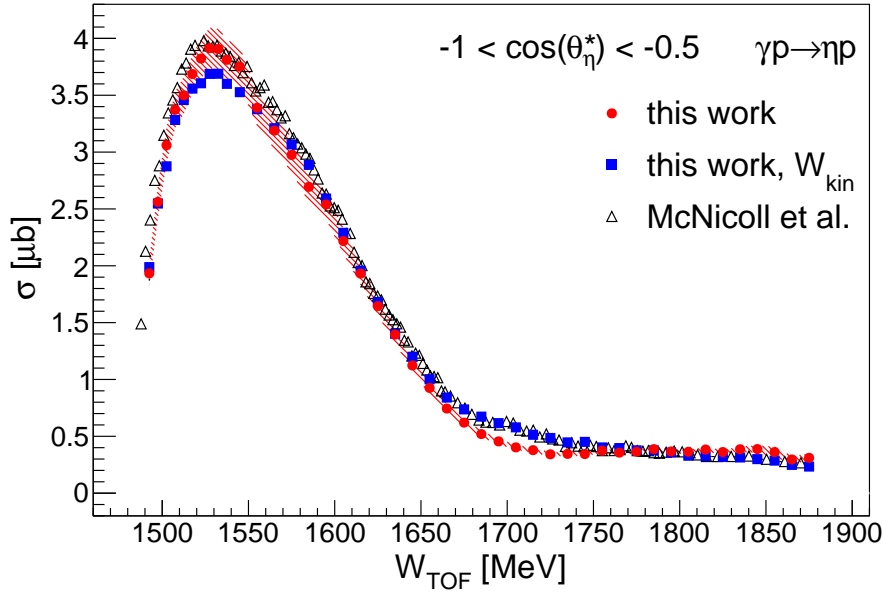
Fig. 5.12: Total cross section of $\gamma p \to \eta p$ from the combined results of the $\eta \to 2\gamma$ and $\eta \to 3\pi^0$ analyses as a function of W_{TOF} for $-1 < \cos(\theta_\eta^*) < -0.5$: Red circles: combined result of this work. Red hatched area: combined systematic error. Blue squares: results from kinematic reconstruction. Black triangles: MAMI-C free proton data [35].

fall-off and the minimum around 1680 MeV, the rise to the maximum near 1720 MeV seen in the free measurement is smeared by resolution and therefore less sharp in the quasi-free data.

The differential cross sections as a function of W_{kin} can be found in figure 5.11. The MAMI-C free proton data were rebinned to the binning used in this work for a better comparison. Overall, the current results reproduce very well the angular distributions of the free proton data. In the region from threshold up to $W \sim 1600$ MeV, which is dominated by the isotropic excitation of the $S_{11}(1535)$ resonance and supplemented by a $S_{11}(1535)$-$D_{13}(1520)$ interference that causes a concave curvature, there is also good agreement with the CBELSA/TAPS data. But, starting at 1600 MeV there are differences up to 30% percent with respect to these data.

There are two notable discrepancies with the MAMI-C free proton data, which can be reasonably understood. First, some slight oscillations in the data of this work can be seen that are not present in the MAMI-C data. They are visible up to 1700 MeV but most prominent in the interval [1512, 1605] MeV. There is, e.g., a local maximum around $\cos(\theta_\eta^*) \sim 0.3$ and a rise in the first forward bins. This is mostly caused by the nucleon detection efficiency, as the proton is going to the tunnel region of the Crystal Ball detector and/or is having very few kinetic energy and, therefore, systematic uncertainties are large (see section 4.8.4).

Interestingly, the Eta-MAID calculation [14] is showing a faint rise in the very forward direction as seen in these data (Eta-MAID not shown in plot). Secondly, the differential cross sections of this work are systematically lower starting from $W \sim 1705$ MeV. Especially in forward direction, the differences can be higher than 15% with increasing energy, whereas in backward direction they are a bit smaller. For the lower energies this is probably caused by resolution, as shown in figure 5.10. For the higher energies there is another effect to be considered. Namely, events produced at photon energies $E_\gamma > E_\gamma^{\text{tagg}}$ but with large Fermi momenta in positive z-direction, which leads to lower center-of-mass energies with respect to $W = \sqrt{2E_\gamma m_N + m_N^2}$, are missing in this region because the corresponding photons are not tagged anymore. Part of this effect should be compensated by the W-dependent flux but it is possible that the correction is not working completely.

Finally, the total cross section depending on the center-of-mass energy W_{TOF} obtained using the time-of-flight measurement of the recoil proton in TAPS is presented in figure 5.12. Due to the kinematic restriction of the recoil nucleon, the total cross section could only be measured for $-1 < \cos(\theta_\eta^*) < -0.5$. Therefore, the results obtained from the kinematic reconstruction as well as the free proton data from MAMI-C were integrated in the same angular range to achieve a comparison with these results. The overall agreement is good considering the very different type of measurements. The current results show a decline of the cross section between 1550 MeV and 1600 MeV. This can also be seen less drastically in $\sigma(W_{\text{kin}})$. It is caused by the proton detection efficiency, which has higher systematic errors in forward direction (Crystal Ball tunnel region and TAPS), and is therefore enhanced in this measurement. The second fall-off with respect to the other measurements is around $W = 1700$ MeV. This is probably due to the worse resolution of the W_{TOF}-reconstruction at higher energies (see section 4.5.2).

5.3 Quasi-free exclusive η-photoproduction on the neutron

In this section the results of the $\gamma n \to \eta n$ analyses are discussed. Details about the analysis of this channel can be found in section 4.1.3.

5.3.1 Comparison of data sets and η-decay channels

The total cross sections as functions of E_γ, W_{kin} and W_{TOF} of the $\gamma n \to \eta n \to 2\gamma n$ and the $\gamma p \to \eta p \to 3\pi^0 p$ analyses, which were obtained from the different data sets, are compared in figures E.3, E.5 and E.7. As noticed for the proton results, the cross sections obtained from the December 2007 data set show some deviations, especially in the $\eta \to 2\gamma$ analysis. The reason for that is the cut on the neutron
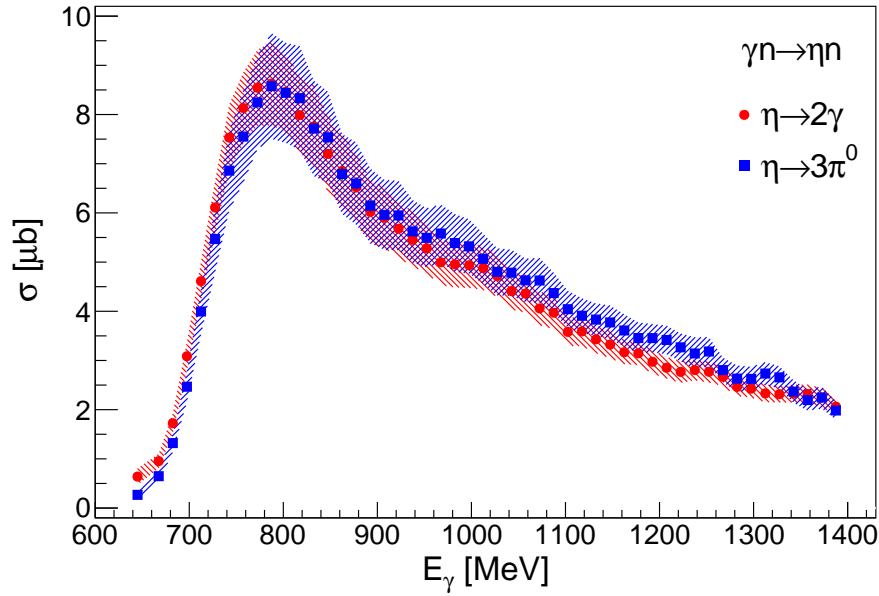
Fig. 5.13: Comparison of the total cross sections of $\gamma n \to \eta n$ of the two η-meson decay analyses as a function of E_γ: Red circles: $\eta \to 2\gamma$ analysis. Blue squares: $\eta \to 3\pi^0$ analysis. The estimated systematic errors are shown by the hatched red and, respectively, blue areas.

polar angle in the laboratory frame, where due to acceptance uncertainties a large portion of the forward going neutrons had to be removed from the analysis (see section 4.3.5). This leads to large statistical errors in the corresponding bins of the angular distributions, which can also be seen in the total cross sections. Equally to the proton analysis, these bins are not considered when the data sets are merged and thus they have no influence on the final results. For the cross section depending on W_{TOF} the complete December 2007 data set is ignored (see section 4.11.1). Apart from these deviations the different measurements agree quite well and the structure seen in $\sigma(W_{\text{kin}})$ around $W \sim 1670$ MeV, whose investigation is the main subject of this work, is clearly present in all data sets of both η-meson decays.

The total cross sections obtained from merging all data sets are shown in figures 5.13, 5.14 and 5.15. The results of both η-meson decay analyses are compared with each other and the comparison is completed by their individually determined systematic errors (see section 4.13). In the region up to $E_\gamma \sim 900$ MeV ($W \sim 1600$ MeV), which is dominated by the $S_{11}(1535)$ resonance, there is a good agreement between the two η-meson decays, although there are some larger discrepancies in $\sigma(E_\gamma)$ right after threshold up to $E_\gamma \sim 780$ MeV. Notably, this is the region where both analyses suffer from massive systematic uncertainties up to 15%, which are mainly caused by the determination of the neutron detection efficiencies and, in case of the $\eta \to 3\pi^0$ analysis, the energy sum trigger in CB. For higher energies
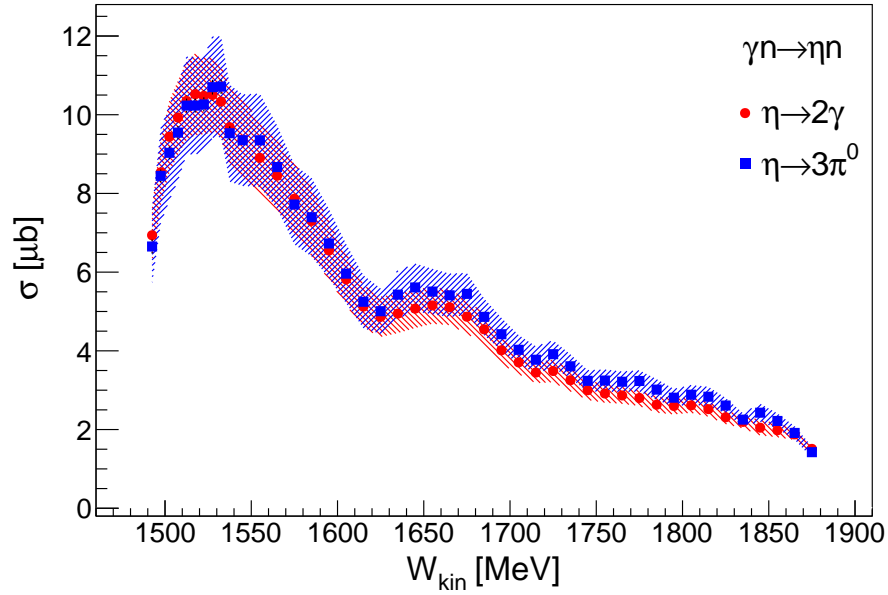
Fig. 5.14: Comparison of the total cross sections of $\gamma n \to \eta n$ of the two η-meson decay analyses as a function of W_{kin}: Red circles: $\eta \to 2\gamma$ analysis. Blue squares: $\eta \to 3\pi^0$ analysis. The estimated systematic errors are shown by the hatched red and, respectively, blue areas.
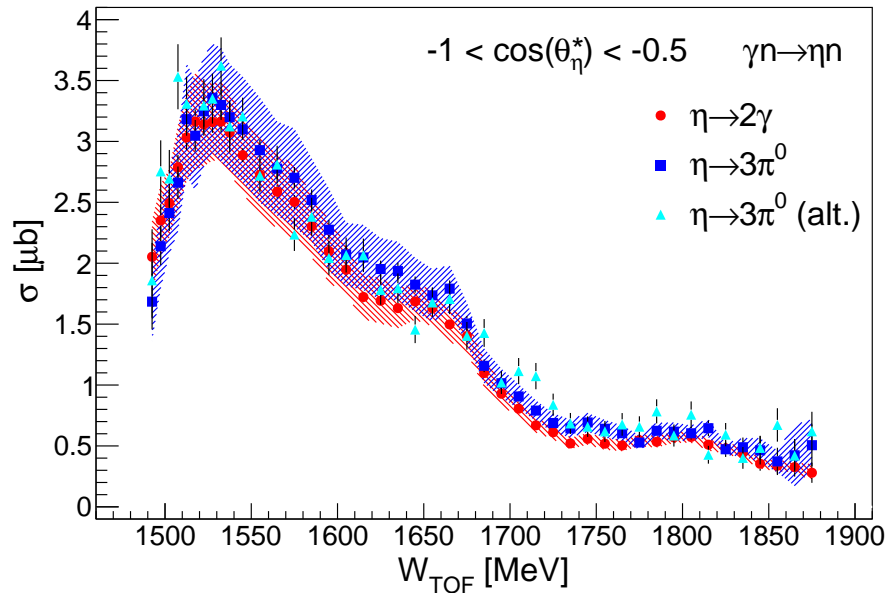
Fig. 5.15: Comparison of the total cross sections of $\gamma n \to \eta n$ of the two η-meson decay analyses as a function of W_{TOF} for $-1 < \cos(\theta_\eta^*) < -0.5$: Red circles: $\eta \to 2\gamma$ analysis. Blue squares: $\eta \to 3\pi^0$ analysis. Cyan triangles: $\eta \to 3\pi^0$ analysis (alternative TOF measurement). The estimated systematic errors are shown by the hatched red and, respectively, blue areas.
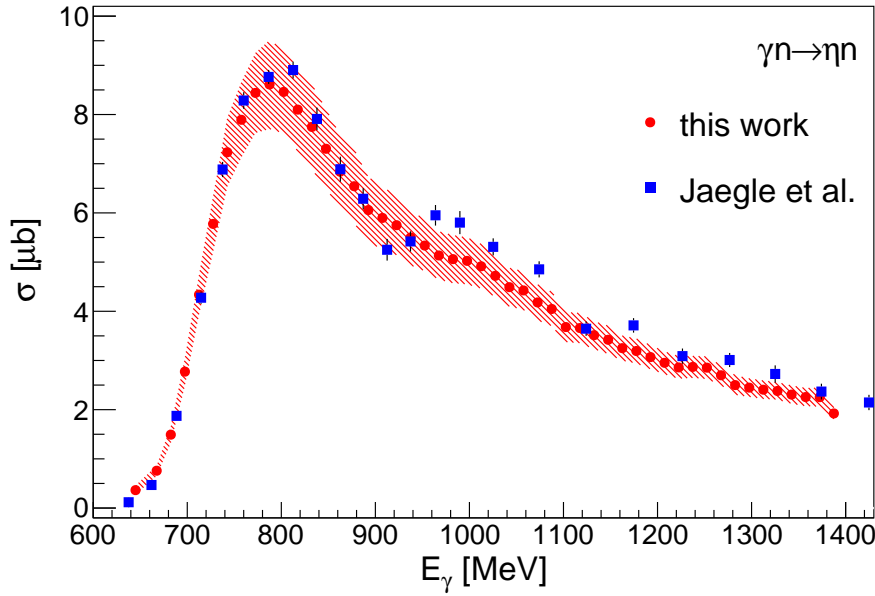
Fig. 5.16: Total cross section of $\gamma n \to \eta n$ from the combined results of the $\eta \to 2\gamma$ and $\eta \to 3\pi^0$ analyses as a function of E_γ: Red circles: combined result of this work. Red hatched area: combined systematic error. Blue squares: CBELSA/TAPS data [15].

there is an almost constant difference of around 10%, as it was seen for the $\gamma p \to \eta p$ analysis. It was argued there, that this could come from contamination of direct $3\pi^0$-production. For the production on the neutron one would expect a smaller effect, although there are no quantitative estimations given in the literature. Therefore, it is questionable if the systematic difference between the analyses of the two η-meson decays in both the proton and the neutron channel has the same origin as, e.g., direct $3\pi^0$-production. The differences in the neutron channels can, at least partially, also be explained by the large and maybe still underestimated systematic uncertainties.

In figure 5.15, additionally the cross section extracted from the alternative time-of-flight measurement, namely by using TAPS as reference time (see section 4.5.2), is shown. Statistics is worse because the nucleon and at least one photon had to be detected in TAPS simultaneously. The agreement with the standard measurement is reasonable. Because of the large statistical errors this cross section is only presented for comparison purposes and is not used any further.

Comparisons of the differential cross sections depending of E_γ and W_{kin} that were extracted from the two η-meson decays can be found in figures E.10 and E.12. Due to the lower statistical quality of the data compared to the proton data, especially for the $\eta \to 3\pi^0$ analysis, it is hard to determine if the almost constant difference of 10% is having a clear angular dependence.

5.3.2 Combined results

The results of the $\gamma n \to \eta n \to 2\gamma n$ and the $\gamma n \to \eta n \to 3\pi^0 n$ analyses were used to calculate a combined result for the $\gamma n \to \eta n$ reaction. The data were averaged according to their statistical weights and the same weights were used to estimate a combined systematic error (see section 4.11.2).

The total and differential cross sections as a function of the photon beam energy E_γ are shown in figures 5.16 and 5.17, respectively. A comparison to the data from CBELSA/TAPS [15] is performed. First, the improved statistical quality of the new data is obvious. The agreement in the region dominated by the $S_{11}(1535)$ resonance up to $E_\gamma \sim 900$ MeV is very good, especially if the substantial systematic errors indicated by the red hatched area are taken into account. The forward-backward asymmetry in the angular distributions at threshold caused by Fermi motion is reproduced as well. At higher energies the isotropic angular behavior with the convex curvature is clearly visible. This is due to an interference of the $S_{11}(1535)$ and the $D_{13}(1520)$ resonances similar to the situation seen on the proton, but with opposite signs, as the helicity couplings of the $S_{11}(1535)$ have opposite signs for proton and neutron, while the $D_{13}(1520)$ couplings have the same.

Starting from a beam energy of 900 MeV the deviations between the two data sets are getting larger (10–15%). In addition the bump structure around 1 GeV is more visible in the CBELSA/TAPS data. This could be due to more stringent kinematic cuts in the analysis but there are also some statistical effects, which enhance the situation even more. For example, the data point around 910 MeV contributes very strongly to the clarity of the bump due to its decreased value. Having a look at the corresponding angular distribution, several data points seem to have accidentally negative statistical fluctuations considering the overall trend of the angular distribution. The same goes for the four data points from 960 MeV to 1080 MeV, where some positive statistical fluctuations seem to increase the integrated total cross sections at these energies, leading to a higher amplitude of the bump.

In figures 5.18 and 5.19 the total and, respectively, differential cross sections as a function of the reconstructed center-of-mass energy W_{kin} are shown. They are again compared to the CBELSA/TAPS results and the superior statistical quality can once again be noticed, particularly in the angular distributions, where the current results provide now twenty bins in $\cos(\theta_\eta^*)$ in contrast to four. In the $S_{11}(1535)$ region the convex curvature is reproduced and a reasonable overall agreement with the CBELSA/TAPS is found considering single statistical outliers and the major systematic uncertainties (15-20%) due to the detection efficiency of slow neutrons. At higher energies there is a systematic and large discrepancy in the normalization with the CBELSA/TAPS results. In the total cross section
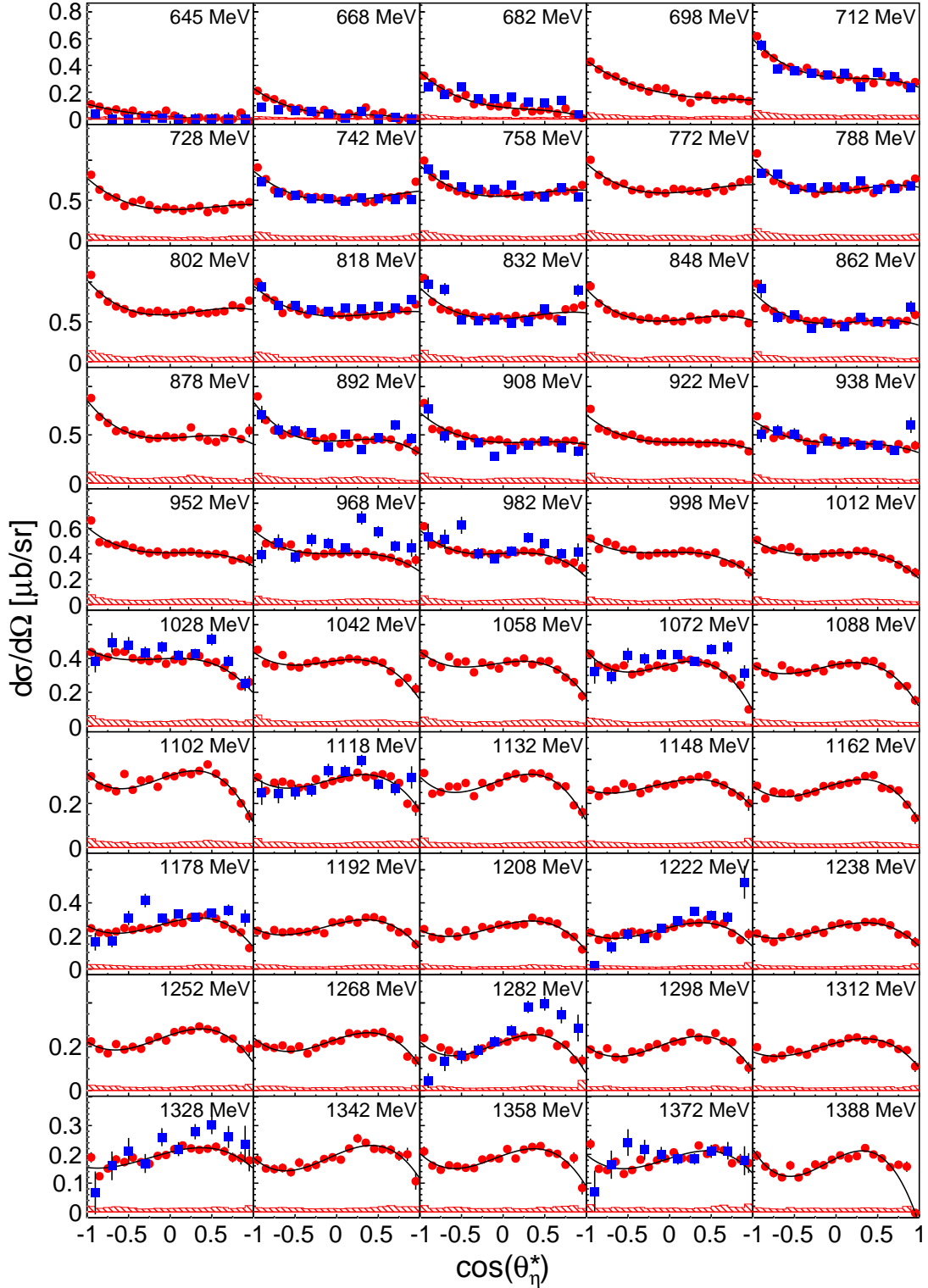
Fig. 5.17: Differential cross sections of $\gamma n \to \eta n$ from the combined results of the $\eta \to 2\gamma$ and $\eta \to 3\pi^0$ analyses as a function of E_γ: Red circles: combined result of this work. Red hatched histograms: combined systematic error. Blue squares: CBELSA/TAPS data [15]. Black lines: fit of data.
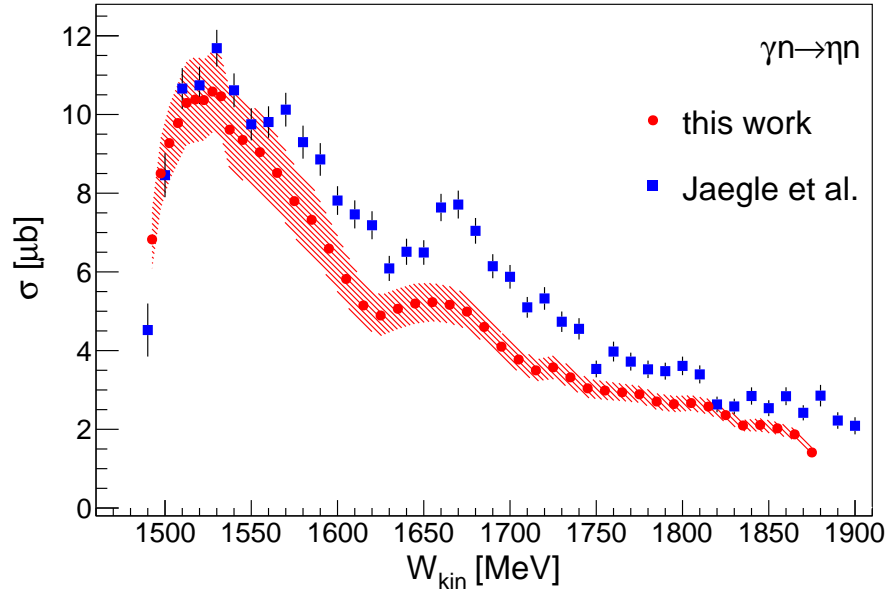
Fig. 5.18: Total cross section of $\gamma n \to \eta n$ from the combined results of the $\eta \to 2\gamma$ and $\eta \to 3\pi^0$ analyses as a function of W_{kin}: Red circles: combined result of this work. Red hatched area: combined systematic error. Blue squares: CBELSA/TAPS data [15] (rebinned).

the bump around $W = 1670$ MeV can be clearly seen and its presence is beyond any doubts from a statistical point of view.

Finally, in figure 5.20 the total cross section as a function of W_{TOF} obtained from the time-of-flight measurement of the neutron in TAPS is shown. Due to the kinematic restriction of the recoil neutron the total cross section could only be integrated in the angular range of $-1 < \cos(\theta_\eta^*) < -0.5$. It is compared to the cross section obtained from kinematic reconstruction integrated over the same angular region. The overall agreement is good but the TOF measurements show a more prominent peak that is shifted to lower energy. These results will be discussed in more detail in section 5.4.3.
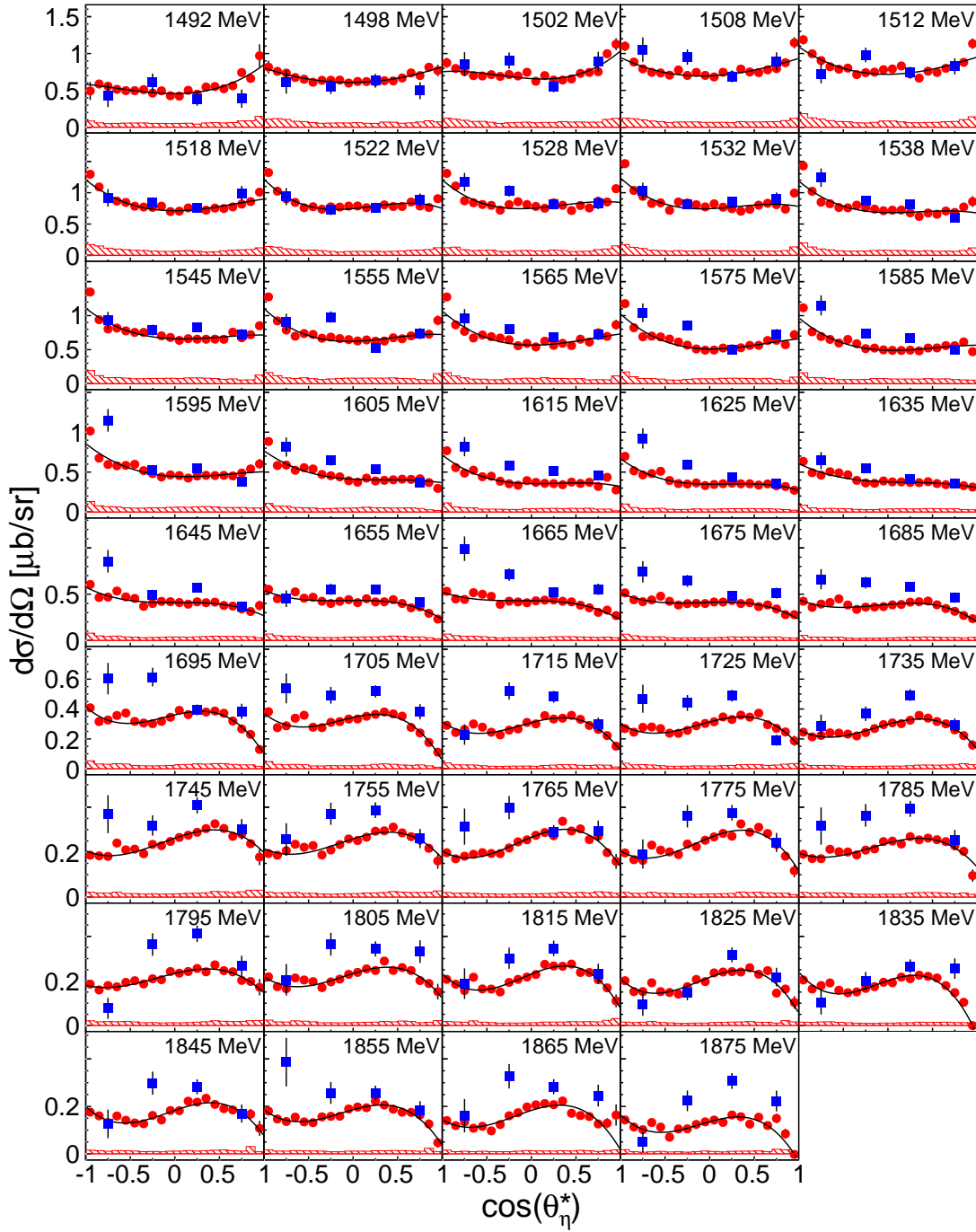
Fig. 5.19: Differential cross sections of $\gamma n \to \eta n$ from the combined results of the $\eta \to 2\gamma$ and $\eta \to 3\pi^0$ analyses as a function of W_{kin}: Red circles: combined result of this work. Red hatched histograms: combined systematic error. Blue squares: CBELSA/TAPS data [15]. Black curves: fit of data.

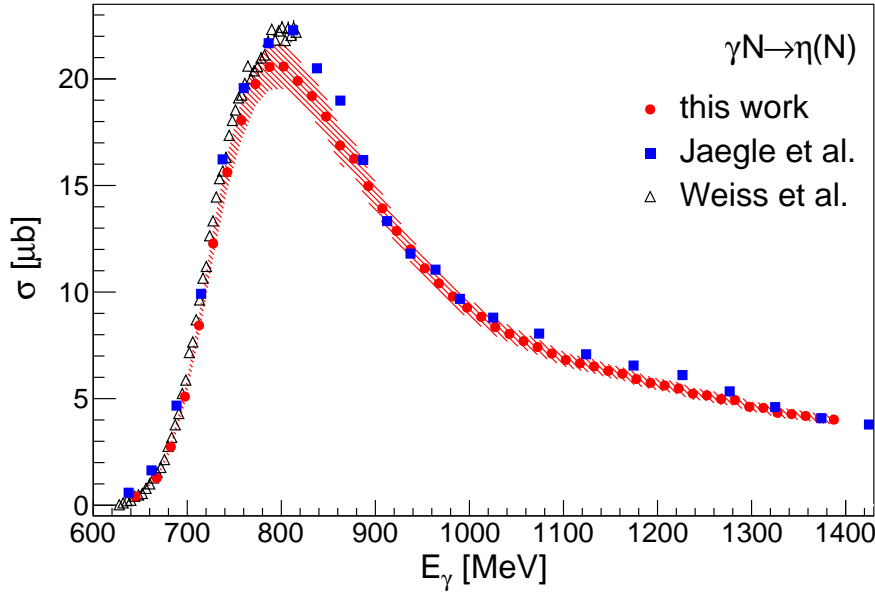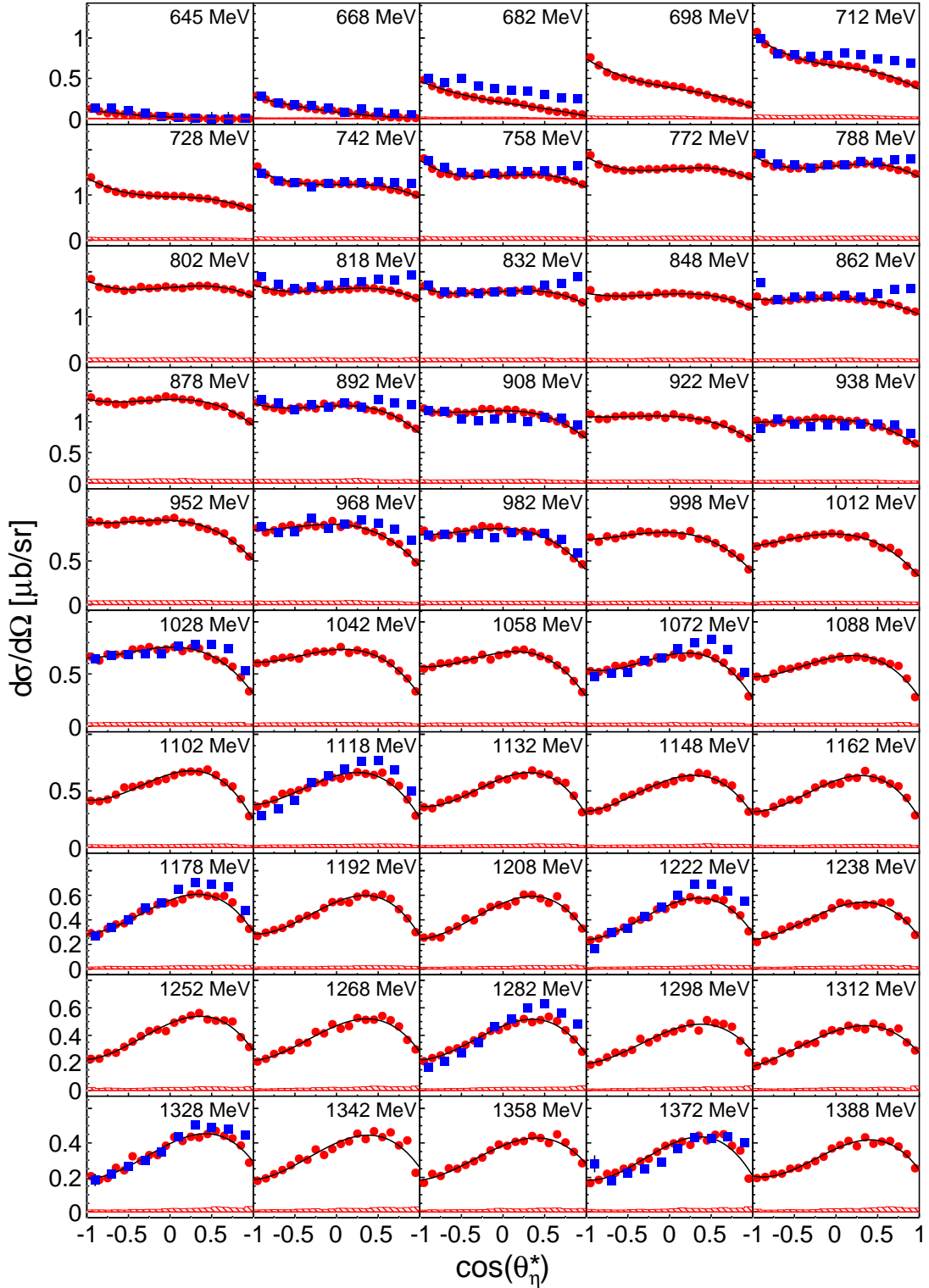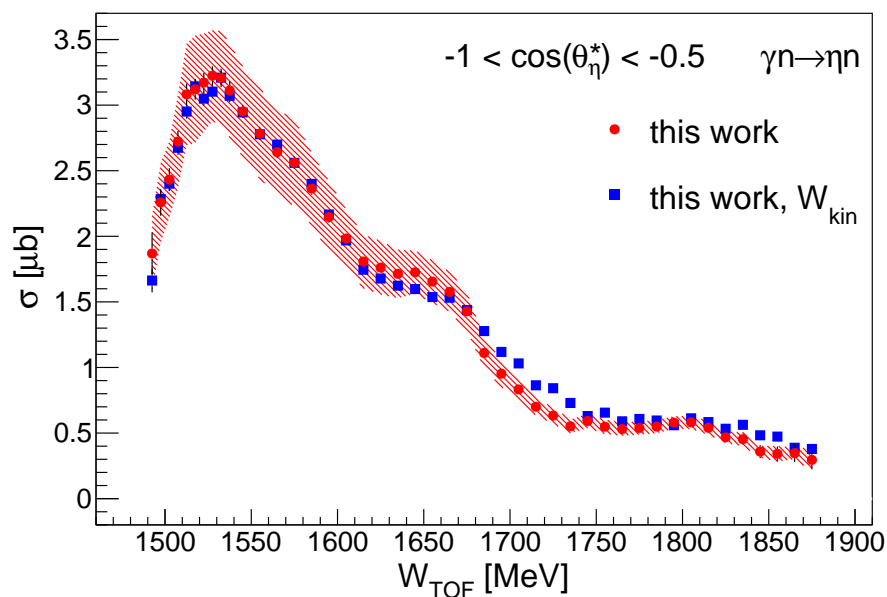**Fig. 5.20:** Total cross section of $\gamma n \to \eta n$ from the combined results of the $\eta \to 2\gamma$ and $\eta \to 3\pi^0$ analyses as a function of W_{TOF} for $-1 < \cos(\theta_\eta^*) < -0.5$: Red circles: combined result of this work. Red hatched area: combined systematic error. Blue squares: results from kinematic reconstruction.

5.4 Investigation of the structure in $\sigma(\gamma n \to \eta n)$

In the previous sections the results obtained in this work were presented. Consistency checks using the two η-meson decay analyses were performed and the data were compared to previous measurements. In the following sections further information is gained from the data and interpreted, especially concerning the structure seen in the total cross section of $\gamma n \to \eta n$.

5.4.1 Consistency of the exclusive measurements

It has been found that the cross section for coherent η-production on the deuteron is very small [16]. Therefore, neglecting FSI effects, the quasi-free inclusive cross section should be equal to the sum of the two quasi-free exclusive cross sections of the proton and the neutron, i.e., $\sigma_{(N)} = \sigma_p + \sigma_n$. On the other hand, measuring $\sigma_{(N)}$ and σ_p can be used to determine the cross section on the neutron indirectly. This was done, for example, in the LNS-Sendai measurement [25] (see section 1.4.2). In addition to the fact that such a measurement is only an indirect one, the resulting neutron cross sections include systematic uncertainties from both the inclusive analysis (background suppression) and from the proton analysis (proton detection efficiency), which could be larger or at least very different compared to a direct measurement on the neutron. Also, only cross sections as a function of the photon beam energy E_γ can be obtained in this way. There is no possibility
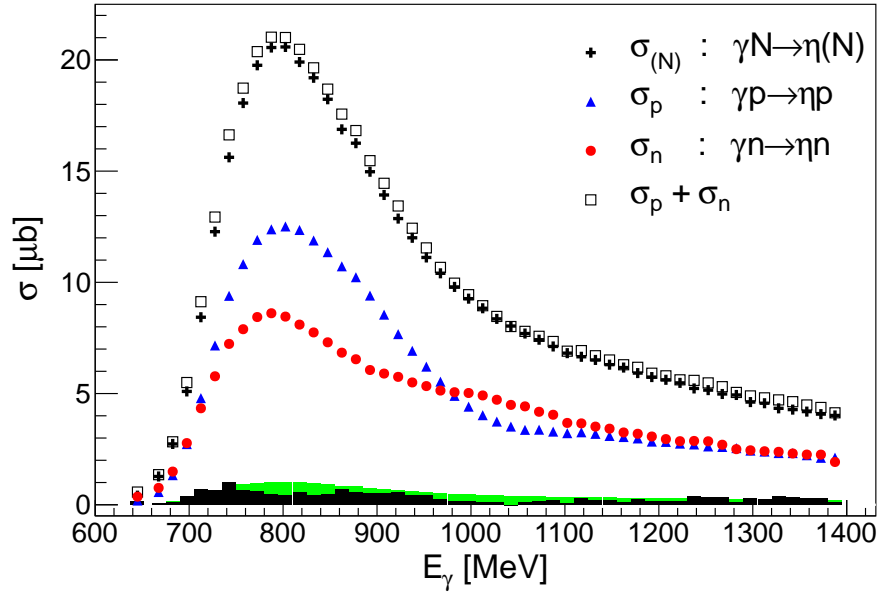
Fig. 5.21: Comparison of the total quasi-free inclusive cross section and the sum of the total exclusive cross sections on the proton and neutron as a function of E_γ: Black crosses: $\gamma N \to \eta(N)$. Blue triangles: $\gamma p \to \eta p$. Red circles: $\gamma n \to \eta n$. Black open squares: sum of proton and neutron. Black histogram: difference of inclusive cross section and sum of proton and neutron. Green histogram: 5% marker of inclusive cross section.

to extract cross sections as a function of the center-of-mass energy W calculated via the final state, which would remove effects from Fermi motion. Therefore, in this work the fact that $\sigma_{(N)} = \sigma_p + \sigma_n$ was only used as a consistency check of the direct neutron measurement. In figure 5.21 the total inclusive cross section as a function of E_γ is compared to the sum of the proton and neutron cross sections. The agreement is very good for all energies. The difference between $\sigma_{(N)}$ and $\sigma_p + \sigma_n$ is represented by the black histogram. For most energies it is below 5% (green histogram) with respect to $\sigma_{(N)}$. The corresponding angular distributions are shown in figure 5.22. It can be seen that the shape of the inclusive cross section is well reproduced by the sum of the proton and neutron cross sections. Larger deviations are only occurring in very forward or backward direction, where systematic errors for the exclusive measurements are larger due to the nucleon detection efficiencies. This good agreement proves the consistency of the three cross section measurements performed in this work. It shows that, despite the large systematic uncertainties caused by the recoil nucleon detection, the analysis is stable and self-consistent.

The extraction of the parameters of the known $S_{11}(1535)$ resonance imposes another check on the analyses of this work. Mainly, it can be checked if the extraction of resonance parameters from cross sections measured exclusively and
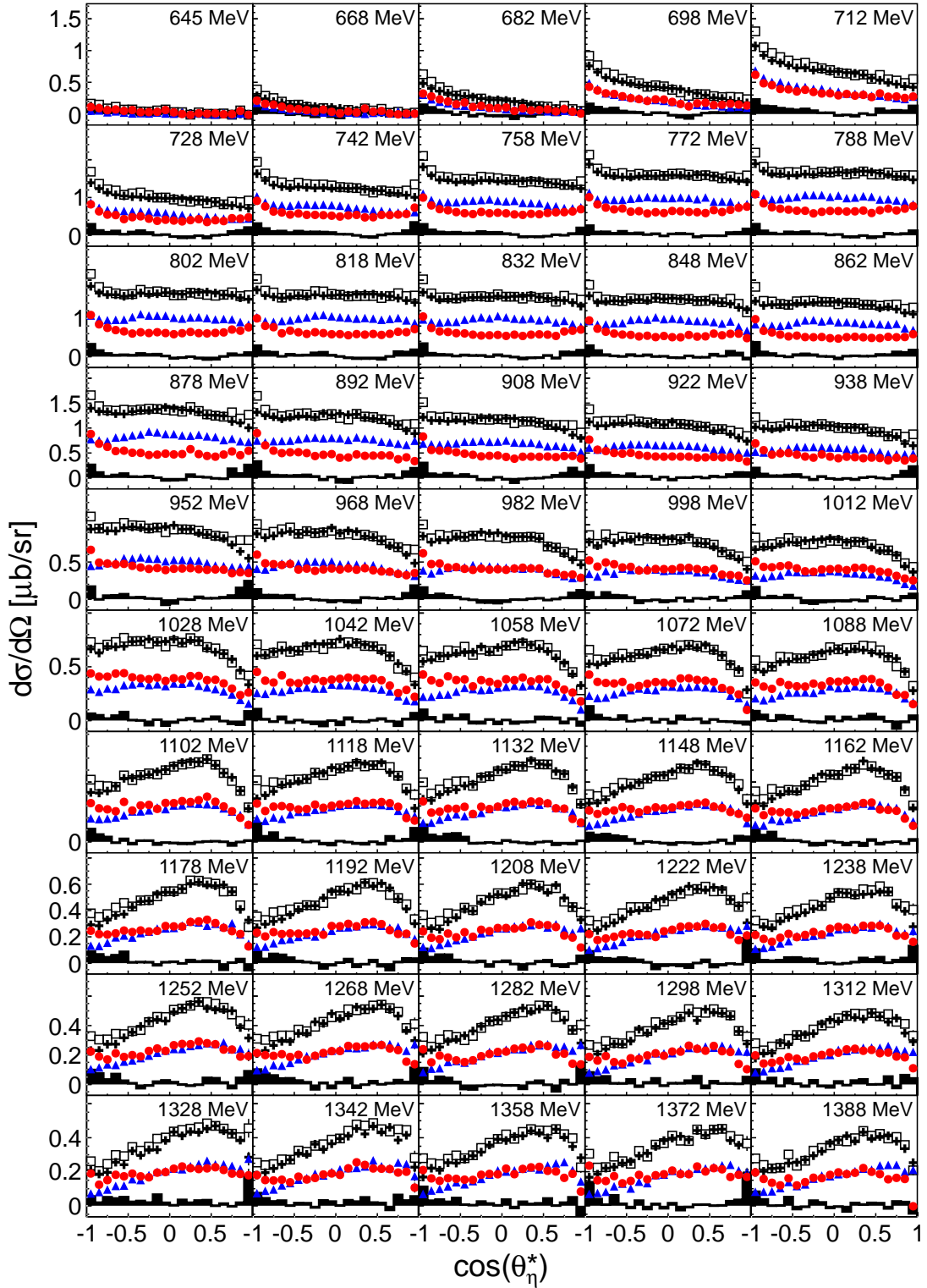
Fig. 5.22: Comparison of the differential quasi-free inclusive cross sections and the sum of the differential exclusive cross sections on the proton and neutron as a function of E_γ: Black crosses: $\gamma N \to \eta(N)$. Blue triangles: $\gamma p \to \eta p$. Red circles: $\gamma n \to \eta n$. Black open squares: sum of proton and neutron. Black histogram: difference of inclusive cross section and sum of proton and neutron.
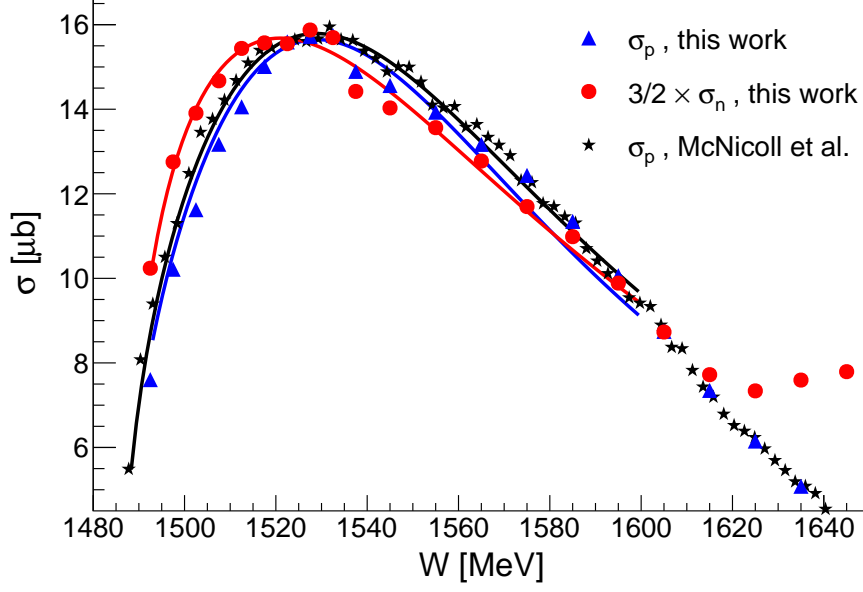
Fig. 5.23: Results of the $S_{11}(1535)$ Breit-Wigner fits performed from threshold up to $W = 1600$ MeV: Blue triangles: quasi-free proton data. Red circles: quasi-free neutron data (scaled by 3/2). Black stars: MAMI-C free proton data [35]. Curves: corresponding fits of ansatz 5.1.

in quasi-free kinematics is feasible. Therefore, the exclusive cross sections as a function of W_{kin} were fitted from threshold up to $W = 1600$ MeV, where dominance of the $S_{11}(1535)$ can be assumed, with the ansatz

$$\sigma(W) = \frac{q_\eta^*}{k^*} \cdot \frac{k_R^*}{q_{\eta R}^*} \cdot \frac{2m_N \cdot W_R \cdot b_\eta \cdot (A_{1/2}^N)^2 \cdot \Gamma_R}{(W_R^2 - W^2)^2 + W_R^2 \Gamma_R^2 x^2}, \tag{5.1}$$

from [92] where

$$x = b_\eta \cdot \frac{q_\eta^*}{q_{\eta R}^*} + b_\pi \cdot \frac{q_\pi^*}{q_{\pi R}^*} + b_{\pi\pi}. \tag{5.2}$$

This ansatz consists of a relativistic Breit-Wigner function with resonance position W_R and an energy dependent width Γ_R, and phase space factors. The latter are k^*, q_η^*, q_π^* and $k_R^*, q_{\eta R}^*, q_{\pi R}^*$ that are the momenta of the incoming photon, η, π in the photon-nucleon center-of-mass system, whereas the subscript R denotes evaluation at resonance position. $A_{1/2}^N$ is the electromagnetic helicity-1/2 coupling, m_N is the nucleon mass and $b_\eta, b_\pi, b_{\pi\pi}$ are the branching ratios of the $N\eta, N\pi, N\pi\pi$ resonance decays, respectively. The values $b_\eta = 0.5$, $b_\pi = 0.4$, $b_{\pi\pi} = 0.1$ were used for the decay branching ratios. In addition to the fits of the results of this work, the cross section data of the free proton measurement at MAMI-C [35] were fitted as well. A close-up view at the region of interest is shown in figure 5.23. The parameters of the resulting fits are summarized in table 5.1 and compared to the

Data	W_R [MeV]	Γ_R [MeV]	$A_{1/2}$ [10^{-3} GeV$^{-1/2}$]
PDG	1535 ± 10	150 ± 25	p: 90 ± 30 n: 46 ± 27
free proton[1]	1536 ± 0	171 ± 2	106 ± 1
q.-f. proton[2]	1544 ± 2	181 ± 13	109 ± 3
q.-f. neutron[2]	1546 ± 3	176 ± 20	90 ± 4
q.-f. proton	1536 ± 1	158 ± 8	101 ± 3
q.-f. neutron	1529 ± 1	188 ± 12	90 ± 3

Tab. 5.1: Results of the $S_{11}(1535)$ Breit-Wigner fits: PDG values from [7]. [1]Free proton data from [35]. [2]Quasi-free data from [15]. Errors of the fit parameters are statistical only.

values provided by the PDG [7] and to the values obtained in the CBELSA/TAPS measurement [15]. The parameters extracted from the quasi-free proton data agree quite well with the ones of the free proton data. A notable difference is only seen in the width Γ_R, which is smaller in the quasi-free case. This is also obvious from figure 5.23, where the rise to the $S_{11}(1535)$ maximum is less steep in the quasi-free data. This could be due to the proton detection efficiency that has rather high systematic error in this region (see section 4.8.4). Also the much worse resolution in W compared to the free measurement is expected to have a strong influence on the sharp rise at threshold. An opposite effect can be observed for the quasi-free neutron data, where the rise at threshold seems to be steeper and shifted compared to the free proton data. In addition, some data points between 1530 MeV and 1580 MeV are lower compared to free and quasi-free proton. This leads to a shifted resonance position and an increased width, evidently seen in table 5.1. The helicity amplitude $A_{1/2}^N$ on the other hand should not be affected by resolution effects. In fact, the agreement between the free proton measurement and the two quasi-free proton measurements is very good. The agreement between the two neutron measurements is excellent. The poor agreement for the neutron helicity coupling with the PDG value comes from the fact that the latter is dominated by the values obtained in pion production. It is argued that η-production is much better suited for the study of the $S_{11}(1535)$ [15]. The PDG values of $A_{1/2}^N$ would lead to a neutron-proton cross section ratio of 0.26 which is unrealistic. A ratio of 0.79 was extracted in this work, while CBELSA/TAPS found 0.68. All this gives confidence for the extraction of resonance parameters from quasi-free data and hints that the W-reconstruction and the nucleon detection efficiencies are sufficiently under control.

5.4.2 Legendre coefficients of the angular distributions

As motivated in section 1.2 the angular distributions can be expanded in terms of the Legendre series to perform a multipole analysis of the data. Therefore, the differential cross sections were fitted using

$$\frac{d\sigma}{d\Omega}(W, \cos(\theta_\eta^*)) = \frac{q_\eta^*(W)}{k_\gamma^*(W)} \sum_{i=0}^{3} A_i(W) P_i(\cos(\theta_\eta^*)) . \qquad (5.3)$$

Because of the decreasing contributions from higher orders, which also include larger statistical errors, the expansion was only performed up to third order. The results were again compared to the free proton data from MAMI-C [35] and the CBELSA/TAPS measurements [15]. The four expansion coefficients as a function of W are shown in figure 5.24.

First of all a good agreement can be found for the free and quasi-free proton data. This is another indication that, with the analysis implemented in this work, observables can be accurately extracted from quasi-free measurements. Resolution effects are of course visible, as already discussed in section 5.2.2. The dip around $W = 1680$ MeV seen in A_0 is smeared in the quasi-free data. Also the oscillations in the differential cross sections due to the proton detection efficiency that was discussed before is reflected in A_1 to A_3 below $W = 1600$ MeV. Because these oscillations have small wavelengths the influence is expected to increase with higher expansion order, which is clearly seen in the plots. The agreement with the CBELSA/TAPS data in the overall trend is good. Notable are the stability and the improved statistics of the current results.

For the neutron data the differences between the result of this work and the CBELSA/TAPS measurement are significant, as was to be expected from the comparison of the angular distributions in section 5.3.2. The best agreement is probably found in A_2, where the sign change around $W = 1680$ MeV and the shapes below and above this energy are reproduced. Statistics of the previous measurement is worse, especially below 1600 MeV, but the current results could suffer from systematic uncertainties in this region due to the neutron detection efficiency. Nevertheless, the overall trends in the expansion coefficients are similar. Thanks to the higher statistics that helps particularly in the calculation of higher order coefficients, the conclusion from the current data can be drawn that A_3 is probably negative in the entire energy range studied in this work.

The predictions of the Eta-MAID model [14] are represented by the curves in figure 5.24. The agreement with the proton data is good. Typical features, such as sign changes, are reproduced. This is not a surprise since proton data were used to fix parameters in this model. The behavior of the neutron data is only poorly reproduced. Reasonable agreement is found for A_2, which is affected by the interference of the $S_{11}(1535)$ and the $D_{13}(1520)$ resonances below $W = 1600$ MeV.
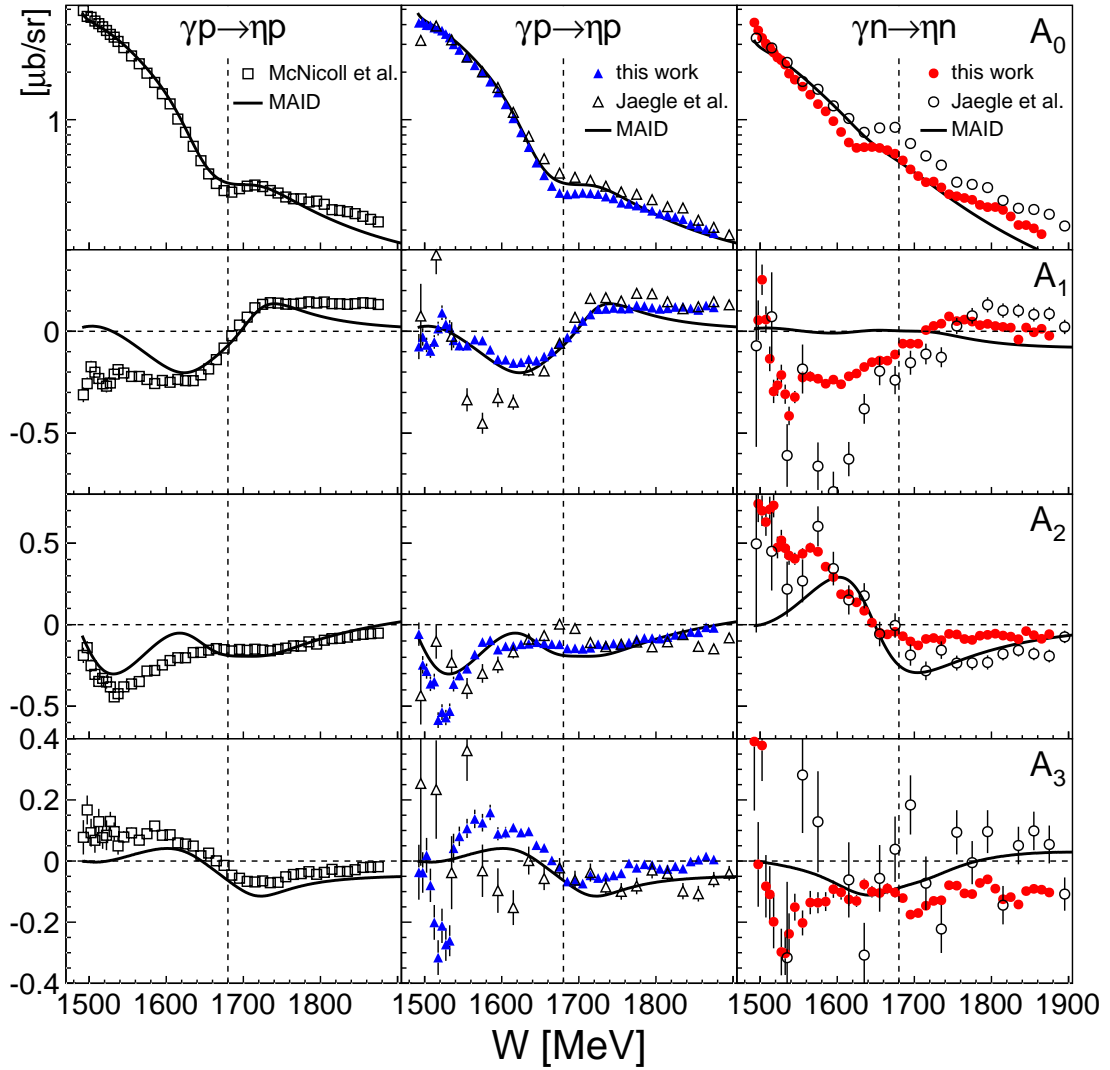
Fig. 5.24: Comparison of Legendre coefficients obtained from fits of angular distributions: Columns (left to right): free proton data, quasi-free proton data, quasi-free neutron data. Rows (top to bottom): Legendre expansion coefficients A_0 to A_3. Blue filled triangles: quasi-free proton data. Red filled circles: quasi-free neutron data. Open squares: MAMI-C free proton data [35]. Open triangles/open circles: CBELSA/TAPS quasi-free proton/neutron data [15]. Curves: Eta-MAID predictions [14]. Vertical dashed lines: marker at 1680 MeV. Note the logarithmic y-axis for A_0.

Neglecting other contributions A_2 is proportional to the helicity couplings $A_{1/2}^N$ of theses states. Because the couplings of the $D_{13}(1520)$ have the same signs for proton and neutron but the corresponding ones of the $S_{11}(1535)$ carry opposite signs, A_2 has opposite signs for proton and neutron.

Interestingly, A_1 is very similar for proton and neutron throughout the entire energy range and shows a common change of sign from negative to positive at $W =$

1680 MeV. In the region of the $S_{11}(1535)$ the coefficient of the neutron is larger than the one obtained from the quasi-free proton, but this could be a systematic problem in the proton data since the free proton data show a different trend that is surprisingly close to the neutron data. The zero crossing was interpreted in the discussion of results from η-electroproduction as S-P wave interference [93]. If only S_{11} (E_{0+} multipole) and P_{11} (M_{1-} multipole) states are considered, A_1 would be directly proportional to $\text{Re}(E_{0+}^* M_{1-})$. A change of sign would then mean that the relative phase between the two multipoles is changing rapidly, caused by resonance passing of one of them.

As discussed before, A_2 of the neutron changes sign around $W = 1680$ MeV and remains as the proton at small negative values, which suggests that the influence of the S_{11}-D_{13} interference becomes weaker. For higher energies it is close to the values of the proton.

A_3 on the other hands shows a change of sign for the proton around $W = 1680$ MeV, while the current neutron results lead to a more or less constant negative value in the entire energy range. As mentioned above, the CBELSA/TAPS data led to an ambiguous picture about A_3 due to the lack of statistics. It was even speculated about a structure near 1680 MeV, admittedly beyond statistical significance [15]. The current results show also a very vivid energy dependence of A_3 in that region. A small dip around $W = 1700$ MeV can be seen but, considering the magnitude of the fluctuations at higher energies, its presence is doubtful.

5.4.3   Position and width of the structure

If the structure seen in the total cross section of $\gamma n \to \eta n$ is not caused by interference or threshold effects, but by a single nucleon resonance, it is interesting to know the exact position and especially the width. Compared to the broad peaks of, e.g., the $P_{33}(1232)$ resonance in π^0-production or the $S_{11}(1535)$ in η-production with typical hadronic widths around 100 MeV, it is immediately clear that the structure around $W = 1680$ MeV is much narrower. Therefore, in the following the results on position and width of a more detailed analysis will be presented.

The position and the width were extracted separately for the $\eta \to 2\gamma$ and the $\eta \to 3\pi^0$ analysis to avoid distortion in a merged data set from effects that may be different in the two analyses. Also, this allows the extraction of a best estimate from two independent data sets. In addition, the reconstruction of the center-of-mass energy W using both the kinematic reconstruction and the time-of-flight (TOF) analysis are used. More details about the two techniques can be found in sections 4.5.1 and 4.5.2, respectively.

In order to maximize the resolution in W, in addition to the standard analysis (Analysis I) a second analysis (Analysis II) that incorporates more stringent kinematic cuts was performed (see section 4.3.7). For example, a cut on the

reconstructed Fermi momentum of the neutron removing large momenta should improve the validity of the kinematically reconstructed W. Obviously, one has to find a compromise between the strictness of the cuts and the leftover statistics that should still allow to extract significant results.

Results of the kinematic reconstruction

In figure 5.25 the results obtained from the kinematic reconstruction are presented. The data were fitted with a sum of functions taking into account all contributions to the data:

1. $S_{11}(1535)$: Breit-Wigner (BW) parametrization from equation 5.1

2. narrow structure: BW as for $S_{11}(1535)$ but with $x = 1$ (fixed width)

3. cumulative background: standard relativistic Breit-Wigner function

The latter is purely phenomenological and combines the contributions from higher resonances and other background. The choice of a simplified version of equation 5.1 as signal function for the narrow structure bears the advantage that the coupling, if one assumes a $J = 1/2$ state, can be easily extracted. Due to smearing of a possibly very narrow structure by the resolution of the reconstruction (see section 4.5.1) the resulting parameter for the width using the fitting function from above represents only an upper limit. As described in section 4.5.3, a numerical convolution of the intrinsic signal function 2) with the resolution distribution was thus implemented. The width resulting from the fit using a convoluted signal function is much smaller and can be considered as an approximation of the intrinsic width. This was shown to be feasible in section 4.5.3, where the reconstruction of the width was tested with simulated data. In this work, both a standard version of 2) as well as a convoluted one were fitted along with the background terms to the data. The corresponding parameters of the fits are listed separately in tables 5.2 and 5.3, respectively.

The fitting functions describe the data very well with the exception of the very sharp dip right before the peak structure. The curves with and without convolution of the resolution look very similar, thus only the ones containing the convolutions are drawn in figure 5.25. The background contributions 1) and 3) are shown by the magenta dotted and dashed curves, respectively. They were subtracted from the data resulting in the data points represented by the triangles, showing a more clear picture of the narrow structure. Also in the lower part of each plot, the intrinsic BW-functions along with the resolution distributions and finally the resulting total signal functions are drawn.

In the $\eta \to 2\gamma$ analysis, the more stringent cuts applied in the Analysis II decrease the width of the structure Γ_R, while the position W_R and the coupling
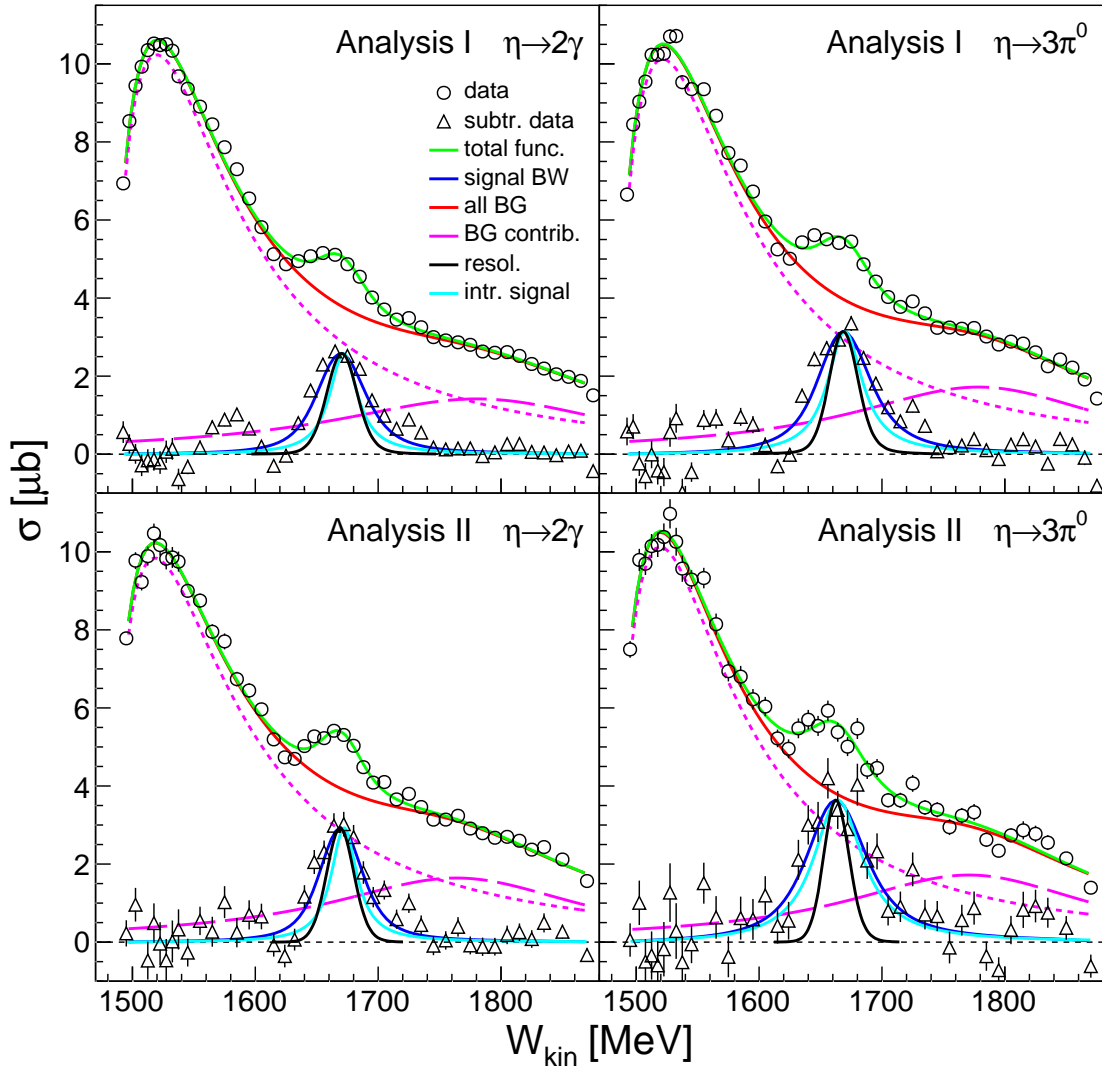
Fig. 5.25: Fit results of the total cross section of $\gamma n \to \eta n$ as a function of W_{kin}: Left column: $\eta \to 2\gamma$ analyses. Right column: $\eta \to 3\pi^0$ analyses. Upper row: standard analyses (Analysis I). Lower row: analyses with stringent cuts (Analysis II). Upper part of plots: data (black circles), total fitting functions (green curves), total background functions (red curves), $S_{11}(1535)$ BW-functions (magenta dotted curves), background BW-functions (magenta dashed curves). Lower part of plots: background subtracted data scaled by 2 (black triangles), convoluted signal BW-functions (blue curves), reconstruction resolutions (black curves), intrinsic signal BW-functions (cyan curves).

$\sqrt{b_\eta} A_{1/2}^n$ are left unchanged. It was shown in section 4.5.1 that stronger cuts improve the resolution of the kinematic W-reconstruction. This leads to the conclusion that the width of the structure is still affected by resolution and the intrinsic width must be more narrow. The situation is less clear in the $\eta \to 3\pi^0$ analysis. All extracted parameters of the two fits differ and the width Γ_R is even

Analysis	W_R [MeV]	Γ_R [MeV]	$\sqrt{b_\eta} A^n_{1/2}$ [10^{-3} GeV$^{-1/2}$]	
$\eta \to 2\gamma$				
Analysis I	1670 ± 1	50 ± 3	12.6 ± 0.5	
Analysis II	1670 ± 2	43 ± 7	12.6 ± 1.2	
Analysis I TOF	1656 ± 1	39 ± 4	6.9 ± 0.3	(13.9 ± 0.6)
Analysis II TOF	1653 ± 3	44 ± 7	9.0 ± 0.8	(18.0 ± 1.5)
$\eta \to 3\pi^0$				
Analysis I	1669 ± 1	54 ± 5	14.4 ± 0.9	
Analysis II	1662 ± 3	62 ± 14	16.5 ± 2.5	
Analysis I TOF	1655 ± 3	42 ± 7	7.2 ± 0.6	(14.5 ± 1.2)
Analysis II TOF	1641 ± 8	68 ± 21	10.1 ± 2.1	(20.2 ± 4.3)
best estimate	1669 ± 5	51 ± 10	13.1 ± 0.8	

Tab. 5.2: Results of the $\gamma n \to \eta n$ total cross section fits without convolution of resolution: Γ_R represents an upper limit for the intrinsic width. Values in parentheses: Extrapolation to full solid angle for TOF results. The best estimate is calculated without the TOF results.

larger for Analysis II. This could be due to statistical problems, as statistics is significantly worse in Analysis II, which could cause unreliable fit results.

Results of the time-of-flight reconstruction

The results of the fits to the data obtained via the time-of-flight W-reconstruction (see section 4.5.2) are shown in figure 5.26. As mentioned before, the results correspond to the angular range of $-1 < \cos(\theta^*_\eta) < -0.5$. During the fitting procedure, it was found that due to the different background contributions in this region, the additional broad Breit-Wigner function 3) is not needed but causes even unstable fits when included. Therefore, the data were fitted with functions 1) and 2) only.

The fits using the convolution of signal and resolution did not converge properly as no minimal and stable values for the intrinsic width could be found. The fitting parameters tended to yield very small values without any lower bound. This is an indication that the convolution is dominated by the resolution, which makes a reliable estimation of the intrinsic signal impossible. This can also be seen in figure 5.26, where the resolutions at the extracted Breit-Wigner mean values are shown by the black curves. The estimated resolutions are in the same order as the widths of the structure themselves. This could also mean that the resolution was underestimated using the method presented in section 4.5.2, where it was argued that simulating the time-of-flight resolution for neutrons has large systematic uncertainties. Hence, the estimation of the W_TOF-resolution could be a rather rough approximation.
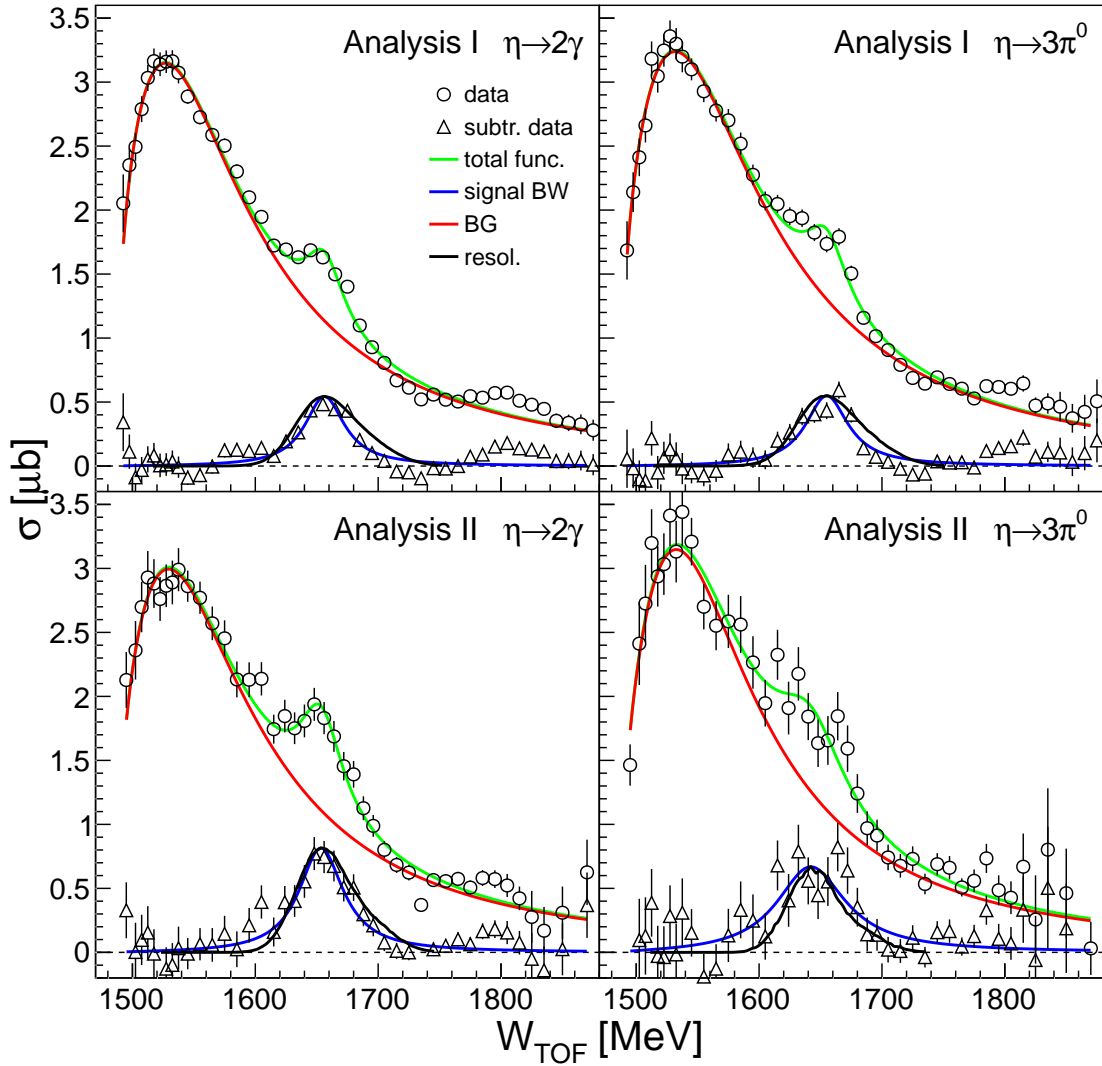
Fig. 5.26: Fit results of the total cross section of $\gamma n \to \eta n$ as a function of W_{TOF} for $-1 < \cos(\theta_\eta^*) < -0.5$: Left column: $\eta \to 2\gamma$ analyses. Right column: $\eta \to 3\pi^0$ analyses. Upper row: standard analyses (Analysis I). Lower row: analyses with stringent cuts (Analysis II). Upper part of plots: data (black circles), total fitting functions (green curves), $S_{11}(1535)$ BW-functions (red curves). Lower part of plots: background subtracted data (black triangles), signal BW-functions (blue curves), reconstruction resolutions (black curves).

As the convoluted fit was not applicable, only the fit with the standard Breit-Wigner function 2) for the narrow structure was performed. The fit results for the two η-meson decays and the Analyses I and II are shown in table 5.2. In section 4.5.2, it was found that more strict analysis cuts do not improve the W_{TOF}-resolution. This is reflected in the extracted fit parameters for the width Γ_R that are even larger for Analysis II. As there is a similar correlation of the deviations of the fit parameters as in the $\eta \to 3\pi^0$ analyses for the kinematic

Analysis	W_R [MeV]	Γ_R [MeV]	$\sqrt{b_\eta}A_{1/2}^n$ [10^{-3} GeV$^{-1/2}$]
$\eta \to 2\gamma$			
Analysis I	1672 ± 1	28 ± 4	11.0 ± 0.5
Analysis II	1672 ± 2	25 ± 8	11.0 ± 1.2
$\eta \to 3\pi^0$			
Analysis I	1670 ± 1	35 ± 5	12.9 ± 0.9
Analysis II	1664 ± 3	49 ± 15	15.1 ± 2.5
best estimate	1671 ± 5	30 ± 5	11.6 ± 0.8

Tab. 5.3: Results of the $\gamma n \to \eta n$ total cross section fits with convolution of resolution: Γ_R represents an approximation of the intrinsic width.

reconstruction, one could again argue that the deviating parameters are probably caused by the lower statistical quality.

Summary

The cross sections of $\gamma n \to \eta n$ as a function of W_{kin} were fitted with a Breit-Wigner function for the structure observed at $W \sim 1670$ MeV along with functions taking into account the background contributions. Parameters for the position W_R, width Γ_R and coupling $\sqrt{b_\eta}A_{1/2}^n$ (assuming $J = 1/2$) were extracted for the $\eta \to 2\gamma$ and $\eta \to 3\pi^0$ analyses separately using standard and more stringent analysis cuts. Apart from effects caused by low statistics, the extracted parameters are consistent with each other, thus best estimates (see table 5.2) were calculated by averaging with quadratic error weighting and taking into account the fluctuations of the fit parameters for the uncertainties. The estimated width poses only an upper limit for the intrinsic width of the structure due to the reconstruction resolution.

In addition to the standard fits, a fit using a Breit-Wigner signal function convoluted with the W_{kin}-resolution was performed. The resulting parameters for the position and the coupling are consistent with the ones obtained by the standard fit. The extracted width is not affected by resolution anymore and is thus much smaller. It can be taken as an estimation of the intrinsic width of the structure. Best estimates of the fitting parameters are shown in table 5.3.

The cross sections obtained via time-of-flight W-reconstruction could only be fitted without convolution of the resolution, as the latter is of the same order as the width of the structure itself. Extrapolation to the full solid angle for the higher statistics results (Analysis I) leads to values for the coupling that are compatible with the W_{kin}-results. The position, on the other hand, is systematically lower by ~ 15 MeV. The reason for this will be discussed in the next section.

5.4.4   Angular dependence of the structure

Compared to previous measurements, the high statistical quality of the current results for $\gamma n \to \eta n$ allows a more detailed investigation of the angular dependence of the cross section and the observed structure.

In figure 5.27 the cross sections of $\gamma p \to \eta p$ and $\gamma n \to \eta n$ obtained in this work are shown for four angular intervals. They are compared to the free proton measurements from MAMI-C [35] and the quasi-free measurements from CBELSA/TAPS [15]. In addition, the ratios of neutron and proton cross sections are shown for all intervals. The discrepancies in the absolute cross sections were already discussed before. Some words should be added here concerning the ratios. With the exception of the second bin in backward direction, there is a good agreement of the neutron-proton ratios between the current results and the ones obtained by CBELSA/TAPS. Apparently, proton and neutron cross sections of this work are lower compared to the latter in a way that the ratios remain constant. This could be hinting at some global discrepancy in the normalization of the cross sections. In the second backward bin, the proton cross sections are in rather good agreement, while the neutron cross sections show larger deviations, leading to a decreased neutron-proton ratio in the current work.

It can be already seen in figure 5.27 that the shapes of the structure around $W \sim 1670$ MeV in the neutron cross sections are different in the four angular intervals. The high available statistics allowed a more detailed study of this phenomenon. Namely, the extraction of the parameters of the structure, performed in section 5.4.3 on the total cross sections, was performed for all twenty angular bins separately. The merged data of the two η-meson decays obtained from the kinematic reconstruction were used for this purpose. Again, the signal was described by a standard or resolution convoluted Breit-Wigner function (equation 5.1 with fixed width $x = 1$). The background consisted of the $S_{11}(1535)$ Breit-Wigner parametrization and a phenomenological broad relativistic Breit-Wigner for the global description of the remaining background contributions. Due to the large number of fit parameters and the lower statistics compared to the fully integrated cross sections, a special fitting procedure had to be applied to prevent arbitrary fit solutions. Assuming a smooth behavior of the $S_{11}(1535)$ and the broad background Breit-Wigner, positions and widths of the two were fitted first and, consequently, fixed for the final fit, resulting in more stable fit results.

First, the $S_{11}(1535)$ was fitted up to $W = 1610$ MeV in all angular bins and the resulting positions and widths as a function of $\cos(\theta_\eta^*)$ were fitted with a first order polynomial, as both showed a linear behavior. New values for position and width were calculated from these fits and fixed in the further fitting procedure. In a second step, the complete fit was performed and the position of the broad background Breit-Wigner was fitted linearly with respect to $\cos(\theta_\eta^*)$, and new fixed
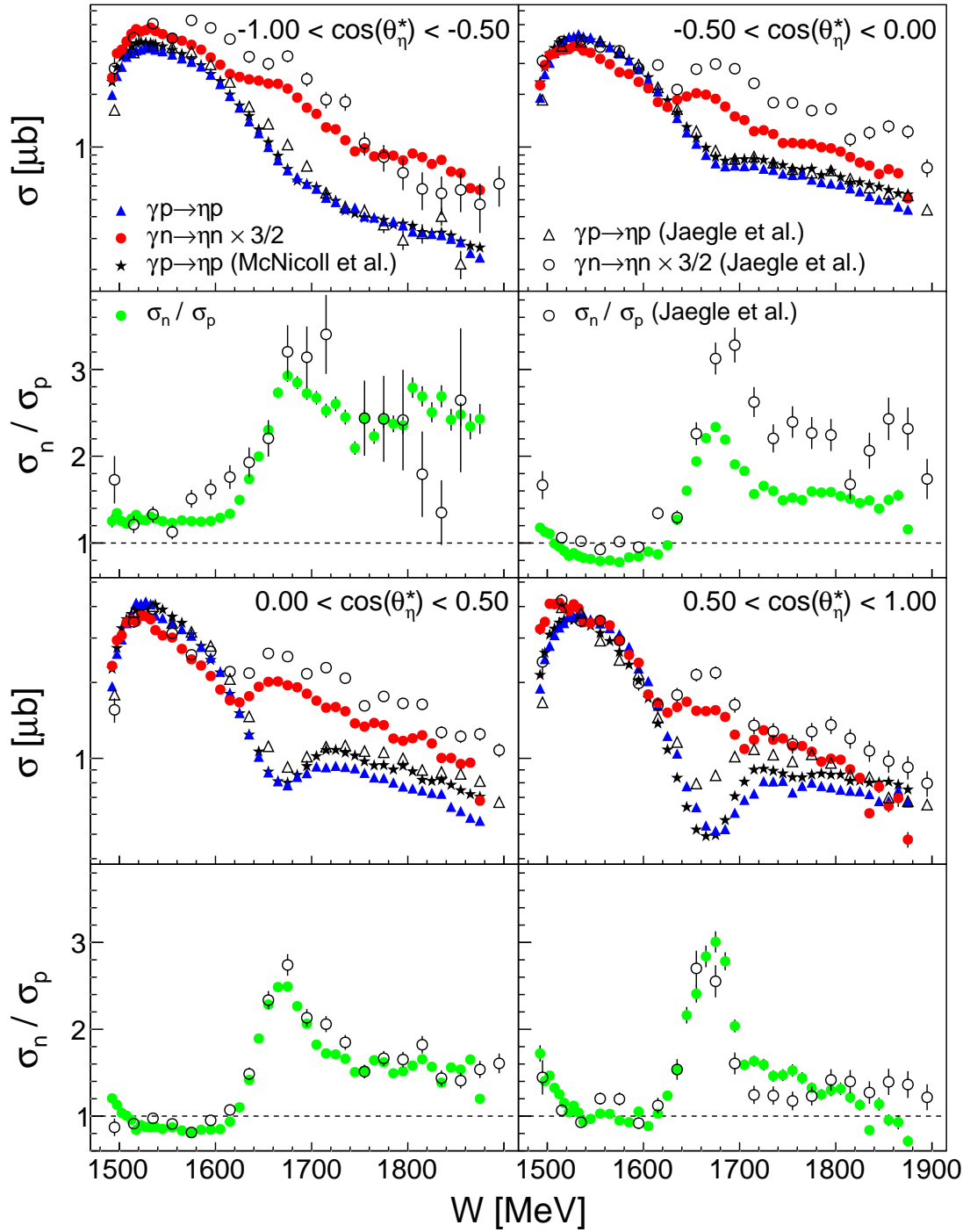
Fig. 5.27: Comparison of cross sections for $\gamma p \to \eta p$ and $\gamma n \to \eta n$ integrated over 4 angular intervals: Blue filled triangles: quasi-free proton data. Red filled circles: quasi-free neutron data scaled by 3/2. Black stars: MAMI-C free proton data (rebinned) [35]. Open triangles/open circles: CBELSA/TAPS quasi-free proton/neutron data (rebinned) [15]. Green filled (open) circles: ratios σ_n/σ_p for this work (CBELSA/TAPS data). Note the different logarithmic y-axes for the cross sections.
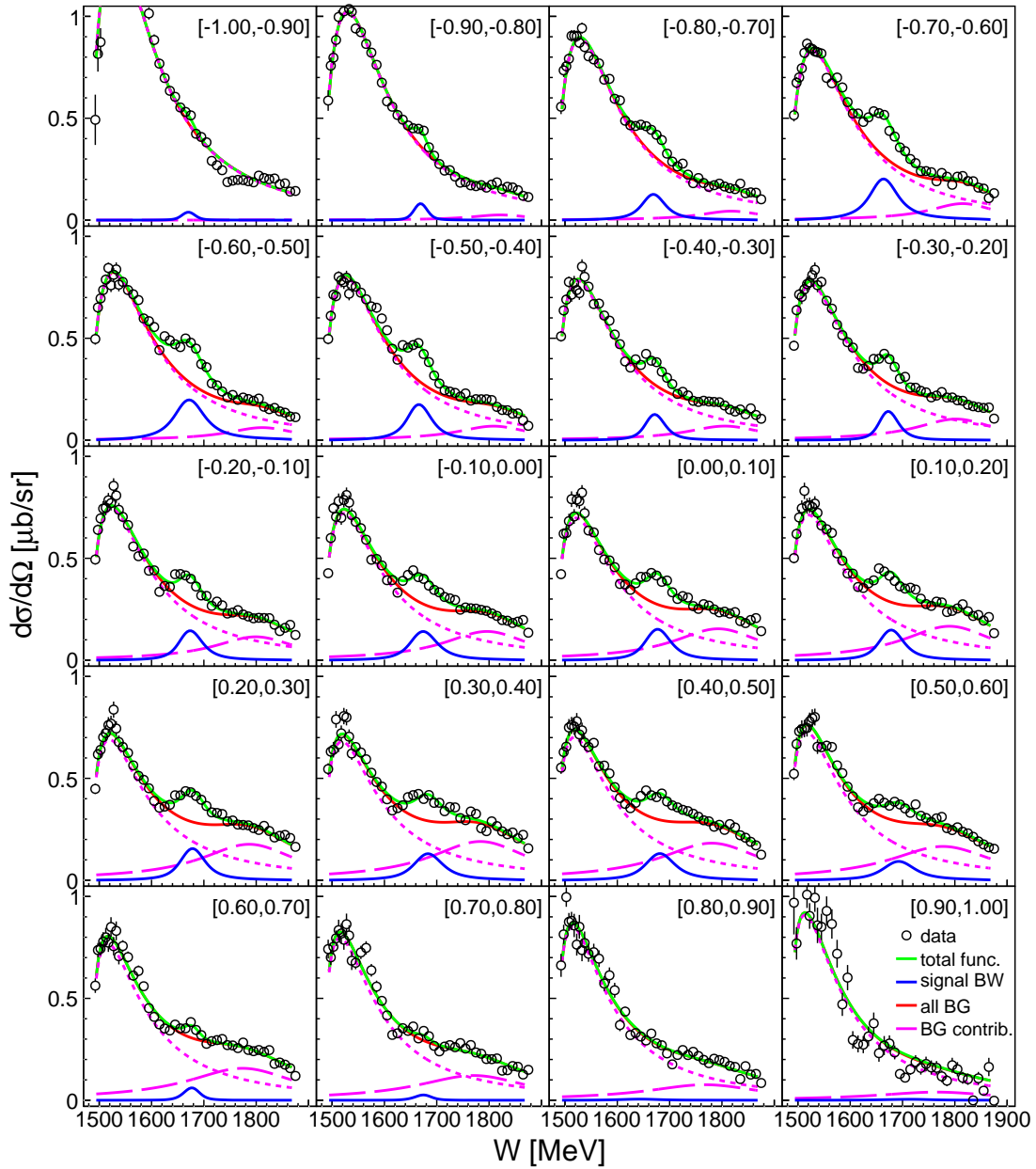
Fig. 5.28: Fits for the extraction of the angular dependent structure parameters: The corresponding angular intervals in terms of $\cos(\theta_\eta^*)$ are shown in the top right corners. Black circles: data. Green curves: total fitting functions. Blue curves: BW-signal functions. Red curves: total background functions. Magenta dotted curves: $S_{11}(1535)$ BW-functions. Magenta dashed curves: background BW-functions.

values were extracted. Subsequently, after another fit iteration, the same was done for the width of the broad Breit-Wigner. Finally, the data were fitted with free parameters for position, width, and amplitude of the signal Breit-Wigner leaving only the amplitudes for the $S_{11}(1535)$ and for the background Breit-Wigner free as well.
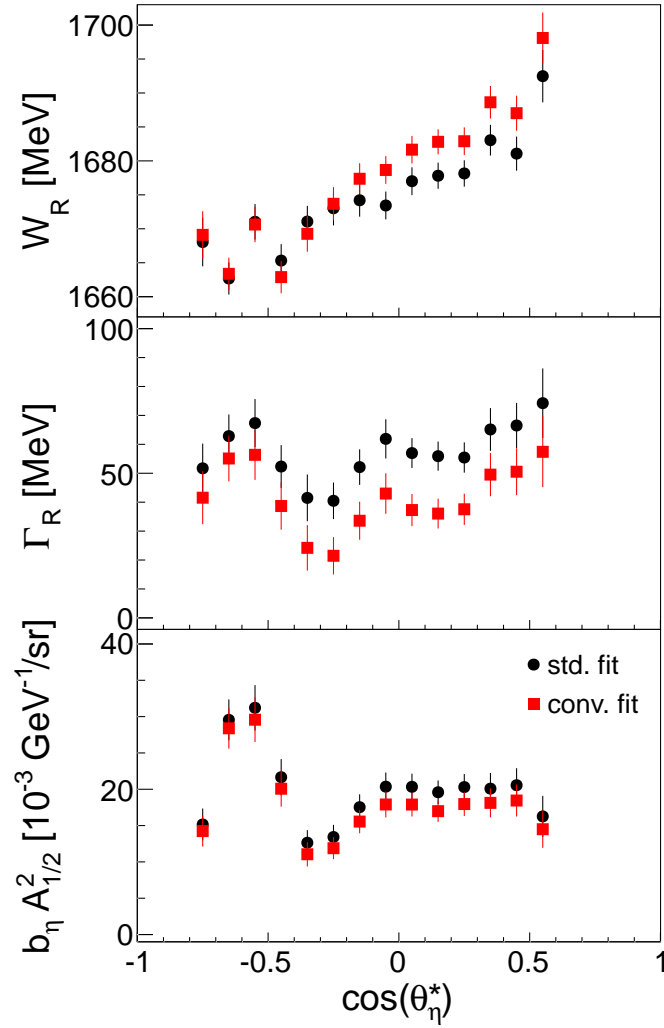
Fig. 5.29: Angular dependence of the Breit-Wigner fitting parameters of the structure: Upper plot: resonance position W_R. Middle plot: resonance width Γ_R. Lower plot: signal strength $b_\eta A_{1/2}^2$. Black circles: standard fit. Red squares: resolution convoluted fit.

The resulting fits using the convoluted Breit-Wigner signal functions are shown in figure 5.28. Thanks to the smoothly varying background contributions also smaller signal contributions could be estimated. Nevertheless, in the two most backward and the four most forward bins, no proper convergence of the fits could be achieved. It can be seen in the plots that the signals are rather small or even completely absent in these bins. In the other bins, a very interesting variation of the signal strength can be observed. It seems to increase until $\cos(\theta_\eta^*) \sim -0.5$ and then to decrease again.

The angular dependence of the fitting parameters of the signal Breit-Wigner function are presented in figure 5.29. Both the results of the standard fit and the resolution convoluted fit are drawn. The results of the bins at both extreme forward

and backward angles were omitted due to the unstable fit results. All parameters show a very interesting angular dependence. First, the resonance position is not constant but linearly varying from lower energies at backward angles to higher energies at forward angles. Only slight differences can be found in the comparison of the standard and the convoluted fit results. This means that the variations in the position are probably not caused by resolution, as the convoluted fit was able to compensate resolution effects in simulated data. A linear fit of the convoluted fit results yields $W_R \sim 1657$ MeV at $\cos(\theta^*_\eta) = -1$ and $W_R \sim 1702$ MeV at $\cos(\theta^*_\eta) = 1$. This explains why the positions extracted in section 5.4.3 from the W_{TOF}-data, which correspond to $-1 < \cos(\theta^*_\eta) < -0.5$, were shifted towards lower energies. The width Γ_R and strength $b_\eta A^2_{1/2}$, the latter being proportional to the integrated cross section area of the signal peak, show a correlated angular dependence with a minimum around $\cos(\theta^*_\eta) \sim -0.3$ and a maximum around $\cos(\theta^*_\eta) \sim -0.6$. Both parameters seem to increase to backward angles, while remaining almost constant at forward angles. As expected, the extracted widths of the resolution convoluted fit are lower compared to the values of the standard fit, whereas the strength values are in good agreement.

The used fitting procedure for the extraction of the angular dependent parameters of the structure tried to minimize systematic uncertainties in the estimation of the values. Nevertheless, there remains a notable systematic uncertainty due to the fact that the additional background to the $S_{11}(1535)$ was parametrized in a rather simple way by only one Breit-Wigner function taking into account contributions from all other sources.

5.5   Conclusions and outlook

Previous measurements of $\gamma n \to \eta n$ performed at GRAAL [21], LNS-Sendai [25] and CBELSA/TAPS [15] revealed a narrow structure in the total cross section around $W \sim 1680$ MeV. A detailed study of this phenomenon in terms of full partial-wave analyses was not possible up to now since the statistical quality of the available data was not sufficient. The current work aimed at providing differential cross section data of high quality with respect to statistics and investigation of the systematic uncertainties.

During three beamtimes at MAMI, a total amount of 471 hours of data was collected using a deuterium target and the combined Crystal Ball and TAPS detector setup. Differential cross sections of $\gamma p \to \eta p$ and $\gamma n \to \eta n$ were simultaneously obtained from exclusive measurements in quasi-free kinematics. Both the $\eta \to 2\gamma$ and the $\eta \to 3\pi^0$ decay channels were used for the identification of the η-mesons. In the analysis of the $\eta \to 2\gamma$ decay channel, 1.2×10^6 events with coincident protons and 4.5×10^5 events with coincident neutrons were reconstructed. The

analysis of the $\eta \to 3\pi^0$ decay channel provided 6.3×10^5 events with coincident protons and 1.8×10^5 events with coincident neutrons.

Differential cross sections were calculated as a function of the center-of-mass energy $W = \sqrt{s}$ and $\cos(\theta_\eta^*)$ determined from the initial state, using the energy of the incoming photon and assuming the nucleon at rest. The resulting cross sections are affected by a loss of resolution due to the Fermi motion of the initial state nucleons.

In addition, differential cross sections were extracted as a function of the center-of-mass energy calculated as the invariant mass of the recoil nucleon and the η-meson in the final state. Two methods were used to obtain the kinetic energy T_N of the recoil nucleons, which is needed for this calculation. First, T_N was calculated from kinematics, as all four unknown quantities in the final state are determined by the four constraints provided by four-momentum conservation. Secondly, T_N was determined by a time-of-flight measurement for nucleons detected in the forward detector TAPS. The resulting differential cross sections as a function of $W_{\mathrm{kin}}, W_{\mathrm{TOF}}$ and $\cos(\theta_\eta^*)$ (in the corresponding center-of-mass frames) are not affected by Fermi motion but only by the resolution of the corresponding W-reconstruction. These resolutions were estimated by simulation and could be taken into account in the extraction of properties from the cross section data.

The results of the inclusive measurement $\gamma N \to \eta(N)$ were used to check the consistency of the exclusive proton and neutron measurements. Namely, as coherent η-production and final state interaction (FSI) are small, the inclusive cross sections are expected to be equal to the sum of the cross sections on the proton and the neutron. This was confirmed in the measurements of this work.

The quasi-free proton results of this work were compared to measurements obtained with a free proton target. Good agreement was found in general, which shows that nuclear effects play a minor role or are sufficiently under control in the quasi-free analysis. This justifies the interpretation of the extracted observables from the quasi-free neutron measurement as approximated observables of the free neutron.

Phenomenological fits of the differential cross sections of $\gamma n \to \eta n$ as a function of W_{kin} were performed. When the structure around $W \sim 1670$ MeV is parametrized with a Breit-Wigner distribution, the resulting resonance position W_R shows a linear angular dependence and extrapolation leads to:

$$W_R(\cos(\theta_\eta^*) = -1) \approx 1657 \, \mathrm{MeV} \qquad W_R(\cos(\theta_\eta^*) = 1) \approx 1702 \, \mathrm{MeV}$$

The width Γ_R and the strength $b_\eta A_{1/2}^2$ of the structure show a correlated angular dependence, having a minimum at $\cos(\theta_\eta^*) \sim -0.3$ and a maximum at $\cos(\theta_\eta^*) \sim -0.6$. These variations could be due to the simplified fit ansatz and do not have to refer to intrinsic physical properties of the structure. Nevertheless, at very

backward and forward angles, the signal is too small to be extracted or completely absent.

The results of this work confirm the presence of a structure around $W \sim 1670$ MeV in the total cross section of $\gamma n \to \eta n$ with unprecedented statistical evidence. The best overall estimate for the position of the structure obtained in this work is

$$W_R = (1670 \pm 5)\,\text{MeV}$$

with a limit on the width of

$$\Gamma_R \leq (51 \pm 10)\,\text{MeV}.$$

Taking into account the resolution of the kinematic W-reconstruction leads to an estimation of the intrinsic width of

$$\Gamma_R \approx (30 \pm 5)\,\text{MeV}.$$

Assuming that the structure is caused by a single $J = 1/2$ state, the coupling strength is determined to be

$$\sqrt{b_\eta}A_{1/2}^n = (12.4 \pm 0.8)\,10^{-3}\,\text{GeV}^{-1/2}.$$

In addition to the phenomenological analysis of the results performed in this work, the extracted high precision differential cross sections should allow a more detailed study by, e.g., partial-wave analyses.

The extraction of quantum numbers will be the next step in the investigation of the structure. In addition to differential cross sections, different polarization observables will set further strong constraints. Corresponding measurements were already performed and the data are being analyzed, or are planned for the future at MAMI and ELSA. Unpolarized cross sections will be remeasured at BGO-OD and LNS-Sendai. An extensive set of measured observables will hopefully shed more light on the nature of this phenomenon. Possible outcomes range from rather unspectacular explanations as, e.g., interference effects to a revolution of the current understanding of hadron structure and QCD, if the existence of the antidecuplet of baryons should be confirmed.

Appendix A

Addenda to the η-meson reconstruction

A.1 Error of the invariant mass in the χ^2-test

The error of the $\gamma_1\gamma_2$ invariant mass $\Delta m_{\gamma_1\gamma_2}$ in the χ^2-test of the η-meson identification using

$$\chi^2 = \left(\frac{m_{\gamma_1\gamma_2} - m_\eta}{\Delta m_{\gamma_1\gamma_2}}\right)^2, \tag{A.1}$$

with the η-meson mass m_η and the $\gamma_1\gamma_2$ invariant mass

$$m_{\gamma_1\gamma_2} = \sqrt{2E_{\gamma_1}E_{\gamma_2}\left(1 - \cos\phi_{\gamma_1\gamma_2}\right)}, \tag{A.2}$$

where E_{γ_1}, E_{γ_2} and $\phi_{\gamma_1\gamma_2}$ are the energies and the opening angle of the two photons, respectively, can be calculated via

$$\begin{aligned}\Delta m_{\gamma_1\gamma_2} &= \sqrt{\left(\frac{\partial m_{\gamma_1\gamma_2}}{\partial\cos\phi_{\gamma_1\gamma_2}}\Delta\cos\phi_{\gamma_1\gamma_2}\right)^2 + \sum_{i=1}^{2}\left(\frac{\partial m_{\gamma_1\gamma_2}}{\partial E_{\gamma_i}}\Delta E_{\gamma_i}\right)^2} \\ &= \frac{1}{2}m_{\gamma_1\gamma_2}\sqrt{\left(\frac{\Delta E_{\gamma_1}}{E_{\gamma_1}}\right)^2 + \left(\frac{\Delta E_{\gamma_2}}{E_{\gamma_2}}\right)^2 + \left(\frac{\Delta\cos\phi_{\gamma_1\gamma_2}}{1 - \cos\phi_{\gamma_1\gamma_2}}\right)^2},\end{aligned} \tag{A.3}$$

with the error of $\cos\phi_{\gamma_1\gamma_2}$

$$\Delta\cos\phi_{\gamma_1\gamma_2} = \sqrt{\sum_{i=1}^{2}\left(\frac{\partial\cos\phi_{\gamma_1\gamma_2}}{\partial\phi_{\gamma_i}}\Delta\phi_{\gamma_i}\right)^2 + \sum_{i=1}^{2}\left(\frac{\partial\cos\phi_{\gamma_1\gamma_2}}{\partial\theta_{\gamma_i}}\Delta\theta_{\gamma_i}\right)^2}. \tag{A.4}$$

As $\cos\phi_{\gamma_1\gamma_2}$ can be derived from

$$
\begin{aligned}
\cos\phi_{\gamma_1\gamma_2} &= \frac{\vec{p}_{\gamma_1}\cdot\vec{p}_{\gamma_2}}{|\vec{p}_{\gamma_1}|\cdot|\vec{p}_{\gamma_2}|} = \frac{x_{\gamma_1}x_{\gamma_2}+y_{\gamma_1}y_{\gamma_2}+z_{\gamma_1}z_{\gamma_2}}{|\vec{p}_{\gamma_1}|\cdot|\vec{p}_{\gamma_2}|}\\
&= \sin\theta_{\gamma_1}\sin\theta_{\gamma_2}\cos\phi_{\gamma_1}\cos\phi_{\gamma_1}+\\
&\quad\; \sin\theta_{\gamma_1}\sin\theta_{\gamma_2}\sin\phi_{\gamma_1}\sin\phi_{\gamma_2}+\\
&\quad\; \cos\theta_{\gamma_1}\cos\theta_{\gamma_2}\,,
\end{aligned}
\tag{A.5}
$$

it follows that

$$
\begin{aligned}
\Delta\cos\phi_{\gamma_1\gamma_2} = \{\,&(-\sin\theta_{\gamma_1}\sin\theta_{\gamma_2}\sin\left(\phi_{\gamma_1}-\phi_{\gamma_2}\right)\Delta\phi_{\gamma_1})^2+\\
&(-\sin\theta_{\gamma_1}\sin\theta_{\gamma_2}\sin\left(\phi_{\gamma_2}-\phi_{\gamma_1}\right)\Delta\phi_{\gamma_2})^2+\\
&([\cos\theta_{\gamma_1}\sin\theta_{\gamma_2}\cos\left(\phi_{\gamma_1}-\phi_{\gamma_2}\right)-\sin\theta_{\gamma_1}\cos\theta_{\gamma_2}]\Delta\theta_{\gamma_1})^2+\\
&([\sin\theta_{\gamma_1}\cos\theta_{\gamma_2}\cos\left(\phi_{\gamma_2}-\phi_{\gamma_1}\right)-\cos\theta_{\gamma_1}\sin\theta_{\gamma_2}]\Delta\theta_{\gamma_2})^2\,\}^{1/2}\,.
\end{aligned}
\tag{A.6}
$$

Therefore, the error of the $\gamma_1\gamma_2$ invariant mass $\Delta m_{\gamma_1\gamma_2}$ finally depends on the errors of the photon energies ΔE_{γ_i} and the errors in azimuthal and polar angles $\Delta\phi_{\gamma_i},\Delta\theta_{\gamma_i}$ of the two photons, respectively.

A.2   The χ^2-distribution

If x_i are k independent and normal distributed random variables with expectation values e_i and standard deviations σ_i, the values χ^2

$$
\chi^2 = \sum_{i=1}^{k}\frac{(x_i-e_i)^2}{\sigma_i^2}
\tag{A.7}
$$

are distributed according to the χ_k^2-distribution with k degrees of freedom. It can be shown [94] that the corresponding probability density function (pdf) $f(\chi^2,k)$ is equal to

$$
f(\chi^2,k) = \frac{(\chi^2)^{k/2-1}}{\Gamma(k/2)\cdot 2^{k/2}}\cdot e^{-\chi^2/2},
\tag{A.8}
$$

where $\Gamma(k/2)$ is the Gamma function. The cumulative distribution function $F(\chi^2,k)$ calculates the probability of a random variable ξ^2, which is distributed according to the χ_k^2-distribution, being smaller than χ^2:

$$
F(\chi^2,k) = P(\xi^2<\chi^2) = \frac{\gamma(k/2,\chi^2/2)}{\Gamma(k/2)}\,,
\tag{A.9}
$$

with the lower incomplete Gamma function $\gamma(k/2,\chi^2/2)$. There are algorithms for the numerical calculation of $f(\chi^2,k)$ and $F(\chi^2,k)$.

In general the probability $P(\xi^2 < \chi_0^2)$ that a random ξ^2 is smaller than a certain χ_0^2 can be calculated via

$$P(\xi^2 < \chi_0^2) = F(\chi_0^2) = \int_{-\infty}^{\chi_0^2} f(\chi^2)\,d\chi^2\,. \tag{A.10}$$

It is clear that the total probability cannot exceed 1:

$$P(\text{any } \xi^2) = \int_{-\infty}^{+\infty} f(\chi^2)\,d\chi^2 = 1 \tag{A.11}$$

An often used quantity is the confidence level $W(\chi^2)$, which denotes the probability that a random ξ^2 is greater than or equal to χ^2:

$$W(\chi^2) = P(\xi^2 \geq \chi^2) = 1 - P(\xi^2 < \chi^2) = 1 - F(\chi^2) \tag{A.12}$$

Assuming a certain χ_0^2 as lower bound, from equations A.10 and A.12 follows:

$$W(\chi^2) = P(\xi^2 \geq \chi_0^2) = 1 - \int_{-\infty}^{\chi_0^2} f(\chi^2)\,d\chi^2 \tag{A.13}$$

From this and equation A.11 it is clear that a high χ_0^2 corresponds to a low confidence level and vice versa.

Appendix B

Kinematic calculations

B.1 Participant-spectator model kinematics

In the participant-spectator model applied for the description of quasi-free reactions, the reactions take solely place on the participant nucleon while the spectator does not participate and remains in its initial state configuration. In the following part the calculation [95] of the center-of-mass energy W is shown for the deuteron case, where either the proton can play the role of the participant and the neutron is spectator, or vice versa.

The participant, having the mass m_P and energy E_P, carries a Fermi momentum of $\vec{p}_F$. The spectator with mass m_S and energy E_S carries therefore a Fermi momentum of $-\vec{p}_F$ so that the deuteron with mass m_d is at rest. Requesting energy and momentum conservation leads to

$$p_d = p_P + p_S = \begin{pmatrix} E_P \\ \vec{p}_F \end{pmatrix} + \begin{pmatrix} E_S \\ -\vec{p}_F \end{pmatrix} = \begin{pmatrix} m_d \\ 0 \end{pmatrix}. \tag{B.1}$$

Because the energy of the spectator is

$$E_S = \sqrt{m_S^2 + \vec{p}_F^{\,2}}, \tag{B.2}$$

and the deuteron binding energy $B_d \sim 2.2$ MeV is neglected in this model (thus $m_d = m_p + m_n$) the energy of the participant is

$$E_P = m_d - \sqrt{m_S^2 + \vec{p}_F^{\,2}} \neq \sqrt{m_P^2 + \vec{p}_F^{\,2}}, \tag{B.3}$$

and hence the participant is off-shell. Using the initial state four-momenta of the incoming photon and the participant nucleon

$$
\begin{aligned}
k &= (E_\gamma, \ \vec{k}), \qquad \vec{k} = (0, \ 0, \ E_\gamma), & \text{(B.4)} \\
p_P &= (E_P, \ \vec{p}_F), & \text{(B.5)}
\end{aligned}
$$

the square of the center-of-mass energy $s = W^2$ can be calculated via

$$
s = (k + p_P)^2 = E_\gamma^2 + 2E_\gamma E_P + E_P^2 - (\vec{k} + \vec{p}_F)^2. \tag{B.6}
$$

Using E_P from equation B.3 leads to

$$
s = m_d^2 + m_s^2 + 2E_\gamma \left(m_d - \sqrt{m_s^2 + \vec{p}_F^2} \right) - 2m_d\sqrt{m_s^2 + \vec{p}_F^2} - 2E_\gamma p_{F,z}. \tag{B.7}
$$

B.2   Kinetic energy of the recoil nucleon

The kinetic energy of the detected participant recoil nucleon $T_P = E_P - m_P$ of the reaction

$$
\gamma d \to \eta p n \tag{B.8}
$$

with either the proton or the neutron as participant P or, respectively, spectator S, can be calculated from

$$
\begin{pmatrix} E_\gamma \\ \vec{p}_\gamma \end{pmatrix} + \begin{pmatrix} m_d \\ 0 \end{pmatrix} = \begin{pmatrix} E_\eta \\ \vec{p}_\eta \end{pmatrix} + \begin{pmatrix} E_P \\ \vec{p}_P \end{pmatrix} + \begin{pmatrix} E_S \\ \vec{p}_S \end{pmatrix}, \tag{B.9}
$$

knowing $E_\gamma, E_\eta, m_d, m_P, m_S$ and the angles θ_η, ϕ_η and θ_P, ϕ_P. Defining the terms

$$
\begin{aligned}
a &:= p_{\eta,x} \sin\theta_P \cos\phi_P + p_{\eta,y} \sin\theta_P \sin\phi_P + (p_{\eta,z} - E_\gamma) \cos\theta_P, & \text{(B.10)} \\
b &:= E_\eta - E_\gamma - m_d, & \text{(B.11)} \\
c &:= (E_\eta + m_P - E_\gamma - m_d)^2 - \left(m_S^2 + p_\eta^2 + E_\gamma^2 - 2E_\gamma p_{\eta,z} \right), & \text{(B.12)}
\end{aligned}
$$

the kinetic energy of the detected recoil nucleon T_P yields to

$$
T_P = \frac{-(bc - 2a^2 m_P) + \sqrt{(bc - 2a^2 m_P)^2 - c^2 (b^2 - a^2)}}{2 (b^2 - a^2)}. \tag{B.13}
$$

The complete calculation can be found in [81].

Appendix C

Bin-overlap method

The bin-overlap method [96] was generally used to fill histograms with entries belonging to a range of values that is not coinciding with the bin edges of that histogram. The main usage is the filling of histograms as a function of E_γ with events belonging to tagger channels with variable energy ranges. The method is illustrated in figure C.1. An event of a tagger channel is redistributed among all N energy bins that overlap with the energy range of that tagger channel. The amount of overlap o_i determines the filling weight $w_i = o_i/L$, which is normalized to the width L of the tagger bin so that

$$\sum_{i=1}^{N} w_i = \frac{1}{L} \sum_{i=1}^{N} o_i = 1 \,. \tag{C.1}$$

The normalization ensures that the total weight of the split entries is 1 and thus statistics is not altered.
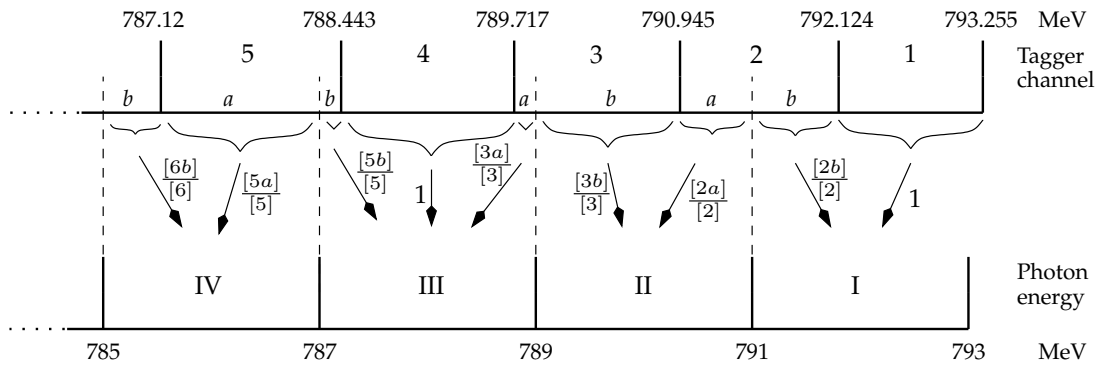
Fig. C.1: Illustration of the bin-overlap method: See text for more details. Taken from [96].

197

Appendix D

Systematic error plots

This appendix contains the additional figures of section 4.13 discussing the systematic uncertainties. Comparisons of the relative systematic errors of the differential cross sections can be found in the following figures:

$\eta \to 2\gamma$ analysis, E_γ-dependent	Fig. 4.42
$\eta \to 3\pi^0$ analysis, E_γ-dependent	Fig. D.1
$\eta \to 2\gamma$ analysis, W_{kin}-dependent	Fig. D.2
$\eta \to 3\pi^0$ analysis, W_{kin}-dependent	Fig. D.3

Contributions of the different sources to the total systematic errors of the differential cross sections are shown in the following figures:

$\gamma N \to \eta(N) \to 2\gamma(N)$ analysis, E_γ-dependent	Fig. D.4
$\gamma N \to \eta(N) \to 3\pi^0(N)$ analysis, E_γ-dependent	Fig. D.5
$\gamma p \to \eta p \to 2\gamma p$ analysis, E_γ-dependent	Fig. D.6
$\gamma p \to \eta p \to 2\gamma p$ analysis, W_{kin}-dependent	Fig. D.7
$\gamma p \to \eta p \to 3\pi^0 p$ analysis, E_γ-dependent	Fig. D.8
$\gamma p \to \eta p \to 3\pi^0 p$ analysis, W_{kin}-dependent	Fig. D.9
$\gamma n \to \eta n \to 2\gamma n$ analysis, E_γ-dependent	Fig. 4.43
$\gamma n \to \eta n \to 2\gamma n$ analysis, W_{kin}-dependent	Fig. D.10
$\gamma n \to \eta n \to 3\pi^0 n$ analysis, E_γ-dependent	Fig. D.11
$\gamma n \to \eta n \to 3\pi^0 n$ analysis, W_{kin}-dependent	Fig. D.12
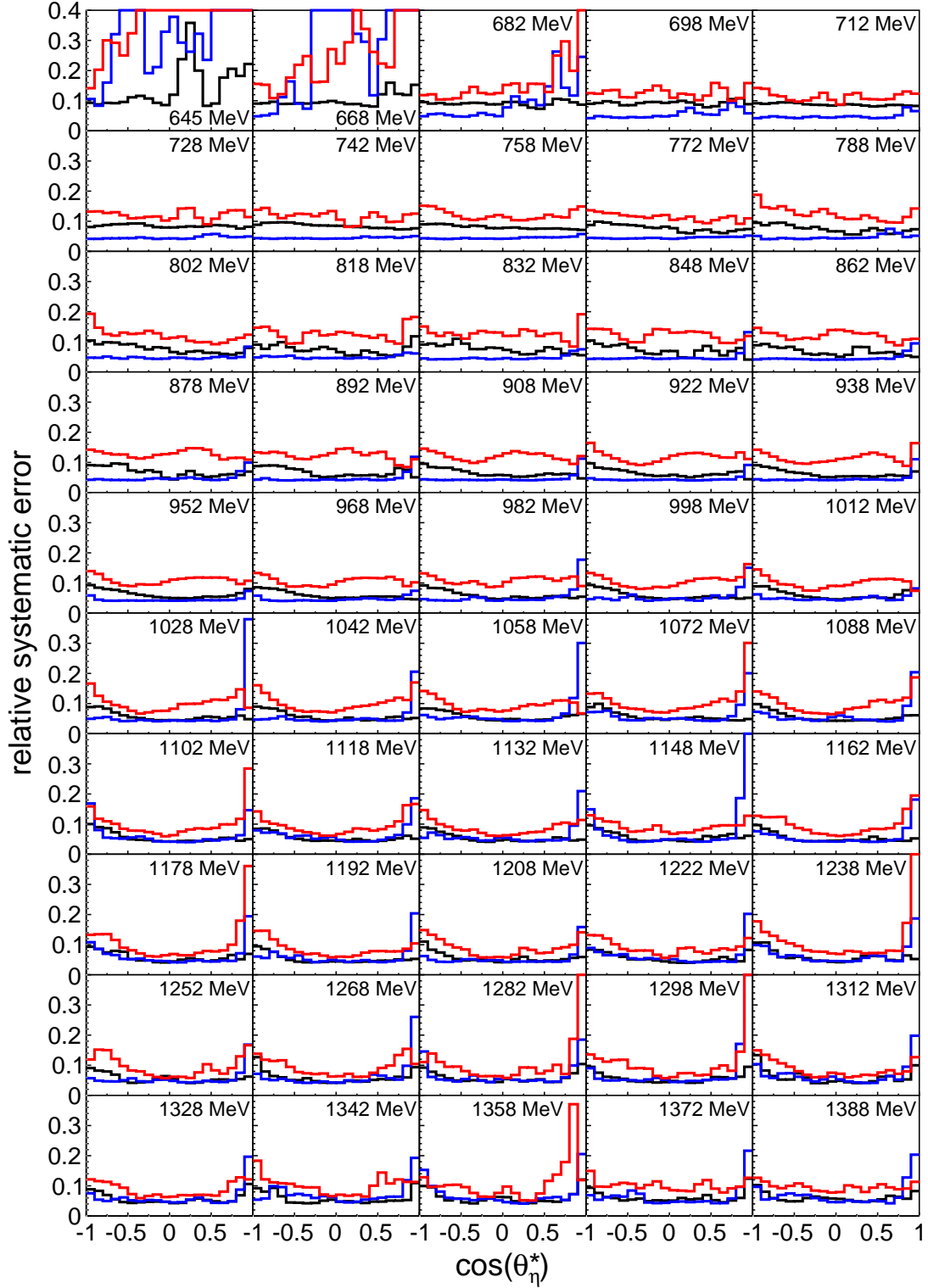
Fig. D.1: Comparison of relative systematic errors of the differential cross sections for the $\eta \to 3\pi^0$ analyses as a function of E_γ: Black histograms: $\gamma N \to \eta(N) \to 3\pi^0(N)$ analysis. Blue histograms: $\gamma p \to \eta p \to 3\pi^0 p$ analysis. Red histograms: $\gamma n \to \eta n \to 3\pi^0 n$ analysis.
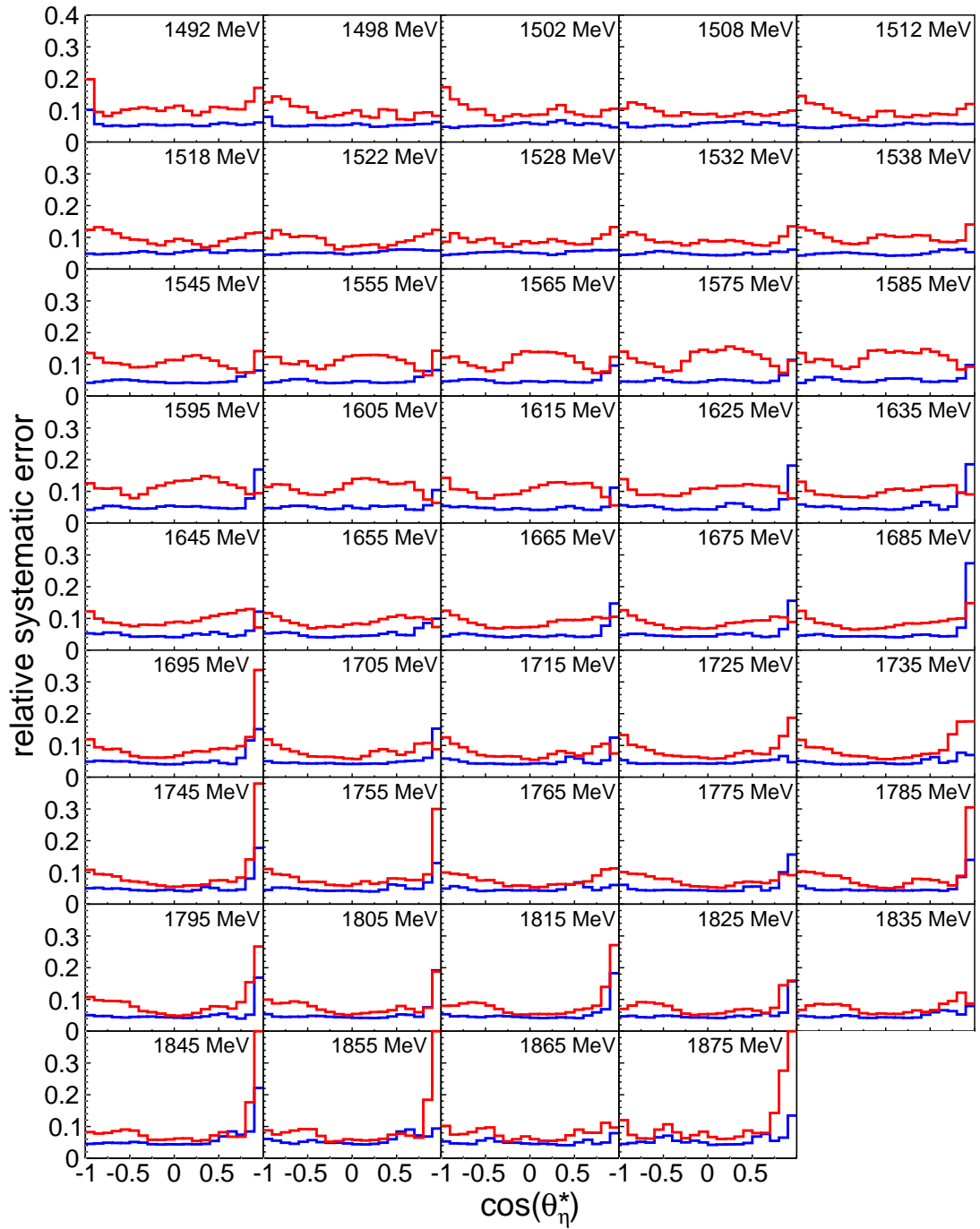
Fig. D.2: Comparison of relative systematic errors of the differential cross sections for the $\eta \to 2\gamma$ analyses as a function of W_{kin}: Blue histograms: $\gamma p \to \eta p \to 2\gamma p$ analysis. Red histograms: $\gamma n \to \eta n \to 2\gamma n$ analysis.
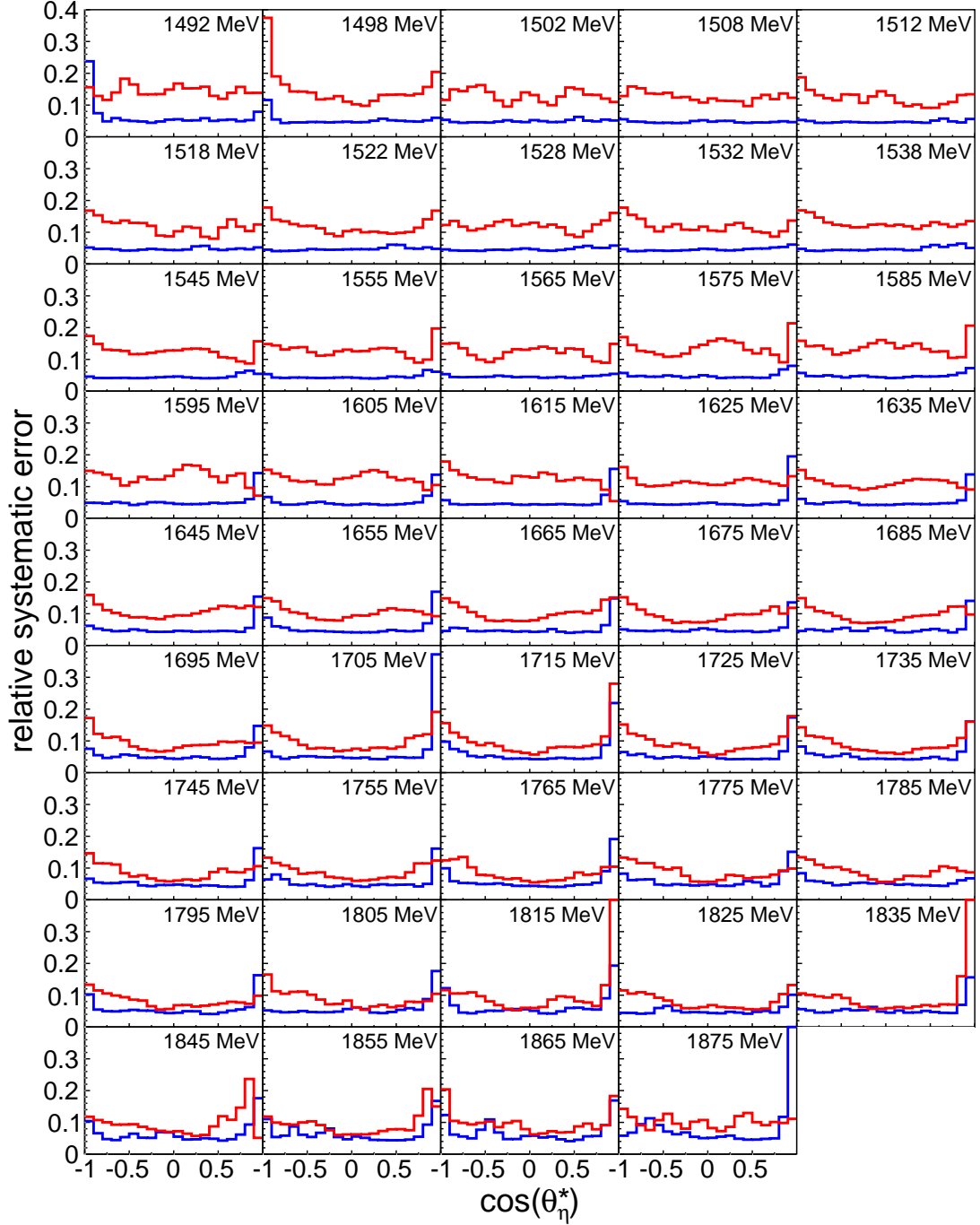
Fig. D.3: Comparison of relative systematic errors of the differential cross sections for the $\eta \to 3\pi^0$ analyses as a function of W_{kin}: Blue histograms: $\gamma p \to \eta p \to 3\pi^0 p$ analysis. Red histograms: $\gamma n \to \eta n \to 3\pi^0 n$ analysis.
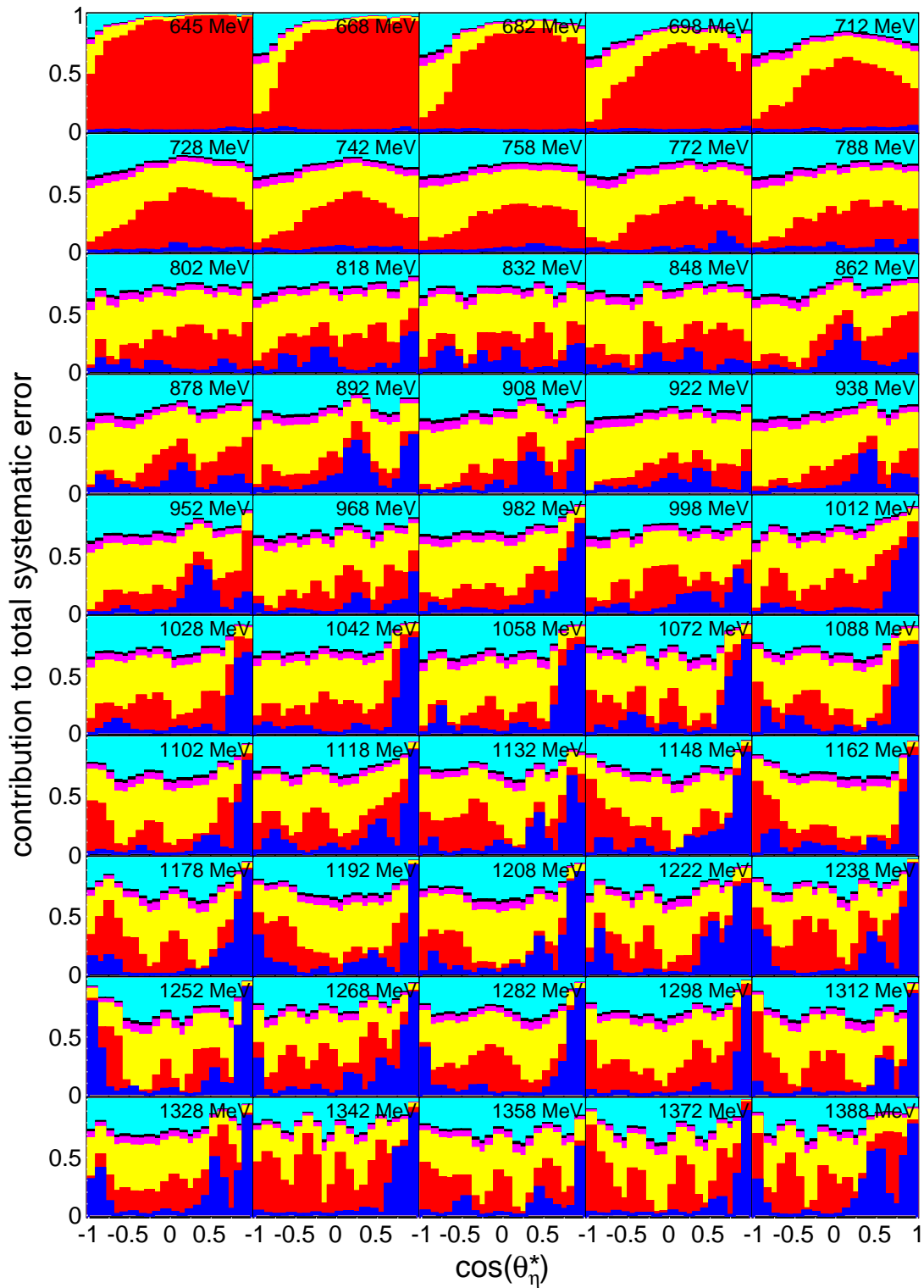
Fig. D.4: Contributions to the total systematic errors of the differential cross sections of $\gamma N \to \eta(N) \to 2\gamma(N)$ as a function of E_γ: CB energy sum trigger (blue), analysis cuts (red), photon flux (yellow), target density (magenta), empty target subtraction (cyan), η-meson decay branching ratio (black).
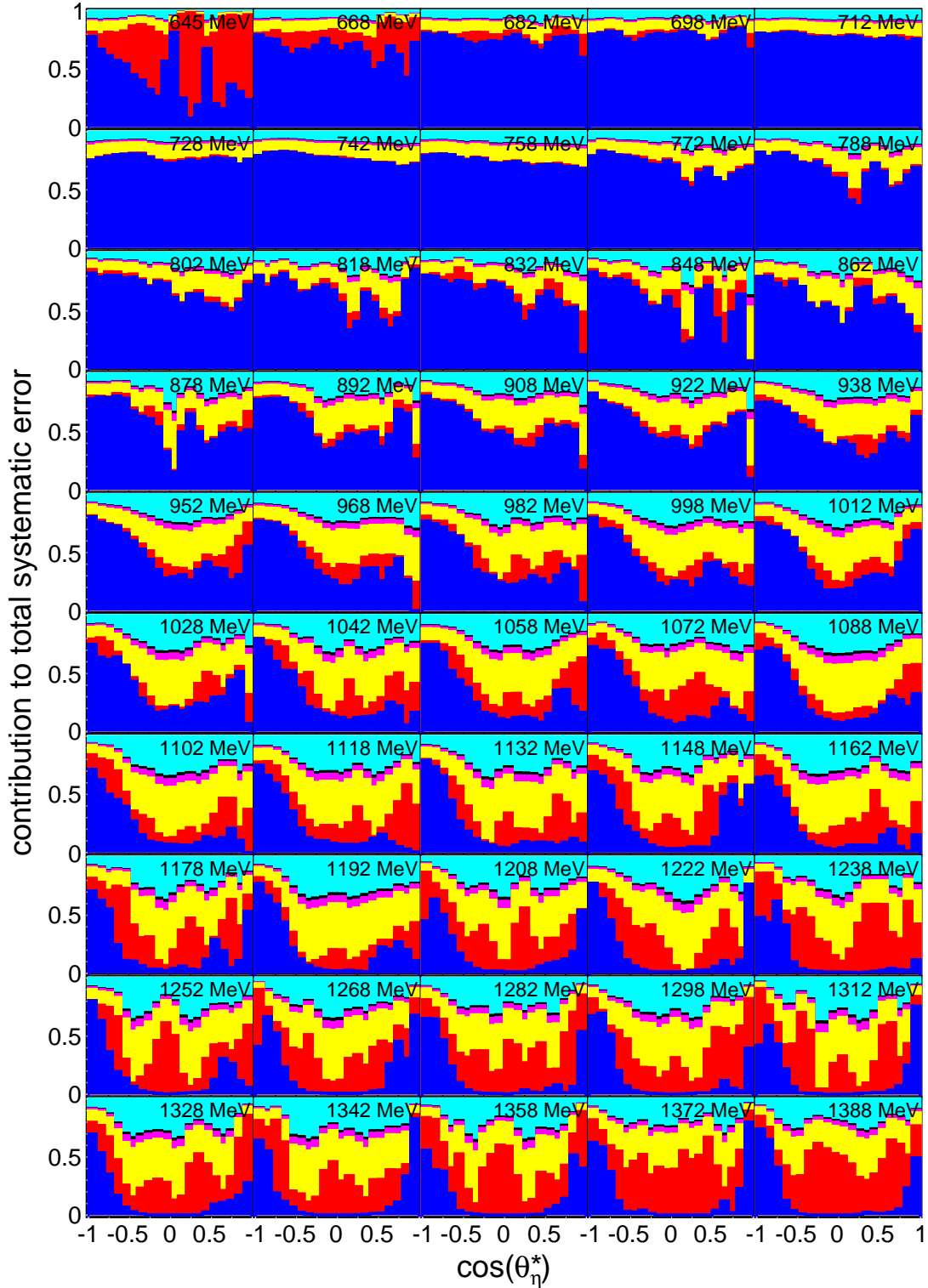
Fig. D.5: Contributions to the total systematic errors of the differential cross sections of $\gamma N \to \eta(N) \to 3\pi^0(N)$ as a function of E_γ: CB energy sum trigger (blue), analysis cuts (red), photon flux (yellow), target density (magenta), empty target subtraction (cyan), η-meson decay branching ratio (black).
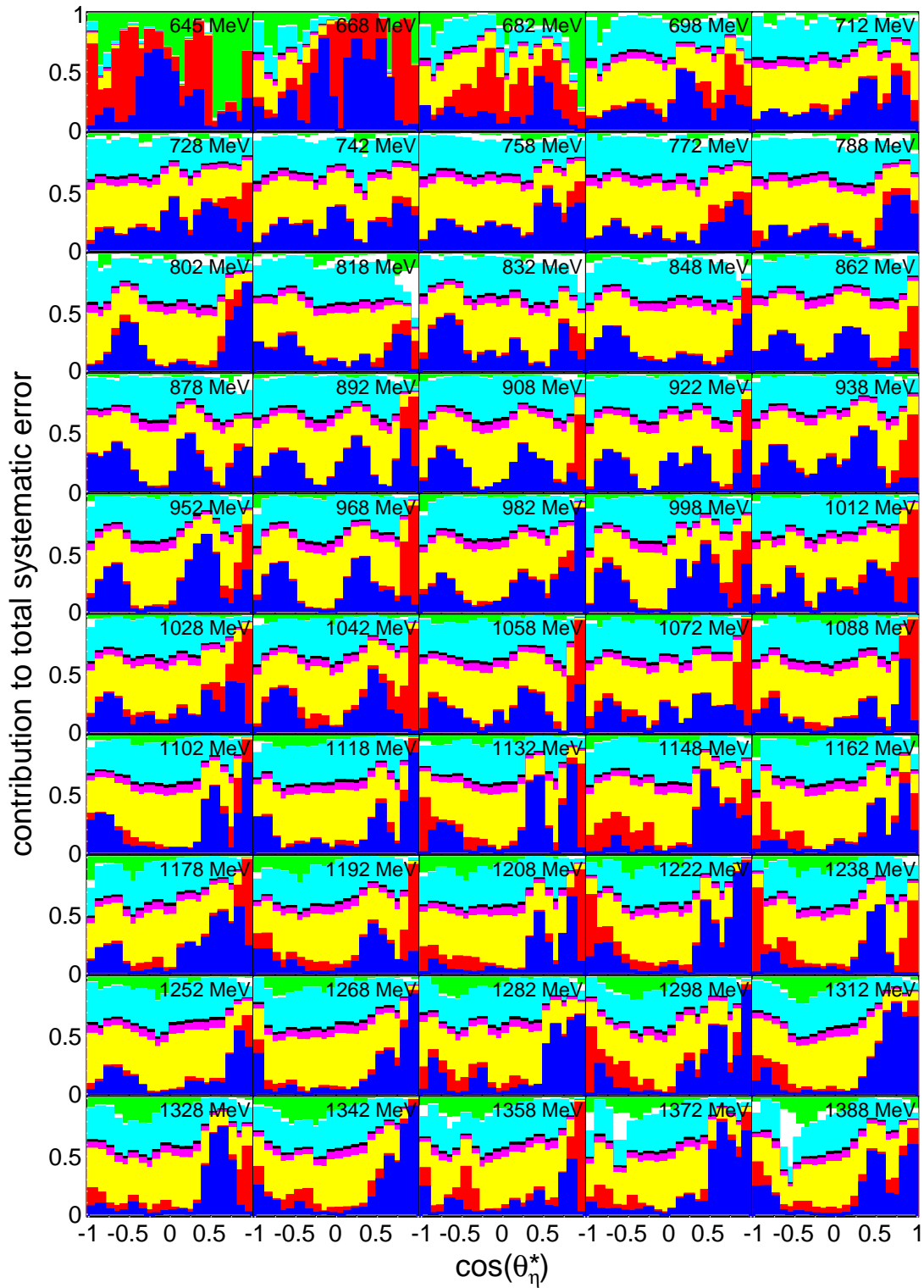
Fig. D.6: Contributions to the total systematic errors of the differential cross sections of $\gamma p \to \eta p \to 2\gamma p$ as a function of E_γ: CB energy sum trigger (blue), analysis cuts (red), photon flux (yellow), target density (magenta), empty target subtraction (cyan), η-meson decay branching ratio (black), nucleon detection efficiency correction (white), Geant4 physics model (green).
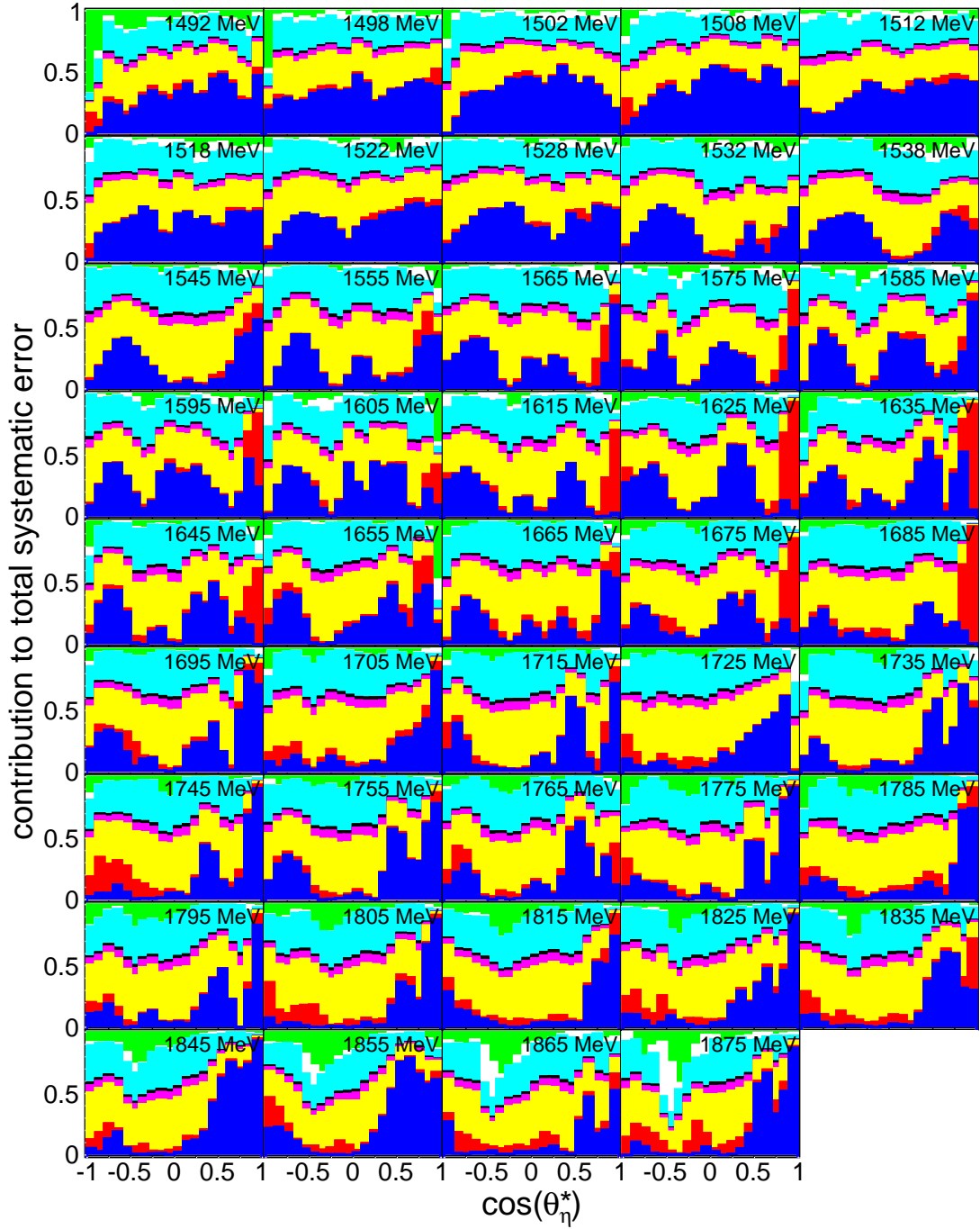
Fig. D.7: Contributions to the total systematic errors of the differential cross sections of $\gamma p \to \eta p \to 2\gamma p$ as a function of W_{kin}: CB energy sum trigger (blue), analysis cuts (red), photon flux (yellow), target density (magenta), empty target subtraction (cyan), η-meson decay branching ratio (black), nucleon detection efficiency correction (white), Geant4 physics model (green).
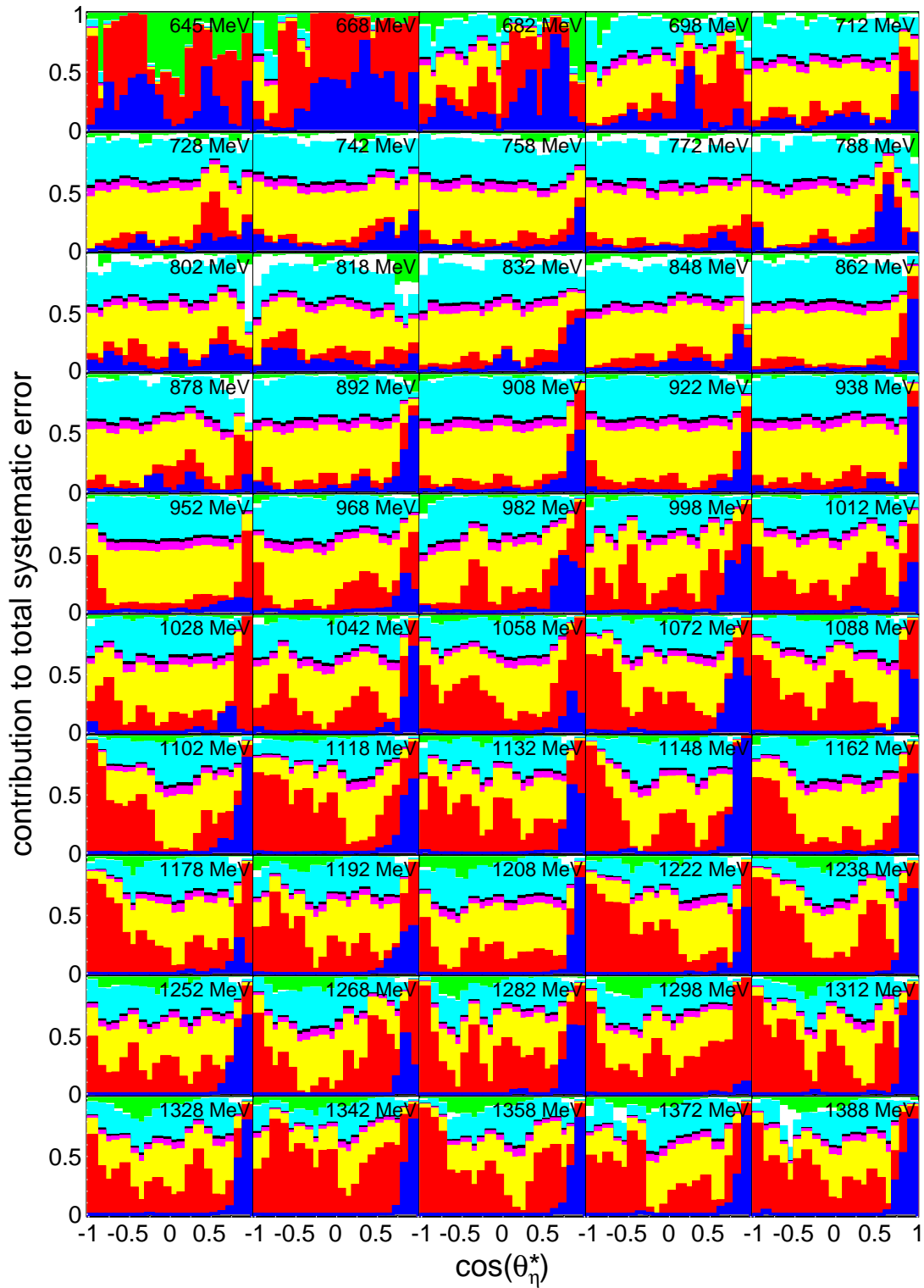
Fig. D.8: Contributions to the total systematic errors of the differential cross sections of $\gamma p \to \eta p \to 3\pi^0 p$ as a function of E_γ: CB energy sum trigger (blue), analysis cuts (red), photon flux (yellow), target density (magenta), empty target subtraction (cyan), η-meson decay branching ratio (black), nucleon detection efficiency correction (white), Geant4 physics model (green).
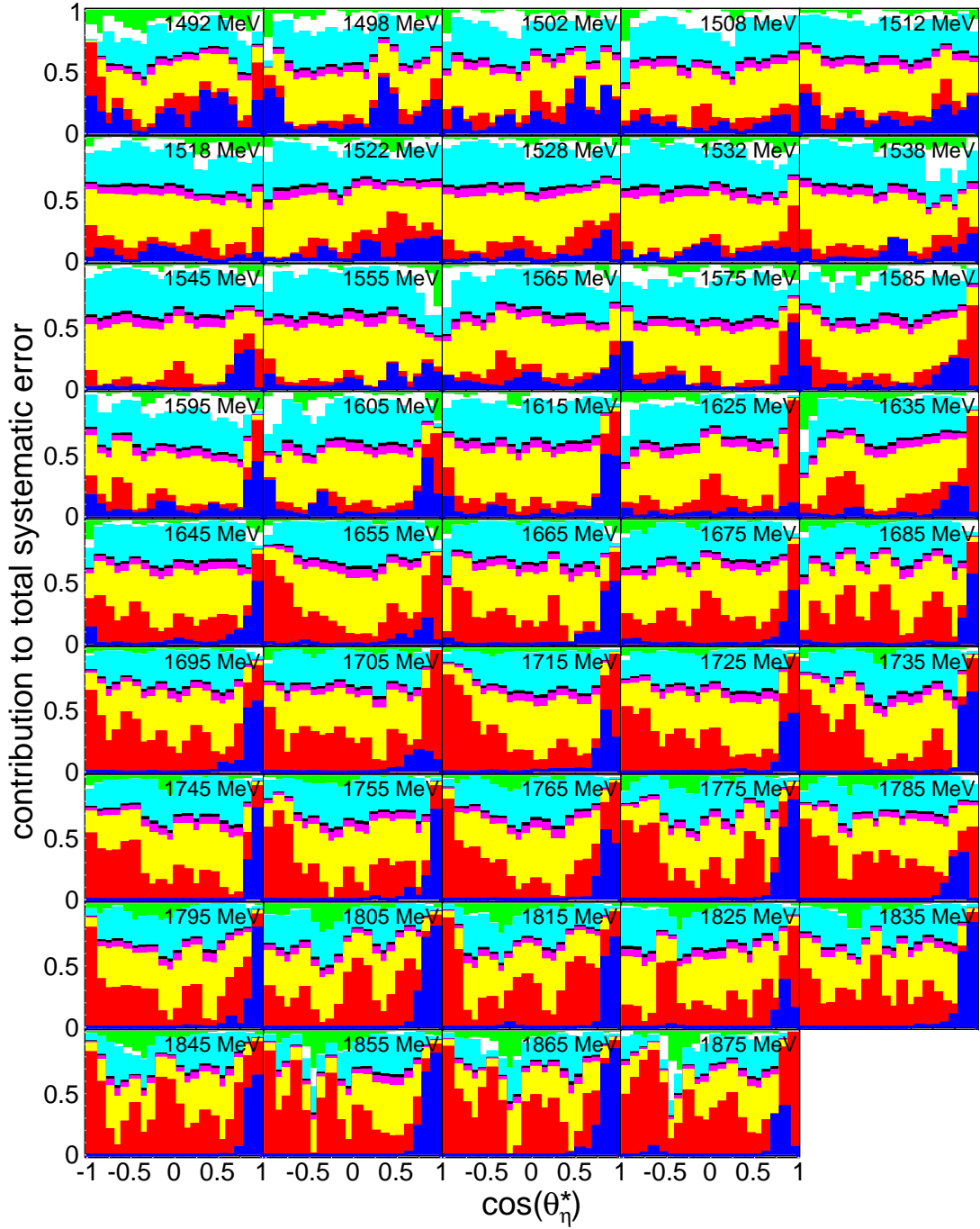
Fig. D.9: Contributions to the total systematic errors of the differential cross sections of $\gamma p \to \eta p \to 3\pi^0 p$ as a function of W_{kin}: CB energy sum trigger (blue), analysis cuts (red), photon flux (yellow), target density (magenta), empty target subtraction (cyan), η-meson decay branching ratio (black), nucleon detection efficiency correction (white), Geant4 physics model (green).
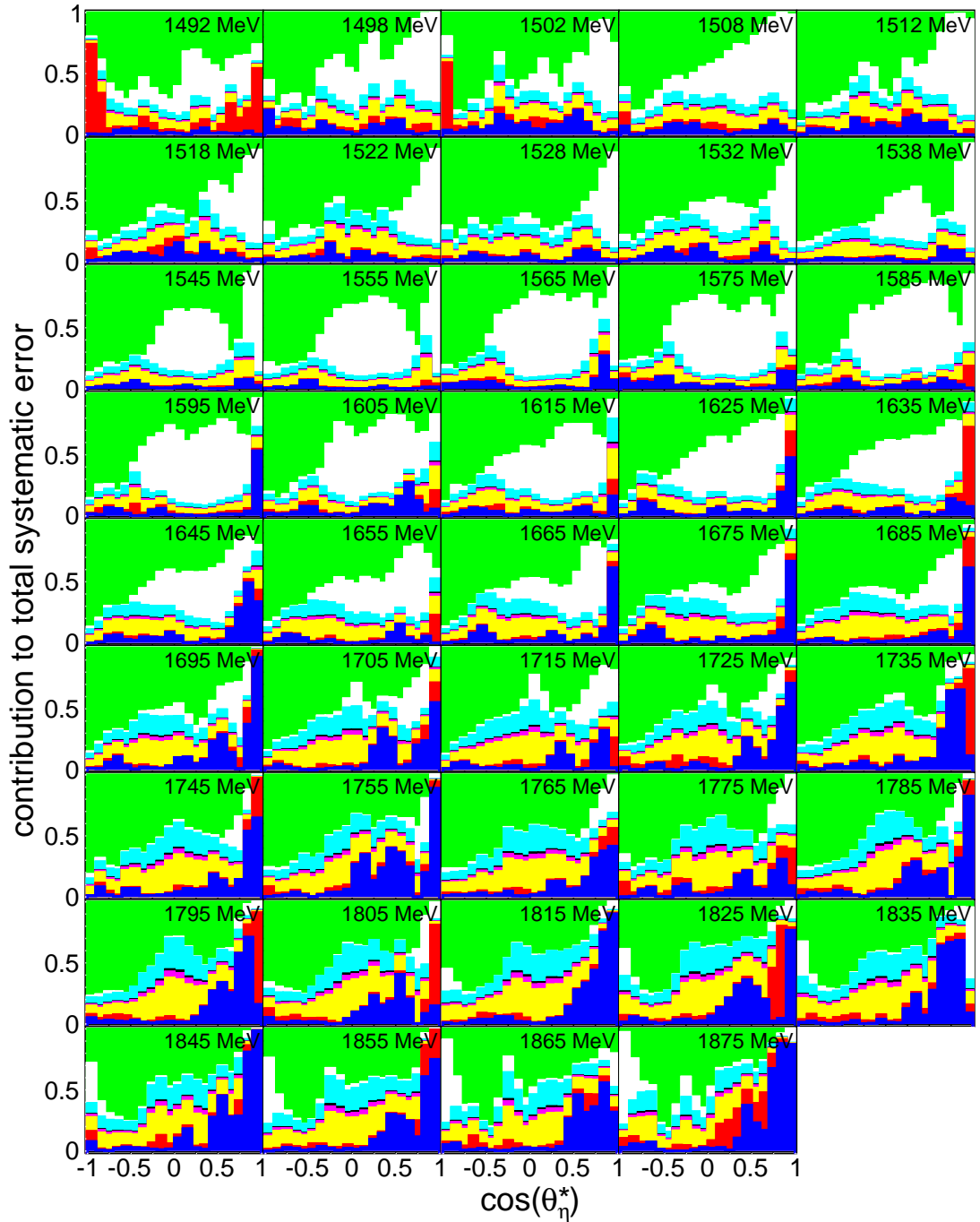
Fig. D.10: Contributions to the total systematic errors of the differential cross sections of $\gamma n \to \eta n \to 2\gamma n$ as a function of W_{kin}: CB energy sum trigger (blue), analysis cuts (red), photon flux (yellow), target density (magenta), empty target subtraction (cyan), η-meson decay branching ratio (black), nucleon detection efficiency correction (white), Geant4 physics model (green).
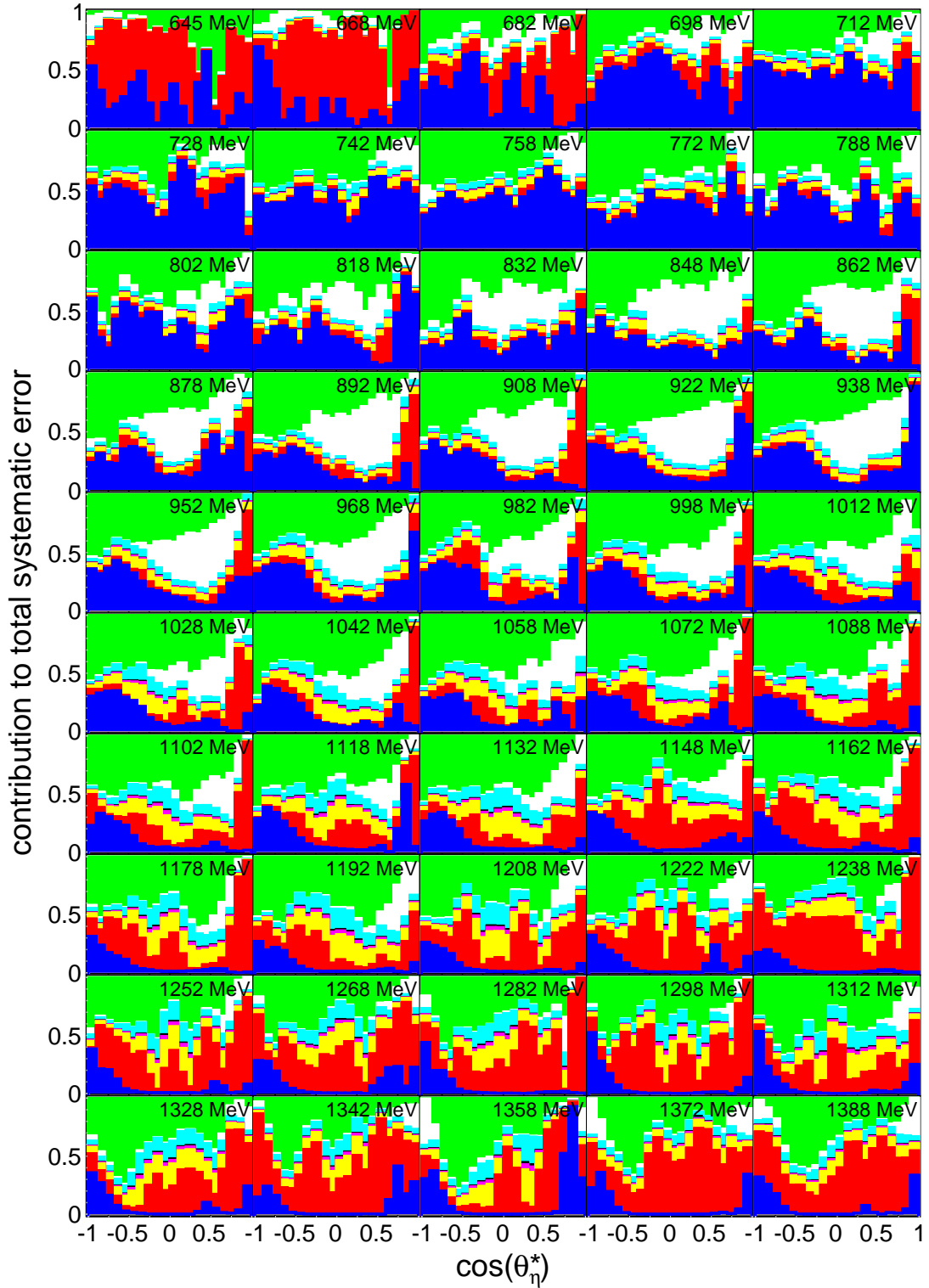
Fig. D.11: Contributions to the total systematic errors of the differential cross sections of $\gamma n \rightarrow \eta n \rightarrow 3\pi^0 n$ as a function of E_γ: CB energy sum trigger (blue), analysis cuts (red), photon flux (yellow), target density (magenta), empty target subtraction (cyan), η-meson decay branching ratio (black), nucleon detection efficiency correction (white), Geant4 physics model (green).
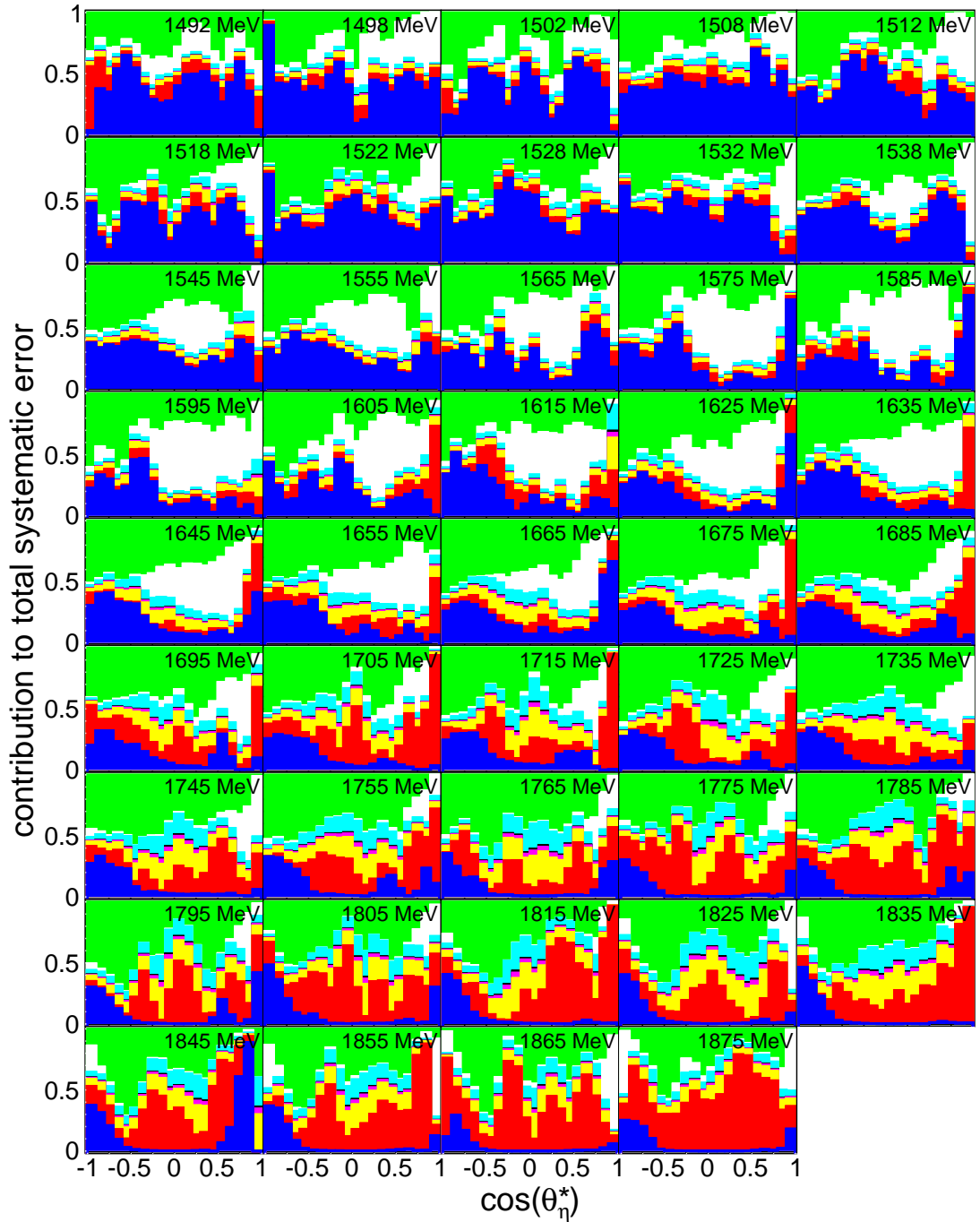
Fig. D.12: Contributions to the total systematic errors of the differential cross sections of $\gamma n \to \eta n \to 3\pi^0 n$ as a function of W_{kin}: CB energy sum trigger (blue), analysis cuts (red), photon flux (yellow), target density (magenta), empty target subtraction (cyan), η-meson decay branching ratio (black), nucleon detection efficiency correction (white), Geant4 physics model (green).

Appendix E

Comparison of data sets

This appendix contains plots comparing the results obtained from the different data sets and the two η-meson decays analyzed in this work. The total cross sections are compared in the following figures:

$\gamma N \to \eta(N)$ analyses, E_γ-dependent   Fig. E.1
$\gamma p \to \eta p$ analyses, E_γ-dependent   Fig. E.2
$\gamma n \to \eta n$ analyses, E_γ-dependent   Fig. E.3
$\gamma p \to \eta p$ analyses, W_{kin}-dependent   Fig. E.4
$\gamma n \to \eta n$ analyses, W_{kin}-dependent   Fig. E.5
$\gamma p \to \eta p$ analyses, W_{TOF}-dependent   Fig. E.6
$\gamma n \to \eta n$ analyses, W_{TOF}-dependent   Fig. E.7

Comparisons of differential cross sections can be found in the following figures:

$\gamma N \to \eta(N)$ analyses, E_γ-dependent   Fig. E.8
$\gamma p \to \eta p$ analyses, E_γ-dependent   Fig. E.9
$\gamma n \to \eta n$ analyses, E_γ-dependent   Fig. E.10
$\gamma p \to \eta p$ analyses, W_{kin}-dependent   Fig. E.11
$\gamma n \to \eta n$ analyses, W_{kin}-dependent   Fig. E.12
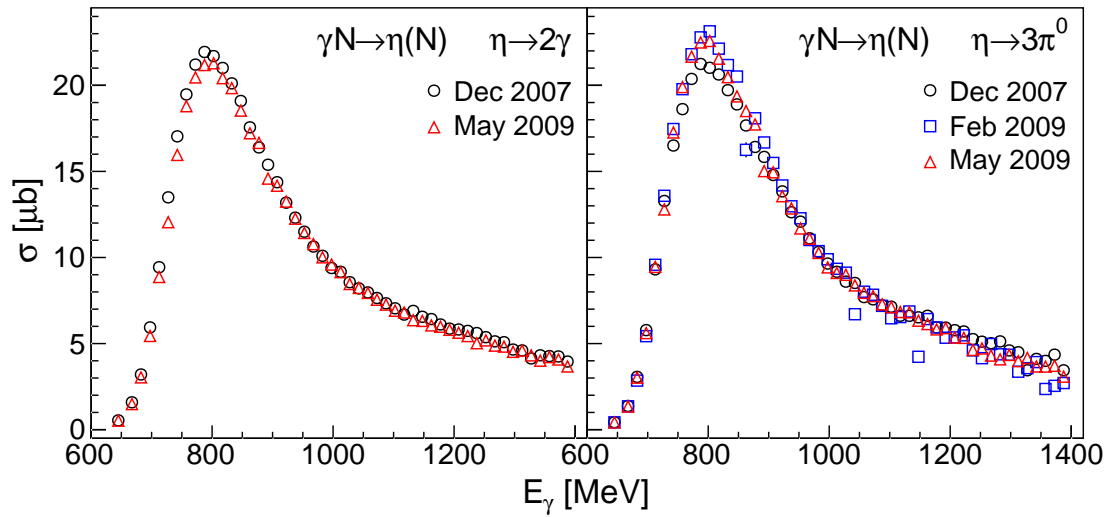
Fig. E.1: Comparison of the total cross sections of the reaction $\gamma N \rightarrow \eta(N)$ obtained from the three data sets and using the two analyzed η-meson decays: Left-hand side: $\eta \rightarrow 2\gamma$ analyses. Right-hand side: $\eta \rightarrow 3\pi^0$ analyses.
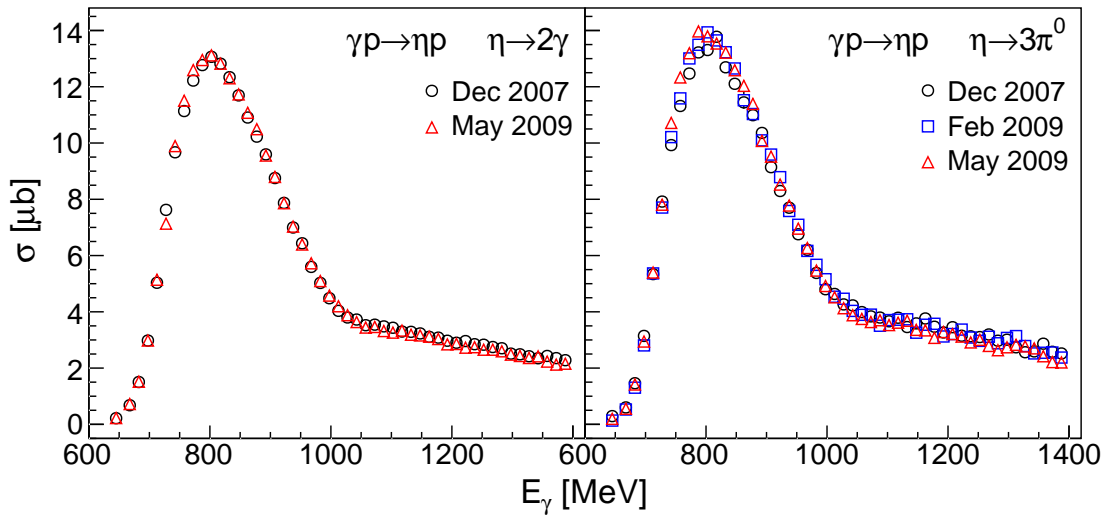
Fig. E.2: Comparison of the total cross sections of the reaction $\gamma p \to \eta p$ as a function of E_γ obtained from the three data sets and using the two analyzed η-meson decays: Left-hand side: $\eta \to 2\gamma$ analyses. Right-hand side: $\eta \to 3\pi^0$ analyses.
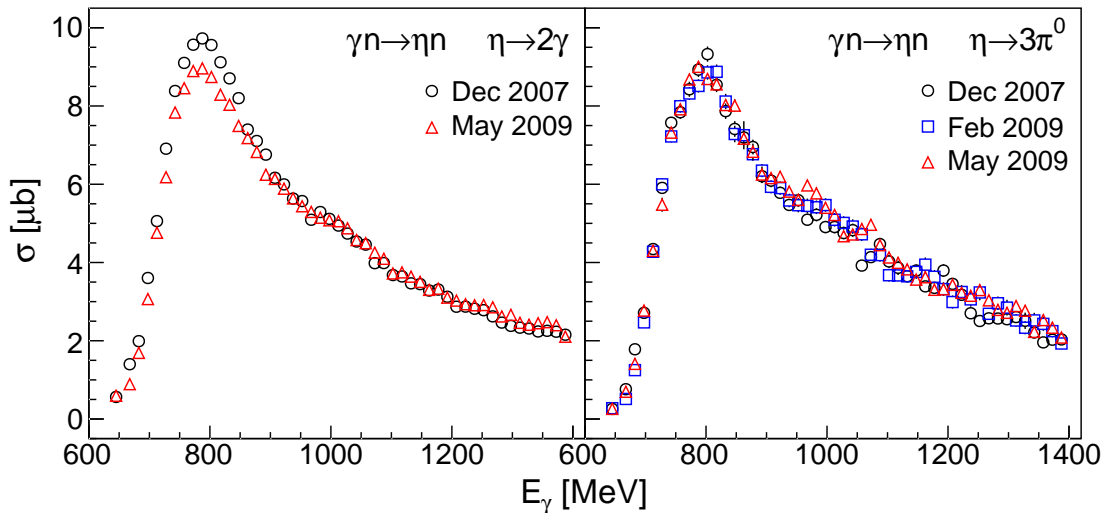
Fig. E.3: Comparison of the total cross sections of the reaction $\gamma n \to \eta n$ as a function of E_γ obtained from the three data sets and using the two analyzed η-meson decays: Left-hand side: $\eta \to 2\gamma$ analyses. Right-hand side: $\eta \to 3\pi^0$ analyses.
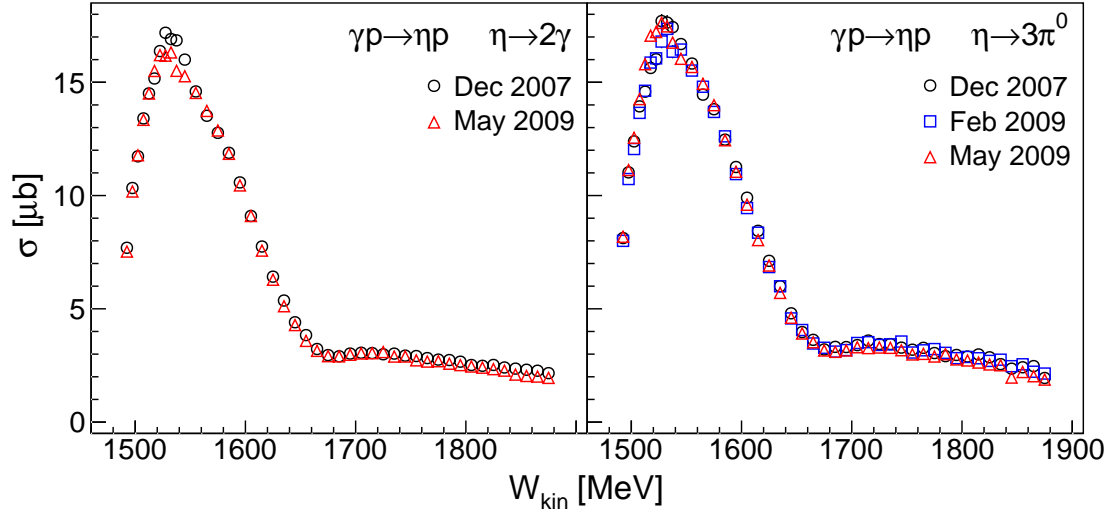
Fig. E.4: Comparison of the total cross sections of the reaction $\gamma p \to \eta p$ as a function of W_{kin} obtained from the three data sets and using the two analyzed η-meson decays: Left-hand side: $\eta \to 2\gamma$ analyses. Right-hand side: $\eta \to 3\pi^0$ analyses.
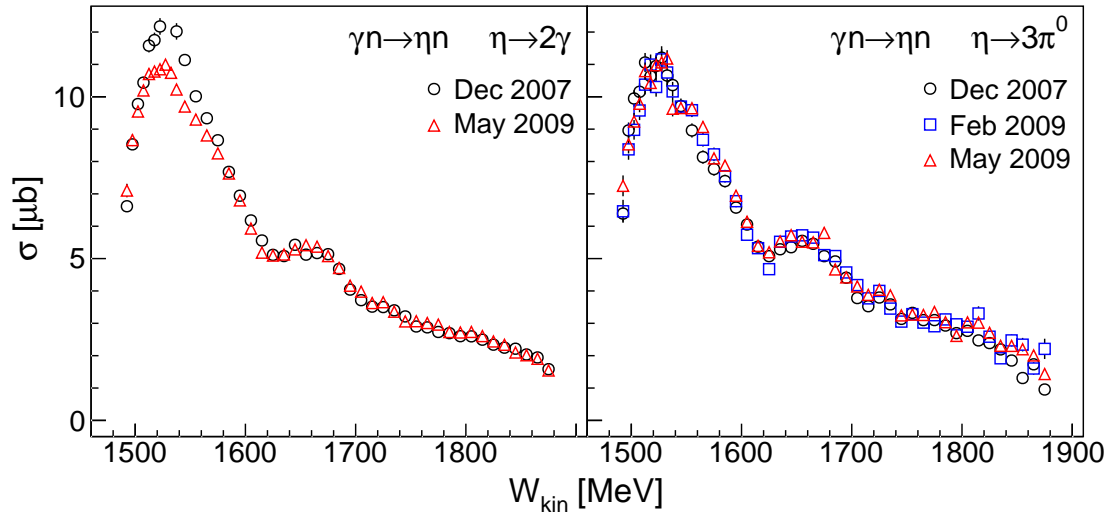
Fig. E.5: Comparison of the total cross sections of the reaction $\gamma n \to \eta n$ as a function of W_{kin} obtained from the three data sets and using the two analyzed η-meson decays: Left-hand side: $\eta \to 2\gamma$ analyses. Right-hand side: $\eta \to 3\pi^0$ analyses.
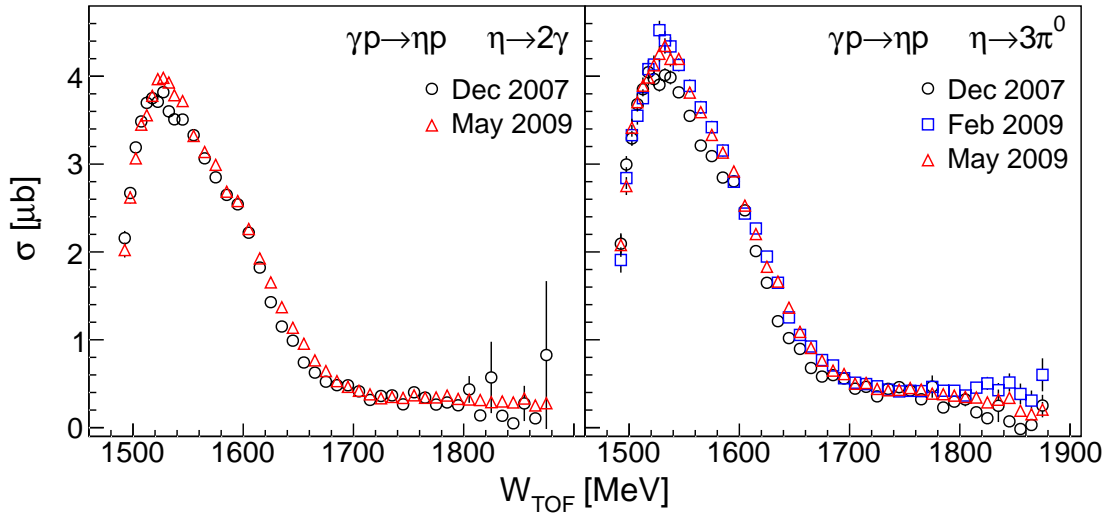
Fig. E.6: Comparison of the total cross sections of the reaction $\gamma p \to \eta p$ as a function of W_{TOF} for $-1 < \cos(\theta_\eta^*) < -0.5$ obtained from the three data sets and using the two analyzed η-meson decays: Left-hand side: $\eta \to 2\gamma$ analyses. Right-hand side: $\eta \to 3\pi^0$ analyses.
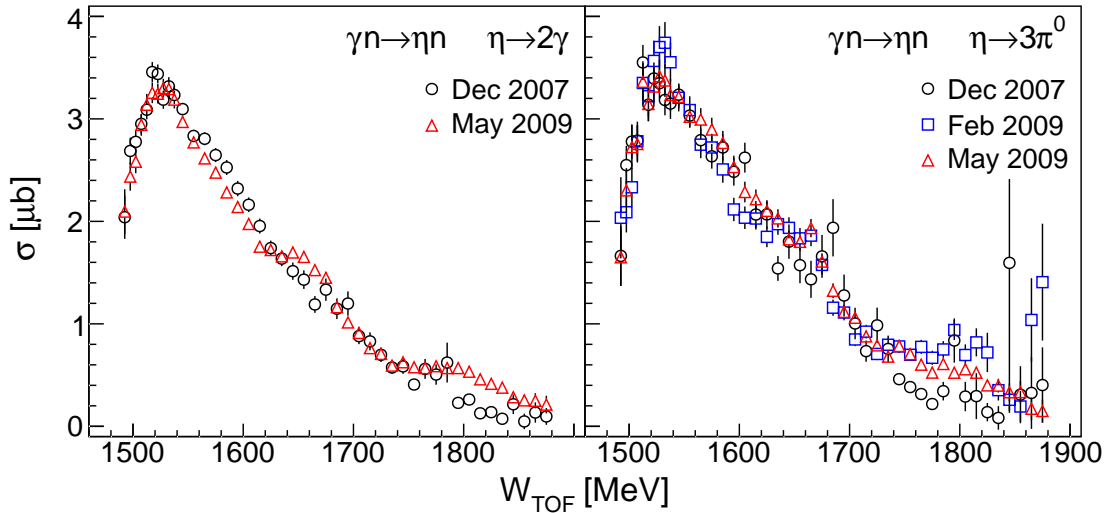
Fig. E.7: Comparison of the total cross sections of the reaction $\gamma n \to \eta n$ as a function of W_{TOF} for $-1 < \cos(\theta_\eta^*) < -0.5$ obtained from the three data sets and using the two analyzed η-meson decays: Left-hand side: $\eta \to 2\gamma$ analyses. Right-hand side: $\eta \to 3\pi^0$ analyses.
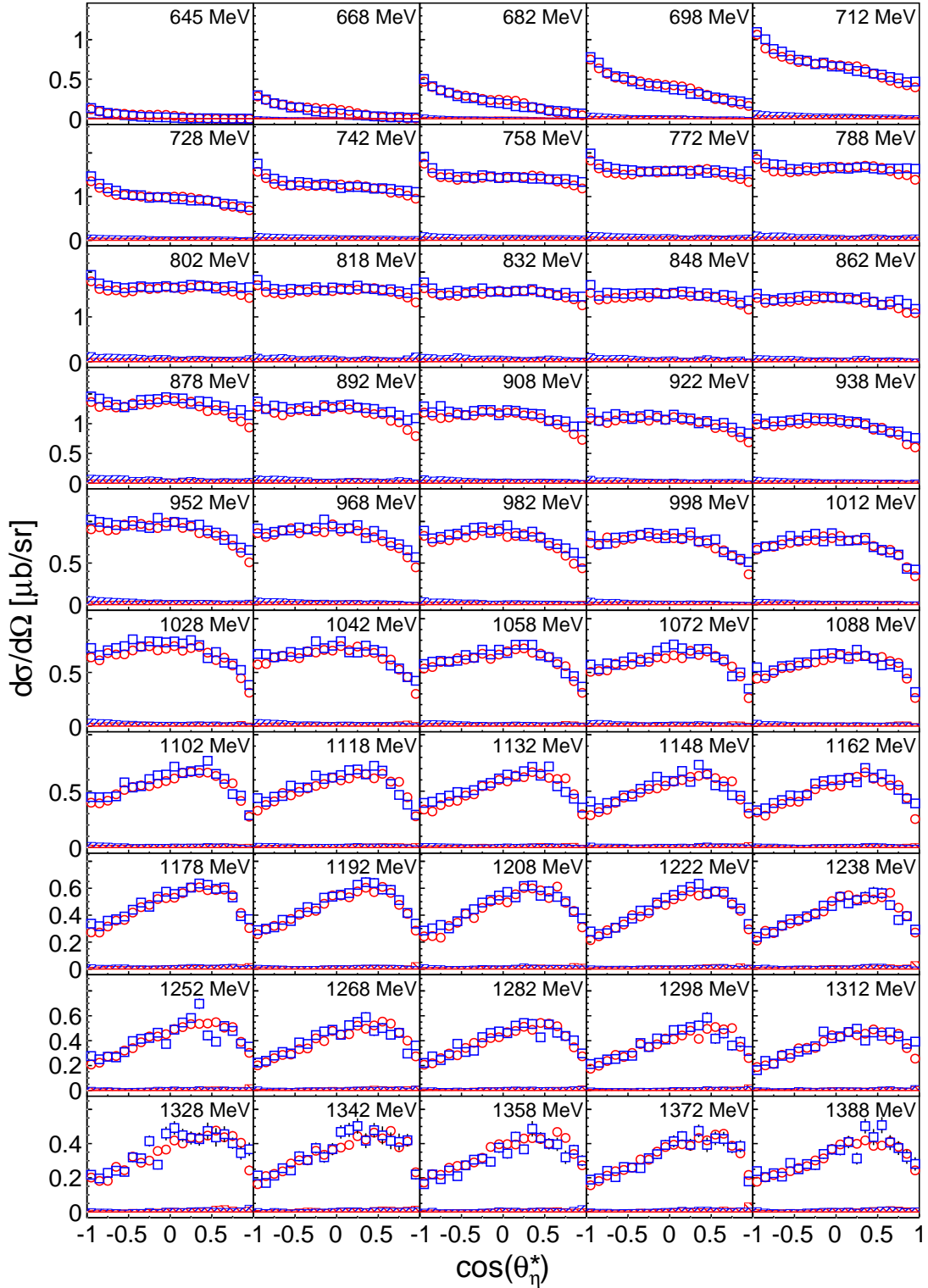
Fig. E.8: Comparison of the differential cross sections of $\gamma N \to \eta(N)$ of the two η-meson decay analyses as a function of E_γ: Red circles: $\eta \to 2\gamma$ analysis. Blue squares: $\eta \to 3\pi^0$ analysis. The estimated systematic errors are shown by the hatched red and, respectively, blue histograms.
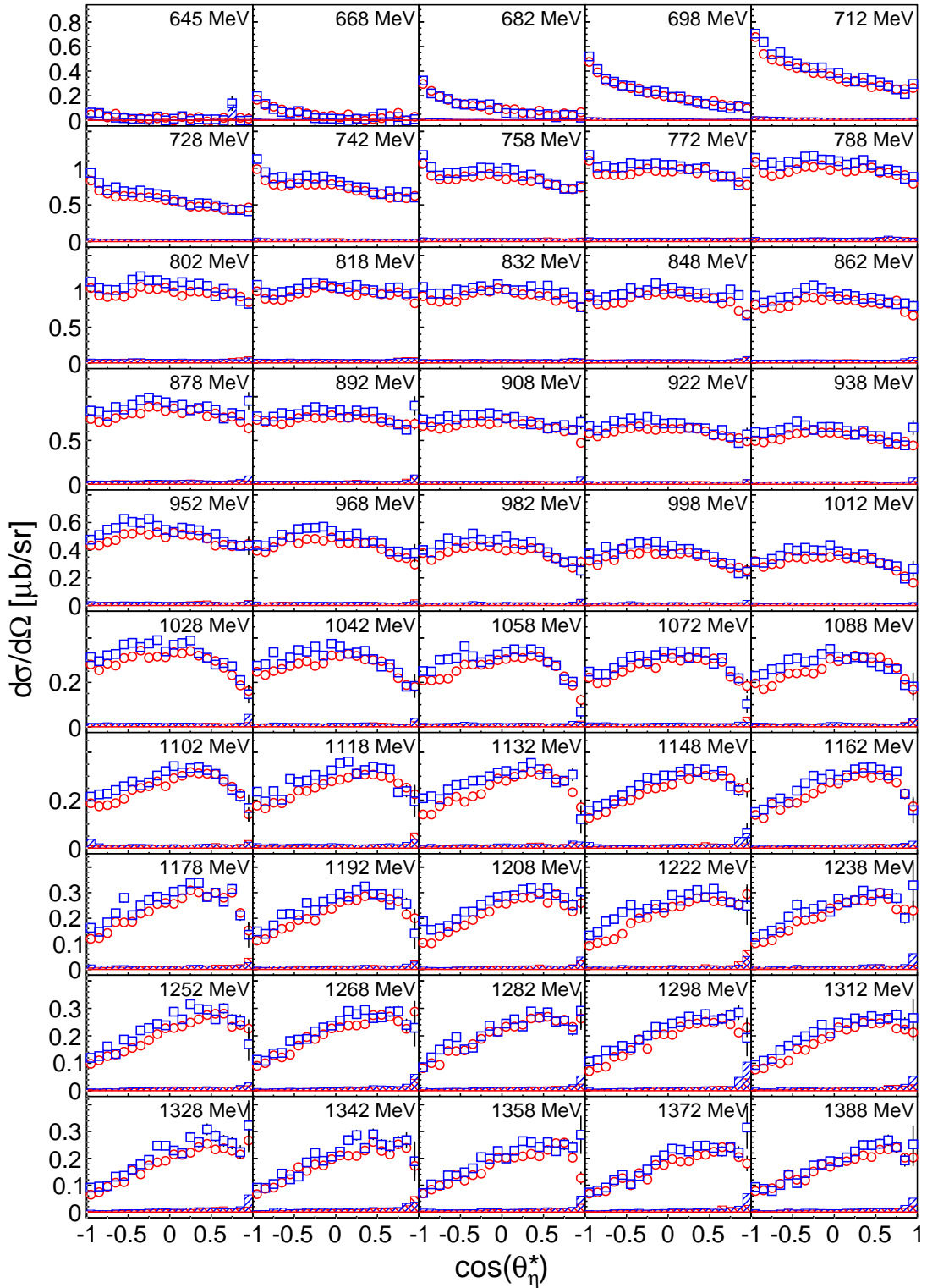
Fig. E.9: Comparison of the differential cross sections of $\gamma p \rightarrow \eta p$ of the two η-meson decay analyses as a function of E_γ: Red circles: $\eta \rightarrow 2\gamma$ analysis. Blue squares: $\eta \rightarrow 3\pi^0$ analysis. The estimated systematic errors are shown by the hatched red and, respectively, blue histograms.
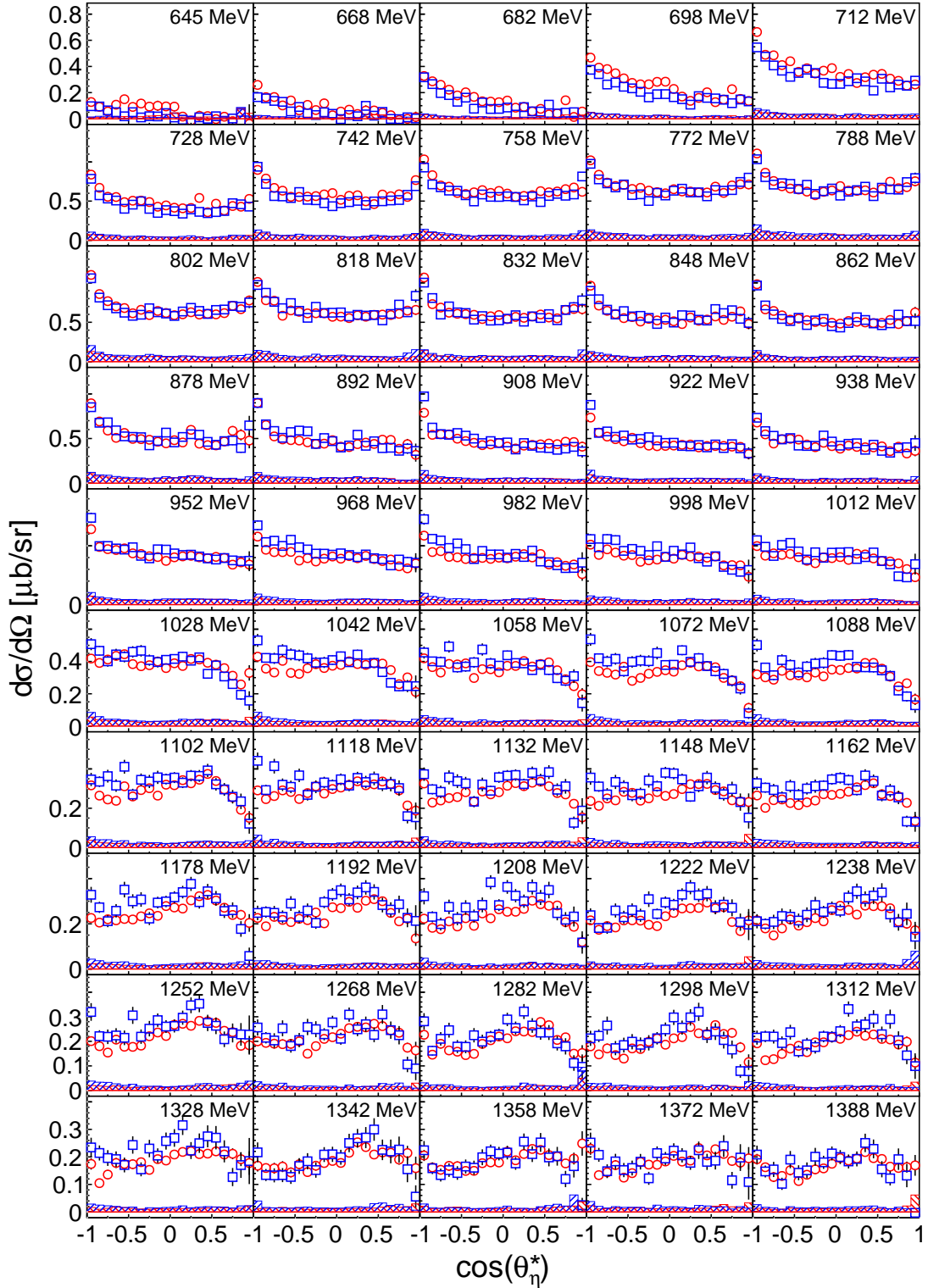
Fig. E.10: Comparison of the differential cross sections of $\gamma n \rightarrow \eta n$ of the two η-meson decay analyses as a function of E_γ: Red circles: $\eta \rightarrow 2\gamma$ analysis. Blue squares: $\eta \rightarrow 3\pi^0$ analysis. The estimated systematic errors are shown by the hatched red and, respectively, blue histograms.
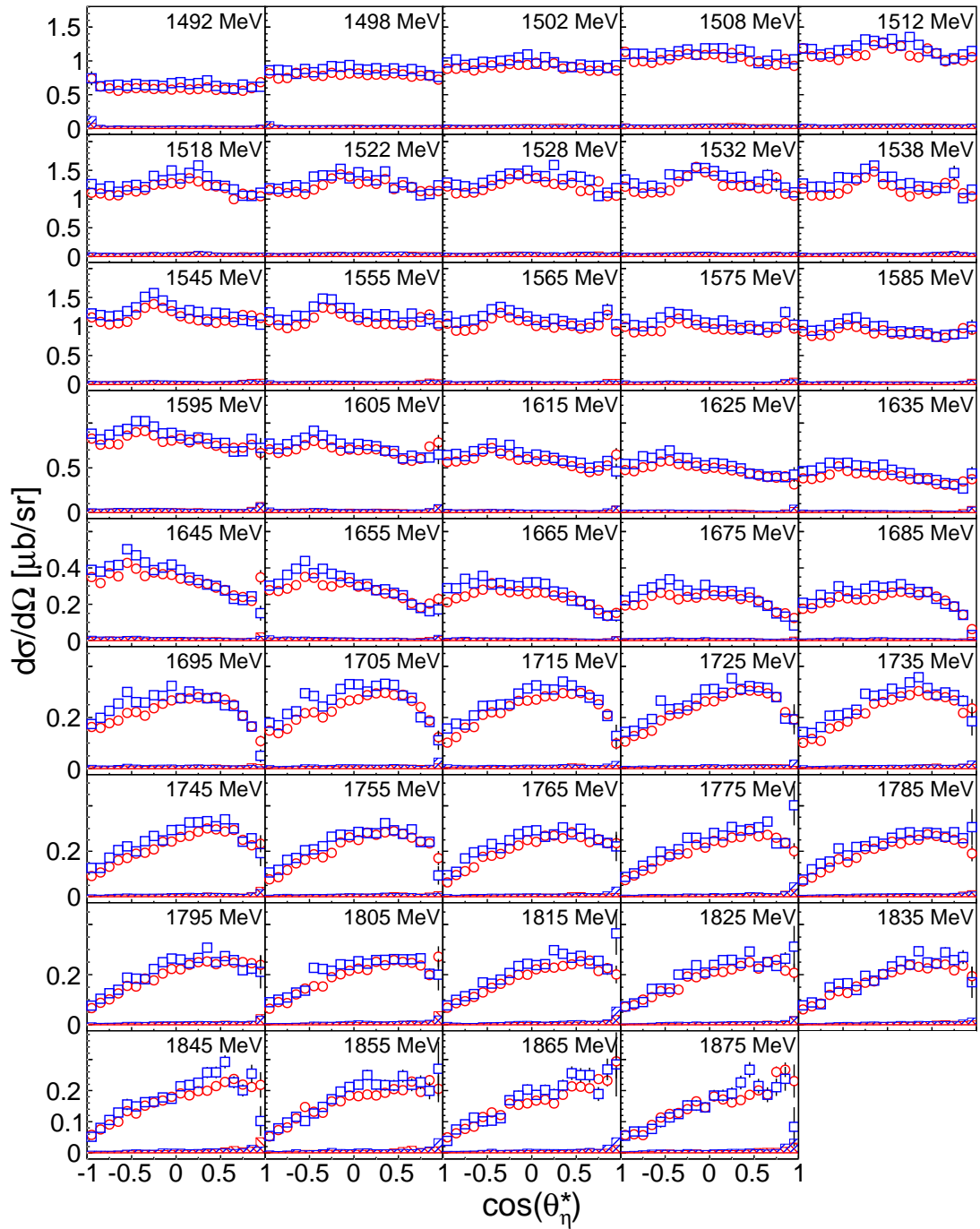
Fig. E.11: Comparison of the differential cross sections of $\gamma p \to \eta p$ of the two η-meson decay analyses as a function of W_{kin}: Red circles: $\eta \to 2\gamma$ analysis. Blue squares: $\eta \to 3\pi^0$ analysis. The estimated systematic errors are shown by the hatched red and, respectively, blue histograms.
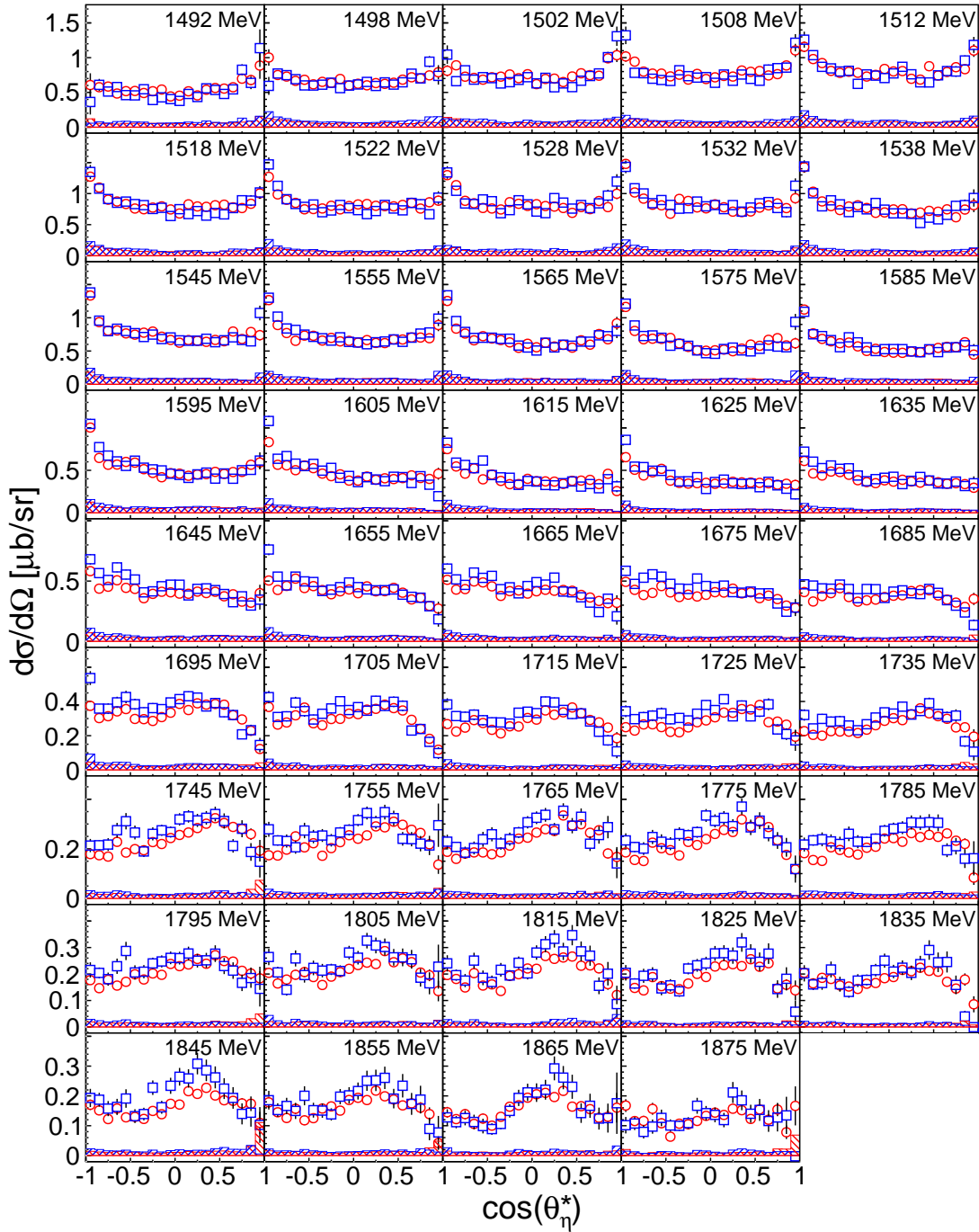
Fig. E.12: Comparison of the differential cross sections of $\gamma n \to \eta n$ of the two η-meson decay analyses as a function of W_{kin}: Red circles: $\eta \to 2\gamma$ analysis. Blue squares: $\eta \to 3\pi^0$ analysis. The estimated systematic errors are shown by the hatched red and, respectively, blue histograms.

Appendix F

Data tables

This appendix contains tables for all measured differential and total cross sections including statistical and systematic errors. The errors are given in absolute values. If not indicated otherwise, the units of differential and total cross sections are μb/sr and μb, respectively. $\cos(\theta_\eta^*)$ is the cosine of the polar angle of the η-meson in the corresponding center-of-mass frame.

Quasi-free inclusive η-photoproduction on the deuteron

Diff. cross section of $\gamma N \to \eta(N)$ as a function of E_γ

$\cos(\theta_\eta^*)$	E_γ=(645.0±15.0) MeV			E_γ=(667.5±7.5) MeV			E_γ=(682.5±7.5) MeV			E_γ=(697.5±7.5) MeV		
	$d\sigma/d\Omega$	Δ_{stat}	Δ_{syst}	$d\sigma/d\Omega$	Δ_{stat}	Δ_{syst}	$d\sigma/d\Omega$	Δ_{stat}	Δ_{syst}	$d\sigma/d\Omega$	Δ_{stat}	Δ_{syst}
	[μb/sr]	[μb/sr]	[μb/sr]	[μb/sr]	[μb/sr]	[μb/sr]	[μb/sr]	[μb/sr]	[μb/sr]	[μb/sr]	[μb/sr]	[μb/sr]
−0.95	0.1248	0.0025	0.0078	0.2875	0.0048	0.0140	0.4803	0.0057	0.0228	0.7584	0.0073	0.0351
−0.85	0.0943	0.0023	0.0068	0.2392	0.0045	0.0118	0.4050	0.0053	0.0198	0.6610	0.0069	0.0313
−0.75	0.0699	0.0021	0.0060	0.1967	0.0042	0.0110	0.3611	0.0051	0.0182	0.5734	0.0065	0.0300
−0.65	0.0647	0.0020	0.0057	0.1782	0.0040	0.0120	0.3299	0.0050	0.0179	0.5254	0.0064	0.0298
−0.55	0.0551	0.0019	0.0051	0.1542	0.0038	0.0117	0.2984	0.0048	0.0197	0.5088	0.0063	0.0293
−0.45	0.0461	0.0018	0.0049	0.1464	0.0038	0.0124	0.2796	0.0047	0.0208	0.4837	0.0062	0.0288
−0.35	0.0389	0.0017	0.0048	0.1295	0.0035	0.0123	0.2675	0.0047	0.0205	0.4591	0.0061	0.0297
−0.25	0.0363	0.0016	0.0053	0.1175	0.0035	0.0120	0.2444	0.0046	0.0202	0.4384	0.0061	0.0315
−0.15	0.0365	0.0017	0.0055	0.1042	0.0033	0.0107	0.2251	0.0044	0.0201	0.4308	0.0060	0.0325
−0.05	0.0326	0.0015	0.0043	0.1028	0.0033	0.0110	0.2243	0.0044	0.0209	0.4159	0.0059	0.0322
0.05	0.0237	0.0013	0.0036	0.0899	0.0032	0.0097	0.2134	0.0044	0.0203	0.4016	0.0059	0.0329
0.15	0.0151	0.0012	0.0030	0.0748	0.0029	0.0085	0.1977	0.0042	0.0189	0.3907	0.0058	0.0331
0.25	0.0098	0.0011	0.0025	0.0584	0.0027	0.0069	0.1749	0.0041	0.0171	0.3560	0.0057	0.0283
0.35	0.0064	0.0010	0.0016	0.0468	0.0025	0.0051	0.1466	0.0039	0.0135	0.3296	0.0055	0.0239
0.45	0.0022	0.0009	0.0002	0.0300	0.0023	0.0030	0.1299	0.0037	0.0115	0.2965	0.0053	0.0217
0.55	0.0010	0.0008	0.0001	0.0234	0.0021	0.0032	0.1003	0.0035	0.0097	0.2565	0.0051	0.0204
0.65	0.0001	0.0007	0.0000	0.0182	0.0020	0.0027	0.0866	0.0033	0.0085	0.2453	0.0049	0.0195
0.75	−0.0004	0.0007	0.0001	0.0167	0.0019	0.0021	0.0799	0.0032	0.0072	0.2148	0.0047	0.0152
0.85	0.0004	0.0007	0.0001	0.0085	0.0018	0.0010	0.0627	0.0030	0.0057	0.1987	0.0044	0.0132
0.95	−0.0007	0.0007	0.0002	0.0096	0.0017	0.0015	0.0534	0.0027	0.0044	0.1763	0.0042	0.0133

$\cos(\theta_\eta^*)$	E_γ=(712.5±7.5) MeV			E_γ=(727.5±7.5) MeV			E_γ=(742.5±7.5) MeV			E_γ=(757.5±7.5) MeV		
	$d\sigma/d\Omega$	Δ_{stat}	Δ_{syst}	$d\sigma/d\Omega$	Δ_{stat}	Δ_{syst}	$d\sigma/d\Omega$	Δ_{stat}	Δ_{syst}	$d\sigma/d\Omega$	Δ_{stat}	Δ_{syst}
	[μb/sr]	[μb/sr]	[μb/sr]	[μb/sr]	[μb/sr]	[μb/sr]	[μb/sr]	[μb/sr]	[μb/sr]	[μb/sr]	[μb/sr]	[μb/sr]
−0.95	1.0735	0.0084	0.0501	1.3902	0.0107	0.0651	1.6301	0.0111	0.0761	1.8083	0.0118	0.0848
−0.85	0.9236	0.0080	0.0450	1.2333	0.0103	0.0592	1.4536	0.0107	0.0687	1.5787	0.0113	0.0750
−0.75	0.8409	0.0077	0.0421	1.1347	0.0099	0.0560	1.3282	0.0103	0.0641	1.4672	0.0109	0.0694
−0.65	0.8042	0.0076	0.0402	1.0708	0.0097	0.0539	1.2862	0.0101	0.0631	1.4633	0.0110	0.0701
−0.55	0.7664	0.0075	0.0391	1.0421	0.0097	0.0530	1.2578	0.0102	0.0614	1.4060	0.0108	0.0684
−0.45	0.7258	0.0074	0.0404	1.0218	0.0097	0.0534	1.2812	0.0103	0.0658	1.4332	0.0110	0.0705
−0.35	0.7270	0.0074	0.0437	1.0098	0.0097	0.0562	1.2675	0.0103	0.0696	1.4179	0.0110	0.0744
−0.25	0.6925	0.0073	0.0437	0.9895	0.0097	0.0574	1.2522	0.0103	0.0696	1.4508	0.0112	0.0787
−0.15	0.7020	0.0074	0.0439	0.9900	0.0097	0.0575	1.2586	0.0104	0.0710	1.4552	0.0113	0.0771
−0.05	0.6722	0.0072	0.0428	0.9797	0.0097	0.0570	1.2440	0.0104	0.0718	1.4296	0.0113	0.0775
0.05	0.6698	0.0073	0.0460	0.9778	0.0098	0.0598	1.2468	0.0105	0.0729	1.4334	0.0114	0.0802
0.15	0.6519	0.0072	0.0457	0.9739	0.0097	0.0623	1.2372	0.0105	0.0762	1.4434	0.0114	0.0816
0.25	0.6416	0.0072	0.0431	0.9489	0.0097	0.0602	1.2497	0.0106	0.0771	1.4418	0.0114	0.0811
0.35	0.6140	0.0070	0.0403	0.9308	0.0095	0.0584	1.2236	0.0105	0.0721	1.4558	0.0115	0.0802
0.45	0.5682	0.0068	0.0369	0.9154	0.0096	0.0568	1.1878	0.0103	0.0688	1.4469	0.0115	0.0793
0.55	0.5318	0.0066	0.0338	0.8808	0.0093	0.0533	1.1798	0.0103	0.0671	1.3968	0.0113	0.0778
0.65	0.4965	0.0065	0.0312	0.8061	0.0090	0.0491	1.1192	0.0101	0.0621	1.3620	0.0113	0.0756
0.75	0.4695	0.0062	0.0289	0.7891	0.0088	0.0477	1.1036	0.0100	0.0588	1.3321	0.0111	0.0730
0.85	0.4372	0.0060	0.0253	0.7517	0.0086	0.0436	1.0609	0.0098	0.0557	1.2981	0.0109	0.0707
0.95	0.4220	0.0058	0.0238	0.7148	0.0084	0.0402	1.0056	0.0096	0.0534	1.2364	0.0107	0.0618

cos(θ_η^*)	E_γ=(772.5±7.5) MeV			E_γ=(787.5±7.5) MeV			E_γ=(802.5±7.5) MeV			E_γ=(817.5±7.5) MeV		
	$d\sigma/d\Omega$	Δ_{stat}	Δ_{syst}	$d\sigma/d\Omega$	Δ_{stat}	Δ_{syst}	$d\sigma/d\Omega$	Δ_{stat}	Δ_{syst}	$d\sigma/d\Omega$	Δ_{stat}	Δ_{syst}
	[μb/sr]	[μb/sr]	[μb/sr]	[μb/sr]	[μb/sr]	[μb/sr]	[μb/sr]	[μb/sr]	[μb/sr]	[μb/sr]	[μb/sr]	[μb/sr]
−0.95	1.8786	0.0129	0.0891	1.8925	0.0129	0.0871	1.8379	0.0136	0.0840	1.7441	0.0147	0.0814
−0.85	1.6766	0.0123	0.0779	1.6979	0.0124	0.0790	1.6617	0.0131	0.0865	1.5975	0.0142	0.0769
−0.75	1.5890	0.0120	0.0738	1.6265	0.0122	0.0776	1.6219	0.0129	0.0774	1.5610	0.0141	0.0767
−0.65	1.5680	0.0121	0.0730	1.6236	0.0122	0.0770	1.6171	0.0131	0.0755	1.5331	0.0140	0.0811
−0.55	1.5396	0.0120	0.0747	1.5826	0.0118	0.0780	1.5764	0.0129	0.0792	1.5640	0.0142	0.0836
−0.45	1.5400	0.0120	0.0788	1.5905	0.0123	0.0826	1.5994	0.0130	0.0811	1.5915	0.0139	0.0817
−0.35	1.5618	0.0122	0.0828	1.6184	0.0125	0.0831	1.6634	0.0134	0.0815	1.5740	0.0146	0.0816
−0.25	1.5720	0.0125	0.0828	1.6044	0.0127	0.0819	1.6320	0.0135	0.0835	1.6158	0.0150	0.0887
−0.15	1.5640	0.0124	0.0831	1.6458	0.0128	0.0873	1.6432	0.0137	0.0896	1.5895	0.0150	0.0906
−0.05	1.5872	0.0126	0.0891	1.6526	0.0129	0.0896	1.6707	0.0139	0.0874	1.6008	0.0150	0.0838
0.05	1.5905	0.0127	0.0893	1.6702	0.0130	0.0865	1.6487	0.0138	0.0838	1.6153	0.0151	0.0783
0.15	1.5851	0.0128	0.0872	1.6573	0.0130	0.0844	1.6335	0.0139	0.0868	1.6046	0.0151	0.0800
0.25	1.5668	0.0127	0.0877	1.6810	0.0131	0.0901	1.6723	0.0139	0.0918	1.6341	0.0154	0.0821
0.35	1.6085	0.0129	0.0890	1.6962	0.0133	0.0962	1.6864	0.0143	0.0931	1.6356	0.0156	0.0837
0.45	1.6001	0.0129	0.0863	1.6756	0.0128	0.0923	1.6890	0.0144	0.0874	1.6346	0.0158	0.0889
0.55	1.5663	0.0128	0.0851	1.6449	0.0132	0.0895	1.6610	0.0143	0.0831	1.6021	0.0156	0.0856
0.65	1.5206	0.0127	0.0840	1.6041	0.0131	0.0871	1.6122	0.0142	0.0846	1.5771	0.0156	0.0759
0.75	1.4852	0.0126	0.0817	1.5515	0.0130	0.0830	1.6037	0.0142	0.0812	1.5273	0.0154	0.0738
0.85	1.4417	0.0124	0.0793	1.5440	0.0130	0.0827	1.5376	0.0140	0.0787	1.4660	0.0151	0.0862
0.95	1.4150	0.0123	0.0756	1.4681	0.0126	0.0813	1.5005	0.0138	0.0871	1.4176	0.0150	0.0956

cos(θ_η^*)	E_γ=(832.5±7.5) MeV			E_γ=(847.5±7.5) MeV			E_γ=(862.5±7.5) MeV			E_γ=(877.5±7.5) MeV		
	$d\sigma/d\Omega$	Δ_{stat}	Δ_{syst}	$d\sigma/d\Omega$	Δ_{stat}	Δ_{syst}	$d\sigma/d\Omega$	Δ_{stat}	Δ_{syst}	$d\sigma/d\Omega$	Δ_{stat}	Δ_{syst}
	[μb/sr]	[μb/sr]	[μb/sr]	[μb/sr]	[μb/sr]	[μb/sr]	[μb/sr]	[μb/sr]	[μb/sr]	[μb/sr]	[μb/sr]	[μb/sr]
−0.95	1.6803	0.0171	0.0796	1.5899	0.0192	0.0789	1.4495	0.0193	0.0660	1.3965	0.0204	0.0650
−0.85	1.5633	0.0166	0.0815	1.4106	0.0179	0.0715	1.3365	0.0186	0.0631	1.3293	0.0200	0.0662
−0.75	1.4887	0.0161	0.0798	1.4398	0.0183	0.0687	1.3595	0.0188	0.0641	1.3263	0.0200	0.0657
−0.65	1.4982	0.0162	0.0799	1.4577	0.0184	0.0695	1.3601	0.0188	0.0634	1.2887	0.0195	0.0612
−0.55	1.5061	0.0158	0.0739	1.4483	0.0182	0.0690	1.3609	0.0186	0.0615	1.2816	0.0195	0.0598
−0.45	1.5275	0.0164	0.0695	1.4712	0.0184	0.0665	1.3934	0.0187	0.0615	1.3295	0.0199	0.0612
−0.35	1.5467	0.0167	0.0730	1.4910	0.0187	0.0702	1.3845	0.0189	0.0625	1.3498	0.0201	0.0648
−0.25	1.5507	0.0172	0.0826	1.4644	0.0196	0.0800	1.4128	0.0199	0.0686	1.3506	0.0212	0.0683
−0.15	1.5563	0.0173	0.0831	1.5342	0.0198	0.0808	1.4260	0.0201	0.0722	1.3775	0.0213	0.0722
−0.05	1.5793	0.0174	0.0386	1.5094	0.0195	0.0745	1.4281	0.0201	0.0756	1.4143	0.0215	0.0701
0.05	1.5542	0.0173	0.0825	1.5280	0.0198	0.0758	1.4274	0.0199	0.0764	1.3949	0.0213	0.0664
0.15	1.5773	0.0173	0.0812	1.5152	0.0195	0.0715	1.3988	0.0196	0.0802	1.3671	0.0208	0.0759
0.25	1.5782	0.0175	0.0769	1.4900	0.0193	0.0738	1.3846	0.0194	0.0753	1.3568	0.0208	0.0712
0.35	1.6011	0.0180	0.0795	1.4702	0.0200	0.0825	1.3469	0.0202	0.0678	1.3193	0.0220	0.0626
0.45	1.5581	0.0182	0.0870	1.4752	0.0209	0.0778	1.3411	0.0207	0.0671	1.2623	0.0220	0.0604
0.55	1.5198	0.0180	0.0810	1.4399	0.0203	0.0770	1.2714	0.0205	0.0640	1.2556	0.0220	0.0606
0.65	1.4765	0.0179	0.0681	1.4086	0.0202	0.0745	1.2973	0.0201	0.0687	1.2441	0.0217	0.0644
0.75	1.4671	0.0178	0.0697	1.3751	0.0201	0.0734	1.2400	0.0201	0.0693	1.1309	0.0212	0.0607
0.85	1.4120	0.0175	0.0768	1.2854	0.0195	0.0702	1.1421	0.0195	0.0626	1.1018	0.0213	0.0588
0.95	1.3204	0.0171	0.0695	1.2257	0.0190	0.0538	1.1119	0.0195	0.0601	1.0049	0.0202	0.0595

cos(θ_η^*)	E_γ=(892.5±7.5) MeV			E_γ=(907.5±7.5) MeV			E_γ=(922.5±7.5) MeV			E_γ=(937.5±7.5) MeV		
	$d\sigma/d\Omega$	Δ_{stat}	Δ_{syst}	$d\sigma/d\Omega$	Δ_{stat}	Δ_{syst}	$d\sigma/d\Omega$	Δ_{stat}	Δ_{syst}	$d\sigma/d\Omega$	Δ_{stat}	Δ_{syst}
	[μb/sr]	[μb/sr]	[μb/sr]	[μb/sr]	[μb/sr]	[μb/sr]	[μb/sr]	[μb/sr]	[μb/sr]	[μb/sr]	[μb/sr]	[μb/sr]
−0.95	1.3169	0.0209	0.0609	1.2181	0.0169	0.0557	1.1230	0.0166	0.0502	1.0177	0.0166	0.0462
−0.85	1.2486	0.0205	0.0634	1.1514	0.0164	0.0514	1.0447	0.0160	0.0482	0.9863	0.0165	0.0445
−0.75	1.2254	0.0202	0.0611	1.1532	0.0164	0.0525	1.0446	0.0158	0.0489	0.9794	0.0162	0.0459
−0.65	1.1870	0.0196	0.0574	1.1344	0.0162	0.0520	1.0863	0.0161	0.0511	0.9923	0.0162	0.0464
−0.55	1.2145	0.0200	0.0584	1.1639	0.0162	0.0530	1.1017	0.0162	0.0513	1.0312	0.0163	0.0468
−0.45	1.2399	0.0199	0.0597	1.1419	0.0160	0.0539	1.0933	0.0157	0.0505	1.0188	0.0163	0.0461
−0.35	1.2364	0.0202	0.0592	1.1586	0.0165	0.0566	1.1045	0.0163	0.0522	1.0323	0.0167	0.0485
−0.25	1.2169	0.0214	0.0568	1.2088	0.0175	0.0560	1.0805	0.0168	0.0526	1.0618	0.0177	0.0506
−0.15	1.2950	0.0217	0.0626	1.2069	0.0174	0.0554	1.1128	0.0169	0.0530	1.0532	0.0175	0.0483
−0.05	1.2622	0.0214	0.0633	1.1667	0.0173	0.0575	1.0639	0.0169	0.0522	1.0479	0.0175	0.0487
0.05	1.2897	0.0214	0.0639	1.1983	0.0171	0.0585	1.1224	0.0168	0.0575	1.0302	0.0173	0.0497
0.15	1.2666	0.0213	0.0705	1.1928	0.0172	0.0570	1.0765	0.0167	0.0513	1.0100	0.0170	0.0499
0.25	1.2744	0.0214	0.0774	1.1508	0.0168	0.0622	1.0643	0.0167	0.0501	1.0162	0.0169	0.0507
0.35	1.2071	0.0220	0.0686	1.1402	0.0175	0.0638	1.0223	0.0171	0.0517	0.9872	0.0179	0.0521
0.45	1.1884	0.0226	0.0587	1.1112	0.0181	0.0584	1.0265	0.0175	0.0505	0.9086	0.0177	0.0491
0.55	1.1714	0.0225	0.0547	1.0505	0.0178	0.0516	0.9438	0.0167	0.0446	0.9210	0.0180	0.0443
0.65	1.0971	0.0216	0.0519	1.0083	0.0175	0.0473	0.9625	0.0173	0.0470	0.8512	0.0173	0.0392
0.75	1.0600	0.0215	0.0527	0.9663	0.0169	0.0484	0.8783	0.0166	0.0434	0.8302	0.0173	0.0402
0.85	0.9483	0.0209	0.0593	0.8599	0.0165	0.0474	0.8006	0.0163	0.0396	0.6906	0.0167	0.0352
0.95	0.8888	0.0203	0.0477	0.7939	0.0163	0.0403	0.7338	0.0163	0.0346	0.6467	0.0159	0.0356

$\cos(\theta_\eta^*)$	$E_\gamma{=}(952.5{\pm}7.5)$ MeV			$E_\gamma{=}(967.5{\pm}7.5)$ MeV			$E_\gamma{=}(982.5{\pm}7.5)$ MeV			$E_\gamma{=}(997.5{\pm}7.5)$ MeV		
	$d\sigma/d\Omega$	Δ_stat	Δ_syst	$d\sigma/d\Omega$	Δ_stat	Δ_syst	$d\sigma/d\Omega$	Δ_stat	Δ_syst	$d\sigma/d\Omega$	Δ_stat	Δ_syst
	[μb/sr]	[μb/sr]	[μb/sr]	[μb/sr]	[μb/sr]	[μb/sr]	[μb/sr]	[μb/sr]	[μb/sr]	[μb/sr]	[μb/sr]	[μb/sr]
-0.95	0.9419	0.0158	0.0424	0.8773	0.0155	0.0418	0.8474	0.0168	0.0414	0.7695	0.0160	0.0368
-0.85	0.9511	0.0159	0.0442	0.8265	0.0152	0.0376	0.7675	0.0158	0.0367	0.7193	0.0154	0.0334
-0.75	0.9189	0.0155	0.0450	0.8508	0.0154	0.0381	0.7954	0.0159	0.0372	0.7812	0.0160	0.0360
-0.65	0.9165	0.0155	0.0447	0.8923	0.0155	0.0419	0.7955	0.0158	0.0376	0.7596	0.0154	0.0387
-0.55	0.9591	0.0157	0.0454	0.9100	0.0155	0.0438	0.8392	0.0160	0.0406	0.7897	0.0157	0.0400
-0.45	0.9703	0.0155	0.0459	0.8792	0.0150	0.0403	0.8343	0.0161	0.0409	0.8034	0.0158	0.0364
-0.35	0.9606	0.0158	0.0445	0.9079	0.0157	0.0420	0.8614	0.0165	0.0410	0.8387	0.0165	0.0388
-0.25	0.9420	0.0166	0.0433	0.8950	0.0165	0.0435	0.8994	0.0180	0.0418	0.8326	0.0172	0.0421
-0.15	0.9564	0.0167	0.0455	0.9105	0.0163	0.0417	0.8841	0.0173	0.0410	0.8143	0.0170	0.0411
-0.05	0.9762	0.0162	0.0448	0.9574	0.0169	0.0420	0.8917	0.0172	0.0403	0.8223	0.0171	0.0411
0.05	0.9934	0.0166	0.0451	0.8900	0.0160	0.0434	0.8512	0.0171	0.0377	0.8152	0.0170	0.0406
0.15	0.9400	0.0160	0.0453	0.9193	0.0163	0.0471	0.8370	0.0167	0.0381	0.7901	0.0167	0.0378
0.25	0.9423	0.0162	0.0480	0.9070	0.0160	0.0453	0.8407	0.0168	0.0391	0.8417	0.0173	0.0390
0.35	0.8881	0.0167	0.0489	0.8449	0.0163	0.0404	0.8335	0.0176	0.0406	0.7550	0.0172	0.0362
0.45	0.8663	0.0167	0.0468	0.8303	0.0170	0.0371	0.8146	0.0179	0.0413	0.7490	0.0173	0.0380
0.55	0.8389	0.0166	0.0406	0.7840	0.0166	0.0371	0.7193	0.0170	0.0366	0.7045	0.0171	0.0338
0.65	0.8152	0.0170	0.0397	0.7178	0.0162	0.0376	0.6911	0.0175	0.0354	0.6467	0.0167	0.0302
0.75	0.7309	0.0159	0.0375	0.6934	0.0159	0.0353	0.6136	0.0168	0.0348	0.5857	0.0163	0.0284
0.85	0.6423	0.0157	0.0340	0.5923	0.0152	0.0286	0.5306	0.0162	0.0315	0.5390	0.0163	0.0271
0.95	0.5506	0.0154	0.0414	0.4841	0.0148	0.0249	0.4623	0.0158	0.0313	0.4027	0.0150	0.0211

$\cos(\theta_\eta^*)$	$E_\gamma{=}(1012.5{\pm}7.5)$ MeV			$E_\gamma{=}(1027.5{\pm}7.5)$ MeV			$E_\gamma{=}(1042.5{\pm}7.5)$ MeV			$E_\gamma{=}(1057.5{\pm}7.5)$ MeV		
	$d\sigma/d\Omega$	Δ_stat	Δ_syst	$d\sigma/d\Omega$	Δ_stat	Δ_syst	$d\sigma/d\Omega$	Δ_stat	Δ_syst	$d\sigma/d\Omega$	Δ_stat	Δ_syst
	[μb/sr]	[μb/sr]	[μb/sr]	[μb/sr]	[μb/sr]	[μb/sr]	[μb/sr]	[μb/sr]	[μb/sr]	[μb/sr]	[μb/sr]	[μb/sr]
-0.95	0.6672	0.0151	0.0299	0.6664	0.0151	0.0317	0.6026	0.0150	0.0291	0.5499	0.0144	0.0252
-0.85	0.6997	0.0152	0.0348	0.6282	0.0146	0.0322	0.6071	0.0146	0.0311	0.5659	0.0141	0.0289
-0.75	0.6994	0.0149	0.0385	0.6884	0.0147	0.0350	0.6405	0.0148	0.0324	0.6012	0.0142	0.0309
-0.65	0.7392	0.0151	0.0392	0.6849	0.0147	0.0340	0.6544	0.0146	0.0308	0.6022	0.0144	0.0277
-0.55	0.7669	0.0155	0.0368	0.6907	0.0144	0.0331	0.6585	0.0146	0.0316	0.6248	0.0141	0.0280
-0.45	0.7615	0.0152	0.0342	0.7345	0.0149	0.0353	0.6462	0.0143	0.0308	0.6325	0.0143	0.0291
-0.35	0.7851	0.0156	0.0366	0.7392	0.0152	0.0365	0.6963	0.0154	0.0320	0.6352	0.0147	0.0289
-0.25	0.7980	0.0166	0.0375	0.7575	0.0162	0.0357	0.7138	0.0161	0.0332	0.6849	0.0160	0.0315
-0.15	0.8023	0.0167	0.0363	0.7288	0.0159	0.0346	0.7142	0.0161	0.0339	0.6379	0.0153	0.0299
-0.05	0.8161	0.0162	0.0382	0.7366	0.0159	0.0339	0.7163	0.0161	0.0327	0.6788	0.0156	0.0301
0.05	0.8073	0.0165	0.0393	0.7571	0.0158	0.0325	0.7579	0.0161	0.0347	0.6927	0.0161	0.0300
0.15	0.7684	0.0161	0.0371	0.7196	0.0151	0.0313	0.7017	0.0155	0.0338	0.7266	0.0158	0.0326
0.25	0.7784	0.0161	0.0366	0.7461	0.0158	0.0331	0.7267	0.0161	0.0336	0.7331	0.0160	0.0334
0.35	0.7841	0.0166	0.0377	0.7427	0.0165	0.0344	0.7062	0.0164	0.0308	0.7045	0.0165	0.0322
0.45	0.7009	0.0165	0.0362	0.6697	0.0158	0.0342	0.6889	0.0168	0.0308	0.6703	0.0163	0.0290
0.55	0.6511	0.0168	0.0353	0.6362	0.0162	0.0325	0.6458	0.0166	0.0298	0.6433	0.0164	0.0277
0.65	0.6496	0.0169	0.0358	0.6218	0.0165	0.0301	0.6028	0.0159	0.0323	0.5825	0.0163	0.0302
0.75	0.5936	0.0166	0.0363	0.5695	0.0161	0.0338	0.5298	0.0155	0.0353	0.5347	0.0162	0.0362
0.85	0.4439	0.0148	0.0307	0.4673	0.0150	0.0349	0.4567	0.0153	0.0305	0.4320	0.0152	0.0328
0.95	0.3637	0.0143	0.0299	0.3332	0.0142	0.0203	0.3330	0.0145	0.0219	0.3267	0.0142	0.0258

$\cos(\theta_\eta^*)$	$E_\gamma{=}(1072.5{\pm}7.5)$ MeV			$E_\gamma{=}(1087.5{\pm}7.5)$ MeV			$E_\gamma{=}(1102.5{\pm}7.5)$ MeV			$E_\gamma{=}(1117.5{\pm}7.5)$ MeV		
	$d\sigma/d\Omega$	Δ_stat	Δ_syst	$d\sigma/d\Omega$	Δ_stat	Δ_syst	$d\sigma/d\Omega$	Δ_stat	Δ_syst	$d\sigma/d\Omega$	Δ_stat	Δ_syst
	[μb/sr]	[μb/sr]	[μb/sr]	[μb/sr]	[μb/sr]	[μb/sr]	[μb/sr]	[μb/sr]	[μb/sr]	[μb/sr]	[μb/sr]	[μb/sr]
-0.95	0.5272	0.0143	0.0295	0.4737	0.0134	0.0283	0.4132	0.0134	0.0248	0.3605	0.0141	0.0192
-0.85	0.5182	0.0139	0.0266	0.4527	0.0134	0.0235	0.4084	0.0131	0.0240	0.3869	0.0140	0.0214
-0.75	0.5394	0.0138	0.0290	0.5023	0.0134	0.0248	0.4250	0.0129	0.0220	0.4218	0.0141	0.0231
-0.65	0.5774	0.0142	0.0289	0.5454	0.0136	0.0259	0.4668	0.0133	0.0211	0.4752	0.0148	0.0234
-0.55	0.5763	0.0141	0.0277	0.5493	0.0139	0.0266	0.5308	0.0142	0.0236	0.4872	0.0146	0.0226
-0.45	0.5957	0.0143	0.0306	0.5715	0.0140	0.0280	0.5355	0.0141	0.0238	0.5058	0.0148	0.0231
-0.35	0.6146	0.0149	0.0310	0.5839	0.0143	0.0287	0.5492	0.0149	0.0248	0.5269	0.0154	0.0255
-0.25	0.6092	0.0157	0.0270	0.6144	0.0156	0.0298	0.5622	0.0154	0.0263	0.5725	0.0167	0.0277
-0.15	0.6583	0.0158	0.0285	0.6288	0.0155	0.0283	0.5863	0.0152	0.0265	0.5752	0.0165	0.0275
-0.05	0.6580	0.0160	0.0308	0.6470	0.0159	0.0278	0.6052	0.0156	0.0253	0.6192	0.0170	0.0278
0.05	0.6859	0.0162	0.0343	0.6662	0.0154	0.0294	0.6383	0.0156	0.0265	0.6083	0.0167	0.0263
0.15	0.6571	0.0156	0.0306	0.6419	0.0154	0.0283	0.6628	0.0157	0.0283	0.6313	0.0168	0.0279
0.25	0.6941	0.0157	0.0299	0.6643	0.0155	0.0279	0.6714	0.0161	0.0288	0.6658	0.0175	0.0304
0.35	0.6772	0.0167	0.0303	0.6549	0.0165	0.0272	0.6685	0.0169	0.0290	0.6513	0.0179	0.0311
0.45	0.7018	0.0171	0.0317	0.6304	0.0165	0.0270	0.6887	0.0178	0.0304	0.6404	0.0189	0.0304
0.55	0.6498	0.0171	0.0280	0.6205	0.0166	0.0273	0.6401	0.0175	0.0299	0.6610	0.0194	0.0326
0.65	0.6075	0.0172	0.0300	0.5961	0.0168	0.0304	0.5754	0.0175	0.0315	0.5795	0.0192	0.0306
0.75	0.5254	0.0162	0.0308	0.5771	0.0171	0.0349	0.5391	0.0171	0.0286	0.5451	0.0191	0.0306
0.85	0.4739	0.0171	0.0272	0.4560	0.0163	0.0336	0.4273	0.0165	0.0229	0.4245	0.0179	0.0273
0.95	0.2855	0.0143	0.0175	0.2778	0.0143	0.0204	0.2774	0.0145	0.0186	0.2812	0.0158	0.0196

$\cos(\theta_\eta^*)$	$E_\gamma{=}(1132.5{\pm}7.5)\,\mathrm{MeV}$			$E_\gamma{=}(1147.5{\pm}7.5)\,\mathrm{MeV}$			$E_\gamma{=}(1162.5{\pm}7.5)\,\mathrm{MeV}$			$E_\gamma{=}(1177.5{\pm}7.5)\,\mathrm{MeV}$		
	$d\sigma/d\Omega$	Δ_stat	Δ_syst	$d\sigma/d\Omega$	Δ_stat	Δ_syst	$d\sigma/d\Omega$	Δ_stat	Δ_syst	$d\sigma/d\Omega$	Δ_stat	Δ_syst
	$[\mu\mathrm{b/sr}]$	$[\mu\mathrm{b/sr}]$	$[\mu\mathrm{b/sr}]$	$[\mu\mathrm{b/sr}]$	$[\mu\mathrm{b/sr}]$	$[\mu\mathrm{b/sr}]$	$[\mu\mathrm{b/sr}]$	$[\mu\mathrm{b/sr}]$	$[\mu\mathrm{b/sr}]$	$[\mu\mathrm{b/sr}]$	$[\mu\mathrm{b/sr}]$	$[\mu\mathrm{b/sr}]$
−0.95	0.3565	0.0131	0.0199	0.3231	0.0136	0.0240	0.3184	0.0128	0.0225	0.2916	0.0123	0.0162
−0.85	0.3464	0.0125	0.0185	0.3253	0.0131	0.0197	0.3023	0.0116	0.0188	0.2842	0.0114	0.0175
−0.75	0.3947	0.0128	0.0203	0.3528	0.0127	0.0195	0.3596	0.0118	0.0211	0.3283	0.0116	0.0223
−0.65	0.4214	0.0132	0.0218	0.4001	0.0128	0.0219	0.3971	0.0123	0.0198	0.3624	0.0121	0.0214
−0.55	0.4354	0.0129	0.0222	0.4483	0.0136	0.0229	0.4224	0.0124	0.0195	0.3721	0.0120	0.0195
−0.45	0.4678	0.0130	0.0231	0.4671	0.0137	0.0216	0.4199	0.0126	0.0185	0.4251	0.0130	0.0208
−0.35	0.4818	0.0135	0.0246	0.4967	0.0147	0.0223	0.4721	0.0135	0.0208	0.4690	0.0136	0.0210
−0.25	0.5462	0.0152	0.0265	0.5267	0.0160	0.0235	0.5301	0.0149	0.0238	0.4729	0.0143	0.0201
−0.15	0.5532	0.0152	0.0248	0.5517	0.0156	0.0259	0.5640	0.0151	0.0253	0.5240	0.0148	0.0219
−0.05	0.6030	0.0155	0.0276	0.5587	0.0158	0.0253	0.5568	0.0148	0.0251	0.5391	0.0149	0.0241
0.05	0.6017	0.0154	0.0264	0.5855	0.0161	0.0245	0.5632	0.0152	0.0243	0.5364	0.0148	0.0258
0.15	0.6359	0.0157	0.0266	0.6190	0.0161	0.0257	0.6172	0.0155	0.0268	0.5660	0.0152	0.0271
0.25	0.6371	0.0156	0.0267	0.6152	0.0164	0.0266	0.6149	0.0152	0.0268	0.6054	0.0155	0.0268
0.35	0.6808	0.0173	0.0317	0.6589	0.0176	0.0302	0.6761	0.0172	0.0289	0.6137	0.0167	0.0260
0.45	0.6500	0.0172	0.0323	0.6493	0.0186	0.0340	0.6135	0.0168	0.0280	0.5951	0.0173	0.0250
0.55	0.6435	0.0176	0.0295	0.5965	0.0183	0.0304	0.5993	0.0173	0.0268	0.5886	0.0174	0.0267
0.65	0.5888	0.0177	0.0288	0.5730	0.0188	0.0278	0.5635	0.0179	0.0245	0.5944	0.0182	0.0308
0.75	0.5710	0.0179	0.0315	0.5472	0.0194	0.0282	0.5410	0.0183	0.0246	0.5426	0.0182	0.0306
0.85	0.4576	0.0165	0.0278	0.4350	0.0182	0.0282	0.4384	0.0175	0.0246	0.4088	0.0174	0.0258
0.95	0.3119	0.0157	0.0181	0.3168	0.0161	0.0261	0.2840	0.0149	0.0189	0.3271	0.0156	0.0298

$\cos(\theta_\eta^*)$	$E_\gamma{=}(1192.5{\pm}7.5)\,\mathrm{MeV}$			$E_\gamma{=}(1207.5{\pm}7.5)\,\mathrm{MeV}$			$E_\gamma{=}(1222.5{\pm}7.5)\,\mathrm{MeV}$			$E_\gamma{=}(1237.5{\pm}7.5)\,\mathrm{MeV}$		
	$d\sigma/d\Omega$	Δ_stat	Δ_syst	$d\sigma/d\Omega$	Δ_stat	Δ_syst	$d\sigma/d\Omega$	Δ_stat	Δ_syst	$d\sigma/d\Omega$	Δ_stat	Δ_syst
	$[\mu\mathrm{b/sr}]$	$[\mu\mathrm{b/sr}]$	$[\mu\mathrm{b/sr}]$	$[\mu\mathrm{b/sr}]$	$[\mu\mathrm{b/sr}]$	$[\mu\mathrm{b/sr}]$	$[\mu\mathrm{b/sr}]$	$[\mu\mathrm{b/sr}]$	$[\mu\mathrm{b/sr}]$	$[\mu\mathrm{b/sr}]$	$[\mu\mathrm{b/sr}]$	$[\mu\mathrm{b/sr}]$
−0.95	0.2689	0.0124	0.0174	0.2558	0.0121	0.0139	0.2343	0.0112	0.0122	0.2201	0.0125	0.0151
−0.85	0.2957	0.0119	0.0172	0.2625	0.0114	0.0148	0.2482	0.0107	0.0155	0.2775	0.0126	0.0159
−0.75	0.3171	0.0116	0.0182	0.2565	0.0107	0.0139	0.2810	0.0107	0.0150	0.2694	0.0119	0.0135
−0.65	0.3341	0.0123	0.0190	0.3145	0.0117	0.0165	0.3065	0.0112	0.0160	0.3206	0.0123	0.0154
−0.55	0.3671	0.0124	0.0186	0.3466	0.0122	0.0175	0.3374	0.0117	0.0165	0.3465	0.0133	0.0166
−0.45	0.4074	0.0132	0.0182	0.4102	0.0132	0.0188	0.3922	0.0127	0.0174	0.3602	0.0136	0.0200
−0.35	0.4331	0.0138	0.0189	0.3958	0.0132	0.0172	0.4016	0.0133	0.0191	0.3837	0.0144	0.0213
−0.25	0.4367	0.0145	0.0189	0.4641	0.0147	0.0204	0.4203	0.0138	0.0218	0.4129	0.0150	0.0201
−0.15	0.4963	0.0147	0.0216	0.5048	0.0149	0.0216	0.4843	0.0146	0.0220	0.4370	0.0153	0.0226
−0.05	0.5441	0.0152	0.0235	0.5213	0.0152	0.0214	0.4883	0.0144	0.0202	0.4947	0.0161	0.0238
0.05	0.5472	0.0157	0.0230	0.5131	0.0153	0.0213	0.5248	0.0149	0.0219	0.5391	0.0172	0.0230
0.15	0.5403	0.0155	0.0235	0.5497	0.0159	0.0242	0.5507	0.0150	0.0233	0.5323	0.0167	0.0223
0.25	0.5884	0.0157	0.0261	0.6058	0.0157	0.0266	0.5845	0.0157	0.0248	0.5156	0.0163	0.0243
0.35	0.6130	0.0172	0.0268	0.6032	0.0169	0.0271	0.5627	0.0161	0.0265	0.5226	0.0182	0.0309
0.45	0.5865	0.0175	0.0265	0.5744	0.0176	0.0278	0.5567	0.0168	0.0295	0.5262	0.0187	0.0296
0.55	0.6050	0.0180	0.0268	0.5378	0.0176	0.0252	0.5756	0.0171	0.0321	0.5394	0.0195	0.0273
0.65	0.5715	0.0188	0.0262	0.5916	0.0184	0.0272	0.5611	0.0182	0.0294	0.5413	0.0191	0.0286
0.75	0.4867	0.0182	0.0254	0.4947	0.0187	0.0267	0.4833	0.0190	0.0263	0.4291	0.0193	0.0234
0.85	0.4119	0.0176	0.0224	0.4293	0.0178	0.0317	0.4364	0.0173	0.0269	0.3941	0.0185	0.0277
0.95	0.2999	0.0167	0.0216	0.3295	0.0171	0.0255	0.3066	0.0161	0.0273	0.2774	0.0171	0.0197

$\cos(\theta_\eta^*)$	$E_\gamma{=}(1252.5{\pm}7.5)\,\mathrm{MeV}$			$E_\gamma{=}(1267.5{\pm}7.5)\,\mathrm{MeV}$			$E_\gamma{=}(1282.5{\pm}7.5)\,\mathrm{MeV}$			$E_\gamma{=}(1297.5{\pm}7.5)\,\mathrm{MeV}$		
	$d\sigma/d\Omega$	Δ_stat	Δ_syst	$d\sigma/d\Omega$	Δ_stat	Δ_syst	$d\sigma/d\Omega$	Δ_stat	Δ_syst	$d\sigma/d\Omega$	Δ_stat	Δ_syst
	$[\mu\mathrm{b/sr}]$	$[\mu\mathrm{b/sr}]$	$[\mu\mathrm{b/sr}]$	$[\mu\mathrm{b/sr}]$	$[\mu\mathrm{b/sr}]$	$[\mu\mathrm{b/sr}]$	$[\mu\mathrm{b/sr}]$	$[\mu\mathrm{b/sr}]$	$[\mu\mathrm{b/sr}]$	$[\mu\mathrm{b/sr}]$	$[\mu\mathrm{b/sr}]$	$[\mu\mathrm{b/sr}]$
−0.95	0.2300	0.0116	0.0214	0.2095	0.0118	0.0128	0.2124	0.0113	0.0127	0.1864	0.0120	0.0115
−0.85	0.2310	0.0108	0.0152	0.2300	0.0111	0.0110	0.2353	0.0107	0.0119	0.2064	0.0109	0.0103
−0.75	0.2728	0.0113	0.0177	0.2652	0.0112	0.0126	0.2544	0.0107	0.0124	0.2403	0.0117	0.0118
−0.65	0.2736	0.0110	0.0161	0.2926	0.0115	0.0150	0.2922	0.0111	0.0142	0.2747	0.0119	0.0137
−0.55	0.3167	0.0122	0.0138	0.2913	0.0120	0.0151	0.3057	0.0115	0.0142	0.2724	0.0122	0.0134
−0.45	0.3545	0.0129	0.0147	0.3464	0.0132	0.0169	0.3317	0.0124	0.0154	0.2945	0.0134	0.0132
−0.35	0.3945	0.0138	0.0162	0.3469	0.0137	0.0164	0.3634	0.0131	0.0178	0.3750	0.0146	0.0165
−0.25	0.4307	0.0151	0.0179	0.4251	0.0151	0.0200	0.3949	0.0141	0.0198	0.3489	0.0147	0.0157
−0.15	0.4408	0.0150	0.0201	0.4145	0.0148	0.0202	0.4324	0.0145	0.0214	0.3820	0.0150	0.0162
−0.05	0.4310	0.0143	0.0213	0.4809	0.0153	0.0229	0.4387	0.0144	0.0215	0.4153	0.0156	0.0173
0.05	0.4922	0.0156	0.0220	0.4483	0.0149	0.0200	0.4661	0.0144	0.0232	0.4275	0.0155	0.0192
0.15	0.5166	0.0156	0.0211	0.4672	0.0153	0.0218	0.4894	0.0148	0.0232	0.4514	0.0164	0.0204
0.25	0.5437	0.0162	0.0234	0.5261	0.0164	0.0247	0.5190	0.0158	0.0224	0.4863	0.0167	0.0223
0.35	0.5620	0.0168	0.0270	0.5127	0.0169	0.0269	0.4958	0.0166	0.0215	0.4346	0.0172	0.0217
0.45	0.5158	0.0180	0.0260	0.5141	0.0178	0.0314	0.5116	0.0171	0.0223	0.5108	0.0192	0.0260
0.55	0.5067	0.0175	0.0260	0.5410	0.0190	0.0296	0.5356	0.0177	0.0239	0.4895	0.0195	0.0234
0.65	0.5082	0.0183	0.0248	0.5097	0.0194	0.0261	0.5041	0.0186	0.0237	0.4829	0.0209	0.0243
0.75	0.5005	0.0195	0.0222	0.4648	0.0197	0.0278	0.4370	0.0185	0.0235	0.4626	0.0212	0.0249
0.85	0.3867	0.0177	0.0230	0.3672	0.0187	0.0255	0.3697	0.0160	0.0289	0.3599	0.0212	0.0262
0.95	0.3156	0.0177	0.0271	0.2979	0.0180	0.0320	0.2812	0.0165	0.0335	0.2758	0.0192	0.0340

$\cos(\theta_\eta^*)$	$E_\gamma=(1312.5\pm7.5)\,\text{MeV}$			$E_\gamma=(1327.5\pm7.5)\,\text{MeV}$			$E_\gamma=(1342.5\pm7.5)\,\text{MeV}$			$E_\gamma=(1357.5\pm7.5)\,\text{MeV}$		
	$d\sigma/d\Omega$	Δ_stat	Δ_syst	$d\sigma/d\Omega$	Δ_stat	Δ_syst	$d\sigma/d\Omega$	Δ_stat	Δ_syst	$d\sigma/d\Omega$	Δ_stat	Δ_syst
	[μb/sr]	[μb/sr]	[μb/sr]	[μb/sr]	[μb/sr]	[μb/sr]	[μb/sr]	[μb/sr]	[μb/sr]	[μb/sr]	[μb/sr]	[μb/sr]
−0.95	0.1787	0.0105	0.0146	0.2074	0.0135	0.0114	0.1801	0.0135	0.0113	0.1687	0.0107	0.0101
−0.85	0.2124	0.0105	0.0118	0.1865	0.0127	0.0118	0.1949	0.0126	0.0122	0.2206	0.0110	0.0125
−0.75	0.2140	0.0102	0.0110	0.1961	0.0120	0.0106	0.2193	0.0124	0.0134	0.2086	0.0104	0.0107
−0.65	0.2841	0.0112	0.0130	0.2560	0.0133	0.0120	0.2429	0.0133	0.0124	0.2533	0.0115	0.0124
−0.55	0.2708	0.0116	0.0120	0.2413	0.0136	0.0110	0.2703	0.0141	0.0123	0.2507	0.0120	0.0126
−0.45	0.3310	0.0128	0.0147	0.3226	0.0158	0.0142	0.3088	0.0157	0.0159	0.2728	0.0125	0.0130
−0.35	0.3385	0.0132	0.0161	0.2963	0.0157	0.0133	0.3022	0.0155	0.0170	0.2937	0.0132	0.0126
−0.25	0.3455	0.0139	0.0161	0.3294	0.0163	0.0150	0.3623	0.0167	0.0186	0.3154	0.0143	0.0136
−0.15	0.4121	0.0145	0.0184	0.3294	0.0162	0.0148	0.3306	0.0171	0.0144	0.3572	0.0147	0.0164
−0.05	0.4376	0.0147	0.0215	0.3840	0.0177	0.0180	0.3647	0.0176	0.0173	0.3911	0.0154	0.0206
0.05	0.4304	0.0146	0.0211	0.4338	0.0185	0.0204	0.3945	0.0174	0.0215	0.3836	0.0149	0.0192
0.15	0.4702	0.0152	0.0200	0.4113	0.0179	0.0191	0.4091	0.0181	0.0205	0.4067	0.0147	0.0173
0.25	0.4549	0.0152	0.0189	0.4358	0.0183	0.0202	0.4538	0.0188	0.0204	0.4112	0.0150	0.0167
0.35	0.4438	0.0162	0.0182	0.4311	0.0195	0.0214	0.4221	0.0197	0.0191	0.4401	0.0173	0.0192
0.45	0.4852	0.0172	0.0205	0.4517	0.0211	0.0231	0.4677	0.0211	0.0246	0.4286	0.0167	0.0218
0.55	0.4609	0.0176	0.0233	0.4696	0.0221	0.0298	0.4337	0.0215	0.0267	0.3996	0.0173	0.0215
0.65	0.4238	0.0179	0.0232	0.4415	0.0228	0.0273	0.4612	0.0232	0.0259	0.4499	0.0194	0.0228
0.75	0.4498	0.0196	0.0207	0.4266	0.0218	0.0241	0.3860	0.0237	0.0225	0.4029	0.0202	0.0182
0.85	0.3487	0.0189	0.0169	0.3856	0.0224	0.0214	0.4147	0.0219	0.0254	0.3481	0.0184	0.0173
0.95	0.2907	0.0170	0.0321	0.2856	0.0230	0.0312	0.2269	0.0190	0.0292	0.2823	0.0185	0.0200

$\cos(\theta_\eta^*)$	$E_\gamma=(1372.5\pm7.5)\,\text{MeV}$			$E_\gamma=(1387.5\pm7.5)\,\text{MeV}$		
	$d\sigma/d\Omega$	Δ_stat	Δ_syst	$d\sigma/d\Omega$	Δ_stat	Δ_syst
	[μb/sr]	[μb/sr]	[μb/sr]	[μb/sr]	[μb/sr]	[μb/sr]
−0.95	0.1676	0.0118	0.0146	0.1960	0.0121	0.0159
−0.85	0.1857	0.0110	0.0117	0.2028	0.0114	0.0101
−0.75	0.2209	0.0113	0.0124	0.2191	0.0112	0.0104
−0.65	0.2275	0.0110	0.0108	0.2223	0.0115	0.0117
−0.55	0.2507	0.0125	0.0113	0.2505	0.0127	0.0135
−0.45	0.2596	0.0128	0.0135	0.2550	0.0129	0.0124
−0.35	0.2934	0.0135	0.0152	0.2706	0.0132	0.0118
−0.25	0.3080	0.0142	0.0135	0.2943	0.0149	0.0132
−0.15	0.3487	0.0149	0.0147	0.3203	0.0146	0.0173
−0.05	0.3832	0.0149	0.0162	0.3677	0.0154	0.0187
0.05	0.3973	0.0157	0.0187	0.3869	0.0155	0.0185
0.15	0.4082	0.0154	0.0233	0.4117	0.0162	0.0201
0.25	0.3887	0.0161	0.0206	0.3809	0.0160	0.0170
0.35	0.4423	0.0176	0.0202	0.4325	0.0174	0.0212
0.45	0.4144	0.0181	0.0180	0.3952	0.0192	0.0237
0.55	0.4474	0.0192	0.0215	0.4076	0.0187	0.0269
0.65	0.4503	0.0203	0.0251	0.4113	0.0194	0.0298
0.75	0.3835	0.0195	0.0208	0.3794	0.0204	0.0267
0.85	0.3560	0.0199	0.0222	0.3357	0.0204	0.0220
0.95	0.1930	0.0164	0.0299	0.2533	0.0203	0.0225

Total cross section of $\gamma N \to \eta(N)$ as a function of E_γ

E_γ [MeV]	ΔE_γ [MeV]	σ [μb]	Δ_{stat} [μb]	Δ_{syst} [μb]
645.0	15.0	0.4089	0.0043	0.0420
667.5	7.5	1.2714	0.0090	0.1015
682.5	7.5	2.7343	0.0121	0.1989
697.5	7.5	5.0954	0.0163	0.3334
712.5	7.5	8.4311	0.0201	0.4930
727.5	7.5	12.2778	0.0269	0.6907
742.5	7.5	15.6209	0.0290	0.8446
757.5	7.5	18.0604	0.0315	0.9465
772.5	7.5	19.7581	0.0351	1.0363
787.5	7.5	20.5568	0.0358	1.0654
802.5	7.5	20.5825	0.0385	1.0576
817.5	7.5	19.9042	0.0419	1.0398
832.5	7.5	19.1969	0.0483	0.9788
847.5	7.5	18.2310	0.0543	0.9161
862.5	7.5	16.8782	0.0550	0.8482
877.5	7.5	16.2559	0.0585	0.8138
892.5	7.5	14.9725	0.0592	0.7600
907.5	7.5	13.9277	0.0476	0.6780
922.5	7.5	12.8662	0.0465	0.6157
937.5	7.5	12.0032	0.0477	0.5767
952.5	7.5	11.1187	0.0453	0.5486
967.5	7.5	10.4059	0.0446	0.4961
982.5	7.5	9.7943	0.0470	0.4800
997.5	7.5	9.2661	0.0463	0.4497
1012.5	7.5	8.8346	0.0446	0.4501
1027.5	7.5	8.3572	0.0433	0.4134
1042.5	7.5	8.0356	0.0436	0.3965
1057.5	7.5	7.6989	0.0430	0.3767
1072.5	7.5	7.4207	0.0436	0.3637
1087.5	7.5	7.1169	0.0427	0.3492
1102.5	7.5	6.8167	0.0433	0.3240
1117.5	7.5	6.6530	0.0467	0.3305
1132.5	7.5	6.5120	0.0429	0.3185
1147.5	7.5	6.2989	0.0448	0.3187
1162.5	7.5	6.1687	0.0421	0.2943
1177.5	7.5	5.9200	0.0420	0.3015
1192.5	7.5	5.7408	0.0429	0.2762
1207.5	7.5	5.6190	0.0426	0.2759
1222.5	7.5	5.4801	0.0413	0.2788
1237.5	7.5	5.2294	0.0451	0.2764
1252.5	7.5	5.1537	0.0428	0.2623
1267.5	7.5	4.9802	0.0436	0.2692
1282.5	7.5	4.9358	0.0412	0.2567
1297.5	7.5	4.6170	0.0456	0.2406
1312.5	7.5	4.5647	0.0417	0.2297
1327.5	7.5	4.3355	0.0506	0.2317
1342.5	7.5	4.2782	0.0502	0.2395
1357.5	7.5	4.1884	0.0425	0.2060
1372.5	7.5	4.0753	0.0436	0.2241
1387.5	7.5	4.0154	0.0448	0.2276

Quasi-free exclusive η-photoproduction on the proton

Differential cross sections of $\gamma p \to \eta p$ as a function of E_γ

$\cos(\theta_\eta^*)$	E_γ=(645.0±15.0) MeV			E_γ=(667.5±7.5) MeV			E_γ=(682.5±7.5) MeV			E_γ=(697.5±7.5) MeV		
	$d\sigma/d\Omega$ [μb/sr]	Δ_{stat} [μb/sr]	Δ_{syst} [μb/sr]	$d\sigma/d\Omega$ [μb/sr]	Δ_{stat} [μb/sr]	Δ_{syst} [μb/sr]	$d\sigma/d\Omega$ [μb/sr]	Δ_{stat} [μb/sr]	Δ_{syst} [μb/sr]	$d\sigma/d\Omega$ [μb/sr]	Δ_{stat} [μb/sr]	Δ_{syst} [μb/sr]
−0.95	0.0528	0.0048	0.0051	0.1764	0.0073	0.0086	0.3039	0.0079	0.0147	0.4892	0.0096	0.0211
−0.85	0.0560	0.0053	0.0048	0.1259	0.0066	0.0067	0.2318	0.0065	0.0123	0.3983	0.0078	0.0199
−0.75	0.0273	0.0053	0.0024	0.1034	0.0066	0.0059	0.1935	0.0062	0.0100	0.3252	0.0071	0.0156
−0.65	0.0419	0.0062	0.0068	0.0801	0.0066	0.0047	0.1683	0.0061	0.0085	0.3044	0.0070	0.0139
−0.55	0.0217	0.0066	0.0072	0.0595	0.0067	0.0040	0.1365	0.0059	0.0068	0.2768	0.0068	0.0123
−0.45	0.0087	0.0068	0.0045	0.0695	0.0071	0.0051	0.1295	0.0060	0.0066	0.2667	0.0070	0.0123
−0.35	0.0132	0.0072	0.0023	0.0503	0.0073	0.0038	0.1227	0.0064	0.0062	0.2516	0.0071	0.0117
−0.25	0.0088	0.0074	0.0020	0.0338	0.0075	0.0028	0.1158	0.0066	0.0068	0.2244	0.0072	0.0103
−0.15	0.0228	0.0093	0.0054	0.0239	0.0080	0.0025	0.0988	0.0067	0.0058	0.2209	0.0074	0.0103
−0.05	0.0084	0.0092	0.0034	0.0272	0.0085	0.0045	0.0977	0.0070	0.0053	0.2077	0.0076	0.0094
0.05	0.0049	0.0083	0.0022	0.0169	0.0086	0.0037	0.0764	0.0070	0.0043	0.1903	0.0077	0.0097
0.15	0.0294	0.0125	0.0088	0.0237	0.0092	0.0057	0.0732	0.0072	0.0045	0.1814	0.0079	0.0117
0.25	0.0045	0.0088	0.0013	0.0123	0.0096	0.0064	0.0571	0.0074	0.0043	0.1659	0.0079	0.0110
0.35	0.0143	0.0117	0.0053	0.0025	0.0097	0.0007	0.0534	0.0074	0.0037	0.1440	0.0078	0.0082
0.45	0.0002	0.0087	0.0001	0.0190	0.0098	0.0023	0.0614	0.0077	0.0045	0.1338	0.0079	0.0074
0.55	−0.0080	0.0103	0.0035	0.0327	0.0112	0.0101	0.0433	0.0078	0.0049	0.1407	0.0080	0.0069
0.65	0.0135	0.0168	0.0099	0.0113	0.0107	0.0021	0.0337	0.0074	0.0029	0.1206	0.0078	0.0066
0.75	−0.0102	0.0182	0.0076	0.0411	0.0114	0.0161	0.0507	0.0077	0.0038	0.1080	0.0074	0.0087
0.85	0.0083	0.0100	0.0068	−0.0012	0.0091	0.0008	0.0419	0.0075	0.0047	0.1158	0.0077	0.0094
0.95	−0.0004	0.0115	0.0005	0.0166	0.0098	0.0065	0.0406	0.0078	0.0086	0.0995	0.0082	0.0061

$\cos(\theta_\eta^*)$	E_γ=(712.5±7.5) MeV			E_γ=(727.5±7.5) MeV			E_γ=(742.5±7.5) MeV			E_γ=(757.5±7.5) MeV		
	$d\sigma/d\Omega$ [μb/sr]	Δ_{stat} [μb/sr]	Δ_{syst} [μb/sr]	$d\sigma/d\Omega$ [μb/sr]	Δ_{stat} [μb/sr]	Δ_{syst} [μb/sr]	$d\sigma/d\Omega$ [μb/sr]	Δ_{stat} [μb/sr]	Δ_{syst} [μb/sr]	$d\sigma/d\Omega$ [μb/sr]	Δ_{stat} [μb/sr]	Δ_{syst} [μb/sr]
−0.95	0.6852	0.0108	0.0289	0.8648	0.0133	0.0366	1.0296	0.0137	0.0443	1.1020	0.0145	0.0469
−0.85	0.5671	0.0085	0.0262	0.7286	0.0103	0.0320	0.8694	0.0103	0.0377	0.9337	0.0105	0.0407
−0.75	0.5058	0.0078	0.0243	0.6701	0.0096	0.0305	0.8033	0.0095	0.0355	0.8655	0.0097	0.0387
−0.65	0.5023	0.0079	0.0226	0.6514	0.0096	0.0286	0.7943	0.0095	0.0362	0.8785	0.0099	0.0390
−0.55	0.4552	0.0077	0.0196	0.6437	0.0098	0.0281	0.7826	0.0097	0.0351	0.8751	0.0102	0.0389
−0.45	0.4357	0.0077	0.0189	0.6309	0.0100	0.0282	0.8157	0.0103	0.0369	0.9108	0.0108	0.0405
−0.35	0.4264	0.0079	0.0199	0.6315	0.0104	0.0303	0.8144	0.0107	0.0379	0.9169	0.0133	0.0400
−0.25	0.3973	0.0079	0.0190	0.6237	0.0107	0.0288	0.8032	0.0111	0.0352	0.9330	0.0151	0.0419
−0.15	0.3976	0.0083	0.0180	0.6132	0.0110	0.0265	0.8123	0.0116	0.0357	0.9490	0.0159	0.0431
−0.05	0.3668	0.0083	0.0161	0.5876	0.0111	0.0274	0.7998	0.0120	0.0379	0.9127	0.0161	0.0407
0.05	0.3533	0.0086	0.0165	0.5537	0.0113	0.0273	0.7814	0.0124	0.0374	0.8981	0.0169	0.0402
0.15	0.3221	0.0085	0.0159	0.5399	0.0115	0.0244	0.7380	0.0126	0.0336	0.9112	0.0178	0.0407
0.25	0.3182	0.0089	0.0160	0.4861	0.0114	0.0215	0.7089	0.0130	0.0317	0.8574	0.0168	0.0394
0.35	0.3202	0.0092	0.0162	0.4929	0.0118	0.0254	0.7063	0.0135	0.0335	0.8505	0.0149	0.0395
0.45	0.2876	0.0091	0.0137	0.4935	0.0121	0.0277	0.6530	0.0136	0.0309	0.8457	0.0156	0.0437
0.55	0.2907	0.0092	0.0130	0.4803	0.0122	0.0261	0.6483	0.0140	0.0309	0.7834	0.0160	0.0435
0.65	0.2737	0.0091	0.0130	0.4435	0.0119	0.0236	0.6262	0.0141	0.0304	0.7687	0.0165	0.0394
0.75	0.2514	0.0087	0.0147	0.4374	0.0118	0.0229	0.6049	0.0138	0.0306	0.7208	0.0163	0.0353
0.85	0.2361	0.0086	0.0150	0.4374	0.0119	0.0228	0.6206	0.0139	0.0322	0.7154	0.0162	0.0385
0.95	0.2738	0.0104	0.0144	0.4433	0.0136	0.0252	0.6142	0.0154	0.0312	0.7419	0.0178	0.0466

	$E_\gamma=(772.5\pm7.5)$ MeV			$E_\gamma=(787.5\pm7.5)$ MeV			$E_\gamma=(802.5\pm7.5)$ MeV			$E_\gamma=(817.5\pm7.5)$ MeV		
$\cos(\theta^*_\eta)$	$d\sigma/d\Omega$ $[\mu\text{b/sr}]$	Δ_stat $[\mu\text{b/sr}]$	Δ_syst $[\mu\text{b/sr}]$	$d\sigma/d\Omega$ $[\mu\text{b/sr}]$	Δ_stat $[\mu\text{b/sr}]$	Δ_syst $[\mu\text{b/sr}]$	$d\sigma/d\Omega$ $[\mu\text{b/sr}]$	Δ_stat $[\mu\text{b/sr}]$	Δ_syst $[\mu\text{b/sr}]$	$d\sigma/d\Omega$ $[\mu\text{b/sr}]$	Δ_stat $[\mu\text{b/sr}]$	Δ_syst $[\mu\text{b/sr}]$
−0.95	1.1272	0.0155	0.0483	1.1015	0.0148	0.0517	1.0746	0.0146	0.0471	1.0301	0.0147	0.0503
−0.85	0.9487	0.0109	0.0418	0.9720	0.0106	0.0410	0.9761	0.0105	0.0449	0.9230	0.0105	0.0441
−0.75	0.9488	0.0104	0.0425	0.9462	0.0100	0.0415	0.9527	0.0100	0.0460	0.9080	0.0100	0.0432
−0.65	0.9363	0.0105	0.0422	0.9564	0.0102	0.0434	0.9622	0.0103	0.0474	0.9299	0.0124	0.0471
−0.55	0.9377	0.0110	0.0410	0.9946	0.0139	0.0432	0.9664	0.0136	0.0487	0.9494	0.0141	0.0481
−0.45	0.9665	0.0144	0.0417	1.0166	0.0145	0.0437	1.0338	0.0146	0.0539	0.9916	0.0149	0.0450
−0.35	0.9902	0.0151	0.0424	1.0670	0.0156	0.0463	1.1103	0.0158	0.0530	1.0234	0.0158	0.0446
−0.25	1.0136	0.0160	0.0450	1.0651	0.0163	0.0481	1.0736	0.0162	0.0473	1.0764	0.0170	0.0489
−0.15	0.9958	0.0164	0.0454	1.0659	0.0167	0.0493	1.0708	0.0164	0.0453	1.0896	0.0172	0.0493
−0.05	0.9829	0.0167	0.0425	1.0183	0.0166	0.0448	1.0710	0.0165	0.0459	1.0538	0.0169	0.0481
0.05	0.9842	0.0174	0.0417	1.0509	0.0171	0.0465	1.0163	0.0162	0.0454	1.0312	0.0166	0.0458
0.15	1.0008	0.0183	0.0435	0.9838	0.0170	0.0457	0.9937	0.0162	0.0442	1.0138	0.0166	0.0432
0.25	0.9859	0.0191	0.0432	0.9985	0.0178	0.0451	1.0246	0.0169	0.0450	0.9920	0.0167	0.0443
0.35	0.9542	0.0199	0.0435	1.0350	0.0191	0.0448	1.0297	0.0177	0.0448	1.0101	0.0174	0.0464
0.45	1.0014	0.0203	0.0484	1.0197	0.0204	0.0443	1.0073	0.0188	0.0441	0.9932	0.0184	0.0430
0.55	0.8900	0.0180	0.0445	0.9467	0.0216	0.0489	0.9719	0.0203	0.0453	0.9632	0.0198	0.0427
0.65	0.8923	0.0195	0.0450	0.9526	0.0193	0.0642	0.9838	0.0236	0.0507	0.9858	0.0232	0.0491
0.75	0.8865	0.0207	0.0465	0.9226	0.0213	0.0590	0.9727	0.0221	0.0546	1.0092	0.0226	0.0629
0.85	0.7951	0.0197	0.0433	0.8876	0.0221	0.0492	0.9050	0.0244	0.0564	0.9472	0.0273	0.0692
0.95	0.8268	0.0213	0.0463	0.8192	0.0229	0.0472	0.8410	0.0259	0.0787	0.8775	0.0307	0.0640

	$E_\gamma=(832.5\pm7.5)$ MeV			$E_\gamma=(847.5\pm7.5)$ MeV			$E_\gamma=(862.5\pm7.5)$ MeV			$E_\gamma=(877.5\pm7.5)$ MeV		
$\cos(\theta^*_\eta)$	$d\sigma/d\Omega$ $[\mu\text{b/sr}]$	Δ_stat $[\mu\text{b/sr}]$	Δ_syst $[\mu\text{b/sr}]$	$d\sigma/d\Omega$ $[\mu\text{b/sr}]$	Δ_stat $[\mu\text{b/sr}]$	Δ_syst $[\mu\text{b/sr}]$	$d\sigma/d\Omega$ $[\mu\text{b/sr}]$	Δ_stat $[\mu\text{b/sr}]$	Δ_syst $[\mu\text{b/sr}]$	$d\sigma/d\Omega$ $[\mu\text{b/sr}]$	Δ_stat $[\mu\text{b/sr}]$	Δ_syst $[\mu\text{b/sr}]$
−0.95	0.9713	0.0154	0.0427	0.9313	0.0163	0.0436	0.8459	0.0155	0.0364	0.7771	0.0154	0.0342
−0.85	0.9035	0.0112	0.0430	0.8379	0.0116	0.0398	0.7836	0.0113	0.0351	0.7518	0.0115	0.0342
−0.75	0.8908	0.0108	0.0442	0.8426	0.0114	0.0407	0.8085	0.0113	0.0382	0.7360	0.0116	0.0326
−0.65	0.9077	0.0144	0.0447	0.8733	0.0156	0.0420	0.8037	0.0153	0.0386	0.8099	0.0190	0.0375
−0.55	0.9080	0.0148	0.0439	0.8761	0.0160	0.0413	0.8264	0.0158	0.0385	0.8216	0.0196	0.0373
−0.45	0.9656	0.0157	0.0435	0.9572	0.0173	0.0431	0.8980	0.0170	0.0403	0.8520	0.0204	0.0363
−0.35	1.0021	0.0167	0.0442	0.9801	0.0180	0.0445	0.9476	0.0180	0.0407	0.8703	0.0214	0.0362
−0.25	1.0305	0.0176	0.0458	0.9668	0.0185	0.0437	0.9555	0.0186	0.0398	0.9280	0.0226	0.0400
−0.15	1.0003	0.0172	0.0435	1.0274	0.0188	0.0446	0.9208	0.0179	0.0386	0.9145	0.0220	0.0399
−0.05	1.0604	0.0177	0.0458	0.9792	0.0182	0.0423	0.9478	0.0179	0.0404	0.8784	0.0213	0.0377
0.05	1.0260	0.0171	0.0457	0.9944	0.0180	0.0432	0.8991	0.0171	0.0413	0.8774	0.0209	0.0394
0.15	0.9917	0.0169	0.0455	0.9781	0.0179	0.0439	0.9013	0.0171	0.0430	0.8503	0.0206	0.0433
0.25	0.9763	0.0169	0.0438	0.9418	0.0177	0.0424	0.8866	0.0171	0.0424	0.8463	0.0206	0.0453
0.35	0.9949	0.0177	0.0438	0.9300	0.0183	0.0411	0.8535	0.0173	0.0397	0.8648	0.0216	0.0415
0.45	0.9487	0.0182	0.0419	0.9279	0.0190	0.0397	0.8669	0.0170	0.0376	0.8340	0.0196	0.0364
0.55	0.9767	0.0199	0.0425	0.9032	0.0199	0.0385	0.8456	0.0176	0.0372	0.8208	0.0156	0.0343
0.65	0.8944	0.0219	0.0416	0.8647	0.0206	0.0376	0.8344	0.0164	0.0361	0.7585	0.0164	0.0322
0.75	0.9346	0.0262	0.0534	0.9191	0.0267	0.0425	0.8571	0.0207	0.0396	0.7846	0.0207	0.0390
0.85	0.8517	0.0287	0.0531	0.7812	0.0301	0.0515	0.7399	0.0286	0.0432	0.7348	0.0305	0.0485
0.95	0.7816	0.0351	0.0542	0.6749	0.0394	0.0793	0.6962	0.0436	0.0461	0.7209	0.0510	0.0545

	$E_\gamma=(892.5\pm7.5)$ MeV			$E_\gamma=(907.5\pm7.5)$ MeV			$E_\gamma=(922.5\pm7.5)$ MeV			$E_\gamma=(937.5\pm7.5)$ MeV		
$\cos(\theta^*_\eta)$	$d\sigma/d\Omega$ $[\mu\text{b/sr}]$	Δ_stat $[\mu\text{b/sr}]$	Δ_syst $[\mu\text{b/sr}]$	$d\sigma/d\Omega$ $[\mu\text{b/sr}]$	Δ_stat $[\mu\text{b/sr}]$	Δ_syst $[\mu\text{b/sr}]$	$d\sigma/d\Omega$ $[\mu\text{b/sr}]$	Δ_stat $[\mu\text{b/sr}]$	Δ_syst $[\mu\text{b/sr}]$	$d\sigma/d\Omega$ $[\mu\text{b/sr}]$	Δ_stat $[\mu\text{b/sr}]$	Δ_syst $[\mu\text{b/sr}]$
−0.95	0.7485	0.0156	0.0324	0.6892	0.0126	0.0302	0.6087	0.0120	0.0265	0.5245	0.0118	0.0232
−0.85	0.7134	0.0116	0.0334	0.6751	0.0094	0.0312	0.5685	0.0087	0.0259	0.5097	0.0087	0.0223
−0.75	0.7363	0.0120	0.0342	0.6664	0.0094	0.0315	0.6047	0.0091	0.0287	0.5569	0.0112	0.0266
−0.65	0.7400	0.0189	0.0352	0.6825	0.0125	0.0323	0.6412	0.0128	0.0303	0.5453	0.0126	0.0268
−0.55	0.7463	0.0194	0.0347	0.6943	0.0130	0.0318	0.6563	0.0134	0.0298	0.5912	0.0135	0.0266
−0.45	0.7758	0.0202	0.0346	0.7249	0.0134	0.0320	0.6750	0.0137	0.0288	0.6206	0.0139	0.0271
−0.35	0.7996	0.0210	0.0338	0.7265	0.0137	0.0298	0.6707	0.0138	0.0273	0.6180	0.0139	0.0266
−0.25	0.8078	0.0217	0.0334	0.7392	0.0140	0.0301	0.6717	0.0140	0.0274	0.6196	0.0142	0.0268
−0.15	0.7931	0.0210	0.0330	0.7230	0.0136	0.0299	0.6549	0.0135	0.0273	0.6103	0.0137	0.0279
−0.05	0.8028	0.0207	0.0343	0.7283	0.0134	0.0306	0.6543	0.0132	0.0299	0.6099	0.0135	0.0283
0.05	0.7949	0.0204	0.0357	0.7490	0.0135	0.0318	0.6516	0.0132	0.0309	0.6050	0.0134	0.0268
0.15	0.7612	0.0200	0.0369	0.7107	0.0131	0.0321	0.6566	0.0123	0.0288	0.5752	0.0101	0.0262
0.25	0.8130	0.0207	0.0428	0.7037	0.0123	0.0339	0.6424	0.0102	0.0281	0.5680	0.0099	0.0292
0.35	0.7879	0.0189	0.0385	0.7055	0.0107	0.0326	0.6361	0.0103	0.0297	0.5970	0.0103	0.0316
0.45	0.7723	0.0147	0.0329	0.6822	0.0108	0.0309	0.6135	0.0103	0.0281	0.5230	0.0099	0.0271
0.55	0.7254	0.0147	0.0299	0.6344	0.0108	0.0289	0.5604	0.0101	0.0235	0.5214	0.0102	0.0231
0.65	0.7121	0.0158	0.0300	0.6443	0.0117	0.0276	0.5697	0.0110	0.0237	0.4802	0.0104	0.0199
0.75	0.6861	0.0189	0.0337	0.6233	0.0137	0.0269	0.5303	0.0125	0.0225	0.4772	0.0121	0.0211
0.85	0.6628	0.0286	0.0520	0.6181	0.0209	0.0305	0.5098	0.0184	0.0270	0.4750	0.0180	0.0259
0.95	0.7459	0.0563	0.0971	0.5219	0.0385	0.0418	0.5103	0.0388	0.0509	0.4856	0.0393	0.0380

$\cos(\theta_\eta^*)$	$E_\gamma=(952.5\pm7.5)$ MeV			$E_\gamma=(967.5\pm7.5)$ MeV			$E_\gamma=(982.5\pm7.5)$ MeV			$E_\gamma=(997.5\pm7.5)$ MeV		
	$d\sigma/d\Omega$ [μb/sr]	$\Delta_{\rm stat}$ [μb/sr]	$\Delta_{\rm syst}$ [μb/sr]	$d\sigma/d\Omega$ [μb/sr]	$\Delta_{\rm stat}$ [μb/sr]	$\Delta_{\rm syst}$ [μb/sr]	$d\sigma/d\Omega$ [μb/sr]	$\Delta_{\rm stat}$ [μb/sr]	$\Delta_{\rm syst}$ [μb/sr]	$d\sigma/d\Omega$ [μb/sr]	$\Delta_{\rm stat}$ [μb/sr]	$\Delta_{\rm syst}$ [μb/sr]
−0.95	0.4478	0.0109	0.0221	0.4093	0.0106	0.0207	0.3871	0.0112	0.0188	0.3406	0.0106	0.0155
−0.85	0.4569	0.0082	0.0210	0.3996	0.0078	0.0189	0.3467	0.0079	0.0158	0.3060	0.0075	0.0157
−0.75	0.4878	0.0113	0.0233	0.4349	0.0109	0.0211	0.3877	0.0113	0.0184	0.3785	0.0113	0.0202
−0.65	0.5006	0.0117	0.0243	0.4805	0.0117	0.0234	0.4204	0.0119	0.0192	0.3436	0.0110	0.0171
−0.55	0.5511	0.0126	0.0249	0.4909	0.0120	0.0223	0.4349	0.0124	0.0189	0.4116	0.0122	0.0197
−0.45	0.5455	0.0126	0.0226	0.4800	0.0120	0.0203	0.4291	0.0124	0.0184	0.3936	0.0119	0.0177
−0.35	0.5622	0.0128	0.0229	0.5040	0.0123	0.0209	0.4591	0.0127	0.0199	0.4031	0.0120	0.0168
−0.25	0.5452	0.0127	0.0226	0.5060	0.0124	0.0208	0.4448	0.0125	0.0193	0.4235	0.0124	0.0172
−0.15	0.5437	0.0124	0.0228	0.4971	0.0120	0.0205	0.4403	0.0122	0.0185	0.3998	0.0117	0.0164
−0.05	0.5095	0.0119	0.0210	0.5067	0.0120	0.0206	0.4356	0.0120	0.0183	0.3803	0.0113	0.0158
0.05	0.5285	0.0120	0.0220	0.4700	0.0108	0.0200	0.4230	0.0092	0.0185	0.3881	0.0088	0.0180
0.15	0.5274	0.0094	0.0239	0.4669	0.0089	0.0219	0.4202	0.0090	0.0194	0.3854	0.0086	0.0203
0.25	0.5199	0.0092	0.0256	0.4660	0.0088	0.0239	0.4106	0.0088	0.0197	0.3913	0.0086	0.0180
0.35	0.5167	0.0093	0.0276	0.4519	0.0089	0.0240	0.4270	0.0092	0.0199	0.3617	0.0084	0.0174
0.45	0.4848	0.0092	0.0273	0.4574	0.0091	0.0215	0.4141	0.0093	0.0191	0.3625	0.0086	0.0211
0.55	0.4531	0.0092	0.0230	0.4182	0.0090	0.0191	0.3624	0.0089	0.0164	0.3238	0.0084	0.0184
0.65	0.4453	0.0098	0.0199	0.3776	0.0091	0.0169	0.3403	0.0092	0.0169	0.3012	0.0087	0.0142
0.75	0.4314	0.0111	0.0193	0.3597	0.0101	0.0159	0.3112	0.0101	0.0175	0.2782	0.0094	0.0137
0.85	0.4326	0.0164	0.0228	0.3505	0.0146	0.0222	0.2847	0.0139	0.0183	0.2620	0.0131	0.0166
0.95	0.4428	0.0367	0.0350	0.3151	0.0309	0.0309	0.2946	0.0315	0.0416	0.2527	0.0289	0.0209

$\cos(\theta_\eta^*)$	$E_\gamma=(1012.5\pm7.5)$ MeV			$E_\gamma=(1027.5\pm7.5)$ MeV			$E_\gamma=(1042.5\pm7.5)$ MeV			$E_\gamma=(1057.5\pm7.5)$ MeV		
	$d\sigma/d\Omega$ [μb/sr]	$\Delta_{\rm stat}$ [μb/sr]	$\Delta_{\rm syst}$ [μb/sr]	$d\sigma/d\Omega$ [μb/sr]	$\Delta_{\rm stat}$ [μb/sr]	$\Delta_{\rm syst}$ [μb/sr]	$d\sigma/d\Omega$ [μb/sr]	$\Delta_{\rm stat}$ [μb/sr]	$\Delta_{\rm syst}$ [μb/sr]	$d\sigma/d\Omega$ [μb/sr]	$\Delta_{\rm stat}$ [μb/sr]	$\Delta_{\rm syst}$ [μb/sr]
−0.95	0.3190	0.0103	0.0155	0.2915	0.0098	0.0138	0.2567	0.0096	0.0113	0.2213	0.0089	0.0110
−0.85	0.2885	0.0073	0.0134	0.2675	0.0070	0.0134	0.2484	0.0069	0.0123	0.2215	0.0066	0.0117
−0.75	0.3123	0.0097	0.0138	0.2978	0.0095	0.0152	0.2767	0.0094	0.0145	0.2397	0.0088	0.0119
−0.65	0.3208	0.0101	0.0145	0.2932	0.0097	0.0140	0.2680	0.0096	0.0143	0.2416	0.0090	0.0117
−0.55	0.3684	0.0109	0.0188	0.3291	0.0104	0.0145	0.2857	0.0099	0.0145	0.2687	0.0096	0.0130
−0.45	0.3641	0.0108	0.0175	0.3364	0.0104	0.0147	0.3036	0.0101	0.0138	0.3042	0.0100	0.0142
−0.35	0.3612	0.0107	0.0152	0.3485	0.0105	0.0156	0.3082	0.0100	0.0135	0.2921	0.0096	0.0133
−0.25	0.3670	0.0108	0.0152	0.3300	0.0102	0.0145	0.2974	0.0099	0.0128	0.2832	0.0096	0.0122
−0.15	0.3614	0.0105	0.0160	0.3374	0.0101	0.0142	0.2966	0.0096	0.0127	0.2878	0.0094	0.0127
−0.05	0.3800	0.0101	0.0179	0.3205	0.0079	0.0138	0.3349	0.0082	0.0144	0.3069	0.0076	0.0144
0.05	0.3717	0.0083	0.0164	0.3448	0.0079	0.0150	0.3292	0.0078	0.0139	0.3136	0.0075	0.0132
0.15	0.3502	0.0080	0.0157	0.3425	0.0078	0.0153	0.3285	0.0077	0.0146	0.3234	0.0076	0.0143
0.25	0.3474	0.0079	0.0157	0.3531	0.0079	0.0152	0.3233	0.0076	0.0149	0.3174	0.0075	0.0157
0.35	0.3373	0.0079	0.0165	0.3235	0.0077	0.0141	0.3128	0.0076	0.0158	0.3274	0.0077	0.0156
0.45	0.3364	0.0081	0.0182	0.3082	0.0076	0.0152	0.3019	0.0077	0.0174	0.3207	0.0079	0.0150
0.55	0.3070	0.0080	0.0154	0.2919	0.0077	0.0143	0.2888	0.0078	0.0153	0.2911	0.0078	0.0128
0.65	0.2957	0.0084	0.0140	0.2715	0.0080	0.0134	0.2708	0.0081	0.0139	0.2738	0.0081	0.0122
0.75	0.2591	0.0089	0.0130	0.2420	0.0085	0.0141	0.2255	0.0084	0.0107	0.2228	0.0082	0.0098
0.85	0.2060	0.0113	0.0150	0.1921	0.0107	0.0163	0.1862	0.0107	0.0102	0.1905	0.0108	0.0118
0.95	0.1822	0.0244	0.0175	0.1576	0.0223	0.0198	0.1807	0.0248	0.0237	0.1029	0.0200	0.0223

$\cos(\theta_\eta^*)$	$E_\gamma=(1072.5\pm7.5)$ MeV			$E_\gamma=(1087.5\pm7.5)$ MeV			$E_\gamma=(1102.5\pm7.5)$ MeV			$E_\gamma=(1117.5\pm7.5)$ MeV		
	$d\sigma/d\Omega$ [μb/sr]	$\Delta_{\rm stat}$ [μb/sr]	$\Delta_{\rm syst}$ [μb/sr]	$d\sigma/d\Omega$ [μb/sr]	$\Delta_{\rm stat}$ [μb/sr]	$\Delta_{\rm syst}$ [μb/sr]	$d\sigma/d\Omega$ [μb/sr]	$\Delta_{\rm stat}$ [μb/sr]	$\Delta_{\rm syst}$ [μb/sr]	$d\sigma/d\Omega$ [μb/sr]	$\Delta_{\rm stat}$ [μb/sr]	$\Delta_{\rm syst}$ [μb/sr]
−0.95	0.2310	0.0093	0.0115	0.2068	0.0091	0.0108	0.1961	0.0092	0.0117	0.1949	0.0102	0.0117
−0.85	0.2093	0.0066	0.0116	0.1885	0.0063	0.0105	0.1892	0.0066	0.0109	0.1750	0.0069	0.0098
−0.75	0.2140	0.0092	0.0119	0.2063	0.0087	0.0108	0.1938	0.0084	0.0100	0.2042	0.0091	0.0104
−0.65	0.2437	0.0099	0.0120	0.2344	0.0095	0.0104	0.2040	0.0087	0.0098	0.1920	0.0089	0.0092
−0.55	0.2628	0.0104	0.0120	0.2593	0.0100	0.0113	0.2214	0.0092	0.0103	0.2298	0.0098	0.0107
−0.45	0.2833	0.0106	0.0129	0.2604	0.0098	0.0120	0.2542	0.0096	0.0120	0.2513	0.0099	0.0119
−0.35	0.2978	0.0107	0.0131	0.2614	0.0095	0.0114	0.2545	0.0093	0.0118	0.2512	0.0097	0.0120
−0.25	0.2875	0.0106	0.0125	0.2571	0.0094	0.0109	0.2633	0.0093	0.0119	0.2673	0.0098	0.0125
−0.15	0.2828	0.0102	0.0128	0.2836	0.0092	0.0123	0.2876	0.0092	0.0123	0.2720	0.0082	0.0123
−0.05	0.3177	0.0080	0.0154	0.3175	0.0079	0.0143	0.2735	0.0074	0.0115	0.2904	0.0081	0.0129
0.05	0.3155	0.0078	0.0149	0.3011	0.0074	0.0142	0.3040	0.0075	0.0127	0.3016	0.0081	0.0133
0.15	0.3084	0.0075	0.0138	0.3033	0.0073	0.0140	0.3055	0.0075	0.0125	0.3103	0.0081	0.0131
0.25	0.3121	0.0076	0.0139	0.3187	0.0075	0.0141	0.3214	0.0077	0.0131	0.3112	0.0081	0.0129
0.35	0.3169	0.0078	0.0149	0.3114	0.0077	0.0146	0.3181	0.0079	0.0134	0.3117	0.0084	0.0132
0.45	0.3086	0.0080	0.0144	0.3050	0.0078	0.0144	0.3141	0.0081	0.0165	0.3148	0.0087	0.0145
0.55	0.3009	0.0082	0.0134	0.3002	0.0081	0.0127	0.3096	0.0083	0.0171	0.3080	0.0089	0.0160
0.65	0.2965	0.0086	0.0136	0.2811	0.0082	0.0115	0.2797	0.0083	0.0142	0.3020	0.0094	0.0145
0.75	0.2317	0.0085	0.0113	0.2638	0.0091	0.0120	0.2530	0.0089	0.0119	0.2595	0.0097	0.0117
0.85	0.2090	0.0118	0.0143	0.2067	0.0113	0.0199	0.2247	0.0118	0.0151	0.2483	0.0132	0.0162
0.95	0.1515	0.0251	0.0348	0.1703	0.0275	0.0365	0.1466	0.0265	0.0273	0.2168	0.0336	0.0523

$\cos(\theta_\eta^*)$	$E_\gamma{=}(1132.5{\pm}7.5)$ MeV			$E_\gamma{=}(1147.5{\pm}7.5)$ MeV			$E_\gamma{=}(1162.5{\pm}7.5)$ MeV			$E_\gamma{=}(1177.5{\pm}7.5)$ MeV		
	$d\sigma/d\Omega$ $[\mu\mathrm{b/sr}]$	Δ_stat $[\mu\mathrm{b/sr}]$	Δ_syst $[\mu\mathrm{b/sr}]$	$d\sigma/d\Omega$ $[\mu\mathrm{b/sr}]$	Δ_stat $[\mu\mathrm{b/sr}]$	Δ_syst $[\mu\mathrm{b/sr}]$	$d\sigma/d\Omega$ $[\mu\mathrm{b/sr}]$	Δ_stat $[\mu\mathrm{b/sr}]$	Δ_syst $[\mu\mathrm{b/sr}]$	$d\sigma/d\Omega$ $[\mu\mathrm{b/sr}]$	Δ_stat $[\mu\mathrm{b/sr}]$	Δ_syst $[\mu\mathrm{b/sr}]$
−0.95	0.1595	0.0086	0.0091	0.1358	0.0083	0.0073	0.1426	0.0078	0.0078	0.1324	0.0075	0.0079
−0.85	0.1601	0.0062	0.0091	0.1494	0.0063	0.0082	0.1358	0.0056	0.0079	0.1301	0.0054	0.0070
−0.75	0.1856	0.0093	0.0099	0.1622	0.0089	0.0085	0.1874	0.0087	0.0093	0.1555	0.0080	0.0083
−0.65	0.2101	0.0100	0.0105	0.1896	0.0098	0.0098	0.1740	0.0087	0.0081	0.1963	0.0093	0.0104
−0.55	0.2299	0.0105	0.0112	0.2023	0.0102	0.0096	0.1886	0.0092	0.0087	0.2101	0.0098	0.0100
−0.45	0.2149	0.0098	0.0100	0.2128	0.0099	0.0091	0.2038	0.0090	0.0094	0.1946	0.0090	0.0093
−0.35	0.2351	0.0098	0.0110	0.2356	0.0100	0.0103	0.2263	0.0092	0.0097	0.2285	0.0093	0.0107
−0.25	0.2423	0.0098	0.0109	0.2614	0.0104	0.0120	0.2479	0.0095	0.0103	0.2396	0.0094	0.0106
−0.15	0.2739	0.0077	0.0120	0.2595	0.0077	0.0111	0.2589	0.0074	0.0108	0.2630	0.0074	0.0117
−0.05	0.2965	0.0076	0.0128	0.2674	0.0075	0.0114	0.2825	0.0073	0.0118	0.2639	0.0071	0.0112
0.05	0.2908	0.0074	0.0128	0.2751	0.0074	0.0119	0.2738	0.0071	0.0117	0.2675	0.0070	0.0111
0.15	0.3009	0.0074	0.0133	0.3080	0.0078	0.0138	0.2973	0.0073	0.0129	0.2861	0.0072	0.0128
0.25	0.3149	0.0076	0.0142	0.2982	0.0076	0.0131	0.3074	0.0074	0.0132	0.3157	0.0075	0.0147
0.35	0.3269	0.0079	0.0181	0.3195	0.0081	0.0155	0.3191	0.0078	0.0139	0.3095	0.0077	0.0143
0.45	0.3109	0.0080	0.0185	0.3087	0.0083	0.0177	0.3040	0.0079	0.0147	0.2841	0.0076	0.0135
0.55	0.3250	0.0085	0.0148	0.2990	0.0084	0.0166	0.3093	0.0082	0.0154	0.2994	0.0081	0.0157
0.65	0.2840	0.0084	0.0121	0.3070	0.0090	0.0157	0.2935	0.0084	0.0128	0.2761	0.0082	0.0152
0.75	0.2795	0.0092	0.0149	0.2817	0.0096	0.0154	0.2836	0.0092	0.0138	0.3035	0.0094	0.0156
0.85	0.2471	0.0120	0.0236	0.2492	0.0122	0.0145	0.2275	0.0111	0.0175	0.2184	0.0107	0.0176
0.95	0.1589	0.0282	0.0142	0.1575	0.0293	0.0114	0.1703	0.0278	0.0124	0.1475	0.0262	0.0372

$\cos(\theta_\eta^*)$	$E_\gamma{=}(1192.5{\pm}7.5)$ MeV			$E_\gamma{=}(1207.5{\pm}7.5)$ MeV			$E_\gamma{=}(1222.5{\pm}7.5)$ MeV			$E_\gamma{=}(1237.5{\pm}7.5)$ MeV		
	$d\sigma/d\Omega$ $[\mu\mathrm{b/sr}]$	Δ_stat $[\mu\mathrm{b/sr}]$	Δ_syst $[\mu\mathrm{b/sr}]$	$d\sigma/d\Omega$ $[\mu\mathrm{b/sr}]$	Δ_stat $[\mu\mathrm{b/sr}]$	Δ_syst $[\mu\mathrm{b/sr}]$	$d\sigma/d\Omega$ $[\mu\mathrm{b/sr}]$	Δ_stat $[\mu\mathrm{b/sr}]$	Δ_syst $[\mu\mathrm{b/sr}]$	$d\sigma/d\Omega$ $[\mu\mathrm{b/sr}]$	Δ_stat $[\mu\mathrm{b/sr}]$	Δ_syst $[\mu\mathrm{b/sr}]$
−0.95	0.1236	0.0075	0.0073	0.1235	0.0073	0.0069	0.1026	0.0064	0.0083	0.1096	0.0073	0.0095
−0.85	0.1250	0.0056	0.0068	0.1149	0.0053	0.0057	0.1150	0.0052	0.0070	0.1156	0.0056	0.0065
−0.75	0.1512	0.0081	0.0079	0.1393	0.0077	0.0062	0.1303	0.0075	0.0074	0.1247	0.0082	0.0063
−0.65	0.1760	0.0090	0.0087	0.1534	0.0083	0.0067	0.1374	0.0079	0.0071	0.1504	0.0093	0.0077
−0.55	0.1825	0.0095	0.0092	0.1745	0.0092	0.0082	0.1608	0.0088	0.0084	0.1666	0.0101	0.0089
−0.45	0.1994	0.0095	0.0105	0.1871	0.0090	0.0093	0.2001	0.0095	0.0099	0.2056	0.0109	0.0104
−0.35	0.2154	0.0094	0.0102	0.2026	0.0090	0.0097	0.2067	0.0092	0.0096	0.2017	0.0103	0.0092
−0.25	0.2026	0.0089	0.0087	0.2273	0.0093	0.0101	0.2119	0.0092	0.0098	0.2082	0.0102	0.0092
−0.15	0.2401	0.0073	0.0106	0.2357	0.0072	0.0107	0.2414	0.0072	0.0110	0.2168	0.0075	0.0098
−0.05	0.2462	0.0071	0.0110	0.2645	0.0073	0.0116	0.2259	0.0066	0.0103	0.2353	0.0074	0.0106
0.05	0.2707	0.0073	0.0117	0.2639	0.0072	0.0111	0.2557	0.0070	0.0116	0.2568	0.0076	0.0112
0.15	0.2724	0.0072	0.0115	0.2798	0.0073	0.0118	0.2520	0.0068	0.0111	0.2620	0.0077	0.0112
0.25	0.2800	0.0074	0.0123	0.2878	0.0074	0.0120	0.2703	0.0071	0.0113	0.2709	0.0078	0.0120
0.35	0.2946	0.0078	0.0143	0.2882	0.0077	0.0135	0.2851	0.0075	0.0128	0.2773	0.0081	0.0135
0.45	0.2961	0.0081	0.0149	0.2985	0.0080	0.0160	0.2824	0.0077	0.0158	0.2706	0.0083	0.0160
0.55	0.2842	0.0082	0.0136	0.2713	0.0080	0.0129	0.2763	0.0080	0.0139	0.3001	0.0091	0.0185
0.65	0.2685	0.0084	0.0124	0.2955	0.0088	0.0126	0.2709	0.0082	0.0125	0.2805	0.0092	0.0125
0.75	0.2735	0.0093	0.0120	0.2578	0.0090	0.0124	0.2631	0.0089	0.0135	0.2437	0.0094	0.0103
0.85	0.2241	0.0111	0.0127	0.2315	0.0112	0.0176	0.2529	0.0114	0.0234	0.2255	0.0115	0.0121
0.95	0.1847	0.0311	0.0313	0.2660	0.0347	0.0358	0.2852	0.0337	0.0681	0.2448	0.0353	0.0191

$\cos(\theta_\eta^*)$	$E_\gamma{=}(1252.5{\pm}7.5)$ MeV			$E_\gamma{=}(1267.5{\pm}7.5)$ MeV			$E_\gamma{=}(1282.5{\pm}7.5)$ MeV			$E_\gamma{=}(1297.5{\pm}7.5)$ MeV		
	$d\sigma/d\Omega$ $[\mu\mathrm{b/sr}]$	Δ_stat $[\mu\mathrm{b/sr}]$	Δ_syst $[\mu\mathrm{b/sr}]$	$d\sigma/d\Omega$ $[\mu\mathrm{b/sr}]$	Δ_stat $[\mu\mathrm{b/sr}]$	Δ_syst $[\mu\mathrm{b/sr}]$	$d\sigma/d\Omega$ $[\mu\mathrm{b/sr}]$	Δ_stat $[\mu\mathrm{b/sr}]$	Δ_syst $[\mu\mathrm{b/sr}]$	$d\sigma/d\Omega$ $[\mu\mathrm{b/sr}]$	Δ_stat $[\mu\mathrm{b/sr}]$	Δ_syst $[\mu\mathrm{b/sr}]$
−0.95	0.1044	0.0068	0.0048	0.0975	0.0065	0.0058	0.0835	0.0059	0.0042	0.0807	0.0061	0.0055
−0.85	0.1155	0.0054	0.0054	0.1032	0.0051	0.0049	0.1069	0.0050	0.0060	0.0911	0.0050	0.0049
−0.75	0.1366	0.0078	0.0066	0.1315	0.0081	0.0063	0.1098	0.0071	0.0058	0.1025	0.0077	0.0053
−0.65	0.1325	0.0080	0.0063	0.1274	0.0083	0.0062	0.1530	0.0087	0.0078	0.1306	0.0091	0.0066
−0.55	0.1552	0.0089	0.0074	0.1462	0.0093	0.0069	0.1594	0.0093	0.0075	0.1370	0.0097	0.0072
−0.45	0.1631	0.0089	0.0080	0.1715	0.0098	0.0075	0.1483	0.0088	0.0073	0.1505	0.0098	0.0074
−0.35	0.1789	0.0089	0.0080	0.1932	0.0099	0.0081	0.1653	0.0088	0.0086	0.1869	0.0104	0.0088
−0.25	0.1961	0.0091	0.0085	0.1970	0.0097	0.0084	0.1921	0.0092	0.0094	0.1657	0.0095	0.0079
−0.15	0.2152	0.0071	0.0100	0.2120	0.0072	0.0095	0.2211	0.0071	0.0097	0.2114	0.0076	0.0097
−0.05	0.2302	0.0070	0.0105	0.2297	0.0071	0.0099	0.2147	0.0067	0.0096	0.2112	0.0072	0.0094
0.05	0.2410	0.0070	0.0102	0.2368	0.0070	0.0098	0.2361	0.0068	0.0106	0.2126	0.0071	0.0091
0.15	0.2406	0.0070	0.0100	0.2486	0.0072	0.0105	0.2398	0.0068	0.0108	0.2372	0.0075	0.0109
0.25	0.2613	0.0072	0.0114	0.2464	0.0072	0.0105	0.2389	0.0068	0.0104	0.2484	0.0076	0.0121
0.35	0.2679	0.0076	0.0117	0.2526	0.0076	0.0112	0.2689	0.0075	0.0115	0.2478	0.0079	0.0112
0.45	0.2801	0.0080	0.0121	0.2729	0.0081	0.0130	0.2656	0.0077	0.0115	0.2574	0.0083	0.0130
0.55	0.2756	0.0082	0.0119	0.2742	0.0084	0.0143	0.2729	0.0082	0.0137	0.2497	0.0085	0.0150
0.65	0.2849	0.0089	0.0123	0.2741	0.0090	0.0144	0.2542	0.0083	0.0145	0.2634	0.0093	0.0156
0.75	0.2388	0.0089	0.0119	0.2613	0.0094	0.0129	0.2578	0.0092	0.0149	0.2488	0.0099	0.0120
0.85	0.2422	0.0113	0.0163	0.2287	0.0112	0.0168	0.2300	0.0108	0.0176	0.2254	0.0117	0.0152
0.95	0.2126	0.0298	0.0176	0.2734	0.0339	0.0416	0.2690	0.0318	0.0260	0.2225	0.0314	0.0436

$\cos(\theta_\eta^*)$	$E_\gamma{=}(1312.5{\pm}7.5)$ MeV			$E_\gamma{=}(1327.5{\pm}7.5)$ MeV			$E_\gamma{=}(1342.5{\pm}7.5)$ MeV			$E_\gamma{=}(1357.5{\pm}7.5)$ MeV		
	$d\sigma/d\Omega$	Δ_{stat}	Δ_{syst}	$d\sigma/d\Omega$	Δ_{stat}	Δ_{syst}	$d\sigma/d\Omega$	Δ_{stat}	Δ_{syst}	$d\sigma/d\Omega$	Δ_{stat}	Δ_{syst}
	[μb/sr]	[μb/sr]	[μb/sr]	[μb/sr]	[μb/sr]	[μb/sr]	[μb/sr]	[μb/sr]	[μb/sr]	[μb/sr]	[μb/sr]	[μb/sr]
-0.95	0.0822	0.0058	0.0046	0.0722	0.0066	0.0039	0.0739	0.0066	0.0041	0.0696	0.0054	0.0047
-0.85	0.0896	0.0046	0.0048	0.0806	0.0053	0.0039	0.0878	0.0055	0.0044	0.0894	0.0047	0.0044
-0.75	0.1103	0.0068	0.0057	0.0953	0.0066	0.0043	0.0956	0.0073	0.0050	0.0987	0.0066	0.0050
-0.65	0.1131	0.0072	0.0063	0.1166	0.0077	0.0057	0.1199	0.0088	0.0067	0.1141	0.0076	0.0063
-0.55	0.1239	0.0080	0.0065	0.1187	0.0082	0.0062	0.1332	0.0098	0.0074	0.1381	0.0089	0.0075
-0.45	0.1607	0.0087	0.0081	0.1563	0.0092	0.0079	0.1533	0.0101	0.0085	0.1260	0.0082	0.0073
-0.35	0.1619	0.0084	0.0078	0.1513	0.0086	0.0073	0.1628	0.0100	0.0091	0.1448	0.0085	0.0074
-0.25	0.1827	0.0087	0.0082	0.1806	0.0090	0.0087	0.1890	0.0106	0.0097	0.1578	0.0086	0.0076
-0.15	0.2000	0.0068	0.0092	0.2000	0.0082	0.0094	0.1779	0.0079	0.0087	0.1829	0.0069	0.0086
-0.05	0.2006	0.0065	0.0093	0.2034	0.0080	0.0091	0.1992	0.0080	0.0093	0.2081	0.0070	0.0093
0.05	0.2351	0.0069	0.0103	0.2185	0.0081	0.0094	0.2142	0.0082	0.0095	0.2011	0.0068	0.0089
0.15	0.2275	0.0068	0.0096	0.2146	0.0080	0.0093	0.2211	0.0082	0.0096	0.2083	0.0068	0.0091
0.25	0.2387	0.0070	0.0099	0.2326	0.0085	0.0103	0.2225	0.0083	0.0097	0.2179	0.0070	0.0092
0.35	0.2492	0.0074	0.0107	0.2459	0.0090	0.0113	0.2311	0.0087	0.0103	0.2248	0.0074	0.0102
0.45	0.2504	0.0077	0.0115	0.2648	0.0097	0.0139	0.2673	0.0097	0.0131	0.2140	0.0074	0.0102
0.55	0.2492	0.0079	0.0133	0.2432	0.0096	0.0141	0.2325	0.0094	0.0123	0.2369	0.0081	0.0107
0.65	0.2609	0.0087	0.0186	0.2436	0.0102	0.0146	0.2211	0.0098	0.0130	0.2492	0.0089	0.0112
0.75	0.2362	0.0089	0.0164	0.2346	0.0109	0.0128	0.2542	0.0113	0.0143	0.2569	0.0097	0.0130
0.85	0.2275	0.0108	0.0180	0.2166	0.0130	0.0124	0.2452	0.0138	0.0248	0.2095	0.0108	0.0152
0.95	0.2214	0.0281	0.0244	0.2767	0.0396	0.0206	0.1749	0.0306	0.0471	0.1426	0.0226	0.0313

$\cos(\theta_\eta^*)$	$E_\gamma{=}(1372.5{\pm}7.5)$ MeV			$E_\gamma{=}(1387.5{\pm}7.5)$ MeV		
	$d\sigma/d\Omega$	Δ_{stat}	Δ_{syst}	$d\sigma/d\Omega$	Δ_{stat}	Δ_{syst}
	[μb/sr]	[μb/sr]	[μb/sr]	[μb/sr]	[μb/sr]	[μb/sr]
-0.95	0.0699	0.0059	0.0039	0.0824	0.0066	0.0056
-0.85	0.0752	0.0045	0.0037	0.0824	0.0048	0.0042
-0.75	0.0821	0.0064	0.0042	0.0845	0.0070	0.0041
-0.65	0.1145	0.0080	0.0065	0.1038	0.0083	0.0062
-0.55	0.1301	0.0092	0.0073	0.1397	0.0106	0.0098
-0.45	0.1013	0.0079	0.0055	0.1157	0.0092	0.0065
-0.35	0.1415	0.0087	0.0071	0.1255	0.0090	0.0067
-0.25	0.1329	0.0079	0.0060	0.1592	0.0093	0.0078
-0.15	0.1802	0.0071	0.0078	0.1775	0.0073	0.0083
-0.05	0.1831	0.0069	0.0078	0.1735	0.0068	0.0078
0.05	0.2052	0.0071	0.0091	0.1856	0.0069	0.0082
0.15	0.1963	0.0068	0.0090	0.1922	0.0069	0.0087
0.25	0.1955	0.0068	0.0088	0.2034	0.0072	0.0091
0.35	0.2176	0.0075	0.0096	0.2181	0.0077	0.0106
0.45	0.2196	0.0078	0.0101	0.2124	0.0079	0.0123
0.55	0.2272	0.0082	0.0128	0.2369	0.0087	0.0133
0.65	0.2380	0.0089	0.0156	0.2400	0.0092	0.0111
0.75	0.2409	0.0098	0.0162	0.2406	0.0100	0.0120
0.85	0.2082	0.0111	0.0144	0.2001	0.0111	0.0140
0.95	0.1964	0.0272	0.0287	0.2115	0.0291	0.0247

Differential cross sections of $\gamma p \to \eta p$ as a function of W_{kin}

$\cos(\theta_\eta^*)$	$d\sigma/d\Omega$ [μb/sr]	Δ_{stat} [μb/sr]	Δ_{syst} [μb/sr]	$d\sigma/d\Omega$ [μb/sr]	Δ_{stat} [μb/sr]	Δ_{syst} [μb/sr]	$d\sigma/d\Omega$ [μb/sr]	Δ_{stat} [μb/sr]	Δ_{syst} [μb/sr]	$d\sigma/d\Omega$ [μb/sr]	Δ_{stat} [μb/sr]	Δ_{syst} [μb/sr]
	$W{=}(1492.5{\pm}2.5)$ MeV			$W{=}(1497.5{\pm}2.5)$ MeV			$W{=}(1502.5{\pm}2.5)$ MeV			$W{=}(1507.5{\pm}2.5)$ MeV		
−0.95	0.7413	0.0612	0.0852	0.8306	0.0423	0.0726	0.9138	0.0360	0.0455	1.1217	0.0350	0.0658
−0.85	0.6221	0.0233	0.0380	0.7796	0.0202	0.0411	0.9276	0.0191	0.0424	1.0241	0.0186	0.0489
−0.75	0.6081	0.0175	0.0304	0.7827	0.0163	0.0368	0.9164	0.0161	0.0432	1.0317	0.0162	0.0485
−0.65	0.5858	0.0150	0.0319	0.8184	0.0154	0.0396	0.8910	0.0150	0.0430	1.0021	0.0154	0.0480
−0.55	0.6072	0.0143	0.0309	0.8433	0.0151	0.0408	0.9266	0.0151	0.0456	1.0449	0.0158	0.0508
−0.45	0.6174	0.0140	0.0312	0.7966	0.0147	0.0403	0.9488	0.0155	0.0461	1.0443	0.0163	0.0516
−0.35	0.6143	0.0136	0.0323	0.8110	0.0148	0.0409	0.9333	0.0157	0.0470	1.1037	0.0174	0.0521
−0.25	0.6039	0.0134	0.0302	0.8560	0.0154	0.0423	0.9726	0.0165	0.0525	1.1253	0.0184	0.0538
−0.15	0.6054	0.0133	0.0308	0.8316	0.0154	0.0416	0.9773	0.0171	0.0526	1.0885	0.0192	0.0584
−0.05	0.6054	0.0134	0.0323	0.8546	0.0159	0.0439	0.9907	0.0179	0.0535	1.1195	0.0206	0.0635
0.05	0.6299	0.0138	0.0347	0.8362	0.0161	0.0437	0.9680	0.0184	0.0539	1.1264	0.0218	0.0613
0.15	0.6033	0.0134	0.0322	0.8175	0.0163	0.0418	0.9704	0.0192	0.0514	1.1180	0.0278	0.0612
0.25	0.6110	0.0137	0.0313	0.8273	0.0166	0.0407	0.9687	0.0196	0.0531	1.0917	0.0237	0.0606
0.35	0.6410	0.0143	0.0342	0.8148	0.0168	0.0421	0.8972	0.0192	0.0511	1.0964	0.0244	0.0595
0.45	0.5902	0.0139	0.0319	0.8411	0.0173	0.0441	0.9111	0.0199	0.0518	1.0400	0.0246	0.0527
0.55	0.5856	0.0145	0.0337	0.8169	0.0173	0.0426	0.9118	0.0200	0.0518	0.9838	0.0243	0.0500
0.65	0.5783	0.0151	0.0328	0.8032	0.0176	0.0417	0.8797	0.0199	0.0488	0.9664	0.0239	0.0512
0.75	0.5872	0.0166	0.0306	0.8044	0.0183	0.0425	0.8794	0.0198	0.0472	0.9903	0.0236	0.0526
0.85	0.6032	0.0201	0.0330	0.7814	0.0197	0.0432	0.8968	0.0207	0.0477	1.0061	0.0233	0.0515
0.95	0.6582	0.0405	0.0435	0.7362	0.0310	0.0457	0.8842	0.0294	0.0426	0.9605	0.0297	0.0481
	$W{=}(1512.5{\pm}2.5)$ MeV			$W{=}(1517.5{\pm}2.5)$ MeV			$W{=}(1522.5{\pm}2.5)$ MeV			$W{=}(1527.5{\pm}2.5)$ MeV		
−0.95	1.1864	0.0332	0.0585	1.1578	0.0304	0.0578	1.1679	0.0291	0.0532	1.2422	0.0293	0.0558
−0.85	1.1065	0.0183	0.0523	1.1263	0.0177	0.0529	1.1447	0.0174	0.0497	1.1475	0.0170	0.0517
−0.75	1.0723	0.0160	0.0478	1.1152	0.0160	0.0536	1.1385	0.0160	0.0517	1.1444	0.0159	0.0520
−0.65	1.0784	0.0158	0.0479	1.0859	0.0158	0.0516	1.1639	0.0162	0.0545	1.1384	0.0160	0.0534
−0.55	1.0602	0.0159	0.0499	1.1784	0.0169	0.0553	1.1233	0.0167	0.0539	1.1969	0.0173	0.0565
−0.45	1.1292	0.0172	0.0565	1.1690	0.0178	0.0564	1.2405	0.0249	0.0614	1.2679	0.0253	0.0625
−0.35	1.1207	0.0182	0.0562	1.1778	0.0256	0.0596	1.3019	0.0273	0.0631	1.3112	0.0280	0.0655
−0.25	1.1624	0.0266	0.0582	1.3009	0.0288	0.0664	1.3764	0.0306	0.0670	1.3809	0.0315	0.0695
−0.15	1.2557	0.0292	0.0616	1.2823	0.0307	0.0607	1.4618	0.0341	0.0692	1.4228	0.0348	0.0730
−0.05	1.2703	0.0313	0.0618	1.3502	0.0337	0.0624	1.3807	0.0355	0.0638	1.4002	0.0366	0.0705
0.05	1.2313	0.0329	0.0610	1.2952	0.0356	0.0626	1.3317	0.0372	0.0642	1.3776	0.0376	0.0680
0.15	1.2224	0.0351	0.0635	1.3945	0.0395	0.0713	1.3398	0.0396	0.0660	1.3305	0.0384	0.0613
0.25	1.1637	0.0368	0.0622	1.3932	0.0424	0.0807	1.2843	0.0413	0.0639	1.3601	0.0405	0.0591
0.35	1.1139	0.0377	0.0575	1.2873	0.0436	0.0761	1.3929	0.0457	0.0759	1.2758	0.0416	0.0592
0.45	1.1702	0.0406	0.0592	1.2284	0.0455	0.0612	1.1820	0.0459	0.0720	1.3209	0.0462	0.0689
0.55	1.1132	0.0305	0.0616	1.2060	0.0483	0.0580	1.2579	0.0517	0.0771	1.2127	0.0502	0.0672
0.65	0.9983	0.0289	0.0583	1.0518	0.0350	0.0555	1.2080	0.0565	0.0679	1.2115	0.0581	0.0694
0.75	1.0282	0.0280	0.0555	1.0801	0.0342	0.0594	1.1093	0.0408	0.0613	1.2038	0.0485	0.0680
0.85	1.0361	0.0262	0.0527	1.0669	0.0303	0.0560	1.1230	0.0360	0.0631	1.0711	0.0406	0.0597
0.95	1.0880	0.0320	0.0618	1.0713	0.0331	0.0599	1.1729	0.0368	0.0623	1.1047	0.0388	0.0656

cos(θ*_η)	$W=(1532.5\pm2.5)\,$MeV			$W=(1537.5\pm2.5)\,$MeV			$W=(1545.0\pm5.0)\,$MeV			$W=(1555.0\pm5.0)\,$MeV		
	$d\sigma/d\Omega$	Δ_{stat}	Δ_{syst}	$d\sigma/d\Omega$	Δ_{stat}	Δ_{syst}	$d\sigma/d\Omega$	Δ_{stat}	Δ_{syst}	$d\sigma/d\Omega$	Δ_{stat}	Δ_{syst}
	[μb/sr]	[μb/sr]	[μb/sr]	[μb/sr]	[μb/sr]	[μb/sr]	[μb/sr]	[μb/sr]	[μb/sr]	[μb/sr]	[μb/sr]	[μb/sr]
−0.95	1.2564	0.0283	0.0573	1.2128	0.0270	0.0539	1.1795	0.0182	0.0511	1.1476	0.0178	0.0520
−0.85	1.1745	0.0170	0.0510	1.1102	0.0163	0.0493	1.1179	0.0115	0.0491	1.0534	0.0113	0.0463
−0.75	1.1327	0.0158	0.0510	1.1071	0.0155	0.0502	1.0796	0.0109	0.0491	1.0139	0.0108	0.0466
−0.65	1.1532	0.0162	0.0560	1.1159	0.0160	0.0523	1.0974	0.0115	0.0517	1.0677	0.0157	0.0503
−0.55	1.1547	0.0205	0.0548	1.1842	0.0231	0.0572	1.1394	0.0163	0.0538	1.0919	0.0167	0.0528
−0.45	1.2366	0.0252	0.0589	1.2400	0.0255	0.0602	1.2449	0.0186	0.0569	1.2139	0.0194	0.0551
−0.35	1.3410	0.0288	0.0631	1.3368	0.0295	0.0638	1.3830	0.0219	0.0613	1.3754	0.0229	0.0582
−0.25	1.4015	0.0324	0.0659	1.4248	0.0336	0.0658	1.4456	0.0242	0.0635	1.3542	0.0232	0.0560
−0.15	1.5531	0.0370	0.0711	1.5133	0.0365	0.0708	1.3626	0.0235	0.0600	1.2543	0.0211	0.0528
−0.05	1.4905	0.0373	0.0685	1.2998	0.0334	0.0587	1.2961	0.0217	0.0551	1.2154	0.0194	0.0524
0.05	1.4333	0.0368	0.0643	1.2805	0.0324	0.0559	1.1948	0.0199	0.0510	1.1255	0.0179	0.0510
0.15	1.2850	0.0353	0.0559	1.1618	0.0304	0.0513	1.1786	0.0194	0.0508	1.1195	0.0176	0.0495
0.25	1.2833	0.0363	0.0559	1.1141	0.0302	0.0483	1.1497	0.0193	0.0480	1.0861	0.0175	0.0453
0.35	1.2691	0.0377	0.0576	1.1809	0.0322	0.0528	1.0957	0.0194	0.0449	1.0918	0.0179	0.0454
0.45	1.2350	0.0409	0.0617	1.1319	0.0345	0.0572	1.1124	0.0211	0.0471	1.0816	0.0189	0.0475
0.55	1.2244	0.0472	0.0579	1.1611	0.0403	0.0654	1.1382	0.0241	0.0494	1.0369	0.0204	0.0455
0.65	1.2517	0.0575	0.0603	1.2506	0.0518	0.0730	1.1031	0.0293	0.0512	1.0804	0.0250	0.0484
0.75	1.3279	0.0730	0.0715	1.3204	0.0721	0.0794	1.1684	0.0434	0.0710	1.1354	0.0366	0.0635
0.85	1.1274	0.0487	0.0611	1.0685	0.0542	0.0678	1.1532	0.0451	0.0811	1.1774	0.0641	0.0873
0.95	1.0789	0.0416	0.0662	1.0886	0.0464	0.0569	1.1012	0.0380	0.0737	1.0290	0.0449	0.0728

cos(θ*_η)	$W=(1565.0\pm5.0)\,$MeV			$W=(1575.0\pm5.0)\,$MeV			$W=(1585.0\pm5.0)\,$MeV			$W=(1595.0\pm5.0)\,$MeV		
	$d\sigma/d\Omega$	Δ_{stat}	Δ_{syst}	$d\sigma/d\Omega$	Δ_{stat}	Δ_{syst}	$d\sigma/d\Omega$	Δ_{stat}	Δ_{syst}	$d\sigma/d\Omega$	Δ_{stat}	Δ_{syst}
	[μb/sr]	[μb/sr]	[μb/sr]	[μb/sr]	[μb/sr]	[μb/sr]	[μb/sr]	[μb/sr]	[μb/sr]	[μb/sr]	[μb/sr]	[μb/sr]
−0.95	1.0892	0.0175	0.0531	1.0381	0.0174	0.0511	0.9479	0.0169	0.0454	0.8453	0.0159	0.0374
−0.85	0.9712	0.0112	0.0454	0.9390	0.0113	0.0433	0.8660	0.0111	0.0424	0.7785	0.0106	0.0374
−0.75	0.9790	0.0110	0.0474	0.9445	0.0113	0.0438	0.8842	0.0112	0.0456	0.8004	0.0108	0.0409
−0.65	1.0030	0.0159	0.0491	0.9694	0.0165	0.0462	0.8964	0.0164	0.0490	0.8132	0.0157	0.0433
−0.55	1.0663	0.0174	0.0522	0.9904	0.0177	0.0503	1.0011	0.0184	0.0500	0.8870	0.0173	0.0440
−0.45	1.1905	0.0204	0.0564	1.1271	0.0208	0.0564	1.0627	0.0206	0.0481	0.9405	0.0193	0.0428
−0.35	1.2680	0.0227	0.0560	1.1621	0.0218	0.0533	1.0452	0.0205	0.0486	0.9474	0.0192	0.0431
−0.25	1.1949	0.0212	0.0508	1.1021	0.0199	0.0473	0.9878	0.0186	0.0448	0.8951	0.0174	0.0422
−0.15	1.1462	0.0191	0.0491	1.0554	0.0180	0.0461	0.9196	0.0169	0.0413	0.8213	0.0157	0.0426
−0.05	1.1193	0.0178	0.0518	1.0123	0.0169	0.0474	0.9605	0.0166	0.0458	0.8327	0.0153	0.0444
0.05	1.0405	0.0166	0.0478	0.9854	0.0164	0.0480	0.8870	0.0158	0.0431	0.8379	0.0152	0.0425
0.15	1.0448	0.0166	0.0457	0.9926	0.0166	0.0471	0.8819	0.0159	0.0434	0.7965	0.0139	0.0395
0.25	1.0250	0.0167	0.0468	0.9713	0.0166	0.0462	0.8904	0.0150	0.0444	0.8252	0.0116	0.0415
0.35	1.0474	0.0173	0.0485	0.9500	0.0167	0.0441	0.8811	0.0123	0.0444	0.7856	0.0113	0.0384
0.45	1.0247	0.0179	0.0444	0.9815	0.0165	0.0456	0.8668	0.0125	0.0398	0.7557	0.0114	0.0367
0.55	0.9788	0.0188	0.0424	0.9383	0.0141	0.0400	0.8216	0.0128	0.0375	0.7355	0.0118	0.0348
0.65	1.0022	0.0219	0.0444	0.9327	0.0189	0.0397	0.8190	0.0141	0.0390	0.7107	0.0126	0.0330
0.75	1.0641	0.0309	0.0530	0.9690	0.0270	0.0474	0.8639	0.0185	0.0420	0.7135	0.0156	0.0340
0.85	1.2270	0.0616	0.0761	1.1194	0.0528	0.0748	0.9376	0.0438	0.0532	0.7767	0.0280	0.0552
0.95	0.9565	0.0533	0.0665	0.9859	0.0633	0.0949	0.9627	0.0700	0.0788	0.6849	0.0635	0.1084

cos(θ*_η)	$W=(1605.0\pm5.0)\,$MeV			$W=(1615.0\pm5.0)\,$MeV			$W=(1625.0\pm5.0)\,$MeV			$W=(1635.0\pm5.0)\,$MeV		
	$d\sigma/d\Omega$	Δ_{stat}	Δ_{syst}	$d\sigma/d\Omega$	Δ_{stat}	Δ_{syst}	$d\sigma/d\Omega$	Δ_{stat}	Δ_{syst}	$d\sigma/d\Omega$	Δ_{stat}	Δ_{syst}
	[μb/sr]	[μb/sr]	[μb/sr]	[μb/sr]	[μb/sr]	[μb/sr]	[μb/sr]	[μb/sr]	[μb/sr]	[μb/sr]	[μb/sr]	[μb/sr]
−0.95	0.7282	0.0146	0.0380	0.5903	0.0129	0.0326	0.4976	0.0119	0.0275	0.4074	0.0108	0.0243
−0.85	0.6827	0.0099	0.0328	0.5986	0.0091	0.0289	0.4869	0.0082	0.0239	0.4039	0.0075	0.0203
−0.75	0.7093	0.0102	0.0343	0.6015	0.0093	0.0292	0.5460	0.0119	0.0275	0.4271	0.0107	0.0207
−0.65	0.7409	0.0147	0.0377	0.6328	0.0133	0.0308	0.5474	0.0123	0.0285	0.4646	0.0115	0.0245
−0.55	0.7832	0.0160	0.0407	0.6917	0.0149	0.0327	0.5975	0.0140	0.0291	0.5283	0.0134	0.0271
−0.45	0.8384	0.0180	0.0426	0.7391	0.0166	0.0347	0.6144	0.0149	0.0272	0.4941	0.0131	0.0229
−0.35	0.7973	0.0170	0.0380	0.6703	0.0149	0.0290	0.5647	0.0130	0.0238	0.4648	0.0114	0.0210
−0.25	0.7566	0.0153	0.0337	0.6756	0.0137	0.0298	0.5515	0.0119	0.0237	0.4699	0.0109	0.0215
−0.15	0.7168	0.0140	0.0322	0.6172	0.0124	0.0284	0.5325	0.0114	0.0240	0.4480	0.0105	0.0202
−0.05	0.7116	0.0136	0.0361	0.6034	0.0123	0.0268	0.5021	0.0112	0.0223	0.4558	0.0101	0.0200
0.05	0.7200	0.0138	0.0336	0.6036	0.0116	0.0256	0.5162	0.0089	0.0230	0.4333	0.0081	0.0184
0.15	0.7209	0.0107	0.0329	0.6011	0.0095	0.0254	0.5015	0.0086	0.0247	0.4163	0.0078	0.0182
0.25	0.7169	0.0105	0.0363	0.5919	0.0094	0.0258	0.4843	0.0084	0.0264	0.3886	0.0075	0.0184
0.35	0.6858	0.0102	0.0333	0.5607	0.0091	0.0272	0.4695	0.0083	0.0250	0.3744	0.0073	0.0192
0.45	0.6667	0.0104	0.0330	0.5337	0.0091	0.0266	0.4375	0.0082	0.0209	0.3694	0.0075	0.0208
0.55	0.5953	0.0103	0.0302	0.5116	0.0093	0.0234	0.4169	0.0084	0.0179	0.3303	0.0074	0.0173
0.65	0.5945	0.0111	0.0262	0.4660	0.0095	0.0196	0.3984	0.0087	0.0170	0.3158	0.0077	0.0139
0.75	0.6043	0.0136	0.0265	0.4825	0.0115	0.0205	0.3953	0.0101	0.0173	0.3081	0.0087	0.0157
0.85	0.6952	0.0238	0.0409	0.5409	0.0193	0.0297	0.4023	0.0154	0.0274	0.3188	0.0129	0.0243
0.95	0.7332	0.0656	0.0809	0.5711	0.0555	0.0688	0.3413	0.0405	0.0631	0.3905	0.0391	0.0638

$\cos(\theta_\eta^*)$	$W=(1645.0\pm5.0)$ MeV			$W=(1655.0\pm5.0)$ MeV			$W=(1665.0\pm5.0)$ MeV			$W=(1675.0\pm5.0)$ MeV		
	$d\sigma/d\Omega$	Δ_{stat}	Δ_{syst}	$d\sigma/d\Omega$	Δ_{stat}	Δ_{syst}	$d\sigma/d\Omega$	Δ_{stat}	Δ_{syst}	$d\sigma/d\Omega$	Δ_{stat}	Δ_{syst}
	$[\mu\text{b/sr}]$	$[\mu\text{b/sr}]$	$[\mu\text{b/sr}]$	$[\mu\text{b/sr}]$	$[\mu\text{b/sr}]$	$[\mu\text{b/sr}]$	$[\mu\text{b/sr}]$	$[\mu\text{b/sr}]$	$[\mu\text{b/sr}]$	$[\mu\text{b/sr}]$	$[\mu\text{b/sr}]$	$[\mu\text{b/sr}]$
−0.95	0.3625	0.0103	0.0202	0.2860	0.0093	0.0168	0.2330	0.0085	0.0104	0.2023	0.0080	0.0099
−0.85	0.3362	0.0070	0.0174	0.2858	0.0066	0.0161	0.2495	0.0063	0.0129	0.2089	0.0058	0.0103
−0.75	0.3844	0.0103	0.0202	0.3105	0.0094	0.0176	0.2719	0.0089	0.0145	0.2212	0.0082	0.0110
−0.65	0.3741	0.0105	0.0195	0.3331	0.0101	0.0174	0.2803	0.0095	0.0138	0.2616	0.0092	0.0122
−0.55	0.4522	0.0127	0.0214	0.3783	0.0118	0.0173	0.3038	0.0107	0.0140	0.2784	0.0104	0.0128
−0.45	0.4188	0.0119	0.0184	0.3541	0.0109	0.0151	0.3133	0.0103	0.0141	0.2757	0.0096	0.0126
−0.35	0.3779	0.0102	0.0164	0.3307	0.0095	0.0138	0.2895	0.0088	0.0125	0.2490	0.0082	0.0109
−0.25	0.3791	0.0098	0.0164	0.3192	0.0090	0.0131	0.2781	0.0084	0.0116	0.2513	0.0080	0.0108
−0.15	0.3772	0.0097	0.0164	0.3315	0.0092	0.0141	0.2814	0.0085	0.0120	0.2430	0.0079	0.0108
−0.05	0.3770	0.0078	0.0157	0.3284	0.0072	0.0143	0.2728	0.0066	0.0125	0.2654	0.0065	0.0122
0.05	0.3537	0.0073	0.0150	0.2996	0.0067	0.0130	0.2791	0.0065	0.0122	0.2565	0.0062	0.0116
0.15	0.3353	0.0070	0.0156	0.3013	0.0066	0.0133	0.2761	0.0063	0.0118	0.2510	0.0060	0.0122
0.25	0.3214	0.0068	0.0158	0.2767	0.0063	0.0124	0.2542	0.0060	0.0118	0.2590	0.0061	0.0128
0.35	0.3112	0.0066	0.0148	0.2651	0.0062	0.0130	0.2444	0.0059	0.0113	0.2337	0.0058	0.0113
0.45	0.2941	0.0067	0.0154	0.2576	0.0064	0.0140	0.2380	0.0061	0.0103	0.2446	0.0062	0.0124
0.55	0.2779	0.0068	0.0138	0.2382	0.0063	0.0113	0.2180	0.0061	0.0091	0.2188	0.0061	0.0096
0.65	0.2430	0.0067	0.0107	0.2038	0.0062	0.0095	0.1978	0.0061	0.0084	0.1944	0.0061	0.0082
0.75	0.2347	0.0075	0.0107	0.1812	0.0065	0.0108	0.1633	0.0061	0.0073	0.1544	0.0059	0.0069
0.85	0.2256	0.0104	0.0134	0.1883	0.0090	0.0151	0.1359	0.0076	0.0099	0.1446	0.0078	0.0092
0.95	0.2536	0.0287	0.0319	0.2086	0.0234	0.0222	0.1476	0.0189	0.0218	0.1098	0.0164	0.0163

$\cos(\theta_\eta^*)$	$W=(1685.0\pm5.0)$ MeV			$W=(1695.0\pm5.0)$ MeV			$W=(1705.0\pm5.0)$ MeV			$W=(1715.0\pm5.0)$ MeV		
	$d\sigma/d\Omega$	Δ_{stat}	Δ_{syst}	$d\sigma/d\Omega$	Δ_{stat}	Δ_{syst}	$d\sigma/d\Omega$	Δ_{stat}	Δ_{syst}	$d\sigma/d\Omega$	Δ_{stat}	Δ_{syst}
	$[\mu\text{b/sr}]$	$[\mu\text{b/sr}]$	$[\mu\text{b/sr}]$	$[\mu\text{b/sr}]$	$[\mu\text{b/sr}]$	$[\mu\text{b/sr}]$	$[\mu\text{b/sr}]$	$[\mu\text{b/sr}]$	$[\mu\text{b/sr}]$	$[\mu\text{b/sr}]$	$[\mu\text{b/sr}]$	$[\mu\text{b/sr}]$
−0.95	0.1856	0.0078	0.0086	0.1668	0.0074	0.0090	0.1581	0.0072	0.0087	0.1166	0.0062	0.0080
−0.85	0.1858	0.0056	0.0090	0.1711	0.0054	0.0091	0.1483	0.0050	0.0070	0.1382	0.0049	0.0084
−0.75	0.2213	0.0082	0.0110	0.1929	0.0078	0.0095	0.1732	0.0075	0.0077	0.1642	0.0073	0.0088
−0.65	0.2192	0.0086	0.0100	0.2081	0.0085	0.0103	0.2022	0.0085	0.0095	0.1765	0.0080	0.0081
−0.55	0.2593	0.0101	0.0116	0.2414	0.0099	0.0127	0.2393	0.0100	0.0110	0.2214	0.0098	0.0099
−0.45	0.2453	0.0091	0.0111	0.2334	0.0090	0.0115	0.2388	0.0091	0.0109	0.2288	0.0089	0.0105
−0.35	0.2361	0.0080	0.0104	0.2219	0.0078	0.0100	0.2128	0.0077	0.0096	0.2275	0.0080	0.0100
−0.25	0.2412	0.0079	0.0106	0.2509	0.0081	0.0111	0.2364	0.0080	0.0108	0.2470	0.0082	0.0104
−0.15	0.2534	0.0077	0.0116	0.2620	0.0067	0.0113	0.2699	0.0068	0.0120	0.2724	0.0069	0.0114
−0.05	0.2606	0.0064	0.0118	0.2807	0.0067	0.0117	0.2815	0.0067	0.0121	0.2775	0.0067	0.0118
0.05	0.2728	0.0064	0.0115	0.2746	0.0064	0.0115	0.2845	0.0066	0.0122	0.2827	0.0066	0.0122
0.15	0.2794	0.0064	0.0114	0.2808	0.0064	0.0129	0.2909	0.0065	0.0127	0.2894	0.0065	0.0126
0.25	0.2693	0.0063	0.0116	0.2822	0.0065	0.0136	0.3013	0.0067	0.0130	0.2902	0.0066	0.0124
0.35	0.2547	0.0061	0.0121	0.2750	0.0064	0.0130	0.3044	0.0068	0.0130	0.3053	0.0069	0.0146
0.45	0.2680	0.0066	0.0132	0.2789	0.0068	0.0137	0.2972	0.0070	0.0141	0.3001	0.0071	0.0169
0.55	0.2392	0.0064	0.0111	0.2638	0.0068	0.0117	0.2880	0.0072	0.0142	0.2975	0.0073	0.0157
0.65	0.2150	0.0064	0.0095	0.2488	0.0070	0.0106	0.2677	0.0072	0.0134	0.2856	0.0075	0.0127
0.75	0.1884	0.0066	0.0082	0.2068	0.0070	0.0119	0.2280	0.0074	0.0116	0.2560	0.0079	0.0111
0.85	0.1422	0.0079	0.0093	0.1651	0.0086	0.0166	0.1869	0.0094	0.0118	0.2108	0.0100	0.0120
0.95	0.0501	0.0119	0.0119	0.0846	0.0160	0.0128	0.1196	0.0200	0.0206	0.1048	0.0204	0.0144

$\cos(\theta_\eta^*)$	$W=(1725.0\pm5.0)$ MeV			$W=(1735.0\pm5.0)$ MeV			$W=(1745.0\pm5.0)$ MeV			$W=(1755.0\pm5.0)$ MeV		
	$d\sigma/d\Omega$	Δ_{stat}	Δ_{syst}	$d\sigma/d\Omega$	Δ_{stat}	Δ_{syst}	$d\sigma/d\Omega$	Δ_{stat}	Δ_{syst}	$d\sigma/d\Omega$	Δ_{stat}	Δ_{syst}
	$[\mu\text{b/sr}]$	$[\mu\text{b/sr}]$	$[\mu\text{b/sr}]$	$[\mu\text{b/sr}]$	$[\mu\text{b/sr}]$	$[\mu\text{b/sr}]$	$[\mu\text{b/sr}]$	$[\mu\text{b/sr}]$	$[\mu\text{b/sr}]$	$[\mu\text{b/sr}]$	$[\mu\text{b/sr}]$	$[\mu\text{b/sr}]$
−0.95	0.1169	0.0062	0.0067	0.1130	0.0059	0.0066	0.1012	0.0056	0.0056	0.0850	0.0052	0.0042
−0.85	0.1341	0.0048	0.0064	0.1232	0.0046	0.0065	0.1129	0.0044	0.0060	0.0950	0.0041	0.0056
−0.75	0.1486	0.0070	0.0069	0.1234	0.0065	0.0061	0.1443	0.0070	0.0072	0.1304	0.0067	0.0073
−0.65	0.1621	0.0077	0.0073	0.1721	0.0080	0.0077	0.1739	0.0081	0.0088	0.1542	0.0077	0.0076
−0.55	0.2105	0.0096	0.0093	0.1790	0.0090	0.0078	0.1858	0.0092	0.0093	0.1755	0.0091	0.0083
−0.45	0.2155	0.0087	0.0096	0.1941	0.0083	0.0087	0.1928	0.0084	0.0091	0.1935	0.0085	0.0088
−0.35	0.2210	0.0079	0.0099	0.2188	0.0080	0.0095	0.2079	0.0078	0.0091	0.1870	0.0075	0.0081
−0.25	0.2338	0.0081	0.0105	0.2362	0.0082	0.0100	0.2243	0.0081	0.0095	0.2114	0.0079	0.0088
−0.15	0.2525	0.0066	0.0112	0.2622	0.0067	0.0118	0.2433	0.0065	0.0109	0.2476	0.0066	0.0106
−0.05	0.2742	0.0067	0.0124	0.2681	0.0066	0.0120	0.2548	0.0064	0.0117	0.2636	0.0066	0.0118
0.05	0.2746	0.0065	0.0122	0.2797	0.0065	0.0120	0.2706	0.0065	0.0119	0.2579	0.0063	0.0110
0.15	0.2863	0.0065	0.0128	0.2859	0.0065	0.0120	0.2807	0.0065	0.0118	0.2816	0.0066	0.0115
0.25	0.3092	0.0069	0.0133	0.2988	0.0068	0.0124	0.2954	0.0068	0.0130	0.2740	0.0065	0.0114
0.35	0.3076	0.0070	0.0139	0.3149	0.0071	0.0137	0.3075	0.0070	0.0158	0.2918	0.0069	0.0135
0.45	0.3092	0.0073	0.0145	0.2935	0.0071	0.0154	0.2994	0.0072	0.0148	0.2894	0.0072	0.0163
0.55	0.3070	0.0075	0.0148	0.2851	0.0073	0.0167	0.2986	0.0075	0.0129	0.2764	0.0073	0.0153
0.65	0.2996	0.0078	0.0148	0.2837	0.0077	0.0128	0.2954	0.0079	0.0127	0.2684	0.0076	0.0131
0.75	0.2797	0.0083	0.0143	0.2719	0.0082	0.0128	0.2480	0.0078	0.0112	0.2429	0.0078	0.0113
0.85	0.2134	0.0101	0.0143	0.2284	0.0105	0.0168	0.2333	0.0105	0.0172	0.2366	0.0107	0.0146
0.95	0.1927	0.0290	0.0098	0.2204	0.0306	0.0159	0.2207	0.0315	0.0384	0.1416	0.0247	0.0188

$\cos(\theta_\eta^*)$	$W=(1765.0\pm5.0)$ MeV			$W=(1775.0\pm5.0)$ MeV			$W=(1785.0\pm5.0)$ MeV			$W=(1795.0\pm5.0)$ MeV		
	$d\sigma/d\Omega$ $[\mu b/sr]$	Δ_{stat} $[\mu b/sr]$	Δ_{syst} $[\mu b/sr]$	$d\sigma/d\Omega$ $[\mu b/sr]$	Δ_{stat} $[\mu b/sr]$	Δ_{syst} $[\mu b/sr]$	$d\sigma/d\Omega$ $[\mu b/sr]$	Δ_{stat} $[\mu b/sr]$	Δ_{syst} $[\mu b/sr]$	$d\sigma/d\Omega$ $[\mu b/sr]$	Δ_{stat} $[\mu b/sr]$	Δ_{syst} $[\mu b/sr]$
−0.95	0.0714	0.0047	0.0041	0.0774	0.0049	0.0051	0.0701	0.0047	0.0045	0.0698	0.0046	0.0041
−0.85	0.0999	0.0042	0.0057	0.0963	0.0042	0.0050	0.0941	0.0042	0.0050	0.0927	0.0042	0.0046
−0.75	0.1281	0.0067	0.0068	0.1216	0.0065	0.0059	0.1188	0.0065	0.0058	0.1092	0.0063	0.0053
−0.65	0.1475	0.0076	0.0070	0.1335	0.0074	0.0064	0.1365	0.0075	0.0064	0.1300	0.0074	0.0060
−0.55	0.1843	0.0094	0.0080	0.1708	0.0093	0.0078	0.1798	0.0096	0.0081	0.1657	0.0093	0.0075
−0.45	0.1951	0.0086	0.0087	0.1793	0.0084	0.0081	0.1606	0.0081	0.0075	0.1620	0.0083	0.0077
−0.35	0.1961	0.0078	0.0091	0.1934	0.0078	0.0088	0.1846	0.0078	0.0085	0.1836	0.0080	0.0087
−0.25	0.2223	0.0083	0.0102	0.2086	0.0081	0.0094	0.2137	0.0084	0.0098	0.1930	0.0077	0.0092
−0.15	0.2374	0.0065	0.0103	0.2358	0.0066	0.0105	0.2189	0.0064	0.0101	0.2152	0.0064	0.0097
−0.05	0.2585	0.0065	0.0113	0.2212	0.0061	0.0099	0.2262	0.0063	0.0103	0.2323	0.0065	0.0101
0.05	0.2528	0.0063	0.0111	0.2540	0.0065	0.0111	0.2463	0.0064	0.0110	0.2301	0.0063	0.0100
0.15	0.2669	0.0065	0.0114	0.2458	0.0063	0.0104	0.2434	0.0064	0.0108	0.2409	0.0065	0.0105
0.25	0.2701	0.0066	0.0113	0.2700	0.0067	0.0114	0.2569	0.0067	0.0114	0.2534	0.0067	0.0114
0.35	0.2669	0.0067	0.0119	0.2690	0.0069	0.0116	0.2549	0.0068	0.0113	0.2636	0.0070	0.0118
0.45	0.2812	0.0072	0.0157	0.2916	0.0074	0.0164	0.2761	0.0074	0.0125	0.2436	0.0071	0.0117
0.55	0.2703	0.0073	0.0161	0.2738	0.0075	0.0152	0.2699	0.0076	0.0120	0.2587	0.0075	0.0135
0.65	0.2485	0.0074	0.0130	0.2846	0.0080	0.0123	0.2608	0.0078	0.0111	0.2500	0.0078	0.0116
0.75	0.2523	0.0081	0.0116	0.2525	0.0083	0.0129	0.2584	0.0085	0.0125	0.2410	0.0085	0.0101
0.85	0.2354	0.0107	0.0132	0.2373	0.0107	0.0232	0.2404	0.0110	0.0184	0.2396	0.0112	0.0129
0.95	0.2321	0.0317	0.0144	0.2278	0.0327	0.0353	0.2081	0.0314	0.0223	0.2320	0.0331	0.0389

$\cos(\theta_\eta^*)$	$W=(1805.0\pm5.0)$ MeV			$W=(1815.0\pm5.0)$ MeV			$W=(1825.0\pm5.0)$ MeV			$W=(1835.0\pm5.0)$ MeV		
	$d\sigma/d\Omega$ $[\mu b/sr]$	Δ_{stat} $[\mu b/sr]$	Δ_{syst} $[\mu b/sr]$	$d\sigma/d\Omega$ $[\mu b/sr]$	Δ_{stat} $[\mu b/sr]$	Δ_{syst} $[\mu b/sr]$	$d\sigma/d\Omega$ $[\mu b/sr]$	Δ_{stat} $[\mu b/sr]$	Δ_{syst} $[\mu b/sr]$	$d\sigma/d\Omega$ $[\mu b/sr]$	Δ_{stat} $[\mu b/sr]$	Δ_{syst} $[\mu b/sr]$
−0.95	0.0715	0.0048	0.0038	0.0711	0.0049	0.0044	0.0722	0.0050	0.0033	0.0662	0.0051	0.0034
−0.85	0.0937	0.0042	0.0044	0.0904	0.0042	0.0047	0.0809	0.0041	0.0038	0.0784	0.0042	0.0038
−0.75	0.0939	0.0059	0.0043	0.1007	0.0062	0.0047	0.0966	0.0061	0.0042	0.0836	0.0058	0.0037
−0.65	0.1238	0.0073	0.0057	0.1150	0.0071	0.0051	0.1202	0.0074	0.0052	0.1284	0.0078	0.0057
−0.55	0.1413	0.0088	0.0066	0.1409	0.0089	0.0064	0.1378	0.0091	0.0071	0.1429	0.0096	0.0068
−0.45	0.1735	0.0087	0.0083	0.1533	0.0082	0.0074	0.1345	0.0080	0.0071	0.1378	0.0083	0.0072
−0.35	0.1708	0.0078	0.0081	0.1687	0.0078	0.0083	0.1555	0.0077	0.0076	0.1480	0.0077	0.0073
−0.25	0.1966	0.0066	0.0090	0.1858	0.0065	0.0091	0.1952	0.0068	0.0087	0.1745	0.0067	0.0078
−0.15	0.2109	0.0065	0.0096	0.2078	0.0066	0.0100	0.2006	0.0068	0.0089	0.1739	0.0066	0.0078
−0.05	0.2212	0.0065	0.0102	0.2095	0.0064	0.0097	0.2030	0.0066	0.0090	0.2023	0.0070	0.0091
0.05	0.2310	0.0065	0.0105	0.2252	0.0065	0.0099	0.2182	0.0067	0.0093	0.2147	0.0070	0.0094
0.15	0.2244	0.0063	0.0100	0.2309	0.0067	0.0097	0.2204	0.0067	0.0093	0.2277	0.0071	0.0102
0.25	0.2528	0.0069	0.0108	0.2408	0.0069	0.0102	0.2285	0.0070	0.0105	0.2383	0.0075	0.0102
0.35	0.2420	0.0068	0.0104	0.2439	0.0071	0.0110	0.2371	0.0073	0.0114	0.2420	0.0077	0.0106
0.45	0.2590	0.0074	0.0121	0.2467	0.0075	0.0112	0.2583	0.0080	0.0116	0.2298	0.0079	0.0119
0.55	0.2533	0.0077	0.0135	0.2584	0.0079	0.0113	0.2259	0.0077	0.0113	0.2428	0.0084	0.0135
0.65	0.2504	0.0081	0.0133	0.2533	0.0084	0.0128	0.2506	0.0087	0.0138	0.2498	0.0091	0.0143
0.75	0.2433	0.0087	0.0115	0.2235	0.0086	0.0130	0.2526	0.0096	0.0120	0.2258	0.0096	0.0125
0.85	0.1995	0.0104	0.0155	0.2248	0.0114	0.0164	0.2261	0.0118	0.0135	0.2434	0.0130	0.0134
0.95	0.2498	0.0346	0.0466	0.2246	0.0328	0.0416	0.2243	0.0335	0.0291	0.1876	0.0319	0.0159

$\cos(\theta_\eta^*)$	$W=(1845.0\pm5.0)$ MeV			$W=(1855.0\pm5.0)$ MeV			$W=(1865.0\pm5.0)$ MeV			$W=(1875.0\pm5.0)$ MeV		
	$d\sigma/d\Omega$ $[\mu b/sr]$	Δ_{stat} $[\mu b/sr]$	Δ_{syst} $[\mu b/sr]$	$d\sigma/d\Omega$ $[\mu b/sr]$	Δ_{stat} $[\mu b/sr]$	Δ_{syst} $[\mu b/sr]$	$d\sigma/d\Omega$ $[\mu b/sr]$	Δ_{stat} $[\mu b/sr]$	Δ_{syst} $[\mu b/sr]$	$d\sigma/d\Omega$ $[\mu b/sr]$	Δ_{stat} $[\mu b/sr]$	Δ_{syst} $[\mu b/sr]$
−0.95	0.0553	0.0047	0.0028	0.0530	0.0049	0.0036	0.0454	0.0050	0.0027	0.0564	0.0061	0.0027
−0.85	0.0767	0.0043	0.0039	0.0748	0.0045	0.0041	0.0663	0.0047	0.0033	0.0622	0.0050	0.0033
−0.75	0.0956	0.0064	0.0046	0.0864	0.0064	0.0044	0.0813	0.0066	0.0039	0.0600	0.0063	0.0034
−0.65	0.1084	0.0075	0.0051	0.1123	0.0080	0.0057	0.0921	0.0079	0.0043	0.0849	0.0085	0.0045
−0.55	0.1404	0.0100	0.0070	0.1288	0.0101	0.0069	0.1102	0.0101	0.0066	0.1085	0.0109	0.0075
−0.45	0.1331	0.0083	0.0072	0.1301	0.0085	0.0073	0.1198	0.0087	0.0081	0.1214	0.0095	0.0086
−0.35	0.1549	0.0080	0.0077	0.1342	0.0079	0.0073	0.1178	0.0079	0.0066	0.1270	0.0077	0.0072
−0.25	0.1621	0.0068	0.0074	0.1670	0.0073	0.0089	0.1610	0.0078	0.0078	0.1434	0.0084	0.0076
−0.15	0.1706	0.0069	0.0080	0.1728	0.0075	0.0087	0.1610	0.0079	0.0078	0.1617	0.0090	0.0089
−0.05	0.1783	0.0069	0.0085	0.1904	0.0075	0.0089	0.1681	0.0077	0.0083	0.1455	0.0080	0.0073
0.05	0.1959	0.0069	0.0090	0.1898	0.0072	0.0088	0.1720	0.0075	0.0082	0.1819	0.0088	0.0080
0.15	0.1913	0.0069	0.0086	0.1989	0.0076	0.0090	0.1770	0.0078	0.0084	0.1740	0.0088	0.0079
0.25	0.2036	0.0073	0.0091	0.1910	0.0075	0.0086	0.1639	0.0077	0.0076	0.1672	0.0087	0.0077
0.35	0.2098	0.0075	0.0097	0.1975	0.0078	0.0094	0.1920	0.0084	0.0082	0.1786	0.0089	0.0080
0.45	0.2226	0.0081	0.0117	0.2070	0.0083	0.0113	0.2212	0.0093	0.0091	0.1990	0.0099	0.0094
0.55	0.2393	0.0088	0.0136	0.2097	0.0088	0.0129	0.2196	0.0099	0.0107	0.2035	0.0107	0.0122
0.65	0.2348	0.0094	0.0157	0.2264	0.0099	0.0150	0.2158	0.0107	0.0125	0.1868	0.0114	0.0119
0.75	0.2144	0.0099	0.0151	0.2025	0.0105	0.0134	0.2226	0.0122	0.0105	0.2459	0.0149	0.0132
0.85	0.2205	0.0132	0.0190	0.2240	0.0143	0.0160	0.2400	0.0165	0.0127	0.2589	0.0200	0.0178
0.95	0.1690	0.0311	0.0363	0.2178	0.0385	0.0217	0.2918	0.0482	0.0254	0.1694	0.0406	0.0235

Total cross section of $\gamma p \to \eta p$ as a function of E_γ

E_γ [MeV]	ΔE_γ [MeV]	σ [μb]	Δ_{stat} [μb]	Δ_{syst} [μb]
645.0	15.0	0.1895	0.0256	0.0494
667.5	7.5	0.5737	0.0243	0.0621
682.5	7.5	1.3304	0.0198	0.0806
697.5	7.5	2.7281	0.0215	0.1395
712.5	7.5	4.7943	0.0243	0.2273
727.5	7.5	7.1621	0.0316	0.3403
742.5	7.5	9.3935	0.0346	0.4346
757.5	7.5	10.8197	0.0408	0.5100
772.5	7.5	11.9084	0.0471	0.5498
787.5	7.5	12.3841	0.0481	0.5938
802.5	7.5	12.5127	0.0488	0.6179
817.5	7.5	12.3539	0.0507	0.6104
832.5	7.5	11.8823	0.0534	0.5677
847.5	7.5	11.3563	0.0558	0.5454
862.5	7.5	10.7205	0.0518	0.4930
877.5	7.5	10.2301	0.0571	0.4733
892.5	7.5	9.4048	0.0549	0.4480
907.5	7.5	8.5477	0.0383	0.3861
922.5	7.5	7.6719	0.0367	0.3470
937.5	7.5	6.9228	0.0368	0.3225
952.5	7.5	6.2106	0.0339	0.2891
967.5	7.5	5.5337	0.0320	0.2593
982.5	7.5	4.8962	0.0321	0.2343
997.5	7.5	4.4110	0.0306	0.2163
1012.5	7.5	4.0271	0.0278	0.1947
1027.5	7.5	3.7408	0.0265	0.1838
1042.5	7.5	3.5155	0.0262	0.1724
1057.5	7.5	3.3682	0.0253	0.1635
1072.5	7.5	3.3750	0.0270	0.1696
1087.5	7.5	3.2890	0.0262	0.1648
1102.5	7.5	3.2182	0.0259	0.1602
1117.5	7.5	3.2586	0.0279	0.1635
1132.5	7.5	3.1885	0.0266	0.1650
1147.5	7.5	3.0929	0.0270	0.1538
1162.5	7.5	3.0453	0.0252	0.1467
1177.5	7.5	2.9821	0.0250	0.1571
1192.5	7.5	2.8403	0.0254	0.1391
1207.5	7.5	2.8272	0.0251	0.1394
1222.5	7.5	2.7491	0.0246	0.1518
1237.5	7.5	2.7121	0.0268	0.1340
1252.5	7.5	2.6228	0.0248	0.1245
1267.5	7.5	2.5986	0.0256	0.1307
1282.5	7.5	2.5473	0.0244	0.1334
1297.5	7.5	2.4345	0.0262	0.1311
1312.5	7.5	2.3919	0.0236	0.1324
1327.5	7.5	2.3247	0.0274	0.1189
1342.5	7.5	2.3226	0.0283	0.1372
1357.5	7.5	2.2270	0.0237	0.1178
1372.5	7.5	2.1113	0.0242	0.1169
1387.5	7.5	2.1186	0.0252	0.1135

Total cross section of $\gamma p \to \eta p$ as a function of W_{kin}

W_{kin} [MeV]	ΔW_{kin} [MeV]	σ [μb]	Δ_{stat} [μb]	Δ_{syst} [μb]
1492.5	2.5	7.6050	0.0488	0.4146
1497.5	2.5	10.2160	0.0507	0.5290
1502.5	2.5	11.6246	0.0537	0.6070
1507.5	2.5	13.1721	0.0611	0.6758
1512.5	2.5	14.0577	0.0773	0.7113
1517.5	2.5	15.0119	0.0898	0.7595
1522.5	2.5	15.5924	0.0989	0.7873
1527.5	2.5	15.7235	0.1009	0.7817
1532.5	2.5	15.7435	0.1016	0.7481
1537.5	2.5	14.8955	0.0958	0.7218
1545.0	5.0	14.5615	0.0650	0.6817
1555.0	5.0	13.9301	0.0652	0.6517
1565.0	5.0	13.1686	0.0636	0.6221
1575.0	5.0	12.4351	0.0597	0.5957
1585.0	5.0	11.3470	0.0522	0.5570
1595.0	5.0	10.0624	0.0464	0.5124
1605.0	5.0	8.7460	0.0417	0.4282
1615.0	5.0	7.3497	0.0367	0.3435
1625.0	5.0	6.1517	0.0332	0.3009
1635.0	5.0	5.0827	0.0297	0.2570
1645.0	5.0	4.1463	0.0263	0.2002
1655.0	5.0	3.5201	0.0240	0.1765
1665.0	5.0	3.0689	0.0222	0.1464
1675.0	5.0	2.8205	0.0213	0.1358
1685.0	5.0	2.8128	0.0210	0.1337
1695.0	5.0	2.8867	0.0215	0.1465
1705.0	5.0	2.9602	0.0222	0.1430
1715.0	5.0	2.9779	0.0225	0.1433
1725.0	5.0	2.9858	0.0230	0.1428
1735.0	5.0	2.9109	0.0228	0.1414
1745.0	5.0	2.8659	0.0228	0.1411
1755.0	5.0	2.7192	0.0222	0.1339
1765.0	5.0	2.7012	0.0226	0.1317
1775.0	5.0	2.6619	0.0228	0.1392
1785.0	5.0	2.5964	0.0229	0.1275
1795.0	5.0	2.5086	0.0229	0.1208
1805.0	5.0	2.4249	0.0227	0.1241
1815.0	5.0	2.3869	0.0231	0.1232
1825.0	5.0	2.3463	0.0238	0.1159
1835.0	5.0	2.2861	0.0246	0.1148
1845.0	5.0	2.1447	0.0251	0.1252
1855.0	5.0	2.0775	0.0266	0.1188
1865.0	5.0	2.0129	0.0292	0.1023
1875.0	5.0	1.9127	0.0321	0.1101

Total cross section of $\gamma p \rightarrow \eta p$ as a function of W_{TOF}

W_{TOF} [MeV]	ΔW_{TOF} [MeV]	σ [μb]	Δ_{stat} [μb]	Δ_{syst} [μb]
1492.5	2.5	1.9333	0.0640	0.1144
1497.5	2.5	2.5617	0.0497	0.1444
1502.5	2.5	3.0610	0.0472	0.1584
1507.5	2.5	3.3728	0.0450	0.1618
1512.5	2.5	3.4993	0.0430	0.1628
1517.5	2.5	3.6865	0.0418	0.1721
1522.5	2.5	3.8228	0.0412	0.1728
1527.5	2.5	3.9150	0.0409	0.1794
1532.5	2.5	3.9062	0.0405	0.1766
1537.5	2.5	3.8117	0.0399	0.1767
1545.0	5.0	3.7520	0.0282	0.1679
1555.0	5.0	3.3898	0.0274	0.1540
1565.0	5.0	3.1896	0.0277	0.1584
1575.0	5.0	2.9747	0.0277	0.1494
1585.0	5.0	2.6942	0.0266	0.1326
1595.0	5.0	2.5392	0.0258	0.1279
1605.0	5.0	2.2176	0.0240	0.1098
1615.0	5.0	1.9311	0.0224	0.0930
1625.0	5.0	1.6453	0.0210	0.0817
1635.0	5.0	1.3949	0.0195	0.0698
1645.0	5.0	1.1234	0.0177	0.0569
1655.0	5.0	0.9256	0.0162	0.0500
1665.0	5.0	0.7444	0.0144	0.0396
1675.0	5.0	0.6205	0.0131	0.0321
1685.0	5.0	0.5198	0.0119	0.0278
1695.0	5.0	0.4552	0.0111	0.0233
1705.0	5.0	0.4028	0.0105	0.0212
1715.0	5.0	0.3783	0.0100	0.0204
1725.0	5.0	0.3417	0.0095	0.0173
1735.0	5.0	0.3454	0.0095	0.0176
1745.0	5.0	0.3438	0.0094	0.0187
1755.0	5.0	0.3739	0.0100	0.0190
1765.0	5.0	0.3564	0.0099	0.0175
1775.0	5.0	0.3639	0.0104	0.0182
1785.0	5.0	0.3874	0.0113	0.0193
1795.0	5.0	0.3667	0.0118	0.0179
1805.0	5.0	0.3635	0.0130	0.0178
1815.0	5.0	0.3837	0.0151	0.0200
1825.0	5.0	0.3615	0.0169	0.0178
1835.0	5.0	0.3861	0.0210	0.0241
1845.0	5.0	0.3878	0.0259	0.0324
1855.0	5.0	0.3612	0.0321	0.0461
1865.0	5.0	0.2960	0.0338	0.0285
1875.0	5.0	0.3106	0.0434	0.0362

Quasi-free exclusive η-photoproduction on the neutron

Differential cross sections of $\gamma n \to \eta n$ as a function of E_γ

$\cos(\theta_\eta^*)$	E_γ=(645.0±15.0) MeV			E_γ=(667.5±7.5) MeV			E_γ=(682.5±7.5) MeV			E_γ=(697.5±7.5) MeV		
	$d\sigma/d\Omega$ $[\mu b/sr]$	$\Delta_{\rm stat}$ $[\mu b/sr]$	$\Delta_{\rm syst}$ $[\mu b/sr]$	$d\sigma/d\Omega$ $[\mu b/sr]$	$\Delta_{\rm stat}$ $[\mu b/sr]$	$\Delta_{\rm syst}$ $[\mu b/sr]$	$d\sigma/d\Omega$ $[\mu b/sr]$	$\Delta_{\rm stat}$ $[\mu b/sr]$	$\Delta_{\rm syst}$ $[\mu b/sr]$	$d\sigma/d\Omega$ $[\mu b/sr]$	$\Delta_{\rm stat}$ $[\mu b/sr]$	$\Delta_{\rm syst}$ $[\mu b/sr]$
−0.95	0.1105	0.0148	0.0114	0.2102	0.0177	0.0184	0.3229	0.0170	0.0329	0.4289	0.0177	0.0474
−0.85	0.0923	0.0141	0.0142	0.1609	0.0156	0.0157	0.2776	0.0146	0.0261	0.3713	0.0150	0.0362
−0.75	0.0608	0.0120	0.0172	0.1479	0.0168	0.0132	0.2304	0.0136	0.0188	0.3260	0.0137	0.0303
−0.65	0.0719	0.0160	0.0089	0.1157	0.0173	0.0124	0.1975	0.0145	0.0172	0.3172	0.0135	0.0321
−0.55	0.0484	0.0145	0.0055	0.0842	0.0155	0.0070	0.1532	0.0152	0.0130	0.2801	0.0129	0.0247
−0.45	0.0629	0.0161	0.0082	0.0785	0.0162	0.0090	0.1806	0.0164	0.0156	0.2500	0.0148	0.0209
−0.35	0.0280	0.0120	0.0041	0.0611	0.0158	0.0080	0.1103	0.0142	0.0108	0.2347	0.0162	0.0206
−0.25	0.0303	0.0128	0.0072	0.0398	0.0152	0.0052	0.1285	0.0156	0.0150	0.2054	0.0154	0.0183
−0.15	0.0337	0.0171	0.0081	0.0687	0.0174	0.0073	0.0969	0.0147	0.0105	0.2318	0.0169	0.0237
−0.05	0.0629	0.0161	0.0230	0.0343	0.0171	0.0071	0.0936	0.0151	0.0100	0.2285	0.0172	0.0233
0.05	0.0260	0.0161	0.0132	0.0102	0.0153	0.0017	0.1051	0.0167	0.0126	0.1910	0.0170	0.0175
0.15	−0.0003	0.0089	0.0003	0.0408	0.0186	0.0060	0.0490	0.0154	0.0060	0.1585	0.0166	0.0159
0.25	−0.0145	0.0097	0.0063	0.0236	0.0167	0.0040	0.0898	0.0161	0.0116	0.1203	0.0164	0.0126
0.35	0.0118	0.0106	0.0065	0.0864	0.0233	0.0276	0.0563	0.0147	0.0094	0.1682	0.0168	0.0165
0.45	0.0036	0.0090	0.0024	0.0363	0.0163	0.0114	0.0632	0.0151	0.0126	0.1784	0.0158	0.0198
0.55	0.0108	0.0090	0.0049	0.0493	0.0178	0.0116	0.0736	0.0199	0.0098	0.1415	0.0157	0.0211
0.65	−0.0045	0.0094	0.0026	0.0083	0.0171	0.0026	0.0411	0.0178	0.0107	0.1464	0.0161	0.0193
0.75	−0.0009	0.0057	0.0004	−0.0045	0.0132	0.0023	0.0794	0.0167	0.0187	0.1628	0.0171	0.0164
0.85	0.0484	0.0201	0.0588	0.0077	0.0163	0.0087	0.0361	0.0161	0.0072	0.1492	0.0179	0.0161
0.95	−0.0121	0.0109	0.0079	0.0054	0.0219	0.0009	0.0074	0.0161	0.0038	0.1342	0.0206	0.0214

$\cos(\theta_\eta^*)$	E_γ=(712.5±7.5) MeV			E_γ=(727.5±7.5) MeV			E_γ=(742.5±7.5) MeV			E_γ=(757.5±7.5) MeV		
	$d\sigma/d\Omega$ $[\mu b/sr]$	$\Delta_{\rm stat}$ $[\mu b/sr]$	$\Delta_{\rm syst}$ $[\mu b/sr]$	$d\sigma/d\Omega$ $[\mu b/sr]$	$\Delta_{\rm stat}$ $[\mu b/sr]$	$\Delta_{\rm syst}$ $[\mu b/sr]$	$d\sigma/d\Omega$ $[\mu b/sr]$	$\Delta_{\rm stat}$ $[\mu b/sr]$	$\Delta_{\rm syst}$ $[\mu b/sr]$	$d\sigma/d\Omega$ $[\mu b/sr]$	$\Delta_{\rm stat}$ $[\mu b/sr]$	$\Delta_{\rm syst}$ $[\mu b/sr]$
−0.95	0.6184	0.0192	0.0638	0.8186	0.0239	0.0772	0.9111	0.0232	0.1020	0.9973	0.0242	0.1192
−0.85	0.4843	0.0150	0.0499	0.6331	0.0182	0.0657	0.7644	0.0177	0.0929	0.7903	0.0176	0.0974
−0.75	0.4552	0.0140	0.0423	0.5468	0.0165	0.0518	0.6289	0.0156	0.0646	0.6919	0.0159	0.0789
−0.65	0.3944	0.0130	0.0363	0.5347	0.0163	0.0500	0.6055	0.0152	0.0555	0.6603	0.0183	0.0698
−0.55	0.3889	0.0131	0.0326	0.4278	0.0195	0.0419	0.5485	0.0202	0.0534	0.6138	0.0193	0.0600
−0.45	0.3555	0.0170	0.0289	0.4786	0.0251	0.0410	0.5771	0.0210	0.0552	0.5847	0.0188	0.0533
−0.35	0.3816	0.0177	0.0330	0.5020	0.0257	0.0466	0.5401	0.0204	0.0507	0.5626	0.0185	0.0500
−0.25	0.3476	0.0173	0.0312	0.4399	0.0246	0.0436	0.5405	0.0205	0.0528	0.6181	0.0198	0.0563
−0.15	0.3235	0.0172	0.0323	0.3832	0.0237	0.0411	0.5325	0.0208	0.0554	0.5844	0.0195	0.0549
−0.05	0.3256	0.0178	0.0289	0.4116	0.0252	0.0395	0.5188	0.0211	0.0517	0.5977	0.0202	0.0550
0.05	0.2939	0.0178	0.0228	0.3906	0.0253	0.0339	0.4963	0.0216	0.0441	0.5817	0.0205	0.0539
0.15	0.3153	0.0187	0.0296	0.3678	0.0253	0.0322	0.5276	0.0226	0.0402	0.5534	0.0205	0.0506
0.25	0.2892	0.0194	0.0312	0.4013	0.0273	0.0397	0.5395	0.0238	0.0406	0.5409	0.0211	0.0436
0.35	0.3014	0.0202	0.0297	0.4272	0.0291	0.0396	0.4739	0.0235	0.0455	0.5683	0.0223	0.0473
0.45	0.2671	0.0200	0.0238	0.3509	0.0281	0.0293	0.4777	0.0245	0.0475	0.5581	0.0228	0.0464
0.55	0.3254	0.0173	0.0301	0.3991	0.0306	0.0359	0.5394	0.0271	0.0463	0.5911	0.0249	0.0487
0.65	0.2727	0.0169	0.0265	0.3761	0.0318	0.0416	0.5347	0.0284	0.0447	0.6089	0.0268	0.0540
0.75	0.2766	0.0178	0.0279	0.4533	0.0232	0.0525	0.5486	0.0307	0.0495	0.6125	0.0287	0.0514
0.85	0.2529	0.0186	0.0267	0.4426	0.0245	0.0524	0.5648	0.0248	0.0581	0.6309	0.0326	0.0585
0.95	0.2759	0.0229	0.0287	0.4767	0.0289	0.0552	0.7323	0.0327	0.0804	0.6908	0.0324	0.0809

$\cos(\theta_\eta^*)$	$E_\gamma{=}(772.5{\pm}7.5)$ MeV			$E_\gamma{=}(787.5{\pm}7.5)$ MeV			$E_\gamma{=}(802.5{\pm}7.5)$ MeV			$E_\gamma{=}(817.5{\pm}7.5)$ MeV		
	$d\sigma/d\Omega$	$\Delta_{\rm stat}$	$\Delta_{\rm syst}$	$d\sigma/d\Omega$	$\Delta_{\rm stat}$	$\Delta_{\rm syst}$	$d\sigma/d\Omega$	$\Delta_{\rm stat}$	$\Delta_{\rm syst}$	$d\sigma/d\Omega$	$\Delta_{\rm stat}$	$\Delta_{\rm syst}$
	[μb/sr]	[μb/sr]	[μb/sr]	[μb/sr]	[μb/sr]	[μb/sr]	[μb/sr]	[μb/sr]	[μb/sr]	[μb/sr]	[μb/sr]	[μb/sr]
−0.95	1.0069	0.0255	0.1190	1.0856	0.0252	0.1453	1.0879	0.0252	0.1383	1.0002	0.0243	0.1214
−0.85	0.8173	0.0185	0.0931	0.8448	0.0178	0.1066	0.8443	0.0176	0.1037	0.8035	0.0174	0.1053
−0.75	0.7330	0.0168	0.0837	0.7418	0.0160	0.0887	0.7518	0.0161	0.0870	0.7690	0.0167	0.0899
−0.65	0.6862	0.0202	0.0759	0.7020	0.0200	0.0787	0.6933	0.0197	0.0694	0.6108	0.0195	0.0574
−0.55	0.7087	0.0206	0.0727	0.6792	0.0196	0.0678	0.6598	0.0190	0.0585	0.6780	0.0203	0.0557
−0.45	0.6255	0.0193	0.0638	0.6506	0.0191	0.0628	0.6032	0.0181	0.0545	0.6364	0.0194	0.0555
−0.35	0.6374	0.0197	0.0611	0.6482	0.0193	0.0614	0.6366	0.0188	0.0664	0.5938	0.0189	0.0569
−0.25	0.5780	0.0192	0.0507	0.5805	0.0187	0.0609	0.6164	0.0189	0.0728	0.6383	0.0200	0.0653
−0.15	0.6111	0.0199	0.0609	0.6210	0.0194	0.0736	0.6379	0.0191	0.0702	0.6147	0.0195	0.0680
−0.05	0.5889	0.0199	0.0635	0.6440	0.0200	0.0756	0.6156	0.0189	0.0621	0.5850	0.0190	0.0647
0.05	0.6441	0.0212	0.0626	0.6420	0.0200	0.0685	0.5864	0.0184	0.0606	0.5878	0.0191	0.0685
0.15	0.6363	0.0216	0.0585	0.6290	0.0203	0.0656	0.6125	0.0193	0.0658	0.5597	0.0187	0.0685
0.25	0.6175	0.0221	0.0561	0.6341	0.0210	0.0626	0.6452	0.0203	0.0696	0.5897	0.0197	0.0687
0.35	0.6106	0.0225	0.0487	0.6545	0.0219	0.0614	0.6138	0.0204	0.0609	0.5751	0.0202	0.0659
0.45	0.5885	0.0231	0.0458	0.5903	0.0218	0.0587	0.6067	0.0212	0.0513	0.5928	0.0213	0.0619
0.55	0.6653	0.0259	0.0627	0.6607	0.0244	0.0620	0.6201	0.0227	0.0505	0.5674	0.0223	0.0591
0.65	0.6163	0.0266	0.0563	0.7053	0.0273	0.0631	0.6328	0.0250	0.0557	0.5968	0.0249	0.0543
0.75	0.6726	0.0301	0.0479	0.6570	0.0290	0.0597	0.7080	0.0298	0.0594	0.6490	0.0295	0.0462
0.85	0.7279	0.0354	0.0586	0.7045	0.0342	0.0647	0.6778	0.0334	0.0497	0.6385	0.0343	0.0528
0.95	0.7581	0.0414	0.0696	0.7708	0.0456	0.0778	0.7655	0.0467	0.0581	0.7194	0.0497	0.0825

$\cos(\theta_\eta^*)$	$E_\gamma{=}(832.5{\pm}7.5)$ MeV			$E_\gamma{=}(847.5{\pm}7.5)$ MeV			$E_\gamma{=}(862.5{\pm}7.5)$ MeV			$E_\gamma{=}(877.5{\pm}7.5)$ MeV		
	$d\sigma/d\Omega$	$\Delta_{\rm stat}$	$\Delta_{\rm syst}$	$d\sigma/d\Omega$	$\Delta_{\rm stat}$	$\Delta_{\rm syst}$	$d\sigma/d\Omega$	$\Delta_{\rm stat}$	$\Delta_{\rm syst}$	$d\sigma/d\Omega$	$\Delta_{\rm stat}$	$\Delta_{\rm syst}$
	[μb/sr]	[μb/sr]	[μb/sr]	[μb/sr]	[μb/sr]	[μb/sr]	[μb/sr]	[μb/sr]	[μb/sr]	[μb/sr]	[μb/sr]	[μb/sr]
−0.95	1.0491	0.0269	0.1438	0.9458	0.0274	0.1177	0.9784	0.0278	0.1264	0.8812	0.0278	0.1151
−0.85	0.7497	0.0180	0.0898	0.7311	0.0192	0.0853	0.6745	0.0185	0.0790	0.6863	0.0199	0.0854
−0.75	0.6584	0.0166	0.0742	0.6508	0.0217	0.0823	0.6321	0.0231	0.0758	0.6223	0.0290	0.0754
−0.65	0.6435	0.0212	0.0754	0.6030	0.0222	0.0698	0.5760	0.0219	0.0650	0.5384	0.0267	0.0626
−0.55	0.6129	0.0204	0.0594	0.5766	0.0216	0.0557	0.5289	0.0207	0.0521	0.5464	0.0265	0.0561
−0.45	0.6068	0.0200	0.0485	0.5683	0.0212	0.0485	0.5486	0.0208	0.0526	0.5046	0.0251	0.0484
−0.35	0.5746	0.0197	0.0572	0.5280	0.0206	0.0446	0.5105	0.0203	0.0498	0.5015	0.0253	0.0497
−0.25	0.5518	0.0196	0.0657	0.5463	0.0212	0.0579	0.5075	0.0204	0.0524	0.4595	0.0245	0.0481
−0.15	0.5578	0.0194	0.0707	0.5097	0.0200	0.0644	0.5131	0.0200	0.0591	0.4673	0.0241	0.0549
−0.05	0.5693	0.0195	0.0702	0.5395	0.0204	0.0691	0.4827	0.0191	0.0597	0.4865	0.0240	0.0611
0.05	0.5418	0.0190	0.0577	0.5077	0.0196	0.0665	0.4708	0.0188	0.0606	0.4711	0.0236	0.0603
0.15	0.5746	0.0196	0.0633	0.5052	0.0197	0.0665	0.5095	0.0196	0.0687	0.4779	0.0237	0.0652
0.25	0.5398	0.0194	0.0685	0.5672	0.0213	0.0737	0.5190	0.0199	0.0690	0.5763	0.0266	0.0822
0.35	0.5739	0.0209	0.0726	0.5229	0.0212	0.0668	0.5049	0.0207	0.0652	0.4781	0.0250	0.0698
0.45	0.5826	0.0220	0.0710	0.5300	0.0225	0.0656	0.4884	0.0213	0.0616	0.4408	0.0249	0.0614
0.55	0.5746	0.0233	0.0669	0.6018	0.0255	0.0668	0.4839	0.0227	0.0561	0.4261	0.0263	0.0502
0.65	0.5409	0.0247	0.0559	0.5575	0.0268	0.0517	0.5165	0.0258	0.0498	0.4689	0.0301	0.0480
0.75	0.6569	0.0309	0.0581	0.5966	0.0317	0.0490	0.5063	0.0289	0.0391	0.5308	0.0370	0.0478
0.85	0.6767	0.0383	0.0550	0.6000	0.0392	0.0490	0.5126	0.0358	0.0349	0.4560	0.0406	0.0334
0.95	0.7072	0.0538	0.1014	0.4833	0.0489	0.0452	0.5872	0.0566	0.0460	0.5442	0.0676	0.0490

$\cos(\theta_\eta^*)$	$E_\gamma{=}(892.5{\pm}7.5)$ MeV			$E_\gamma{=}(907.5{\pm}7.5)$ MeV			$E_\gamma{=}(922.5{\pm}7.5)$ MeV			$E_\gamma{=}(937.5{\pm}7.5)$ MeV		
	$d\sigma/d\Omega$	$\Delta_{\rm stat}$	$\Delta_{\rm syst}$	$d\sigma/d\Omega$	$\Delta_{\rm stat}$	$\Delta_{\rm syst}$	$d\sigma/d\Omega$	$\Delta_{\rm stat}$	$\Delta_{\rm syst}$	$d\sigma/d\Omega$	$\Delta_{\rm stat}$	$\Delta_{\rm syst}$
	[μb/sr]	[μb/sr]	[μb/sr]	[μb/sr]	[μb/sr]	[μb/sr]	[μb/sr]	[μb/sr]	[μb/sr]	[μb/sr]	[μb/sr]	[μb/sr]
−0.95	0.8981	0.0288	0.1033	0.8289	0.0230	0.1046	0.7678	0.0224	0.1045	0.6927	0.0221	0.0865
−0.85	0.6529	0.0200	0.0745	0.5607	0.0152	0.0629	0.5657	0.0154	0.0623	0.5556	0.0160	0.0620
−0.75	0.5468	0.0283	0.0640	0.5478	0.0192	0.0602	0.5378	0.0200	0.0564	0.4674	0.0197	0.0464
−0.65	0.4973	0.0265	0.0554	0.5449	0.0189	0.0562	0.5003	0.0189	0.0499	0.4917	0.0198	0.0449
−0.55	0.5135	0.0269	0.0511	0.5145	0.0181	0.0478	0.4862	0.0185	0.0436	0.4990	0.0197	0.0421
−0.45	0.5160	0.0263	0.0495	0.4866	0.0172	0.0419	0.5023	0.0184	0.0410	0.4670	0.0187	0.0370
−0.35	0.4981	0.0260	0.0485	0.4640	0.0167	0.0389	0.4601	0.0175	0.0375	0.4281	0.0176	0.0352
−0.25	0.4391	0.0249	0.0438	0.4317	0.0163	0.0386	0.4418	0.0174	0.0392	0.4067	0.0175	0.0372
−0.15	0.4637	0.0246	0.0526	0.4435	0.0161	0.0452	0.4295	0.0167	0.0418	0.4720	0.0182	0.0453
−0.05	0.4775	0.0246	0.0609	0.4507	0.0159	0.0521	0.4256	0.0163	0.0460	0.4268	0.0172	0.0434
0.05	0.4051	0.0224	0.0545	0.4213	0.0153	0.0534	0.4291	0.0163	0.0506	0.3943	0.0164	0.0434
0.15	0.4105	0.0226	0.0580	0.3854	0.0147	0.0508	0.4268	0.0123	0.0520	0.4249	0.0126	0.0489
0.25	0.4718	0.0248	0.0648	0.4252	0.0127	0.0541	0.4276	0.0124	0.0534	0.4148	0.0126	0.0494
0.35	0.4433	0.0166	0.0561	0.4265	0.0128	0.0537	0.4064	0.0125	0.0516	0.3949	0.0127	0.0482
0.45	0.4481	0.0173	0.0561	0.4245	0.0133	0.0541	0.4123	0.0131	0.0510	0.4078	0.0136	0.0494
0.55	0.4523	0.0185	0.0539	0.4288	0.0142	0.0511	0.4204	0.0141	0.0499	0.3984	0.0143	0.0466
0.65	0.4511	0.0204	0.0483	0.4165	0.0154	0.0466	0.4101	0.0155	0.0485	0.3537	0.0150	0.0410
0.75	0.3744	0.0321	0.0319	0.4379	0.0187	0.0448	0.4172	0.0183	0.0450	0.4041	0.0186	0.0420
0.85	0.4126	0.0418	0.0280	0.4404	0.0295	0.0351	0.4006	0.0297	0.0331	0.3512	0.0227	0.0291
0.95	0.3372	0.0560	0.0275	0.3884	0.0428	0.0290	0.3295	0.0417	0.0166	0.3894	0.0494	0.0386

$\cos(\theta_\eta^*)$	$E_\gamma=(952.5\pm7.5)$ MeV			$E_\gamma=(967.5\pm7.5)$ MeV			$E_\gamma=(982.5\pm7.5)$ MeV			$E_\gamma=(997.5\pm7.5)$ MeV		
	$d\sigma/d\Omega$ [μb/sr]	Δ_{stat} [μb/sr]	Δ_{syst} [μb/sr]	$d\sigma/d\Omega$ [μb/sr]	Δ_{stat} [μb/sr]	Δ_{syst} [μb/sr]	$d\sigma/d\Omega$ [μb/sr]	Δ_{stat} [μb/sr]	Δ_{syst} [μb/sr]	$d\sigma/d\Omega$ [μb/sr]	Δ_{stat} [μb/sr]	Δ_{syst} [μb/sr]
−0.95	0.6634	0.0212	0.0782	0.5999	0.0202	0.0671	0.6176	0.0220	0.0694	0.5212	0.0202	0.0592
−0.85	0.4923	0.0147	0.0549	0.4821	0.0148	0.0513	0.4725	0.0157	0.0482	0.4383	0.0151	0.0461
−0.75	0.4794	0.0192	0.0444	0.4712	0.0191	0.0434	0.4794	0.0211	0.0427	0.4941	0.0216	0.0448
−0.65	0.4678	0.0186	0.0376	0.4598	0.0188	0.0367	0.4263	0.0197	0.0345	0.4705	0.0208	0.0386
−0.55	0.4752	0.0185	0.0368	0.4734	0.0189	0.0338	0.4312	0.0197	0.0310	0.4274	0.0196	0.0333
−0.45	0.4487	0.0176	0.0342	0.3989	0.0168	0.0279	0.4084	0.0185	0.0283	0.4349	0.0192	0.0318
−0.35	0.4262	0.0168	0.0344	0.4111	0.0166	0.0318	0.3944	0.0177	0.0297	0.3860	0.0177	0.0274
−0.25	0.4067	0.0167	0.0346	0.3811	0.0162	0.0305	0.4117	0.0183	0.0338	0.3873	0.0178	0.0301
−0.15	0.4188	0.0165	0.0381	0.4002	0.0163	0.0325	0.3983	0.0175	0.0332	0.4067	0.0177	0.0348
−0.05	0.3917	0.0157	0.0392	0.4126	0.0162	0.0372	0.4031	0.0137	0.0369	0.4050	0.0130	0.0344
0.05	0.4087	0.0121	0.0432	0.3993	0.0120	0.0404	0.3950	0.0127	0.0402	0.4031	0.0127	0.0346
0.15	0.4126	0.0121	0.0444	0.4143	0.0122	0.0444	0.4123	0.0130	0.0424	0.4234	0.0129	0.0393
0.25	0.4169	0.0123	0.0462	0.3963	0.0120	0.0436	0.4236	0.0132	0.0452	0.4223	0.0131	0.0427
0.35	0.4036	0.0125	0.0465	0.4165	0.0128	0.0474	0.4125	0.0135	0.0460	0.4058	0.0133	0.0442
0.45	0.3944	0.0129	0.0450	0.3890	0.0129	0.0440	0.4135	0.0142	0.0494	0.3914	0.0136	0.0427
0.55	0.4002	0.0138	0.0448	0.3739	0.0136	0.0419	0.3461	0.0137	0.0426	0.4099	0.0149	0.0445
0.65	0.3969	0.0153	0.0442	0.3692	0.0148	0.0415	0.3535	0.0153	0.0392	0.3306	0.0147	0.0367
0.75	0.3491	0.0169	0.0359	0.3398	0.0168	0.0353	0.3245	0.0175	0.0358	0.3243	0.0172	0.0357
0.85	0.3620	0.0223	0.0275	0.3224	0.0213	0.0279	0.3315	0.0229	0.0341	0.3158	0.0223	0.0349
0.95	0.3512	0.0461	0.0162	0.3518	0.0479	0.0315	0.2878	0.0481	0.0190	0.2537	0.0477	0.0294

$\cos(\theta_\eta^*)$	$E_\gamma=(1012.5\pm7.5)$ MeV			$E_\gamma=(1027.5\pm7.5)$ MeV			$E_\gamma=(1042.5\pm7.5)$ MeV			$E_\gamma=(1057.5\pm7.5)$ MeV		
	$d\sigma/d\Omega$ [μb/sr]	Δ_{stat} [μb/sr]	Δ_{syst} [μb/sr]	$d\sigma/d\Omega$ [μb/sr]	Δ_{stat} [μb/sr]	Δ_{syst} [μb/sr]	$d\sigma/d\Omega$ [μb/sr]	Δ_{stat} [μb/sr]	Δ_{syst} [μb/sr]	$d\sigma/d\Omega$ [μb/sr]	Δ_{stat} [μb/sr]	Δ_{syst} [μb/sr]
−0.95	0.5097	0.0198	0.0615	0.4384	0.0178	0.0617	0.4521	0.0187	0.0651	0.4285	0.0186	0.0537
−0.85	0.4346	0.0148	0.0474	0.4094	0.0142	0.0430	0.3712	0.0139	0.0406	0.3741	0.0139	0.0432
−0.75	0.4291	0.0188	0.0397	0.4087	0.0183	0.0358	0.3534	0.0172	0.0310	0.3493	0.0170	0.0339
−0.65	0.4447	0.0190	0.0355	0.4372	0.0189	0.0351	0.4209	0.0187	0.0317	0.4114	0.0183	0.0336
−0.55	0.4537	0.0189	0.0358	0.4404	0.0186	0.0354	0.3531	0.0169	0.0250	0.3765	0.0172	0.0263
−0.45	0.4151	0.0175	0.0304	0.4020	0.0172	0.0287	0.3466	0.0161	0.0240	0.3827	0.0170	0.0250
−0.35	0.3753	0.0163	0.0255	0.3914	0.0166	0.0248	0.3721	0.0165	0.0250	0.3181	0.0151	0.0216
−0.25	0.3709	0.0163	0.0266	0.3842	0.0166	0.0262	0.3855	0.0168	0.0274	0.3759	0.0165	0.0271
−0.15	0.4011	0.0165	0.0310	0.3989	0.0165	0.0286	0.3670	0.0159	0.0266	0.3598	0.0157	0.0260
−0.05	0.4043	0.0127	0.0332	0.3687	0.0120	0.0270	0.3804	0.0125	0.0265	0.3406	0.0117	0.0240
0.05	0.4112	0.0125	0.0348	0.3939	0.0121	0.0304	0.3881	0.0123	0.0291	0.3840	0.0122	0.0297
0.15	0.3917	0.0121	0.0353	0.3825	0.0119	0.0332	0.4000	0.0124	0.0331	0.3758	0.0118	0.0312
0.25	0.4227	0.0128	0.0426	0.4136	0.0125	0.0387	0.3937	0.0124	0.0345	0.3999	0.0124	0.0356
0.35	0.4218	0.0133	0.0453	0.4149	0.0130	0.0400	0.3808	0.0127	0.0337	0.3645	0.0125	0.0345
0.45	0.4024	0.0136	0.0432	0.3757	0.0129	0.0370	0.3892	0.0136	0.0353	0.3835	0.0133	0.0362
0.55	0.3707	0.0138	0.0396	0.3794	0.0140	0.0400	0.3751	0.0140	0.0365	0.3845	0.0141	0.0360
0.65	0.3608	0.0150	0.0392	0.3453	0.0144	0.0384	0.3253	0.0144	0.0330	0.3344	0.0145	0.0313
0.75	0.3142	0.0166	0.0314	0.2970	0.0159	0.0310	0.2561	0.0149	0.0261	0.2878	0.0158	0.0290
0.85	0.2779	0.0205	0.0246	0.2365	0.0185	0.0248	0.2851	0.0208	0.0268	0.2605	0.0197	0.0278
0.95	0.2528	0.0374	0.0223	0.2606	0.0369	0.0364	0.2206	0.0339	0.0230	0.1783	0.0307	0.0190

$\cos(\theta_\eta^*)$	$E_\gamma=(1072.5\pm7.5)$ MeV			$E_\gamma=(1087.5\pm7.5)$ MeV			$E_\gamma=(1102.5\pm7.5)$ MeV			$E_\gamma=(1117.5\pm7.5)$ MeV		
	$d\sigma/d\Omega$ [μb/sr]	Δ_{stat} [μb/sr]	Δ_{syst} [μb/sr]	$d\sigma/d\Omega$ [μb/sr]	Δ_{stat} [μb/sr]	Δ_{syst} [μb/sr]	$d\sigma/d\Omega$ [μb/sr]	Δ_{stat} [μb/sr]	Δ_{syst} [μb/sr]	$d\sigma/d\Omega$ [μb/sr]	Δ_{stat} [μb/sr]	Δ_{syst} [μb/sr]
−0.95	0.4277	0.0189	0.0464	0.3541	0.0172	0.0400	0.3239	0.0169	0.0402	0.3200	0.0185	0.0408
−0.85	0.3596	0.0142	0.0415	0.3162	0.0132	0.0352	0.2802	0.0128	0.0286	0.2579	0.0134	0.0239
−0.75	0.3492	0.0189	0.0365	0.2950	0.0164	0.0315	0.2718	0.0156	0.0267	0.2947	0.0173	0.0252
−0.65	0.3446	0.0186	0.0298	0.3594	0.0181	0.0327	0.2556	0.0151	0.0228	0.2989	0.0169	0.0249
−0.55	0.3592	0.0186	0.0260	0.3297	0.0169	0.0245	0.3342	0.0168	0.0250	0.2897	0.0163	0.0221
−0.45	0.3060	0.0167	0.0212	0.3185	0.0162	0.0213	0.2624	0.0144	0.0178	0.2711	0.0153	0.0193
−0.35	0.3210	0.0170	0.0223	0.3164	0.0158	0.0206	0.3043	0.0153	0.0208	0.2746	0.0150	0.0190
−0.25	0.3420	0.0175	0.0240	0.3435	0.0166	0.0226	0.3091	0.0154	0.0209	0.3112	0.0161	0.0207
−0.15	0.3584	0.0174	0.0248	0.3242	0.0156	0.0210	0.2757	0.0118	0.0175	0.2851	0.0125	0.0173
−0.05	0.3522	0.0124	0.0245	0.3648	0.0124	0.0232	0.3253	0.0118	0.0196	0.3017	0.0124	0.0178
0.05	0.3447	0.0118	0.0257	0.3611	0.0120	0.0246	0.3239	0.0116	0.0207	0.3125	0.0123	0.0193
0.15	0.3917	0.0125	0.0311	0.3719	0.0121	0.0294	0.3406	0.0118	0.0252	0.3186	0.0123	0.0215
0.25	0.3929	0.0127	0.0315	0.3584	0.0120	0.0302	0.3333	0.0117	0.0261	0.3401	0.0129	0.0257
0.35	0.3779	0.0129	0.0315	0.3857	0.0129	0.0335	0.3485	0.0124	0.0277	0.3193	0.0129	0.0260
0.45	0.3713	0.0134	0.0339	0.3856	0.0135	0.0355	0.3776	0.0137	0.0328	0.3262	0.0138	0.0251
0.55	0.3593	0.0141	0.0360	0.3536	0.0138	0.0326	0.3355	0.0136	0.0289	0.3330	0.0147	0.0255
0.65	0.3031	0.0141	0.0297	0.3067	0.0141	0.0289	0.2960	0.0139	0.0275	0.3234	0.0159	0.0287
0.75	0.2823	0.0162	0.0272	0.2392	0.0144	0.0228	0.2556	0.0155	0.0242	0.2933	0.0178	0.0297
0.85	0.2430	0.0199	0.0246	0.2363	0.0189	0.0220	0.2011	0.0180	0.0187	0.1989	0.0195	0.0263
0.95	0.0986	0.0231	0.0108	0.1524	0.0281	0.0212	0.1417	0.0285	0.0191	0.1782	0.0343	0.0391

$\cos(\theta_\eta^*)$	$E_\gamma=(1132.5\pm7.5)$ MeV			$E_\gamma=(1147.5\pm7.5)$ MeV			$E_\gamma=(1162.5\pm7.5)$ MeV			$E_\gamma=(1177.5\pm7.5)$ MeV		
	$d\sigma/d\Omega$ $[\mu b/sr]$	Δ_{stat} $[\mu b/sr]$	Δ_{syst} $[\mu b/sr]$	$d\sigma/d\Omega$ $[\mu b/sr]$	Δ_{stat} $[\mu b/sr]$	Δ_{syst} $[\mu b/sr]$	$d\sigma/d\Omega$ $[\mu b/sr]$	Δ_{stat} $[\mu b/sr]$	Δ_{syst} $[\mu b/sr]$	$d\sigma/d\Omega$ $[\mu b/sr]$	Δ_{stat} $[\mu b/sr]$	Δ_{syst} $[\mu b/sr]$
-0.95	0.3384	0.0176	0.0430	0.2620	0.0169	0.0308	0.2800	0.0164	0.0278	0.2461	0.0156	0.0270
-0.85	0.2444	0.0125	0.0238	0.2334	0.0127	0.0251	0.2230	0.0117	0.0246	0.2205	0.0117	0.0263
-0.75	0.2521	0.0170	0.0214	0.2559	0.0174	0.0240	0.2543	0.0160	0.0265	0.2174	0.0150	0.0233
-0.65	0.2773	0.0176	0.0225	0.2627	0.0176	0.0231	0.2479	0.0157	0.0226	0.2265	0.0153	0.0210
-0.55	0.2763	0.0171	0.0203	0.2906	0.0179	0.0222	0.2461	0.0154	0.0195	0.2479	0.0156	0.0193
-0.45	0.2931	0.0169	0.0207	0.2748	0.0166	0.0188	0.2276	0.0141	0.0165	0.2365	0.0146	0.0162
-0.35	0.2334	0.0147	0.0168	0.2470	0.0154	0.0171	0.2456	0.0143	0.0170	0.2486	0.0148	0.0163
-0.25	0.2932	0.0165	0.0196	0.2679	0.0160	0.0181	0.2531	0.0147	0.0162	0.2404	0.0145	0.0146
-0.15	0.2744	0.0114	0.0166	0.2883	0.0121	0.0185	0.2791	0.0113	0.0169	0.2450	0.0106	0.0144
-0.05	0.2940	0.0114	0.0179	0.2798	0.0115	0.0175	0.2802	0.0109	0.0161	0.2823	0.0109	0.0163
0.05	0.3230	0.0116	0.0207	0.2874	0.0114	0.0180	0.2854	0.0110	0.0166	0.2795	0.0108	0.0165
0.15	0.3344	0.0117	0.0218	0.3052	0.0116	0.0196	0.2935	0.0108	0.0183	0.2779	0.0106	0.0172
0.25	0.3141	0.0114	0.0212	0.3095	0.0118	0.0200	0.3040	0.0112	0.0203	0.3132	0.0114	0.0216
0.35	0.3374	0.0125	0.0243	0.3211	0.0124	0.0225	0.3248	0.0121	0.0236	0.3174	0.0120	0.0263
0.45	0.3368	0.0129	0.0256	0.3287	0.0133	0.0252	0.3289	0.0128	0.0255	0.3301	0.0127	0.0270
0.55	0.3220	0.0133	0.0252	0.2945	0.0133	0.0277	0.2704	0.0121	0.0227	0.3046	0.0129	0.0237
0.65	0.2803	0.0136	0.0236	0.2830	0.0142	0.0264	0.2666	0.0133	0.0223	0.2685	0.0134	0.0210
0.75	0.2777	0.0159	0.0249	0.2500	0.0156	0.0218	0.2592	0.0153	0.0214	0.2429	0.0148	0.0188
0.85	0.1918	0.0179	0.0224	0.2339	0.0203	0.0250	0.1948	0.0172	0.0170	0.2215	0.0185	0.0189
0.95	0.1614	0.0302	0.0275	0.2012	0.0345	0.0420	0.1340	0.0267	0.0137	0.1270	0.0269	0.0146

$\cos(\theta_\eta^*)$	$E_\gamma=(1192.5\pm7.5)$ MeV			$E_\gamma=(1207.5\pm7.5)$ MeV			$E_\gamma=(1222.5\pm7.5)$ MeV			$E_\gamma=(1237.5\pm7.5)$ MeV		
	$d\sigma/d\Omega$ $[\mu b/sr]$	Δ_{stat} $[\mu b/sr]$	Δ_{syst} $[\mu b/sr]$	$d\sigma/d\Omega$ $[\mu b/sr]$	Δ_{stat} $[\mu b/sr]$	Δ_{syst} $[\mu b/sr]$	$d\sigma/d\Omega$ $[\mu b/sr]$	Δ_{stat} $[\mu b/sr]$	Δ_{syst} $[\mu b/sr]$	$d\sigma/d\Omega$ $[\mu b/sr]$	Δ_{stat} $[\mu b/sr]$	Δ_{syst} $[\mu b/sr]$
-0.95	0.2311	0.0156	0.0284	0.2415	0.0158	0.0300	0.2209	0.0150	0.0257	0.2144	0.0163	0.0249
-0.85	0.2028	0.0118	0.0243	0.1930	0.0115	0.0219	0.1757	0.0106	0.0191	0.1845	0.0121	0.0204
-0.75	0.2358	0.0165	0.0244	0.1819	0.0145	0.0187	0.1875	0.0149	0.0194	0.1629	0.0156	0.0181
-0.65	0.2213	0.0154	0.0199	0.2252	0.0153	0.0201	0.2008	0.0148	0.0185	0.1930	0.0166	0.0187
-0.55	0.2260	0.0155	0.0164	0.1965	0.0143	0.0150	0.2188	0.0152	0.0168	0.2226	0.0172	0.0184
-0.45	0.2244	0.0149	0.0137	0.2349	0.0150	0.0151	0.2262	0.0148	0.0149	0.1977	0.0156	0.0151
-0.35	0.2255	0.0147	0.0135	0.2005	0.0135	0.0117	0.2198	0.0143	0.0132	0.2147	0.0158	0.0141
-0.25	0.2361	0.0147	0.0142	0.2539	0.0151	0.0148	0.2147	0.0141	0.0126	0.2371	0.0166	0.0143
-0.15	0.2162	0.0103	0.0126	0.2437	0.0109	0.0142	0.1987	0.0097	0.0116	0.2182	0.0112	0.0132
-0.05	0.2822	0.0114	0.0165	0.2673	0.0110	0.0154	0.2425	0.0104	0.0132	0.2622	0.0120	0.0145
0.05	0.2808	0.0113	0.0169	0.2674	0.0109	0.0156	0.2539	0.0105	0.0142	0.2758	0.0120	0.0149
0.15	0.2989	0.0114	0.0200	0.2629	0.0107	0.0169	0.2768	0.0109	0.0188	0.2693	0.0119	0.0176
0.25	0.2802	0.0112	0.0225	0.2708	0.0109	0.0217	0.2803	0.0112	0.0209	0.2528	0.0115	0.0175
0.35	0.3107	0.0122	0.0245	0.3102	0.0123	0.0263	0.2785	0.0114	0.0200	0.2845	0.0127	0.0200
0.45	0.3137	0.0129	0.0246	0.2909	0.0125	0.0224	0.2994	0.0125	0.0202	0.2842	0.0134	0.0201
0.55	0.2970	0.0132	0.0237	0.2887	0.0131	0.0225	0.2693	0.0123	0.0185	0.2848	0.0142	0.0185
0.65	0.2505	0.0133	0.0197	0.2746	0.0140	0.0203	0.2757	0.0139	0.0210	0.2642	0.0149	0.0176
0.75	0.2218	0.0146	0.0176	0.2093	0.0141	0.0157	0.2169	0.0141	0.0200	0.2086	0.0153	0.0149
0.85	0.2236	0.0194	0.0210	0.1943	0.0179	0.0176	0.1752	0.0165	0.0217	0.2078	0.0202	0.0200
0.95	0.1497	0.0299	0.0197	0.1189	0.0259	0.0139	0.2104	0.0336	0.0384	0.1622	0.0310	0.0309

$\cos(\theta_\eta^*)$	$E_\gamma=(1252.5\pm7.5)$ MeV			$E_\gamma=(1267.5\pm7.5)$ MeV			$E_\gamma=(1282.5\pm7.5)$ MeV			$E_\gamma=(1297.5\pm7.5)$ MeV		
	$d\sigma/d\Omega$ $[\mu b/sr]$	Δ_{stat} $[\mu b/sr]$	Δ_{syst} $[\mu b/sr]$	$d\sigma/d\Omega$ $[\mu b/sr]$	Δ_{stat} $[\mu b/sr]$	Δ_{syst} $[\mu b/sr]$	$d\sigma/d\Omega$ $[\mu b/sr]$	Δ_{stat} $[\mu b/sr]$	Δ_{syst} $[\mu b/sr]$	$d\sigma/d\Omega$ $[\mu b/sr]$	Δ_{stat} $[\mu b/sr]$	Δ_{syst} $[\mu b/sr]$
-0.95	0.2239	0.0159	0.0238	0.2132	0.0159	0.0185	0.2395	0.0161	0.0213	0.1875	0.0152	0.0175
-0.85	0.1895	0.0115	0.0209	0.1994	0.0120	0.0203	0.1501	0.0103	0.0155	0.1625	0.0117	0.0169
-0.75	0.1697	0.0145	0.0192	0.1945	0.0166	0.0198	0.1965	0.0156	0.0194	0.1925	0.0175	0.0199
-0.65	0.2118	0.0158	0.0199	0.2056	0.0167	0.0187	0.1831	0.0150	0.0163	0.1518	0.0152	0.0151
-0.55	0.1869	0.0147	0.0149	0.1867	0.0155	0.0145	0.1636	0.0139	0.0130	0.1425	0.0145	0.0130
-0.45	0.1995	0.0144	0.0147	0.2014	0.0155	0.0138	0.1523	0.0130	0.0108	0.1780	0.0156	0.0142
-0.35	0.1903	0.0136	0.0130	0.1686	0.0138	0.0113	0.1642	0.0131	0.0107	0.1730	0.0149	0.0124
-0.25	0.2276	0.0149	0.0147	0.1950	0.0149	0.0128	0.1920	0.0141	0.0115	0.1972	0.0157	0.0123
-0.15	0.2444	0.0112	0.0149	0.2136	0.0108	0.0137	0.2072	0.0103	0.0122	0.2118	0.0113	0.0127
-0.05	0.2281	0.0106	0.0121	0.2264	0.0107	0.0126	0.2209	0.0103	0.0125	0.1952	0.0106	0.0115
0.05	0.2666	0.0113	0.0146	0.2270	0.0107	0.0122	0.2232	0.0103	0.0124	0.2235	0.0113	0.0130
0.15	0.2753	0.0113	0.0168	0.2619	0.0112	0.0155	0.2432	0.0107	0.0146	0.2229	0.0111	0.0134
0.25	0.2738	0.0114	0.0166	0.2575	0.0114	0.0151	0.2503	0.0109	0.0170	0.2635	0.0123	0.0170
0.35	0.2923	0.0124	0.0201	0.2586	0.0119	0.0159	0.2416	0.0112	0.0196	0.2423	0.0123	0.0158
0.45	0.2802	0.0127	0.0211	0.2634	0.0125	0.0169	0.2712	0.0123	0.0200	0.2293	0.0123	0.0148
0.55	0.2733	0.0132	0.0211	0.2677	0.0134	0.0176	0.2605	0.0127	0.0174	0.2617	0.0141	0.0201
0.65	0.2366	0.0135	0.0206	0.2446	0.0141	0.0167	0.2032	0.0122	0.0154	0.2258	0.0141	0.0181
0.75	0.2368	0.0154	0.0235	0.2331	0.0157	0.0159	0.2093	0.0145	0.0142	0.2205	0.0166	0.0157
0.85	0.1890	0.0182	0.0191	0.1548	0.0168	0.0119	0.1407	0.0155	0.0135	0.1389	0.0167	0.0115
0.95	0.1924	0.0342	0.0279	0.1373	0.0282	0.0223	0.1363	0.0270	0.0461	0.1035	0.0262	0.0146

$\cos(\theta_\eta^*)$	$E_\gamma{=}(1312.5{\pm}7.5)\,$MeV			$E_\gamma{=}(1327.5{\pm}7.5)\,$MeV			$E_\gamma{=}(1342.5{\pm}7.5)\,$MeV			$E_\gamma{=}(1357.5{\pm}7.5)\,$MeV		
	$d\sigma/d\Omega$	Δ_{stat}	Δ_{syst}	$d\sigma/d\Omega$	Δ_{stat}	Δ_{syst}	$d\sigma/d\Omega$	Δ_{stat}	Δ_{syst}	$d\sigma/d\Omega$	Δ_{stat}	Δ_{syst}
	[μb/sr]	[μb/sr]	[μb/sr]	[μb/sr]	[μb/sr]	[μb/sr]	[μb/sr]	[μb/sr]	[μb/sr]	[μb/sr]	[μb/sr]	[μb/sr]
−0.95	0.1978	0.0146	0.0210	0.1896	0.0177	0.0190	0.1804	0.0183	0.0149	0.2101	0.0172	0.0221
−0.85	0.1420	0.0102	0.0156	0.1239	0.0115	0.0125	0.1510	0.0127	0.0132	0.1608	0.0115	0.0124
−0.75	0.1476	0.0133	0.0156	0.1508	0.0143	0.0154	0.1489	0.0157	0.0144	0.1463	0.0139	0.0128
−0.65	0.1597	0.0135	0.0160	0.1822	0.0154	0.0181	0.1531	0.0157	0.0155	0.1621	0.0143	0.0160
−0.55	0.1856	0.0144	0.0169	0.1732	0.0147	0.0159	0.1380	0.0148	0.0137	0.1581	0.0142	0.0165
−0.45	0.1751	0.0135	0.0139	0.1890	0.0149	0.0135	0.1713	0.0159	0.0144	0.1534	0.0133	0.0148
−0.35	0.1631	0.0126	0.0114	0.1729	0.0138	0.0101	0.1543	0.0145	0.0108	0.1522	0.0130	0.0115
−0.25	0.1908	0.0136	0.0116	0.1672	0.0136	0.0105	0.1633	0.0150	0.0106	0.1822	0.0140	0.0117
−0.15	0.2005	0.0103	0.0120	0.1947	0.0123	0.0125	0.1838	0.0120	0.0116	0.1874	0.0104	0.0117
−0.05	0.2170	0.0104	0.0127	0.1978	0.0122	0.0117	0.1898	0.0120	0.0118	0.1851	0.0101	0.0121
0.05	0.2156	0.0102	0.0125	0.2180	0.0126	0.0126	0.1816	0.0113	0.0112	0.2184	0.0107	0.0148
0.15	0.2382	0.0108	0.0138	0.2310	0.0130	0.0135	0.2203	0.0128	0.0128	0.1856	0.0099	0.0116
0.25	0.2426	0.0111	0.0151	0.2208	0.0130	0.0132	0.2555	0.0139	0.0134	0.2167	0.0109	0.0110
0.35	0.2287	0.0111	0.0157	0.2157	0.0133	0.0130	0.2402	0.0140	0.0131	0.2258	0.0117	0.0120
0.45	0.2346	0.0117	0.0154	0.2197	0.0140	0.0147	0.2192	0.0140	0.0154	0.2289	0.0121	0.0162
0.55	0.2125	0.0117	0.0149	0.2265	0.0152	0.0172	0.2177	0.0148	0.0186	0.2053	0.0123	0.0145
0.65	0.2165	0.0128	0.0170	0.2104	0.0156	0.0156	0.2158	0.0159	0.0219	0.2017	0.0132	0.0183
0.75	0.1895	0.0139	0.0119	0.1890	0.0169	0.0119	0.1953	0.0174	0.0179	0.1641	0.0137	0.0198
0.85	0.1843	0.0180	0.0165	0.1868	0.0222	0.0138	0.2000	0.0229	0.0184	0.1880	0.0190	0.0217
0.95	0.1100	0.0252	0.0220	0.1792	0.0383	0.0219	0.1067	0.0293	0.0181	0.0832	0.0227	0.0121

$\cos(\theta_\eta^*)$	$E_\gamma{=}(1372.5{\pm}7.5)\,$MeV			$E_\gamma{=}(1387.5{\pm}7.5)\,$MeV		
	$d\sigma/d\Omega$	Δ_{stat}	Δ_{syst}	$d\sigma/d\Omega$	Δ_{stat}	Δ_{syst}
	[μb/sr]	[μb/sr]	[μb/sr]	[μb/sr]	[μb/sr]	[μb/sr]
−0.95	0.2359	0.0189	0.0253	0.1959	0.0166	0.0145
−0.85	0.1496	0.0117	0.0128	0.1576	0.0122	0.0124
−0.75	0.1453	0.0143	0.0126	0.1351	0.0152	0.0104
−0.65	0.1743	0.0152	0.0157	0.1200	0.0136	0.0096
−0.55	0.1321	0.0134	0.0131	0.1616	0.0161	0.0151
−0.45	0.1457	0.0136	0.0146	0.1197	0.0135	0.0121
−0.35	0.1817	0.0146	0.0157	0.1390	0.0142	0.0128
−0.25	0.1557	0.0135	0.0121	0.1649	0.0151	0.0132
−0.15	0.1793	0.0105	0.0132	0.1624	0.0104	0.0121
−0.05	0.1854	0.0104	0.0125	0.1816	0.0105	0.0123
0.05	0.2069	0.0109	0.0138	0.1964	0.0108	0.0126
0.15	0.1863	0.0101	0.0121	0.1861	0.0104	0.0124
0.25	0.1853	0.0104	0.0113	0.1939	0.0108	0.0128
0.35	0.2309	0.0122	0.0137	0.2218	0.0121	0.0144
0.45	0.2016	0.0118	0.0141	0.1996	0.0120	0.0134
0.55	0.2209	0.0131	0.0202	0.1859	0.0124	0.0128
0.65	0.2143	0.0140	0.0236	0.1556	0.0119	0.0116
0.75	0.1692	0.0145	0.0168	0.1640	0.0143	0.0123
0.85	0.1821	0.0194	0.0154	0.1573	0.0181	0.0192
0.95	0.1698	0.0344	0.0274	−0.0031	0.0011	0.0009

Differential cross sections of $\gamma n \to \eta n$ as a function of W_{kin}

$\cos(\theta_\eta^*)$	$W{=}(1492.5{\pm}2.5)\,$MeV			$W{=}(1497.5{\pm}2.5)\,$MeV			$W{=}(1502.5{\pm}2.5)\,$MeV			$W{=}(1507.5{\pm}2.5)\,$MeV		
	$d\sigma/d\Omega$	Δ_{stat}	Δ_{syst}	$d\sigma/d\Omega$	Δ_{stat}	Δ_{syst}	$d\sigma/d\Omega$	Δ_{stat}	Δ_{syst}	$d\sigma/d\Omega$	Δ_{stat}	Δ_{syst}
	[μb/sr]	[μb/sr]	[μb/sr]	[μb/sr]	[μb/sr]	[μb/sr]	[μb/sr]	[μb/sr]	[μb/sr]	[μb/sr]	[μb/sr]	[μb/sr]
-0.95	0.4923	0.1235	0.0847	0.8160	0.0872	0.1098	0.8737	0.0686	0.1235	1.0994	0.0656	0.1230
-0.85	0.5869	0.0506	0.0600	0.7579	0.0407	0.1169	0.7972	0.0339	0.1105	0.8842	0.0325	0.1165
-0.75	0.5564	0.0362	0.0502	0.7350	0.0324	0.1058	0.7548	0.0283	0.0947	0.7917	0.0272	0.1001
-0.65	0.5148	0.0304	0.0522	0.6744	0.0282	0.0809	0.7002	0.0260	0.0790	0.7451	0.0257	0.0846
-0.55	0.4963	0.0277	0.0563	0.6511	0.0268	0.0770	0.6952	0.0256	0.0798	0.7367	0.0252	0.0769
-0.45	0.4964	0.0264	0.0575	0.6100	0.0255	0.0627	0.7135	0.0260	0.0669	0.7069	0.0252	0.0651
-0.35	0.5095	0.0262	0.0592	0.6365	0.0261	0.0535	0.6896	0.0259	0.0518	0.7762	0.0272	0.0709
-0.25	0.4633	0.0246	0.0517	0.6378	0.0261	0.0565	0.7149	0.0268	0.0608	0.7032	0.0355	0.0717
-0.15	0.4941	0.0248	0.0523	0.6397	0.0263	0.0594	0.6956	0.0269	0.0651	0.7440	0.0366	0.0717
-0.05	0.4268	0.0231	0.0502	0.5994	0.0258	0.0582	0.7457	0.0282	0.0691	0.7037	0.0362	0.0664
0.05	0.4221	0.0232	0.0524	0.6207	0.0264	0.0627	0.6240	0.0356	0.0611	0.6823	0.0363	0.0659
0.15	0.5009	0.0258	0.0547	0.6198	0.0272	0.0538	0.7003	0.0383	0.0658	0.7454	0.0388	0.0671
0.25	0.4482	0.0252	0.0423	0.6176	0.0273	0.0521	0.6398	0.0369	0.0653	0.7015	0.0382	0.0628
0.35	0.5456	0.0285	0.0583	0.6310	0.0287	0.0706	0.6405	0.0380	0.0771	0.7892	0.0412	0.0765
0.45	0.5525	0.0304	0.0643	0.6286	0.0295	0.0683	0.6553	0.0399	0.0702	0.7495	0.0417	0.0713
0.55	0.5221	0.0310	0.0588	0.6682	0.0318	0.0542	0.7301	0.0323	0.0712	0.7415	0.0434	0.0717
0.65	0.5624	0.0356	0.0634	0.7369	0.0352	0.0594	0.7438	0.0340	0.0680	0.7785	0.0465	0.0743
0.75	0.7418	0.0462	0.0860	0.7012	0.0375	0.0714	0.7532	0.0365	0.0689	0.7948	0.0383	0.0768
0.85	0.6621	0.0565	0.0870	0.8140	0.0472	0.0883	0.9971	0.0477	0.1066	0.8752	0.0440	0.0910
0.95	0.9696	0.1558	0.1486	0.7694	0.0793	0.0727	1.1266	0.0805	0.1207	1.1452	0.0756	0.1223

$\cos(\theta_\eta^*)$	$W{=}(1512.5{\pm}2.5)\,$MeV			$W{=}(1517.5{\pm}2.5)\,$MeV			$W{=}(1522.5{\pm}2.5)\,$MeV			$W{=}(1527.5{\pm}2.5)\,$MeV		
	$d\sigma/d\Omega$	Δ_{stat}	Δ_{syst}	$d\sigma/d\Omega$	Δ_{stat}	Δ_{syst}	$d\sigma/d\Omega$	Δ_{stat}	Δ_{syst}	$d\sigma/d\Omega$	Δ_{stat}	Δ_{syst}
	[μb/sr]	[μb/sr]	[μb/sr]	[μb/sr]	[μb/sr]	[μb/sr]	[μb/sr]	[μb/sr]	[μb/sr]	[μb/sr]	[μb/sr]	[μb/sr]
-0.95	1.1868	0.0631	0.1850	1.2943	0.0609	0.1719	1.3218	0.0576	0.1412	1.3090	0.0538	0.1211
-0.85	0.9969	0.0329	0.1284	1.0913	0.0332	0.1499	1.0243	0.0311	0.1304	1.1072	0.0312	0.1303
-0.75	0.9044	0.0285	0.1107	0.9052	0.0278	0.1146	0.9030	0.0270	0.1045	0.8704	0.0263	0.0893
-0.65	0.8208	0.0265	0.0904	0.8660	0.0267	0.1008	0.8445	0.0260	0.0905	0.8401	0.0258	0.0754
-0.55	0.7876	0.0261	0.0776	0.8449	0.0269	0.0900	0.7601	0.0333	0.0822	0.8116	0.0339	0.0798
-0.45	0.8019	0.0269	0.0748	0.7845	0.0346	0.0806	0.7756	0.0339	0.0848	0.7975	0.0341	0.0828
-0.35	0.7139	0.0348	0.0604	0.7711	0.0350	0.0777	0.7369	0.0337	0.0756	0.7215	0.0331	0.0649
-0.25	0.7402	0.0355	0.0577	0.7658	0.0353	0.0675	0.7740	0.0350	0.0627	0.8102	0.0357	0.0632
-0.15	0.7480	0.0362	0.0664	0.7847	0.0360	0.0628	0.7706	0.0357	0.0525	0.8556	0.0371	0.0762
-0.05	0.7807	0.0373	0.0843	0.6989	0.0346	0.0612	0.7862	0.0365	0.0615	0.8105	0.0370	0.0778
0.05	0.7903	0.0383	0.0843	0.7053	0.0359	0.0691	0.7881	0.0376	0.0626	0.7806	0.0369	0.0703
0.15	0.8309	0.0402	0.0732	0.7567	0.0377	0.0737	0.7604	0.0374	0.0625	0.7518	0.0370	0.0698
0.25	0.7223	0.0383	0.0613	0.7612	0.0391	0.0659	0.7685	0.0388	0.0648	0.8372	0.0398	0.0853
0.35	0.6670	0.0377	0.0609	0.7209	0.0387	0.0527	0.8055	0.0403	0.0603	0.7994	0.0396	0.0770
0.45	0.7602	0.0412	0.0653	0.7548	0.0406	0.0569	0.7797	0.0409	0.0632	0.7156	0.0390	0.0607
0.55	0.7442	0.0424	0.0673	0.7472	0.0421	0.0719	0.7794	0.0433	0.0701	0.7955	0.0433	0.0641
0.65	0.7996	0.0465	0.0749	0.7735	0.0454	0.0820	0.8504	0.0481	0.0802	0.7561	0.0452	0.0652
0.75	0.8348	0.0513	0.0785	0.8183	0.0496	0.0869	0.7877	0.0490	0.0848	0.8639	0.0522	0.0907
0.85	0.8806	0.0442	0.1035	0.8579	0.0571	0.0927	0.7639	0.0538	0.0918	0.8513	0.0582	0.1020
0.95	1.1332	0.0713	0.1417	1.0088	0.0650	0.1196	0.9045	0.0629	0.1209	1.0641	0.0698	0.1509

	$W=(1532.5\pm2.5)$ MeV			$W=(1537.5\pm2.5)$ MeV			$W=(1545.0\pm5.0)$ MeV			$W=(1555.0\pm5.0)$ MeV		
$\cos(\theta_\eta^*)$	$d\sigma/d\Omega$	Δ_{stat}	Δ_{syst}	$d\sigma/d\Omega$	Δ_{stat}	Δ_{syst}	$d\sigma/d\Omega$	Δ_{stat}	Δ_{syst}	$d\sigma/d\Omega$	Δ_{stat}	Δ_{syst}
	$[\mu b/sr]$	$[\mu b/sr]$	$[\mu b/sr]$	$[\mu b/sr]$	$[\mu b/sr]$	$[\mu b/sr]$	$[\mu b/sr]$	$[\mu b/sr]$	$[\mu b/sr]$	$[\mu b/sr]$	$[\mu b/sr]$	$[\mu b/sr]$
-0.95	1.4639	0.0551	0.1711	1.4284	0.0524	0.1977	1.3472	0.0349	0.1929	1.2749	0.0331	0.1639
-0.85	1.0362	0.0300	0.1280	1.0226	0.0294	0.1323	0.9404	0.0196	0.1188	0.9224	0.0195	0.1185
-0.75	0.9422	0.0272	0.1092	0.8493	0.0259	0.1010	0.8039	0.0177	0.0888	0.7884	0.0178	0.0857
-0.65	0.8278	0.0257	0.0808	0.8242	0.0259	0.0876	0.8178	0.0239	0.0897	0.6980	0.0225	0.0766
-0.55	0.8381	0.0344	0.0755	0.7630	0.0328	0.0734	0.7765	0.0232	0.0823	0.7367	0.0230	0.0862
-0.45	0.7186	0.0324	0.0667	0.7592	0.0328	0.0671	0.7534	0.0232	0.0729	0.7237	0.0231	0.0735
-0.35	0.8519	0.0356	0.0762	0.8016	0.0343	0.0689	0.7532	0.0236	0.0738	0.6681	0.0226	0.0609
-0.25	0.8359	0.0362	0.0680	0.7606	0.0342	0.0681	0.7769	0.0242	0.0778	0.6843	0.0227	0.0695
-0.15	0.8084	0.0360	0.0712	0.7380	0.0339	0.0779	0.7033	0.0228	0.0779	0.6631	0.0216	0.0776
-0.05	0.7734	0.0358	0.0764	0.7118	0.0333	0.0812	0.6791	0.0220	0.0802	0.6477	0.0206	0.0820
0.05	0.8225	0.0369	0.0759	0.7216	0.0329	0.0787	0.6363	0.0207	0.0751	0.6272	0.0197	0.0800
0.15	0.7687	0.0361	0.0705	0.7234	0.0327	0.0776	0.6613	0.0209	0.0846	0.6428	0.0197	0.0826
0.25	0.7446	0.0359	0.0742	0.6782	0.0320	0.0725	0.6543	0.0210	0.0854	0.6248	0.0199	0.0818
0.35	0.7046	0.0354	0.0696	0.6217	0.0312	0.0672	0.6537	0.0215	0.0814	0.6270	0.0205	0.0822
0.45	0.7357	0.0378	0.0649	0.6760	0.0337	0.0744	0.6542	0.0224	0.0756	0.6743	0.0223	0.0851
0.55	0.8008	0.0414	0.0676	0.6553	0.0355	0.0645	0.6523	0.0240	0.0646	0.6602	0.0239	0.0776
0.65	0.8314	0.0462	0.0675	0.7070	0.0402	0.0672	0.7570	0.0287	0.0700	0.7026	0.0274	0.0726
0.75	0.8088	0.0501	0.0682	0.6847	0.0455	0.0652	0.6746	0.0316	0.0541	0.7254	0.0325	0.0606
0.85	0.7369	0.0547	0.0761	0.7715	0.0566	0.0772	0.7190	0.0396	0.0565	0.7266	0.0417	0.0537
0.95	0.9941	0.0694	0.1348	0.8583	0.0869	0.1184	0.8512	0.0644	0.1270	0.9291	0.0713	0.1471

	$W=(1565.0\pm5.0)$ MeV			$W=(1575.0\pm5.0)$ MeV			$W=(1585.0\pm5.0)$ MeV			$W=(1595.0\pm5.0)$ MeV		
$\cos(\theta_\eta^*)$	$d\sigma/d\Omega$	Δ_{stat}	Δ_{syst}	$d\sigma/d\Omega$	Δ_{stat}	Δ_{syst}	$d\sigma/d\Omega$	Δ_{stat}	Δ_{syst}	$d\sigma/d\Omega$	Δ_{stat}	Δ_{syst}
	$[\mu b/sr]$	$[\mu b/sr]$	$[\mu b/sr]$	$[\mu b/sr]$	$[\mu b/sr]$	$[\mu b/sr]$	$[\mu b/sr]$	$[\mu b/sr]$	$[\mu b/sr]$	$[\mu b/sr]$	$[\mu b/sr]$	$[\mu b/sr]$
-0.95	1.2745	0.0332	0.1617	1.1756	0.0323	0.1718	1.1151	0.0319	0.1609	1.0144	0.0303	0.1322
-0.85	0.8646	0.0194	0.1133	0.8221	0.0195	0.1024	0.7620	0.0192	0.0904	0.6747	0.0182	0.0788
-0.75	0.7693	0.0180	0.0863	0.6893	0.0177	0.0762	0.6932	0.0183	0.0869	0.5954	0.0237	0.0678
-0.65	0.6717	0.0228	0.0676	0.6996	0.0241	0.0754	0.6511	0.0239	0.0776	0.5791	0.0229	0.0653
-0.55	0.7157	0.0233	0.0662	0.6876	0.0238	0.0671	0.5973	0.0230	0.0594	0.5840	0.0231	0.0532
-0.45	0.6914	0.0233	0.0567	0.6562	0.0235	0.0537	0.6499	0.0241	0.0607	0.5973	0.0234	0.0488
-0.35	0.6702	0.0231	0.0588	0.6115	0.0224	0.0524	0.5866	0.0222	0.0585	0.5183	0.0210	0.0490
-0.25	0.6456	0.0218	0.0709	0.5666	0.0205	0.0639	0.5152	0.0199	0.0634	0.4807	0.0192	0.0539
-0.15	0.5578	0.0194	0.0734	0.5104	0.0184	0.0710	0.5233	0.0190	0.0761	0.4390	0.0176	0.0523
-0.05	0.5912	0.0191	0.0814	0.4929	0.0175	0.0719	0.4968	0.0180	0.0746	0.4649	0.0175	0.0595
0.05	0.5406	0.0179	0.0743	0.4941	0.0173	0.0711	0.4897	0.0177	0.0693	0.4564	0.0172	0.0618
0.15	0.6247	0.0192	0.0871	0.5239	0.0180	0.0788	0.4882	0.0179	0.0681	0.4256	0.0155	0.0596
0.25	0.5634	0.0187	0.0772	0.5122	0.0183	0.0804	0.4926	0.0137	0.0687	0.4511	0.0128	0.0653
0.35	0.5936	0.0200	0.0767	0.5274	0.0193	0.0792	0.4821	0.0138	0.0681	0.4597	0.0131	0.0689
0.45	0.5601	0.0206	0.0724	0.5626	0.0158	0.0771	0.5238	0.0152	0.0735	0.4569	0.0139	0.0642
0.55	0.6539	0.0241	0.0741	0.5636	0.0172	0.0716	0.5255	0.0164	0.0692	0.4589	0.0150	0.0569
0.65	0.6117	0.0256	0.0565	0.6346	0.0266	0.0787	0.5596	0.0188	0.0710	0.4520	0.0165	0.0561
0.75	0.7477	0.0330	0.0594	0.6379	0.0309	0.0641	0.5577	0.0295	0.0607	0.4878	0.0203	0.0574
0.85	0.6949	0.0412	0.0568	0.5728	0.0373	0.0451	0.6131	0.0388	0.0553	0.5398	0.0364	0.0501
0.95	0.8651	0.0721	0.1142	0.7191	0.0680	0.0967	0.4705	0.0567	0.0521	0.6019	0.0619	0.0512

	$W=(1605.0\pm5.0)$ MeV			$W=(1615.0\pm5.0)$ MeV			$W=(1625.0\pm5.0)$ MeV			$W=(1635.0\pm5.0)$ MeV		
$\cos(\theta_\eta^*)$	$d\sigma/d\Omega$	Δ_{stat}	Δ_{syst}	$d\sigma/d\Omega$	Δ_{stat}	Δ_{syst}	$d\sigma/d\Omega$	Δ_{stat}	Δ_{syst}	$d\sigma/d\Omega$	Δ_{stat}	Δ_{syst}
	$[\mu b/sr]$	$[\mu b/sr]$	$[\mu b/sr]$	$[\mu b/sr]$	$[\mu b/sr]$	$[\mu b/sr]$	$[\mu b/sr]$	$[\mu b/sr]$	$[\mu b/sr]$	$[\mu b/sr]$	$[\mu b/sr]$	$[\mu b/sr]$
-0.95	0.8840	0.0276	0.1076	0.7680	0.0248	0.1150	0.6974	0.0230	0.1006	0.6347	0.0215	0.0858
-0.85	0.5826	0.0166	0.0738	0.5564	0.0158	0.0636	0.5158	0.0150	0.0568	0.4929	0.0146	0.0530
-0.75	0.5877	0.0231	0.0727	0.4876	0.0204	0.0544	0.4652	0.0192	0.0429	0.4619	0.0189	0.0434
-0.65	0.5232	0.0213	0.0564	0.5233	0.0205	0.0527	0.4819	0.0193	0.0439	0.5046	0.0197	0.0461
-0.55	0.5553	0.0221	0.0536	0.4422	0.0191	0.0365	0.5102	0.0202	0.0469	0.4899	0.0200	0.0428
-0.45	0.5395	0.0217	0.0503	0.4485	0.0191	0.0367	0.3949	0.0177	0.0351	0.4665	0.0192	0.0399
-0.35	0.4709	0.0195	0.0431	0.3861	0.0168	0.0352	0.3562	0.0155	0.0317	0.3966	0.0161	0.0336
-0.25	0.4544	0.0180	0.0449	0.3544	0.0150	0.0328	0.3505	0.0143	0.0336	0.3642	0.0145	0.0299
-0.15	0.4408	0.0169	0.0479	0.3355	0.0139	0.0320	0.3643	0.0140	0.0395	0.3597	0.0141	0.0313
-0.05	0.3924	0.0155	0.0492	0.3932	0.0148	0.0413	0.3315	0.0133	0.0366	0.3892	0.0146	0.0377
0.05	0.3739	0.0151	0.0517	0.3713	0.0108	0.0427	0.3452	0.0102	0.0375	0.3774	0.0107	0.0400
0.15	0.4248	0.0119	0.0605	0.3592	0.0105	0.0446	0.3546	0.0104	0.0406	0.3769	0.0107	0.0411
0.25	0.3892	0.0115	0.0547	0.3559	0.0106	0.0464	0.3612	0.0106	0.0419	0.3702	0.0107	0.0390
0.35	0.3972	0.0118	0.0527	0.3423	0.0106	0.0431	0.3538	0.0106	0.0420	0.3677	0.0109	0.0399
0.45	0.4036	0.0126	0.0505	0.3746	0.0117	0.0461	0.3535	0.0113	0.0437	0.3797	0.0118	0.0440
0.55	0.4116	0.0136	0.0507	0.3578	0.0124	0.0449	0.3379	0.0118	0.0405	0.3566	0.0122	0.0422
0.65	0.4092	0.0151	0.0523	0.3723	0.0140	0.0466	0.3518	0.0135	0.0413	0.3424	0.0134	0.0403
0.75	0.4164	0.0180	0.0447	0.3206	0.0154	0.0367	0.3284	0.0154	0.0374	0.3536	0.0161	0.0413
0.85	0.3688	0.0298	0.0281	0.4351	0.0237	0.0367	0.3198	0.0203	0.0310	0.3298	0.0210	0.0317
0.95	0.2958	0.0432	0.0197	0.2765	0.0415	0.0154	0.2729	0.0421	0.0225	0.3131	0.0479	0.0284

$\cos(\theta_\eta^*)$	$W{=}(1645.0{\pm}5.0)$ MeV			$W{=}(1655.0{\pm}5.0)$ MeV			$W{=}(1665.0{\pm}5.0)$ MeV			$W{=}(1675.0{\pm}5.0)$ MeV		
	$d\sigma/d\Omega$	Δ_{stat}	Δ_{syst}	$d\sigma/d\Omega$	Δ_{stat}	Δ_{syst}	$d\sigma/d\Omega$	Δ_{stat}	Δ_{syst}	$d\sigma/d\Omega$	Δ_{stat}	Δ_{syst}
	[μb/sr]	[μb/sr]	[μb/sr]	[μb/sr]	[μb/sr]	[μb/sr]	[μb/sr]	[μb/sr]	[μb/sr]	[μb/sr]	[μb/sr]	[μb/sr]
-0.95	0.6052	0.0211	0.0782	0.5527	0.0204	0.0689	0.5311	0.0201	0.0688	0.5140	0.0197	0.0676
-0.85	0.4645	0.0143	0.0489	0.4508	0.0143	0.0509	0.4483	0.0143	0.0518	0.4390	0.0143	0.0499
-0.75	0.4684	0.0192	0.0424	0.4610	0.0193	0.0443	0.4431	0.0190	0.0445	0.4186	0.0185	0.0411
-0.65	0.5342	0.0205	0.0472	0.5249	0.0206	0.0462	0.5164	0.0207	0.0458	0.4377	0.0192	0.0383
-0.55	0.4706	0.0199	0.0382	0.4567	0.0198	0.0370	0.4990	0.0209	0.0407	0.4781	0.0206	0.0391
-0.45	0.4539	0.0190	0.0350	0.4668	0.0192	0.0330	0.4764	0.0194	0.0340	0.4226	0.0180	0.0298
-0.35	0.3691	0.0156	0.0301	0.4233	0.0166	0.0310	0.3898	0.0159	0.0271	0.3826	0.0156	0.0256
-0.25	0.3988	0.0154	0.0320	0.3994	0.0156	0.0304	0.4238	0.0160	0.0310	0.3976	0.0156	0.0286
-0.15	0.4219	0.0156	0.0336	0.4228	0.0159	0.0315	0.4157	0.0159	0.0299	0.3995	0.0157	0.0283
-0.05	0.4187	0.0117	0.0368	0.4411	0.0122	0.0361	0.4075	0.0119	0.0299	0.3989	0.0118	0.0275
0.05	0.4091	0.0114	0.0371	0.4085	0.0117	0.0352	0.4281	0.0120	0.0319	0.4154	0.0119	0.0294
0.15	0.3918	0.0112	0.0345	0.4507	0.0122	0.0378	0.4353	0.0121	0.0341	0.4145	0.0118	0.0322
0.25	0.4169	0.0116	0.0390	0.4164	0.0118	0.0380	0.4371	0.0122	0.0398	0.4315	0.0122	0.0377
0.35	0.4077	0.0117	0.0421	0.4176	0.0121	0.0419	0.4235	0.0123	0.0408	0.3986	0.0121	0.0356
0.45	0.4139	0.0127	0.0454	0.4407	0.0132	0.0473	0.4169	0.0130	0.0403	0.4076	0.0129	0.0378
0.55	0.3779	0.0128	0.0439	0.3997	0.0135	0.0442	0.3805	0.0133	0.0369	0.3657	0.0132	0.0346
0.65	0.3712	0.0142	0.0438	0.3526	0.0140	0.0365	0.3528	0.0141	0.0346	0.3835	0.0151	0.0371
0.75	0.3405	0.0161	0.0420	0.3620	0.0168	0.0380	0.3035	0.0154	0.0320	0.3404	0.0168	0.0370
0.85	0.3126	0.0208	0.0400	0.2932	0.0201	0.0286	0.3274	0.0215	0.0354	0.2793	0.0203	0.0286
0.95	0.3773	0.0532	0.0284	0.2309	0.0419	0.0175	0.2683	0.0468	0.0295	0.2784	0.0398	0.0267

$\cos(\theta_\eta^*)$	$W{=}(1685.0{\pm}5.0)$ MeV			$W{=}(1695.0{\pm}5.0)$ MeV			$W{=}(1705.0{\pm}5.0)$ MeV			$W{=}(1715.0{\pm}5.0)$ MeV		
	$d\sigma/d\Omega$	Δ_{stat}	Δ_{syst}	$d\sigma/d\Omega$	Δ_{stat}	Δ_{syst}	$d\sigma/d\Omega$	Δ_{stat}	Δ_{syst}	$d\sigma/d\Omega$	Δ_{stat}	Δ_{syst}
	[μb/sr]	[μb/sr]	[μb/sr]	[μb/sr]	[μb/sr]	[μb/sr]	[μb/sr]	[μb/sr]	[μb/sr]	[μb/sr]	[μb/sr]	[μb/sr]
-0.95	0.4236	0.0184	0.0540	0.4079	0.0184	0.0529	0.3818	0.0180	0.0480	0.2907	0.0160	0.0389
-0.85	0.3576	0.0131	0.0366	0.3160	0.0125	0.0317	0.2753	0.0118	0.0294	0.2428	0.0114	0.0268
-0.75	0.3929	0.0181	0.0351	0.3262	0.0166	0.0302	0.2872	0.0158	0.0268	0.2632	0.0153	0.0258
-0.65	0.4100	0.0186	0.0349	0.3567	0.0173	0.0336	0.3384	0.0171	0.0292	0.2999	0.0164	0.0251
-0.55	0.4491	0.0199	0.0357	0.3733	0.0183	0.0314	0.3582	0.0179	0.0271	0.2785	0.0162	0.0203
-0.45	0.3831	0.0168	0.0269	0.3170	0.0152	0.0222	0.2780	0.0144	0.0188	0.2445	0.0137	0.0172
-0.35	0.3358	0.0145	0.0220	0.3061	0.0137	0.0198	0.2752	0.0130	0.0185	0.2268	0.0120	0.0155
-0.25	0.3600	0.0148	0.0244	0.3018	0.0136	0.0191	0.3107	0.0138	0.0207	0.2585	0.0127	0.0173
-0.15	0.3614	0.0114	0.0246	0.3175	0.0108	0.0199	0.3154	0.0107	0.0200	0.2668	0.0099	0.0175
-0.05	0.3659	0.0113	0.0255	0.3448	0.0111	0.0221	0.3328	0.0109	0.0202	0.3101	0.0105	0.0182
0.05	0.3846	0.0115	0.0282	0.3909	0.0117	0.0275	0.3333	0.0108	0.0200	0.3005	0.0103	0.0166
0.15	0.3889	0.0115	0.0308	0.3625	0.0112	0.0288	0.3513	0.0111	0.0237	0.3557	0.0111	0.0218
0.25	0.4135	0.0120	0.0352	0.3950	0.0119	0.0327	0.3644	0.0114	0.0296	0.3329	0.0109	0.0246
0.35	0.4181	0.0125	0.0355	0.3795	0.0121	0.0311	0.3800	0.0121	0.0327	0.3385	0.0114	0.0278
0.45	0.4255	0.0135	0.0369	0.3863	0.0130	0.0342	0.3673	0.0128	0.0295	0.3575	0.0125	0.0274
0.55	0.3851	0.0138	0.0346	0.3716	0.0135	0.0345	0.3521	0.0133	0.0255	0.3310	0.0128	0.0231
0.65	0.3449	0.0144	0.0324	0.3198	0.0139	0.0290	0.2769	0.0129	0.0229	0.2900	0.0132	0.0221
0.75	0.3144	0.0161	0.0316	0.2667	0.0145	0.0261	0.2398	0.0138	0.0259	0.2633	0.0148	0.0250
0.85	0.2698	0.0200	0.0278	0.2298	0.0174	0.0259	0.1761	0.0152	0.0195	0.2221	0.0182	0.0237
0.95	0.2348	0.0341	0.0335	0.1291	0.0229	0.0167	0.1108	0.0207	0.0104	0.1513	0.0266	0.0119

$\cos(\theta_\eta^*)$	$W{=}(1725.0{\pm}5.0)$ MeV			$W{=}(1735.0{\pm}5.0)$ MeV			$W{=}(1745.0{\pm}5.0)$ MeV			$W{=}(1755.0{\pm}5.0)$ MeV		
	$d\sigma/d\Omega$	Δ_{stat}	Δ_{syst}	$d\sigma/d\Omega$	Δ_{stat}	Δ_{syst}	$d\sigma/d\Omega$	Δ_{stat}	Δ_{syst}	$d\sigma/d\Omega$	Δ_{stat}	Δ_{syst}
	[μb/sr]	[μb/sr]	[μb/sr]	[μb/sr]	[μb/sr]	[μb/sr]	[μb/sr]	[μb/sr]	[μb/sr]	[μb/sr]	[μb/sr]	[μb/sr]
-0.95	0.2691	0.0156	0.0371	0.2448	0.0146	0.0302	0.1866	0.0128	0.0215	0.1938	0.0131	0.0226
-0.85	0.2448	0.0114	0.0263	0.2136	0.0106	0.0213	0.1837	0.0097	0.0183	0.1864	0.0100	0.0187
-0.75	0.2773	0.0160	0.0277	0.2231	0.0144	0.0220	0.1812	0.0130	0.0178	0.2065	0.0140	0.0199
-0.65	0.2797	0.0162	0.0250	0.2406	0.0152	0.0224	0.2406	0.0153	0.0225	0.2351	0.0151	0.0208
-0.55	0.2689	0.0162	0.0207	0.2388	0.0156	0.0190	0.2102	0.0148	0.0162	0.2218	0.0152	0.0162
-0.45	0.2383	0.0136	0.0171	0.2320	0.0136	0.0166	0.2134	0.0130	0.0154	0.2293	0.0135	0.0170
-0.35	0.2372	0.0123	0.0169	0.2195	0.0120	0.0150	0.1930	0.0113	0.0136	0.1875	0.0113	0.0138
-0.25	0.2573	0.0130	0.0175	0.2421	0.0127	0.0162	0.2346	0.0125	0.0150	0.2099	0.0119	0.0132
-0.15	0.2875	0.0104	0.0193	0.2692	0.0101	0.0169	0.2288	0.0093	0.0136	0.2338	0.0094	0.0143
-0.05	0.3034	0.0105	0.0187	0.2955	0.0104	0.0173	0.2478	0.0095	0.0138	0.2586	0.0097	0.0154
0.05	0.3144	0.0106	0.0181	0.3072	0.0104	0.0179	0.2653	0.0096	0.0150	0.2517	0.0094	0.0158
0.15	0.3467	0.0111	0.0205	0.3020	0.0103	0.0180	0.2754	0.0096	0.0165	0.2665	0.0096	0.0184
0.25	0.3301	0.0111	0.0220	0.3249	0.0109	0.0202	0.2884	0.0102	0.0172	0.2931	0.0104	0.0189
0.35	0.3592	0.0120	0.0272	0.3573	0.0120	0.0246	0.3049	0.0108	0.0192	0.2948	0.0108	0.0203
0.45	0.3455	0.0126	0.0281	0.3391	0.0124	0.0251	0.3262	0.0120	0.0250	0.3116	0.0119	0.0247
0.55	0.3721	0.0139	0.0280	0.3163	0.0128	0.0239	0.3053	0.0125	0.0238	0.2858	0.0122	0.0224
0.65	0.2951	0.0137	0.0221	0.3006	0.0138	0.0252	0.2705	0.0131	0.0198	0.2689	0.0132	0.0208
0.75	0.2706	0.0153	0.0247	0.2602	0.0151	0.0291	0.2805	0.0158	0.0237	0.2537	0.0151	0.0205
0.85	0.2464	0.0195	0.0308	0.2218	0.0185	0.0343	0.2378	0.0194	0.0308	0.2171	0.0191	0.0211
0.95	0.1873	0.0336	0.0346	0.1587	0.0329	0.0275	0.1780	0.0359	0.0308	0.1609	0.0344	0.0276

$\cos(\theta_\eta^*)$	$W=(1765.0\pm5.0)$ MeV			$W=(1775.0\pm5.0)$ MeV			$W=(1785.0\pm5.0)$ MeV			$W=(1795.0\pm5.0)$ MeV		
	$d\sigma/d\Omega$ [μb/sr]	Δ_{stat} [μb/sr]	Δ_{syst} [μb/sr]	$d\sigma/d\Omega$ [μb/sr]	Δ_{stat} [μb/sr]	Δ_{syst} [μb/sr]	$d\sigma/d\Omega$ [μb/sr]	Δ_{stat} [μb/sr]	Δ_{syst} [μb/sr]	$d\sigma/d\Omega$ [μb/sr]	Δ_{stat} [μb/sr]	Δ_{syst} [μb/sr]
-0.95	0.1974	0.0135	0.0208	0.1966	0.0136	0.0213	0.1906	0.0136	0.0210	0.1854	0.0135	0.0210
-0.85	0.1705	0.0097	0.0176	0.1665	0.0096	0.0171	0.1715	0.0099	0.0185	0.1594	0.0097	0.0164
-0.75	0.1819	0.0133	0.0184	0.1635	0.0129	0.0164	0.1712	0.0134	0.0172	0.1790	0.0139	0.0176
-0.65	0.1906	0.0138	0.0168	0.2314	0.0153	0.0215	0.2128	0.0151	0.0199	0.1735	0.0140	0.0167
-0.55	0.1978	0.0146	0.0150	0.2090	0.0152	0.0175	0.2018	0.0152	0.0187	0.1933	0.0152	0.0180
-0.45	0.1942	0.0127	0.0148	0.2011	0.0130	0.0167	0.2007	0.0133	0.0170	0.2008	0.0136	0.0160
-0.35	0.1934	0.0117	0.0131	0.1895	0.0117	0.0146	0.1876	0.0119	0.0132	0.1862	0.0120	0.0124
-0.25	0.2187	0.0124	0.0127	0.2361	0.0123	0.0150	0.2091	0.0094	0.0132	0.2094	0.0096	0.0128
-0.15	0.2457	0.0097	0.0149	0.2243	0.0095	0.0127	0.2145	0.0093	0.0122	0.2055	0.0093	0.0114
-0.05	0.2547	0.0099	0.0150	0.2531	0.0099	0.0141	0.2470	0.0100	0.0130	0.2420	0.0100	0.0124
0.05	0.2749	0.0101	0.0148	0.2679	0.0102	0.0145	0.2491	0.0098	0.0128	0.2346	0.0097	0.0120
0.15	0.2873	0.0104	0.0158	0.2834	0.0106	0.0152	0.2362	0.0096	0.0130	0.2420	0.0099	0.0129
0.25	0.2729	0.0103	0.0169	0.2712	0.0106	0.0164	0.2691	0.0104	0.0182	0.2557	0.0104	0.0149
0.35	0.3374	0.0119	0.0213	0.3256	0.0119	0.0225	0.2547	0.0105	0.0201	0.2406	0.0105	0.0166
0.45	0.2940	0.0119	0.0187	0.2888	0.0120	0.0204	0.2625	0.0115	0.0204	0.2719	0.0118	0.0210
0.55	0.3036	0.0129	0.0209	0.3107	0.0133	0.0217	0.2554	0.0121	0.0199	0.2459	0.0121	0.0189
0.65	0.2559	0.0132	0.0186	0.2831	0.0139	0.0191	0.2469	0.0132	0.0177	0.2408	0.0133	0.0174
0.75	0.2710	0.0159	0.0239	0.2345	0.0151	0.0177	0.2282	0.0149	0.0141	0.2022	0.0145	0.0180
0.85	0.1981	0.0179	0.0214	0.1820	0.0173	0.0172	0.2037	0.0193	0.0182	0.1972	0.0193	0.0216
0.95	0.1591	0.0332	0.0176	0.1172	0.0290	0.0109	0.0959	0.0270	0.0123	0.1718	0.0366	0.0225

$\cos(\theta_\eta^*)$	$W=(1805.0\pm5.0)$ MeV			$W=(1815.0\pm5.0)$ MeV			$W=(1825.0\pm5.0)$ MeV			$W=(1835.0\pm5.0)$ MeV		
	$d\sigma/d\Omega$ [μb/sr]	Δ_{stat} [μb/sr]	Δ_{syst} [μb/sr]	$d\sigma/d\Omega$ [μb/sr]	Δ_{stat} [μb/sr]	Δ_{syst} [μb/sr]	$d\sigma/d\Omega$ [μb/sr]	Δ_{stat} [μb/sr]	Δ_{syst} [μb/sr]	$d\sigma/d\Omega$ [μb/sr]	Δ_{stat} [μb/sr]	Δ_{syst} [μb/sr]
-0.95	0.2183	0.0149	0.0239	0.2069	0.0151	0.0180	0.2008	0.0152	0.0152	0.2042	0.0159	0.0148
-0.85	0.1741	0.0104	0.0163	0.1852	0.0110	0.0160	0.1519	0.0103	0.0131	0.1636	0.0111	0.0139
-0.75	0.1650	0.0135	0.0152	0.1567	0.0133	0.0145	0.1521	0.0134	0.0146	0.1791	0.0148	0.0158
-0.65	0.2131	0.0155	0.0209	0.2164	0.0156	0.0206	0.1916	0.0149	0.0179	0.1908	0.0154	0.0166
-0.55	0.2040	0.0156	0.0193	0.1639	0.0141	0.0148	0.1518	0.0139	0.0134	0.1582	0.0146	0.0139
-0.45	0.1967	0.0134	0.0165	0.1631	0.0123	0.0132	0.1479	0.0118	0.0119	0.1468	0.0119	0.0122
-0.35	0.1698	0.0116	0.0121	0.1503	0.0110	0.0105	0.1405	0.0107	0.0095	0.1505	0.0112	0.0105
-0.25	0.1955	0.0094	0.0123	0.1931	0.0095	0.0112	0.1740	0.0092	0.0098	0.1663	0.0093	0.0096
-0.15	0.2079	0.0096	0.0118	0.2068	0.0100	0.0109	0.2063	0.0102	0.0109	0.1741	0.0097	0.0095
-0.05	0.2294	0.0101	0.0124	0.2172	0.0101	0.0117	0.1967	0.0100	0.0109	0.1937	0.0101	0.0109
0.05	0.2381	0.0101	0.0133	0.2287	0.0104	0.0126	0.2358	0.0109	0.0133	0.1918	0.0100	0.0106
0.15	0.2538	0.0106	0.0143	0.2743	0.0116	0.0152	0.2397	0.0111	0.0138	0.2170	0.0108	0.0121
0.25	0.2466	0.0107	0.0151	0.2667	0.0117	0.0151	0.2415	0.0115	0.0150	0.2097	0.0109	0.0125
0.35	0.2888	0.0121	0.0180	0.2655	0.0121	0.0153	0.2398	0.0118	0.0159	0.2257	0.0117	0.0148
0.45	0.2471	0.0117	0.0162	0.2753	0.0130	0.0171	0.2587	0.0129	0.0174	0.2205	0.0122	0.0137
0.55	0.2596	0.0130	0.0199	0.2379	0.0130	0.0166	0.2300	0.0130	0.0145	0.2130	0.0129	0.0142
0.65	0.2465	0.0140	0.0177	0.2377	0.0143	0.0172	0.2460	0.0149	0.0142	0.1788	0.0131	0.0148
0.75	0.2015	0.0152	0.0125	0.2052	0.0156	0.0158	0.1452	0.0137	0.0109	0.1473	0.0142	0.0132
0.85	0.1884	0.0195	0.0142	0.1688	0.0190	0.0233	0.1635	0.0187	0.0217	0.1040	0.0157	0.0129
0.95	0.1520	0.0351	0.0218	0.1102	0.0290	0.0311	0.1033	0.0280	0.0159	-0.0008	0.0005	0.0001

$\cos(\theta_\eta^*)$	$W=(1845.0\pm5.0)$ MeV			$W=(1855.0\pm5.0)$ MeV			$W=(1865.0\pm5.0)$ MeV			$W=(1875.0\pm5.0)$ MeV		
	$d\sigma/d\Omega$ [μb/sr]	Δ_{stat} [μb/sr]	Δ_{syst} [μb/sr]	$d\sigma/d\Omega$ [μb/sr]	Δ_{stat} [μb/sr]	Δ_{syst} [μb/sr]	$d\sigma/d\Omega$ [μb/sr]	Δ_{stat} [μb/sr]	Δ_{syst} [μb/sr]	$d\sigma/d\Omega$ [μb/sr]	Δ_{stat} [μb/sr]	Δ_{syst} [μb/sr]
-0.95	0.1759	0.0152	0.0154	0.1803	0.0161	0.0167	0.1400	0.0150	0.0156	0.1429	0.0169	0.0176
-0.85	0.1602	0.0115	0.0135	0.1471	0.0117	0.0118	0.1191	0.0111	0.0094	0.1131	0.0121	0.0089
-0.75	0.1318	0.0132	0.0112	0.1362	0.0138	0.0116	0.1345	0.0142	0.0109	0.1020	0.0136	0.0068
-0.65	0.1594	0.0147	0.0140	0.1547	0.0149	0.0137	0.1080	0.0131	0.0091	0.1320	0.0153	0.0084
-0.55	0.1414	0.0142	0.0129	0.1347	0.0143	0.0127	0.1159	0.0138	0.0110	0.1127	0.0138	0.0105
-0.45	0.1301	0.0116	0.0116	0.1315	0.0119	0.0124	0.0968	0.0104	0.0096	0.0703	0.0090	0.0079
-0.35	0.1268	0.0105	0.0094	0.1559	0.0123	0.0116	0.1236	0.0091	0.0091	0.1049	0.0086	0.0088
-0.25	0.1617	0.0096	0.0100	0.1581	0.0102	0.0087	0.1603	0.0110	0.0091	0.1057	0.0093	0.0071
-0.15	0.1428	0.0093	0.0087	0.1586	0.0106	0.0088	0.1734	0.0120	0.0113	0.1239	0.0105	0.0095
-0.05	0.1825	0.0104	0.0112	0.1891	0.0115	0.0114	0.1974	0.0126	0.0139	0.1348	0.0106	0.0119
0.05	0.1820	0.0102	0.0117	0.1974	0.0115	0.0115	0.2065	0.0129	0.0125	0.1424	0.0109	0.0099
0.15	0.2219	0.0116	0.0140	0.1941	0.0120	0.0111	0.2118	0.0131	0.0120	0.1325	0.0111	0.0082
0.25	0.2178	0.0118	0.0120	0.2222	0.0130	0.0131	0.2073	0.0136	0.0119	0.1637	0.0124	0.0107
0.35	0.2342	0.0125	0.0136	0.2057	0.0127	0.0129	0.2227	0.0142	0.0132	0.1564	0.0121	0.0112
0.45	0.2085	0.0126	0.0154	0.1884	0.0130	0.0141	0.1711	0.0131	0.0123	0.1253	0.0117	0.0116
0.55	0.1906	0.0127	0.0164	0.1756	0.0132	0.0137	0.1615	0.0137	0.0145	0.1543	0.0146	0.0125
0.65	0.1850	0.0140	0.0131	0.1747	0.0147	0.0125	0.1572	0.0151	0.0129	0.1194	0.0145	0.0097
0.75	0.1679	0.0158	0.0119	0.1641	0.0172	0.0112	0.1262	0.0161	0.0101	0.1493	0.0201	0.0191
0.85	0.1672	0.0217	0.0309	0.1258	0.0195	0.0235	0.1291	0.0211	0.0137	0.0846	0.0213	0.0171
0.95	0.1077	0.0314	0.0089	0.0468	0.0210	0.0098	0.1633	0.0449	0.0167	-0.0025	0.0015	0.0004

Total cross section of $\gamma n \to \eta n$ as a function of E_γ

E_γ [MeV]	ΔE_γ [MeV]	σ [μb]	Δ_{stat} [μb]	Δ_{syst} [μb]
645.0	15.0	0.3640	0.0340	0.0954
667.5	7.5	0.7587	0.0469	0.1055
682.5	7.5	1.4915	0.0441	0.1698
697.5	7.5	2.7728	0.0451	0.2837
712.5	7.5	4.3383	0.0488	0.4083
727.5	7.5	5.7763	0.0688	0.5704
742.5	7.5	7.2323	0.0642	0.7038
757.5	7.5	7.8929	0.0633	0.7685
772.5	7.5	8.4397	0.0672	0.8156
787.5	7.5	8.6106	0.0660	0.9041
802.5	7.5	8.4598	0.0643	0.8401
817.5	7.5	8.0997	0.0652	0.8425
832.5	7.5	7.7481	0.0680	0.8616
847.5	7.5	7.3037	0.0710	0.8030
862.5	7.5	6.8379	0.0689	0.7462
877.5	7.5	6.5422	0.0824	0.7478
892.5	7.5	6.0581	0.0744	0.6673
907.5	7.5	5.8982	0.0515	0.6286
922.5	7.5	5.7501	0.0520	0.6042
937.5	7.5	5.4994	0.0519	0.5630
952.5	7.5	5.3359	0.0491	0.5163
967.5	7.5	5.1346	0.0486	0.4884
982.5	7.5	5.0601	0.0513	0.4868
997.5	7.5	5.0248	0.0509	0.4752
1012.5	7.5	4.9145	0.0476	0.4512
1027.5	7.5	4.7213	0.0461	0.4281
1042.5	7.5	4.4902	0.0456	0.3915
1057.5	7.5	4.4238	0.0449	0.3904
1072.5	7.5	4.1803	0.0452	0.3636
1087.5	7.5	4.0468	0.0437	0.3446
1102.5	7.5	3.6796	0.0418	0.3045
1117.5	7.5	3.6594	0.0452	0.3060
1132.5	7.5	3.5140	0.0427	0.2822
1147.5	7.5	3.4208	0.0441	0.2849
1162.5	7.5	3.2508	0.0399	0.2540
1177.5	7.5	3.1926	0.0400	0.2503
1192.5	7.5	3.0688	0.0409	0.2433
1207.5	7.5	2.9524	0.0394	0.2292
1222.5	7.5	2.8585	0.0390	0.2284
1237.5	7.5	2.8694	0.0432	0.2227
1252.5	7.5	2.8538	0.0407	0.2293
1267.5	7.5	2.6994	0.0406	0.1960
1282.5	7.5	2.4997	0.0375	0.1972
1297.5	7.5	2.4479	0.0407	0.1859
1312.5	7.5	2.4059	0.0372	0.1861
1327.5	7.5	2.3803	0.0443	0.1756
1342.5	7.5	2.3065	0.0445	0.1843
1357.5	7.5	2.2564	0.0379	0.1838
1372.5	7.5	2.2541	0.0403	0.1929
1387.5	7.5	1.9234	0.0336	0.1427

Total cross section of $\gamma n \to \eta n$ as a function of W_{kin}

W_{kin} [MeV]	ΔW_{kin} [MeV]	σ [μb]	Δ_{stat} [μb]	Δ_{syst} [μb]
1492.5	2.5	6.8263	0.1093	0.7644
1497.5	2.5	8.5028	0.0978	0.9082
1502.5	2.5	9.2720	0.0989	0.9659
1507.5	2.5	9.7816	0.1065	1.0050
1512.5	2.5	10.2924	0.1103	1.0636
1517.5	2.5	10.3800	0.1121	1.0858
1522.5	2.5	10.3666	0.1123	1.0295
1527.5	2.5	10.5825	0.1137	1.0438
1532.5	2.5	10.4627	0.1109	1.0329
1537.5	2.5	9.6140	0.1061	1.0245
1545.0	5.0	9.3537	0.0745	1.0216
1555.0	5.0	9.0426	0.0745	1.0205
1565.0	5.0	8.5164	0.0734	0.9413
1575.0	5.0	7.7982	0.0688	0.9193
1585.0	5.0	7.3236	0.0650	0.8956
1595.0	5.0	6.5916	0.0612	0.7614
1605.0	5.0	5.8203	0.0547	0.6647
1615.0	5.0	5.1479	0.0483	0.5579
1625.0	5.0	4.8922	0.0461	0.5220
1635.0	5.0	5.0626	0.0472	0.5149
1645.0	5.0	5.1953	0.0478	0.5117
1655.0	5.0	5.2309	0.0478	0.4850
1665.0	5.0	5.1637	0.0481	0.4689
1675.0	5.0	4.9911	0.0472	0.4440
1685.0	5.0	4.6016	0.0445	0.3967
1695.0	5.0	4.1005	0.0407	0.3504
1705.0	5.0	3.7733	0.0387	0.3072
1715.0	5.0	3.4980	0.0390	0.2786
1725.0	5.0	3.5740	0.0408	0.2969
1735.0	5.0	3.3200	0.0393	0.2775
1745.0	5.0	3.0413	0.0385	0.2414
1755.0	5.0	2.9846	0.0384	0.2358
1765.0	5.0	2.9395	0.0381	0.2198
1775.0	5.0	2.8898	0.0377	0.2132
1785.0	5.0	2.7065	0.0371	0.2057
1795.0	5.0	2.6424	0.0380	0.2049
1805.0	5.0	2.6672	0.0390	0.1964
1815.0	5.0	2.5771	0.0386	0.1963
1825.0	5.0	2.3605	0.0375	0.1714
1835.0	5.0	2.0970	0.0319	0.1430
1845.0	5.0	2.1096	0.0392	0.1660
1855.0	5.0	2.0244	0.0390	0.1568
1865.0	5.0	1.8716	0.0412	0.1447
1875.0	5.0	1.4118	0.0330	0.1162

Total cross section of $\gamma n \to \eta n$ as a function of W_{TOF}

W_{TOF} [MeV]	ΔW_{TOF} [MeV]	σ [μb]	Δ_{stat} [μb]	Δ_{syst} [μb]
1492.5	2.5	1.8692	0.1600	0.2884
1497.5	2.5	2.2577	0.1014	0.3031
1502.5	2.5	2.4324	0.0865	0.2916
1507.5	2.5	2.7226	0.0805	0.3575
1512.5	2.5	3.0818	0.0815	0.3873
1517.5	2.5	3.1202	0.0786	0.4100
1522.5	2.5	3.1719	0.0745	0.3733
1527.5	2.5	3.2240	0.0720	0.3463
1532.5	2.5	3.2074	0.0705	0.3589
1537.5	2.5	3.1120	0.0687	0.3574
1545.0	5.0	2.9516	0.0471	0.3447
1555.0	5.0	2.7834	0.0465	0.3450
1565.0	5.0	2.6420	0.0467	0.3230
1575.0	5.0	2.5607	0.0478	0.3335
1585.0	5.0	2.3636	0.0467	0.2749
1595.0	5.0	2.1470	0.0434	0.2727
1605.0	5.0	1.9830	0.0402	0.2214
1615.0	5.0	1.8081	0.0370	0.2036
1625.0	5.0	1.7613	0.0360	0.2041
1635.0	5.0	1.7140	0.0356	0.1844
1645.0	5.0	1.7256	0.0358	0.1647
1655.0	5.0	1.6546	0.0355	0.1608
1665.0	5.0	1.5765	0.0348	0.1513
1675.0	5.0	1.4275	0.0327	0.1466
1685.0	5.0	1.1104	0.0283	0.1181
1695.0	5.0	0.9526	0.0257	0.1000
1705.0	5.0	0.8326	0.0236	0.0776
1715.0	5.0	0.7007	0.0213	0.0649
1725.0	5.0	0.6334	0.0202	0.0619
1735.0	5.0	0.5518	0.0188	0.0525
1745.0	5.0	0.5922	0.0191	0.0543
1755.0	5.0	0.5485	0.0185	0.0544
1765.0	5.0	0.5305	0.0185	0.0508
1775.0	5.0	0.5390	0.0196	0.0500
1785.0	5.0	0.5494	0.0212	0.0510
1795.0	5.0	0.5799	0.0235	0.0482
1805.0	5.0	0.5815	0.0269	0.0489
1815.0	5.0	0.5402	0.0301	0.0526
1825.0	5.0	0.4678	0.0343	0.0423
1835.0	5.0	0.4536	0.0420	0.0533
1845.0	5.0	0.3584	0.0504	0.0444
1855.0	5.0	0.3418	0.0556	0.0598
1865.0	5.0	0.3465	0.0667	0.0444
1875.0	5.0	0.2955	0.0719	0.0869

References

[1] R. Frisch and O. Stern, *Über die magnetische Ablenkung von Wasserstoff-molekülen und das magnetische Moment des Protons. I*, Zeitschrift für Physik **85**, 4 (1933).

[2] R. W. McAllister and R. Hofstadter, *Elastic Scattering of 188-Mev Electrons from the Proton and the Alpha Particle*, Phys. Rev. **102**, 851 (1956).

[3] H. L. Anderson et al., *Total Cross Sections of Positive Pions in Hydrogen*, Phys. Rev. **85**, 936 (1952).

[4] R. G. Edwards, *Excited state baryon spectroscopy from lattice QCD*, Phys. Rev. D **84**, 074508 (2011).

[5] A. J. Hey and R. L. Kelly, *Baryon spectroscopy*, Phys. Rept. **96**, 71 (1983).

[6] S. Capstick and W. Roberts, *Quarks Models of Baryon Masses and Decays*, Prog. Part. Nucl. Phys. **45**, S241 (2000).

[7] J. Beringer et al. (Particle Data Group), *Review of Particle Physics*, Phys. Rev. D **86**, 010001 (2012).

[8] R. Shankar, *Principles of Quantum Mechanics* (Plenum, 1994), 2nd ed.

[9] M. Benmerrouche, N. C. Mukhopadhyay and J. F. Zhang, *Effective Lagrangian approach to the theory of η photoproduction in the $N^*(1535)$ region*, Phys. Rev. D **51**, 3237 (1995).

[10] G. F. Chew, M. L. Goldberger, F. E. Low and Y. Nambu, *Relativistic Dispersion Relation Approach to Photomeson Production*, Phys. Rev. **106**, 1345 (1957).

[11] W.-T. Chiang and F. Tabakin, *Completeness rules for spin observables in pseudoscalar meson photoproduction*, Phys. Rev. C **55**, 2054 (1997).

[12] L. Tiator, *Complete Experiments for Pion Photoproduction*, arXiv:1211.3927 [nucl-th] (2012).

[13] B. Krusche and S. Schadmand, *Study of non-strange baryon resonances with meson photoproduction*, Prog. Part. Nucl. Phys. **51**, 399 (2003).

[14] W.-T. Chiang et al., *An isobar model for η photo- and electroproduction on the nucleon*, Nucl. Phys. A **700**, 429 (2002).

[15] I. Jaegle et al., *Quasi-free photoproduction of η-mesons off the deuteron*, Eur. Phys. J. A **47**, 89 (2011).

[16] J. Weiss et al., *Exclusive measurement of coherent η-photoproduction from the deuteron*, Eur. Phys. J. A **11**, 371 (2001).

[17] J. Weiss et al., *Exclusive measurement of quasi-free η-photoproduction from deuterium*, Eur. Phys. J. A **16**, 275 (2003).

[18] R. G. Moorehouse, *Photoproduction of N^* Resonances in the Quark Model*, Phys. Rev. Lett. **16**, 772 (1966).

[19] O. Bartalini et al., *Measurement of η photoproduction on the proton from threshold to 1500 MeV*, Eur. Phys. J. A **33**, 169 (2007).

[20] A. Fantini et al., *First measurement of the Σ beam asymmetry in η photoproduction on the neutron*, Phys. Rev. C **78**, 015203 (2008).

[21] V. Kuznetsov et al., *Evidence for a narrow structure at W∼1.68 GeV in η photoproduction off the neutron*, Phys. Lett. B **647**, 23 (2007).

[22] V. Kuznetsov et al., *Evidence for a narrow N^*(1685) resonance in quasifree Compton scattering on the neutron*, Phys. Rev. C **83**, 022201(R) (2011).

[23] T. Nakabayashi et al., *Photoproduction of η mesons off protons for $E_\gamma \leqslant 1.15$ GeV*, Phys. Rev. C **74**, 035202 (2006).

[24] B. Krusche et al., *Near-threshold photoproduction of η-mesons from the deuteron*, Phys. Lett. B **358**, 40 (1995).

[25] F. Miyahara et al., *Narrow Resonance at $E_\gamma = 1020$ MeV in the $D(\gamma, \eta)pn$ Reaction*, Prog. Theor. Phys. Suppl. **168**, 90 (2007).

[26] I. Jaegle et al., *Quasifree Photoproduction of η Mesons off the Neutron*, Phys. Rev. Lett. **100**, 252002 (2008).

[27] R. A. Arndt et al., *Nonstrange and other flavor partners of the exotic Θ^+ baryon*, Phys. Rev. C **69**, 035208 (2004).

[28] D. Diakonov, V. Petrov, and M. V. Polyakov, *Exotic Anti-Decuplet of Baryons: Prediction from Chiral Solitons*, Z. Phys. A **359**, 305 (1997).

[29] M. V. Polyakov and A. Rathke, *On photoexcitation of baryon antidecuplet*, Eur. Phys. J. A **18**, 691 (2003).

[30] M. V. Polyakov, *Notes on New Narrow N*∗, arXiv:1108.4524 [nucl-th] (2011).

[31] K.-S. Choi et al., *A new N*∗*(1675) resonance in the* $\gamma N \rightarrow \eta N$ *reaction*, Phys. Lett. B **636**, 253 (2006).

[32] A. Fix, L. Tiator, and M. V. Polyakov, *Photoproduction of* η*-mesons on the deuteron above* $S_{11}(1535)$ *in the presence of a narrow* $P_{11}(1670)$*-resonance*, Eur. Phys. J. A **32**, 311 (2007).

[33] W.-T. Chiang et al., *Reggeized model for* η *and* η' *photoproduction*, Phys. Rev. C **68**, 045202 (2003).

[34] X.-H. Zhong and Q. Zhao, η *photoproduction on quasifree nucleons in the chiral quark model*, Phys. Rev. C **84**, 045207 (2011).

[35] E. F. McNicoll et al., *Experimental study of the* $\gamma p \rightarrow \eta p$ *reaction with the Crystal Ball detector at the Mainz Microtron (MAMI-C)*, Phys. Rev. C **82**, 035208 (2010).

[36] A. V. Anisovich et al., *Photoproduction of* η*-mesons off neutrons from a deuteron target*, Eur. Phys. J. A **41**, 13 (2009).

[37] R. Shyam and O. Scholten, *Photoproduction of* η *mesons within a coupled-channels K-matrix approach*, Phys. Rev. C **78**, 065201 (2008).

[38] V. Shklyar, H. Lenske, U. Mosel, η *photoproduction in the resonance energy region*, Phys. Lett. B **650**, 172 (2007).

[39] M. Döring and K. Nakayama, *On the cross section ratio* σ_n/σ_p *in* η *photoproduction*, Phys. Lett. B **683**, 145 (2010).

[40] B. Krusche and W. Briscoe, *Photoproduction of* η*-mesons off the neutron — Part I: angular distributions and double polarization observable E*, A2 MAMI Proposal, PAC 2005 (2005).

[41] H. Herminghaus et al., *The design of a cascaded 800 MeV normal conducting C.W. race track microtron*, Nucl. Instr. Meth. **138**, 1 (1976).

[42] K.-H. Kaiser et al., *The 1.5 GeV harmonic double-sided microtron at Mainz University*, Nucl. Instr. Meth. A **593**, 159 (2008).

[43] T. Walcher, *Highlights and Perspectives of the Mainz Microtron MAMI*, Prog. Part. Nucl. Phys. **50**, 503 (2003).

[44] K. Aulenbacher, *Polarized beams for electron accelerators*, Eur. Phys. J. Spec. Top. **198**, 361 (2011).

[45] I. Anthony et al., *Design of a tagged photon spectrometer for use with the Mainz 840 MeV microtron*, Nucl. Instr. Meth. A **301**, 230 (1991).

[46] S. J. Hall et al., *A focal plane system for the 855 MeV tagged photon spectrometer at MAMI-B*, Nucl. Instr. Meth. A **368**, 698 (1996).

[47] J. C. McGeorge et al., *Upgrade of the Glasgow photon tagging spectrometer for Mainz MAMI-C*, Eur. Phys. J. A **37**, 129 (2008).

[48] S. Schumann, *Strahlungsbegleitete π^0-Photoproduktion am Proton*, Ph.D. thesis, Universität Bonn (2007).

[49] H. W. Koch and J. W. Motz, *Bremsstrahlung Cross-Section Formulas and Related Data*, Rev. Mod. Phys. **31**, 920 (1959).

[50] *A2 Collaboration Website* (2013), `http://wwwa2.kph.uni-mainz.de`.

[51] A. Thomas, *Crystal Ball Hydrogen (Deuterium) Target Manual* (2013).

[52] M. J. Oreglia, *A study of the reactions $\psi' \to \gamma\gamma\psi$*, Ph.D. thesis, Stanford University (1981).

[53] E. D. Bloom et al., *A Proposal For A Large Solid Angle Neutral Detector For Spear 2 (The Crystal Ball)*, SLAC Proposal SP-024 (1975).

[54] A. Starostin et al., *Measurement of $K^-p \to \eta\Lambda$ near threshold*, Phys. Rev. C **64**, 055205 (2001).

[55] *PDG Atomic and Nuclear Properties*, `http://pdg.lbl.gov/2012/AtomicNuclearProperties/index.html`.

[56] D. Watts, Calorimetry in Particle Physics, Proceedings of the 11th International Conference, Perugia, Italy, 2004, World Scientific, Singapore p. 560 (2005).

[57] R. Novotny, *The BaF_2 photon spectrometer TAPS*, IEEE Trans. Nucl. Sci. **38**, 379 (1991).

[58] A. R. Gabler et al., *Response of TAPS to monochromatic photons with energies between 45 and 790 MeV*, Nucl. Instr. Meth. A **346**, 168 (1994).

[59] S. Bender, *Aufbau und Test eines Bleiwolframat-Kalorimeters für das Crystal Ball/TAPS-Experiment an MAMI*, Diploma thesis, Universität Mainz (2009).

[60] M. Thiel, *In-medium properties of the ω-meson studied in photonuclear reactions near the production threshold*, Ph.D. thesis, Universität Giessen (2010).

[61] J. R. M. Annand, *Data Analysis within an AcquRoot Framework* (2008), `http://www.nuclear.gla.ac.uk/~acqusys/doc/AcquRoot.11.08.pdf`.

[62] R. Brun and F. Rademakers, *ROOT - An Object Oriented Data Analysis Framework*, Nucl. Instr. and Meth. A **389**, 81 (1997).

[63] D. Glazier, *A Geant4 simulation for the CrystalBall@MAMI Setup* (2012), `http://ww2.ph.ed.ac.uk/nuclear/G4/G4A2CBSimulation-06-12.pdf`.

[64] S. Agostinelli et al., *Geant4 - a simulation toolkit*, Nucl. Instr. Meth. A **506**, 250 (2003).

[65] J. Allison et al., *Geant4 developments and applications*, IEEE Trans. Nucl. Sci. **53**, 270 (2006).

[66] I. Fröhlich et al., *Pluto: A Monte Carlo Simulation Tool for Hadronic Physics*, XI International Workshop on Advanced Computing and Analysis Techniques in Physics Research, Amsterdam, the Netherlands, April 2007 (2007).

[67] L. Witthauer, private communication (2012).

[68] M. Pfeiffer, *Photoproduction of η mesons from ^3He*, Ph.D. thesis, Universität Giessen (2002).

[69] T. C. Awes et al., *A simple method of shower localization and identification in laterally segmented calorimeters*, Nucl. Instr. Meth. A **311**, 130 (1992).

[70] K. Molenaar, *Performance of TAPS in the Tagged Photon Beam of MAMI*, Diploma thesis, Rijksuniversiteit Groningen (1992).

[71] V. Hejny, *Photoproduktion von η-Mesonen an Helium 4*, Ph.D. thesis, Universität Giessen (1998).

[72] M. Unverzagt, *Bestimmung des Dalitz-Plot-Parameters α für den Zerfall $η \to 3π^0$ mit dem Crystal Ball am MAMI*, Ph.D. thesis, Universität Bonn (2008).

[73] M. Unverzagt, *Energie-Eichung des Crystal Ball-Detektors am MAMI*, Diploma thesis, Universität Mainz (2004).

[74] M. E. Röbig, *Eichung des TAPS-Detektorsystems mit Höhenstrahlung*, Diploma thesis, Universität Giessen (1991).

[75] T. C. Jude, *Strangeness Photoproduction off the Proton at Threshold Energies*, Ph.D. thesis, University of Edinburgh (2010).

[76] M. Kotulla, private communication (2007).

[77] J. C. McGeorge, *ugcalv2ua* (2010).

[78] V. Kuznetsov, private communication (2009).

[79] P. Pedroni, private communication (2011).

[80] M. Lacombe et al., *Parametrization of the deuteron wave function of the Paris N–N potential*, Phys. Lett. B **101**, 139 (1981).

[81] M. Dieterle, *Comparison of the Experimental Resolution in Case of Using a 1.76 or 4.76 cm LD$_2$ Target*, Master project work, Universität Basel (2009), `http://jazz.physik.unibas.ch/site/theses.html`.

[82] R. O. Owens, *Statistical treatment of tagged photon experiments*, Nucl. Instr. and Meth. A **288**, 574 (1990).

[83] F. James, *Monte Carlo Phase Space*, CERN 68-15 (1968).

[84] R. A. Arndt, *Extended partial-wave analysis of πN scattering data*, Phys. Rev. C **74**, 045205 (2006).

[85] *SAID solution SP06, accessed on September 1, 2011*, `http://gwdac.phys.gwu.edu`.

[86] *Geant4, Reference Physics Lists*, `http://geant4.cern.ch/support/proc_mod_catalog/physics_lists/referencePL.shtml`.

[87] D. Glazier, private communication (2011).

[88] M. Dieterle, Ph.D. thesis, Universität Basel (in preparation).

[89] M. Oberle, Ph.D. thesis, Universität Basel (in preparation).

[90] J. R. M. Annand, *The Glasgow/Mainz Bremsstrahlung Tagger Operations Manual* (2008).

[91] A. Starostin et al., *Measurement of $3\pi^0$ photoproduction on the proton from threshold to 1.4 GeV*, arXiv:1101.3744 [nucl-ex] (2011).

[92] B. Krusche et al., *Constraining N*(1535) parameters from the eta photoproduction*, Phys. Lett. B **397**, 171 (1997).

[93] H. Denizli et al., *Q^2 dependence of the S_{11}(1535) photocoupling and evidence for a P-wave resonance in η electroproduction*, Phys. Rev. C **76**, 015204 (2007).

[94] S. Brandt, *Datenanalyse* (Spektrum Akademischer Verlag, 1999), 4th ed.

[95] D. Werthmüller, *Photoproduction of η' Mesons off the Deuteron near Threshold*, Master thesis, Universität Basel (2007), `http://jazz.physik.unibas.ch/site/theses.html`.

[96] H. Holvoet, *Study of the helicity dependence of double pion photoproduction on the proton*, Ph.D. thesis, Universiteit Gent (2000).

Acknowledgments

Curriculum Vitae

Full name: Dominik Marco Werthmüller
Date of birth: December 25, 1981
Place of birth: Aarau, Switzerland

Education

2007–2013	Ph.D. studies at the University of Basel Ph.D. in Experimental Physics
2005–2007	Master studies at the University of Basel Master of Science in Physics
2002–2005	Bachelor studies at the University of Basel Bachelor of Science in Physics
1998–2002	Grammar school, Alte Kantonsschule Aarau Matura Typus C (Natural Sciences)
1994–1998	High school, Bezirksschule Aarau

Positions

2012	Teaching assistant: experimental physics practical for beginners
2008–2012	System administrator: nuclear physics group
2007–2008	Teaching assistant: experimental nuclear physics practical
2006–2007	Software developer: Giniality AG, Basel
2003–2006	Teaching assistant: computer science (Department of Informatics)

Awards

2013	Camille und Henry Dreyfus Stipendium, University of Basel

For valuable lectures during my studies I am indebted to:
PD Dr. A. Aste, Prof. G. Baur, Prof. B. Binggeli, Prof. C. Bruder, Prof. H. Burkhart, Prof. M. Grote, Prof. H.-J. Güntherodt, PD Dr. K. Hencken, Prof. O. Gerhard, Prof. S. Goedecker, PD Dr. T. Heim, Prof. H.-J. Hug, Prof. H.-C. Im Hof, PD Dr. M. Hofmann-Riedinger, Prof. J. Jourdan, PD Dr. D. Kiselev (geb. Rohe), PD Dr. E. Kolbe, Prof. B. Krusche, Prof. D. Loss, Prof. D. Masser, Prof. E. Meyer, PD Dr. T. Rauscher, Prof. C. Schönenberger, Prof. I. Sick, Prof. F.-K. Thielemann, Prof. D. Trautmann, Prof. T. Vetter, PD Dr. H.-J. Weyer